

# **Results of Open Testing for the Program to Assess the Reliability of Emerging Nondestructive Techniques**

## AVAILABILITY OF REFERENCE MATERIALS IN NRC PUBLICATIONS

### NRC Reference Material

As of November 1999, you may electronically access NUREG-series publications and other NRC records at the NRC's Public Electronic Reading Room at <http://www.nrc.gov/reading-rm.html>. Publicly released records include, to name a few, NUREG-series publications; *Federal Register* notices; applicant, licensee, and vendor documents and correspondence; NRC correspondence and internal memoranda; bulletins and information notices; inspection and investigative reports; licensee event reports; and Commission papers and their attachments.

NRC publications in the NUREG series, NRC regulations, and Title 10, "Energy," in the *Code of Federal Regulations* may also be purchased from one of these two sources.

#### 1. The Superintendent of Documents

U.S. Government Publishing Office  
Mail Stop SSOP  
Washington, DC 20402-0001  
Internet: <http://bookstore.gpo.gov>  
Telephone: 1-866-512-1800  
Fax: (202) 512-2104

#### 2. The National Technical Information Service

5301 Shawnee Road  
Alexandria, VA 22161-0002  
<http://www.ntis.gov>  
1-800-553-6847 or, locally, (703) 605-6000

A single copy of each NRC draft report for comment is available free, to the extent of supply, upon written request as follows:

#### U.S. Nuclear Regulatory Commission

Office of Administration  
Publications Branch  
Washington, DC 20555-0001  
E-mail: [distribution.resource@nrc.gov](mailto:distribution.resource@nrc.gov)  
Facsimile: (301) 415-2289

Some publications in the NUREG series that are posted at the NRC's Web site address <http://www.nrc.gov/reading-rm/doc-collections/nuregs> are updated periodically and may differ from the last printed version. Although references to material found on a Web site bear the date the material was accessed, the material available on the date cited may subsequently be removed from the site.

### Non-NRC Reference Material

Documents available from public and special technical libraries include all open literature items, such as books, journal articles, transactions, *Federal Register* notices, Federal and State legislation, and congressional reports. Such documents as theses, dissertations, foreign reports and translations, and non-NRC conference proceedings may be purchased from their sponsoring organization.

Copies of industry codes and standards used in a substantive manner in the NRC regulatory process are maintained at—

#### The NRC Technical Library

Two White Flint North  
11545 Rockville Pike  
Rockville, MD 20852-2738

These standards are available in the library for reference use by the public. Codes and standards are usually copyrighted and may be purchased from the originating organization or, if they are American National Standards, from—

#### American National Standards Institute

11 West 42nd Street  
New York, NY 10036-8002  
<http://www.ansi.org>  
(212) 642-4900

Legally binding regulatory requirements are stated only in laws; NRC regulations; licenses, including technical specifications; or orders, not in NUREG-series publications. The views expressed in contractor-prepared publications in this series are not necessarily those of the NRC.

The NUREG series comprises (1) technical and administrative reports and books prepared by the staff (NUREG-XXXX) or agency contractors (NUREG/CR-XXXX), (2) proceedings of conferences (NUREG/CP-XXXX), (3) reports resulting from international agreements (NUREG/IA-XXXX), (4) brochures (NUREG/BR-XXXX), and (5) compilations of legal decisions and orders of the Commission and Atomic and Safety Licensing Boards and of Directors' decisions under Section 2.206 of NRC's regulations (NUREG-0750).

**DISCLAIMER:** This report was prepared as an account of work sponsored by an agency of the U.S. Government. Neither the U.S. Government nor any agency thereof, nor any employee, makes any warranty, expressed or implied, or assumes any legal liability or responsibility for any third party's use, or the results of such use, of any information, apparatus, product, or process disclosed in this publication, or represents that its use by such third party would not infringe privately owned rights.

# **Results of Open Testing for the Program to Assess the Reliability of Emerging Nondestructive Techniques**

Manuscript Completed: December 2016  
Date Published: August 2017

Prepared by:  
R. M. Meyer, A. E. Holmes, and P. G. Heasler

Pacific Northwest National Laboratory  
P.O. Box 999  
Richland, WA 99352

I. Prokofiev and B. Lin, NRC Project Managers

NRC Job Code V6286

Office of Nuclear Regulatory Research



## ABSTRACT

The U.S. Nuclear Regulatory Commission (NRC) has established the Program to Assess the Reliability of Emerging Nondestructive Techniques (PARENT) whose goal was to investigate the performance of current emerging and perspective novel nondestructive examination (NDE) procedures and techniques to find flaws in nickel-alloy welds and base materials. This was performed by conducting a series of open and blind international round-robin tests on a set of nickel alloy piping components that include large-bore dissimilar metal welds (LBDMW), small-bore dissimilar metal welds (SBDMW), and bottom-mounted instrumentation (BMI) penetration welds. The project was split into open and blind testing portions for the purpose of separating the evaluation of novel techniques that are at a stage of relative immaturity for field testing and which were implemented by teams that may not have significant experience in conducting field examinations (open testing) from the evaluation of more established techniques implemented by commercial inspection vendors (blind testing). This report is focused on documenting the open testing activity and results. The motivation for evaluating emerging NDE techniques includes the desire to identify more effective methods for detecting and characterizing rapidly growing forms of degradation, such as primary water stress corrosion cracking (PWSCC) and interdendritic stress corrosion cracking (IDSCC).

PARENT was a follow-on to the Program for Inspection of Nickel Alloy Components (PINAC), which was based on the Bilateral International Agreements with participants and the in-kind contribution of resources from organizations of Finland, Japan, Republic of Korea, Sweden, and the United States of America to evaluate several nondestructive techniques for detection and characterization of PWSCC and IDSCC in SBDMW and BMI components. In February 2012, the NRC conducted new agreements with VTT Technical Research Centre of Finland, Nuclear Regulation Authority of Japan, Korea Institute of Nuclear Safety, Swedish Radiation Safety Authority, and Swiss Federal Nuclear Safety Inspectorate to establish PARENT to conduct a series of round-robin tests on SBDMWs, BMIs, and LBDMWs. The open testing portion of PARENT was performed with knowledge of true-state information in the open test blocks provided to teams conducting tests. As a result, no detection performance analyses were performed on open test data. Thus, the evaluation of open test data is based on statistical analyses of sizing data and qualitative review of data response images.



## FOREWORD

Leakage events due to primary water stress corrosion cracking (PWSCC) or interdendritic stress corrosion cracking (IDSCC) have been recorded in the United States and internationally. This cracking has been observed at several weld locations in reactor coolant systems including penetrations to the reactor vessel (e.g., control rod drive mechanism [CRDM] penetrations, bottom-mounted instrumentation [BMI] penetrations, and nozzle penetrations), and nozzle penetrations on steam generator and pressurizer components. Inservice inspections (ISI) are conducted at nuclear power plants to detect cracks before leakage occurs. The effectiveness of ISI is dependent on several factors such as the frequency with which periodic examinations occur, human factors, the performance capability of the nondestructive examination (NDE) procedures and techniques used, etc. Leakage events, both domestic and internationally, have indicated a need for additional research to evaluate the performance of NDE procedures and techniques for the detection and sizing of PWSCC and IDSCC flaws in reactor components.

In February 2012, the U.S. Nuclear Regulatory Commission executed agreements with organizations in Finland, Japan, Republic of Korea, Sweden, Switzerland, and the United States to establish the Program to Assess the Reliability of Emerging Nondestructive Techniques (PARENT) to investigate the performance of current and emerging NDE techniques to find flaws in nickel-alloy welds and base material. This assessment was performed by conducting a series of open and blind international round-robin tests on a set of mockups. The project was split into open and blind testing to separate the evaluation of novel techniques implemented by nonqualified teams from the evaluation of more established techniques implemented by commercial inspection service providers. The objective of the blind testing was to obtain quantitative empirical estimates of the performance of contemporary NDE inspection procedures and techniques used within the industry to determine which may be more reliable for detecting and accurate sizing PWSCC or IDSCC flaws. The objective of the open testing was to evaluate the performance of novel NDE procedures and techniques that have not yet reached the maturity level for field testing. The motivation for evaluating novel NDE procedures and techniques was to explore their potential for improving the performance of NDE in comparison to established techniques. Analysis of the open test data included a quantitative evaluation of sizing performance and qualitative evaluation of signal response images.

The purpose of this report was to publish the results of the sizing analyses and the qualitative evaluation of signal response images for data collected in open testing for PARENT. The open test assessed several novel and non-standard NDE procedures and techniques such as nonlinear ultrasonic testing (NLUT) and advanced phased array UT (ADVPAUT). Some highlights obtained from the results of the sizing analysis include observations that ADVPAUT and NLUT procedures exhibited more consistent depth sizing error over the range of flaw depths sampled in comparison to established PAUT procedures. Further, sub-harmonic NLUT procedures exhibited better overall depth sizing performance than higher-harmonic NLUT procedures. Highlights of the qualitative analysis of data response images included the observation that identifying stress corrosion crack tip signals with established PAUT procedures can be difficult and that crack tip signal identification by image analysis is, in part, a subjective determination. Further, for both PAUT and ADVPAUT procedures, data response images illustrate the difficulty in distinguishing noise from SCC crack tip responses. The results obtained in open testing can be considered optimistic to what would be anticipated under blind test conditions or field conditions. Thus, the PARENT open test results have illustrated that NDE procedures and techniques are limited to less than ideal performance by their fundamental capability and that overall ISI effectiveness could benefit from NDE technology advancements

that improve upon fundamental capability. Finally, the data generated from PARENT open testing provides an understanding of the state of art in NDE capabilities and can be used to evaluate emerging inspection techniques in the future.



# TABLE OF CONTENTS

<b>ABSTRACT</b> .....	<b>iii</b>
<b>FOREWORD</b> .....	<b>v</b>
<b>LIST OF FIGURES</b> .....	<b>xi</b>
<b>LIST OF TABLES</b> .....	<b>xix</b>
<b>EXECUTIVE SUMMARY</b> .....	<b>xxiii</b>
<b>ACKNOWLEDGMENTS</b> .....	<b>xxvii</b>
<b>ACRONYMS AND ABBREVIATIONS</b> .....	<b>xxix</b>
<b>1 INTRODUCTION</b> .....	<b>1-1</b>
1.1 Laboratory Grown SCC Specimens .....	1-2
1.2 Open NDE Techniques Report .....	1-2
1.3 Atlas Information Tool .....	1-3
1.4 PARENT Organization .....	1-3
1.5 Organization of Report .....	1-3
<b>2 TEST BLOCK DESCRIPTIONS</b> .....	<b>2-1</b>
2.1 Full Circumference Large Bore and Small Bore Dissimilar Metal Weld Test Blocks .....	2-1
2.2 Partial Circumference Large Bore Dissimilar Metal Weld Test Blocks .....	2-4
2.3 Flat Bar Test Blocks .....	2-5
2.4 Bottom-Mounted Instrumentation Test Blocks .....	2-7
2.5 Simulated Flaw Types .....	2-9
2.5.1 Laboratory-Grown SCC (P12, P28, P29, P31, P32, and P38) .....	2-10
2.5.2 Thermal Fatigue Cracks (P1, P4, and P5) .....	2-14
2.5.3 Weld Solidification Cracks (P7, P37, and P41) .....	2-14
2.5.4 Electrical Discharge Machined Notches (P1, P12, P42, P21, P22, P23, and P24) .....	2-15
2.5.5 Mechanical Fatigue Cracks (P30) .....	2-15
2.5.6 Welding Defects (P37) .....	2-15
2.6 True-State Determination .....	2-15
<b>3 TECHNIQUE DESCRIPTIONS</b> .....	<b>3-1</b>
3.1 Ultrasonic Techniques .....	3-1
3.1.1 Through Transmission of Longitudinal Waves .....	3-1
3.1.2 Phased Array Ultrasonic Testing .....	3-3
3.1.3 Three-Dimensional Synthetic Aperture Focusing Technique .....	3-4
3.1.4 Phased Array Time Reversal Technique .....	3-6
3.1.5 Phased Array Asymmetrical Beam Time of Flight Diffraction .....	3-7
3.1.6 Phased Array Twin Probe .....	3-9
3.1.7 Subharmonic Phased Array .....	3-10
3.1.8 Large Amplitude Excitation Subharmonic .....	3-13
3.1.9 Higher Harmonic Ultrasonic Technique .....	3-13

3.1.10	Nonlinear Resonant Ultrasound Spectroscopy .....	3-15
3.1.11	Guided Ultrasonic Waves .....	3-16
3.1.12	Laser Ultrasound Visualization .....	3-18
3.1.13	Ultrasound Infrared Thermography.....	3-18
3.2	Eddy Current Techniques.....	3-20
3.2.1	Exciter-Pickup Eddy Current Techniques .....	3-20
3.2.2	Controlled Excitation ECT .....	3-21
3.2.3	Orthogonal Coil Array Eddy Current Technique.....	3-23
3.2.4	Pulsed Excitation Eddy Current Technique.....	3-23
3.3	Other Techniques.....	3-24
3.3.1	Microwave Near Field Microscope.....	3-24
3.3.2	Radiography Techniques.....	3-25
<b>4</b>	<b>DATA OVERVIEW.....</b>	<b>4-1</b>
4.1	Data Reporting .....	4-1
4.2	Records Collection Overview Summary .....	4-5
4.3	Procedure Type Categorization .....	4-5
4.4	Scoring Procedure Used for PARENT Open Testing.....	4-5
4.5	Substitution for X1, X2, Y1, and Y2 Indication Fields.....	4-9
4.6	Multiple Indications Associated with One Flaw .....	4-11
4.7	Analysis of PARENT Open Round Robin Data.....	4-12
<b>5</b>	<b>DATA ANALYSIS RESULTS .....</b>	<b>5-1</b>
5.1	DMW Depth Sizing Results .....	5-1
5.1.1	Depth Sizing Regression Plots for ADVPAUT Procedure Types.....	5-5
5.1.2	Depth Sizing Regression Plots for NLUT Procedure Types.....	5-9
5.1.3	Depth Sizing Regression Plots for PAUT Procedure Types.....	5-11
5.1.4	Depth Sizing Regression Plots for RT Procedure Types.....	5-13
5.1.5	Depth Sizing Regression Plots for UIR Procedure Types .....	5-15
5.1.6	Depth Sizing Regression Plots for Conventional UT Procedure Types .....	5-17
5.2	DMW Length Sizing Results.....	5-19
5.2.1	Length Sizing Regression Plots for ADVPAUT Procedure Types .....	5-21
5.2.2	Length Sizing Regression Plots for NLUT Procedure Types.....	5-22
5.2.3	Length Sizing Regression Plots for PAUT Procedure Types .....	5-23
5.2.4	Length Sizing Regression Plots for Conventional UT Procedure Types .....	5-25
5.2.5	Length Sizing Regression Plots for ECT Procedure Types.....	5-26
5.2.6	Length Sizing Regression Plots for MM Procedure Types .....	5-27
5.3	BMI Data Analysis Results .....	5-28
5.4	Indication Plots.....	5-28

<b>6</b>	<b>ANALYSIS OF RESULTS .....</b>	<b>6-1</b>
6.1	Comparison of ADVPAUT and PAUT Procedure Types .....	6-1
6.2	Comparison of NLUT with PAUT and ADVPAUT Procedure Types.....	6-7
6.3	Analysis of FB Test Block Results .....	6-11
6.4	Comparison of Linear and Sectorial PAUT by Team 122.....	6-15
6.5	UIR Results .....	6-17
6.6	RT, Conventional UT, and ECT Results .....	6-18
6.7	Analysis of Data Response Images from FB Test Blocks .....	6-21
6.7.1	Comparison of PAATOFD.29.2 Responses from P42, P30, and P32.....	6-21
6.7.2	Comparison of SAFT.17 Responses from P42, P30, and P32.....	6-24
6.7.3	PAUT.122.1 Responses from SCC Flaws.....	6-31
6.7.4	Team 22 SAFT and PATRT Responses from P29.....	6-38
6.7.5	SAFT.17 Depth Measurement on P46.....	6-40
6.8	Procedures with Sparsely Populated Datasheets .....	6-44
6.9	Discussion of Test Block Appropriateness.....	6-48
6.10	Techniques to Consider for Blind Testing .....	6-49
<b>7</b>	<b>CONCLUSIONS AND FUTURE WORK .....</b>	<b>7-1</b>
<b>8</b>	<b>REFERENCES .....</b>	<b>8-1</b>
<b>APPENDIX A</b>	<b>11<sup>th</sup> ICNDE PAPERS .....</b>	<b>A-1</b>
<b>APPENDIX B</b>	<b>SUMMARY TABLE OF OPEN NDE TECHNIQUES .....</b>	<b>B-1</b>
<b>APPENDIX C</b>	<b>SUMMARIES OF OPEN NDE TECHNIQUES.....</b>	<b>C-1</b>
<b>APPENDIX D</b>	<b>TEST BLOCK INFORMATION .....</b>	<b>D-1</b>
<b>APPENDIX E</b>	<b>TRUE-STATE SUMMARY .....</b>	<b>E-1</b>
<b>APPENDIX F</b>	<b>DEPTH SIZING RESULTS.....</b>	<b>F-1</b>
<b>APPENDIX G</b>	<b>LENGTH SIZING RESULTS .....</b>	<b>G-1</b>
<b>APPENDIX H</b>	<b>INDICATION PLOTS .....</b>	<b>H-1</b>



## LIST OF FIGURES

Figure 1.1	Organization Chart for Steering Committee and Task Groups .....	1-3
Figure 2.1	Coordinate System Definition for SBDMW Test Blocks P41 and LBDMW Test Block P37 .....	2-2
Figure 2.2	Coordinate System Definition for SBDMW Test Blocks P1.....	2-3
Figure 2.3	Coordinate System Definition for SBDMW Test Blocks P4.....	2-4
Figure 2.4	Coordinate System Definition and Illustration of LBDMW Partial Circumference Test Block P12.....	2-5
Figure 2.5	Coordinate System Definition and Illustration of LBDMW Partial Circumference Test Blocks P23 and P24.....	2-5
Figure 2.6	Coordinate System Definition, Dimensions, and Illustrations of FB Test Blocks P28, P29, P30, P31, P32, P42, and P46 .....	2-6
Figure 2.7	Coordinate System Definition, Dimensions, and Illustrations of FB Test Block P38 .....	2-6
Figure 2.8	Coordinate System Used for BMI Test Blocks: P5 and P7 .....	2-7
Figure 2.9	Depiction of Configuration for BMI Test Blocks P21 and P22 with Coordinate System and Dimensions Labeled .....	2-8
Figure 2.10	Depiction of Configuration for BMI Test Blocks P5 and P7 with Labeled Dimensions .....	2-9
Figure 2.11	Depiction of the Approach Used to Produce a Laboratory-Grown SCC in Test Block P12.....	2-11
Figure 2.12	Flowchart of the Process Used to Produce a Laboratory-Grown PWSCC/IDSCC .....	2-11
Figure 2.13	Photograph and Depiction of FB Test Block Cut Out into Standard Fracture Mechanic Specimen from Reactor Pressure Vessel Material.....	2-12
Figure 2.14	Depiction of laboratory Autoclave Set-up for Growing SCC Flaws in FB Specimens under BWR and PWR Conditions.....	2-12
Figure 2.15	Typical Micro-Fractographic Appearance of Laboratory-Grown SCC in FB Specimens .....	2-13
Figure 2.16	Uncracked Ligaments and Finger-Like Local Laboratory SCC Crack Growth in Destructively Analyzed FB Specimen .....	2-14
Figure 3.1	Illustration of Mechanized Scanning Through-Transmission Longitudinal Pitch/Catch Technique.....	3-2
Figure 3.2	The C-scan Shows the Received Amplitude Color Coded (0% full screen height, FSH [ <i>white</i> ] to 100% FSH [ <i>red</i> ].....	3-2
Figure 3.3	Illustration of Time Delay Sequencing of Excitation of PAUT Transducer Elements to Achieve Beam Steering and Focusing.....	3-3
Figure 3.4	PAUT Data Represented as A-scan ( <i>top left</i> ), C-scan ( <i>top right</i> ), B-scan ( <i>bottom left</i> ), and D scan ( <i>bottom right</i> ).....	3-4

Figure 3.5	2D Illustration of SAFT Correction for Focusing Distortion in Ultrasonic Inspections ( <i>left</i> ); B-scan Illustrating Distortion Caused by Beam Focusing Effects ( <i>right</i> ) .....	3-5
Figure 3.6	Implementation of 3D SAFT Using a Matrix Array Transducer. Individual elements are excited in sequence, while all elements “listen” for echoes.....	3-6
Figure 3.7	Illustration of the Time Reversal Technique Concept for Focusing Ultrasonic Energy .....	3-7
Figure 3.8	Schematic Illustration of the PAATOFD Technique.....	3-8
Figure 3.9	Data from Multiple Scan Angles and Depths of Focus are Synthesized in PAATOFD to Help Discriminate Crack Tip Signals from Noise.....	3-8
Figure 3.10	Schematic Illustration of the PATP Technique .....	3-9
Figure 3.11	Data from Multiple Scan Angles and Depths of Focus are Synthesized in PATP to Help Discriminate Crack Tip Signals from Noise .....	3-10
Figure 3.12	Illustration of the Crack Face “Clapping” Phenomena that is the Basis for Subharmonic Generation when Elastic Waves are Applied to Tight Cracks .....	3-11
Figure 3.13	Illustration of SPACE Implementation in SAW Mode to Assess Detection and Length Sizing Capability and in Bulk Wave Mode to Assess Depth Sizing Capability .....	3-12
Figure 3.14	Illustration of SHPA Data Analysis for Length and Depth Sizing of Flaws .....	3-12
Figure 3.15	Depiction of the LASH Technique Implementation .....	3-13
Figure 3.16	Illustration of Higher Harmonic Generation Because of the CAN Phenomenon .....	3-14
Figure 3.17	Illustration of HHUT Implementation in PE ( <i>left</i> ) and TR ( <i>right</i> ) Modes.....	3-14
Figure 3.18	Resonance Frequency Shift in a Compact Tension Specimen in the Early Stage of Crack Initiation ( <i>top</i> ) and a Compact Tension Specimen with Crack Length of 7.0 mm ( <i>bottom</i> ) .....	3-15
Figure 3.19	Schematic Drawing of Possible Piezoelectric Sensor Configuration.....	3-16
Figure 3.20	Illustration of GUW Formation and Propagation in Test Material.....	3-16
Figure 3.21	Guided Wave Dispersion Curves on Cylindrical Coordinate: (a) phase velocity dispersion curve; (b) group velocity dispersion curve .....	3-17
Figure 3.22	Schematic of the Envisioned LUV System .....	3-18
Figure 3.23	Illustration of the UIR Concept .....	3-19
Figure 3.24	UIR Image of a Test Specimen with Crack.....	3-19
Figure 3.25	Depiction of a Single Coil Eddy Current Probe with an Alternating Current Excitation, Induced Magnetic Fields, and Induced Eddy Currents. Disturbance of eddy current flow can be caused by existence of a defect.....	3-21
Figure 3.26	Schematic Illustration of an Eddy Current Probe with Separate Coils for Field Excitation and for Signal Detection.....	3-21

Figure 3.27	Illustration Showing that the Phase Response of CEECT has a Significant Correlation to Flaw Depth over a Large Range of Flaw Depth Values, Including for Deep Cracks .....	3-22
Figure 3.28	Illustration of the CEECT Probe for Measuring the Depth of Flaws .....	3-22
Figure 3.29	Illustration of Orthogonal Coil Pair and Relative Orientation to Surface Crack Profiles .....	3-23
Figure 3.30	Comparison of Pulsed Excitation for PECT ( <i>left</i> ) to Continuous Sine-Wave Excitation for Conventional ECT ( <i>right</i> ) and Illustration of the Frequency Spectrum Associated with Each Type of Excitation Source .....	3-24
Figure 3.31	Illustration of the MM Technique for Crack Detection .....	3-25
Figure 3.32	Illustration of a Radiographic Examination and Interaction of Source X-rays with Density Discontinuities such as Flaws .....	3-26
Figure 3.33	Illustration Depicting the Sensitivity of Conventional Radiography Signal to Planar Flaw Orientation .....	3-27
Figure 4.1	Technique Datasheets for Techniques ET400Hz and TOFD.Ax for Fictitious Inspection 12.P89.1 .....	4-3
Figure 4.2	Technique Datasheet for Technique TOFD.Circ for Fictitious Inspection 12.P89.1 .....	4-4
Figure 4.3	Inspection Summary Datasheet for Fictitious Inspection 12.P89.1 .....	4-4
Figure 4.4	Diagram Illustrating How Procedures are Classified by Procedure Types for Data Analysis Purposes .....	4-8
Figure 4.5	Illustration of Tolerance ( $\delta X$ and $\delta Y$ ) Applied Flaw True-State (in red) Dimensions for the Purpose of Scoring in PARENT .....	4-9
Figure 4.6	Depiction of Indication Plot Illustrating 2-D Representation of Test Block. The red filled rectangles represent the true-state (actual flaws), while red empty rectangles surrounding the flaws depict the scoring tolerance. Indications are shown as black empty rectangles. ....	4-9
Figure 4.7	Inspection Summary Datasheet for Inspection of Test block P1 by Procedure LASH.18 showing unpopulated X1, X2, Y1 and Y2 fields .....	4-10
Figure 4.8	Indication Plot for Procedure LASH.18 Applied to Test Block P1 in PARENT Open Testing (X – Y view) .....	4-11
Figure 4.9	Indication Plot for Procedure LASH.18 Applied to Test Block P1 in PARENT Open Testing (X – Z view) .....	4-11
Figure 4.10	Indication Plot Illustrating Two Indications Intersecting the Region Bounded by the Tolerance Box .....	4-12
Figure 4.11	Illustration of Tolerance Divided Between Flaw and Multiple Indications Intersecting the Region Bounded by the Flaw Tolerance Box .....	4-12
Figure 4.12	Indication Plot for Procedure HHUT.27 Inspection of Test Block P1 .....	4-14
Figure 4.13	Length Sizing Regression for ADVPAUT Procedures on LBDMW Test Blocks in PARENT Open Testing (O.D. access) .....	4-14

Figure 4.14	Depth Sizing Regression (in mm) for Procedure PAUT.131.1 on SBDMW Test Blocks in PARENT Open Testing (O.D. access – w/ FB test blocks) .....	4-15
Figure 4.15	Depth Sizing Regression for NLUT Procedures on SBDMW Test Blocks in PARENT Open Testing (O.D. access – w/ FB test blocks) .....	4-16
Figure 4.16	Depth Sizing Regression (in mm) for Procedure HHUT.30 on SBDMW Test Blocks in PARENT Open Testing (I.D. access – w/ FB test blocks).....	4-16
Figure 5.1	Depth Sizing Regression for ADVPAUT Procedures on SBDMW Test Blocks in PARENT Open Testing (O.D. access – w/ FB test blocks).....	5-6
Figure 5.2	Depth Sizing Regression for ADVPAUT Procedures on SBDMW Test Blocks in PARENT Open Testing (O.D. access – w/o FB test blocks).....	5-6
Figure 5.3	Depth Sizing Regression for ADVPAUT Procedures on FB Test Blocks in PARENT Open Testing (O.D. access).....	5-7
Figure 5.4	Depth Sizing Regression for ADVPAUT Procedures on FB Test Blocks in PARENT Open Testing (I.D. access) .....	5-7
Figure 5.5	Depth Sizing Regression for ADVPAUT Procedures on LBDMW Test Blocks in PARENT Open Testing (O.D. access) .....	5-8
Figure 5.6	Depth Sizing Regression for ADVPAUT Procedures on LBDMW Test Blocks in PARENT Open Testing (I.D. access) .....	5-8
Figure 5.7	Depth Sizing Regression for NLUT Procedures on SBDMW Test Blocks in PARENT Open Testing (O.D. access – w/ FB test blocks) .....	5-9
Figure 5.8	Depth Sizing Regression for NLUT Procedures on SBDMW Test Blocks in PARENT Open Testing (O.D. access – w/o FB test blocks) .....	5-10
Figure 5.9	Depth Sizing Regression for NLUT Procedures on FB Test Blocks in PARENT Open Testing (O.D. access) .....	5-10
Figure 5.10	Depth Sizing Regression for PAUT Procedures on SBDMW Test Blocks in PARENT Open Testing (O.D. access – w/ FB test blocks).....	5-11
Figure 5.11	Depth Sizing Regression for PAUT Procedures on SBDMW Test Blocks in PARENT Open Testing (O.D. access – w/o FB test blocks) .....	5-12
Figure 5.12	Depth Sizing Regression for PAUT Procedures on FB Test Blocks in PARENT Open Testing (O.D. access) .....	5-12
Figure 5.13	Depth Sizing Regression for PAUT Procedures on LBDMW Test Blocks in PARENT Open Testing (I.D. access) .....	5-13
Figure 5.14	Depth Sizing Regression for RT Procedures on SBDMW Test Blocks in PARENT Open Testing (O.D. access – w/ FB test blocks).....	5-14
Figure 5.15	Depth Sizing Regression for RT Procedures on SBDMW Test Blocks in PARENT Open Testing (O.D. access – w/o FB test blocks).....	5-14
Figure 5.16	Depth Sizing Regression for RT Procedures on FB Test Blocks in PARENT Open Testing (O.D. access) .....	5-15
Figure 5.17	Depth Sizing Regression for UIR Procedures on SBDMW Test Blocks in PARENT Open Testing (O.D. access – w/ FB test blocks).....	5-16



Figure 5.18	Depth Sizing Regression for UIR Procedures on FB Test Blocks in PARENT Open Testing (O.D. access) .....	5-16
Figure 5.19	Depth Sizing Regression for Conventional UT Procedures on SBDMW Test Blocks in PARENT Open Testing (O.D. access – w/ FB test blocks).....	5-17
Figure 5.20	Depth Sizing Regression for Conventional UT Procedures on SBDMW Test Blocks in PARENT Open Testing (O.D. access – w/o FB test blocks) .....	5-18
Figure 5.21	Depth Sizing Regression for Conventional UT Procedures on FB Test Blocks in PARENT Open Testing (O.D. access) .....	5-18
Figure 5.22	Length Sizing Regression for ADVPAUT Procedures on SBDMW Test Blocks in PARENT Open Testing (O.D. access) .....	5-21
Figure 5.23	Length Sizing Regression for ADVPAUT Procedures on LBDMW Test Blocks in PARENT Open Testing (O.D. access) .....	5-22
Figure 5.24	Length Sizing Regression for NLUT Procedures on SBDMW Test Blocks in PARENT Open Testing (O.D. access) .....	5-23
Figure 5.25	Length Sizing Regression for PAUT Procedures on SBDMW Test Blocks in PARENT Open Testing (O.D. access) .....	5-24
Figure 5.26	Length Sizing Regression for PAUT Procedures on LBDMW Test Blocks in PARENT Open Testing (O.D. access) .....	5-24
Figure 5.27	Length Sizing Regression for PAUT Procedures on LBDMW Test Blocks in PARENT Open Testing (I.D. access) .....	5-25
Figure 5.28	Length Sizing Regression for Conventional UT Procedures on SBDMW Test Blocks in PARENT Open Testing (O.D. access) .....	5-25
Figure 5.29	Length Sizing Regression for ECT Procedures on SBDMW Test Blocks in PARENT Open Testing (I.D. access) .....	5-26
Figure 5.30	Length Sizing Regression for ECT Procedures on LBDMW Test Blocks in PARENT Open Testing (I.D. access) .....	5-27
Figure 5.31	Length Sizing Regression for MM Procedures on LBDMW Test Blocks in PARENT Open Testing (I.D. access) .....	5-27
Figure 6.1	Depth Sizing Regression for ADVPAUT Procedures on SBDMW Test Blocks in PARENT Open Testing (O.D. access – w/o FB test blocks).....	6-2
Figure 6.2	Depth Sizing Regression for PAUT Procedures on SBDMW Test Blocks in PARENT Open Testing (O.D. access – w/o FB test blocks).....	6-3
Figure 6.3	Depth Sizing Regression for ADVPAUT Procedures on FB Test Blocks in PARENT Open Testing (O.D. access).....	6-3
Figure 6.4	Depth Sizing Regression for PAUT Procedures on FB Test Blocks in PARENT Open Testing (O.D. access) .....	6-4
Figure 6.5	Length Sizing Regression for PAUT Procedures on SBDMW Test Blocks in PARENT Open Testing (O.D. access) .....	6-6
Figure 6.6	Length Sizing Regression for ADVPAUT Procedures on SBDMW Test Blocks in PARENT Open Testing (O.D. access) .....	6-7

Figure 6.7	Depth Sizing Regression Plot for HHUT.27.1 Applied to SBDMW Test Blocks (w/o FB test blocks) with O.D. Access .....	6-8
Figure 6.8	Depth Sizing Regression Plot for SHPA.6.1 Applied to SBDMW Test Blocks (w/o FB test blocks) with O.D. Access .....	6-9
Figure 6.9	Depth Sizing Regression Plot for LASH.18 Applied to SBDMW Test Blocks (w/o FB test blocks) with O.D. Access .....	6-9
Figure 6.10	Depth Sizing Regression Plot for HHUT.27.2 Applied to FB Test Blocks with O.D. Access .....	6-10
Figure 6.11	Depth Sizing Regression Plot for SHPA.6.3 Applied to FB Test Blocks with O.D. Access .....	6-10
Figure 6.12	Depth Sizing Regression Plot for LASH.18 Applied to FB Test Blocks with O.D. Access .....	6-11
Figure 6.13	Depth Sizing Regression for Procedure PAUT.122.1 (Linear) for FB Test Blocks by O.D. Access.....	6-16
Figure 6.14	Depth Sizing Regression for Procedure PAUT.122.2 (Sectorial) FB Test Blocks by O.D. Access.....	6-16
Figure 6.15	UIR Image of FB Test Block P29 (view from side surface).....	6-17
Figure 6.16	UIR Image of FB Test Block P29 (view from side surface).....	6-17
Figure 6.17	UIR Image of FB Test Block P29 (view of surface from which crack initiates) .....	6-17
Figure 6.18	Length Sizing Regression Plot for Procedure AECT.33 Applied to SBDMW Test Blocks with I.D. Access .....	6-19
Figure 6.19	Length Sizing Regression Plot for Procedure ECT.16 Applied to SBDMW Test Blocks with I.D. Access .....	6-20
Figure 6.20	Length Sizing Regression Plot for Procedure AECT.33 Applied to LBDMW Test Blocks with I.D. Access.....	6-20
Figure 6.21	PAATOFD.29.2 Inspection of P42 (EDM) from O.D. ....	6-21
Figure 6.22	PAATOFD.29.2 Inspection of P42 (EDM) from I.D. ....	6-22
Figure 6.23	PAATOFD.29.2 Inspection of P30 (MFC) from O.D. ....	6-22
Figure 6.24	PAATOFD.29.2 Inspection of P30 (MFC) from I.D. ....	6-23
Figure 6.25	PAATOFD.29.2 Inspection of P32 (SCC) from O.D. ....	6-23
Figure 6.26	PAATOFD.29.2 Inspection of P32 (SCC) from I.D. ....	6-24
Figure 6.27	Data Images of Responses Obtained by SAFT-17 on Test Block P42 with EDM Notch.....	6-25
Figure 6.28	Data Images of Responses Obtained by SAFT-17 on Test Block P30 with MFC Flaw .....	6-26
Figure 6.29	Data Images of Responses Obtained by SAFT-17 on Test Block P32 with SCC Flaw .....	6-27
Figure 6.30	Indication Depth Profile Obtained by SAFT-17 on Test Block P42 with EDM Notch .....	6-28

Figure 6.31	Indication Depth Profile Obtained by SAFT-17 on Test Block P30 with MFC Flaw .....	6-29
Figure 6.32	Indication Depth Profile Obtained by SAFT-17 on Test Block P32 with SCC Flaw .....	6-30
Figure 6.33	Indication Plot for Procedure SAFT.17 Applied to Test Block P42 in PARENT Open Testing (X – Z view) .....	6-30
Figure 6.34	Indication Plot for Procedure SAFT.17 Applied to Test Block P30 in PARENT Open Testing (X – Z view) .....	6-31
Figure 6.35	Indication Plot for Procedure SAFT.17 Applied to Test Block P32 in PARENT Open Testing (X – Z view) .....	6-31
Figure 6.36	Data Image Response for PAUT.122.1 Inspection of SCC Flaw in P28 Viewed from the Right Side of Weld. The Inspection was performed by linear scanning with longitudinal wave modes from TRL probe at 60°. Two possible crack tip signals are highlighted by arrows in the image. ....	6-32
Figure 6.37	Data Image Response for PAUT.122.1 Inspection of SCC Flaw in P28 Viewed from the Right Side of Weld. The Inspection was performed by linear scanning with longitudinal wave modes from TRL probe at 50°. The likely crack tip signal is identified with the white circle. ....	6-33
Figure 6.38	Data Image Response for PAUT.122.1 Inspection of SCC Flaw in P32 Viewed from the Right Side of Weld. The inspection was performed by linear scanning with longitudinal wave modes from TRL probe at 50°. The white circle indicates that it is difficult to separate the tip response from noise. ....	6-34
Figure 6.39	Data Image Response for PAUT.122.1 Inspection of SCC Flaw in P32 Viewed from the Left Side of Weld. The inspection was performed by linear scanning with longitudinal wave modes from TRL probe at 55°. The white arrow highlights a weak signal considered to be the crack tip response. ....	6-35
Figure 6.40	Data Image Response for PAUT.122.1 Inspection of SCC Flaw in P32 Viewed from the Left Side of Weld. The inspection was performed by linear scanning with longitudinal wave modes from TRL probe at 45°. The white circle highlights the signal considered to be the crack tip response. ....	6-36
Figure 6.41	Data Image Response for PAUT.122.1 Inspection of MFC Flaw in P30 Viewed from the Left Side of Weld. The inspection was performed by linear scanning with longitudinal wave modes from TRL Probe at 50°. The white circle highlights the signal considered to be the tip response. ....	6-37
Figure 6.42	Data Image Response for PAUT.122.1 Inspection of EDM Notch in P42 Viewed from the Right Side of Weld. The inspection was performed by linear scanning with longitudinal wave modes from TRL probe at 50°. The white circle highlights the signal considered to be the tip response. ....	6-38
Figure 6.43	Image of Response for Team 22 SAFT Response with L-waves .....	6-39

Figure 6.44	Image of Response for Team 22 SAFT Response with S-waves .....	6-39
Figure 6.45	Image of Response for Team 22 PATRT Response with L-waves .....	6-39
Figure 6.46	Image of Response for Team 22 PATRT Response with S-waves.....	6-40
Figure 6.47	Coordinate System Definition, Dimensions, and Illustrations of FB Test Block P46 .....	6-40
Figure 6.48	Data Images of Responses Obtained by SAFT-17 on Test Block P46 from y-position 103.6 mm .....	6-41
Figure 6.49	Indication Depth Profile Obtained by SAFT-17 on Test Block P46 from y-position 103.6 mm.....	6-42
Figure 6.50	Data Images of Responses Obtained by SAFT-17 on Test Block P46 from y-position 120 mm .....	6-43
Figure 6.51	Indication Depth Profile Obtained by SAFT-17 on Test Block P46 from y-position 120 mm .....	6-44
Figure 6.52	Example of Datasheet Submission for Procedures MM.28.1 and MM.28.2 with Non-Numerical Data in X, Y, and Z Fields for Indications.....	6-45
Figure 6.53	Example of Datasheet Submission for Procedure GUW.21 with Blank X, Y, and Z Fields for Indications.....	6-46
Figure 6.54	Example of Datasheet Submission for Procedures PECT.11 with Non-Numerical Data in X, Y, and Z Fields for Indications .....	6-47
Figure 6.55	Example of Datasheet Submission for Procedures NRUS.11 with Non-Numerical Data in X, Y, and Z Fields for Indications .....	6-48

## LIST OF TABLES

Table 1.1	Summary of Members of the PARENT Steering Committee, NDE Task Group, Atlas Task Group, and Invigilator/DAG.....	1-4
Table 2.1	Summary of Categories into which Test Blocks for Open Testing are Classified.....	2-1
Table 2.2	Summary of Dimensions for LBDMW Full Circumference Test Blocks.....	2-2
Table 2.3	Summary of Dimensions for SBDMW Full Circumference Test Blocks.....	2-3
Table 2.4	Summary of Dimensions for LBDMW Partial Circumference Test Blocks.....	2-5
Table 2.5	Tabulation of BMI Test Block P5 and P7 Dimensions.....	2-9
Table 2.6	Summary of Flaw Simulation Methods Used for Each Test Block and Quantities of Each Type of Simulated Flaw.....	2-10
Table 4.1	Definitions of Data Fields for “Technique Datasheets” and “Inspection Summary Datasheets”.....	4-2
Table 4.2	Number of Inspection Summary Records by Procedure and Test Block Type.....	4-6
Table 4.3	Number of Inspection Summary Records for Procedure Types and Block Types by Access.....	4-7
Table 4.4	Summary of Number of Flaw Observations (NOBS) for Different Flaw Types in Each Test Block Type.....	4-7
Table 4.5	Summary of Number of Flaw Observations (NOBS) by Flaw Orientation in Each Test Block Type.....	4-7
Table 5.1	Depth Sizing Results for Procedure Types Applied to SBDMW Test Blocks with O.D. Access w/ FB Test Blocks.....	5-1
Table 5.2	Depth Sizing Results for Procedure Types Applied to SBDMW Test Blocks with O.D. Access w/o FB Test Blocks.....	5-2
Table 5.3	Depth Sizing Results for Procedure Types Applied to SBDMW Test Blocks with O.D. Access (only FB test blocks).....	5-2
Table 5.4	Depth Sizing Results for Procedure Types Applied to SBDMW Test Blocks with I.D. Access (only FB test blocks).....	5-2
Table 5.5	Depth Sizing Results for Procedure Types Applied to LBDMW Test Blocks with O.D. Access.....	5-2
Table 5.6	Depth Sizing Results for Procedure Types Applied to LBDMW Test Blocks with I.D. Access.....	5-3
Table 5.7	Depth Sizing Results for Procedures Applied to SBDMW Test Blocks with O.D. Access w/ FB Test Blocks.....	5-3
Table 5.8	Depth Sizing Results for Procedures Applied to SBDMW Test Blocks with O.D. Access w/o FB Test Blocks.....	5-4
Table 5.9	Depth Sizing Results for Procedures Applied to SBDMW Test Blocks with O.D. Access (only FB blocks).....	5-4

Table 5.10	Depth Sizing Results for Procedures Applied to SBDMW Test Blocks with I.D. Access (only FB test blocks) .....	5-5
Table 5.11	Depth Sizing Results for Procedures Applied to LBDMW Test Blocks with O.D. Access .....	5-5
Table 5.12	Depth Sizing Results for Procedures Applied to LBDMW Test Blocks with I.D. Access .....	5-5
Table 5.13	Length Sizing Results for Procedure Types Applied to SBDMW Test Blocks with O.D. Access .....	5-19
Table 5.14	Length Sizing Results for Procedure Types Applied to SBDMW Test Blocks with I.D. Access.....	5-19
Table 5.15	Length Sizing Results for Procedure Types Applied to LBDMW Test Blocks with O.D. Access .....	5-19
Table 5.16	Length Sizing Results for Procedure Types Applied to LBDMW Test Blocks with I.D. Access.....	5-20
Table 5.17	Length Sizing Results for Procedures Applied to SBDMW Test Blocks with O.D. Access .....	5-20
Table 5.18	Length Sizing Results for Procedures Applied to SBDMW Test Blocks with I.D. Access .....	5-20
Table 5.19	Length Sizing Results for Procedures Applied to LBDMW Test Blocks with O.D. Access .....	5-20
Table 5.20	Length Sizing Results for Procedures Applied to LBDMW Test Blocks with I.D. Access .....	5-21
Table 5.21	Length Sizing Results for Procedures Applied to BMI Test Blocks with J-Groove Weld Surface Access .....	5-28
Table 6.1	Summary of Depth Sizing RMSEs for ADVPAUT and PAUT Techniques Applied to SBDMW and LBDMW Test Blocks with O.D. and I.D. Access.....	6-2
Table 6.2	Summary of Depth Sizing Performances for ADVPAUT Procedure Types Applied to SBDMW Test Blocks with O.D. Access w/o FB Test Blocks.....	6-5
Table 6.3	Summary of Depth Sizing Performances for ADVPAUT Procedure Types Applied to FB Test Blocks with O.D. Access .....	6-5
Table 6.4	Summary of Depth Sizing Performances for PAUT Procedure Types Applied to SBDMW Test Blocks with O.D. Access w/o FB Test Blocks.....	6-5
Table 6.5	Summary of Depth Sizing Performances for PAUT Procedure Types Applied to FB Test Blocks with O.D. Access .....	6-5
Table 6.6	Summary of Length Sizing RMSEs for ADVPAUT and PAUT Techniques Applied to SBDMW and LBDMW Test Blocks with O.D. Access.....	6-6
Table 6.7	Summary of Length Sizing Performances for ADVPAUT Procedure Types Applied to SBDMW Test Blocks with O.D. Access w/o FB Test Blocks.....	6-6

Table 6.8	Summary of Length Sizing Performances for PAUT Procedure Types Applied to SBDMW Test Blocks with O.D. Access w/o FB Test Blocks.....	6-6
Table 6.9	Comparison of Depth Sizing Performances for FB Test Blocks.....	6-12
Table 6.10	Depth Sizing Results for P28 by Procedure Type for I.D. Access .....	6-12
Table 6.11	Depth Sizing Results for P29 by Procedure Type for I.D. Access .....	6-12
Table 6.12	Depth Sizing Results for P30 by Procedure Type for I.D. Access .....	6-12
Table 6.13	Depth Sizing Results for P31 by Procedure Type for I.D. Access .....	6-12
Table 6.14	Depth Sizing Results for P32 by Procedure Type for I.D. Access .....	6-13
Table 6.15	Depth Sizing Results for P38 by Procedure Type for I.D. Access .....	6-13
Table 6.16	Depth Sizing Results for P42 by Procedure Type for I.D. Access .....	6-13
Table 6.17	Depth Sizing Results for P28 by Procedure Type for O.D. Access.....	6-13
Table 6.18	Depth Sizing Results for P29 by Procedure Type for O.D. Access.....	6-13
Table 6.19	Depth Sizing Results for P30 by Procedure Type for O.D. Access.....	6-14
Table 6.20	Depth Sizing Results for P31 by Procedure Type for O.D. Access.....	6-14
Table 6.21	Depth Sizing Results for P32 by Procedure Type for O.D. Access.....	6-14
Table 6.22	Depth Sizing Results for P38 by Procedure Type for O.D. Access.....	6-15
Table 6.23	Depth Sizing Results for P42 by Procedure Type for O.D. Access.....	6-15
Table 6.24	Summary of Depth Sizing Performances for Procedures PAUT.122.1 and PAUT.122.2 .....	6-15





## EXECUTIVE SUMMARY

The U.S. Nuclear Regulatory Commission (NRC) has established the Program to Assess the Reliability of Emerging Nondestructive Techniques (PARENT) whose goal is to investigate the performance of current emerging and perspective novel nondestructive examination (NDE) procedures and techniques to find flaws in nickel-alloy welds and base materials. This was performed by conducting a series of open and blind international round-robin tests on a set of piping components that include large-bore dissimilar metal welds (LBDMW), small-bore dissimilar metal welds (SBDMW), and bottom-mounted instrumentation (BMI) penetration welds. In February 2012, the NRC entered into agreements with VTT Technical Research Centre of Finland, Nuclear Regulation Authority of Japan (NRA), Korea Institute of Nuclear Safety (KINS), Swedish Radiation Safety Authority (SSM), and Swiss Federal Nuclear Safety Inspectorate (ENSI) to establish PARENT to conduct a series of round-robin tests on SBDMWs, BMIs, and LBDMWs. PARENT activities were split into blind testing and open testing activities. Blind testing was performed in PARENT to quantitatively estimate the performance of established NDE methods in the nuclear power industry and the results from blind testing are documented in another report that is under preparation. This report is focused on documenting the open testing activity and results.

Open testing was performed on a set of test blocks with true-state information that was open and provided to teams performing the testing. The objective of open testing was to evaluate the performance of emerging NDE techniques, which are still in relatively early stages of development. The performances of emerging NDE techniques were evaluated based on quantitative sizing analyses and qualitative analysis of data response images. The motivation for evaluating emerging NDE techniques includes the desire to identify more effective methods for detecting and characterizing rapidly growing forms of degradation, such as primary water stress corrosion cracking (PWSCC) and interdendritic stress corrosion cracking (IDSCC). Inspections with emerging NDE techniques were carried out by a variety of organizations including universities, industry organizations, and government research organizations.

This report describes open testing performed in PARENT including a description of the test blocks used, an overview of the NDE techniques applied, and analysis of the data. Data were collected for procedures incorporating novel NDE techniques on SBDMW, LBDMW, and BMI test blocks. There were 226 inspections performed on 4 BMI test blocks, 4 LBDMW test blocks, and 11 SBDMW test blocks. Some significant conclusions drawn for the results documented in this report include:

- A general trend was observed for oversizing shallow flaws and undersizing deep flaws with the exception of advanced phased array ultrasonic testing (ADVPAUT) procedure types and non-linear ultrasonic testing (NLUT) procedure types based on sub-harmonic techniques, which exhibit a more consistent error over the range of flaw depths considered.
- NLUT procedures incorporating sub-harmonic techniques exhibited better depth sizing performance than NLUT procedures incorporating higher harmonic techniques based on overall root mean square error (RMSE) and regression analysis.
- ADVPAUT procedure types did not exhibit better overall depth sizing accuracy than phased array ultrasonic testing (PAUT) procedure types in this study based on RMSE.

- Overall, NLUT procedure types did not exhibit better overall depth sizing accuracy in comparison to ADVPAUT and PAUT procedure types based on RMSE.
- PAUT procedures exhibited a more consistent length sizing error over the range of flaw lengths considered for SBDMW test blocks in comparison to ADVPAUT, which exhibited a tendency to oversize short flaws and undersize long flaws.
- Better depth sizing performance was observed on flat bar (FB) test blocks (most with laboratory-grown SCC flaws) for ADVPAUT, NLUT, and conventional UT procedure types in comparison to SBDMW test blocks (with weld solidification cracks). PAUT procedure types exhibited better depth sizing performance on SBDMW test blocks in comparison to FB test blocks.
- Eddy current testing (ECT) exhibits a more consistent length sizing error over the range of flaw lengths considered for SBDMW test blocks in comparison to "Advanced" ECT procedures (AECT.33), which tend to oversize short flaws and undersize long flaws.
- Depth sizing data for ultrasound infrared thermography (UIR) was obtained in a way that would not be practical in a field environment. However, the results indicated a capability for flaw detection and flaw length sizing.
- Data response images for ADVPAUT techniques illustrate that SCC flaws result in weaker crack tip responses in comparison to mechanical fatigue crack (MFC) and electro-discharge machine (EDM) notch flaws.
- Data response images for PAUT techniques illustrate that identifying crack tip signals with PAUT can be difficult and that crack tip signal identification by image pattern analysis is, in part, a subjective determination.
- Data response images for ADVPAUT and PAUT techniques illustrate difficulty in distinguishing noise from crack tip responses.
- Tip diffraction signals with low signal-to-noise ratio (SNR) were easier to detect under open testing conditions with flaw information provided to test participants. Detecting tip diffraction signals with low SNR under blind test conditions will be more challenging.

Based on the results documented in this report and the conclusions outlined above, the following recommendations can be made:

- Blind testing of some of the open test procedures described in this report could be conducted based on the open testing results to obtain an estimate of detection performance and more realistic estimates of sizing performance. The specific techniques for which blind testing is recommended are summarized below:
  - ADVPAUT
    - PAATOFD.29.0
    - PAATOFD.29.1
    - PAATOFD.29.2
    - PAATOFD.29.3
    - PATP.29

- PATRT.22
- SAFT.17
- NLUT
  - SHPA.6.1
  - SHPA.6.2
  - SHPA.6.3
  - LASH.18
  - HHUT.27.1
  - HHUT.27.2
  - HHUT.30
- ECT
  - ECT.7
  - AECT.33
  - ECT.6
- Procedures UIR.20 and LUV.170 incorporated stand-off inspection techniques that have the potential for deployment during reactor operation. Evaluation of these procedures should be based on test pieces subject to relevant field conditions.
- NLUT procedure types, which incorporated techniques that are sensitive to degradation in early stages (i.e., before large cracks form), should be evaluated using test blocks with simulated early degradation to better evaluate their potential.
- Procedure GUW.21 had difficulty detecting flaws due to the geometrical limitations of the test blocks used in PARENT. Future efforts to evaluate GUW testing should ensure the dimensions of the test blocks are sufficient so that boundaries do not significantly influence the response.



## ACKNOWLEDGMENTS

There have been significant contributions made by a number of people and organizations to accomplish this work. The authors express appreciation to Iouri Prokofiev, Stephen Cumblidge, and Aladar Csontos, of the NRC for their leadership in helping to organize and start the Program to Assess the Reliability of Emerging Nondestructive Techniques (PARENT) program; to David Rudland of the NRC for his continued commitment to PARENT; to Stephen Cumblidge for continuing to provide technical and philosophical input to PARENT; and to Iouri Prokofiev for his continuous leadership of PARENT. Brett Braatz was the original Project Manager for PARENT and was responsible for the complex task of organizing and executing test block shipping and data collection. The authors also acknowledge the tireless efforts of the PARENT invigilators—Tommy Zetterwall (Europe), Ichiro Komura (Japan), and Kyung-cho Kim (South Korea)—who reviewed inspection procedures and monitored the work of inspection teams in their respective regions. The author also acknowledges contributions to the open testing portion of PARENT from the following organizations:

- Organizations from Japan
  - Nuclear Regulation Authority (NRA)
  - Ultrasonic Materials Diagnosis Laboratory (UMDL)
  - Institute of Nuclear Safety System, Incorporated (INSS)
  - Tohoku University
  - Nagoya University
  - Toyama University
  - Japan Power Engineering and Inspection Corporation (JPEIC)
  
- Organizations from Europe
  - Swedish Radiation Safety Authority (SSM)
  - Swiss Federal Nuclear Safety Inspectorate (ENSI)
  - Swedish Qualification Center (SQC)
  - Swiss Association for Technical Inspections, Nuclear Inspectorate (SVTI)
  - VTT Technical Research Centre of Finland Ltd.
  - Alstom Power Products [Switzerland]
  - Swiss Federal Laboratories for Materials Science and Technology (EMPA)
  - Chalmers Institute of Technology [Sweden]
  - Paul Scherer Institute (PSI) [Switzerland]
  
- Organizations from Korea
  - Korea Institute of Nuclear Safety (KINS)
  - Korea Plant Service KPS
  - Korea Atomic Energy Research Institute (KAERI)
  - Korea Research Institute of Standards and Science (KRISS)
  - Pusan National University (PNU)
  - Sungkyunkwan University (SKKU)
  - Hanyang University (HYU)
  
- Organizations from the USA
  - Nuclear Regulatory Commission (NRC)

- IHI Southwest Technologies and Southwest Research Institute (SwRI)
- AlphaSense
- Pacific Northwest National Laboratory (PNNL)

Finally, the authors thank Ms. Kay Hass for typing and editing versions and revisions of this document.

## ACRONYMS AND ABBREVIATIONS

2D	two-dimensional
3D	three-dimensional
ADVPAUT	advanced phased array ultrasonic testing
AECT	advanced ECT technique
BMI	bottom-mounted instrumentation
BWR	boiling water reactor
CAN	contact acoustic nonlinearity
CCD	charge coupled device
CEECT	controlled excitation eddy current technique
CT	computed tomography
DMW	dissimilar metal weld
ECT	eddy current techniques
EDM	electrical discharge machining
EPRI	Electric Power Research Institute
FB	flat bar
FFT	Fast Fourier Transform
FSH	full screen height
GUW	guided ultrasonic waves
HHUT	higher harmonic ultrasonic technique
I.D.	inner diameter
ID	identification
IGSCC	intergranular stress corrosion cracking
IQI	image quality indicators
IR	infrared
ISI	inservice inspection
LASH	large amplitude excitation subharmonic UT
LBDMW	large bore dissimilar metal weld
LOB	lack of bond
LOF	lack of fusion
LUV	laser ultrasound visualization
MA Method	Multi-angle Synthesis Method
MFC	mechanical fatigue crack
MM	microwave near-field microscopy
NDE	nondestructive examination

NLUT	nonlinear ultrasonic testing
NOBS	number of observations
NRUS	nonlinear resonant ultrasound spectroscopy
O.D.	outer diameter
OCECT	orthogonal coil eddy current technique
PA	phased array
PAATOFD	phased array asymmetrical beam time-of-flight diffraction
PARENT	Program to Assess the Reliability of Emerging Nondestructive Techniques
PATP	phased array twin probe
PAUT	phased-array ultrasonic techniques
PC	pitch/catch
PE	pulse-echo
PECT	pulsed excitation eddy current technique
photo-emf	photo electromotive force
PINC	Program for the Inspection of Nickel Alloy Components
POD	probability of detection
PWR	pressurized water reactor
PWSCC	primary water stress corrosion cracking
PZT	piezoelectric transducer
RMSE	root mean square error
SAFT	synthetic aperture focusing technique
SAW	surface acoustic waves
SBDMMW	small bore dissimilar metal weld
SC	weld solidification cracks
SCC	stress corrosion cracking
SHPA	subharmonic phased array
SI	slag inclusion
SPACE	subharmonic phased array for crack evaluation
stdev	standard deviation
TFC	thermal fatigue cracks
TOFD	time-of-flight diffraction
TR	transmit-receive
TRL	transmit-receive longitudinal
PATRT	phased array time reversal technique
UIR	ultrasound infrared thermography
w/	with
w/o	without



## Definitions

Bottom-mounted instrumentation (BMI)	A cylindrical penetration in the bottom head of a nuclear reactor pressure vessel, into which a tube is welded. Typical inside diameters are a few centimeters.
Dendrite	weld grain (columnar or tree-like)
Dissimilar metal weld (DMW)	Weldments joining components made of different alloys. In the context of PINC and PARENT, refers primarily to nozzle welds.
Heat-affected zone	a volume of base metal, adjacent to the fusion zone, changed by the heat of welding
Interdendritic	between the tree-like grains, such as can form in castings or weld metal
Intergranular	between the metal crystals rather than through them
J-groove weld	a weld with profile shaped as the letter “J,” the seal weld of a CRDM or BMI penetration
Lack of fusion	missing metallic bond either between the sidewall of a weld with the base metal or between weld passes (inter-run)
Partial penetration weld	the weld performed to eliminate leakage paths, also called a seal weld
Primary water stress corrosion cracking (PWSCC)	The intergranular or interdendritic cracking of nickel-base alloys that occurs in service and originates from the surfaces of a component that are wetted by the primary water of a pressurized water reactor (PWR)
Program for the Inspection of Nickel-Alloy Components (PINC)	An international cooperative research program, The purpose of PINC is to assess the capabilities of current and emerging NDE techniques to detect and size flaws associated with PWSCC in nuclear reactors. This information tool is the definitive source of information on PINC.
Round-robin test (RRT)	a test performed independently several times (usually at multiple testing facilities)



# 1 INTRODUCTION

The U.S. Nuclear Regulatory Commission (NRC) has established the Program to Assess the Reliability of Emerging Nondestructive Techniques (PARENT) whose goal is to identify and quantitatively assess current emerging and perspective novel nondestructive examination (NDE) procedures and techniques for detecting, characterizing, and sizing of flaws in nickel-alloy welds and base materials. This was performed by conducting a series of open and blind international round-robin tests on a set of piping components that include large-bore dissimilar metal welds (LBDMW), small-bore dissimilar metal welds (SBDMW), and bottom-mounted instrumentation (BMI) penetration welds. PARENT was a follow-on to the Program for Inspection of Nickel Alloy Components (PINAC) (Cumblidge et al. 2010) based on the Bilateral International Agreements with participants and the in-kind contribution of resources from organizations of Finland, Japan, Republic of Korea, Sweden, and the United States of America to evaluate several nondestructive techniques for detection and characterization of primary water stress corrosion cracks (PWSCC) in SBDMW and BMI components. In February 2012, the NRC entered into new agreements with VTT Technical Research Centre of Finland, Nuclear Regulation Authority of Japan (NRA), Korea Institute of Nuclear Safety (KINS), Swedish Radiation Safety Authority (SSM), and Swiss Federal Nuclear Safety Inspectorate (ENSI) to establish PARENT to conduct a series of round-robin tests on SBDMWs, BMIs, and LBDMWs. PARENT activities were split into blind testing and open testing activities. Blind testing was performed in PARENT to quantitatively estimate the performance of established NDE methods in the nuclear power industry and the results from blind testing are documented in NUREG/CR-7235 (Meyer and Heasler 2017). This report is focused on documenting the open testing activity and results.

Open testing was performed on a set of test blocks with true-state information that was open and provided to teams performing the testing. The objective of open testing was to evaluate the performance of emerging NDE techniques, which are still in relatively early stages of development. The motivation for evaluating emerging NDE techniques is the desire to identify more effective methods for detecting and characterizing rapidly growing forms of degradation, such as PWSCC. Many of the emerging NDE techniques evaluated in open testing were explored for their potential to be implemented for on-line monitoring or inspections. Other techniques were explored for their potential to improve on detection and characterization performance compared to more established techniques. Inspections with emerging NDE techniques were carried out by a variety of organizations including universities, industry organizations, and government research organizations. This contrasts with the blind testing portion of PARENT, which focused only on evaluating the latest commercially used NDE inspection techniques and only included inspectors and procedures provided by commercial vendors. This report describes open testing performed in PARENT including a description of the test blocks used, an overview of the NDE techniques applied, and analysis of the data. A separate report is under development for the blind testing portion of PARENT.

The open testing portion of PARENT collected data from 226 inspections performed on 4 BMI test blocks, 4 LBDMW test blocks, and 11 SBDMW test blocks (8 of these test blocks are referred to as “flat bar” test blocks discussed in the next subsection). The data was collected by 23 teams using 37 procedures. An overview of the inspections performed for each test block type is provided in Section 4 and tabulated summaries of NDE procedures and techniques applied to each test block are provided in Appendix B.

The open testing was performed with knowledge of true-state information in the open test blocks provided to teams conducting tests. As a result, no detection performance analyses were performed on open test data. Thus, the evaluation of open test data is based on statistical sizing analyses and qualitative review of data response images. Although the sizing analyses provide some objective measures of performance, the sample sizes are often limited and the results of sizing analyses are only able to provide an approximate measure of performance. This is appropriate for an open test evaluation because the focus is on establishing basic capability of techniques to justify further development and more detailed assessments of performance. For this reason, sizing analyses results for axial and circumferential flaws are not separated and no attempt is made to analyze outliers in the sizing plots. However, several data response images provided by test participants are qualitatively analyzed to supplement the sizing data. In reviewing sizing analyses results, emphasis should be placed on relative comparisons within open testing instead of the absolute values. Data was collected using established phased array ultrasonic testing (PAUT) techniques to provide a benchmark for comparison. Readers are cautioned against comparing sizing results from open testing with sizing results from blind testing because of the different conditions associated with each test.

### **1.1 Laboratory Grown SCC Specimens**

PARENT open testing was performed on several block types, including SBDMWs. A subset of the SBDMW test blocks used for open testing were manufactured by growing stress corrosion cracks (SCC) into fracture mechanics specimens in a laboratory autoclave and then machining off the tabs. These test blocks are described in Section 2.3. The specimens do not have curvature like other SBDMW test blocks and the flaws extend the full width of the specimens so that analysis of length sizing performance cannot be conducted with these test blocks. In addition, the weld in these test blocks is used to join pieces of similar reactor vessel steel. This contrasts with other SBDMW test blocks that join stainless steel components with carbon steel components. These factors provide the basis for distinguishing these test blocks as flat bar (FB) test blocks. They are still considered a subset of SBDMW test blocks in this report because the FB test blocks are similar to SBDMW test blocks dimensionally (i.e., they have similar thicknesses). Therefore, for the results in Section 5 and in Section 6, depth sizing results for SBDMW test blocks are noted in figure and table captions to indicate if the data results include data from FB test blocks or if the analysis was conducted by excluding data from FB test blocks. As noted, length sizing analysis cannot be performed on the FB test blocks, so figure and table captions related to length sizing performance do not indicate inclusion or exclusion of FB test block data.

### **1.2 Open NDE Techniques Report**

An intermediate report was prepared to document the variety of NDE techniques evaluated in PARENT open testing (Meyer 2014). Much of the information in the report was provided by teams applying the techniques in PARENT open testing. The main body of the report included a basic description of the techniques, while specific information on how the techniques were applied in PARENT open testing are included as appendices to the report. Information from the main body of that report is included as Section 3 here, while the appendices are collected in Appendix C of this report. A summarized tabulation of the NDE procedures and techniques applied to LBDMWs, SBDMWs, FBs, and BMIs is included in Appendix B of this report.

### 1.3 Atlas Information Tool

An information tool is under development as part of PARENT and is referred to as the PARENT Atlas. The information tool is designed to contain data from PARENT open testing and information about the test blocks, as well as information on experiences of NDE applied in the field to inspect components for PWSCC. At the time of writing this report, only data from PARENT open testing and information about the open test blocks has been incorporated into the Atlas. Further discussions will be held with PARENT participants regarding additional information to incorporate into the Atlas.

### 1.4 PARENT Organization

PARENT is organized with a Steering Committee, a Task Group on NDE, a Task Group on the PARENT Atlas, and an Invigilator/Data Analysis Group (DAG) following a convention used in PINC and as shown in Figure 1.1. The objectives of these groups for PINC are described in Section 1.0 of NUREG-7019 (Cumblidge et al. 2010) and are similar to PARENT, although personnel have changed. A summary of the members of the Steering Committee, Task Group on NDE, Task Group on the PARENT Atlas, and the Invigilator/DAG is provided in Table 1.1. PARENT participants meet twice per year with one meeting in the United States and the other meeting rotated among the remaining participant countries. The first PARENT meeting was held June 1–3, 2010, at Pacific Northwest National Laboratory (PNNL) in Richland, Washington.

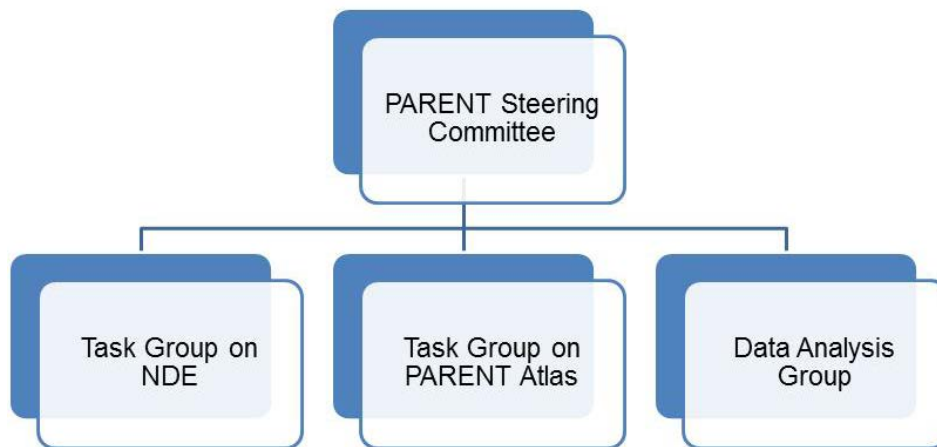


**Figure 1.1 Organization Chart for Steering Committee and Task Groups**

### 1.5 Organization of Report

Section 2 of this report includes a description of the test blocks used in PARENT open testing, including dimensional information, a description of true states, and types of flaws used in each test block. Section 3 provides a description of the NDE techniques applied in PARENT open testing, while Section 4 provides an overview of how data was recorded and a breakdown of inspections by procedure, test block, flaw type, and flaw orientation. Section 4 also describes how the depth and length sizing analysis was performed. Results of data analysis are presented in Section 5 with presentation of the results organized by block type and access (outer diameter [O.D.] versus inner diameter [I.D.]). Section 6 includes a discussion of the results in Section 5. Finally, additional conclusions and recommendations for future work are provided in Section 7.

**Table 1.1 Summary of Members of the PARENT Steering Committee, NDE Task Group, Atlas Task Group, and Invigilator/DAG**

		PARENT Committee Members				
Member Name	Organization	Steering	NDE Task Group	Atlas Task Group	Invigilator/Data Analysis Task Group	
Finland	VTT	Esa Leskelä	Esa Leskelä	Esa Leskelä		
	Aalto University			Hannu Hänninen		
Japan	NRA/JNES	Kazunobu Sakamoto Kikuo Takeshima	Kazunobu Sakamoto Kikuo Takeshima	Kenjiro Aono Kikuo Takeshima	Kensaku Arai Kikuo Takeshima	
	JAPEIC		Ichiro Komura Toshihiro Yamamoto		Ichiro Komura Toshihiro Yamamoto	
	Japanese PWR Industry Group		Yusuke Kono (MHI) Takehiko Yamaguchi (MHI) Takayoshi Tsuruta (MHI)	(Rotating Member) Tomonori Shichida (MHI) Yasuto Nagoshi (MHI) Takehiko Sera (Kansai) Yasukazu Takada (Kansai) Seiji Asada (MHI) Junichiro Nishida (MHI)		
	Tohoku University		Tetsuya Uchimoto			
	KINS	Sung-Sik Kang		Kyung Cho Kim	Kyung Cho Kim	
Korea	KPS		ES Doh			
	KHNP				Yong-Sik Kim	
	KAERI			Hong-Pyo Kim		
DOOSAN			DS Lee, Joo Youl Hong Hak-Joon Kim			
	SKKU					
Sweden	SSM	Richard Sundberg Giselle García Roldán				
	SQC		Tommy Zetterwall		Tommy Zetterwall (all of Europe) Ulf Hjern (only invigilation)	
Switzerland	ENSI	Klaus Germerdonk		Klaus Germerdonk		
	SVTI		Hardy Ernst			
USA	PNNL (Non-Voting)	Brett Braatz, Rob Harris Ryan M. Meyer	Brett Braatz, Ryan M. Meyer	Darren Curtis, Robert Harris Ryan M. Meyer	Steven Doctor, Brett Braatz Jack Spanner – DAG (Open Only) Ryan M. Meyer	
	NRC	Iouri Prokofiev	Stephen Cumbledge			
	EPRI	Jack Spanner	Jack Spanner			
DOOSAN – Doosan Heavy Industries & Construction		KAERI – Korea Atomic Energy Research Institute				
ENSI – Swiss Federal Nuclear Safety Inspectorate		Kansai – The Kansai Electric Power Company, Inc.			PNL – Pacific Northwest National Laboratory	
EPRI – Electric Power Research Institute		KHNP – Korea Hydro & Nuclear Power			SKKU – Sungkyunkwan University	
JAPEIC – Japan Power Engineering and Inspection Corporation		KINS – Korea Institute of Nuclear Safety			SQC – Swedish Qualification Center	
JNES – Japan Nuclear Energy Safety Organization		KPS – Korea Plant Service			SSM – Swedish Radiation Safety Authority	
		MHI – Mitsubishi Heavy Industries, Ltd.			SVTI – Swiss Association for Technical Inspections, Nuclear Inspectorate	
		NRC – US Nuclear Regulatory Commission			VTT – Technical Research Centre of Finland Ltd	

## 2 TEST BLOCK DESCRIPTIONS

The following section provides an overview of the test blocks used in the open testing activity of PARENT. The categories of test blocks that were used in the open testing study are summarized in Table 2.1. The categories include large bore dissimilar metal weld (LBDMW) test blocks, small bore dissimilar metal weld (SBDMW) test blocks, flat bar (FB) test blocks, and bottom mounted instrumentation (BMI) test blocks. A total of 19 test blocks were contributed for the open testing. Table 2.1 also indicates the typical weldment in each test block category, test block diameter and wall thickness dimensions, and the identifications (IDs) of test blocks in each category. Descriptions of the test blocks in each category are provided in Sections 2.1–2.4, while the flaw fabrication methods are described in Section 2.6. True-state information for the flaws in each test block is summarized in Section 2.7.

**Table 2.1 Summary of Categories into which Test Blocks for Open Testing are Classified**

Category		Typical Weldment in Category	Diameter/Thickness Range	Test Block IDs	Test Block Photographs
LBDMW	Full Circumference	DMW piping welds, PWR	Diameter (outer): 897 mm Thickness: 78.5 mm	P37	Appendix D.3
LBDMW	Partial Circumference		Diameter (outer): 852.5, Thickness: 77 mm	P12, P23, P24	
SBDMW	Full Circumference	DMW piping welds, BWR	Diameter range (outer): 286 mm–387 mm Thickness range: 32 mm–47 mm	P1, P4, P41	Appendix D.2
FB			Diameter: Flat Thickness: 30.3 mm	P28, P29, P30, P31, P32, P38, P42, P46,	Appendix D.2
BMI		J-groove weld	Tube OD: 38–45 mm	P21, P22, P5, P7	Appendix D.1

### 2.1 Full Circumference Large Bore and Small Bore Dissimilar Metal Weld Test Blocks

One LBDMW full circumference test block and three SBDMW full circumference test blocks were used in PARENT open testing. The coordinate system defined for acquiring and reporting data on LBDMW test block P37 and SBDMW test block P41 is provided in Figure 2.1. The zero point is defined as that location on the test block where  $X=0$ ,  $Y=0$ , and  $Z=0$ . Figure 2.1 also provides the definitions for the directional vectors  $X+$ ,  $Y+$ , and  $Z+$  in relation to the zero point and with respect to the material construction of the test block. The location for  $Z=0$ ,  $Y=0$  is at the outer diameter surface of the test block, at the center of the weld, and is located a distance “D” from the face edge of the carbon steel section. The  $X=0$  location is indicated by a punch marking on the test block outer surface. A summary of dimensions for P37 and P41 are provided in Table 2.2 and Table 2.3, respectively. The locations, sizes, and types of flaws in test blocks P37 and P41 are provided in the true-state table in Appendix E.

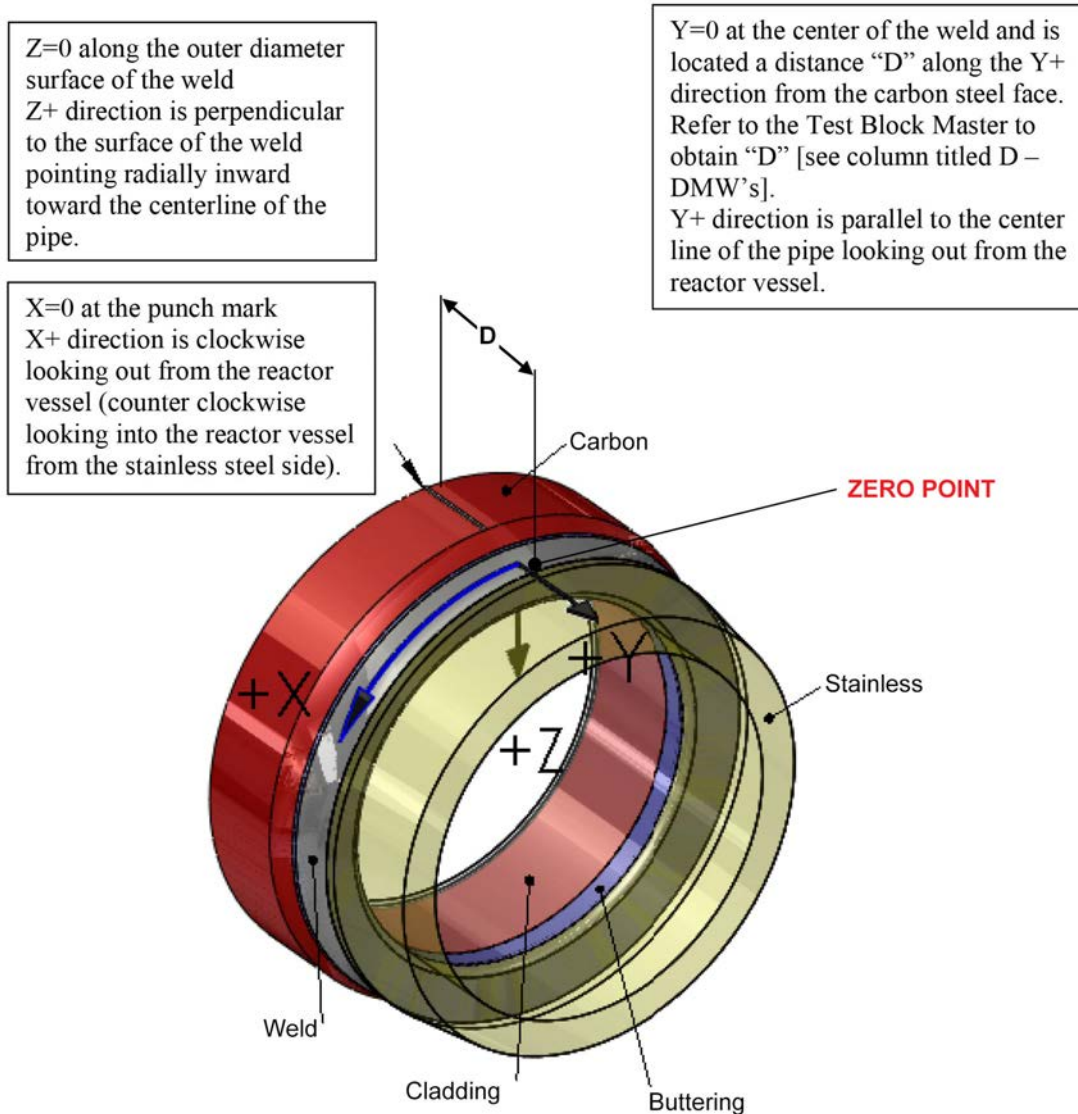


**Figure 2.1 Coordinate System Definition for SBDMW Test Blocks P41 and LBDMW Test Block P37**

**Table 2.2 Summary of Dimensions for LBDMW Full Circumference Test Blocks**

Test Block ID	Inner Diameter, mm	Outer Diameter, mm	D, mm	Test Block Length, mm	Circumferential Extent, degrees
P37	740	897	300	---	360



**Table 2.3 Summary of Dimensions for SBDMW Full Circumference Test Blocks**

Test Block ID	Inner Diameter, mm	Outer Diameter, mm	D, mm	Test Block Length, mm	Circumferential Extent, degrees
P1	260–284	324–349	89	256	360
P4	257–290	324–387	208	583	360
P41	222	286	215	---	360

The coordinate systems defined for acquiring and reporting data on SBDMW test blocks P1 and P4 are provided in Figure 2.2 and Figure 2.3, respectively. The zero point is defined as the location on the test blocks where  $X=0$ ,  $Y=0$ , and  $Z=0$ . Figure 2.2 and Figure 2.3 also provide the definitions for the directional vectors  $X+$ ,  $Y+$ , and  $Z+$  in relation to the zero point and with respect to the material construction of the test block. The location for  $Z=0$ ,  $Y=0$  is at the outer diameter surface of the test block, at the center of the weld, and is located a distance “D” from the face edge of the carbon steel section. The  $X=0$  locations are indicated by punch markings on the outer surface of the test blocks. A summary of dimensions for P1 and P4 are provided in Table 2.3. The locations, sizes, and types of flaws in test blocks P1 and P4 are provided in the true-state table in Appendix E.

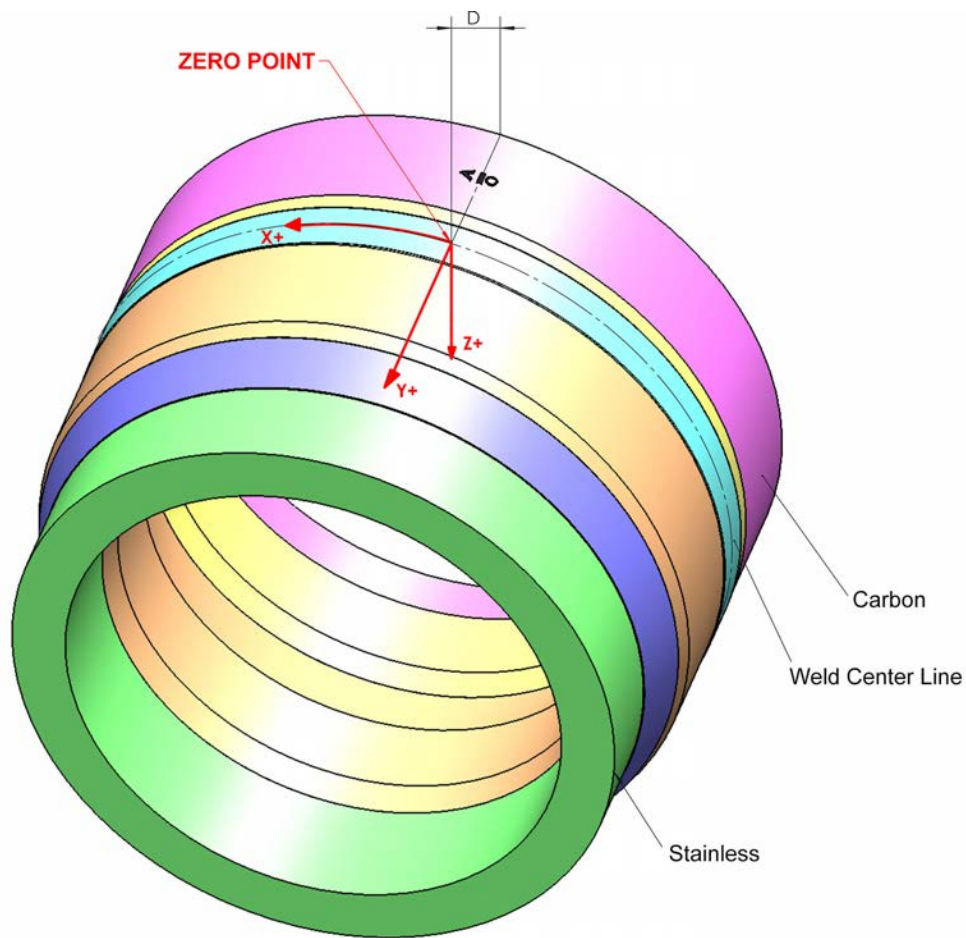


**Figure 2.2 Coordinate System Definition for SBDMW Test Blocks P1**

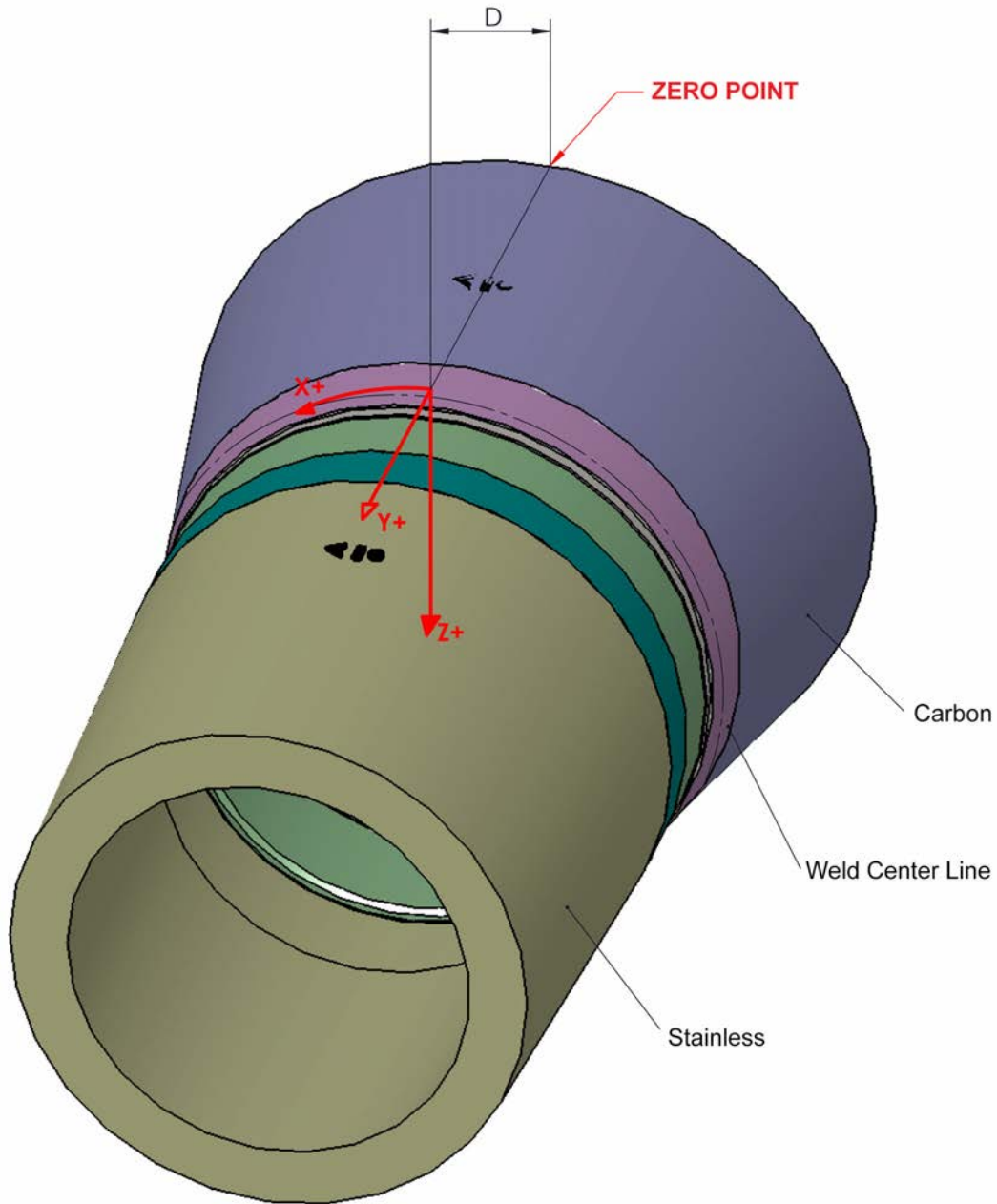


**Figure 2.3 Coordinate System Definition for SBDMW Test Blocks P4**

## **2.2 Partial Circumference Large Bore Dissimilar Metal Weld Test Blocks**

Three partial circumference LBDMW test blocks (P12, P23, and P24) were used in the open testing activities as indicated in Table 2.1. These test blocks use a similar coordinate system definition as the full circumference test blocks; however, the  $X=0$  point is defined at a sector edge rather than a punch marking on the surface. Figure 2.4 depicts the coordinate system defined for P12 and Figure 2.5 depicts the coordinate system defined for P23 and P24. A summary of dimensions for P12, P23, and P24 test blocks is provided in Table 2.4.

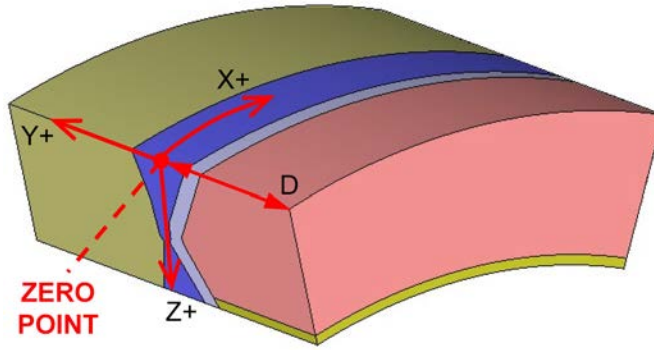


**Figure 2.4 Coordinate System Definition and Illustration of LBDMW Partial Circumference Test Block P12**

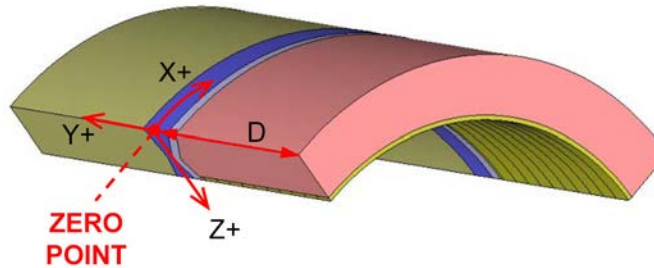


**Figure 2.5 Coordinate System Definition and Illustration of LBDMW Partial Circumference Test Blocks P23 and P24**

**Table 2.4 Summary of Dimensions for LBDMW Partial Circumference Test Blocks**

Test Block ID	Inner Diameter, mm	Outer Diameter, mm	D, mm	Test Block Length, mm	Circumferential Extent, degrees
P12	698.5	852.5	100	200	32.8
P23	736.6	912	306	600	88.8
P24	736.6	912	306	600	89.5

### 2.3 Flat Bar Test Blocks

A total of eight FB test blocks were used in PARENT open testing, as summarized in Table 2.1. However, unlike the partial circumference LBDMWs, these test blocks are not cut-outs from full circumference pieces. These specimens are fabricated by modifying fracture mechanics specimens used in autoclaves for growing laboratory flaws. As a result, the test blocks are flat bars that are cut out from reactor vessel material. The coordinate system and dimensions of test blocks P28, P29, P30, P31, P32, P42, and P46 are provided in Figure 2.6. In this case, the weld area is in the middle of the specimen and exhibits symmetry. Also, the flaws (one flaw in each block) are located at the middle of the specimens and extend across the full width of the specimens, except for P46, which is blank. Test block P38, illustrated in Figure 2.7, is slightly different as the weld area does not exhibit symmetry with respect to the Y direction. The dimensions for P38 and its weld area are included in Figure 2.7.

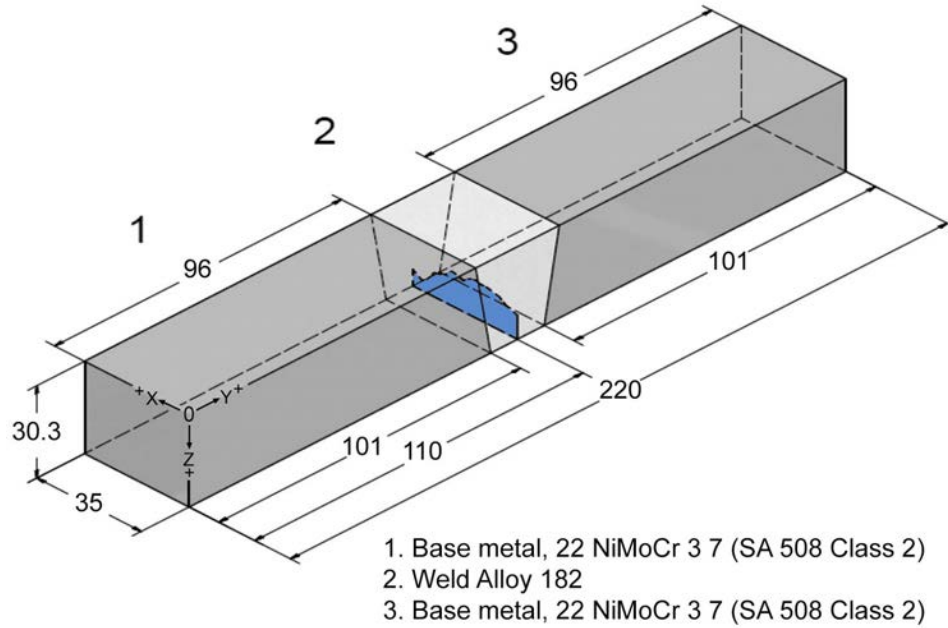


**Figure 2.6** Coordinate System Definition, Dimensions, and Illustrations of FB Test Blocks P28, P29, P30, P31, P32, P42, and P46

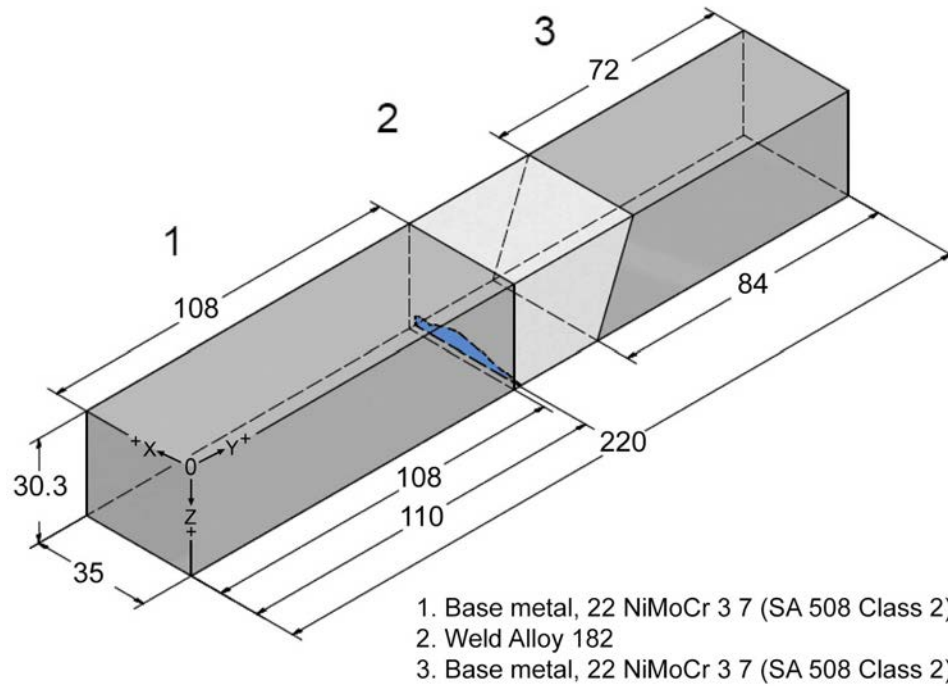


**Figure 2.7** Coordinate System Definition, Dimensions, and Illustrations of FB Test Block P38

## 2.4 Bottom-Mounted Instrumentation Test Blocks

As Table 2.1 indicates, four BMI test blocks were used in open testing (P21, P22, P5 and P7). The coordinate system defined for acquiring and reporting data on these test blocks is provided in Figure 2.8 for P5 and P7 and Figure 2.9 for P21 and P22. These figures show that a cylindrical coordinate system is defined for BMI test blocks with the azimuthal coordinate,  $\theta$ , increasing in the clockwise direction when viewed from the top of the test block (above the wetted surface) with the zero-point marked on the test block. The radial coordinate,  $R$ , is defined such that  $R=0$  at the center of the penetration tube.  $R$  increases outward from this point along a plane that is parallel with the top (wetted) surface. The  $Z$  coordinate is defined as perpendicular to the J-groove weld surface such that  $Z=0$  at the top (wetted) surface and increases into the J-groove material. The dimensions of test blocks P21 and P22 are labeled in Figure 2.9, while the configuration of test blocks P5 and P7 are represented in Figure 2.10, and the dimensions for P5 and P7 are tabulated in Table 2.5.

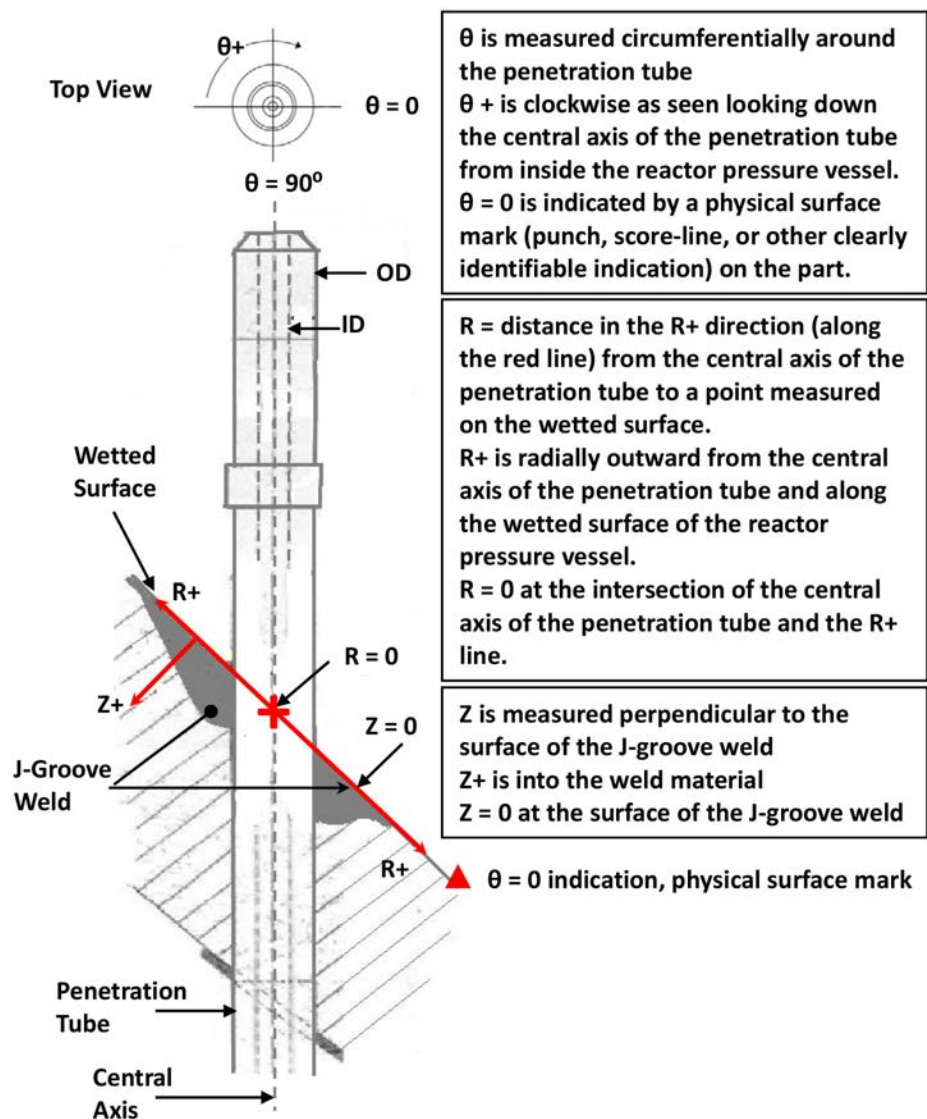


Figure 2.8 Coordinate System Used for BMI Test Blocks: P5 and P7

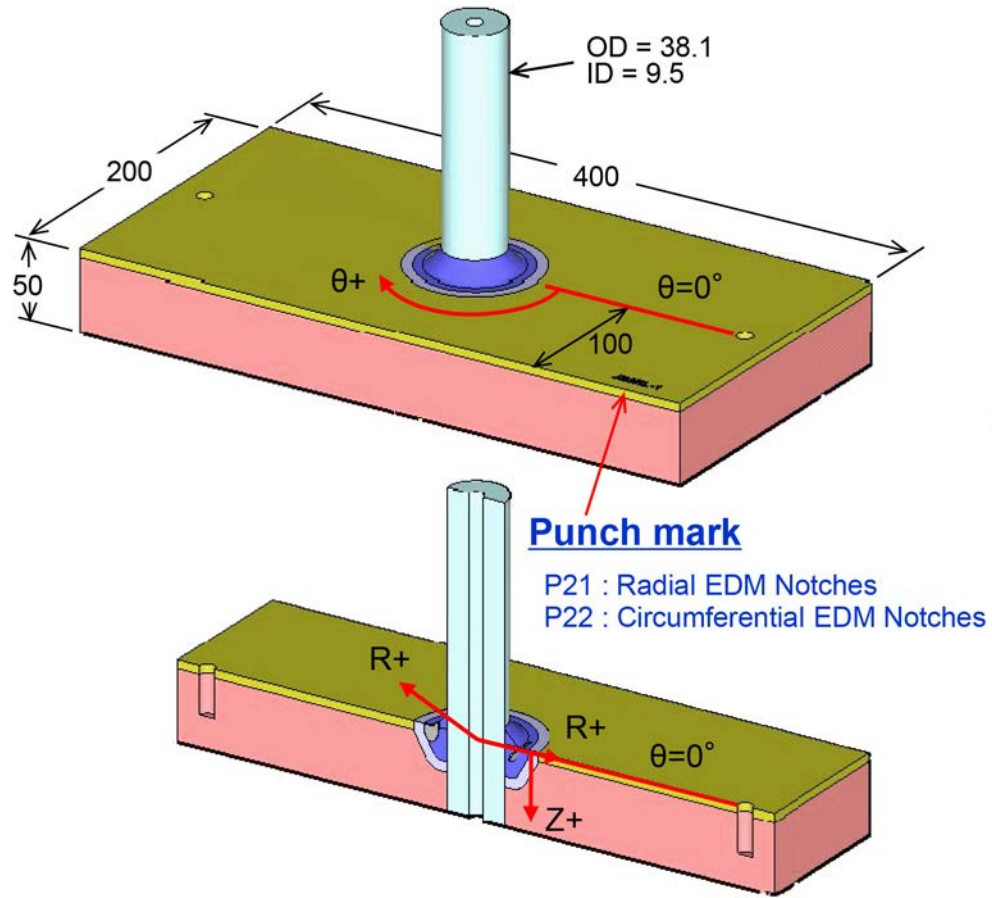
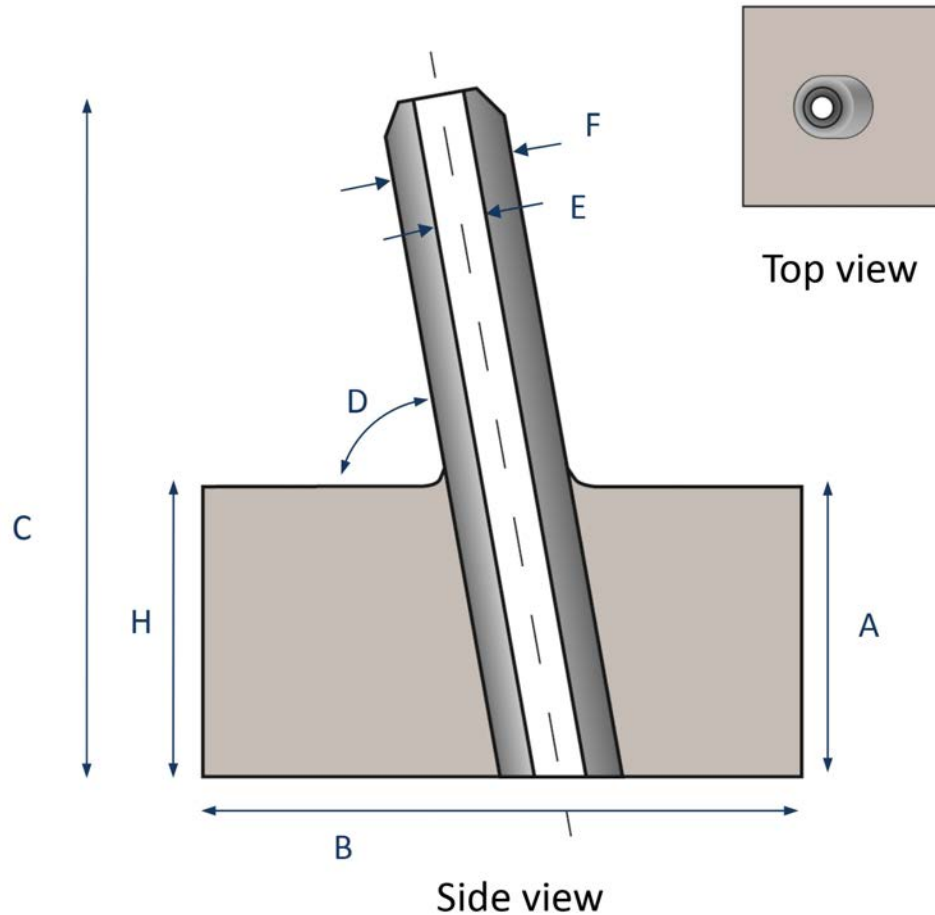


Figure 2.9 Depiction of Configuration for BMI Test Blocks P21 and P22 with Coordinate System and Dimensions Labeled



**Figure 2.10 Depiction of Configuration for BMI Test Blocks P5 and P7 with Labeled Dimensions**

**Table 2.5 Tabulation of BMI Test Block P5 and P7 Dimensions**

Test Block ID	Figure Ref.	A, mm	B, mm	C, mm	D (angle), degrees	E (I.D.), mm	F (O.D.), mm	H, mm
P5	Figure 2.10	100.0	215 × 222	240	89.5	15.9	44.2	100.0
P7	Figure 2.10	97.0	215 × 217	218	87.0	15.9	44.2	97.0

I.D. = inner/inside diameter  
O.D. = outer/outside diameter

## 2.5 Simulated Flaw Types

Field flaws were simulated in PARENT open test blocks using similar methods as those used in PINC. Simulation flaw types include laboratory-grown SCC, weld solidification cracks (SC), thermal fatigue cracks (TFC), a mechanical fatigue crack (MFC), electrical discharge machining (EDM) notches, implanted welding defects such as lack of fusion (LOF), lack of bond (LOB), and slag inclusion (SI). A summary of the type and quantity of simulated flaws used in each test block is provided in Table 2.6. Brief descriptions of the flaw simulation types are provided in the following sections with the objective of highlighting some of the advantages and limitations of

each flaw simulation type with respect to representing PWSCC/IDSCC for assessing NDE performance.

**Table 2.6 Summary of Flaw Simulation Methods Used for Each Test Block and Quantities of Each Type of Simulated Flaw**

Flaw Type	Test Block ID (Quantity)	Total Flaws
Laboratory-Grown SCC	P12 (1), P28 (1), P29 (1), P31 (1), P32(1), P38(1)	6
TFC	P5(3), P1 (4), P4 (2)	9
MFC	P30(1)	1
SC	P7(4), P41(12), P37 (9)	25
Welding Defects	P37 (2)	2
EDM	P4(2), P42(1), P12(1), P21(3), P22(3), P23(3), P24(4)	17
<b>Total</b>		<b>60</b>

### 2.5.1 Laboratory-Grown SCC (P12, P28, P29, P31, P32, and P38)

Laboratory methods for introducing SCC flaws allow for the deliberate introduction of realistic flaws into test pieces at desired locations. However, even in a controlled laboratory environment, the dimensions of SCC flaws can be difficult to control. In addition, it can be difficult to grow SCC flaws into complex geometries because it can be difficult to generate the necessary stresses to promote SCC growth. Nonetheless, laboratory-grown SCC was introduced into several test blocks. The configuration used to grow SCC in P12 is shown in Figure 2.11. The bending loading setup shown in Figure 2.11 was used to introduce SCC flaws of shallow and medium depth. The process used is depicted as a flowchart in Figure 2.12.

A different procedure is used for growing SCC flaws into test blocks P28, P29, P31, P32, and P38. Initially, these test blocks are fabricated by forming a standard fracture mechanics specimen from a sample of pressurized water reactor (PWR) vessel material, including weld material, and then exposing the specimens to PWR environments in an autoclave facility. When desired crack growth is completed, the tabs of the fracture mechanics specimen are cut off so that a flat rectangular bar geometry remains. This is illustrated through a series of photographs in Figure 2.13. A depiction of the laboratory autoclave facility growing SCC flaws is provided in Figure 2.14.

In addition to test blocks P28, P29, P31, P32, and P38, another FB specimen was prepared with the laboratory-grown SCC process depicted in Figure 2.14. This test block was destructively analyzed to study the SCC morphology produced. A photograph of the crack surface depicting the micro-fractographic appearance of the flaws is provided in Figure 2.15 and Figure 2.16. Observed features of the laboratory-grown SCC flaws considered relevant to NDE included the presence of “fingers” on the crack growth front and the presence of uncracked ligaments. The “fingers” may have an impact on depth sizing because they creates an irregular crack front and it may be difficult to identify the deepest part of the crack. The uncracked ligaments indicate regions where ultrasound would be transmitted across the crack faces, increasing the transparency of the crack to inspection by ultrasound.



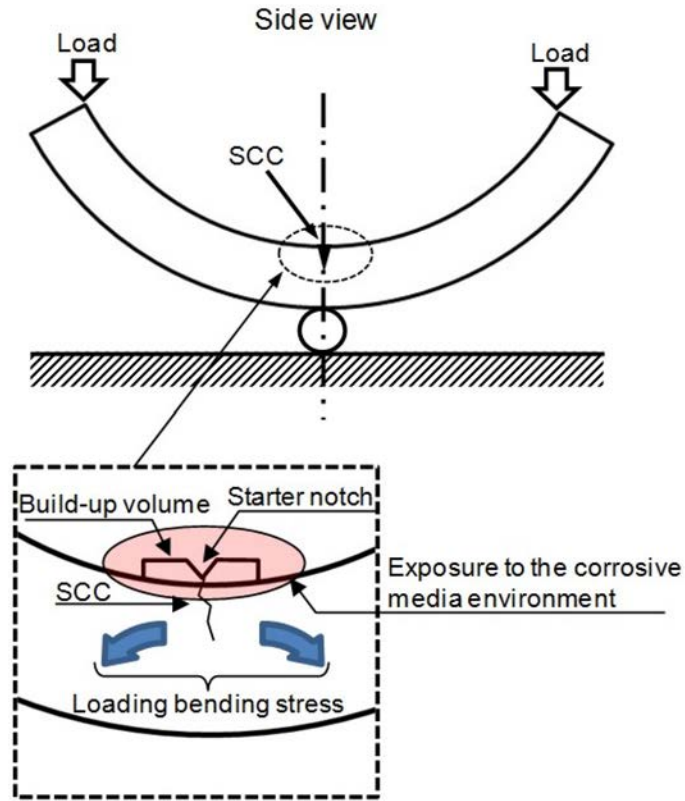


**Figure 2.11** Depiction of the Approach Used to Produce a Laboratory-Grown SCC in Test Block P12

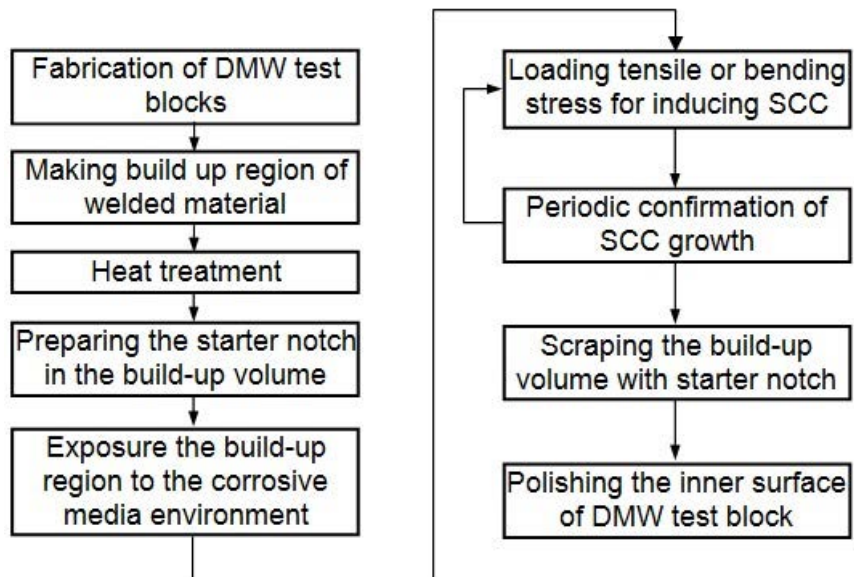


**Figure 2.12** Flowchart of the Process Used to Produce a Laboratory-Grown PWSCC/IDSCC

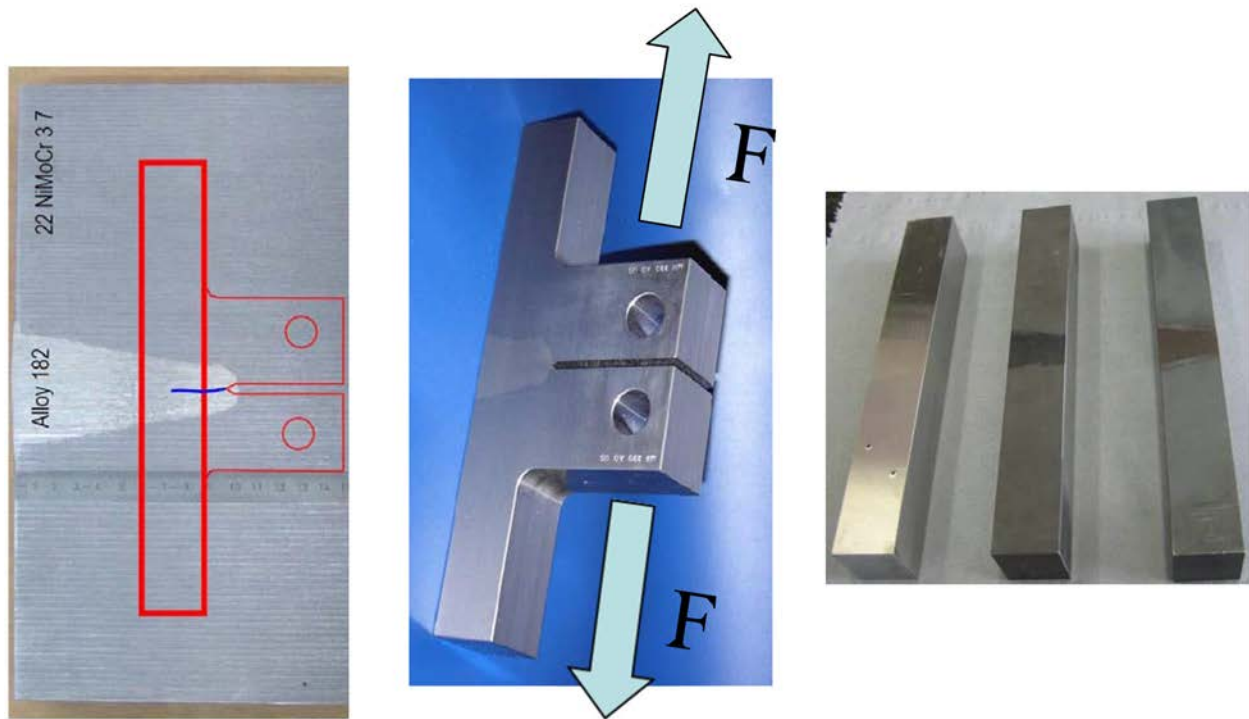


Figure 2.13 Photograph and Depiction of FB Test Block Cut Out into Standard Fracture Mechanics Specimen from Reactor Pressure Vessel Material

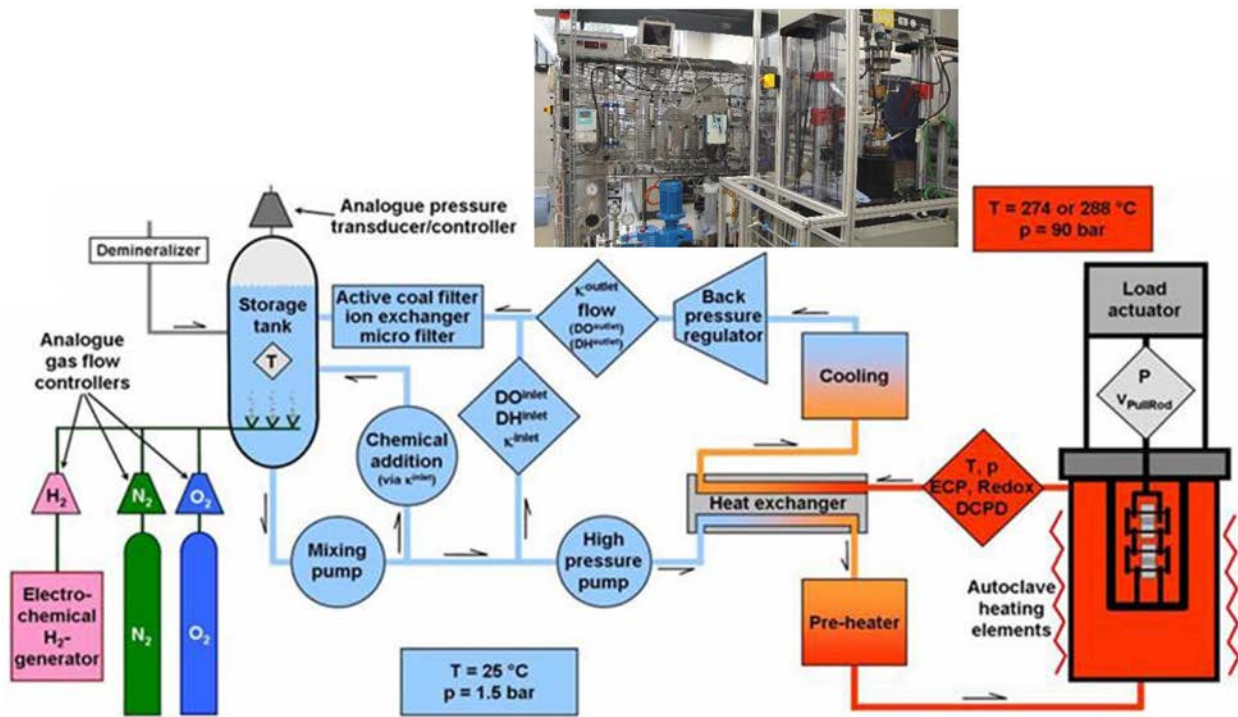
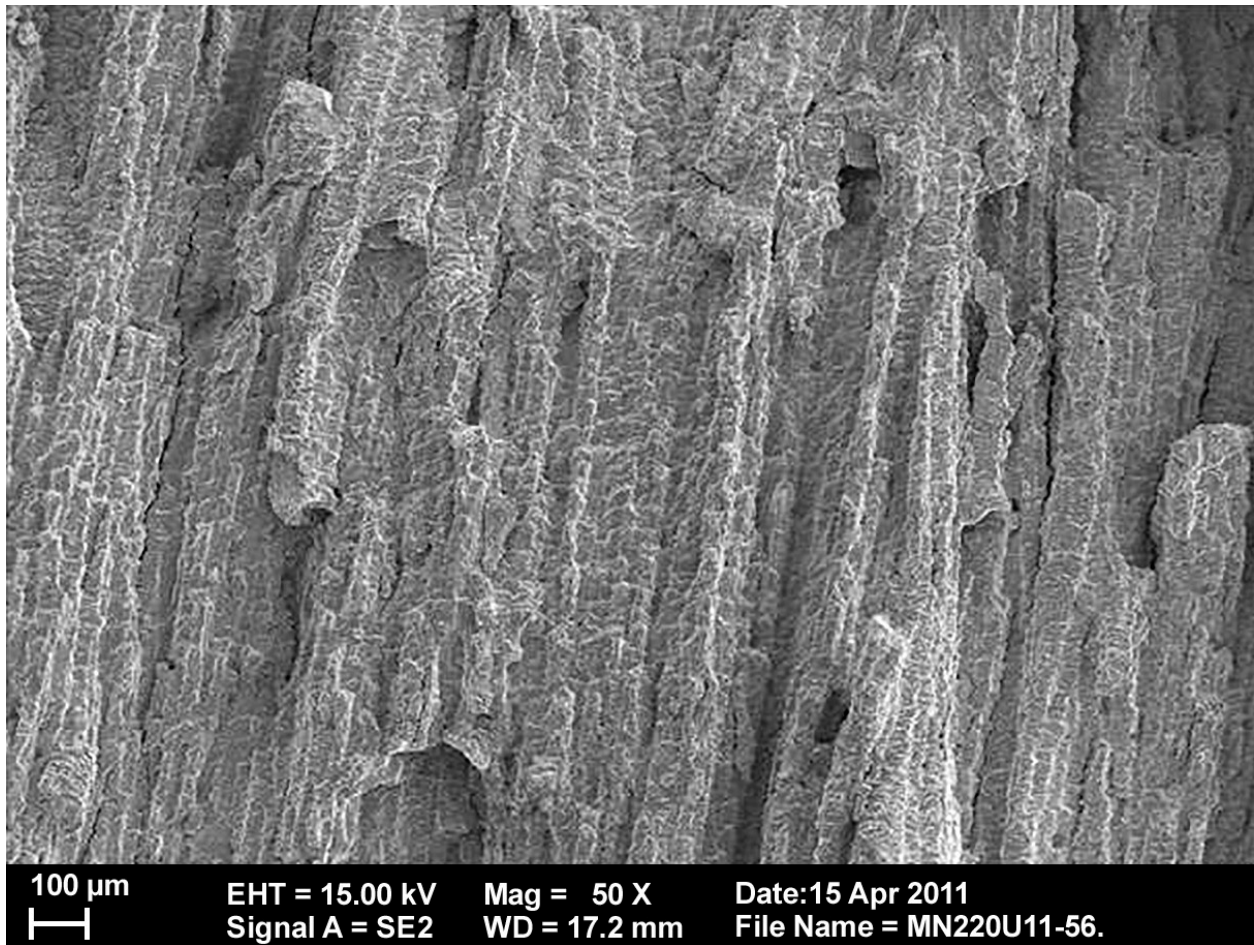
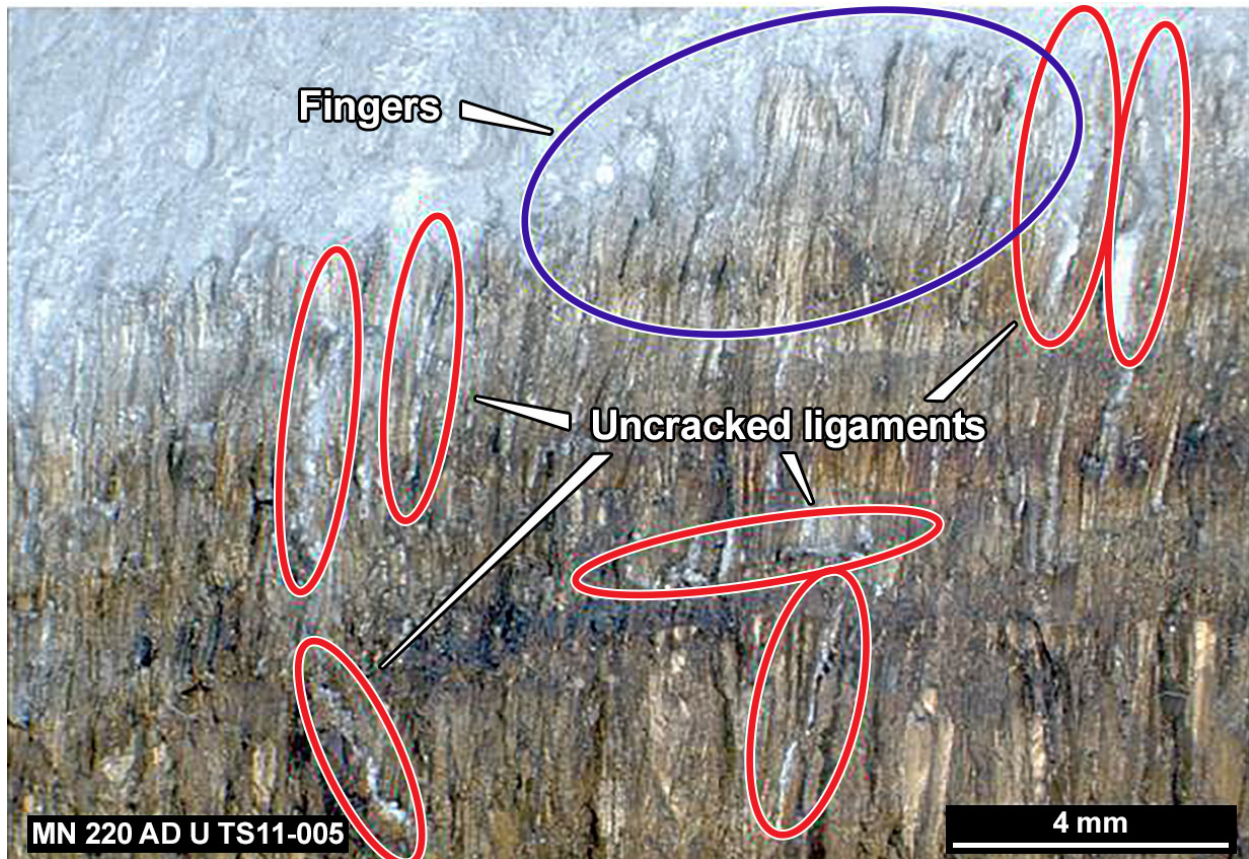


Figure 2.14 Depiction of laboratory Autoclave Set-up for Growing SCC Flaws in FB Specimens under BWR and PWR Conditions



**Figure 2.15** Typical Micro-Fractographic Appearance of Laboratory-Grown SCC in FB Specimens



**Figure 2.16 Uncracked Ligaments and Finger-Like Local Laboratory SCC Crack Growth in Destructively Analyzed FB Specimen**

### **2.5.2 Thermal Fatigue Cracks (P1, P4, and P5)**

Thermal fatigue cracks can be introduced directly into test blocks without welding or machining. A single crack or a network of cracks can be induced in the base material and welded areas without artificial crack initiators. A total of nine TFCs were introduced into PARENT open test blocks P5 (BMI), P1, and P4. Analysis of TFC flaws in blind test blocks P6, P8, and P9 has indicated that the TFCs are wider than a typical SCC flaw. Further, flaw clusters have been observed in several test blocks. The clusters may make certain flaws easier to detect than they would be otherwise. In addition, flaw clusters introduce difficulty in depth sizing because of the interference caused by several crack tips in close proximity.

### **2.5.3 Weld Solidification Cracks (P7, P37, and P41)**

Weld solidification cracks may be used to simulate service-type defects such as IDSCC or PWSCC. The region where the cracks are fabricated are excised and filled with a “poisoned” weld metal that is designed to crack upon cooling. Care must be taken when SCs are to be used to determine the capability of NDE methods because the region of flaw fabrication may be too obvious by examination, similar to flaws that are implanted. This may be more of an issue for base material compared to weld material, and for this reason, SC type flaws are recommended for implantation into weld material. A total of 25 SC defects were used to simulate PWSCC flaws in test blocks P7, P37, and P41.

#### **2.5.4 Electrical Discharge Machined Notches (P1, P12, P42, P21, P22, P23, and P24)**

A total of 17 EDM notches are included in test blocks P1, P12, P42, P21, P22, P23, and P24. Electrical discharge machining works by eroding the material in the path of electrical discharges that form between an electrode and the work piece. EDM notches are relatively easy to make and control the dimensions of, but they are often criticized for limited representation of real flaw features. EDM notches have a well-defined rectangular or semi-elliptical shape and lack the branching characteristic that SCC flaws often exhibit. In addition, the width of an EDM notch is dependent on the depth of the notch, with greater surface opening required with increasing depth.

#### **2.5.5 Mechanical Fatigue Cracks (P30)**

One MFC is included in test block P30. MFCs are formed by cyclic mechanical loading of a test block or piece of material that is then implanted into a larger test block. In this case (P30), the MFC is grown into a test block whose geometry has been designed to accommodate controlled cyclic mechanical loading. MFCs typically have wider crack openings than SCC type flaws and the crack faces generally are not in contact except when under compression. Further, MFCs do not exhibit the branching behavior that is more common for SCC flaws.

#### **2.5.6 Welding Defects (P37)**

Two welding defects including LOF and SI are included in test block P37. These defects are not surface-breaking.

### **2.6 True-State Determination**

Information on flaw true states for each test block were documented on test block drawings by the test block contributors based on information documented in the flaw fabrication process and by fingerprinting. A summary of true states for all test blocks is provided in Appendix E.



## 3 TECHNIQUE DESCRIPTIONS

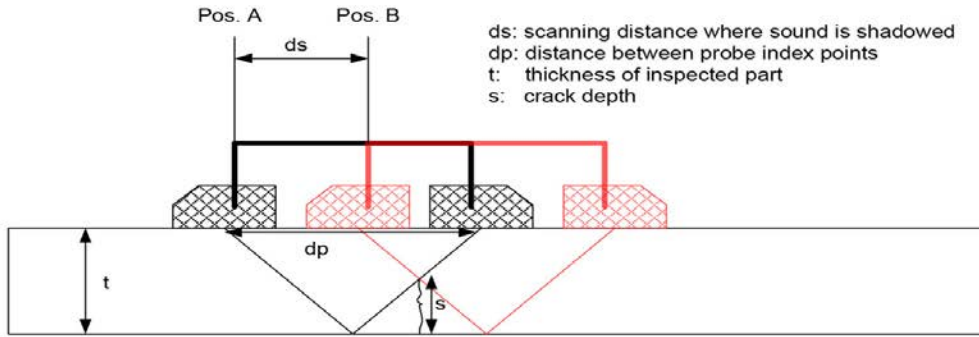
The technique descriptions provided in this section have been documented in the main body of an intermediate report (PNNL-23387; Meyer 2014). The appendices of PNNL-23387 contain more information about specific implementation of open NDE techniques in PARENT and these appendices are compiled in Appendix C of this report. A tabulated summary of the open NDE techniques and procedures is included in Appendix B organized by test block type. The rest of this section is organized such that brief overview descriptions of ultrasonic techniques are provided in Section 3.1, while brief overview descriptions of the eddy current techniques used in the open testing are included in Section 3.2. Overview descriptions for other techniques are provided in Section 3.3, which includes descriptions for microwave near-field microscopy (MM) and radiographic techniques.

### 3.1 Ultrasonic Techniques

This section documents ultrasonic techniques employed in the open testing portion of PARENT by providing brief overview descriptions of the techniques. This section is roughly organized by first providing the description for a variant of conventional ultrasonic testing involving single-element transducers, then by providing the description for phased array and other array transducer-based techniques. This is followed by overview descriptions for non-linear ultrasonic techniques, and overview descriptions for long-range or stand-off ultrasonic inspection techniques are provided last.

#### 3.1.1 Through Transmission of Longitudinal Waves

A specific variant of conventional ultrasonic testing was assessed during the open testing based on a pitch/catch-type transducer arrangement for transmission and reception of longitudinal waves (UT-P/C). Mechanized scanning and encoding of transducer position and data was used to enhance flaw characterization ability. Identical angle beam (40° to 45°) transducers are used for both transmission and reception. Like most conventional ultrasonic techniques, the transducers are mounted on the outer surface of the component under inspection. A single reflection off of the backwall is required to direct the sound beam to the receiver located on the outer surface. The distance between the transmitter and receiver is such as to optimize this received signal. As the pair of transducers is scanned linearly over a flaw, shadowing of the transmitted signal by the flaw will result in a drop in the signal received (see Figure 3.1). Flaw characterization can be performed by analyzing C-scan images of the data like Figure 3.2. The depth of flaws can be determined from the C-scans as shown in Figure 3.2 with the aid of the formula in Figure 3.1. A detailed description of how the conventional UT-P/C technique was implemented in PARENT can be found in Appendix C.2.1. As reported in Appendix C.2.1.5, this technique is relatively insensitive to flaw surface roughness and to flaw orientation. In addition, material grain boundaries introduce very low noise, enabling the use of higher frequencies. However, inspection results can be heavily influenced by the presence of cladding and the technique can be difficult to implement when the I.D. surface is not parallel with the O.D. surface.



**Set-up:**

- Two identical probes (aperture, frequency, angle) with an angle of about 40° to 45° (long), fixed in a probe holder.
- Distance between probe index points is optimized to receive the reflected longitudinal wave from the backwall (LL)
- Probe holder is moved over the surface and the distance where sound is shadowed by the crack will be stored (B-scan of the received signal)

Crack depth is given by the following formula:

$$s = ds * t / dp$$

**Figure 3.1 Illustration of Mechanized Scanning Through-Transmission Longitudinal Pitch/Catch Technique**

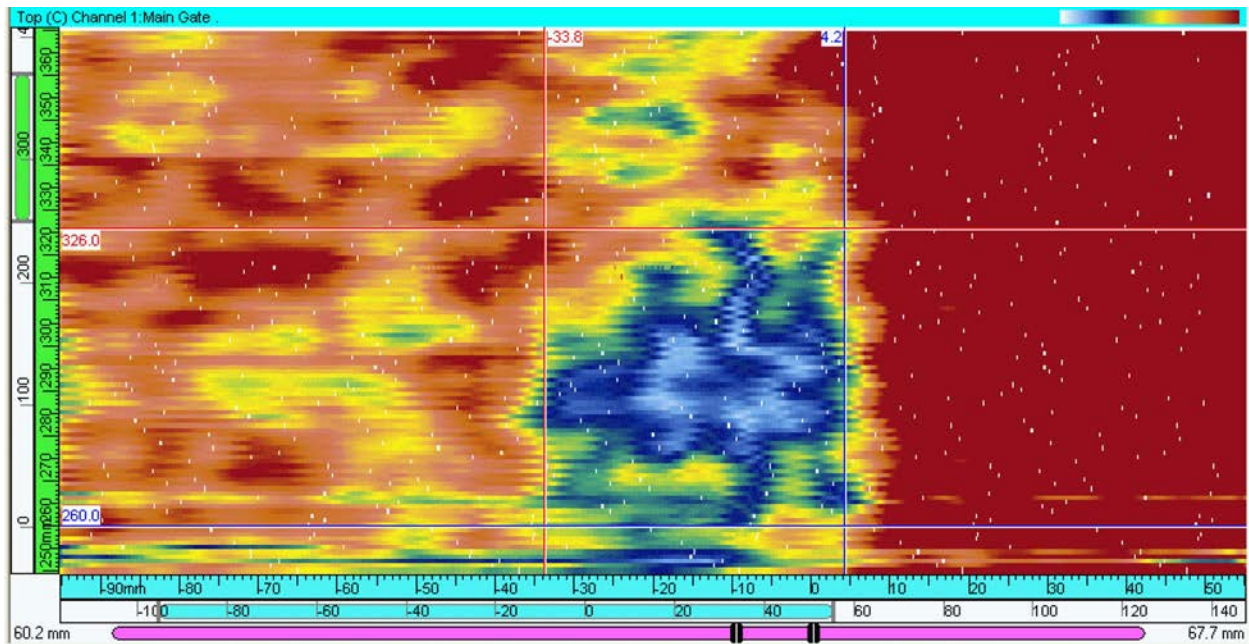


**Figure 3.2 The C-scan Shows the Received Amplitude Color Coded (0% full screen height, FSH [white] to 100% FSH [red])**



### 3.1.2 Phased Array Ultrasonic Testing

Phased array ultrasonic testing (PAUT) techniques have been gaining increased acceptance for performing inservice inspection of nuclear power plants. PAUT uses a transducer consisting of multiple piezoelectric or piezocomposite elements in contrast to conventional UT, which uses transducers with only a single-element. Electronic beam steering and focusing is achieved by careful time delay sequencing of excitation signals to the individual elements in the PAUT transducers to create complex constructive and destructive interference patterns to intensify the sound field in a desired location (see Figure 3.3). PAUT data is often presented in A-scan, B-scan, C-scan, and D-scan image form for analysis. In this way, the linear dimensions of a flaw are characterized based on image analysis. Figure 3.4 shows an example of PAUT data representation as A-scan, B-scan, C-scan, and D-scan images. A PowerPoint overview of how several PAUT techniques were implemented in PARENT can be found in Appendix C.1.3 while a more detailed description of how the techniques were implemented can be found in Appendix C.2.2–C.2.5.

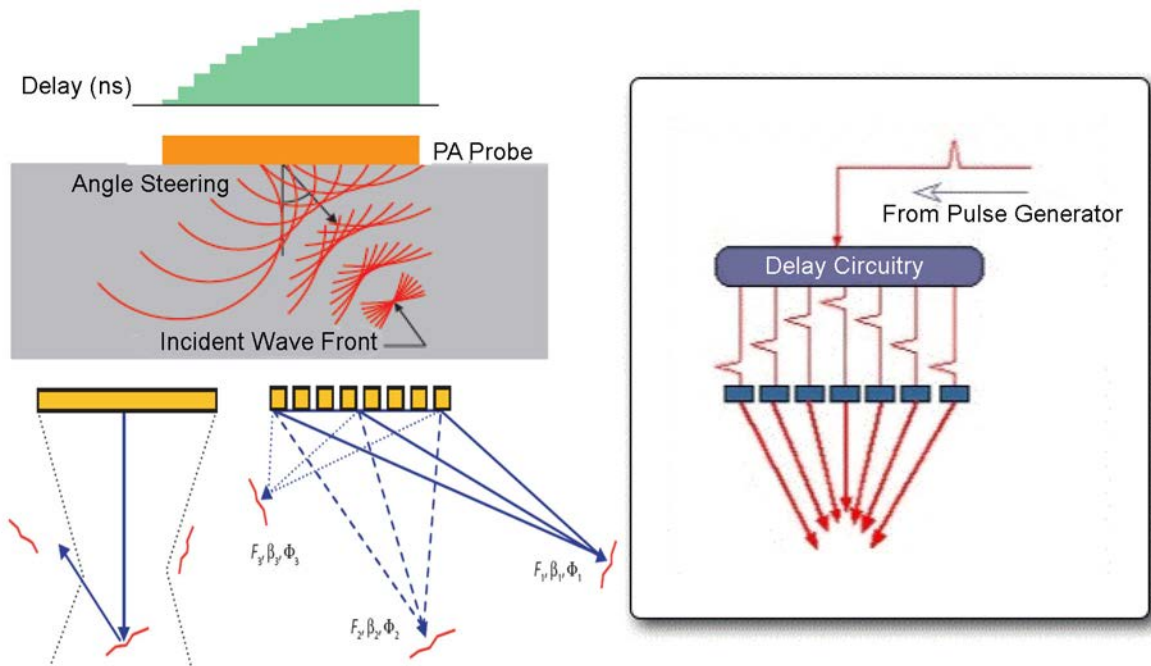


**Figure 3.3 Illustration of Time Delay Sequencing of Excitation of PAUT Transducer Elements to Achieve Beam Steering and Focusing**

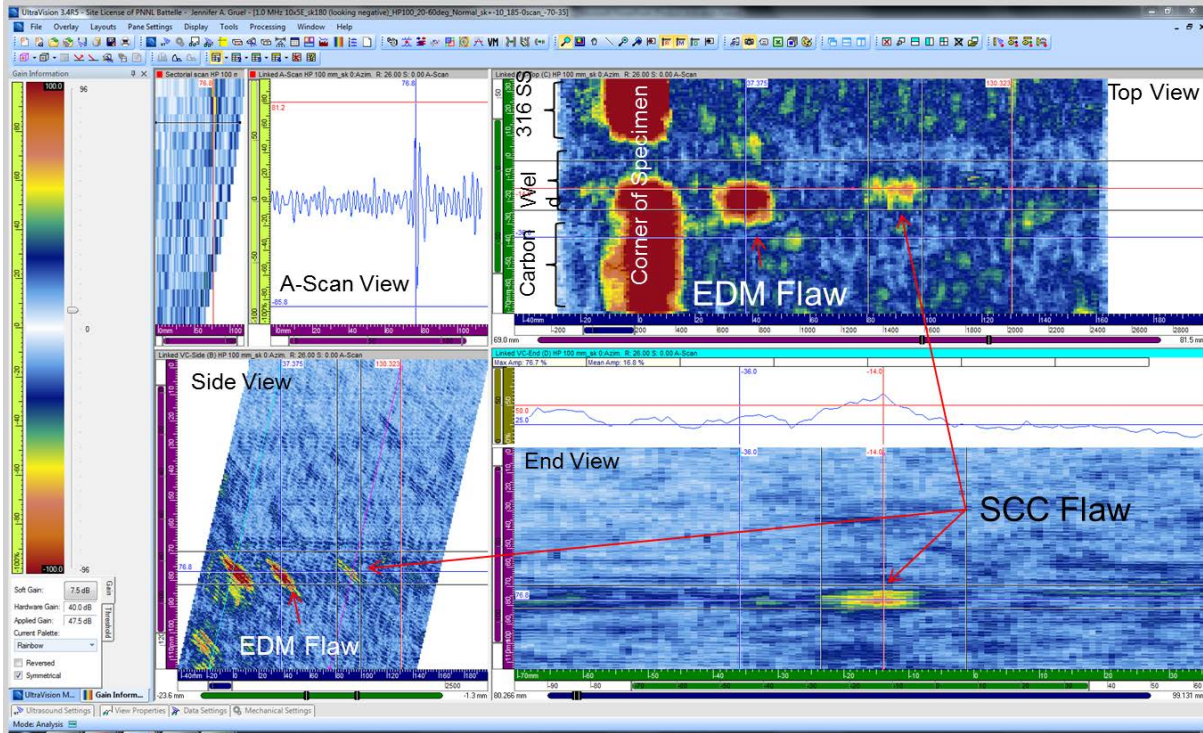


**Figure 3.4 PAUT Data Represented as A-scan (top left), C-scan (top right), B-scan (bottom left), and D scan (bottom right)**

There are many parameters to consider in tailoring PAUT to a specific application including the size, number, and orientation of elements in a PAUT transducer as well as frequency. In addition, probes for PAUT may operate in pulse-echo mode or include separate arrays for transmitting and receiving. Like conventional UT, PAUT can be implemented with automated and encoded or can be performed manually. The significant advantage of PAUT over conventional UT is that it enables rapid examination of flaws from multiple angles resulting in more accurate and complete flaw characterization. However, the equipment (including the transducers, excitation electronics, and signal processing equipment) is more complex and costly in comparison to equipment for conventional UT exams. This increased complexity also requires a greater amount of personnel expertise to implement. PAUT can be applied for O.D. or I.D. inspections.

### 3.1.3 Three-Dimensional Synthetic Aperture Focusing Technique

Synthetic aperture focusing technique (SAFT) is a signal processing technique to correct for distortions in scanning images as a result of transducer focusing distortion, to obtain images with improved resolution. Similar to PAUT, SAFT enables electronic control over transducer focus and can greatly improve inspection performance compared to conventional UT. However, with SAFT, this control is implemented through post-processing of collected data. The basis for SAFT is easiest to illustrate for the two-dimensional (2D) scenario, as shown in Figure 3.5.

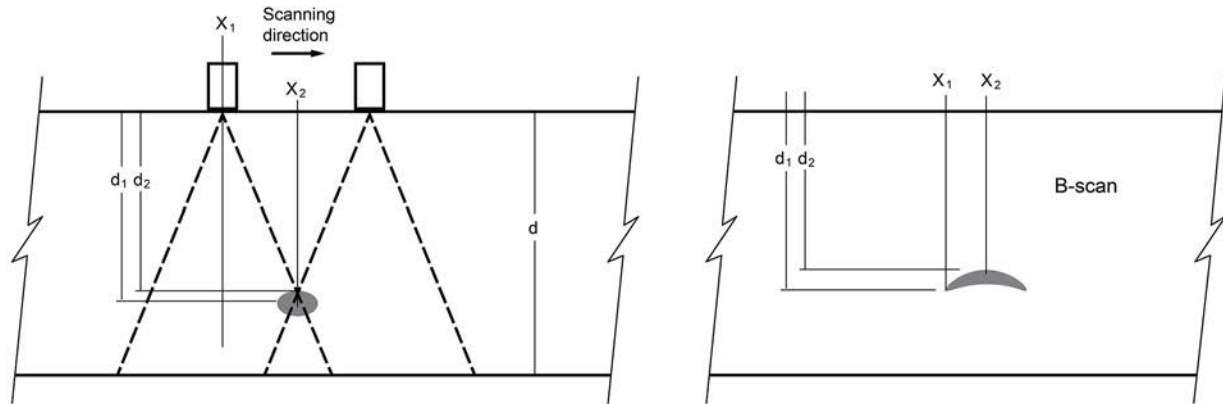


**Figure 3.5 2D Illustration of SAFT Correction for Focusing Distortion in Ultrasonic Inspections (left); B-scan Illustrating Distortion Caused by Beam Focusing Effects (right)**

In this figure, an unfocused transducer located at  $x_1$  transmits a signal and receives an echo from the defect located at  $x_2$ . As the transducer is scanned along  $x$  over the location of the defect, the B-scan image is created illustrating the distortion of the actual defect as a result of poor focusing. This distortion can be corrected with knowledge of the incident beam width and path traveled by ultrasound through the test piece (Elbern and Guimaraes 1999),

$$d_2 = \left[ d_1^2 - (x_1 - x_2)^2 \right]^{1/2}. \quad (3.1)$$

SAFT can also be implemented with a transducer array in which each element in the transducer can be individually excited in sequence while all elements “listen” for echo signals. Using a matrix array transducer allows SAFT imaging to be performed in three dimensions (3D) (see Figure 3.6). An obvious advantage of implementing SAFT with array transducers is that it enables flaws to be characterized much faster and reduces the amount of mechanical scanning required for the transducer. Data from 3D-SAFT can be presented in the form of a variety of images including A-scans, B-scans, C-scans, and D-scans. Thus, analysis procedures are similar to those for PAUT. A PowerPoint overview of how the 3D-SAFT was implemented in PARENT can be found in Appendix C.1.2, while a more detailed description of how the 3D-SAFT technique was implemented in PARENT can be found in Appendix C.5.2.

3D-SAFT is a powerful technique in that it enables near arbitrary focusing and rapid characterization of defects through post processing of data. Similar to PAUT, 3D-SAFT requires the use of sophisticated probes and data recording and processing equipment.

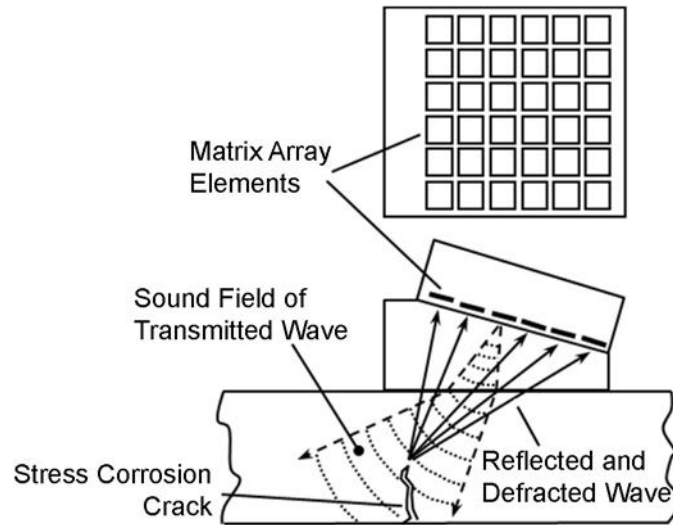


**Figure 3.6 Implementation of 3D SAFT Using a Matrix Array Transducer. Individual elements are excited in sequence, while all elements “listen” for echoes.**

### 3.1.4 Phased Array Time Reversal Technique

The phased array time reversal technique (PATRT) is a means for transmitting electronically focused ultrasonic energy through even non-homogenous media (Fink 1992; Fink 1999). PATRT is an iterative technique in which the reflection of ultrasonic energy from a target is interpreted as the emission of a weak ultrasonic signal from the target, which is detected by an array transducer. Under this interpretation, the target acts as a localized source and the sound field spreads as it propagates away from the target towards the array transducer. After digitization and recording of the signals at the transducer, they are time reversed and re-transmitted to generate a sound field that becomes more focused as it travels from the array transducer back to the target (see Figure 3.7). As the process is repeated, the focusing of the sound field improves. Formally, the basis for PATRT lies in the reciprocity property of the wave equation. A PowerPoint overview of how PATRT was implemented in PARENT can be found in Appendix C.1.1 and a more detailed description of how PATRT was implemented in PARENT can be found in Appendix C.3.6.

A significant advantage of PATRT is its ability to adaptively focus in non-homogenous media. In contrast to SAFT, knowledge of the actual path that ultrasonic signals travel through the test material is not required. Similar to SAFT and PAUT, PATRT requires relatively sophisticated equipment and expertise for data recording and processing, in comparison to conventional UT. The techniques should be capable of performing both I.D. and O.D. inspections.

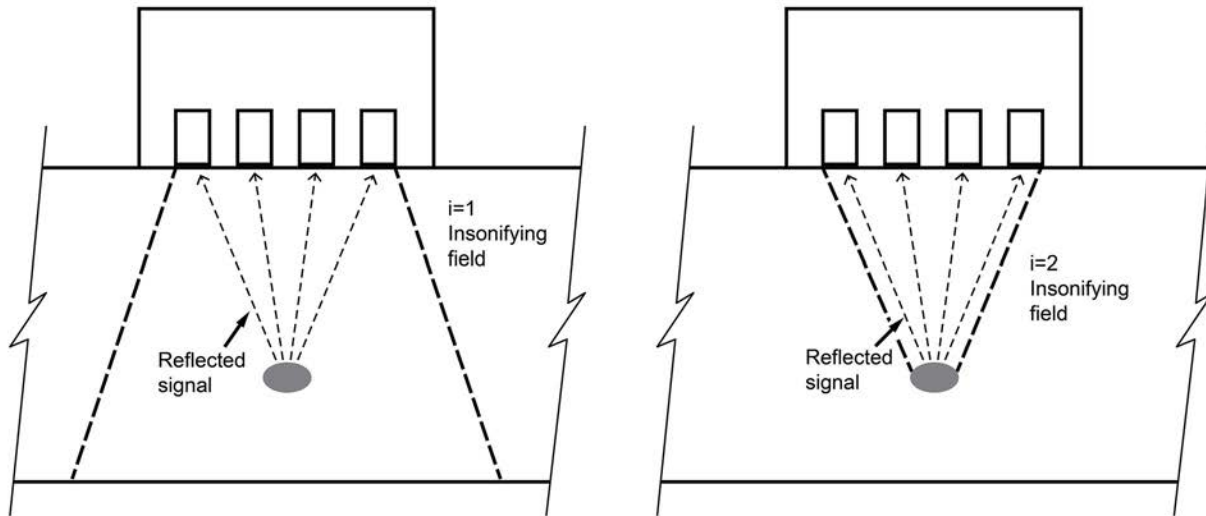


**Figure 3.7 Illustration of the Time Reversal Technique Concept for Focusing Ultrasonic Energy**

### 3.1.5 Phased Array Asymmetrical Beam Time of Flight Diffraction

The phased array asymmetrical beam time-of-flight diffraction (PAATOFD) technique is implemented using a pair of 2D matrix array probes, with one probe serving as the transmitter and the other probe serving as the receiver (Ishida and Kitasaka 2013). Each probe is mounted on opposite sides of the flaw under investigation, similar to a regular time-of-flight diffraction (TOFD) configuration. However, the PAATOFD technique is based on the direct insonification of the crack tip as opposed to listening for the crack tip response when the base of the crack is insonified. With PAATOFD, the scan angle and focal depth of the transmitting and receiving probes may be arbitrarily adjusted, as indicated in Figure 3.8, to obtain the tip echo of the flaw from multiple scan angles. This enables improved discrimination of tip echo signals from sources of noise through synthesis (by the method named Multi-angle Synthesis Method (MA Method)) of the data from multiple scan angles and depths of focus as illustrated in Figure 3.9. A PowerPoint overview of how the PAATOFD technique was implemented in PARENT can be found in Appendix C.1.2, and a more detailed description of how PAATOFD was implemented in PARENT can be found in Appendix C.5.1.

In principle, the PAATOFD technique could be applied on the component O.D. or I.D. and could handle geometrical complexities such as weld crowns or unlevel surfaces, although this would likely complicate the analysis. The PAATOFD technique focuses on detecting crack tip signals and, thus, should be very accurate at depth sizing. The disadvantages of this technique include its large footprint with two matrix array probes, which may make it difficult to implement for certain components. Also, the technique could take a significant amount of time to implement as one must systematically scan through multiple depths of focus to identify the crack tip signal. However, if the technique is implemented in tandem with PAUT or conventional UT for initial flaw detection and rough sizing, it is possible that the scan volume could be significantly reduced.

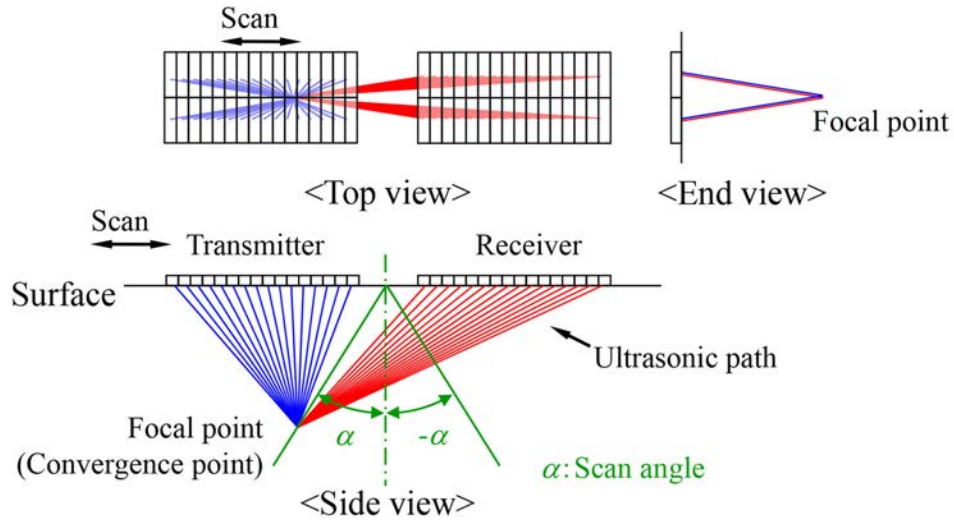


**Figure 3.8 Schematic Illustration of the PAATOFD Technique**

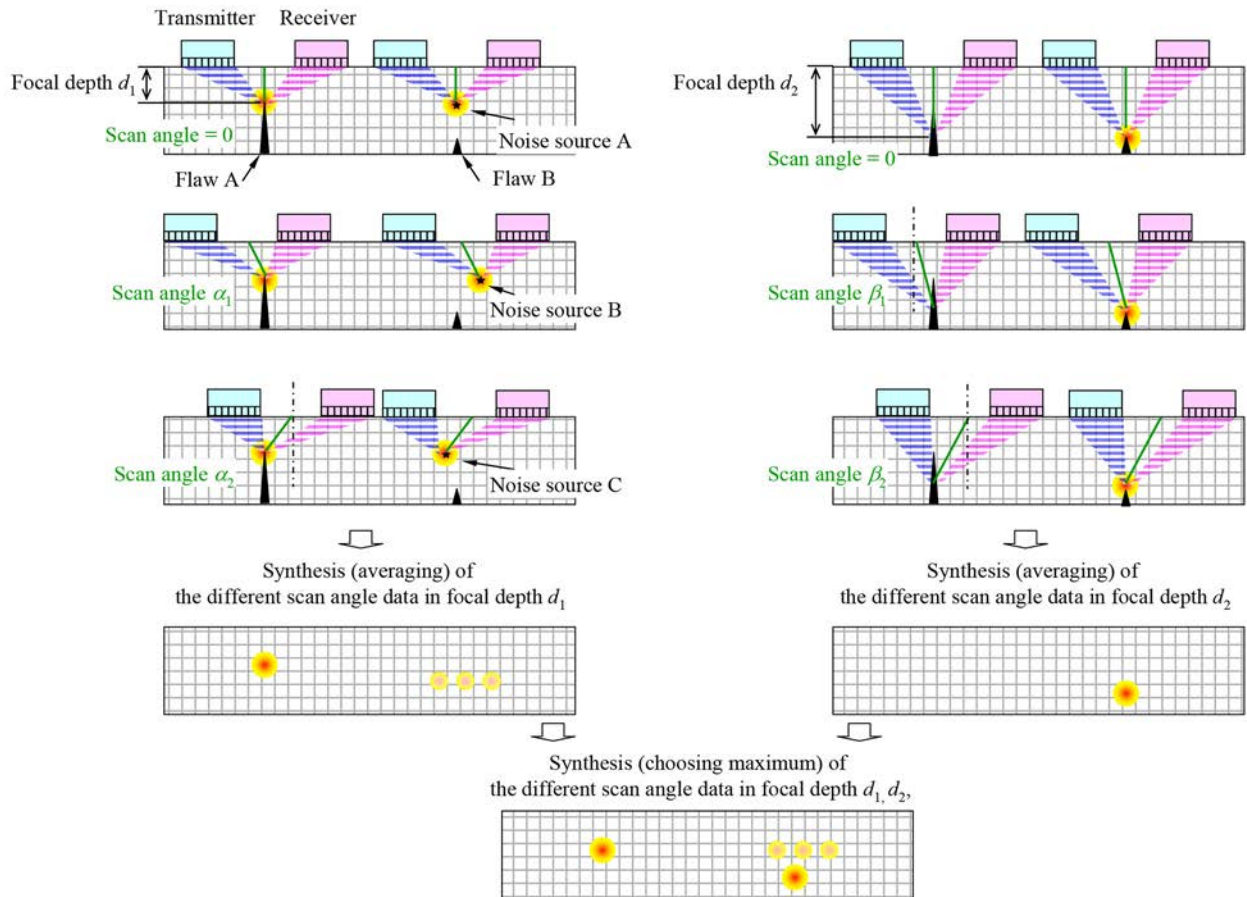


**Figure 3.9 Data from Multiple Scan Angles and Depths of Focus are Synthesized in PAATOFD to Help Discriminate Crack Tip Signals from Noise**

### 3.1.6 Phased Array Twin Probe

The phased array twin probe (PATP) method is very similar to the PAATOFD method except that both the transmitter and receiver are oriented in the direction perpendicular to the scan direction as opposed to parallel to the scan direction for the PAATOFD technique. An illustration of the PATP technique is provided in Figure 3.10. With PATP, the scan angle and focal depth of the transmitting and receiving probes may be arbitrarily adjusted to enable improved discrimination of tip signals from sources of noise through synthesis (by MA method) of the data from multiple scan angles and depths of focus as illustrated Figure 3.11. The selection of the PAATOFD or PATP method will depend significantly on access conditions. For situations in which only single-sided access is available, the PATP could be implemented whereas PAATOFD may require access to both sides of a weld. A PowerPoint overview of how the PATP technique was implemented in PARENT can be found in Appendix C.1.2, and a more detailed description of how PATP was implemented in PARENT can be found in Appendix C.5.1.

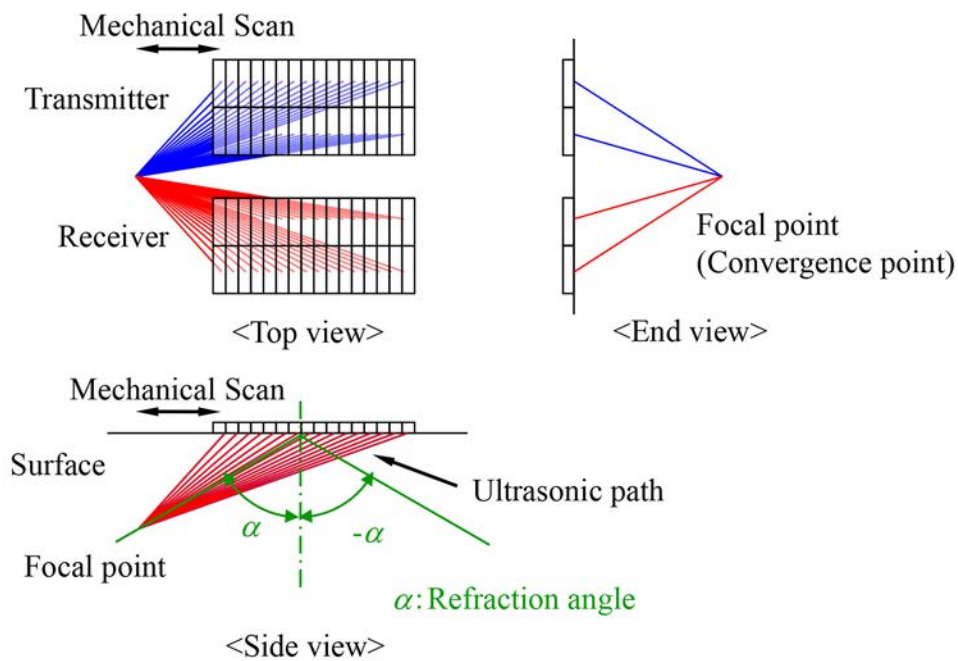


**Figure 3.10 Schematic Illustration of the PATP Technique**

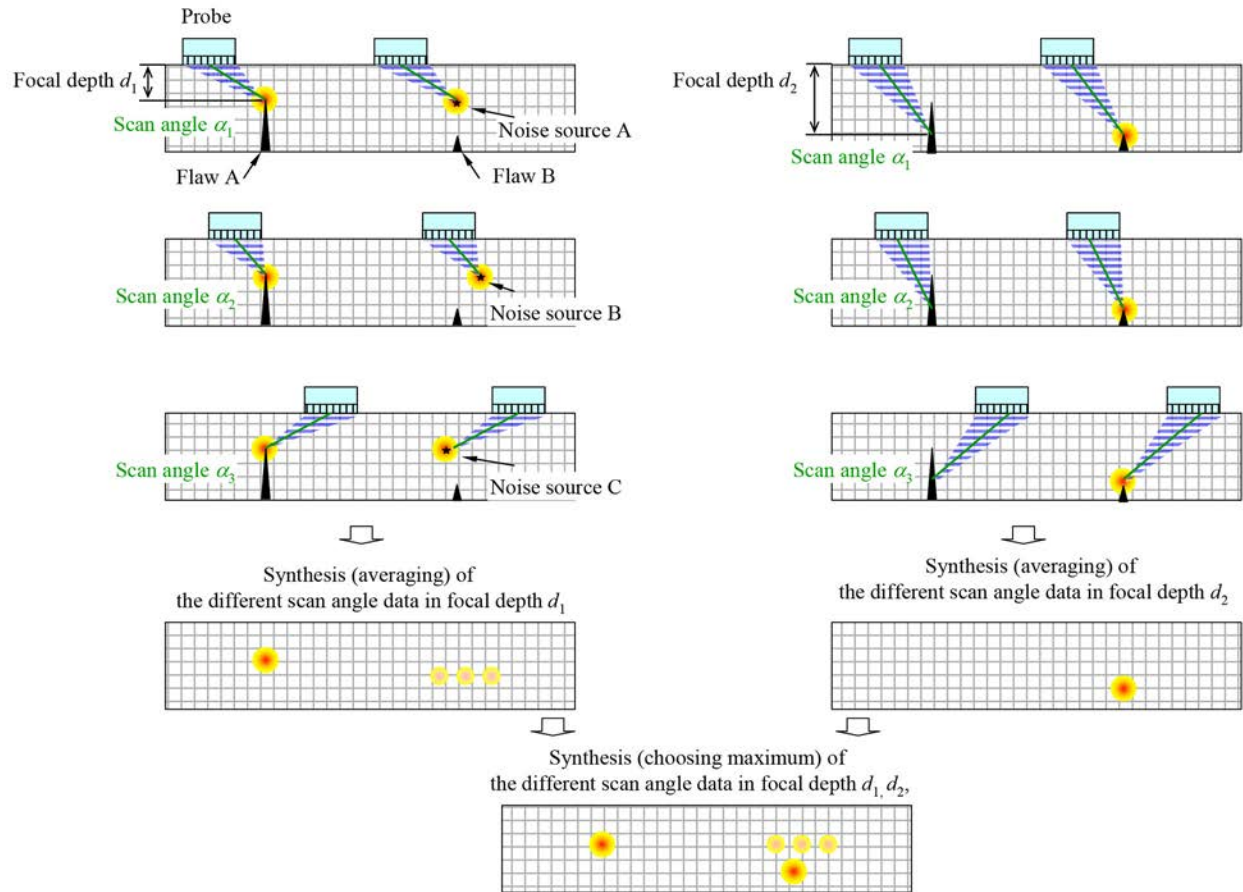


**Figure 3.11 Data from Multiple Scan Angles and Depths of Focus are Synthesized in PATP to Help Discriminate Crack Tip Signals from Noise**

### 3.1.7 Subharmonic Phased Array

Subharmonic phased array (SHPA), or subharmonic phased array for crack evaluation (SPACE), is an advanced ultrasonic testing technique that is based on the observation of nonlinear acoustic responses from material damage and phased array imaging techniques. More specifically, for crack evaluation, SHPA is based on the periodic contact (clapping) of the faces of tight cracks during the compressional period of an applied elastic wave, also referred to as contact acoustic nonlinearity (CAN). In this case, the clapping can occur if the amplitude of the elastic displacement is greater than the crack face separation (see Figure 3.12). In comparison to observations of higher harmonic generations, observations of subharmonic responses exhibit better selectivity to closed cracks (Ohara et al. 2008).



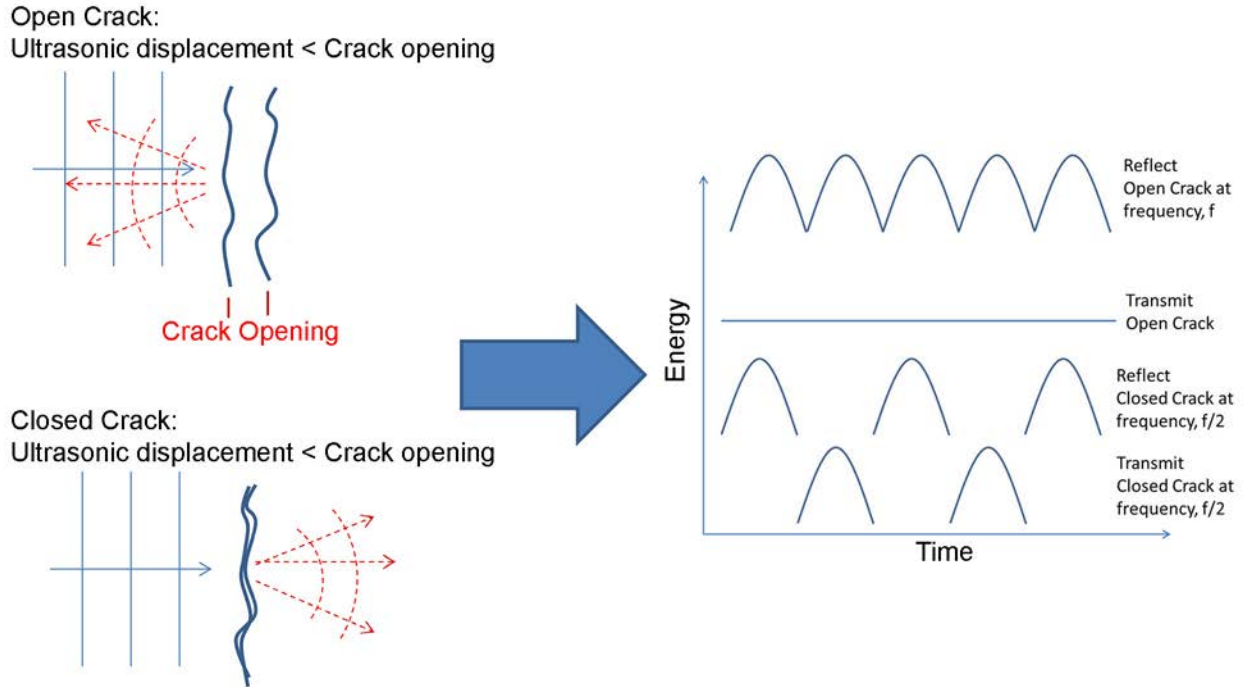


**Figure 3.12 Illustration of the Crack Face “Clapping” Phenomena that is the Basis for Subharmonic Generation when Elastic Waves are Applied to Tight Cracks**

SHPA provides fundamental array images at fundamental frequency  $f$  and subharmonic array images at the subharmonic frequency  $f/2$ , visualizing the open and closed parts of cracks, respectively. In PARENT, SHPA was implemented in a surface acoustic waves (SAW) mode to assess flaw detection and length sizing capability and in a bulk wave mode to assess flaw depth sizing capability (see Figure 3.13). As the figure shows, SAW mode requires mounting of the transducer on the same surface as the flaw’s surface-breaking feature, while bulk wave mode is implemented similar to the way conventional UT and PAUT would typically be performed in the field with the transducer mounted on the component O.D. surface.

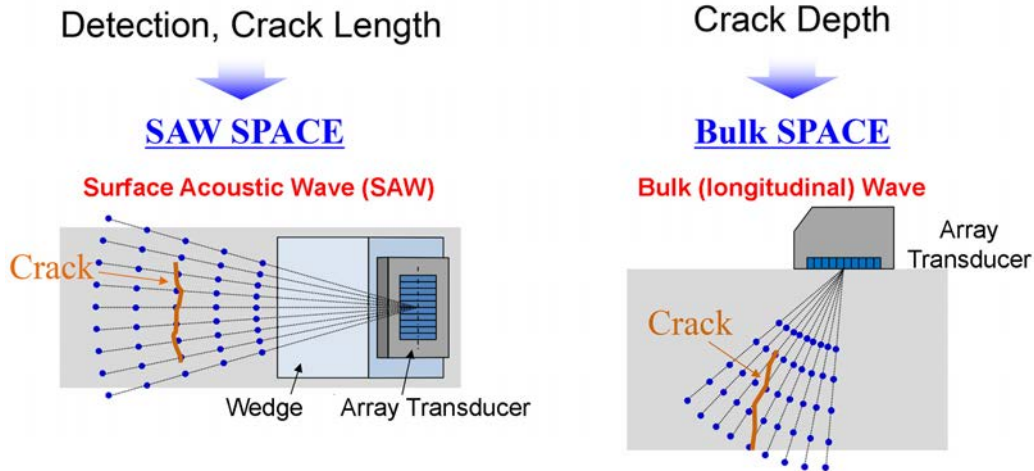


**Figure 3.13 Illustration of SPACE Implementation in SAW Mode to Assess Detection and Length Sizing Capability and in Bulk Wave Mode to Assess Depth Sizing Capability**

For PARENT, SHPA was implemented using a single phased array transducer for transmitting and receiving and using short burst waves for excitations. SHPA data analysis can be performed in a similar fashion to data analysis for regular phased array examinations. That is, through examination of A-scan data and image analysis of B-scans, C-scans, and D-scans (see Figure 3.14).

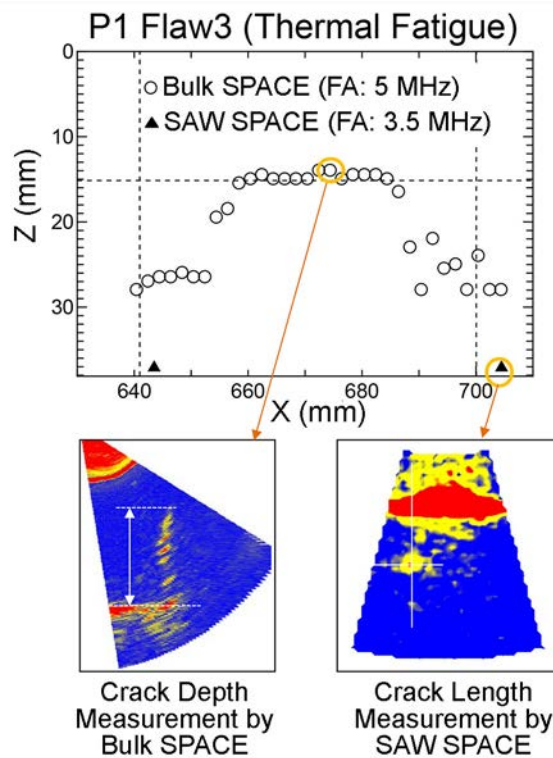


**Figure 3.14 Illustration of SHPA Data Analysis for Length and Depth Sizing of Flaws**

As noted, SHPA is particularly selective to closed or tight formed cracks but would not be useful for characterizing open cracks. Thus, characterization of both closed and open portions of cracks must be performed by analyzing images of data at the fundamental frequency,  $f$  (like regular phased array), in addition to the subharmonic image analysis. Otherwise, SHPA may be performed very similarly to regular phased array (PAUT) examinations, with similar equipment requirements and data analysis procedures. A variant of SHPA, referred to as large amplitude excitation subharmonic UT (LASH), described in the next subsection, uses a large amplitude excitation pulse to enable characterization of flaws with larger crack openings using subharmonic data. A PowerPoint overview describing how the SHPA technique was implemented for PARENT can be found in Appendix C.1.2, and a more detailed description of how SHPA was implemented in PARENT can be found in Appendix C.5.3.

### 3.1.8 Large Amplitude Excitation Subharmonic

LASH is a variant of SHPA, described in the previous subsection, utilizing a large amplitude excitation pulse to generate elastic waves with larger displacement so that selectivity for flaws with larger crack openings that may be more relevant to field conditions can be obtained. Implementation of LASH differs in comparison to the implementation described for SHPA in the last subsection in that a transmit/receive arrangement is used to facilitate use of separate high-voltage transducer for excitation of elastic waves with large displacement. Data analysis can be performed similar to SHPA and PAUT through analysis of A-scans, B-scans, C-scans, and D-scans.

As shown in Figure 3.15, this variant of LASH requires a separate high-voltage transducer for excitation in addition to the array transducer for signal reception. A PowerPoint overview of how LASH was implemented in PARENT can be found in Appendix C.1.2, and a more detailed description of how LASH was implemented in PARENT can be found in Appendix C.5.4.

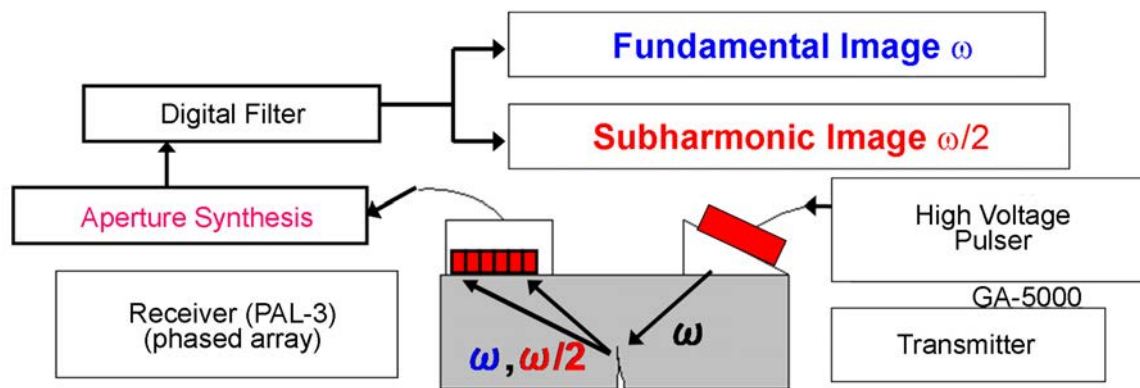
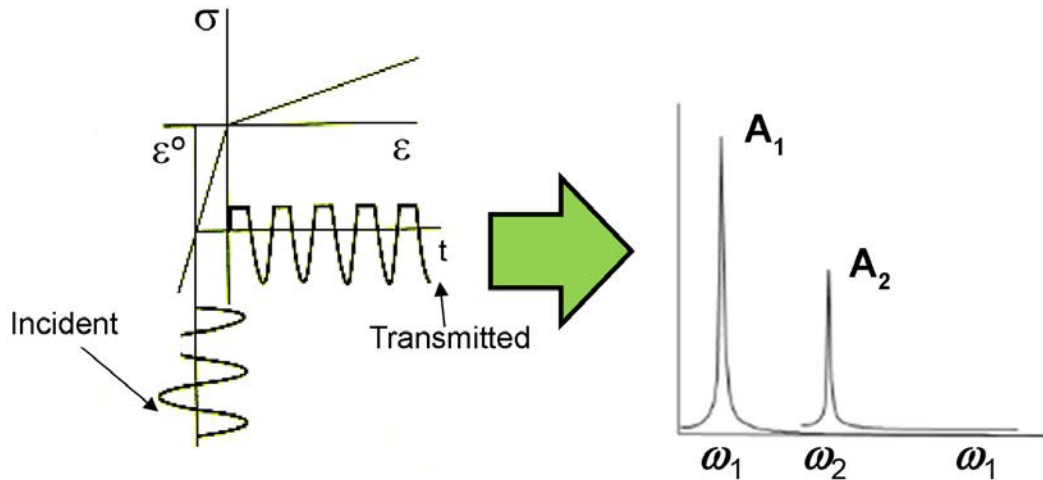


Figure 3.15 Depiction of the LASH Technique Implementation

### 3.1.9 Higher Harmonic Ultrasonic Technique

The higher harmonic ultrasonic technique (HHUT) for crack detection is also based on the phenomenon of CAN, as illustrated in Figure 3.12. Higher harmonics are generated, in addition to subharmonics, because of the nonlinearity induced in signals as they interact with the crack faces (illustrated in Figure 3.16). As a result, the acoustic waveform becomes distorted and the higher harmonic frequency components are generated in the transmitted wave or in the reflected wave from the crack.



**Figure 3.16 Illustration of Higher Harmonic Generation Because of the CAN Phenomenon**

Thus, it would be possible to detect closed cracks by monitoring the magnitude of the higher harmonic frequency component generated in the transmitted or the reflected wave. Usually, the relative nonlinear parameter ( $\beta'$ ) defined by the ratio of the second order harmonic frequency magnitude to the power of the fundamental frequency magnitude is used as the monitoring parameter (Jhang 2000), although the generation of higher order harmonics can provide useful monitoring parameters as well. Overviews of how HHUT was implemented in PARENT can be found in the Appendices B.1.1 and B.1.2. More detailed descriptions of how HHUT was implemented in PARENT can be found in Appendices C.3.7 and C.5.5.

HHUT can be implemented in pulse-echo (PE) or transmit-receive (TR) modes as shown in Figure 3.17. The technique could be implemented on the component I.D. or O.D. To ensure sufficient interaction with the crack faces, the transducers should be mounted at an angle with respect to the crack faces, or perpendicular to them. The advantage of this technique compared to conventional UT is its sensitivity to closed cracks. However, compared to the subharmonic techniques described previously, higher harmonics are not as selective for closed cracks, although this may not necessarily be viewed as a drawback for all applications. A disadvantage of HHUT is that physical understanding of the technique is incomplete. As a consequence, quantitative characterization of flaws by HHUT will be difficult with a single measurement and may require relative comparison to responses obtained from already well characterized flaws.

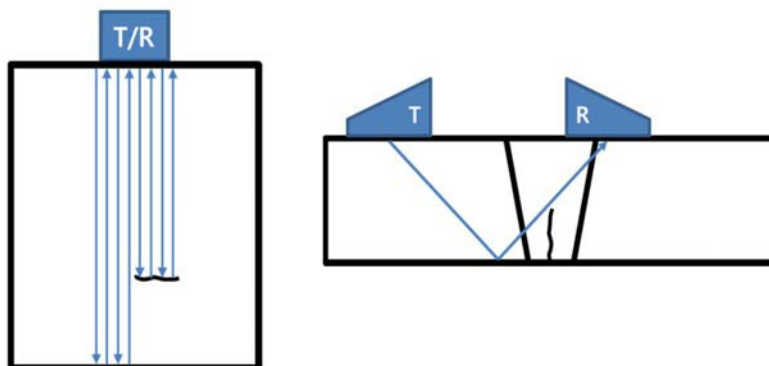


**Figure 3.17 Illustration of HHUT Implementation in PE (left) and TR (right) Modes**

### 3.1.10 Nonlinear Resonant Ultrasound Spectroscopy

Nonlinear resonant ultrasound spectroscopy (NRUS) is another acoustic technique, in addition to the SHPA, LASH, and HHUT techniques described earlier, in which material characterization or damage assessment is based on the observation of nonlinear acoustic/ultrasonic responses. With NRUS, signals are applied over a wide frequency sweep to specimens to observe material nonlinearity as a result of damage manifested as a shift in resonant frequency and damping of the resonant peak amplitude as the excitation signal amplitude increases. An illustration of this for cyclic fatigue crack growth in a compact tension (CT) is shown in Figure 3.18.

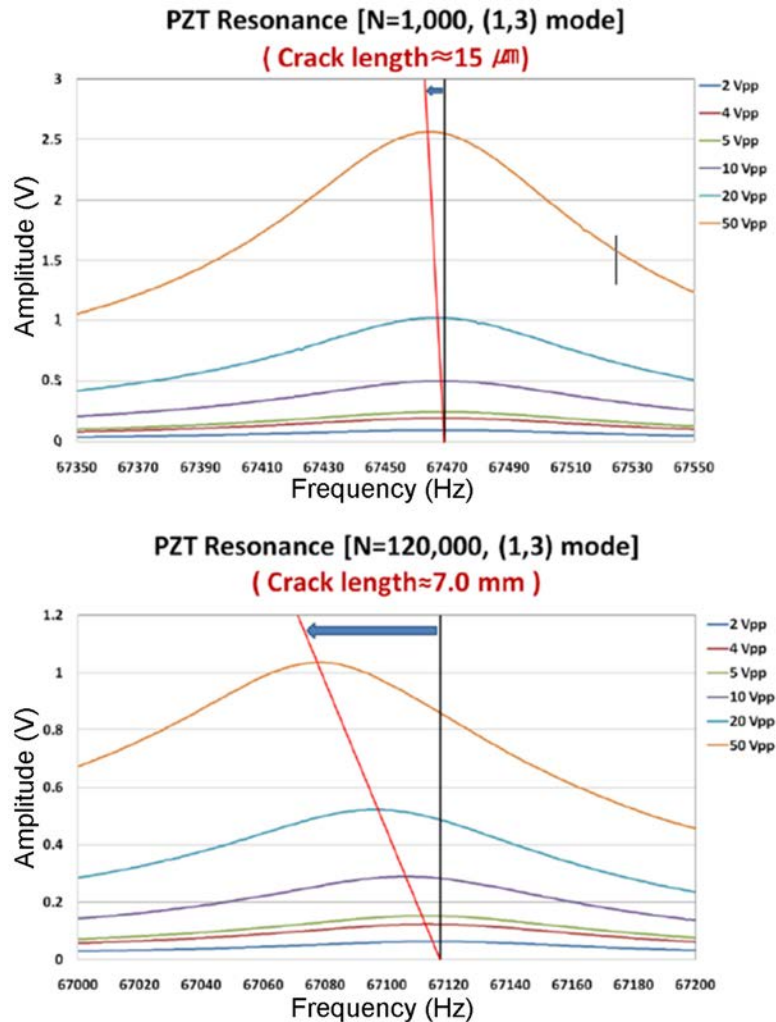


**Figure 3.18** Resonance Frequency Shift in a Compact Tension Specimen in the Early Stage of Crack Initiation (*top*) and a Compact Tension Specimen with Crack Length of 7.0 mm (*bottom*)

NRUS can be implemented by permanent mounting of piezoelectric sensors on specimen surfaces, as illustrated in Figure 3.19. Resonant peaks can be generated through application of swept frequency excitation and the resonant modes can be identified with an iterative solver that matches observed spectra with predicted spectra. A PowerPoint overview of how NRUS is implemented in PARENT can be found in Appendix C.1.1 and a more detailed description of the

implementation can be found in Appendix C.3.1. An advantage of NRUS is that it can be sensitive to very early stages of degradation like other nonlinear acoustic/ultrasonic techniques. Another advantage is that it is suitable for continuous monitoring and can monitor damage progression over an extended region without mechanical scanning of the sensors. However, physical models of nonlinear elastic responses in materials are incomplete at this stage; thus, it may be difficult to characterize damage based on a single measurement. In addition, because NRUS may be implemented to monitor over an extended region, it may be difficult to precisely locate the detected damage by NRUS.

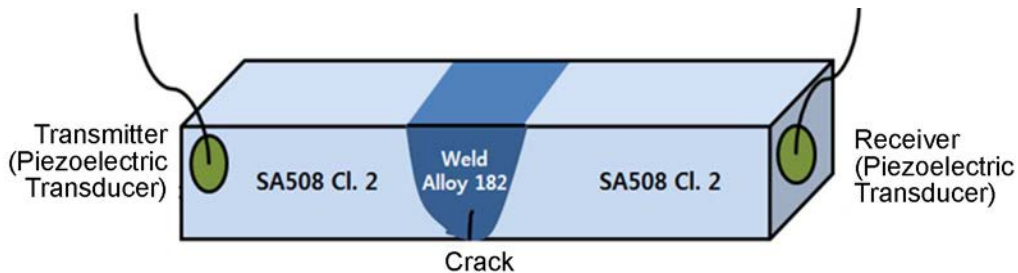


**Figure 3.19 Schematic Drawing of Possible Piezoelectric Sensor Configuration**

### 3.1.11 Guided Ultrasonic Waves

Guided ultrasonic waves (GUW) refers to an emerging class of techniques based on the propagation of low frequency acoustic/ultrasonic signals through materials. Analogous to the propagation of electromagnetic waves in bounded media, GUW are formed when the dimensions of the test material and wavelength are on similar order of magnitude or when the dimensions of the test material are much less than the wavelength of the probing acoustic/ultrasonic energy. In this regime, the interactions of the waves with material boundaries is very significant and the multiple reflecting waves constructively and destructively interfere such that new modes of propagation are generated with velocity that is dependent on component geometry, dimensions, and frequency (see Figure 3.20). This is in contrast to bulk ultrasonic wave propagation in which only two modes (longitudinal and shear) propagate through materials with a velocity that is independent of the component geometry, dimensions, and frequency. The topic of GUW is treated in multiple textbooks including the book by Rose (1999).

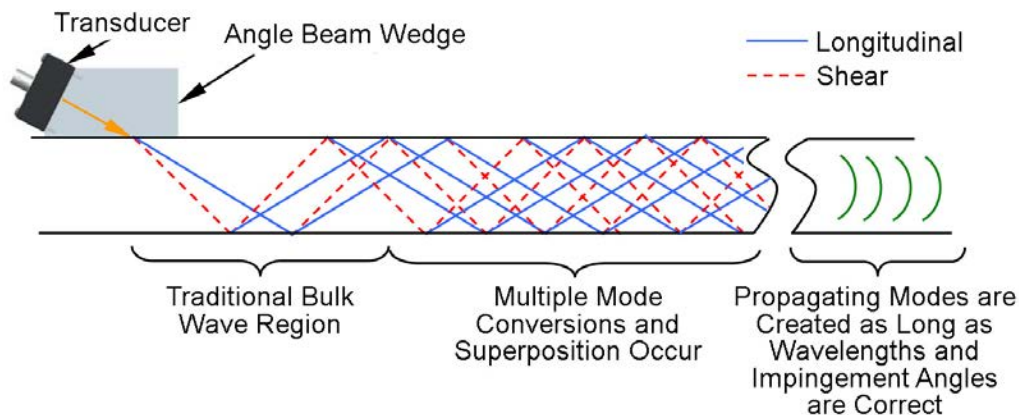


**Figure 3.20 Illustration of GUW Formation and Propagation in Test Material**

The dependence of GUV mode velocity on frequency is a phenomena known as dispersion. The design of GUV inspection procedures and the analysis of GUV data is greatly assisted by the calculation of dispersion curves for a given applications. The dispersion curves show the relationship between the phase velocity and group velocity for several modes as a function of frequency, as illustrated in Figure 3.21. Like conventional UT, it is possible to implement GUV techniques in PE or P/C mode and it can also perform both I.D. and O.D. inspections. A PowerPoint overview of how GUV was implemented in PARENT can be found in Appendix C.1.1 while a more detailed description of its implementation can be found in Appendix C.3.5.

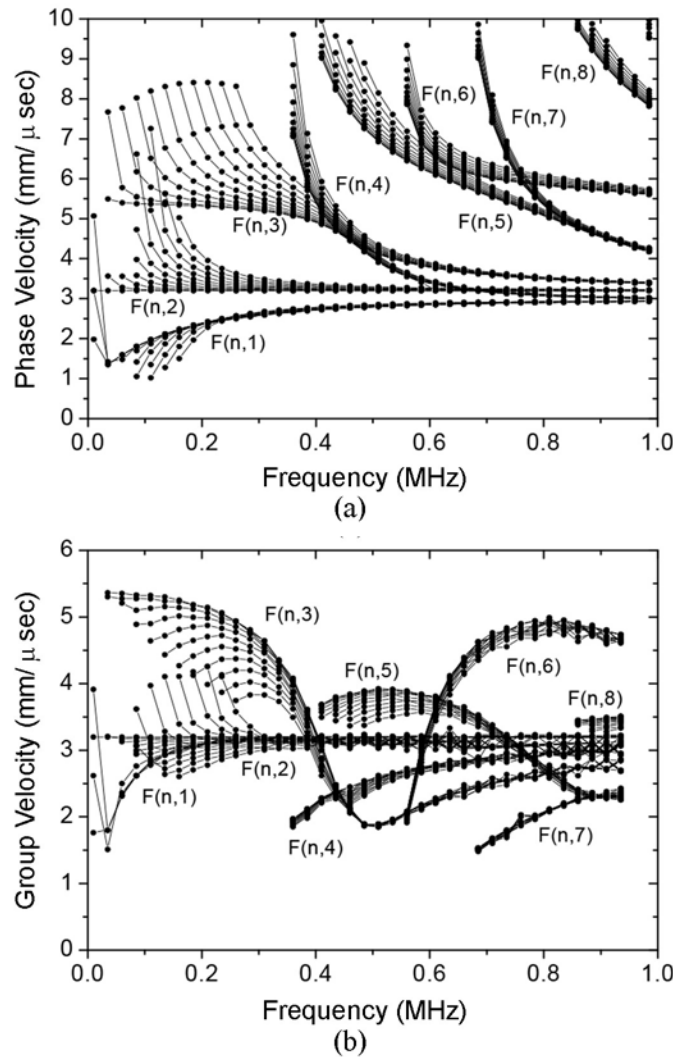


**Figure 3.21 Guided Wave Dispersion Curves on Cylindrical Coordinate: (a) phase velocity dispersion curve; (b) group velocity dispersion curve**

The first widespread application of GUV for NDE was in the long-range inspection of petrochemical pipelines for corrosion (Lowe et al. 1998). Since then, the number of GUV applications has increased, and in the nuclear power industry, GUV have been given serious consideration for the inspection of buried pipelines (EPRI 2008). These applications highlight the major benefits of GUV, which is the ability to perform fast inspections over a large distance

in test materials, and the ability to inspect regions that may be inaccessible by conventional NDE equipment. However, GUW can be complex to implement in practice, often requiring systems tailored for specific applications. In addition, the analysis of GUW signals can be complicated, especially if multiple modes are propagated in the test material simultaneously.

### 3.1.12 Laser Ultrasound Visualization

Laser ultrasound is a technique in which ultrasound is transmitted and/or received in a material, similar to a traditional piezoelectric transducer (PZT). However, laser ultrasound allows the ultrasound to be transmitted and received from a distance, and without actual physical contact with the component under testing. A laser can be used to introduce the ultrasound via thermoelastic or ablative effects in the material surface (Murray and Wagner 1999; Rose 1984). A laser system can also be used to detect ultrasound via interferometry, photo electromotive force (photo-emf) detectors, or the optical beam deflection technique (Murfin et al. 2000). The laser ultrasound visualization (LUV) technique implemented in PARENT uses PZT sensors mounted on the component at discrete locations for signal detection. A laser is raster scanned over the surface of the test component and the received signals can be mapped with the laser ultrasound generated at different points. After a complete scan, the data can be processed and displayed as a movie clip for evaluation (see Figure 3.22). A more detailed description of the proposed LUV technique can be found in Appendix C.4.4.

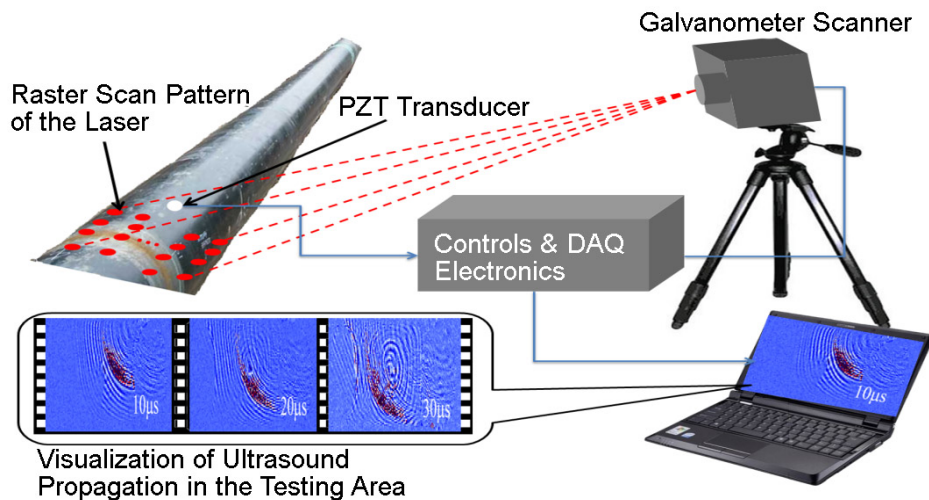


**Figure 3.22 Schematic of the Envisioned LUV System**

The obvious advantage of LUV is the stand-off mode of ultrasound generation, which can enable inspection of components that are otherwise difficult to access by more conventional means. Enhanced visualization schemes promise to make detection and characterization easier. Laser ultrasound techniques, in general, can be used to detect cracks that break the illuminated surface. However, depth sizing with laser ultrasound is more difficult and the ability of laser ultrasound to do so is undetermined. LUV is most suited for O.D. applications.

### 3.1.13 Ultrasound Infrared Thermography

Ultrasound infrared thermography (UIR) is based on the detection of thermal energy generated when elastic energy is absorbed by a defect and converted to thermal energy through thermo elastic effects. An illustration of the general concept is provided in Figure 3.23. The result is an



infrared image in the test specimen to which standard image analysis techniques may be applied to characterize defects based on temperature differences (see Figure 3.24). The main UIR techniques include pulsed, phase lock-in, or a combination of both (Dillenz et al. 2000; Maldague 2001). A PowerPoint overview of how UIR was implemented in PARENT can be found in Appendix C.1.1, while a more detailed description is provided in Appendix C.3.4.

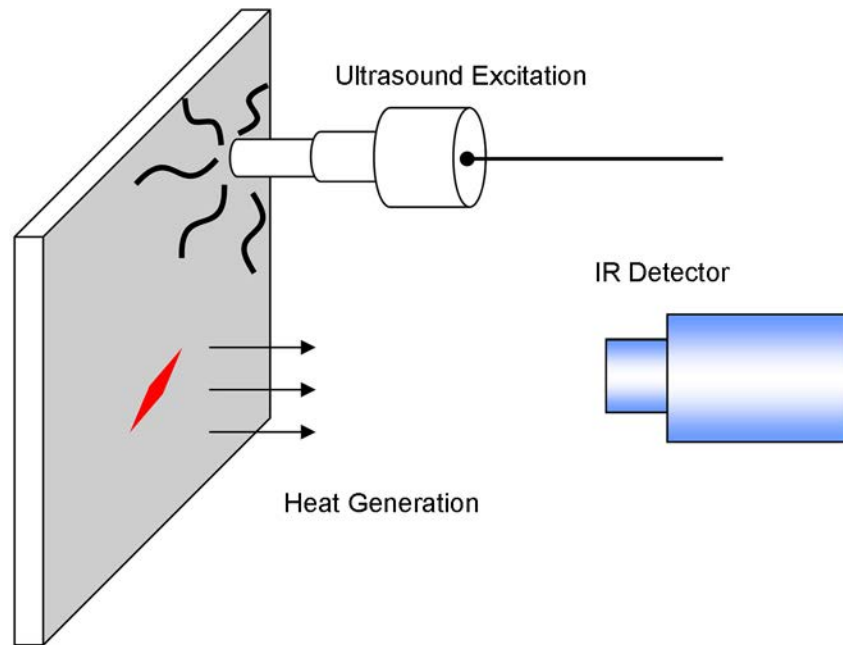


**Figure 3.23 Illustration of the UIR Concept**

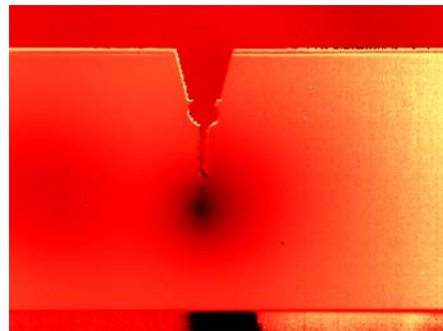


**Figure 3.24 UIR Image of a Test Specimen with Crack**

With lock-in phase UIR, amplitude and phase information about the thermal waves emitted from the specimen is preserved for several frequencies. The advantage of this is that it enables characterizing the depth of a source of thermal emissions within the test component. With pulsed phase lock-in thermography, broadband thermal signals arriving at each pixel of an infrared detector camera are analyzed using Fast Fourier Transform analysis. The advantage of UIR is that it potentially enables more rapid examination of large areas based on camera images in contrast to techniques that would require a point-by-point raster scan. The technique is significantly more sensitive to cracks on the visually accessible surface (normally O.D).

surface). The potential disadvantage of the technique is that it requires a low thermal noise background so that flaws could be imaged reliably.

### **3.2 Eddy Current Techniques**

Overview descriptions for eddy current techniques employed in the open testing portion of PARENT are provided in this section including a description of exciter-pickup eddy current techniques, which refer to eddy current techniques that employ a coil for generating an excitation field and separate sensor to detect perturbations in the field because of flaws. This contrasts with conventional ECT in which the same coil may be used for both field excitation and detection. The controlled excitation eddy current technique (CEECT) is also a variant of the pulsed excitation eddy current technique (PECT) but is described separately here because the probe is configured specifically to enhance its ability for characterizing deep flaws. Finally, overview descriptions for the orthogonal coil eddy current technique (OCECT) and PECT is included. In addition to CEECT, PECT can be distinguished from conventional ECT in that it is often implemented for the purpose of characterizing flaws in the depth dimension.

#### **3.2.1 Exciter-Pickup Eddy Current Techniques**

In practice, an eddy current probe consists of one or more coils with the axis alignment most often perpendicular or parallel to the inspection surface normal. An alternating current source is applied to the one or more coils, generating magnetic fields. These magnetic fields induce eddy currents in the conducting materials when the probe is positioned nearby (see Figure 3.25). Flaws and defects in the test material impede the flow of eddy currents manifesting as a change in the measurable eddy current coil impedance. An important parameter for eddy current testing is the skin depth,

$$\delta = \sqrt{\frac{1}{\pi f \sigma \mu}} \quad (3.2)$$

which provides a measure of the depth to which eddy current fields can penetrate in a test material. As can be seen from Eq. (3.2), this quantity depends on the coil frequency,  $f$ , and electrical conductivity,  $\sigma$ , of the test material ( $\mu$  is the magnetic permeability). Thus, in metal components, the depth of penetration is usually small and the eddy current technique is often limited to surface examinations. Multi-coil techniques include separate coils for the generation of eddy current fields in the test material and for detection of the fields at the surface, as illustrated in Figure 3.26. These types of probes may also be referred to as reflection probes, driver-pickup, exciter-pickup, or send-receive probes. This contrasts with conventional ECT in which the same coil is used for both field generation and for signal reception. In PARENT, two teams applied basic multi-coil techniques. A PowerPoint overview of how one of the techniques was implemented in PARENT can be found in Appendix C.1.4, while a more detailed description can be found in Appendix C.4.1. A PowerPoint overview of how the second technique (referred to as the advanced ECT technique [AECT]) was implemented can be found in Appendix C.1.2, and a more detailed description of how AECT was implemented in PARENT can be found in Appendix C.5.7.

The advantage of eddy current techniques over ultrasonic techniques is that they are usually more sensitive to small defects and the probes do not require coupling to the test material surface. As noted, a significant disadvantage of eddy current techniques is that they are often relegated to surface inspections and are not very useful for characterizing the depth of flaws

beyond 1 or 2 mm. In addition, the increased sensitivity of ECT can make it more prone to false calls from the pick-up of signals from superficial surface imperfections (such as scratches) and ECT techniques can be sensitive to lift-off variations and variations in material conductivity.

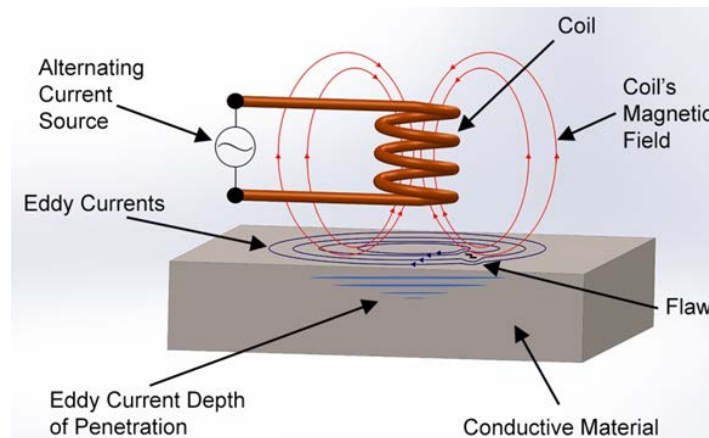


**Figure 3.25** Depiction of a Single Coil Eddy Current Probe with an Alternating Current Excitation, Induced Magnetic Fields, and Induced Eddy Currents. Disturbance of eddy current flow can be caused by existence of a defect.

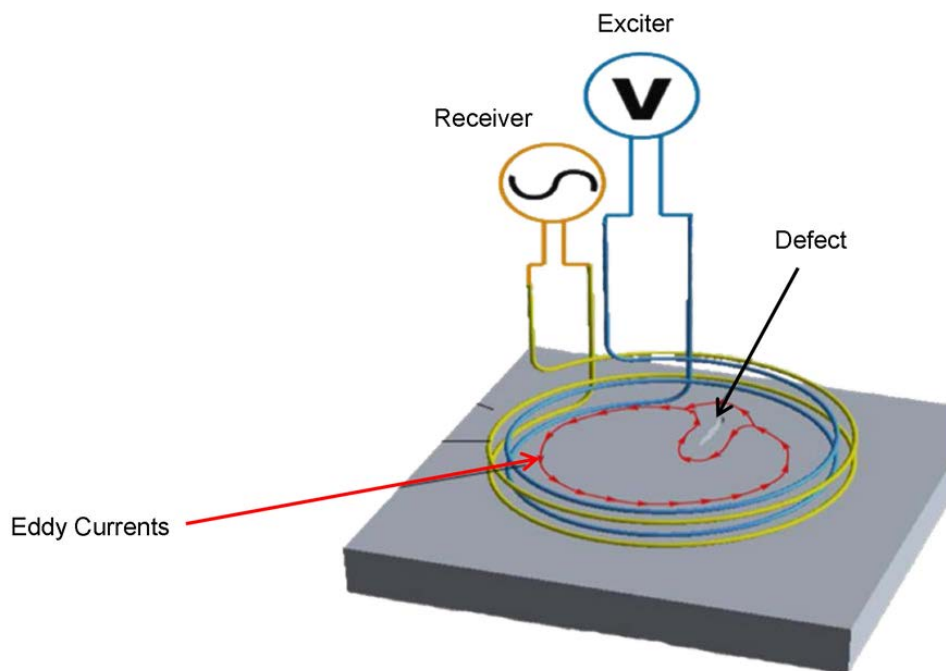


**Figure 3.26** Schematic Illustration of an Eddy Current Probe with Separate Coils for Field Excitation and for Signal Detection

### 3.2.2 Controlled Excitation ECT

Controlled excitation eddy current (CEECT) is another type of exciter-pickup technique with coils configured so that eddy current response can be correlated with crack depth, even for deep cracks. In particular, the probe is designed such that the phase response shows

correlation with depth for deep cracks, as illustrated in Figure 3.27. A schematic of the particular CEECT probe implementation for PARENT is provided in Figure 3.28. This particular probe has two exciter coils oriented with their axes perpendicular to the test surface normal and a pick-up sensor is located between the two exciter coils. A PowerPoint overview of CEECT and how it was implemented in PARENT is included in Appendix C.1.2, and a more detailed description of its implementation can be found in Appendix C.5.8.

The phase response of the CEECT to deep cracks is a significant advantage of CEECT over other eddy current techniques. However, the phase response is also dependent on other flaw parameters such as length, cross section, etc. More information is needed to fully understand the effects of other flaw parameters on the phase response. In addition, the footprint of the CEECT can be quite large, because the pick-up sensor must be separated sufficiently from the exciter coils. This may limit the ability to deploy the technology on component regions with poor accessibility.

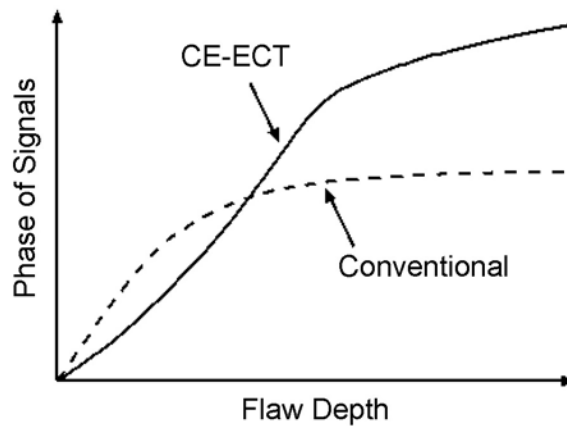


**Figure 3.27** Illustration Showing that the Phase Response of CEECT has a Significant Correlation to Flaw Depth over a Large Range of Flaw Depth Values, Including for Deep Cracks

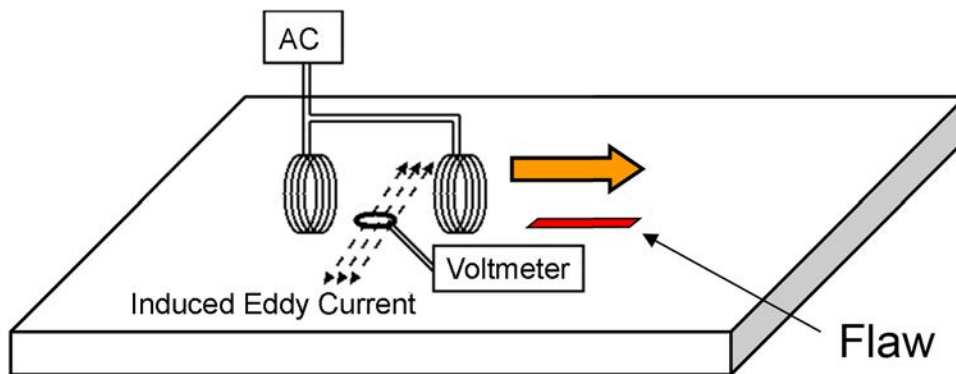


**Figure 3.28** Illustration of the CEECT Probe for Measuring the Depth of Flaws

### 3.2.3 Orthogonal Coil Array Eddy Current Technique

The orthogonal coil array eddy current technique (OCECT) was implemented in PARENT using a commercial eddy current probe with an array of orthogonal coil pairs. The single orthogonal coil pair configuration has also been referred to as “plus-point” because when viewed from the test piece the intersecting orthogonal coils look similar to a plus sign (Figure 3.29). The OCECT technique is a differential eddy current technique meaning that the output of one coil is referenced to the output of the other coil. Differential eddy current probes are typically less sensitive to lift-off and surface irregularities. One advantage of OC-ECT is that it has directional sensitivity to flaws, making it possible to distinguish between axial and circumferential defects. The orthogonal coil configuration helps minimize the influence of flaw orientation with respect to the probe performance as defects that are parallel to the current flow can be missed. Rotation of the OCECT probe can also be performed to further minimize the influence of flaw orientation. A PowerPoint overview of how OCECT was implemented in PARENT can be found in Appendix C.1.2, and a more detailed description of its implementation can be found in Appendix C.5.6.

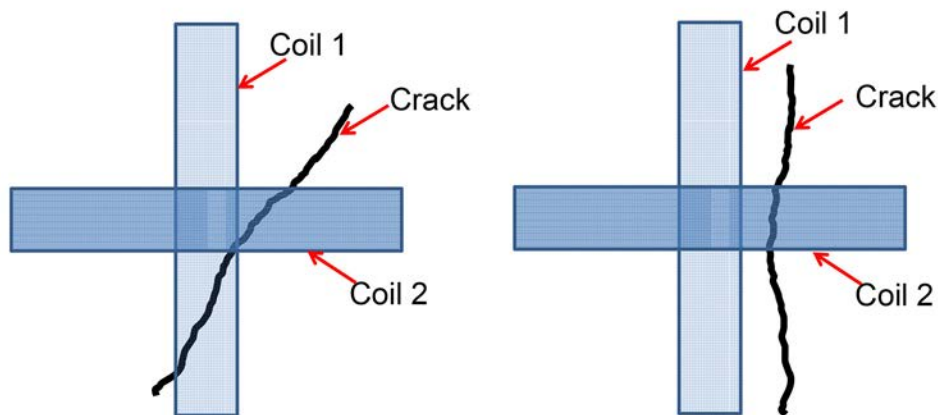


**Figure 3.29 Illustration of Orthogonal Coil Pair and Relative Orientation to Surface Crack Profiles**

### 3.2.4 Pulsed Excitation Eddy Current Technique

Pulsed excitation eddy current technique (PECT) is an eddy current technique that relies on low duty cycle pulse excitations (Lebrun et al. 1997). This contrasts with most ECT concepts, which are based on continuous sinusoidal wave excitation at a single frequency (see Figure 3.30). The low duty cycle pulse results in a wide frequency band excitation field that allows deeper penetration into a test component owing to the lower frequency components (up to 30 mm) (Lee et al. 2012). The penetration depth can be tuned by changing the duty cycle of these pulses, with wider pulses containing stronger low-frequency components (Abidin et al. 2009). Besides the ability to penetrate significant depth, PECT has other advantages over conventional ECT techniques such as lower power consumption and the ability to generate a richer set of data. However, the instrumentation used to drive pulsed sources can be more complex than for a conventional ECT system. In addition the interpretation of PECT signals can require considerable expertise. A PowerPoint overview describing how PECT was implemented in PARENT can be found in Appendix C.1.1. A more detailed description of how PECT was implemented in PARENT can be found in Appendix C.3.2.

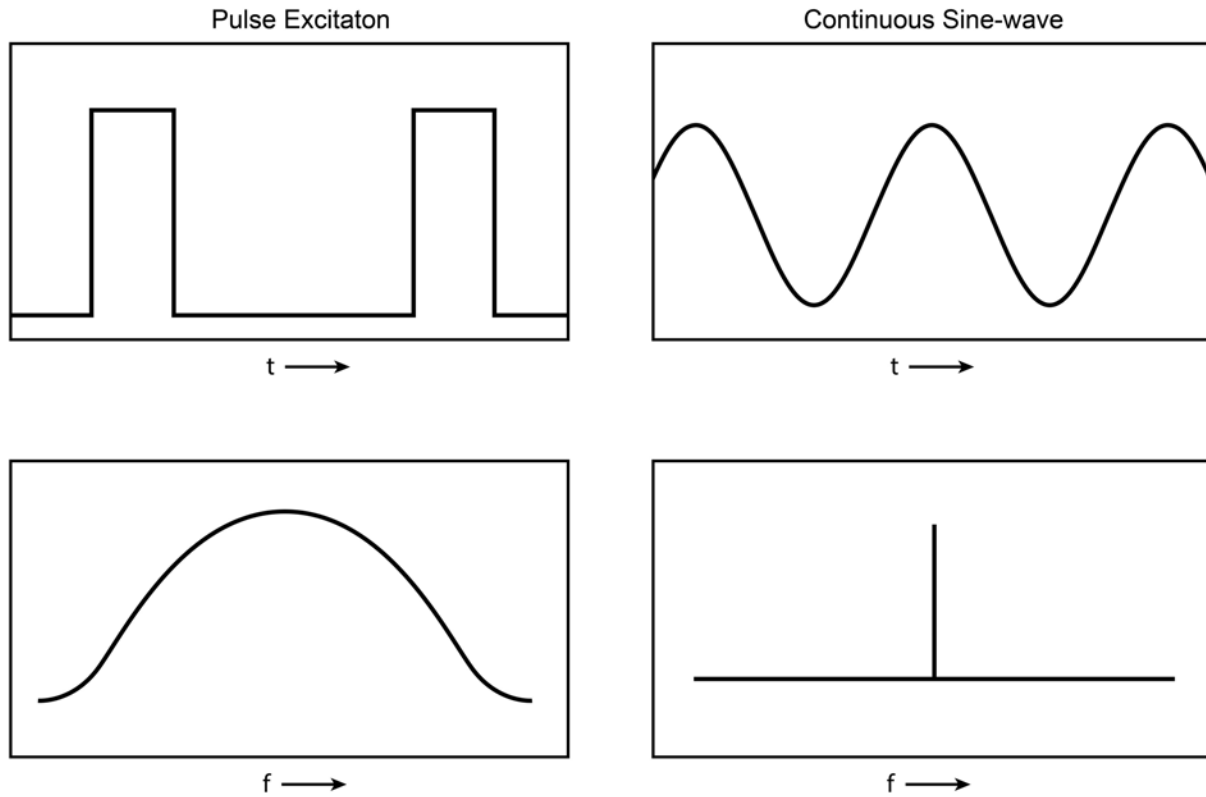


**Figure 3.30 Comparison of Pulsed Excitation for PECT (*left*) to Continuous Sine-Wave Excitation for Conventional ECT (*right*) and Illustration of the Frequency Spectrum Associated with Each Type of Excitation Source**

### 3.3 Other Techniques

This section describes other techniques implemented in the open testing portion of PARENT and includes the microwave near field microscopy technique and radiographic techniques.

#### 3.3.1 **Microwave Near Field Microscope**

Microwave near field microscope (MM) is an electromagnetic NDE technique that is based on sensing impedance changes as a result of the obstruction of surface excitation currents from discontinuities. In this respect, MM is similar to ECT, but operates at much higher frequencies such that the electromagnetic field does not penetrate the surface. Whereas ECT may operate approximately from 0.1 to 10 MHz, MM may be performed in a frequency range from approximately 1 GHz to over 100 GHz (Zoughi and Kharkovsky 2008). MM sensing is based on open-ended waveguides in which the standing wave pattern in the waveguide will change in response to the terminating impedance. Thus, when the tip of an MM probe is placed near a conducting surface and a surface-breaking discontinuity disrupts the flow of currents, it represents a change in the terminating impedance and will alter the standing wave pattern (see Figure 3.31).

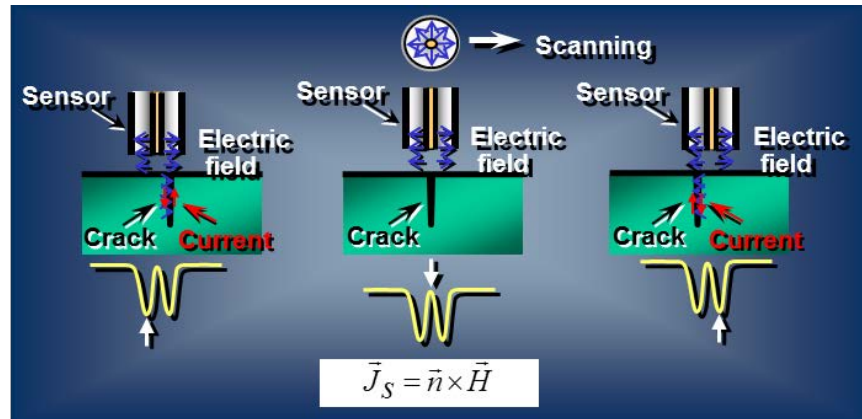


**Figure 3.31 Illustration of the MM Technique for Crack Detection**

Zoughi and Kharkovsky (2008) describe two types of interactions through which MM can not only indicate crack detection, but also provide information about crack width and depth. In dominant mode interaction (for instance, transverse electromagnetic mode), MM is performed primarily by observing the perturbations in the dominant mode as a result of interactions with surface-breaking discontinuities. In addition to affecting the dominant mode, the presence of cracks will result in the generation of higher order modes. Thus, MM can be used to characterize flaws based on both the analysis of dominant mode perturbations and higher order mode generations. MM is able to detect very tight cracks and is able to sense cracks that may be masked by layers of paint or corrosion products. Similar to conventional ECT, MM is primarily a surface inspection technique, although its ability to characterize the width and depth of flaws sets it apart from conventional ECT. A PowerPoint overview of how MM was implemented in PARENT is provided in Appendix C.1.2, and a more detailed description of its implementation can be found in Appendix C.5.9.

### 3.3.2 Radiography Techniques

A radiographic inspection system uses a source of radiation (x-rays or gamma rays) to irradiate the specimen under test. X- or gamma rays penetrate the specimen, and are absorbed, scattered or otherwise attenuated when passing through the material. A detector of some form is used to collect and record the transmitted rays as illustrated in Figure 3.32. Several different sources are available (with different energy levels) (Halmshaw 1987) enabling the inspection of specimens with different thicknesses. The inspection itself requires a balance between the source energy, source-to-specimen distance, source-to-detector distance, and exposure time. Conventional radiographic inspection requires access to both sides of the specimen, with the source and detector placed on either side of the test specimen. The quality of the radiographs is usually determined through the use of image quality indicators (IQI) or penetrameters. Details on radiographic inspection, along with information on the choice of IQI devices, may be found in several publications, for instance Cartz (1995).

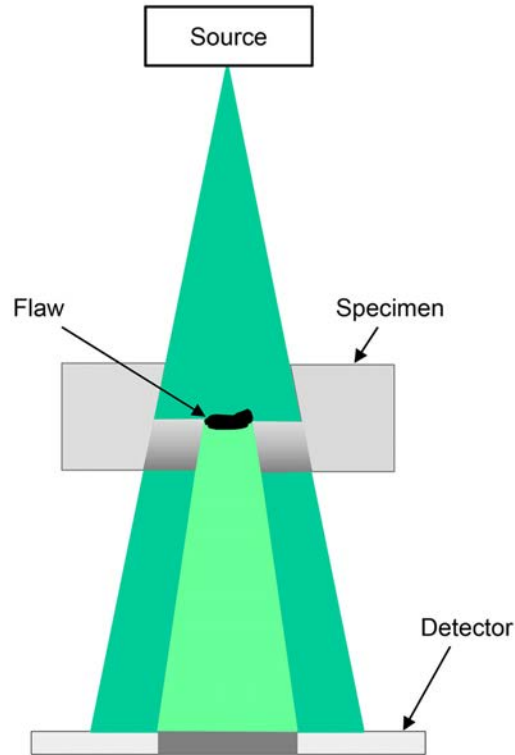


**Figure 3.32 Illustration of a Radiographic Examination and Interaction of Source X-rays with Density Discontinuities such as Flaws**

In conventional radiography, the location and orientation of the specimen is fixed relative to the source and detector location. The result is a radiograph where the orientation of any flaws is fixed with respect to the source and detector locations. The effectiveness of conventional radiography techniques for inspection of planar flaws is especially sensitive to the flaw orientation (see Figure 3.33). An alternative approach is to subject each region on the specimen to multiple radiographic inspections. Each inspection is performed with the specimen oriented at a different angle relative to the source and/or detector. While this technique improves the information on flaws (potentially enabling better detection and through-wall sizing), the approach tends to have higher costs. A common variation on this approach is computed tomography (CT), where multiple view angles are used, and the resulting two-dimensional data combined to create 3D images of the specimen. Typically, CT scans require a computer-controlled scanner system to obtain precision control of view angles (Ewert et al. 2007). A description of how radiography techniques were implemented in PARENT can be found in the Appendices C.2.7 and C.2.8.



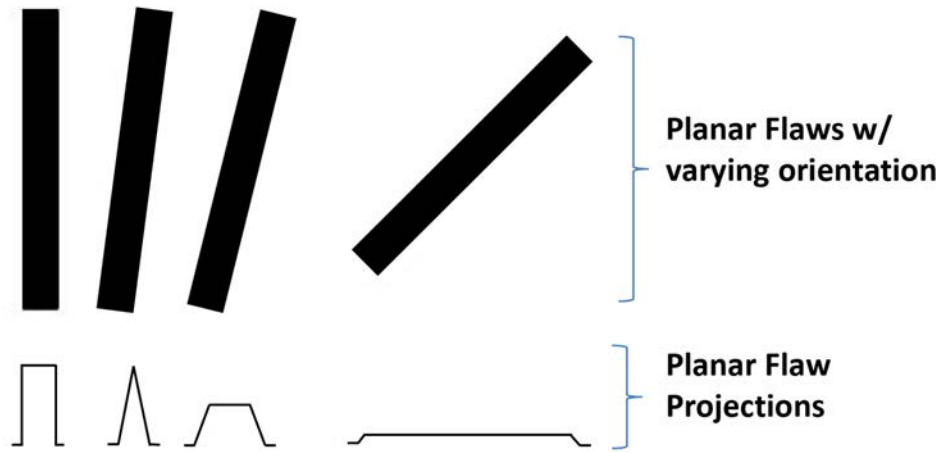


**Figure 3.33** Illustration Depicting the Sensitivity of Conventional Radiography Signal to Planar Flaw Orientation



## 4 DATA OVERVIEW

This section provides information on what data was recorded and reported during PARENT open round-robin testing and how the data is analyzed. Section 4.1 provides a description of data reporting by describing the datasheets used to record and report test data. Section 4.2 provides an overview summary of inspection records collected, and Section 4.3 describes how procedures are categorized in procedure type categories. Finally, Section 4.4 includes a discussion of how data is analyzed.

### 4.1 Data Reporting

This section provides an example of the completed data forms for one inspection. In this inspection, Team 12 has inspected test block P89 using Procedure 12.1. Procedure 12.1 uses three techniques in the inspection, identified as ET400kHz, TOFD.Ax, and TOFD.Circ. Consequently, this inspection generates three Technique Datasheets, and one Inspection Summary Datasheet. Illustrations of Technique Datasheets and an Inspection Summary Datasheet are provided in Figures 4.1 through 4.3. Information in the Inspection Summary Datasheet is based on data recorded in Technique Datasheets. For the example provided, techniques TOFD.Ax and TOFD.Circ are used for depth sizing and characterization while technique ET400kHz is used for detection, length sizing, and positioning. This information is combined in completion of the Inspection Summary Datasheet. Similar data fields are included in Technique Datasheets and Inspection Summary Datasheets. A summary of descriptions for all of the data fields is provided in Table 4.1. Figures 4.1 through 4.3 show that datasheets include a table where information about each observed indication is recorded. The information includes a series of coordinates (X1, X2, Y1, Y2, Z1, Z2) that describe a cuboid that envelopes an observed indication, allowing for comparison of its position and size to true-state information for both detection and sizing analysis. In addition, fields "Ymax/Xmax," "Amp dB," and "Surface Breaking" are included to allow recording of the location where a maximum signal response is observed, the value of that signal, and whether or not an observed indication is surface-breaking.

**Table 4.1 Definitions of Data Fields for “Technique Datasheets” and “Inspection Summary Datasheets”**

Field Name	Description
Procedure ID	This has format of Team-ID.seq-no and uniquely identifies this procedure in the round robin test. This ID originates from the Procedure Summary Data Sheet that describes this technique.
Team ID	This is a unique number assigned to each participating team in the test to maintain anonymity.
Tech ID	This is a unique alpha-numeric identifier assigned to each technique on the data form. This ID originates from the Procedure Summary Data Sheet and identifies the technique being applied.
Inspection ID	This ID identifies each unique inspection performed. One inspection ID is common to all inspections made on a specific test block, by a specific test team, for all the Technique IDs applied within a specific Procedure ID. Format: Team-id.Block-id.seq-no.
Test Block ID	ID of the test block being inspected.
Access	This field indicates if access is obtained from I.D. or O.D. If access is from both sides, “I.D. and O.D.” can be entered.
Date	Date of inspection
Detection	This field should contain “yes” if at least one of the techniques in the procedure is able to detect flaws. Otherwise, it should contain “no.”
Length Sizing	This field should contain “yes” if at least one of the techniques in the procedure is able to length size flaws. Otherwise, it should contain “no.”
Depth Sizing	This field should contain “yes” if at least one of the techniques in the procedure is able to depth size flaws. Otherwise, it should contain “no.”
Weld Volume Inspected	Coordinates of the volume of material inspected.
Defect No.	Uniquely identifies each observed indications
X1, X2, Y1, Y2, Z1, Z2	These coordinates describe a cuboid that contains the observed indication.
$Y_{max}/X_{max}$	This identifies the location at which a maximum signal is observed.
Amp dB	The amplitude of the signal observed at $Y_{max}/X_{max}$ is recorded here.
Surface Breaking	Indicate whether or not a flaw is surface breaking.
Comments	To include useful information about each indication found.

PARENT RRT- DMW TECHNIQUE Data Sheet										
Procedure ID:12.1					Tech ID: ET400Hz					
Inspection ID:12.P89.1					Access:ID					
Test Block ID:P89					Date:2010/01/01					
Team ID:12										
					Weld Volume Inspected					
Detection:yes					X1:0		X2:457			
Length Sizing:yes					Y1:-31		Y2:20			
Depth Sizing:no					Z1:0		Z2:68			
Defect No	X1 mm	X2 mm	Y1 mm	Y2 mm	Z1 mm	Z2 mm	$Y_{max}$ mm	Amp dB	Surface Breaking	Comments
1	230.2	235.5	-11	1	NA	NA	NA	NA	yes	
2	215.2	218.2	-12	5	NA	NA	NA	NA	yes	

PARENT RRT- DMW TECHNIQUE Data Sheet										
Procedure ID:12.1					Tech ID: TOFD.Ax					
Inspection ID:12.P89.1					Access:ID					
Test Block ID:P89					Date:2010/01/01					
Team ID:12										
					Weld Volume Inspected					
Detection:no					X1:0		X2:457			
Length Sizing:no					Y1:-31		Y2:20			
Depth Sizing:yes					Z1:0		Z2:68			
Defect No	X1 mm	X2 mm	Y1 mm	Y2 mm	Z1 mm	Z2 mm	$Y_{max}$ mm	Amp dB	Surface Breaking	Comments
1	227.4	229.9	-12	-1	50.3	68.2	-6	-14	yes	
2	226.4	225.4	-11	2	51.7	68.2	-5	-12	yes	
3	224.8	227.7	-10	1	48.2	68.2	-3	-19	yes	
4	226.3	226.5	-12	1	50.3	68.2	-2	-16	yes	

Figure 4.1 Technique Datasheets for Techniques ET400Hz and TOFD.Ax for Fictitious Inspection 12.P89.1

PARENT RRT- DMW TECHNIQUE Data Sheet											
Procedure ID:12.1					Tech ID: TOFD.Circ						
Inspection ID:12.P89.1					Access:ID						
Test Block ID:P89					Date:2010/01/01						
Team ID:12											
Detection: <i>no</i>					Weld Volume Inspected			X1:0			X2:457
Length Sizing: <i>no</i>					Y1:-31			Y2:20			
Depth Sizing: <i>yes</i>					Z1:0			Z2:68			
Defect No	X1 mm	X2 mm	Y1 mm	Y2 mm	Z1 mm	Z2 mm	$Y_{max}$ mm	Amp dB	Surface Breaking	Comments	
1	219.8	220.6	-8	-1	62.5	68.2	-4	-8	yes		
2	233.0	234.2	-10	1	58.4	68.2	-8	-7	yes		

Figure 4.2 Technique Datasheet for Technique TOFD.Circ for Fictitious Inspection 12.P89.1

PARENT RRT-DMW INSPECTION SUMMARY Data Sheet											
Inspection ID:12.P89.1					Procedure ID:12.1						
Test Block ID:P89					Date:2012/01/01						
Team ID:12					Access: ID						
Detection: <i>yes</i>					Weld Volume Inspected			X1:0			X2:457
Length Sizing: <i>yes</i>					Y1:-31			Y2:20			
Depth Sizing: <i>yes</i>					Z1:0			Z2:68			
Defect No	X1 mm	X2 mm	Y1 mm	Y2 mm	Z1 mm	Z2 mm	$Y_{max}$ mm	Amp dB	Surface Breaking	Comments	
1	230.2	235.5	-11	1	48.2	68.2	-3	-19	yes	Detection: Tech-ID ET400kHz Length: Tech ID ET400kHz Depth: Tech-ID TOFD.Ax	
2	#	#	#	#	#	#	#	#	entry	As was done for flaw 1, data could be entered for flaw 2	

Figure 4.3 Inspection Summary Datasheet for Fictitious Inspection 12.P89.1

## 4.2 Records Collection Overview Summary

The number of inspection summary datasheets collected (equivalent to the number of inspections) for each block type (i.e., BMIs, LBDMWs, SBDMWs, FBs) is tabulated in Table 4.2 according to procedure ID. Procedure ID is expressed here as “Tech.TeamID” where Tech represents the type of technique used for a given procedure ID. The possible techniques are described in Section 3. Table 4.3 breaks down the number of inspections by access type (i.e., O.D. vs. I.D.) for BMIs, SBDMWs, LBDMWs, and FBs test blocks for each procedure type classification. Table 4.4 tabulates the number of inspections by flaw type and Table 4.5 tabulates number of inspections by flaw orientation. Flaw orientation is considered axial if the axial dimension of the flaw is 3x the circumferential dimension or greater. Flaw orientation is considered circumferential if the circumferential dimension of the flaw is 3x the axial dimension or greater. If neither of these criteria is met, the flaw is classified as diagonal. In this case, the term diagonal is used to distinguish from axial and circumferential orientation and reflect that the flaw does not have a dominant orientation in the axial or circumferential direction based on dimensions. Only two flaws were classified as diagonal based on this criterion—one flaw in BMI test block P22 and another flaw in BMI test block P7.

## 4.3 Procedure Type Categorization

Individual procedures can be organized into procedure type categories. For instance, procedures PAUT.20 and PAUT.122 can be classified as PAUT procedure types. In PARENT open testing, the majority of procedures can be classified as PAUT or advanced PAUT (ADVPAUT) procedures. The next largest procedure type is ECT. Several procedures included in the ECT procedure type category could be considered advanced ECT techniques. However, due to the limited amount of data, conventional ECT and advanced ECT procedure types are combined into a single procedure type category. A diagram illustrating procedure type categories and how procedures are classified by procedure type categories for the purpose of data analysis is included in Figure 4.4.

## 4.4 Scoring Procedure Used for PARENT Open Testing

The same scoring procedure was utilized in PARENT open testing as was used in PARENT blind testing and in PINC, which is described in Section 4.1 of NUREG/CR-7019 (Cumblidge et al. 2010). Although detection performance is not analyzed for open test data, scoring was required to associate indications to flaws for sizing analysis purposes. A tolerance was added to flaw true-state dimensions to limit systematic positioning error resulting in legitimate detections being classified as misses. Once the tolerance is defined,  $\delta X$  and  $\delta Y$ , then the flaw cuboid,  $X_1, X_2; Y_1, Y_2; Z_1, Z_2$ , becomes,

$$(X_1 - \delta X, X_2 + \delta X, Y_1 - \delta Y, Y_2 + \delta Y, Z_1, Z_2) \quad (4.1)$$

An illustration of tolerance applied to flaw true-state (solid red) dimensions is provided in Figure 4.5 resulting in an enlarged region represented by white space with a red border. Indications that intersect any portion of this enlarged region are classified as hits. Tolerance values of  $\delta X = \delta Y = 10$  mm were utilized, which is consistent with PARENT blind testing and PINC. An illustration of an indication plot is provided in Figure 4.6. The red rectangles represent the “true-state” (actual flaws) with the surrounding tolerance box. Indications are shown as empty rectangles.

**Table 4.2 Number of Inspection Summary Records by Procedure and Test Block Type**

	BMIs	LBDMWs	SBDMWs	FBs
AECT.33	2	2	1	8
CEECT.5.1	1	0	2	0
CEECT.5.2	0	1	0	0
ECT.16	2	1	3	7
ECT.7	4	0	0	0
GUW.21	1	0	1	0
HHUT.27.1	0	0	2	0
HHUT.27.2	0	0	0	8
HHUT.30	0	0	0	3
LASH.18	0	1	1	5
LUV.170	6	0	4	0
MM.28.1	1	3	3	0
MM.28.2	0	0	0	5
NRUS.11	0	0	0	3
PAATOFD.29.0	0	4	2	0
PAATOFD.29.1	0	4	0	16
PAATOFD.29.2	0	1	0	16
PATP.29	0	4	2	0
PATRT.22	0	0	0	1
PAUT.114	0	0	3	7
PAUT.122.1	0	0	0	7
PAUT.122.2	0	0	0	7
PAUT.131.1	0	0	0	7
PAUT.131.2	0	0	3	0
PAUT.131.4	0	0	1	0
PAUT.150	0	2	0	0
PAUT.20	0	0	1	6
PAUT.7	0	2	0	0
PECT.11	0	0	0	3
RT.109	0	0	0	6
RT.112	0	0	1	3
SAFT.17	0	4	2	8
SHPA.6.1	0	0	1	1
SHPA.6.2	0	0	1	0
SHPA.6.3	0	0	0	4
UIR.20	0	0	0	6
UT.104	0	0	1	8
<b>TOTAL</b>	<b>17</b>	<b>29</b>	<b>35</b>	<b>145</b>



**Table 4.3 Number of Inspection Summary Records for Procedure Types and Block Types by Access**

	BMI	LBDMWs I.D.	LBDMWs O.D.	SBDMW I.D.	SBDMW O.D.	FB I.D.	FB O.D.
ADVPAUT	0	5	12	0	6	16	25
ADVPAUT, NLUT	0	0	1	0	3	0	10
ECT	9	4	0	6	0	15	3
GUW	1	0	0	0	1	0	0
LUV	6	0	0	0	4	0	0
MM	1	3	0	3	0	5	0
NLUT	0	0	0	0	2	3	11
PAUT	0	2	2	0	8	2	32
RT	0	0	0	0	1	0	9
UIR	0	0	0	0	0	0	6
UT	0	0	0	0	1	0	8
TOTAL	17	14	15	9	26	41	105

ADVPAUT = advanced phased-array ultrasonic testing; NLUT = nonlinear ultrasonic testing

**Table 4.4 Summary of Number of Flaw Observations (NOBS) for Different Flaw Types in Each Test Block Type**

	BMI	FB	LBDMW	SBDMW	TOTAL
EDM	18	28	83	24	153
LOB/LOF	0	0	11	0	11
MFC	0	52	0	0	52
SC	41	0	126	300	467
SCC	0	216	26	0	242
SI	0	0	11	0	11
TFC	31	0	0	124	155
TOTAL	90	296	257	448	1091

**Table 4.5 Summary of Number of Flaw Observations (NOBS) by Flaw Orientation in Each Test Block Type**

	BMI	FB	LBDMW	SBDMW	TOTAL
A	40	0	140	150	330
C	16	296	117	298	727
Vol	34	0	0	0	34
TOTAL	90	296	257	448	1092

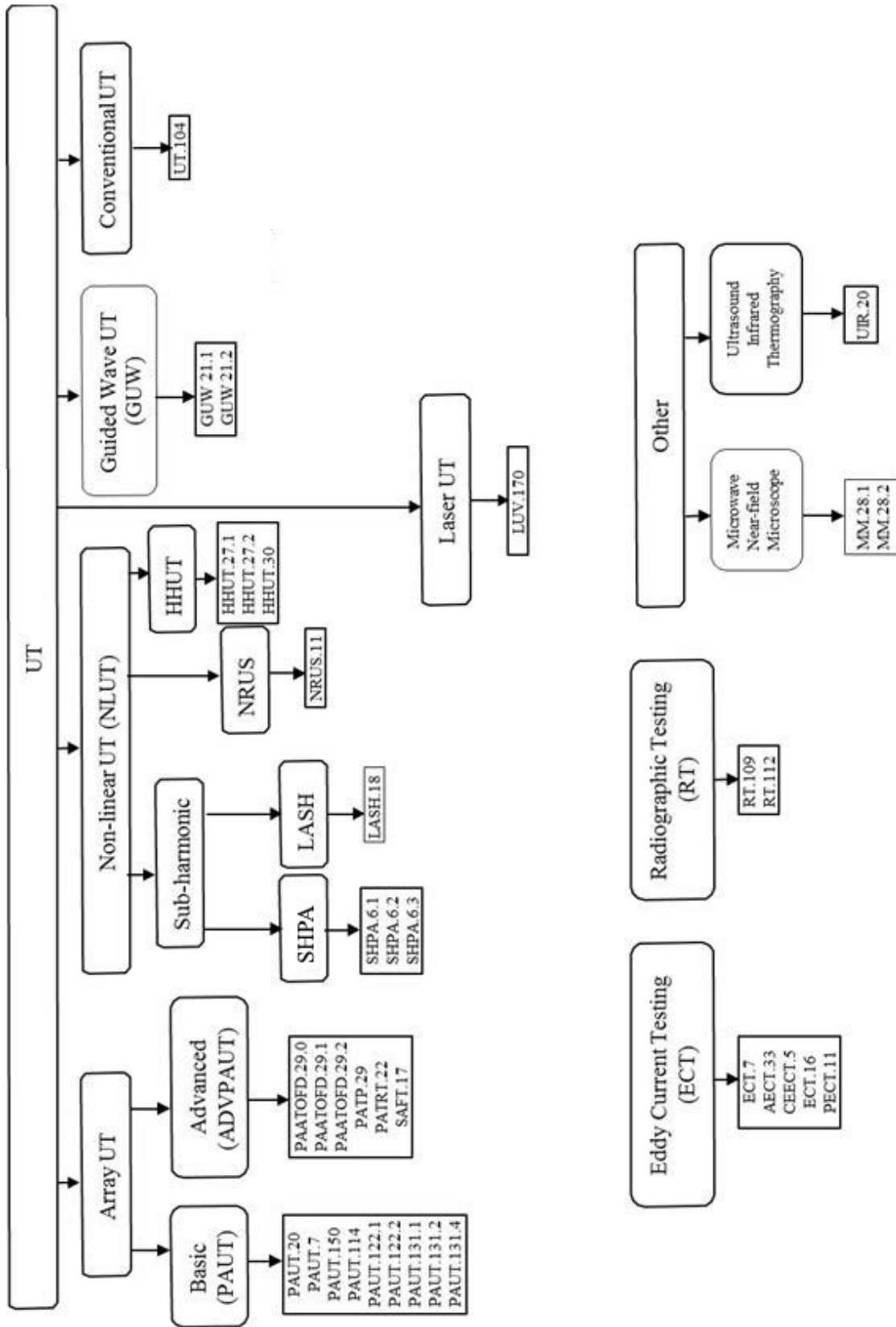
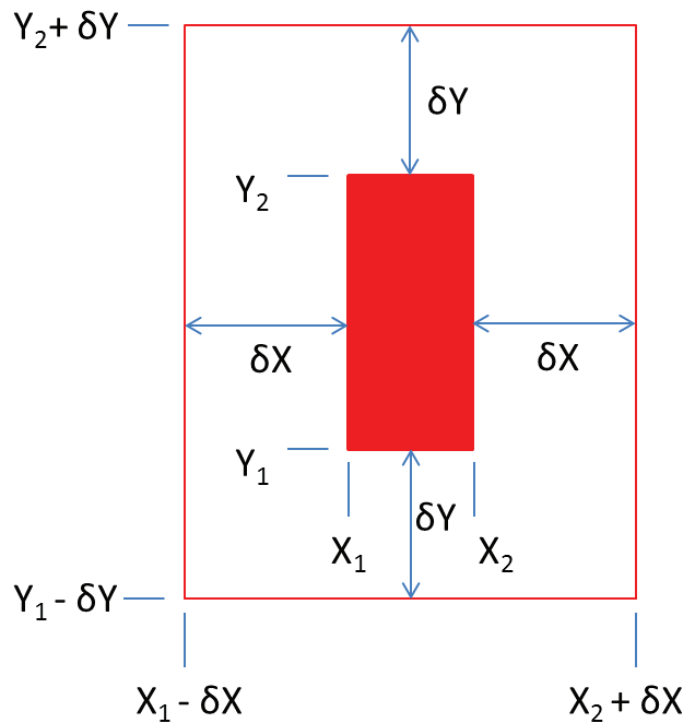
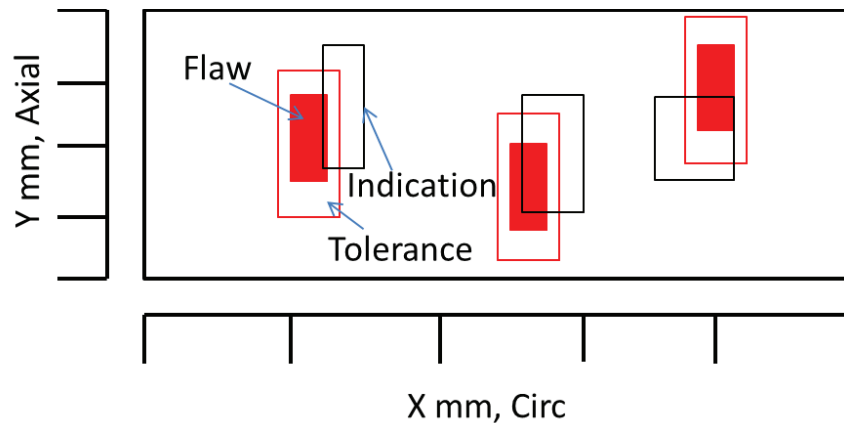


Figure 4.4 Diagram Illustrating How Procedures are Classified by Procedure Types for Data Analysis Purposes



**Figure 4.5 Illustration of Tolerance ( $\delta X$  and  $\delta Y$ ) Applied Flaw True-State (in red) Dimensions for the Purpose of Scoring in PARENT**



**Figure 4.6 Depiction of Indication Plot Illustrating 2-D Representation of Test Block. The red filled rectangles represent the true-state (actual flaws), while red empty rectangles surrounding the flaws depict the scoring tolerance. Indications are shown as black empty rectangles.**

#### **4.5 Substitution for X1, X2, Y1, and Y2 Indication Fields**

For some open testing inspections, X1, X2, Y1, and Y2 fields were not populated because a procedure may have only been assessed for depth sizing and the location of flaws was known. An example is provided in Figure 4.7 for LASH.18 examination of P1. To facilitate depth sizing analysis, the X1, X2, Y1, and Y2 fields were populated with the values for the true state. This

was necessary so that the data in the Z1 and Z2 fields for the indications would be correlated to the correct flaw. The indication plots appear as Figure 4.8 and Figure 4.9 in this scenario. As Figure 4.8 shows, the indication and flaw dimensions (X1, X2, Y1, and Y2) are identical. A collection of indication plots for all of the open inspections performed in PARENT is included in Appendix H.

74 DMW Summary Sheet

### PARENT RRT -- DMW INSPECTION SUMMARY Data Sheet

Inspection ID:   
TeamID.BlockID.SeqNo

Test Block ID:   
p<number>

Team ID:   
number

Detection:

Length Sizing:

Depth Sizing:

Comments

Procedure ID:   
TeamID.SeqNo

Access:

Start Date:    
yyyy/mm/dd

End Date:    
yyyy/mm/dd (optional)

Weld Volume Inspected

X1:  mm    X2:  mm  
 Y1:  mm    Y2:  mm  
 Z1:  mm    Z2:  mm

Technique Data Sheets

New

18.p1.1-1

18.p1.1-2

Procedure Sheets

New

ProcedureSheet\_18.1

Defect No	X1 mm	X2 mm	Y1 mm	Y2 mm	Z1 mm	Z2 mm	Ymax mm	Amp db	sbreak	Comments
1					32.0	38.1	na	36	yes	Positions of transducer
2					21.2	36.0	na	32	yes	Positions of transducer
3					14.0	38.1	na	52	yes	Positions of transducer
4					25.0	36.0	na	32	yes	Positions of transducer

**Figure 4.7 Inspection Summary Datasheet for Inspection of Test block P1 by Procedure LASH.18 showing unpopulated X1, X2, Y1 and Y2 fields**

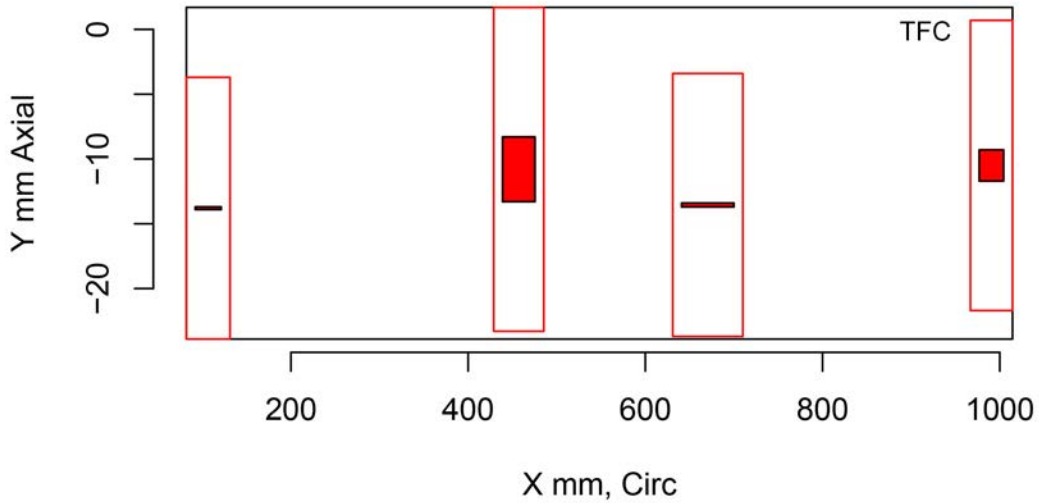


**Figure 4.8** Indication Plot for Procedure LASH.18 Applied to Test Block P1 in PARENT Open Testing (X – Y view)

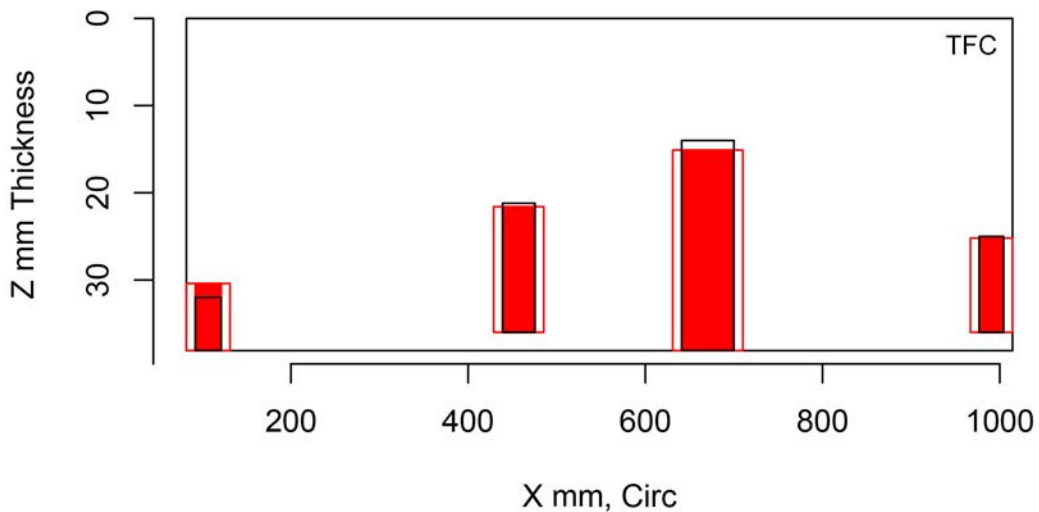


**Figure 4.9** Indication Plot for Procedure LASH.18 Applied to Test Block P1 in PARENT Open Testing (X – Z view)

#### **4.6 Multiple Indications Associated with One Flaw**

In a few cases, multiple indications may intersect the region bounded by the tolerance box for the same flaw as illustrated in Figure 4.10. For these scenarios, it is necessary to select one of the indications for performing the sizing analysis. The selection is based on the indication with the largest intersecting area with the tolerance region. To accommodate indications that may have no width defined in one dimension (i.e., X or Y), and thus have no area, the tolerance is divided between the flaw and the indications with values of  $\delta X/2$  and  $\delta Y/2$  (refer to Figure 4.5). This is illustrated in Figure 4.11. The indication whose tolerance boundaries form the largest region of intersection with the area defined by the flaw tolerance boundaries is selected as the indication to associate with the flaw for sizing analysis purposes.

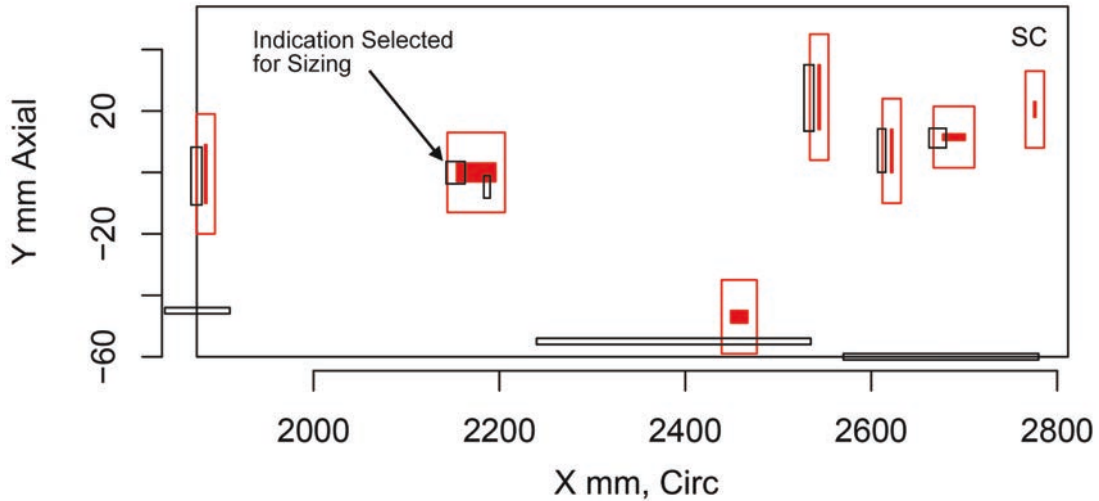


**Figure 4.10 Indication Plot Illustrating Two Indications Intersecting the Region Bounded by the Tolerance Box**

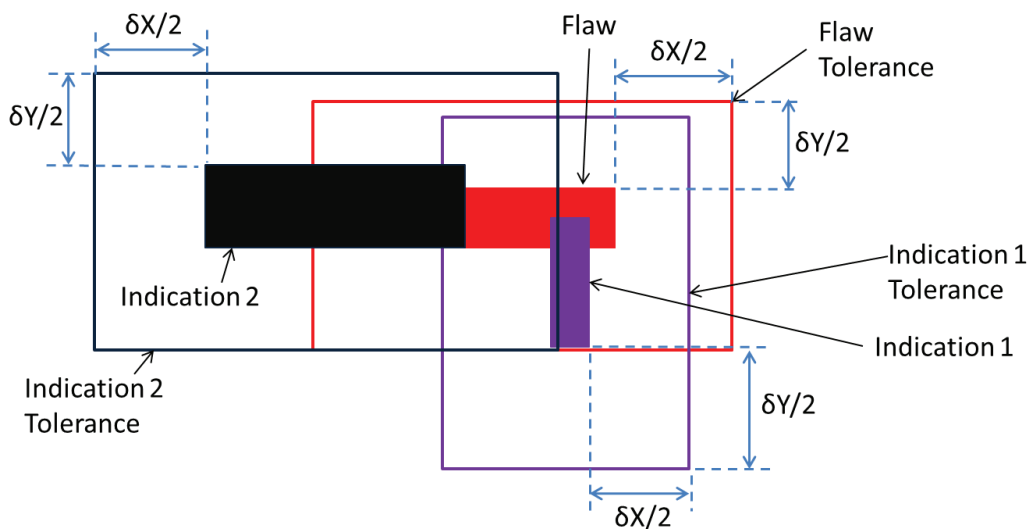


**Figure 4.11 Illustration of Tolerance Divided Between Flaw and Multiple Indications Intersecting the Region Bounded by the Flaw Tolerance Box**

#### **4.7 Analysis of PARENT Open Round Robin Data**

PARENT used the same scoring criteria as PINC, which is described in Section 4.1 of NUREG/CR-7019 (Cumblidge et al. 2010). However, probability of detection is not emphasized for open test data as teams were provided with true-state information for flaws prior to performing measurements. Linear regression was used to analyze sizing data (depth and length) in PARENT Open testing. An error relation between the measured and true sizes of the flaws is defined by the following regression formula:

$$M_i = B1 + B2 \times T_i + E_i \quad (4.2)$$

where  $M_i$  represents the measured size associated with flaw  $i$   
 $T_i$  represents the true size of flaw  $i$   
 $E_i$  represents the measurement error in sizing flaw  $i$

B1 and B2 are the regression parameters usually associated with the Y intercept and slope of the linear regression. Ideal performance for sizing would occur when  $B1 = 0$ ,  $B2 = 1$ , and  $E_i = 0$ . To compare two different regression fits, and to order a set of regression fits (from most accurate to least accurate as an example), the metric of root mean square error (RMSE) is used. RMSE is a statistic that summarizes the three deviations of regression analyses from their respective ideals. RMSE is defined by

$$RMSE^2 = \frac{\sum_i (M_i - T_i)^2}{n} \quad (4.3)$$

where all the variables are the same as in the preceding descriptions and  $n$  is the total number of measurements. RMSE can also be represented in terms of bias and standard deviation as

$$RMSE^2 = bias^2 + StDev^2. \quad (4.4)$$

In this formula, standard deviation is represented with the variable  $StDev$ . The bias and  $StDev$  represent systematic and random components to the error and are calculated with the following formulas,

$$bias = \frac{\sum_i (M_i - T_i)}{n}, \quad (4.5)$$

$$StDev = \sqrt{\frac{\sum_i [(M_i - T_i) - bias]^2}{n}}. \quad (4.6)$$

The length of an indication is determined by the maximum of its circumferential and axial dimensions. While this is adequate for most of the inspections, this definition of length lead to counterintuitive results for procedure HHUT.27 inspection of test block P1. The indication plot for this inspection is provided in Figure 4.12. The indications in Figure 4.12 have axial dimensions that are greater than their circumferential dimensions. However, the flaws are circumferentially oriented. In this case, the sizing algorithm compares the axial dimension of the indication to the circumferential dimension in the analysis of length sizing error.

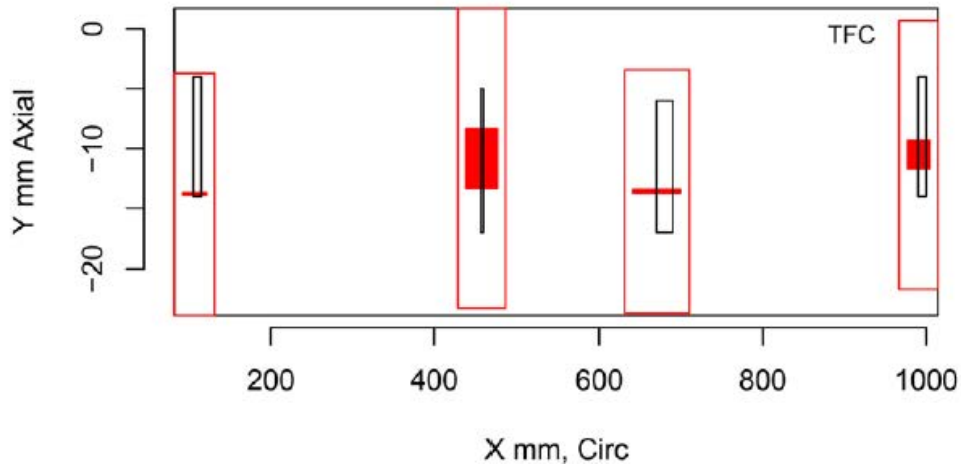


**Figure 4.12 Indication Plot for Procedure HHUT.27 Inspection of Test Block P1**

An example of a sizing regression curve is provided in Figure 4.13 for length sizing performed on flaws in LBDMW test blocks from the O.D. surface for ADVPAUT procedure types. The dark line represents the regression fit while the red dashed lines above and below the regression fit are the 95% confidence intervals. In this case, the “A’s” represent the axial flaw data points and “C” is used to represent circumferential flaw data points.

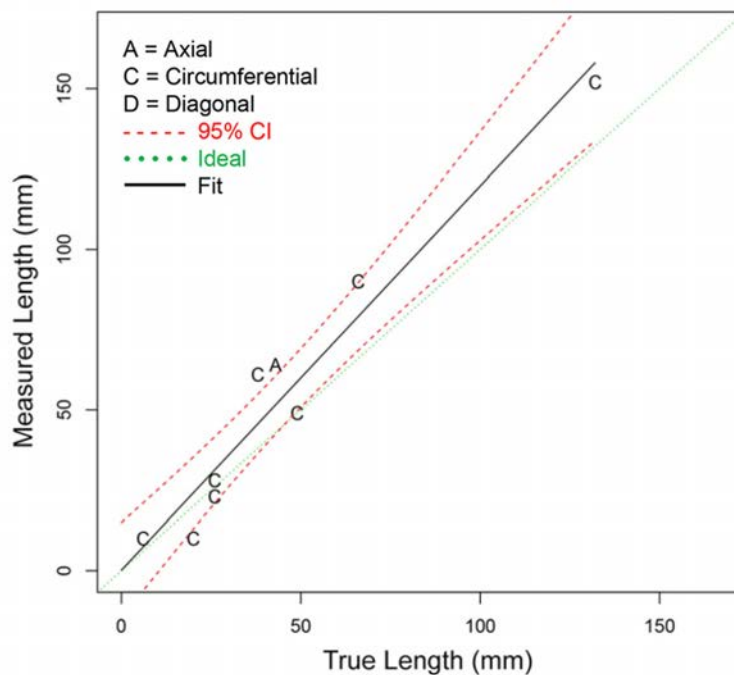


**Figure 4.13 Length Sizing Regression for ADVPAUT Procedures on LBDMW Test Blocks in PARENT Open Testing (O.D. access)**

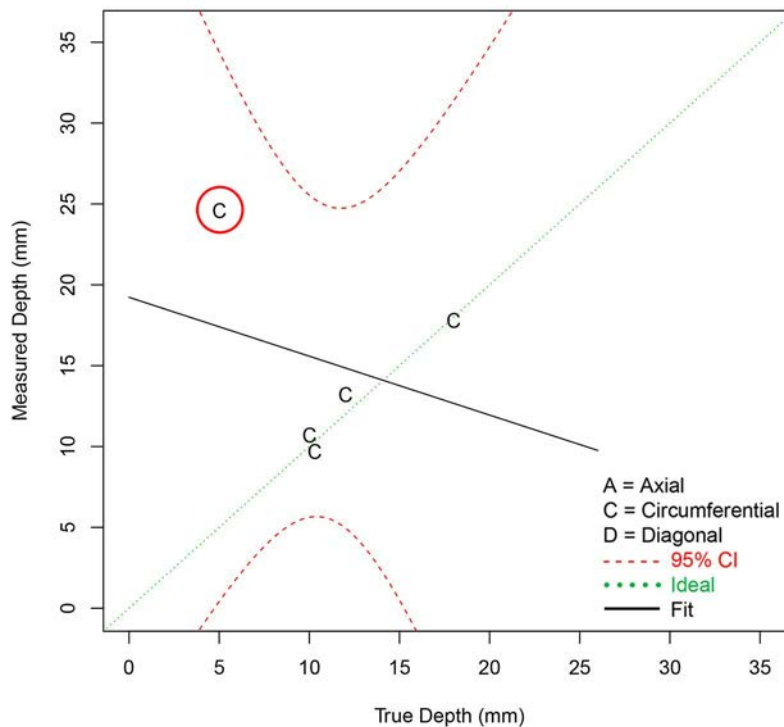
The sizing analysis was performed by an algorithm that was implemented in an automated fashion and generally combined data for axially and circumferentially oriented flaws. In addition, outliers were not analyzed in detail and were not removed from the analysis. However, the



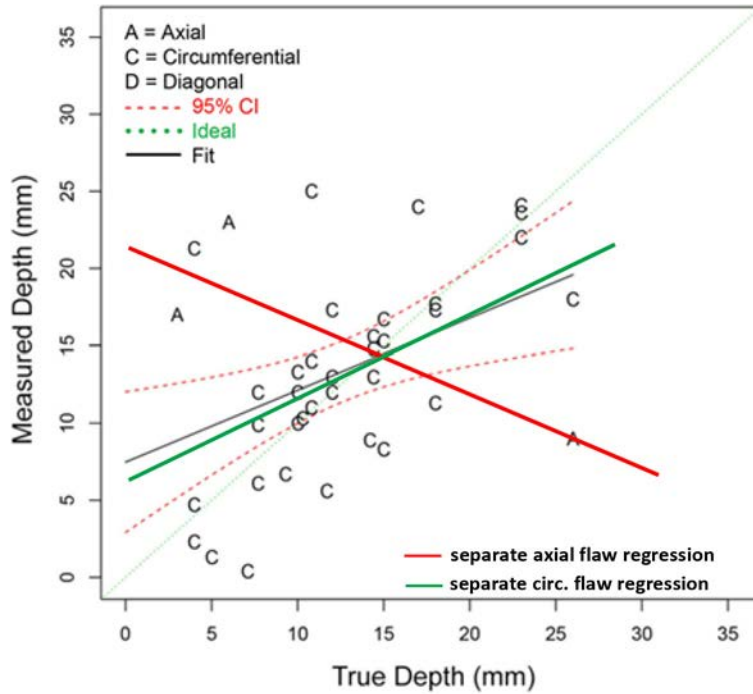
objective of open testing was in establishing basic capability of techniques to justify further development and more detailed assessments of performance. Thus, only approximate measures of depth and length sizing performance were sought in open testing. Some specific sizing examples are provided below to illustrate the consequences of these analyses decisions and to emphasize to the reader to interpret the results of sizing analysis cautiously. The data provided by the sizing analysis was meant to serve as a rough assessment of performance capability, and was not intended to provide a precise measure of performance capability.

Figure 4.14 shows a regression curve for the depth sizing performance of procedure PAUT.131.1 applied to SBDMW test blocks and FB test blocks with a negative slope. This result is most likely an artifact of an outlier datapoint, which is circled in red. If the outlier datapoint were removed, the slope of the regression line would likely be positive. Another example provided in Figure 4.15 shows a positive regression fit to circumferential and axial flaw datapoints for NLUT procedures applied to SBDMW and FB test blocks. Red and green lines are superimposed to illustrate that the regression fits to circumferential and axial flaw datapoints would be much different. In this case, it is apparent that the axial datapoints would have resulted in a negatively sloped curve.

In addition, for some presentations of sizing results, plots such as Figure 4.16 are provided. In this case, no regression fit is displayed because four data points are required to provide a fit for the model in Eq. (4.2).



**Figure 4.14** Depth Sizing Regression (in mm) for Procedure PAUT.131.1 on SBDMW Test Blocks in PARENT Open Testing (O.D. access – w/ FB test blocks)



**Figure 4.15** Depth Sizing Regression for NLUT Procedures on SBDMW Test Blocks in PARENT Open Testing (O.D. access – w/ FB test blocks)

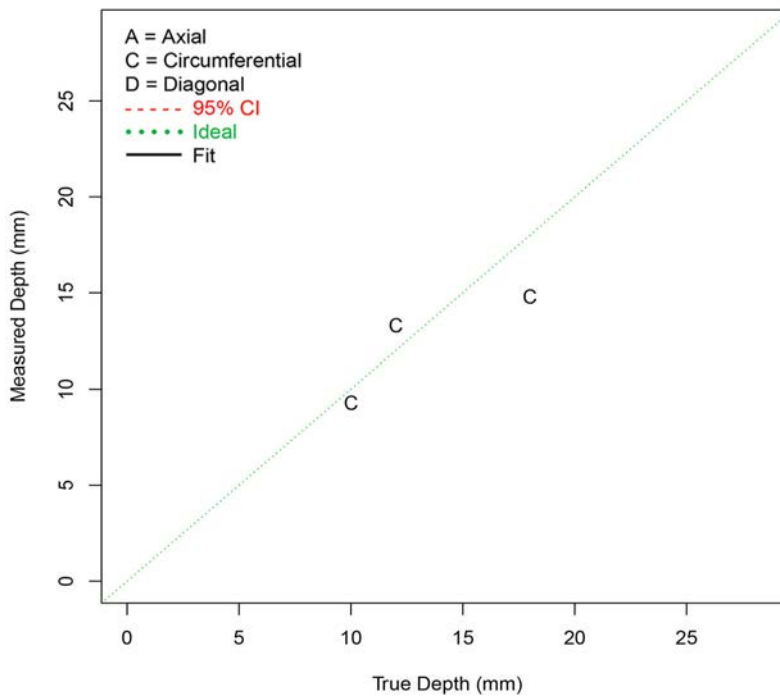


**Figure 4.16** Depth Sizing Regression (in mm) for Procedure HHUT.30 on SBDMW Test Blocks in PARENT Open Testing (I.D. access – w/ FB test blocks)

## 5 DATA ANALYSIS RESULTS

This section presents the results of data analysis performed for open test data collected in PARENT. The primary data analysis performed includes depth sizing analysis and length sizing analysis. Section 5.1 includes the depth sizing analysis results for DMW test blocks, including LBDMWs and SBDMWs and FB test blocks. The results are presented separately for O.D. and I.D. access of LBDMWs and SBDMWs, and where relevant, SBDMW results are presented with (w/) and without (w/o) FB data. In some cases, data is presented just for FB test blocks. Tabulated summaries of depth sizing results for procedure types and individual procedures are included in Section 5.1. Plots of regression curves for depth sizing data from ADVPAUT, NLUT, PAUT, RT, UIR, and conventional UT procedure types are included in Sections 5.1.1 through 5.1.6, respectively. Section 5.2 summarizes length sizing results for DMWs, again presenting results separately for LBDMW and SBDMW test blocks, and according to test block access. In this case, FB test block data is not included in the length sizing analysis because flaws extend the full width of FB test blocks. Tabulated summaries of length sizing results for procedure types and individual procedures are included in Section 5.2. Plots of regression curves for length sizing data from ADVPAUT, NLUT, PAUT, conventional UT, ECT, and MM procedure types are included in Sections 5.2.1 through 5.2.6, respectively. Finally, BMI results are summarized in Section 5.3, consisting of the results of length sizing analysis of inspections conducted from the J-groove weld surface.

### 5.1 DMW Depth Sizing Results

The results of depth sizing analysis are summarized in this section by tabulating RMSE and Bias for procedures and procedure types. The table column heading “NOBS” refers to the number of observations, which represents the number of depth size measurements. Tabulated summaries of depth sizing results for procedure types applied to SBDMW and FB test blocks by O.D. access are included in Tables 5.1 through 5.3 for SBDMW test blocks with FB test blocks, only SBDMW test blocks, and only FB test blocks, respectively. Table 5.4 includes the same summary for procedure types with I.D. access, which is only relevant to FB test blocks. Finally, depth sizing summaries for procedure types applied to LBDMW test blocks are included in Tables 5.5 and 5.6 for O.D. and I.D. access, respectively.

**Table 5.1 Depth Sizing Results for Procedure Types Applied to SBDMW Test Blocks with O.D. Access w/ FB Test Blocks**

	NOBS	Bias (mm)	RMSE (mm)
ADVPAUT	57	2.7	5.3
NLUT	38	0.7	6.7
PAUT	79	0.3	3.4
RT	14	-0.2	2.0
UIR	6	1.0	3.4
UT	11	-0.0	2.1
All	205	1.0	4.6

**Table 5.2 Depth Sizing Results for Procedure Types Applied to SBDMW Test Blocks with O.D. Access w/o FB Test Blocks**

	NOBS	Bias (mm)	RMSE (mm)
ADVPAUT	36	2.5	5.5
NLUT	21	0.7	7.7
PAUT	47	-0.1	2.4
RT	6	0.2	2.2
UT	4	-0.4	3.2
All	114	0.9	4.8

**Table 5.3 Depth Sizing Results for Procedure Types Applied to SBDMW Test Blocks with O.D. Access (only FB test blocks)**

	NOBS	Bias (mm)	RMSE (mm)
ADVPAUT	21	3.2	5.0
NLUT	17	0.7	5.2
PAUT	32	0.9	4.5
RT	8	-0.5	1.8
UIR	6	1.0	3.4
UT	7	0.2	0.9
All	91	1.2	4.4

**Table 5.4 Depth Sizing Results for Procedure Types Applied to SBDMW Test Blocks with I.D. Access (only FB test blocks)**

	NOBS	Bias (mm)	RMSE (mm)
ADVPAUT	14	2.0	3.1
NLUT	3	-0.9	2.0
PAUT	2	-0.5	1.2
All	19	1.3	2.8

**Table 5.5 Depth Sizing Results for Procedure Types Applied to LBDMW Test Blocks with O.D. Access**

	NOBS	Bias (mm)	RMSE (mm)
ADVPAUT	36	2.0	9.1
NLUT	1	-1.1	1.1
PAUT	3	2.9	5.1
All	40	2.0	8.7

**Table 5.6 Depth Sizing Results for Procedure Types Applied to LBDMW Test Blocks with I.D. Access**

	NOBS	Bias (mm)	RMSE (mm)
ADVPAUT	8	2.3	6.7
PAUT	8	-1.4	5.2
All	16	0.4	6.0

The tabulation of depth sizing results for individual procedures is provided in Tables 5.7 through 5.12. The summary for individual procedures applied to SBDMW test blocks and FB test blocks with O.D. access is provided in Table 5.7. Table 5.8 provides a summary for SBDMW test blocks without FB test blocks with O.D. access and Table 5.9 provides a summary for FB test blocks with O.D. access. Table 5.10 provides a summary for SBDMW test blocks with ID access, while Tables 5.11 and 5.12 provide depth sizing summaries for individual procedures applied to LBDMW test blocks with O.D. and I.D. access, respectively.

**Table 5.7 Depth Sizing Results for Procedures Applied to SBDMW Test Blocks with O.D. Access w/ FB Test Blocks**

	NOBS	Bias (mm)	RMSE (mm)
HHUT.27.1	9	3.2	11.1
HHUT.27.2	7	3.1	7.1
LASH.18	9	-1.7	3.3
PAATOFD.29.0	13	0.8	4.6
PAATOFD.29.1	7	3.6	5.5
PAATOFD.29.2	7	3.9	5.8
PATP.29	9	2.4	6.6
PAUT.114	26	0.2	2.8
PAUT.122.1	7	0.4	0.9
PAUT.122.2	7	-0.0	1.1
PAUT.131.1	5	4.1	8.8
PAUT.131.2	16	0.3	0.6
PAUT.131.4	8	-0.1	0.4
PAUT.20	10	-0.6	5.4
RT.109	5	-0.3	2.1
RT.112	9	-0.1	1.9
SAFT.17	21	3.3	4.8
SHPA.6.1	5	1.6	1.9
SHPA.6.2	4	-5.2	5.4
SHPA.6.3	4	1.0	1.4
UIR.20	6	1.0	3.4
UT.104	11	-0.0	2.1
All	205	1.0	4.6

**Table 5.8 Depth Sizing Results for Procedures Applied to SBDMW Test Blocks with O.D. Access w/o FB Test Blocks**

	NOBS	Bias (mm)	RMSE (mm)
HHUT.27.1	9	3.2	11.1
LASH.18	4	0.0	1.0
PAATOFD.29.0	13	0.8	4.6
PATP.29	9	2.4	6.6
PAUT.114	19	0.2	3.3
PAUT.131.2	16	0.3	0.6
PAUT.131.4	8	-0.1	0.4
PAUT.20	4	-3.1	3.7
RT.112	6	0.2	2.2
SAFT.17	14	4.0	5.4
SHPA.6.1	4	1.8	2.1
SHPA.6.2	4	-5.2	5.4
UT.104	4	-0.4	3.2
All	114	0.9	4.8

**Table 5.9 Depth Sizing Results for Procedures Applied to SBDMW Test Blocks with O.D. Access (only FB blocks)**

	NOBS	Bias (mm)	RMSE (mm)
HHUT.27.2	7	3.1	7.1
LASH.18	5	-3.0	4.3
PAATOFD.29.1	7	3.6	5.5
PAATOFD.29.2	7	3.9	5.8
PAUT.114	7	0.1	0.8
PAUT.122.1	7	0.4	0.9
PAUT.122.2	7	-0.0	1.1
PAUT.131.1	5	4.1	8.8
PAUT.20	6	1.0	6.2
RT.109	5	-0.3	2.1
RT.112	3	-0.8	1.1
SAFT.17	7	2.0	3.5
SHPA.6.1	1	1.0	1.0
SHPA.6.3	4	1.0	1.4
UIR.20	6	1.0	3.4
UT.104	7	0.2	0.9
All	91	1.2	4.4

**Table 5.10 Depth Sizing Results for Procedures Applied to SBDMW Test Blocks with I.D. Access (only FB test blocks)**

	NOBS	Bias (mm)	RMSE (mm)
HHUT.30	3	-0.9	2.0
PAATOFD.29.1	7	2.4	3.2
PAATOFD.29.2	7	1.5	3.0
PAUT.131.1	2	-0.5	1.2
All	19	1.3	2.8

**Table 5.11 Depth Sizing Results for Procedures Applied to LBDMW Test Blocks with O.D. Access**

	NOBS	Bias (mm)	RMSE (mm)
LASH.18	1	-1.1	1.1
PAATOFD.29.0	12	-1.5	4.7
PATP.29	15	-2.5	5.6
PAUT.150	3	2.9	5.1
SAFT.17	9	14.1	15.7
All	37	2.3	8.9

**Table 5.12 Depth Sizing Results for Procedures Applied to LBDMW Test Blocks with I.D. Access**

	NOBS	Bias (mm)	RMSE (mm)
PAATOFD.29.1	8	2.3	6.7
PAUT.7	8	-1.4	5.2
All	16	0.4	6.0

### 5.1.1 Depth Sizing Regression Plots for ADVPAUT Procedure Types

Plots of regression curves fit to depth sizing data for ADVPAUT procedure types are provided in Figures 5.1 through 5.6. Figure 5.1 provides the curve for ADVPAUT procedure types applied to SBDMW and FB test blocks with O.D. access; Figure 5.2 provides the curve for ADVPAUT procedure types applied only to SBDMW test blocks with O.D. access; and Figure 5.3 provides the curve for ADVPAUT procedure types applied only to FB test blocks with O.D. access. Figure 5.4 provides the curve for ADVPAUT procedure types applied to FB test blocks with I.D. access. Figure 5.5 provides the curve for ADVPAUT procedure types applied to LBDMW test blocks with O.D. access. Finally, Figure 5.6 provides the depth sizing regression plot for ADVPAUT procedure types applied to LBDMW test blocks with I.D. access. A compilation of all depth sizing regression plots for individual ADVPAUT procedures and for ADVPAUT procedure types applied to SBDMW, FB, and LBDMW test blocks with I.D. and O.D. access is provided in Appendix F.

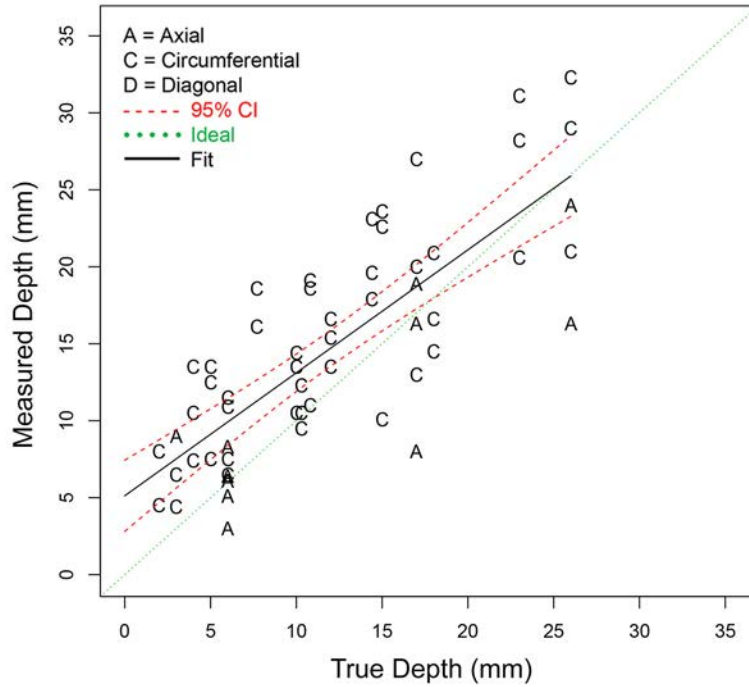


**Figure 5.1** Depth Sizing Regression for ADVPAUT Procedures on SBDMW Test Blocks in PARENT Open Testing (O.D. access – w/ FB test blocks)

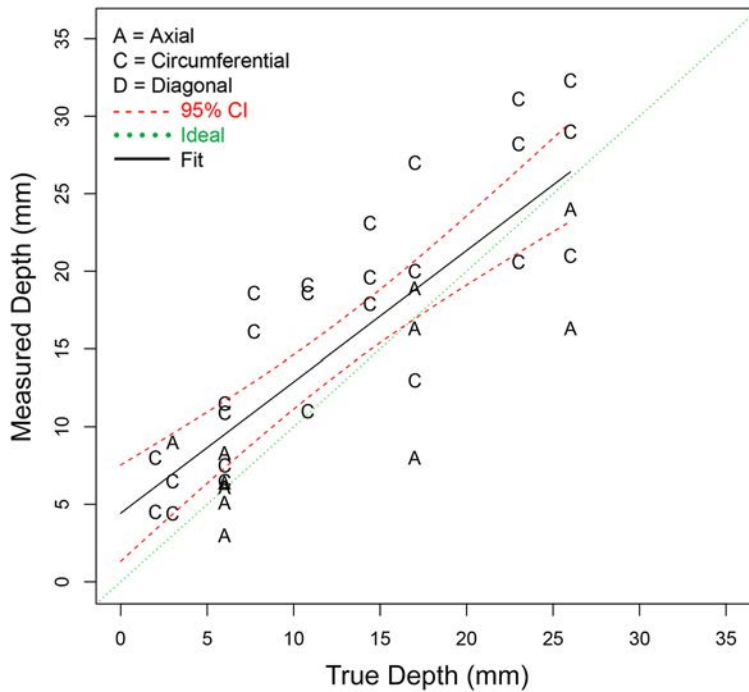


**Figure 5.2** Depth Sizing Regression for ADVPAUT Procedures on SBDMW Test Blocks in PARENT Open Testing (O.D. access – w/o FB test blocks)



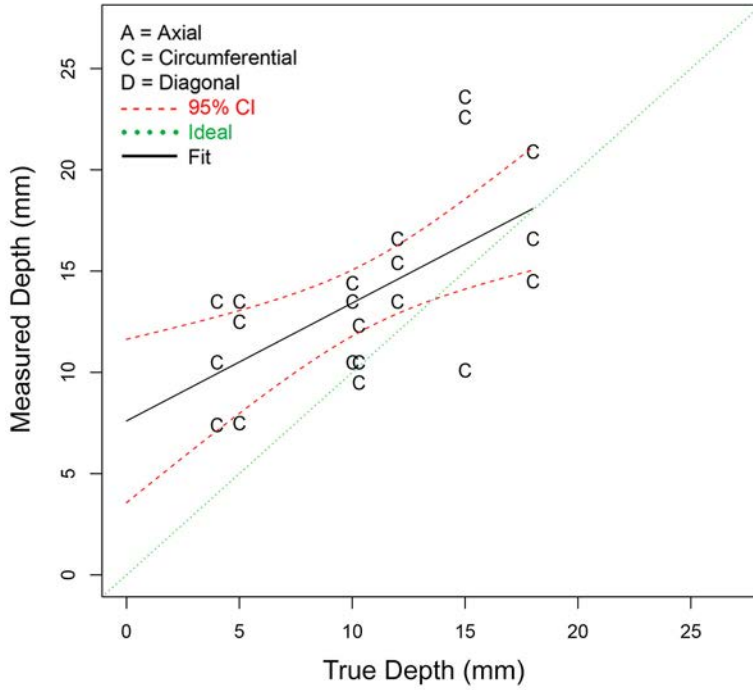


**Figure 5.3** Depth Sizing Regression for ADVPAUT Procedures on FB Test Blocks in PARENT Open Testing (O.D. access)

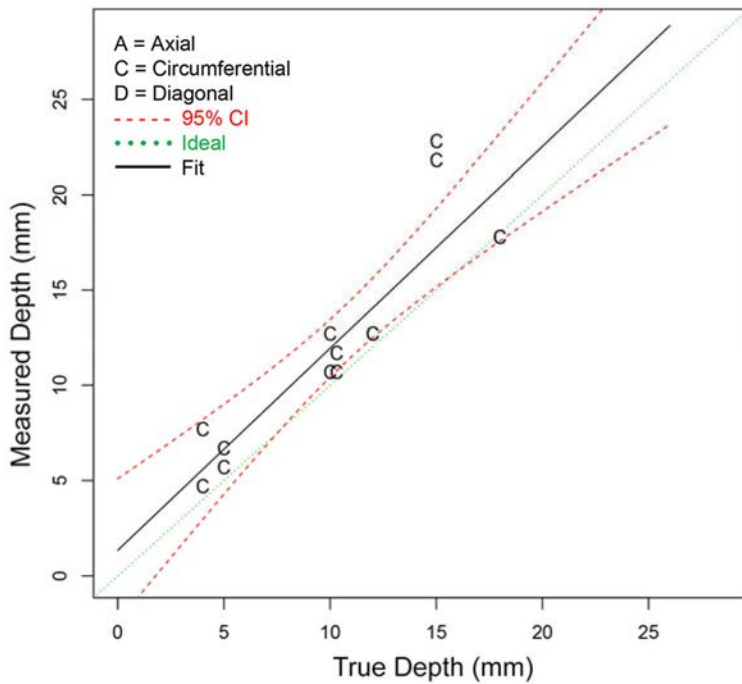


**Figure 5.4** Depth Sizing Regression for ADVPAUT Procedures on FB Test Blocks in PARENT Open Testing (I.D. access)

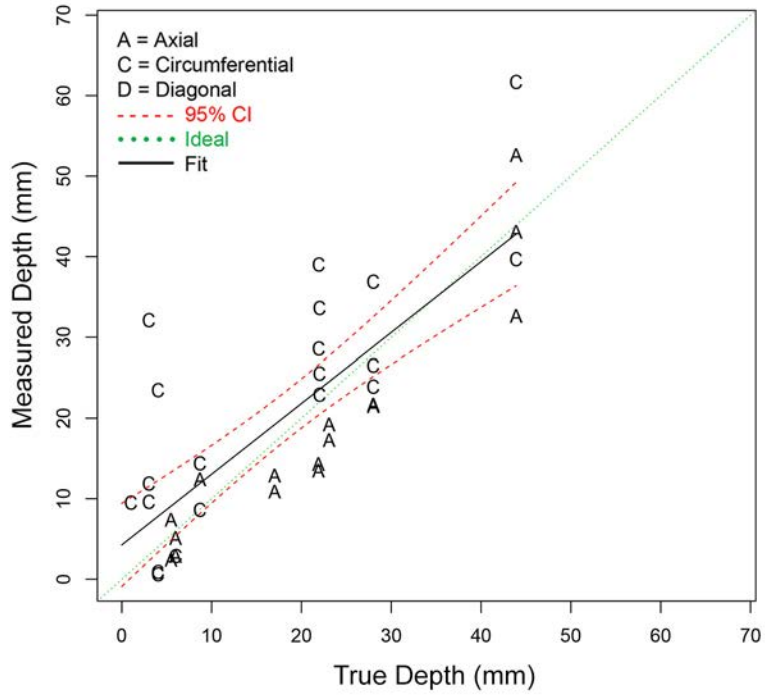


**Figure 5.5** Depth Sizing Regression for ADVPAUT Procedures on LBDMW Test Blocks in PARENT Open Testing (O.D. access)

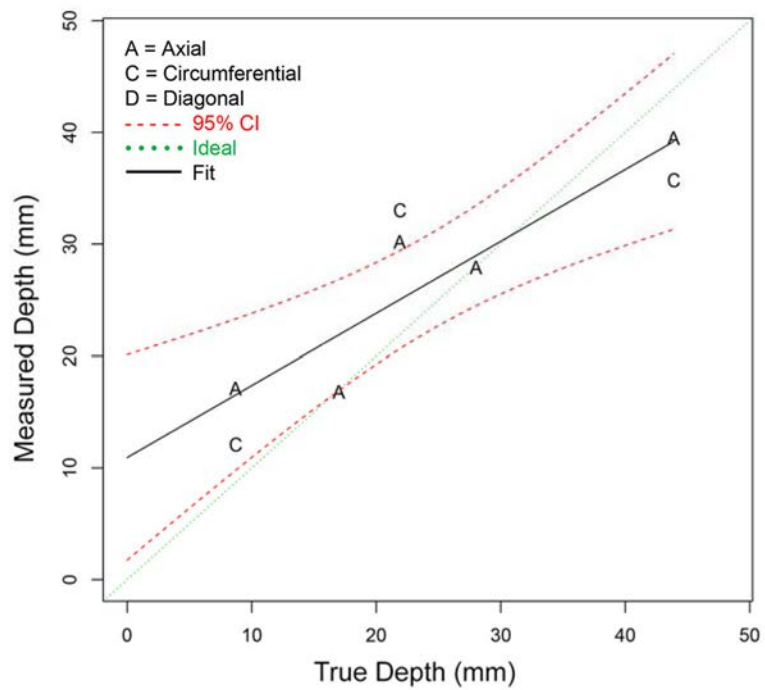


**Figure 5.6** Depth Sizing Regression for ADVPAUT Procedures on LBDMW Test Blocks in PARENT Open Testing (I.D. access)

### 5.1.2 Depth Sizing Regression Plots for NLUT Procedure Types

Plots of regression curves fit to depth sizing data for NLUT procedure types are provided in Figures 5.7 through 5.9. Figure 5.7 provides the curve for NLUT procedure types applied to SBDMW and FB test blocks with O.D. access; Figure 5.8 provides the curve for NLUT procedure types applied only to SBDMW test blocks with O.D. access; and Figure 5.9 provides the curve for NLUT procedure types applied only to FB test blocks with O.D. access. A compilation of all depth sizing regression plots for individual NLUT procedures and for NLUT procedure types applied to SBDMW, FB, and LBDMW test blocks with I.D. and O.D. access is provided in Appendix F.

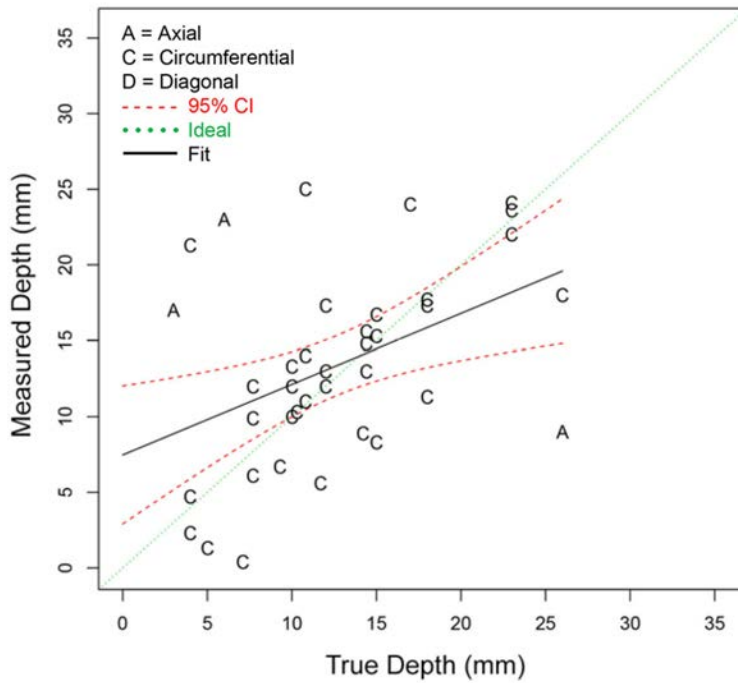


**Figure 5.7 Depth Sizing Regression for NLUT Procedures on SBDMW Test Blocks in PARENT Open Testing (O.D. access – w/ FB test blocks)**

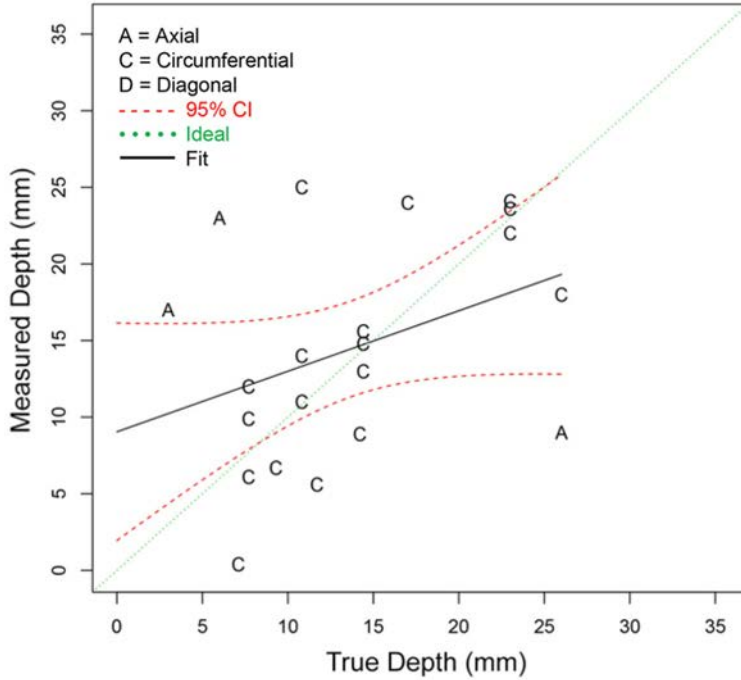


**Figure 5.8** Depth Sizing Regression for NLUT Procedures on SBDMW Test Blocks in PARENT Open Testing (O.D. access – w/o FB test blocks)

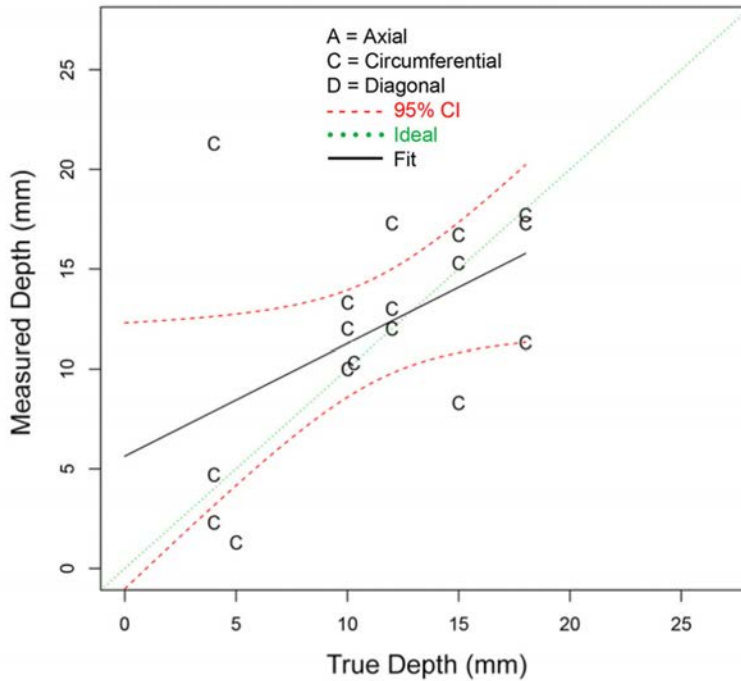


**Figure 5.9** Depth Sizing Regression for NLUT Procedures on FB Test Blocks in PARENT Open Testing (O.D. access)

### 5.1.3 Depth Sizing Regression Plots for PAUT Procedure Types

Plots of regression curves fit to depth sizing data for PAUT procedure types are provided in Figures 5.10 through 5.13. Figure 5.10 provides the curve for PAUT procedure types applied to SBDMW and FB test blocks with O.D. access; Figure 5.11 provides the curve for PAUT procedure types applied only to SBDMW test blocks with O.D. access; and Figure 5.12 provides the curve for PAUT procedure types applied only to FB test blocks with O.D. access. Finally, Figure 5.13 provides the depth sizing regression plot for PAUT procedure types applied to LBDMW test blocks with I.D. access. A compilation of all depth sizing regression plots for individual PAUT procedures and for PAUT procedure types applied to SBDMW, FB, and LBDMW test blocks with I.D. and O.D. access is provided in Appendix F.

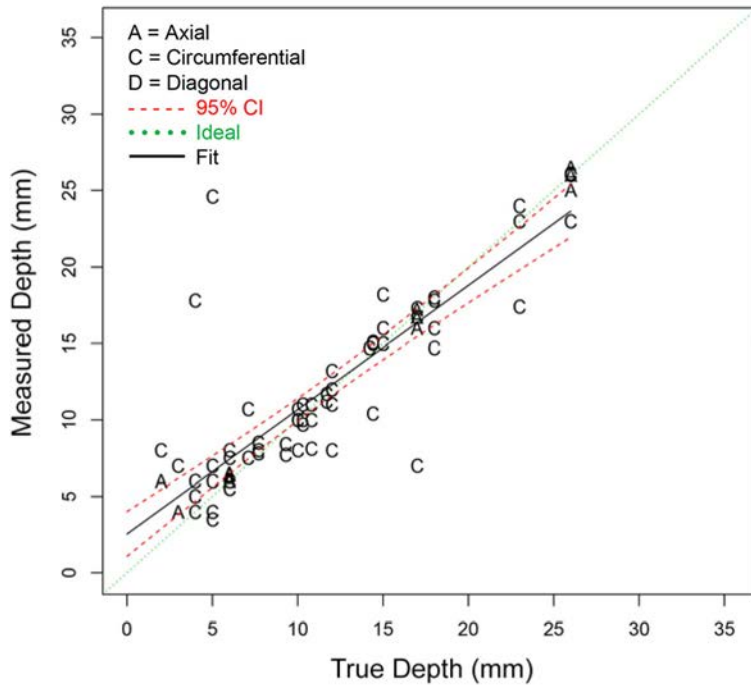


**Figure 5.10** Depth Sizing Regression for PAUT Procedures on SBDMW Test Blocks in PARENT Open Testing (O.D. access – w/ FB test blocks)

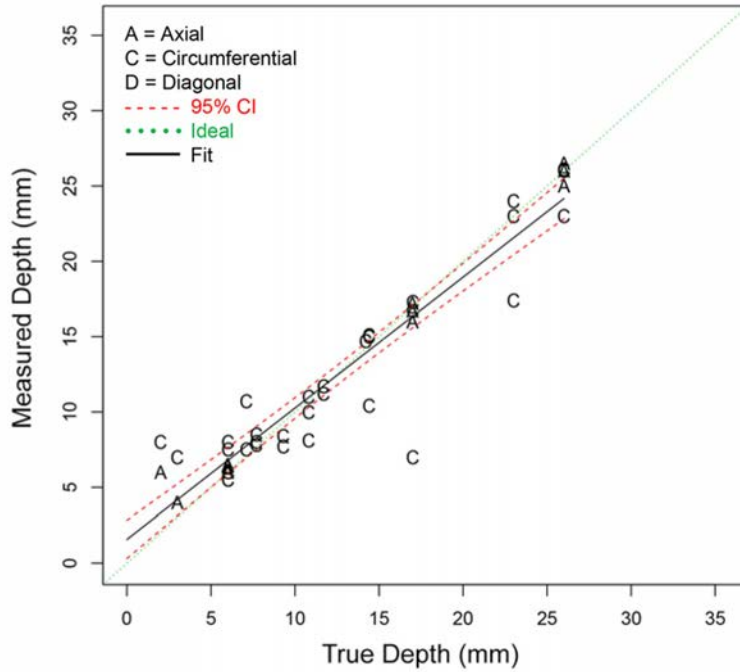


**Figure 5.11** Depth Sizing Regression for PAUT Procedures on SBDMW Test Blocks in PARENT Open Testing (O.D. access – w/o FB test blocks)

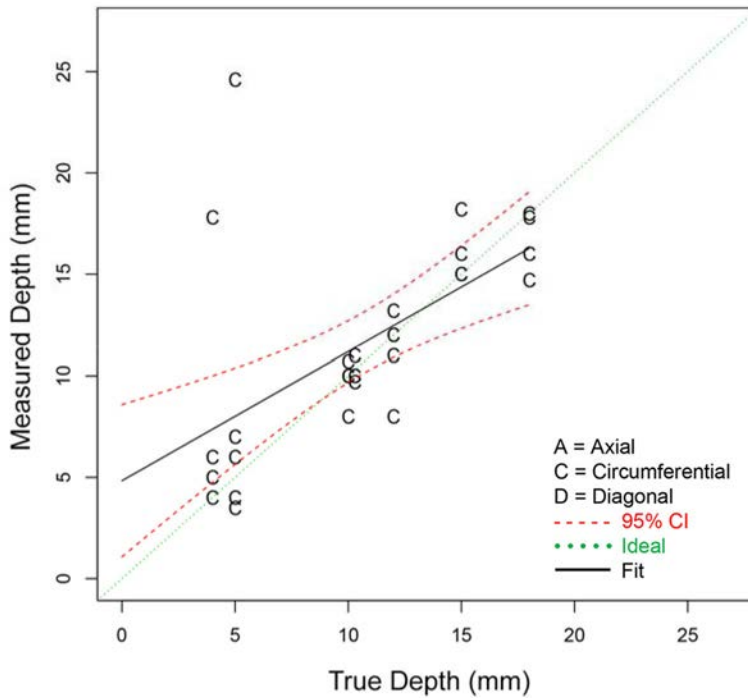


**Figure 5.12** Depth Sizing Regression for PAUT Procedures on FB Test Blocks in PARENT Open Testing (O.D. access)

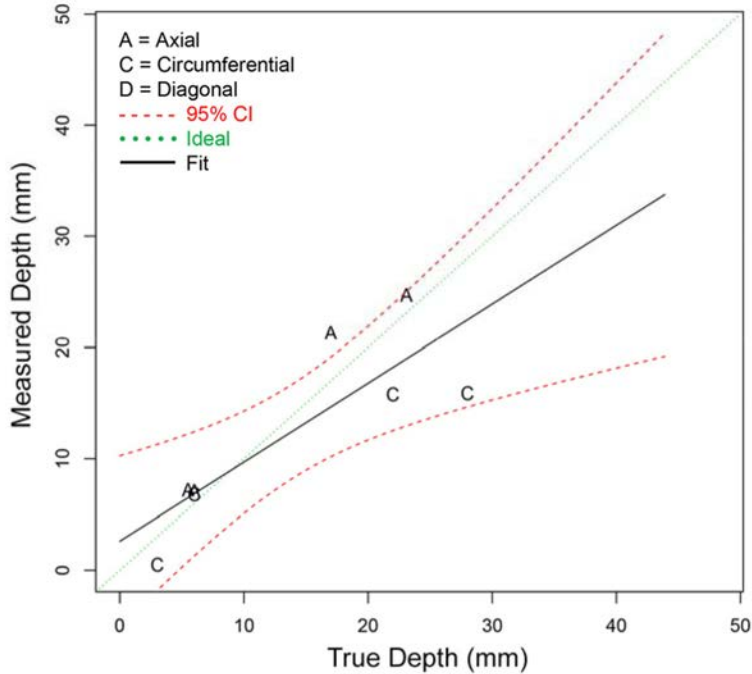


**Figure 5.13 Depth Sizing Regression for PAUT Procedures on LBDMW Test Blocks in PARENT Open Testing (I.D. access)**

#### **5.1.4 Depth Sizing Regression Plots for RT Procedure Types**

Plots of regression curves fit to depth sizing data for RT procedure types are provided in Figures 5.14 through 5.16. Figure 5.14 provides the curve for RT procedure types applied to SBDMW and FB test blocks with O.D. access; Figure 5.15 provides the curve for RT procedure types applied only to SBDMW test blocks with O.D. access; and Figure 5.16 provides the curve for RT procedure types applied only to FB test blocks with O.D. access. A compilation of all depth sizing regression plots for individual RT procedures and for RT procedure types applied to SBDMW, FB, and LBDMW test blocks with I.D. and O.D. access is provided in Appendix F.

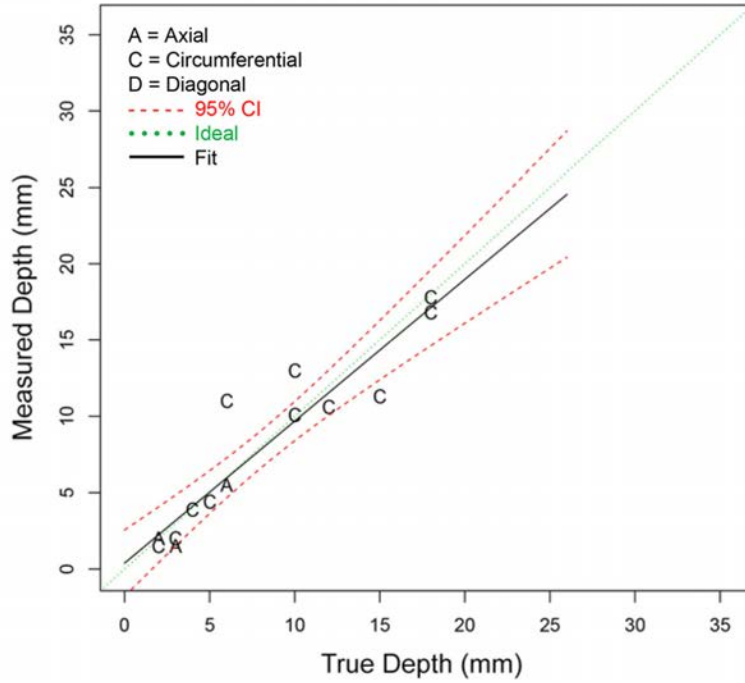


**Figure 5.14** Depth Sizing Regression for RT Procedures on SBDMW Test Blocks in PARENT Open Testing (O.D. access – w/ FB test blocks)

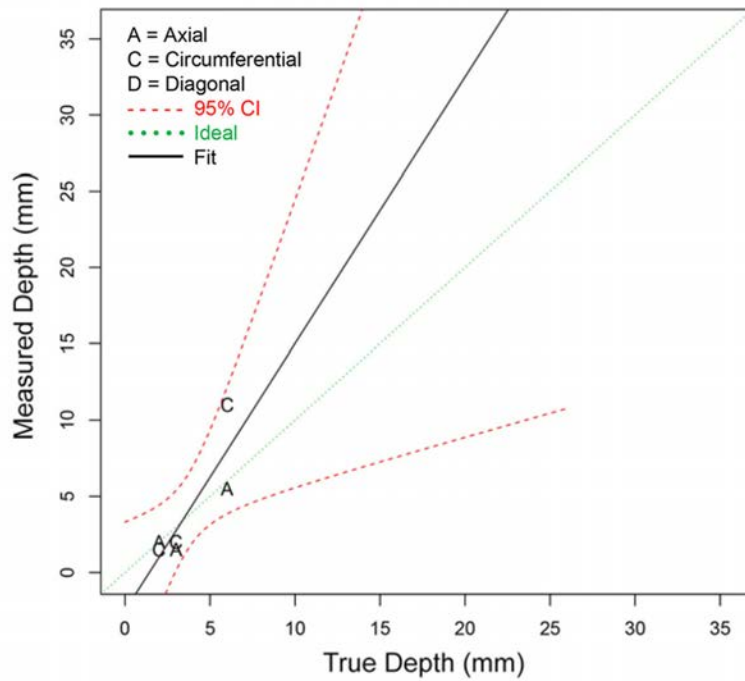


**Figure 5.15** Depth Sizing Regression for RT Procedures on SBDMW Test Blocks in PARENT Open Testing (O.D. access – w/o FB test blocks)



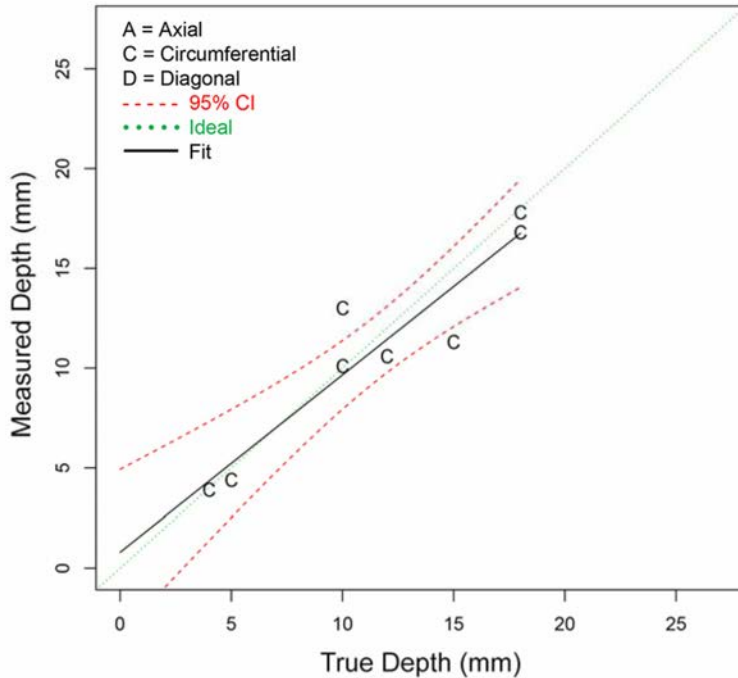


**Figure 5.16 Depth Sizing Regression for RT Procedures on FB Test Blocks in PARENT Open Testing (O.D. access)**

### 5.1.5 Depth Sizing Regression Plots for UIR Procedure Types

Plots of regression curves fit to depth sizing data for UIR procedure types are provided in Figures 5.17 and 5.18. Figure 5.17 provides the curve for UIR procedure types applied to SBDMW and FB test blocks with O.D. access and Figure 5.18 provides the curve for UIR procedure types applied only to FB test blocks with O.D. access. A compilation of all depth sizing regression plots for individual UIR procedures and for UIR procedure types applied to SBDMW, FB, and LBDMW test blocks with I.D. and O.D. access is provided in Appendix F.

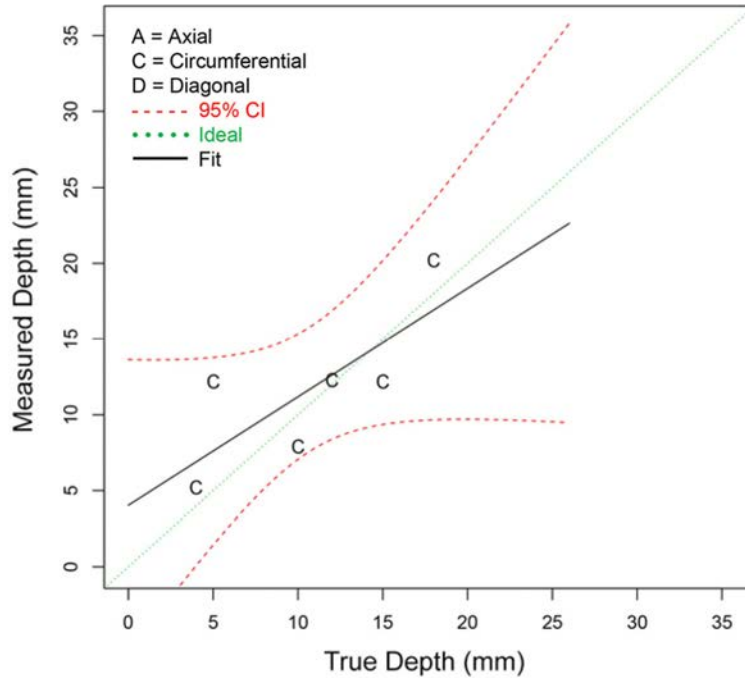


**Figure 5.17** Depth Sizing Regression for UIR Procedures on SBDMW Test Blocks in PARENT Open Testing (O.D. access – w/ FB test blocks)

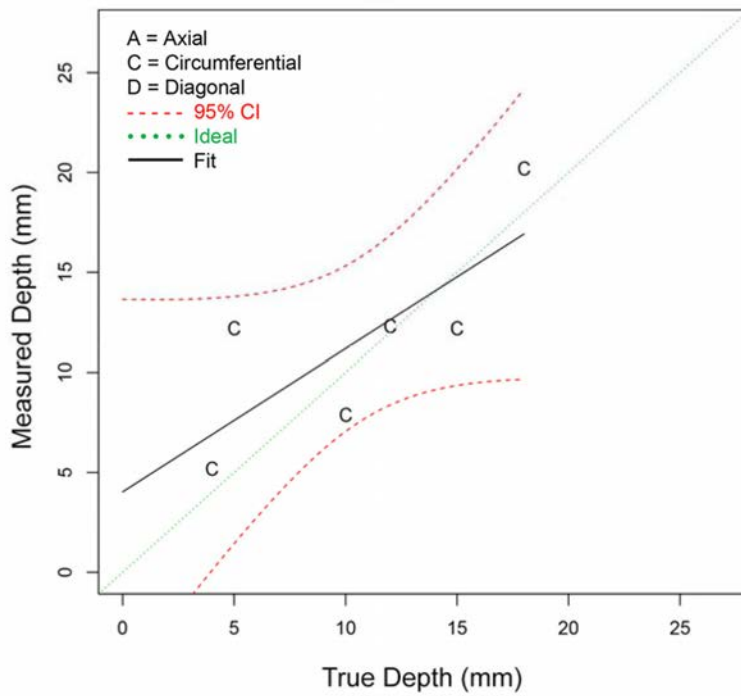


**Figure 5.18** Depth Sizing Regression for UIR Procedures on FB Test Blocks in PARENT Open Testing (O.D. access)

### 5.1.6 Depth Sizing Regression Plots for Conventional UT Procedure Types

Plots of regression curves fit to depth sizing data for conventional UT procedure types are provided in Figures 5.19 through 5.21. Figure 5.19 provides the curve for conventional UT procedure types applied to SBDMW and FB test blocks with O.D. access; Figure 5.20 provides the curve for conventional UT procedure types applied only to SBDMW test blocks with O.D. access; and Figure 5.21 provides the curve for conventional UT procedure types applied only to FB test blocks with O.D. access. A compilation of all depth sizing regression plots for individual conventional UT procedures and for conventional UT procedure types applied to SBDMW, FB, and LBDMW test blocks with I.D. and O.D. access is provided in Appendix F.

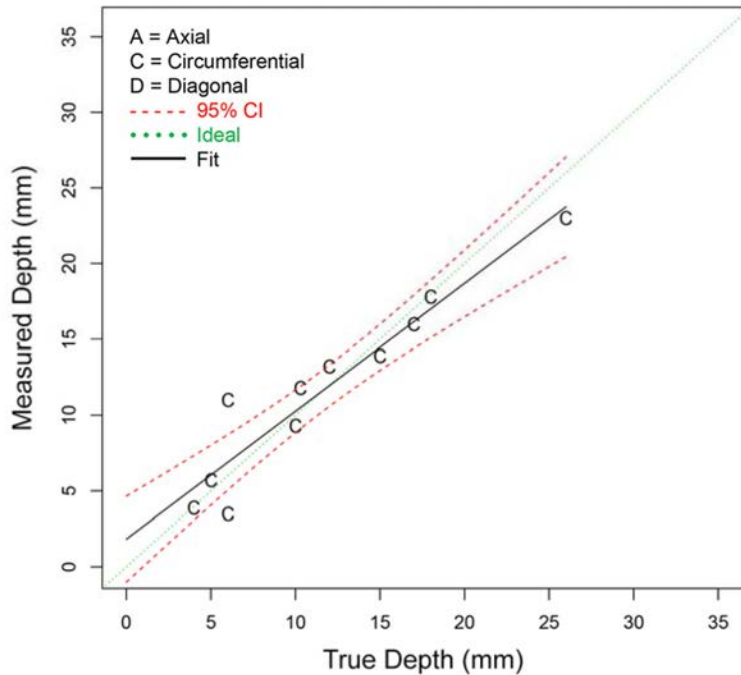


**Figure 5.19** Depth Sizing Regression for Conventional UT Procedures on SBDMW Test Blocks in PARENT Open Testing (O.D. access – w/ FB test blocks)

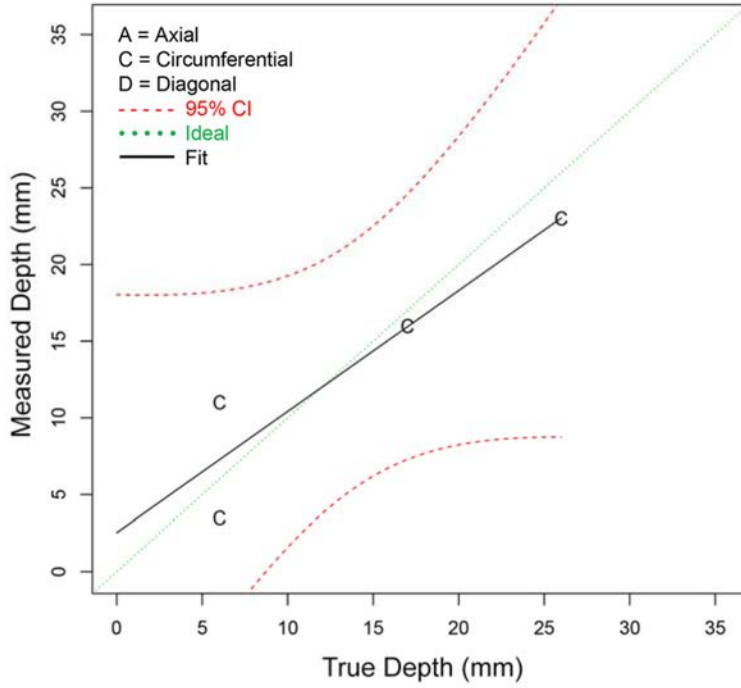


**Figure 5.20** Depth Sizing Regression for Conventional UT Procedures on SBDMW Test Blocks in PARENT Open Testing (O.D. access – w/o FB test blocks)

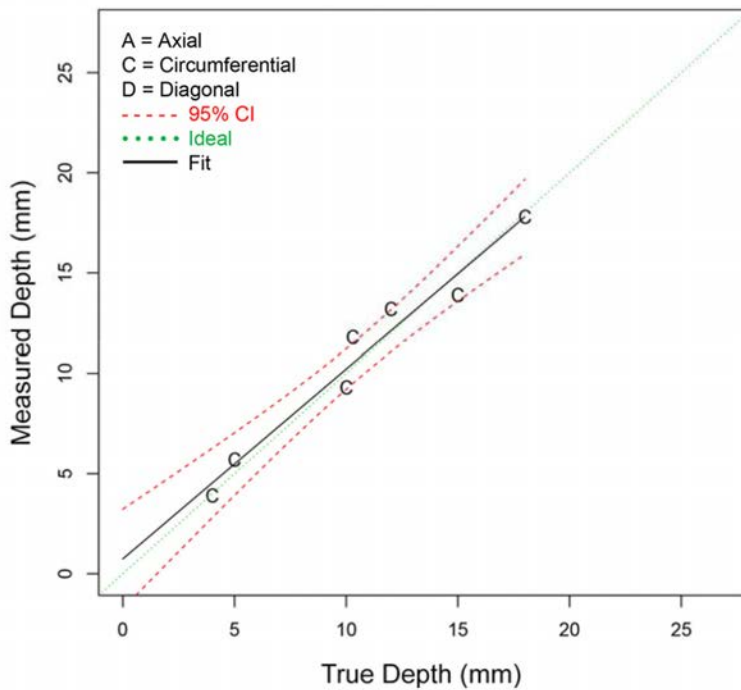


**Figure 5.21** Depth Sizing Regression for Conventional UT Procedures on FB Test Blocks in PARENT Open Testing (O.D. access)

## 5.2 DMW Length Sizing Results

The results of length sizing analysis are summarized in this section by tabulating RMSE and Bias for procedures and procedure types. Tabulated summaries of length sizing results for procedure types applied to SBDMW test blocks by O.D. and I.D. access are included in Tables 5.13 and 5.14, respectively, and for LBDMW test blocks by O.D. and I.D. access in Tables 5.15 and 5.16, respectively. The tabulation of length sizing results for individual procedures is provided in Tables 5.17 through 5.20. The summary for individual procedures applied to SBDMW test blocks with O.D. and I.D. access is provided in Tables 5.17 and 5.18, respectively. Tables 5.19 and 5.20 provide summaries for LBDMW test blocks with O.D. and I.D. access, respectively. No length sizing analysis was performed on FB test blocks as the flaws extend the full width of the specimens.

**Table 5.13 Length Sizing Results for Procedure Types Applied to SBDMW Test Blocks with O.D. Access**

	NOBS	Bias (mm)	RMSE (mm)
ADVPAUT	14	3.9	14.0
NLUT	17	-10.9	17.0
PAUT	49	1.0	9.3
UT	4	1.2	2.4
All	84	-0.9	11.9

**Table 5.14 Length Sizing Results for Procedure Types Applied to SBDMW Test Blocks with I.D. Access**

	NOBS	Bias (mm)	RMSE (mm)
ECT	32	1.2	9.0

**Table 5.15 Length Sizing Results for Procedure Types Applied to LBDMW Test Blocks with O.D. Access**

	NOBS	Bias (mm)	RMSE (mm)
ADVPAUT	9	9.0	15.2
PAUT	4	10.8	20.8
All	13	9.5	17.1

**Table 5.16 Length Sizing Results for Procedure Types Applied to LBDMW Test Blocks with I.D. Access**

	NOBS	Bias (mm)	RMSE (mm)
ECT	12	-1.8	7.6
MM	7	-2.4	3.6
PAUT	9	1.7	12.5
All	28	-0.8	8.9

**Table 5.17 Length Sizing Results for Procedures Applied to SBDMW Test Blocks with O.D. Access**

	NOBS	Bias (mm)	RMSE (mm)
HHUT.27.1	9	-14.9	20.7
PAUT.114	19	2.1	13.0
PAUT.131.2	18	0.7	6.4
PAUT.131.4	8	2.2	3.4
PAUT.20	4	-5.0	7.6
SAFT.17	13	3.5	14.3
SHPA.6.1	4	1.8	4.9
SHPA.6.2	4	-14.8	15.6
UT.104	4	1.2	2.4
All	84	-0.9	11.9

**Table 5.18 Length Sizing Results for Procedures Applied to SBDMW Test Blocks with I.D. Access**

	NOBS	Bias (mm)	RMSE (mm)
AECT.33	12	2.4	3.3
ECT.16	20	0.4	11.1
All	32	1.2	9.0

**Table 5.19 Length Sizing Results for Procedures Applied to LBDMW Test Blocks with O.D. Access**

	NOBS	Bias (mm)	RMSE (mm)
PAUT.150	4	10.8	20.8
SAFT.17	9	9.0	15.2
All	13	9.5	17.1

**Table 5.20 Length Sizing Results for Procedures Applied to LBDMW Test Blocks with I.D. Access**

	NOBS	Bias (mm)	RMSE (mm)
AECT.33	8	-1.2	7.4
CEECT.5.2	2	-10.0	10.4
ECT.16	2	4.5	4.5
MM.28.1	7	-2.4	3.6
PAUT.7	9	1.7	12.5
All	28	-0.8	8.9

**5.2.1 Length Sizing Regression Plots for ADVPAUT Procedure Types**

Plots of regression curves fit to length sizing data for ADVPAUT procedure types are provided in Figures 5.22 and 5.23. Figure 5.22 provides the curve for ADVPAUT procedure types applied to SBDMW test blocks with O.D. access, while Figure 5.23 provides the curve for ADVPAUT procedure types applied to LBDMW test blocks with O.D. access. A compilation of all length sizing regression plots for individual ADVPAUT procedures and for ADVPAUT procedure types applied to SBDMW and LBDMW test blocks with I.D. and O.D. access is provided in Appendix G.

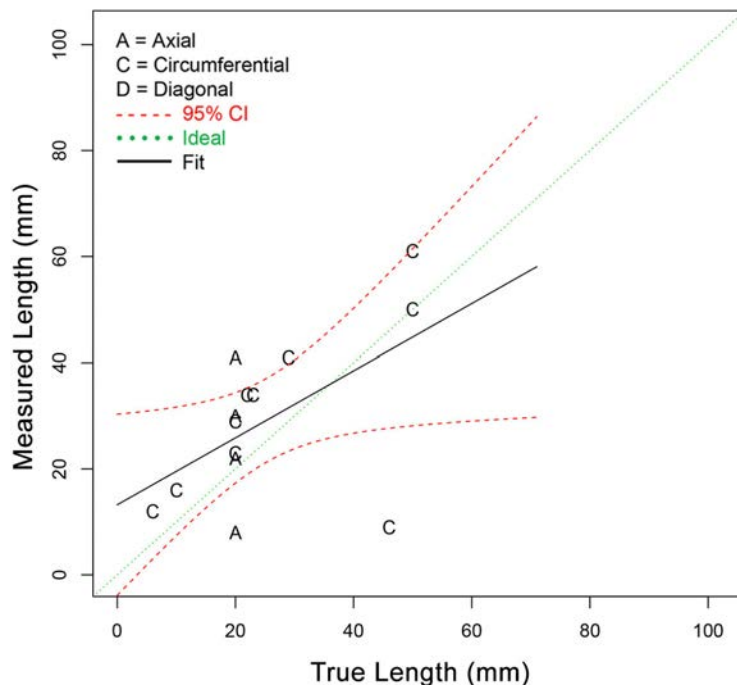


**Figure 5.22 Length Sizing Regression for ADVPAUT Procedures on SBDMW Test Blocks in PARENT Open Testing (O.D. access)**

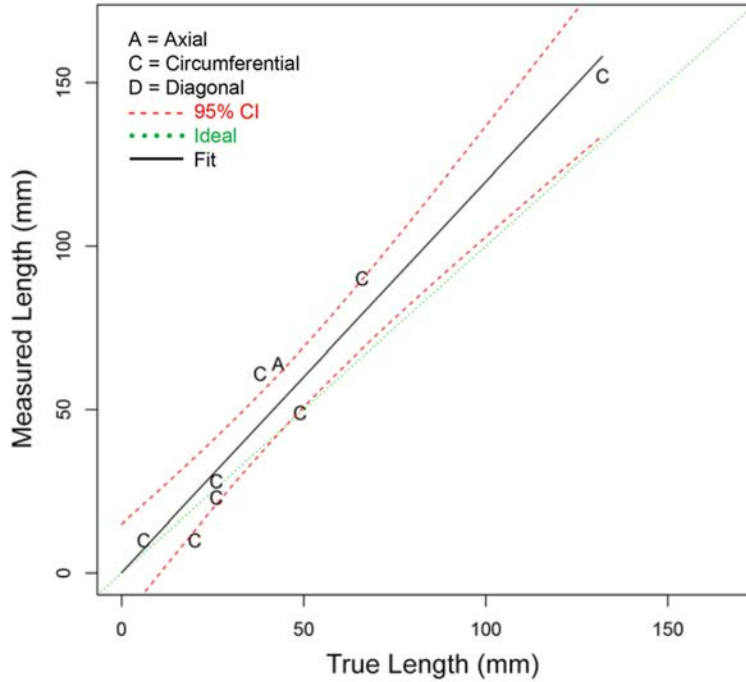


**Figure 5.23 Length Sizing Regression for ADVPAUT Procedures on LBDMW Test Blocks in PARENT Open Testing (O.D. access)**

### 5.2.2 Length Sizing Regression Plots for NLUT Procedure Types

A plot of a regression curve fit to length sizing data for NLUT procedure types is provided in Figure 5.24 for SBDMW test blocks with O.D. access. A compilation of all length sizing regression plots for individual NLUT procedures and for NLUT procedure types applied to SBDMW and LBDMW test blocks with I.D. and O.D. access is provided in Appendix G.



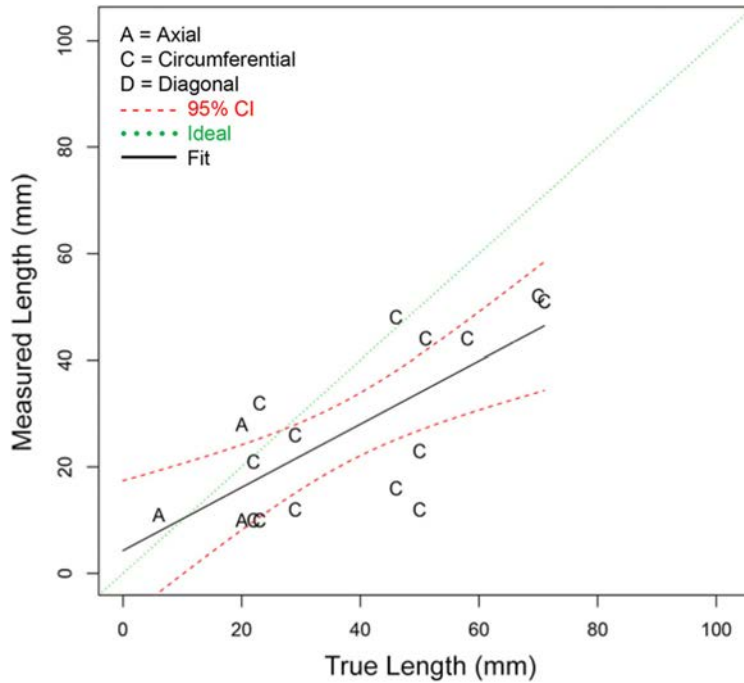


**Figure 5.24 Length Sizing Regression for NLUT Procedures on SBDMW Test Blocks in PARENT Open Testing (O.D. access)**

### 5.2.3 Length Sizing Regression Plots for PAUT Procedure Types

Plots of regression curves fit to length sizing data for PAUT procedure types are provided in Figures 5.25 and 5.27. Figure 5.25 provides the curve for PAUT procedure types applied to SBDMW test blocks with O.D. access, while Figure 5.26 provides the curve for PAUT procedure types applied to LBDMW test blocks with O.D. access. Figure 5.27 provides the curve for PAUT procedure types applied to LBDMW test blocks with I.D. access. A compilation of all length sizing regression plots for individual PAUT procedures and for PAUT procedure types applied to SBDMW and LBDMW test blocks with I.D. and O.D. access is provided in Appendix G.

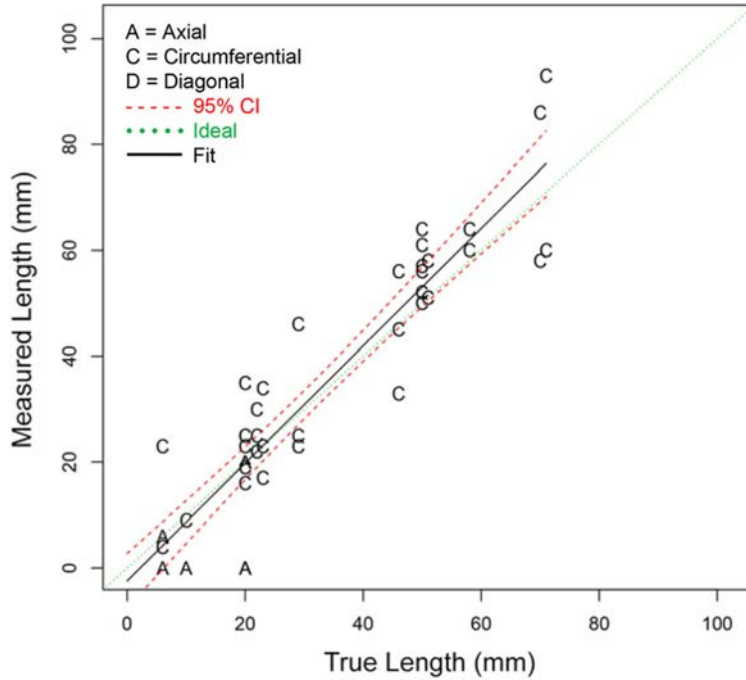


**Figure 5.25** Length Sizing Regression for PAUT Procedures on SBDMW Test Blocks in PARENT Open Testing (O.D. access)

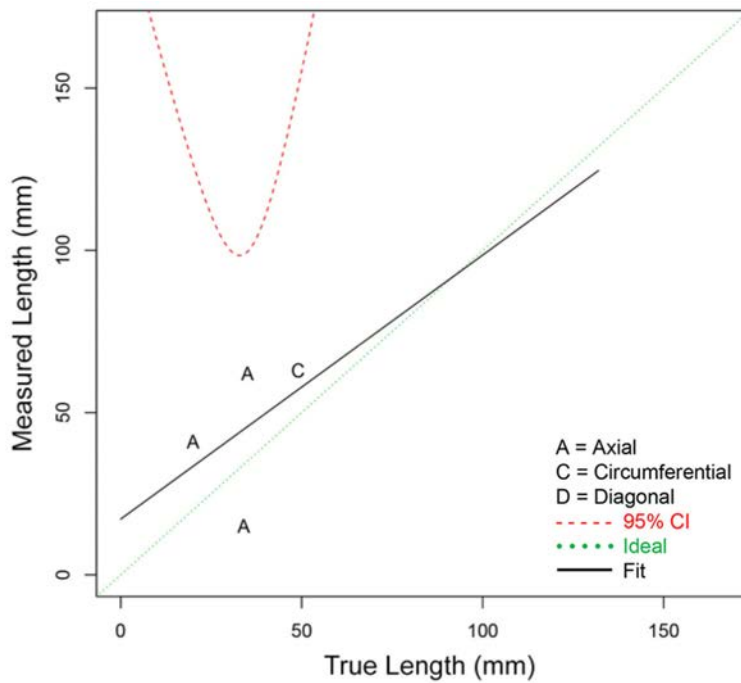


**Figure 5.26** Length Sizing Regression for PAUT Procedures on LBDMW Test Blocks in PARENT Open Testing (O.D. access)

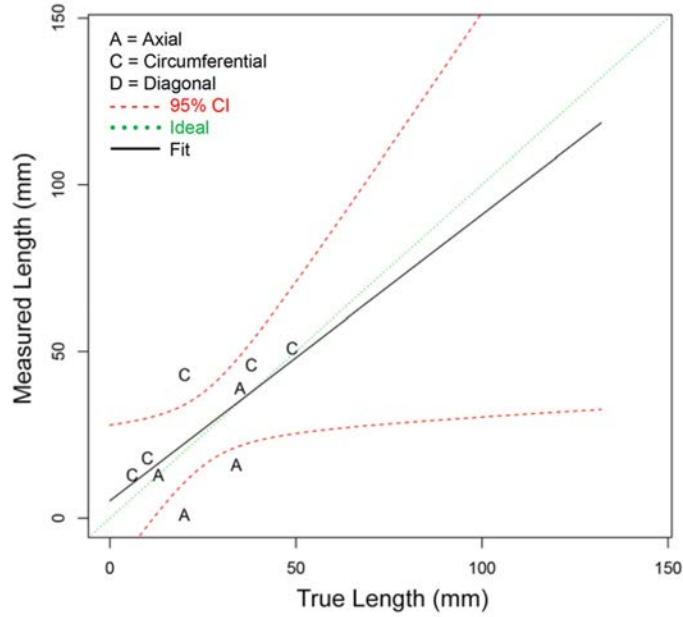


**Figure 5.27 Length Sizing Regression for PAUT Procedures on LBDMW Test Blocks in PARENT Open Testing (I.D. access)**

#### 5.2.4 Length Sizing Regression Plots for Conventional UT Procedure Types

A plot of a regression curve fit to length sizing data for conventional UT procedure types is provided in Figure 5.28 for SBDMW test blocks with O.D. access. A compilation of all length sizing regression plots for individual conventional UT procedures and for conventional UT procedure types applied to SBDMW and LBDMW test blocks with I.D. and O.D. access is provided in Appendix G.

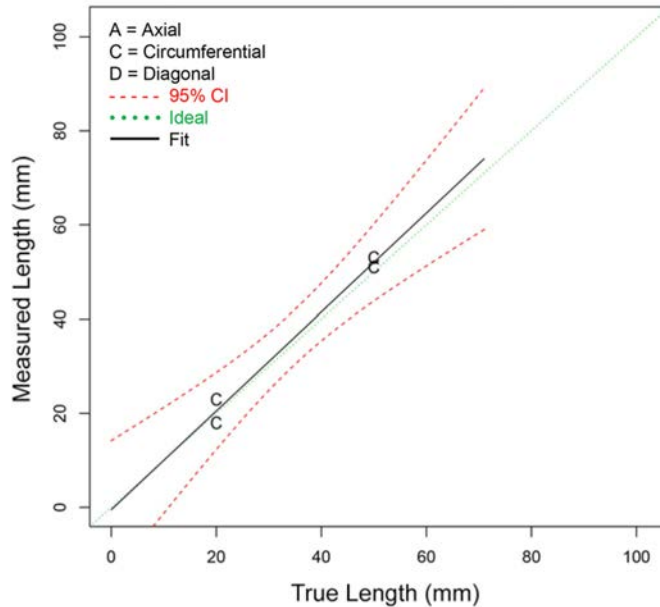


**Figure 5.28 Length Sizing Regression for Conventional UT Procedures on SBDMW Test Blocks in PARENT Open Testing (O.D. access)**

### 5.2.5 Length Sizing Regression Plots for ECT Procedure Types

Plots of regression curves fit to length sizing data for ECT procedure types are provided in Figures 5.29 and 5.30. Figure 5.29 provides the curve for ECT procedure types applied to SBDMW test blocks with I.D. access, while Figure 5.30 provides the curve for ECT procedure types applied to LBDMW test blocks with I.D. access. A compilation of all length sizing regression plots for individual ECT procedures and for ECT procedure types applied to SBDMW and LBDMW test blocks with I.D. and O.D. access is provided in Appendix G.

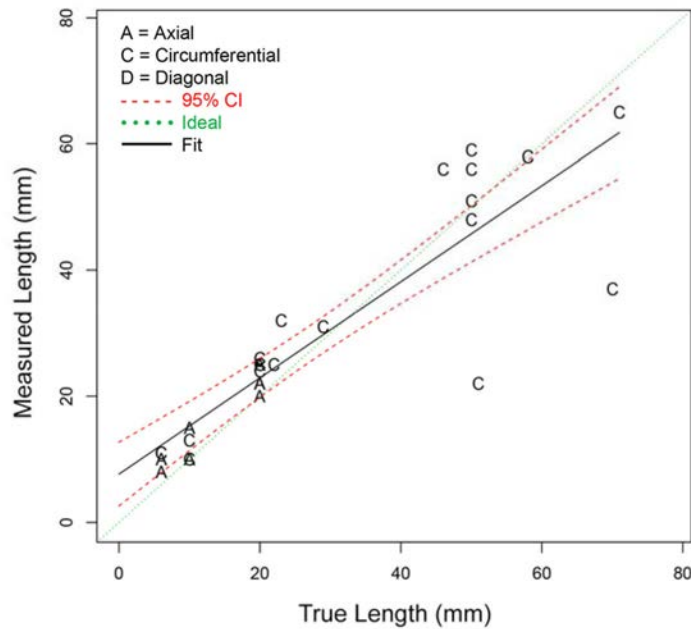


**Figure 5.29 Length Sizing Regression for ECT Procedures on SBDMW Test Blocks in PARENT Open Testing (I.D. access)**

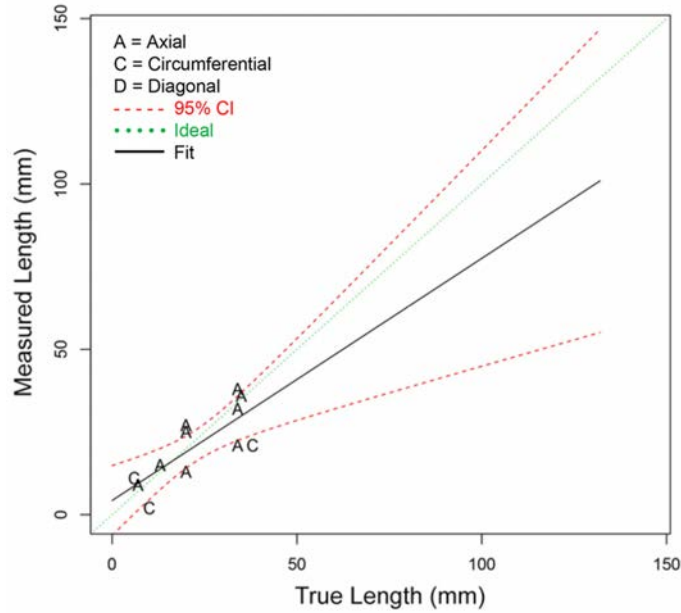


**Figure 5.30 Length Sizing Regression for ECT Procedures on LBDMW Test Blocks in PARENT Open Testing (I.D. access)**

### 5.2.6 Length Sizing Regression Plots for MM Procedure Types

A plot of a regression curve fit to length sizing data for MM procedure types is provided in Figure 5.31 for LBDMW test blocks with I.D. access. A compilation of all length sizing regression plots for individual MM procedures and for MM procedure types applied to SBDMW and LBDMW test blocks with I.D. and O.D. access is provided in Appendix G.

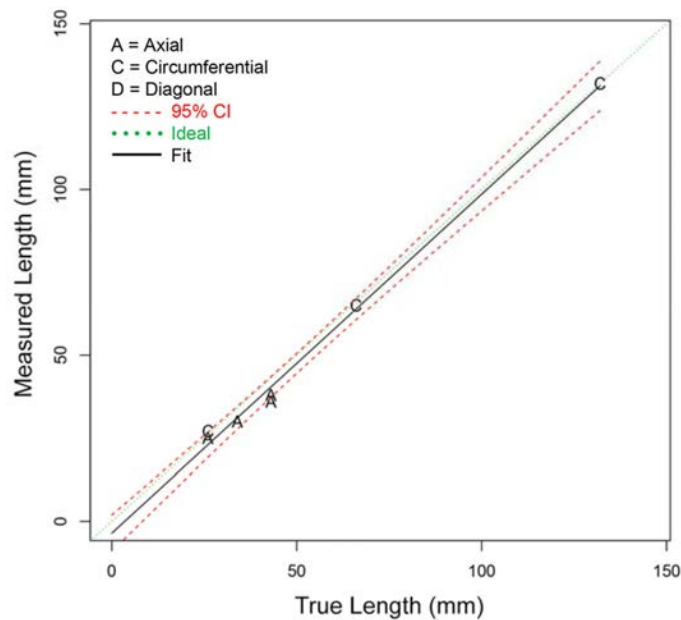


**Figure 5.31 Length Sizing Regression for MM Procedures on LBDMW Test Blocks in PARENT Open Testing (I.D. access)**

### 5.3 BMI Data Analysis Results

The length sizing analysis results for BMI test blocks is provided in Table 5.21 for individual procedure types. All data was collected by accessing the J-groove weld surface. Due to the limited amount of data collected on BMI test blocks, no attempt has been made to group results by procedure types. Plots of regression curves fit to length sizing data can be found in Appendix G.9.

**Table 5.21 Length Sizing Results for Procedures Applied to BMI Test Blocks with J-Groove Weld Surface Access**

	NOBS	Bias (mm)	RMSE (mm)
AECT.33	4	-5.2	5.3
ECT.16	3	4.0	5.0
ECT.7	14	3.4	4.9
LUV.170	5	-0.2	1.0
MM.28.1	1	-7.0	7.0

### 5.4 Indication Plots

Indication plots for individual inspections are compiled in Appendix H.

## 6 ANALYSIS OF RESULTS

This section provides some additional discussion and analysis of the results presented in Section 5. In particular, PAUT and ADVPAUT procedure type performances are compared based on sizing RMSEs in Section 6.1 and NLUT procedure type performances are compared with PAUT and ADVPAUT procedure type performances in Section 6.2. Depth sizing results for FB test blocks are presented in Section 6.3 to observe the impact of complex stress corrosion crack morphology on sizing results and data for test block P38 are also considered to determine if the weld asymmetry in this test block has an observable impact on performance. The results for linear and sectorial PAUT examinations by team 122 are compared in Section 6.4. Results obtained by UIR examinations are discussed in Section 6.5; and the results from RT, conventional UT, and ECT examinations are briefly discussed in Section 6.6. Section 6.7 includes a brief analysis of data response images obtained from FB test blocks to illustrate the difficulty in distinguishing crack tip responses of SCC flaws from noise. Sparsely populated datasheets are highlighted in Section 6.8 to illustrate that some techniques had difficulty with identifying flaws under the open test conditions. Section 6.9 includes a brief discussion of test block appropriateness and how limitations of the test blocks available for open testing inhibited an effective evaluation of some techniques. Finally, Section 6.10 provides a summary of open techniques that exhibited sufficient capability in open testing such that further blind testing to obtain more detailed assessments of performance is justified.

### 6.1 Comparison of ADVPAUT and PAUT Procedure Types

A comparison of ADVPAUT and PAUT procedure types is provided in Table 6.1 based on depth sizing RMSE results. In this table, comparisons are made considering data from SBDMW and FB test blocks, considering data from only SBDMW test blocks, considering data from only FB test blocks, and considering data from LBDMW test blocks. The RMSE data indicate that PAUT procedures generally outperformed the ADVPAUT procedures in open testing. The generally better performance observed for PAUT procedures may reflect increased familiarity of teams with PAUT procedures in comparison to ADVPAUT procedures. This would also indicate that the performance of ADVPAUT procedures could improve with additional experience. However, a review of depth sizing regression plots for ADVPAUT and PAUT procedure types on SBDMW test blocks with O.D. access in Figures 6.1 and 6.2 show that while ADVPAUT procedure types may not have depth sized flaws as accurately as PAUT procedure types, depth sizing results for ADVPAUT procedure types are more conservative than PAUT procedure types, showing an oversizing trend over the entire flaw depth range considered. In the depth sizing regression plots for ADVPAUT and PAUT procedure types applied to FB test blocks with O.D. access in Figures 6.3 and 6.4, both procedure types show a similar sizing trend of oversizing shallower flaws and undersizing the deep flaws.

**Table 6.1 Summary of Depth Sizing RMSEs for ADVPAUT and PAUT Techniques Applied to SBDMW and LBDMW Test Blocks with O.D. and I.D. Access**

	ADVPAUT		PAUT	
	NOBS	RMSE (mm)	NOBS	RMSE (mm)
SBDMW and FB Test Blocks with O.D. Access	57	5.3	79	3.4
SBDMW Test Blocks with O.D. Access	36	5.5	47	2.4
FB Test Blocks with O.D. Access	21	5.0	32	4.5
FB Test Blocks with I.D. Access	14	3.1	2	1.2
LBDMW Test Blocks with O.D. Access	36	9.1	3	5.1
LBDMW Test Blocks with I.D. Access	8	6.7	8	5.2

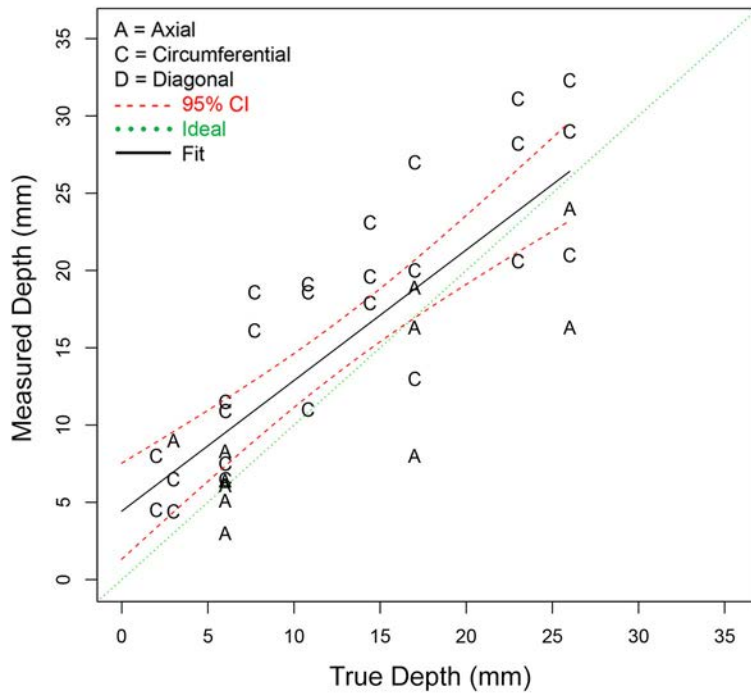


**Figure 6.1 Depth Sizing Regression for ADVPAUT Procedures on SBDMW Test Blocks in PARENT Open Testing (O.D. access – w/o FB test blocks)**



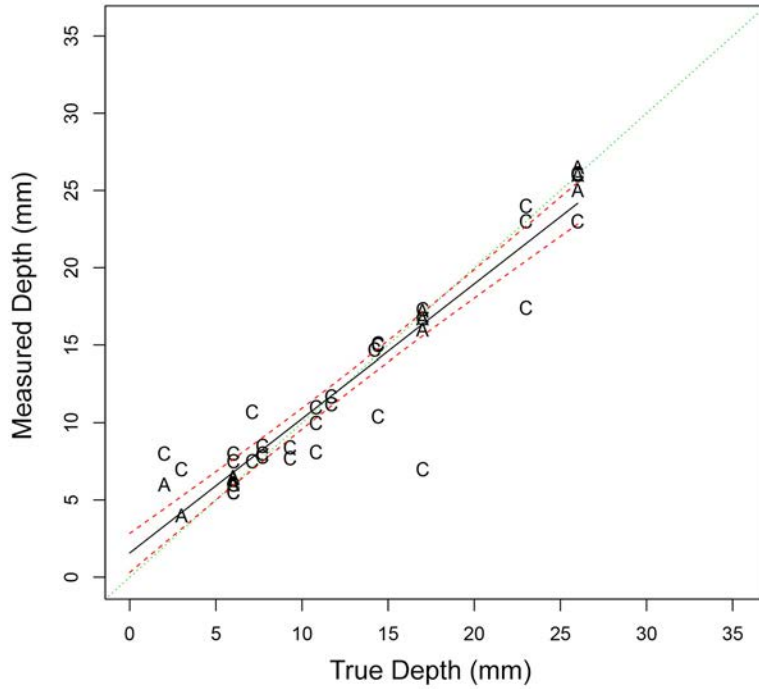


**Figure 6.2 Depth Sizing Regression for PAUT Procedures on SBDMW Test Blocks in PARENT Open Testing (O.D. access – w/o FB test blocks)**

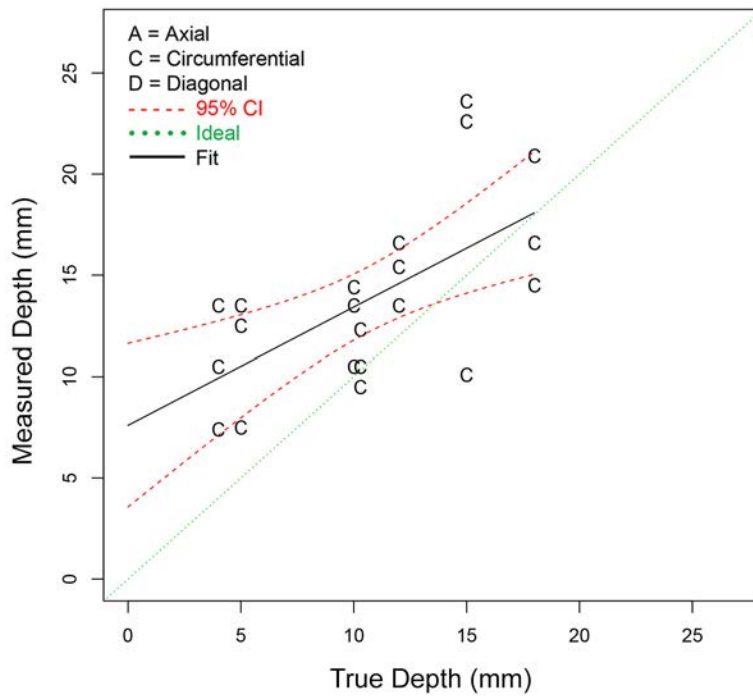


**Figure 6.3 Depth Sizing Regression for ADVPAUT Procedures on FB Test Blocks in PARENT Open Testing (O.D. access)**

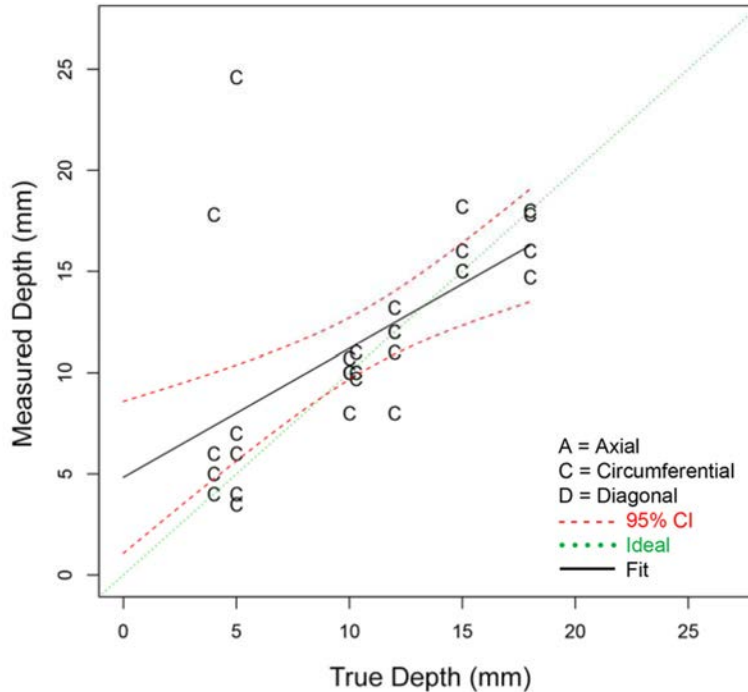


**Figure 6.4 Depth Sizing Regression for PAUT Procedures on FB Test Blocks in PARENT Open Testing (O.D. access)**

A summary of depth sizing RMSEs for ADVPAUT and PAUT procedures is provided in Tables 6.2 through 6.5 for SBDMW and FB test blocks. These tables indicate that several ADVPAUT and PAUT procedures exhibited variation in performance for SBDMW test blocks (solidification cracks) versus FB test blocks (mostly laboratory-grown SCC). For instance, procedures LASH.18 and PAUT.20 exhibit better performance on SBDMW test blocks versus FB test blocks and procedures SAFT.17 and PAUT.114 exhibit better performance on FB test blocks versus SBDMW test blocks.

Length sizing RMSEs are summarized in Table 6.6 for ADVPAUT and PAUT procedure types applied to SBDMW and LBDMW test blocks with O.D. access. In this case, PAUT procedure types exhibit better length sizing performance on SBDMW test blocks. ADVPAUT procedure types exhibit better length sizing performance than PAUT procedure types on LBDMW test blocks; however, the sample sizes are relatively small. Length sizing performances of individual ADVPAUT and PAUT procedures applied to SBDMW test blocks are summarized in Tables 6.7 and 6.8, respectively. A review of length sizing regression plots for PAUT and ADVPAUT procedure types in Figures 6.5 and 6.6, respectively, for SBDMW test blocks with O.D. access show that ADVPAUT procedure types exhibit a trend of oversizing short flaws and undersizing long flaws while PAUT procedure types oversize longer flaws and slightly undersize shorter flaws.

**Table 6.2 Summary of Depth Sizing Performances for ADVPAUT Procedure Types Applied to SBDMW Test Blocks with O.D. Access w/o FB Test Blocks**

	NOBS	Bias (mm)	RMSE (mm)
LASH.18	4	0.0	1.0
PAATOFD.29.0	13	0.8	4.6
PATP.29	9	2.4	6.6
SAFT.17	14	4.0	5.4
SHPA.6.1	4	1.8	2.1
SHPA.6.2	4	-5.2	5.4

**Table 6.3 Summary of Depth Sizing Performances for ADVPAUT Procedure Types Applied to FB Test Blocks with O.D. Access**

	NOBS	Bias (mm)	RMSE (mm)
LASH.18	5	-3.0	4.3
PAATOFD.29.1	7	3.6	5.5
PAATOFD.29.2	7	3.9	5.8
SAFT.17	7	2.0	3.5
SHPA.6.1	1	1.0	1.0
SHPA.6.3	4	1.0	1.4

**Table 6.4 Summary of Depth Sizing Performances for PAUT Procedure Types Applied to SBDMW Test Blocks with O.D. Access w/o FB Test Blocks**

	NOBS	Bias (mm)	RMSE (mm)
PAUT.114	19	0.2	3.3
PAUT.131.2	16	0.3	0.6
PAUT.131.4	8	-0.1	0.4
PAUT.20	4	-3.1	3.7

**Table 6.5 Summary of Depth Sizing Performances for PAUT Procedure Types Applied to FB Test Blocks with O.D. Access**

	NOBS	Bias (mm)	RMSE (mm)
PAUT.114	7	0.1	0.8
PAUT.122.1	7	0.4	0.9
PAUT.122.2	7	-0.0	1.1
PAUT.131.1	5	4.1	8.8
PAUT.20	6	1.0	6.2

**Table 6.6 Summary of Length Sizing RMSEs for ADVPAUT and PAUT Techniques Applied to SBDMW and LBDMW Test Blocks with O.D. Access**

	ADVPAUT		PAUT	
	NOBS	RMSE (mm)	NOBS	RMSE (mm)
SBDMW Test Blocks with O.D. Access	14	14.0	49	9.3
LBDMW Test Blocks with O.D. Access	9	15.2	4	20.8

**Table 6.7 Summary of Length Sizing Performances for ADVPAUT Procedure Types Applied to SBDMW Test Blocks with O.D. Access w/o FB Test Blocks**

	NOBS	Bias (mm)	RMSE (mm)
SAFT.17	14	3.9	14.0
SHPA.6.1	4	1.8	4.9
SHPA.6.2	4	-14.8	15.6

**Table 6.8 Summary of Length Sizing Performances for PAUT Procedure Types Applied to SBDMW Test Blocks with O.D. Access w/o FB Test Blocks**

	NOBS	Bias (mm)	RMSE (mm)
PAUT.114	19	2.1	13.0
PAUT.131.2	18	0.7	6.4
PAUT.131.4	8	2.2	3.4
PAUT.20	4	-5.0	7.6

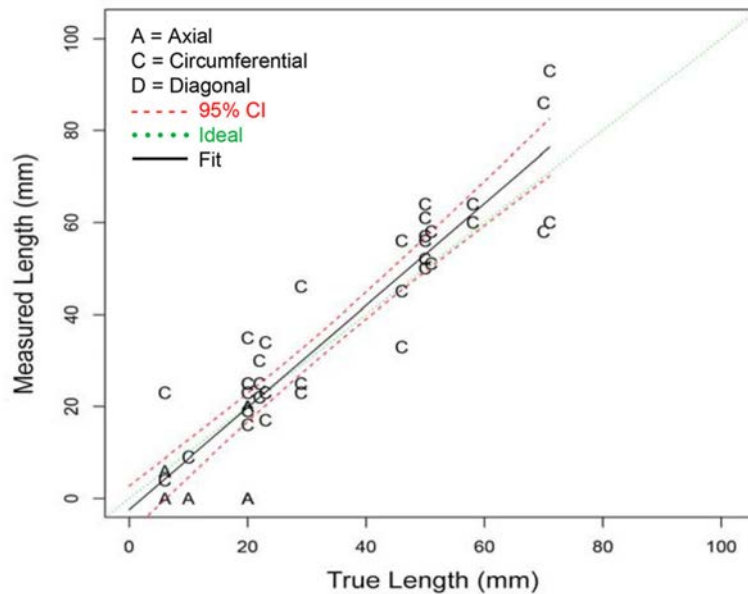


**Figure 6.5 Length Sizing Regression for PAUT Procedures on SBDMW Test Blocks in PARENT Open Testing (O.D. access)**

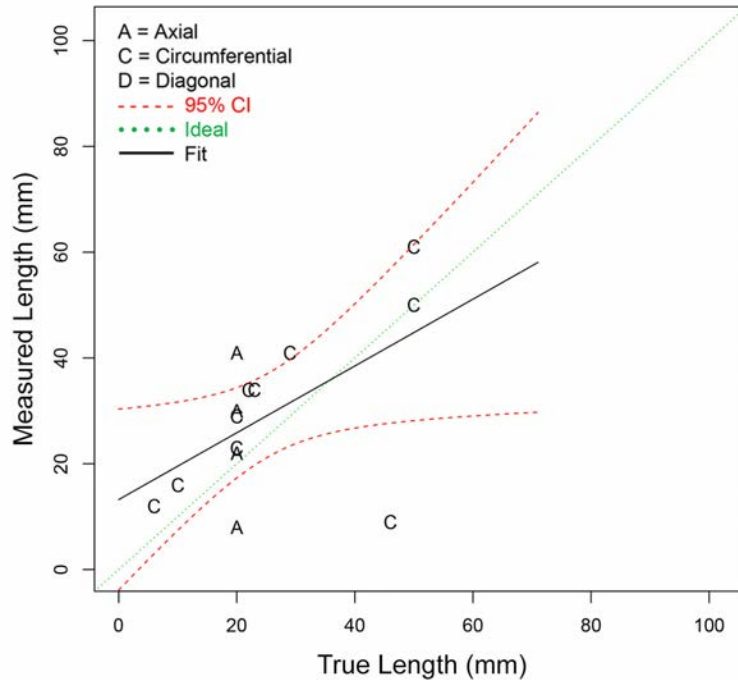


**Figure 6.6 Length Sizing Regression for ADVPAUT Procedures on SBDMW Test Blocks in PARENT Open Testing (O.D. access)**

## **6.2 Comparison of NLUT with PAUT and ADVPAUT Procedure Types**

The performance of NLUT procedure types can be compared with the performance of PAUT and ADVPAUT procedure types by reviewing depth sizing results in Tables 5.1 through 5.3 for SBDMW and FB test blocks with O.D. access, Table 5.4 for FB test blocks with I.D. access, and Table 5.5 for LBDMW test blocks with O.D. access. Tables 5.1 through 5.3 indicate that NLUT procedure types are less accurate at depth sizing than PAUT and ADVPAUT procedure types based on RMSE, though the depth sizing accuracies are comparable. Similarly, these tables indicate that the bias for NLUT procedure types is also comparable to the bias observed for PAUT and ADVPAUT procedure types. Table 5.4 indicates that the RMSE for NLUT procedure types is less than for ADVPAUT procedure types but greater than for PAUT procedure types for FB test blocks by I.D. access and, Table 5.5 indicates that the RMSE for NLUT procedure types is less than for PAUT and ADVPAUT procedure types for LBDMW test blocks with O.D. access, but the sample size is limited in these cases. A review of depth sizing regression plots in Figures 5.7 through 5.9 show that NLUT procedure types exhibit a trend of oversizing shallow flaws and undersizing deep flaws in testing performed on SBDMW and FB test blocks with O.D. access.

The length sizing performance of NLUT procedure types may be compared with PAUT and ADVPAUT procedure types in Table 5.13, which shows that NLUT procedure types exhibit a much higher RMSE than ADVPAUT and PAUT procedure types for SBDMW test blocks with O.D. access and that NLUT procedure types exhibit a strong negative bias. A review of the length sizing regression curve for NLUT procedure types applied to SBDMW test blocks with O.D. access in Figure 5.24 shows a strong tendency to undersize flaws over most of the flaw length range. However, a review of individual NLUT procedure depth sizing regression plots in Figures 6.7 through 6.12 indicates, that overall, NLUT procedures based on higher harmonic techniques do not perform as well as NLUT procedures based on sub-harmonic techniques. Figures 6.7 and 6.10 show a weak correlation between measured depth and true depth based on

HHUT.27.1 and HHUT.27.2 procedures. Figures 6.8 and 6.11 for procedures SHPA.6.1 and SHPA.6.3 indicate a more consistent measurement error over the entire depth ranges considered with slight conservative (oversizing) bias over the full flaw depth range. Finally, Figure 6.9 indicates that procedure LASH.18 for SBDMWs exhibits a slight undersizing of shallower flaws and a slight oversizing of deep flaws, and Figure 6.12 indicates that procedure LASH.18 for FB test block exhibits an oversizing of shallower flaws and a undersizing of deep flaws.

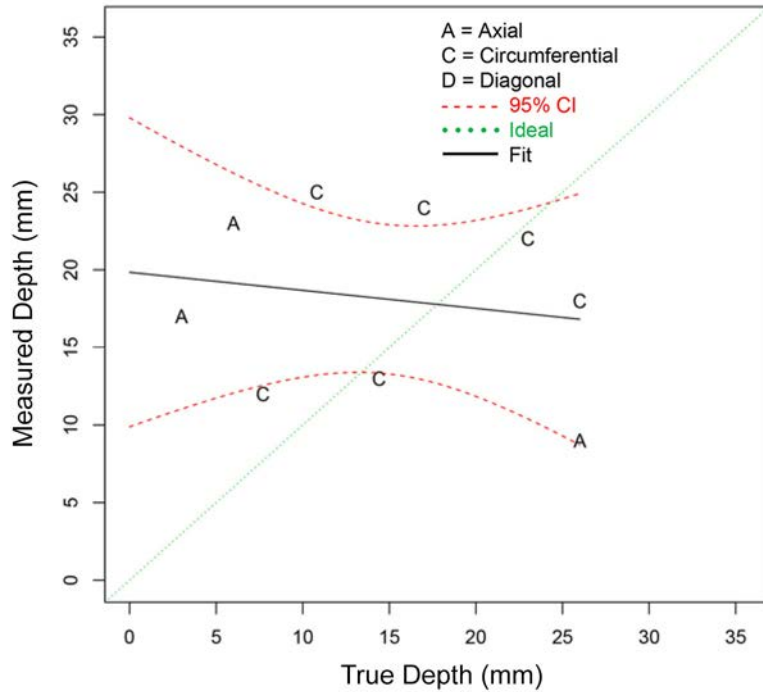


**Figure 6.7** Depth Sizing Regression Plot for HHUT.27.1 Applied to SBDMW Test Blocks (w/o FB test blocks) with O.D. Access

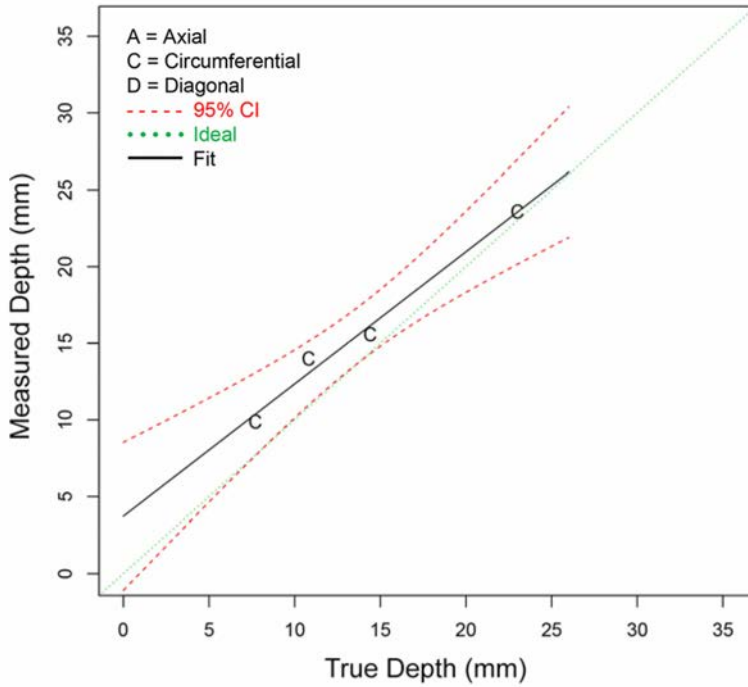


**Figure 6.8** Depth Sizing Regression Plot for SHPA.6.1 Applied to SBDMW Test Blocks (w/o FB test blocks) with O.D. Access

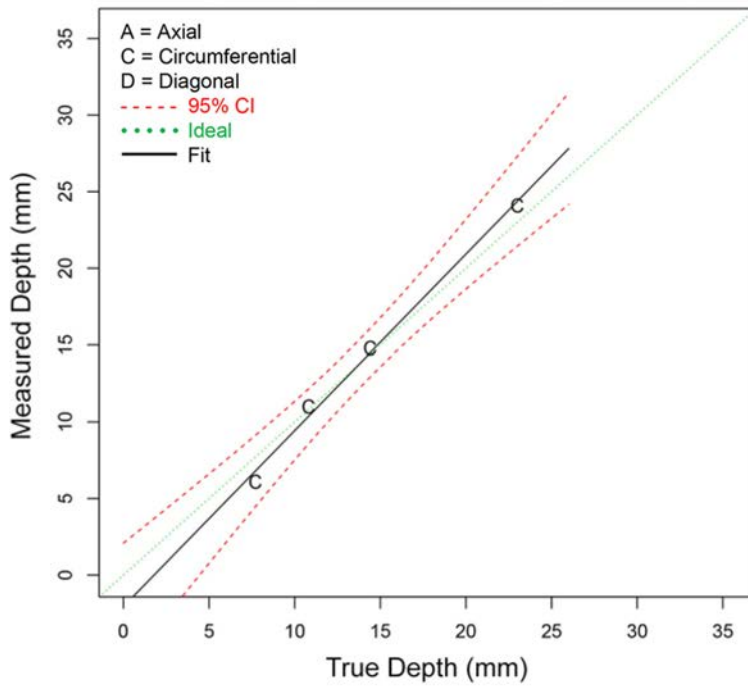


**Figure 6.9** Depth Sizing Regression Plot for LASH.18 Applied to SBDMW Test Blocks (w/o FB test blocks) with O.D. Access

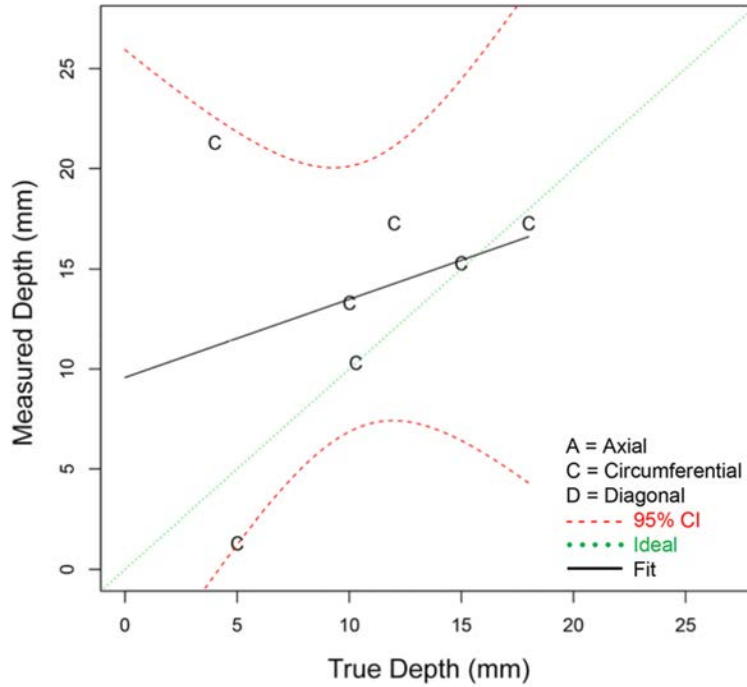


Figure 6.10 Depth Sizing Regression Plot for HHUT.27.2 Applied to FB Test Blocks with O.D. Access

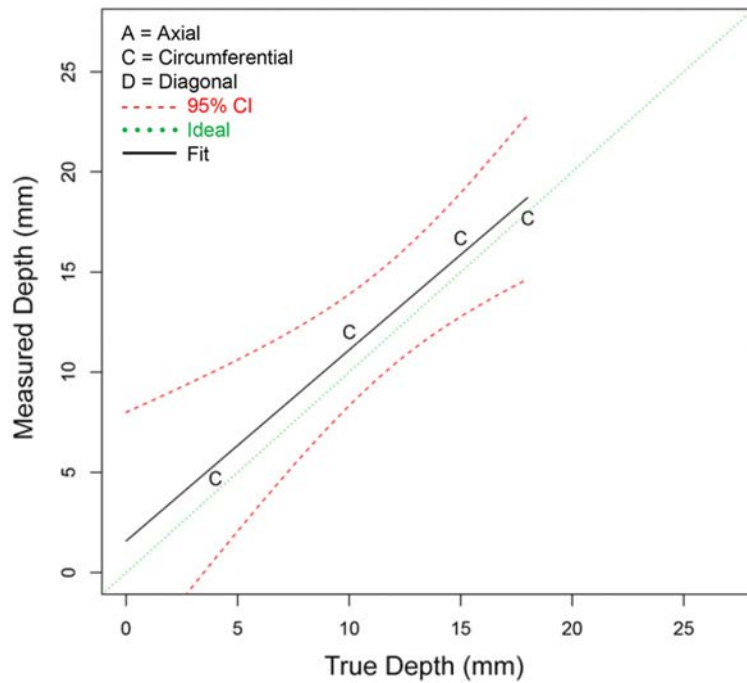
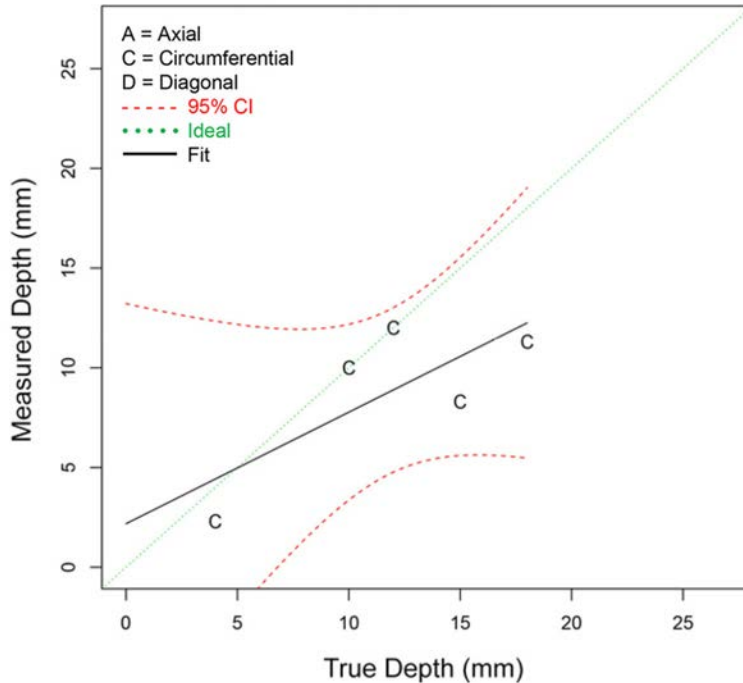


Figure 6.11 Depth Sizing Regression Plot for SHPA.6.3 Applied to FB Test Blocks with O.D. Access





**Figure 6.12 Depth Sizing Regression Plot for LASH.18 Applied to FB Test Blocks with O.D. Access**

### **6.3 Analysis of FB Test Block Results**

A summary of I.D. and O.D. access depth sizing performances for all FB test blocks is provided in Table 6.9 in terms of RMSE. This table indicates that the RMSE for I.D. access examinations of P32 is much greater than for other FB test blocks. In addition, the RMSE for O.D. access examinations of P31, P32, and P38 is greater than for other FB test blocks. All of the FB test blocks contain laboratory-grown SCC flaws with the exception of P30, which contains an MFC, and P42, which contains an EDM notch. Specimen P38 is the only specimen to exhibit geometric asymmetry in the weld.

Summaries of depth sizing performances for procedure types applied by I.D. access to FB test blocks are provided in Tables 6.10 through 6.16. These summaries show that the ADVPAUT procedure type is the only procedure type applied for I.D. access examination of all FB test blocks. Summaries of depth sizing performances for procedure types applied by O.D. access to FB test blocks are provided in Tables 6.17 through 6.23. The RMSE for ADVPAUT procedures applied by I.D. and O.D. access is greater for P32 than for other FB test blocks. For test block P38, the PAUT and UIR procedure types applied by O.D. access exhibit greater RMSE than for other FB test blocks. However, the sizing data for UIR is only based on one sample in each of Tables 6.17 through 6.23.

**Table 6.9 Comparison of Depth Sizing Performances for FB Test Blocks**

	I.D. Access		O.D. Access	
	NOBS	RMSE (mm)	NOBS	RMSE (mm)
P28	3	0.9	14	2.5
P29	3	1.7	15	2.1
P30	3	1.9	15	2.4
P31	3	2.2	13	7.0
P32	3	6.0	13	4.3
P38	2	1.3	12	7.0
P42	2	1.0	9	0.9

**Table 6.10 Depth Sizing Results for P28 by Procedure Type for I.D. Access**

	NOBS	Bias (mm)	RMSE (mm)
ADVPAUT	2	0.7	0.7
NLUT	1	1.3	1.3
All	3	0.9	0.9

**Table 6.11 Depth Sizing Results for P29 by Procedure Type for I.D. Access**

	NOBS	Bias (mm)	RMSE (mm)
ADVPAUT	2	1.7	2.0
NLUT	1	-0.7	0.7
All	3	0.9	1.7

**Table 6.12 Depth Sizing Results for P30 by Procedure Type for I.D. Access**

	NOBS	Bias (mm)	RMSE (mm)
ADVPAUT	2	-0.2	0.2
NLUT	1	-3.2	3.2
All	3	-1.2	1.9

**Table 6.13 Depth Sizing Results for P31 by Procedure Type for I.D. Access**

	NOBS	Bias (mm)	RMSE (mm)
ADVPAUT	2	2.2	2.7
NLUT	1	0.6	0.6
All	3	1.7	2.2

**Table 6.14 Depth Sizing Results for P32 by Procedure Type for I.D. Access**

	NOBS	Bias (mm)	RMSE (mm)
ADVPAUT	2	7.3	7.3
NLUT	1	-1.6	1.6
All	3	4.3	6.0

**Table 6.15 Depth Sizing Results for P38 by Procedure Type for I.D. Access**

	NOBS	Bias (mm)	RMSE (mm)
ADVPAUT	2	1.2	1.3
All	2	1.2	1.3

**Table 6.16 Depth Sizing Results for P42 by Procedure Type for I.D. Access**

	NOBS	Bias (mm)	RMSE (mm)
ADVPAUT	2	0.9	1.0
All	2	0.9	1.0

**Table 6.17 Depth Sizing Results for P28 by Procedure Type for O.D. Access**

	NOBS	Bias (mm)	RMSE (mm)
ADVPAUT	3	3.2	3.4
NLUT	3	2.1	3.1
PAUT	5	-0.8	1.9
RT	1	-1.4	1.4
UIR	1	0.3	0.3
UT	1	1.2	1.2
All	14	0.9	2.5

**Table 6.18 Depth Sizing Results for P29 by Procedure Type for O.D. Access**

	NOBS	Bias (mm)	RMSE (mm)
ADVPAUT	3	2.8	3.3
NLUT	3	1.8	2.2
PAUT	5	-0.3	0.9
RT	2	1.5	2.1
UIR	1	-2.1	2.1
UT	1	-0.7	0.7
All	15	0.8	2.1

**Table 6.19 Depth Sizing Results for P30 by Procedure Type for O.D. Access**

	NOBS	Bias (mm)	RMSE (mm)
ADVPAUT	3	-0.7	2.7
NLUT	3	-2.6	3.9
PAUT	5	-1.1	1.7
RT	2	-0.7	0.9
UIR	1	2.2	2.2
UT	1	-0.2	0.2
All	15	-1.0	2.4

**Table 6.20 Depth Sizing Results for P31 by Procedure Type for O.D. Access**

	NOBS	Bias (mm)	RMSE (mm)
ADVPAUT	3	6.5	6.9
NLUT	3	5.4	10.0
PAUT	4	4.2	7.0
RT	1	-0.1	0.1
UIR	1	1.2	1.2
UT	1	-0.1	0.1
All	13	4.1	7.0

**Table 6.21 Depth Sizing Results for P32 by Procedure Type for O.D. Access**

	NOBS	Bias (mm)	RMSE (mm)
ADVPAUT	3	3.8	7.2
NLUT	3	-1.6	4.0
PAUT	4	1.0	1.7
RT	1	-3.7	3.7
UIR	1	-2.8	2.8
UT	1	-1.1	1.1
All	13	0.2	4.3

**Table 6.22 Depth Sizing Results for P38 by Procedure Type for O.D. Access**

	NOBS	Bias (mm)	RMSE (mm)
ADVPAUT	3	6.2	6.7
NLUT	1	-3.7	3.7
PAUT	5	4.0	8.9
RT	1	-0.6	0.6
UIR	1	7.2	7.2
UT	1	0.7	0.7
All	12	3.5	7.0

**Table 6.23 Depth Sizing Results for P42 by Procedure Type for O.D. Access**

	NOBS	Bias (mm)	RMSE (mm)
ADVPAUT	3	0.5	1.2
NLUT	1	0.0	0.0
PAUT	4	-0.1	0.5
UT	1	1.5	1.5
All	9	0.3	0.9

#### **6.4 Comparison of Linear and Sectorial PAUT by Team 122**

The depth sizing performances of procedures PAUT.122.1 and PAUT.122.2 are summarized in Table 6.24 and in Figures 6.13 and 6.14. Descriptions of the PAUT.122.1 and PAUT.122.2 procedures are provided in Appendix C.3.3. PAUT.122.1 employs a linear PAUT technique and PAUT.122.2 employs a sectorial PAUT technique. The data provided in Table 6.24 and in Figures 6.13 and 6.14 indicate that both procedures exhibit similar performances.

**Table 6.24 Summary of Depth Sizing Performances for Procedures PAUT.122.1 and PAUT.122.2**

	NOBS	Bias (mm)	RMSE (mm)
PAUT.122.1 (Linear)	7	0.4	0.9
PAUT.122.2 (Sectorial)	7	0.0	1.1

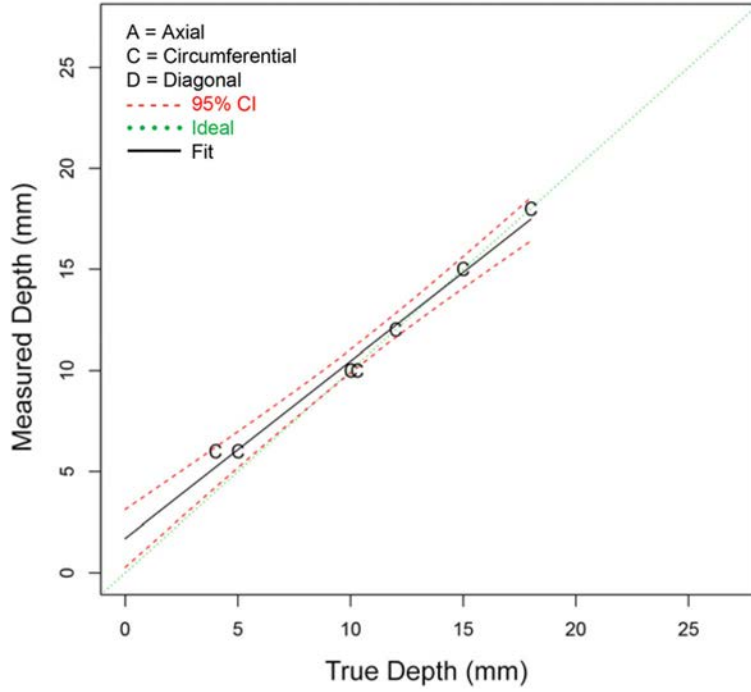


**Figure 6.13** Depth Sizing Regression for Procedure PAUT.122.1 (Linear) for FB Test Blocks by O.D. Access

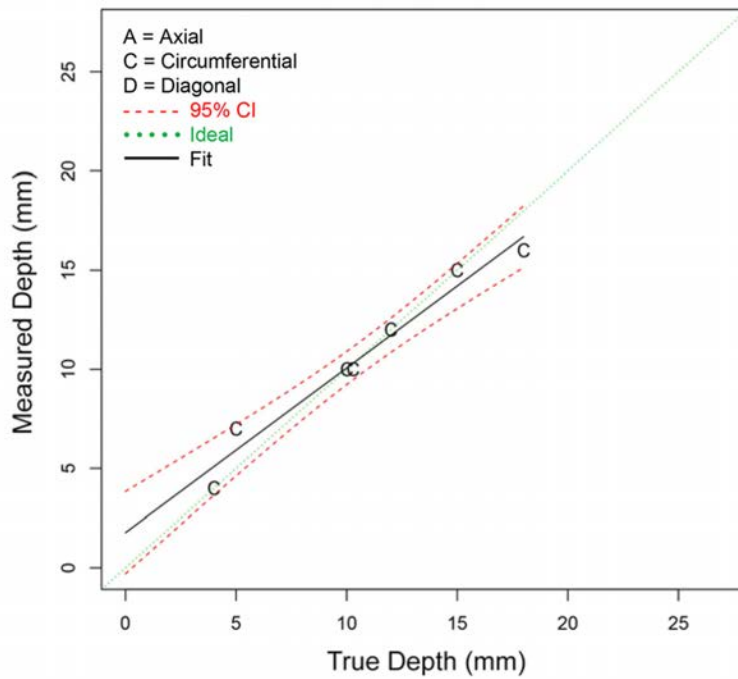


**Figure 6.14** Depth Sizing Regression for Procedure PAUT.122.2 (Sectorial) FB Test Blocks by O.D. Access

## 6.5 UIR Results

Depth sizing results are reported for UIR procedures applied to FB test blocks with O.D. access in Table 5.3. However, these depth sizing results are obtained from viewing the sides of the FB test blocks as depicted in Figures 6.15 and 6.16. This type of access is not practical in a field environment, and in this context, the results provide a better representation of length sizing performance. A view of the test block surface that the crack initiates from is provided in Figure 6.17. Together, Figures 6.15 through 6.17 demonstrate the capability of UIR to detect cracks in these specimens under laboratory conditions.



**Figure 6.15 UIR Image of FB Test Block P29 (view from side surface)**

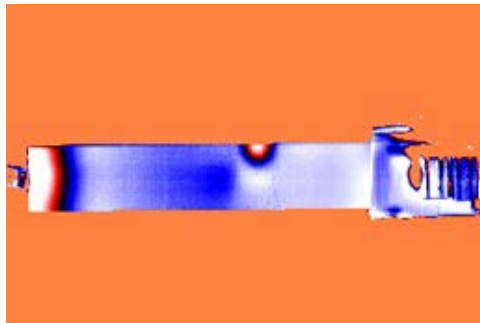


**Figure 6.16 UIR Image of FB Test Block P29 (view from side surface)**



**Figure 6.17 UIR Image of FB Test Block P29 (view of surface from which crack initiates)**

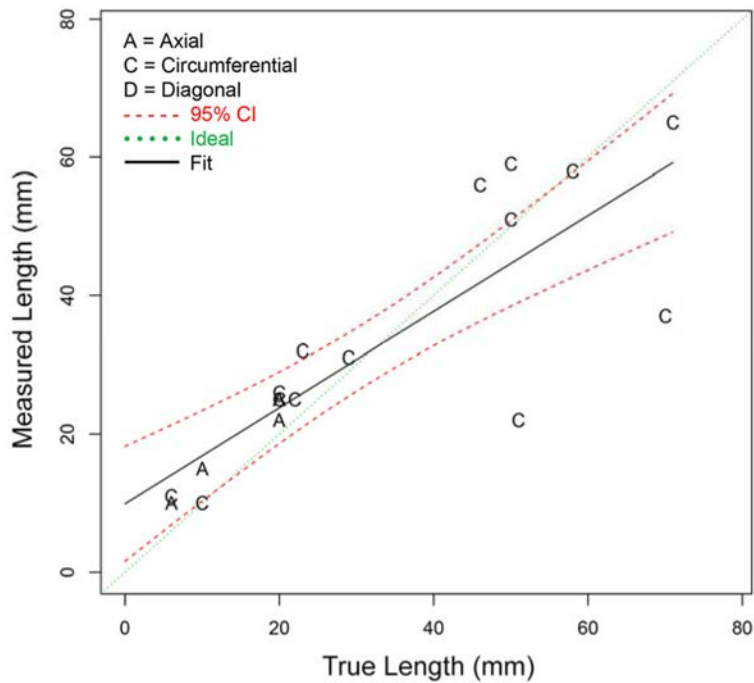
## **6.6 RT, Conventional UT, and ECT Results**

The RT and conventional UT procedure types generated the most accurate depth sizing data based on FB test blocks as indicated in Table 5.3. Figure 5.16 and Figure 5.21 indicate that that RT and conventional UT procedure types have a tendency to oversize the shallow flaws and to undersize for deeper flaws. Table 5.13 indicates that conventional UT has superior length sizing accuracy for SBDMW test blocks with O.D. access; however, the sample size is limited.

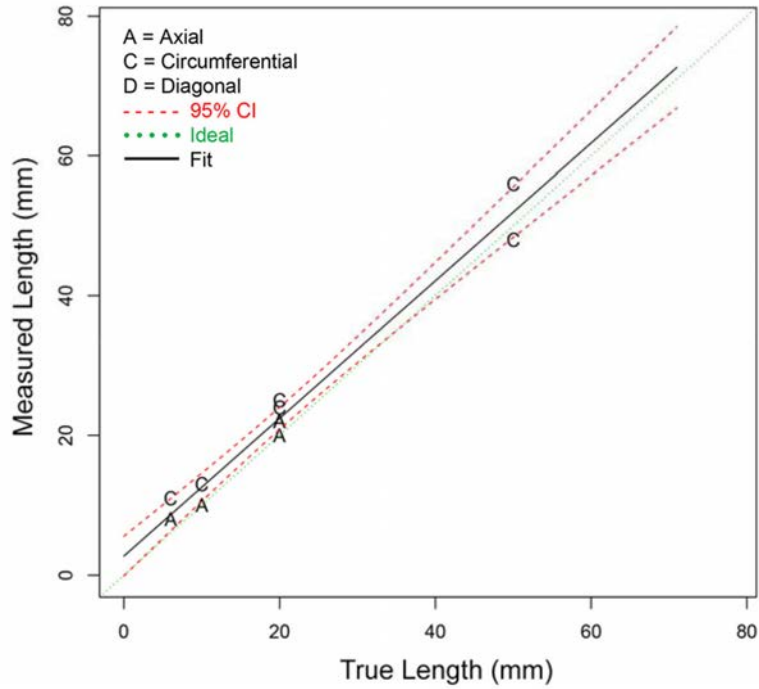
ECT length sizing results can be reviewed for SBDMW test blocks and LBDMW test blocks with I.D. access in Tables 5.14 and 5.16, respectively. Figure 5.29 and Figure 5.30 indicate a tendency to oversize shorter flaws and undersize longer flaws for both types of test blocks. Table 5.18 indicates that “advanced” ECT procedures (i.e., AECT.33) perform better than conventional ECT procedures (i.e., ECT.16) for SBDMW test blocks.



Table 5.20 indicates that the opposite is true for LBDMW test blocks; however, the sample sizes are limited in this case. Length sizing regression plots for specific ECT procedures can be reviewed in Figures 6.18, 6.19, and 6.20. Figure 6.18 indicates that AECT.33 may have a tendency to oversize shorter flaws and undersize longer flaws for SBDMW test blocks. Figure 6.19 shows that ECT.16 provides a response that correlates well with the true length over the full range of lengths considered for SBDMW test blocks. Finally, Figure 6.20 shows that AECT.33 has a tendency to oversize shorter flaws and undersize longer flaws for LBDMW test blocks although linear sizing performance is within the 95% confidence bounds.



**Figure 6.18** Length Sizing Regression Plot for Procedure AECT.33 Applied to SBDMW Test Blocks with I.D. Access



**Figure 6.19** Length Sizing Regression Plot for Procedure ECT.16 Applied to SBDMW Test Blocks with I.D. Access

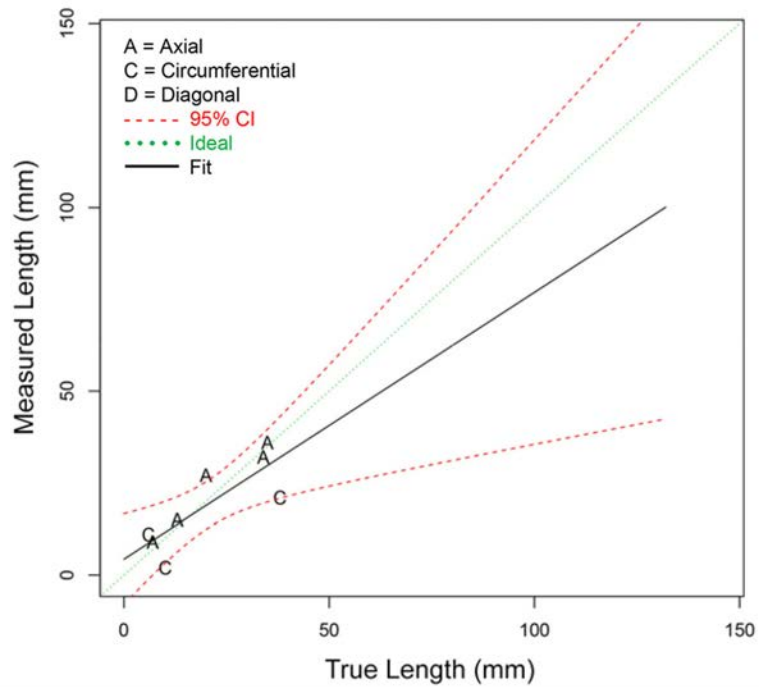


**Figure 6.20** Length Sizing Regression Plot for Procedure AECT.33 Applied to LBDMW Test Blocks with I.D. Access

## 6.7 Analysis of Data Response Images from FB Test Blocks

This section provides a brief discussion and analysis of data image responses obtained from FB test blocks with EDM notch, MFC, and SCC type flaws and a blank test block to illustrate the difficulty of detecting crack tip responses from SCC flaws and how it can be difficult to distinguish the crack tip response of SCC flaws from noise.

### 6.7.1 Comparison of PAATOFD.29.2 Responses from P42, P30, and P32

Some responses of technique PAATOFD.29.2 are reviewed in this section to compare responses obtained from EDM, MFC, and SCC flaws and to compare responses from I.D. access with responses from O.D. access. A summary of PAATOFD.29.2 is included in the table of Appendix B.1 and a description of the Phased Array Asymmetric TOFD technique is provided in Section 3 and in Appendix C. The responses are obtained from FB test blocks; specifically, test block P42 that contains an EDM notch, P30 that contains the MFC flaw, and P32 that contains a laboratory-grown SCC flaw. Figures 6.21 and 6.22 display responses for O.D. and I.D. access, respectively, on P42 while Figures 6.23 and 6.24 display the responses for O.D. and I.D. access, respectively, on P30. Finally, Figures 6.25 and 6.26 display O.D. and I.D. responses, respectively, from P32. In each figure, a red cursor appears over a region in the data image that identifies the response from the flaw tip. In addition, the depth position at 0 mm indicates the inspection surface, which is specified in the figure captions as I.D. or O.D and the opposite surface is located at 30 mm. In this case, it appears that the clearest tip signals are obtained from the EDM notch in P42, followed by the MFC flaw in P30, and the SCC flaw in P32 produces the weakest response. In comparing O.D. access response versus I.D. access response, it appears that both O.D. and I.D. access results in strong responses from the EDM notch in P42. Conversely, a clear response cannot be observed for the SCC block in P32 regardless of O.D. or I.D. access. It is unlikely that crack tip response is correctly identified by the red cursor in Figure 6.25 based on the location of the red cursor. The potential influence of O.D. versus I.D. access on signal response is most clearly demonstrated for the MFC flaw in P30. In this case, a stronger response from the tip of the MFC flaw is observed for I.D. access in Figure 6.24 in comparison to O.D. access in Figure 6.23.

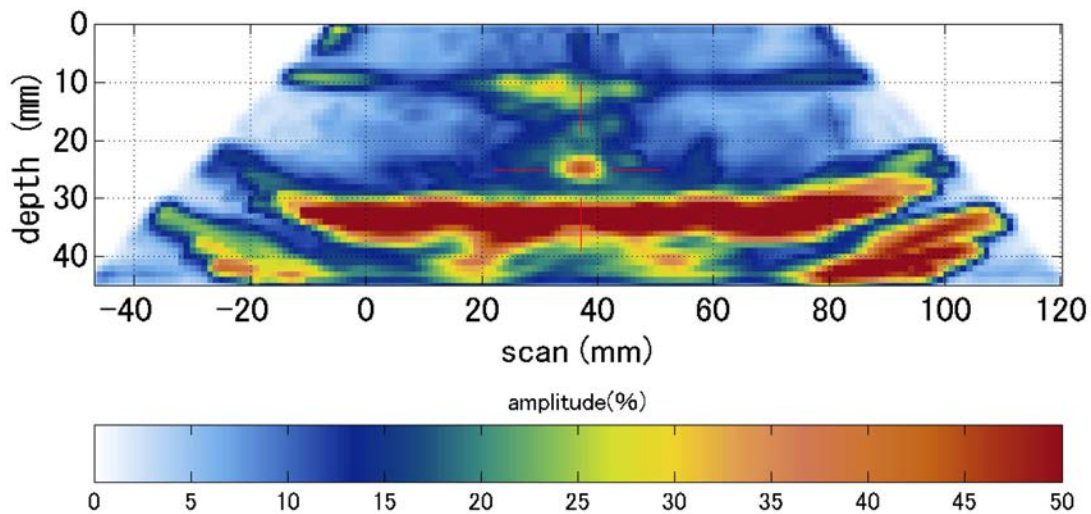


Figure 6.21 PAATOFD.29.2 Inspection of P42 (EDM) from O.D.

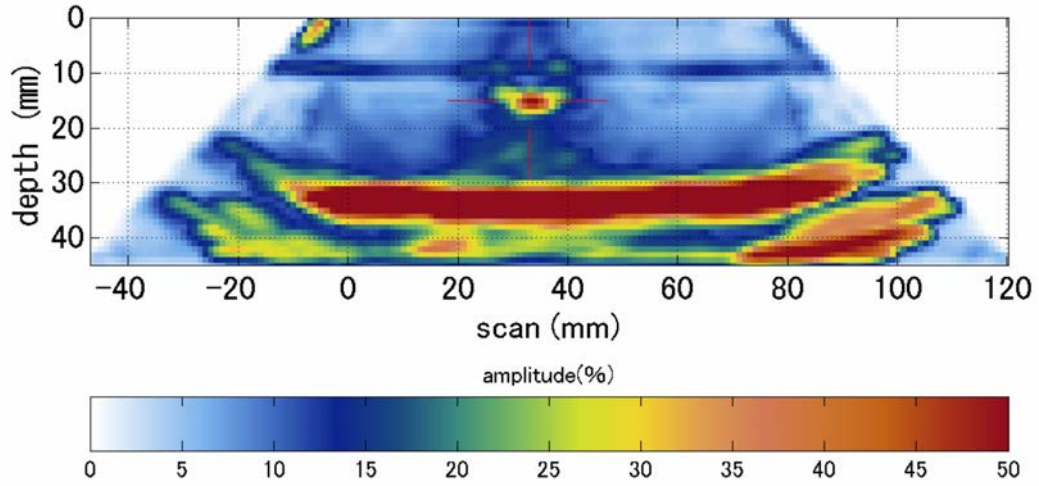


Figure 6.22 PAATOFD.29.2 Inspection of P42 (EDM) from I.D.

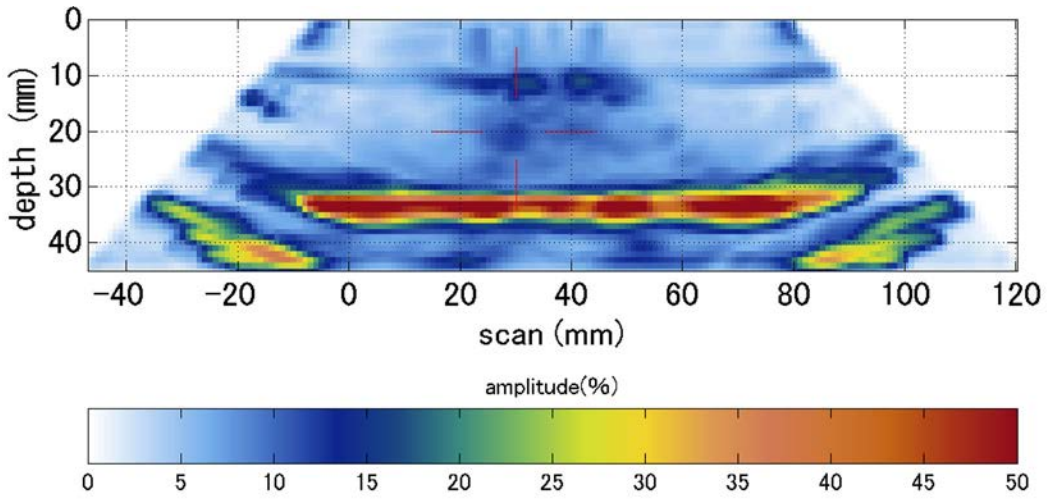


Figure 6.23 PAATOFD.29.2 Inspection of P30 (MFC) from O.D.

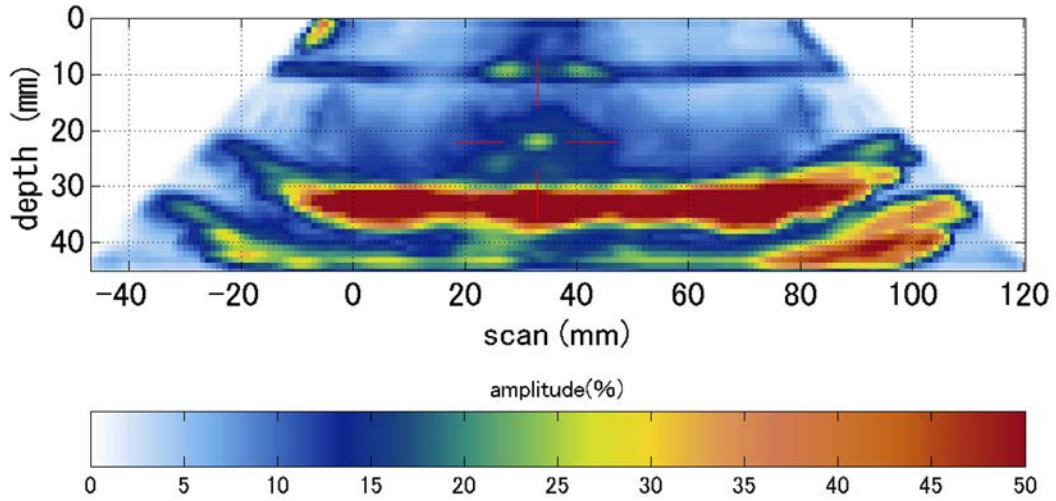


Figure 6.24 PAATOFD.29.2 Inspection of P30 (MFC) from I.D.

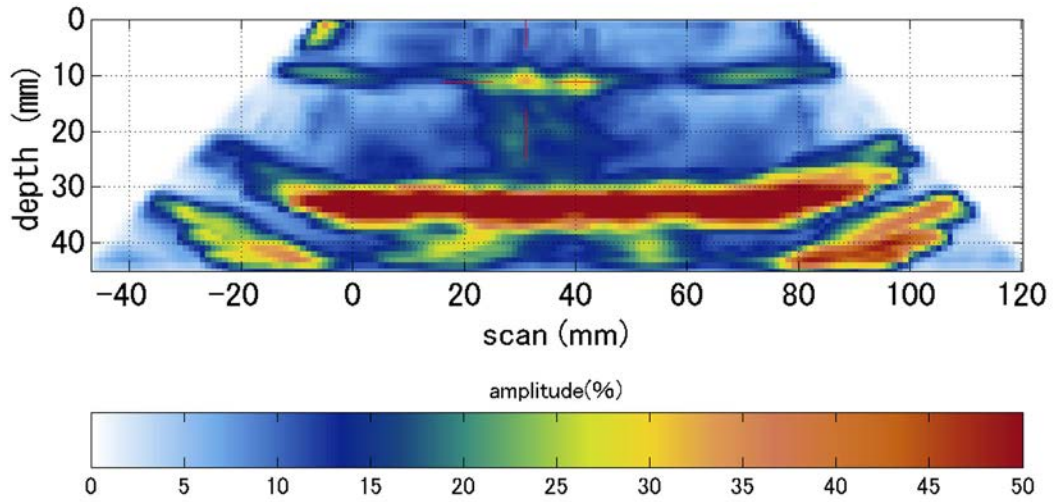
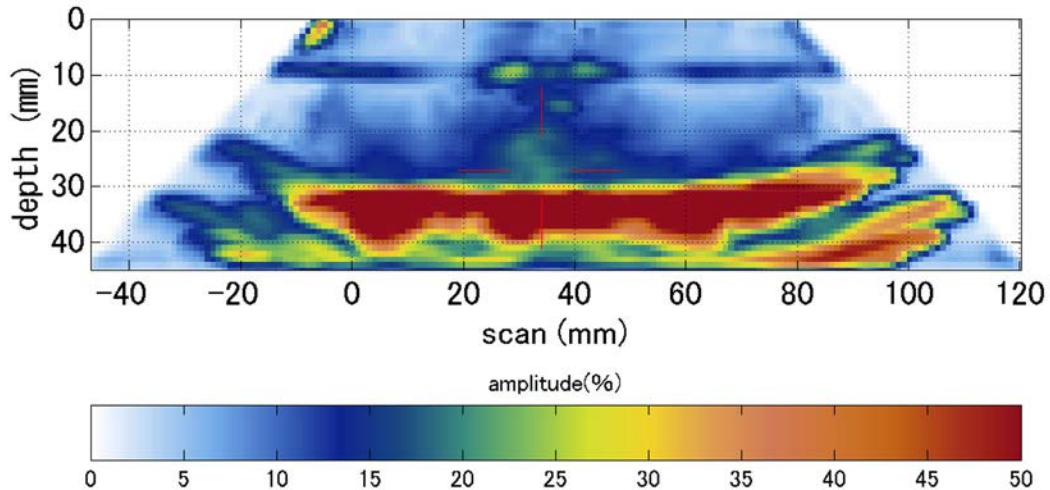


Figure 6.25 PAATOFD.29.2 Inspection of P32 (SCC) from O.D.



**Figure 6.26 PAATOFD.29.2 Inspection of P32 (SCC) from I.D.**

### **6.7.2 Comparison of SAFT.17 Responses from P42, P30, and P32**

For comparison of SAFT.17 responses, data images from an EDM notch (P42), MFC flaw (P30), and SCC flaw (P32) are provided in Figures 6.27 through 6.29, respectively, and the indication depth profiles along x for P42, P30, and P32 are provided in Figures 6.30 through 6.32, respectively. Although the SCC flaw in P32 appears to give a crack tip response that is comparable to the tip response obtained from the MFC flaw in P30, a review of the indication depth profiles indicates that the depth profile for the SCC flaw in P32 (Figure 6.32) is very uneven in contrast to the depth profiles for P42 and P30. Finally, the indication plots provided in Figures 6.33, 6.34, and 6.35 reveal how accurately SAFT.17 depth sized flaws in P42, P30, and P32, respectively. While depth measurements of the EDM notch in P42 and the MFC flaw in P30 are pretty accurate, the depth of the SCC flaw in P32 is significantly undersized.

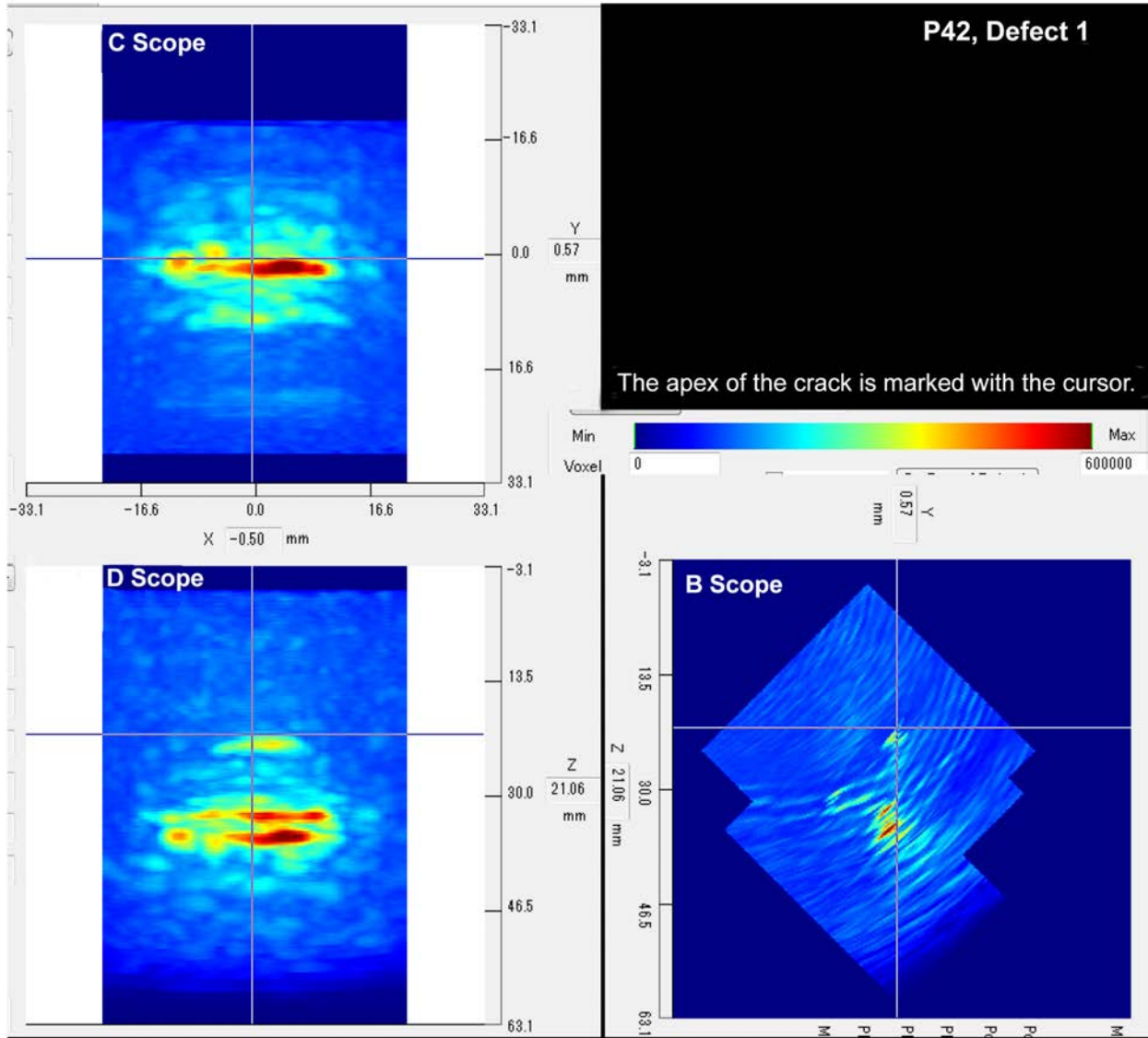
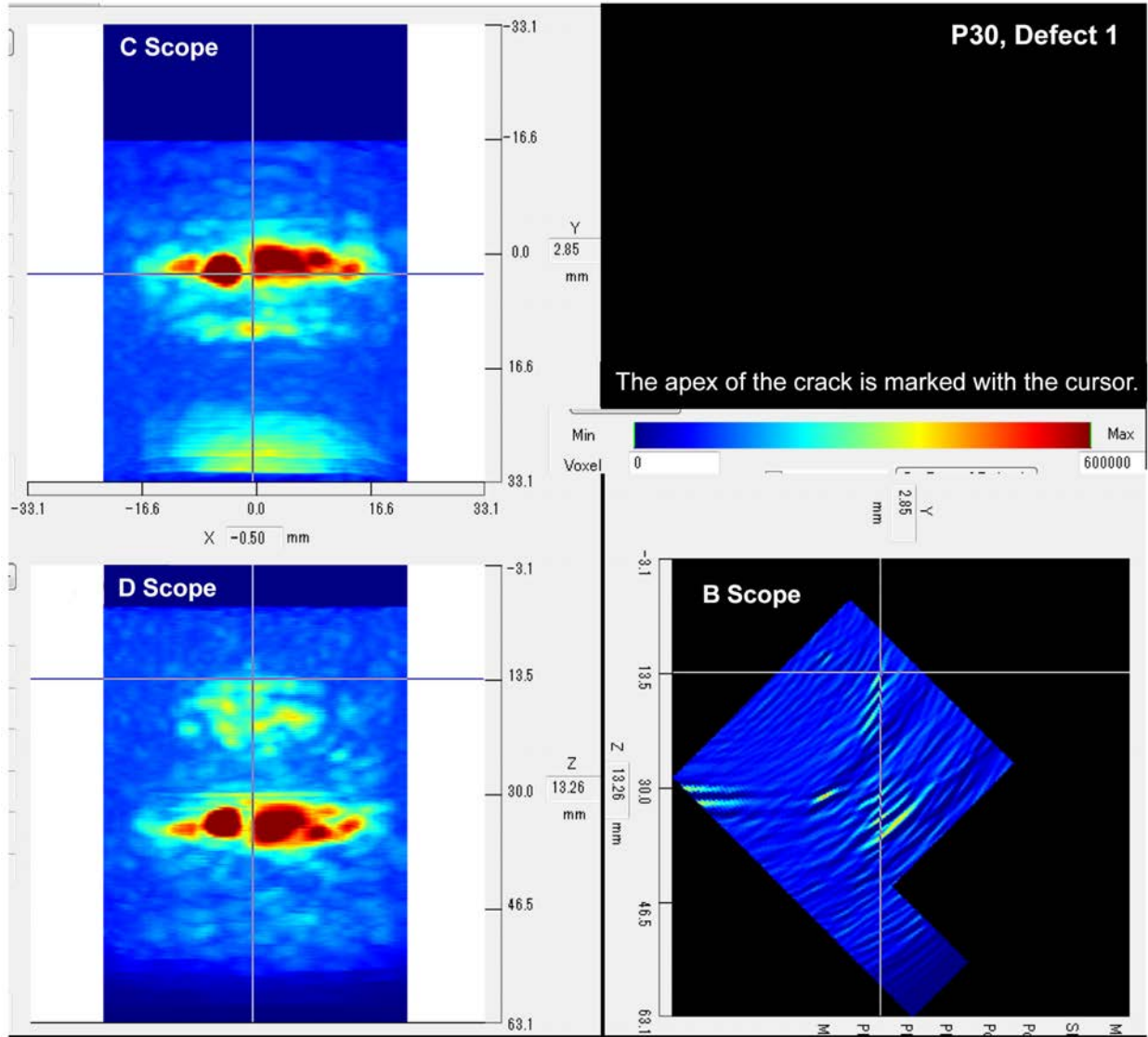
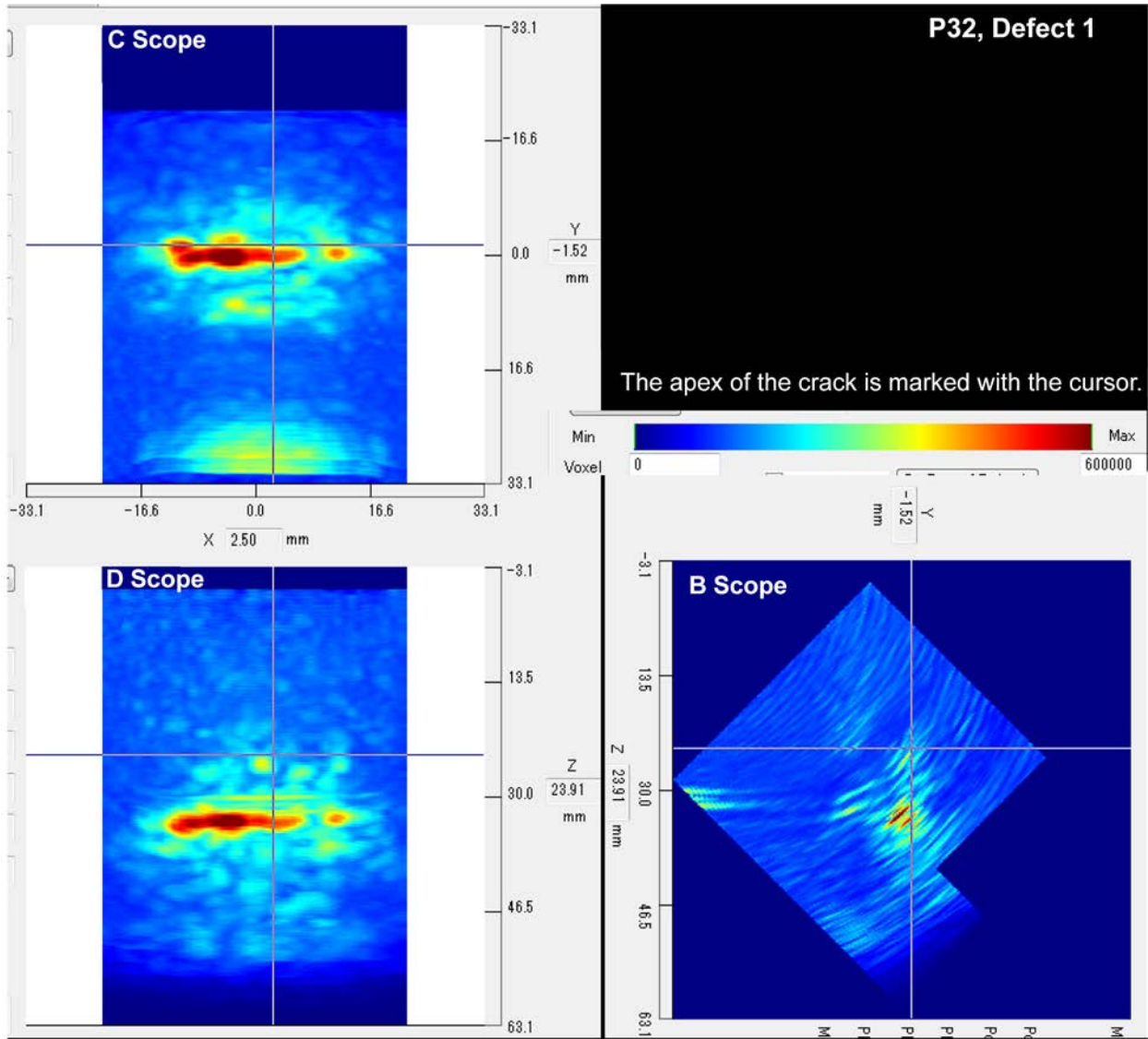


Figure 6.27 Data Images of Responses Obtained by SAFT-17 on Test Block P42 with EDM Notch



**Figure 6.28** Data Images of Responses Obtained by SAFT-17 on Test Block P30 with MFC Flaw





**Figure 6.29 Data Images of Responses Obtained by SAFT-17 on Test Block P32 with SCC Flaw**

P42, Defect 1

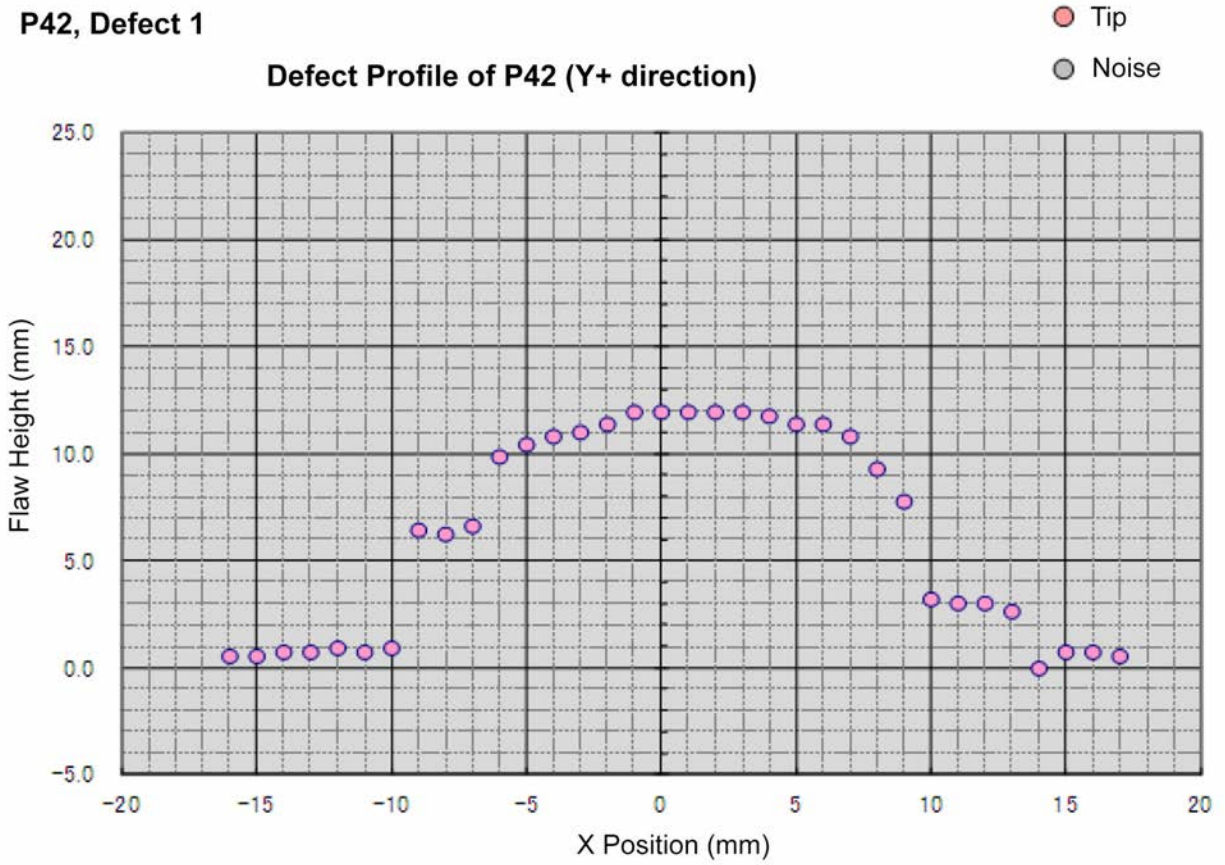


**Figure 6.30** Indication Depth Profile Obtained by SAFT-17 on Test Block P42 with EDM Notch

P30, Defect 1

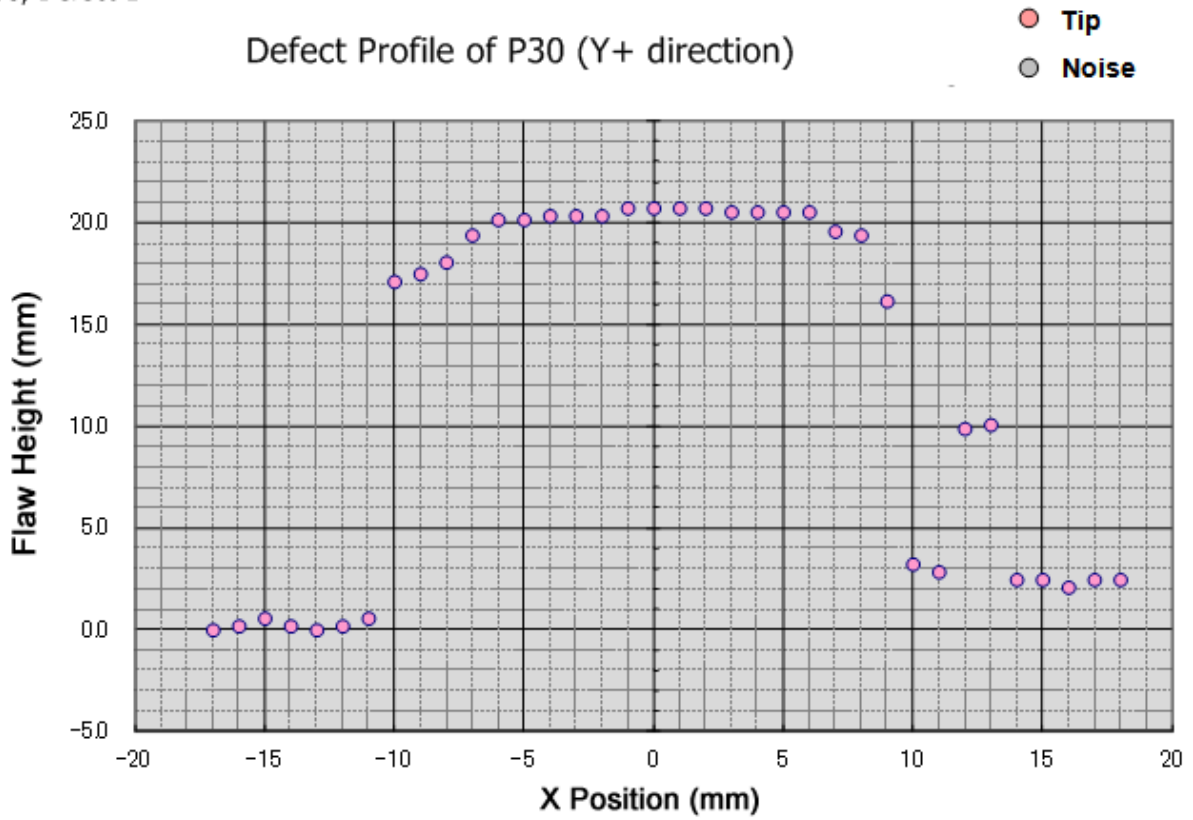


Figure 6.31 Indication Depth Profile Obtained by SAFT-17 on Test Block P30 with MFC Flaw

P32, Defect 1

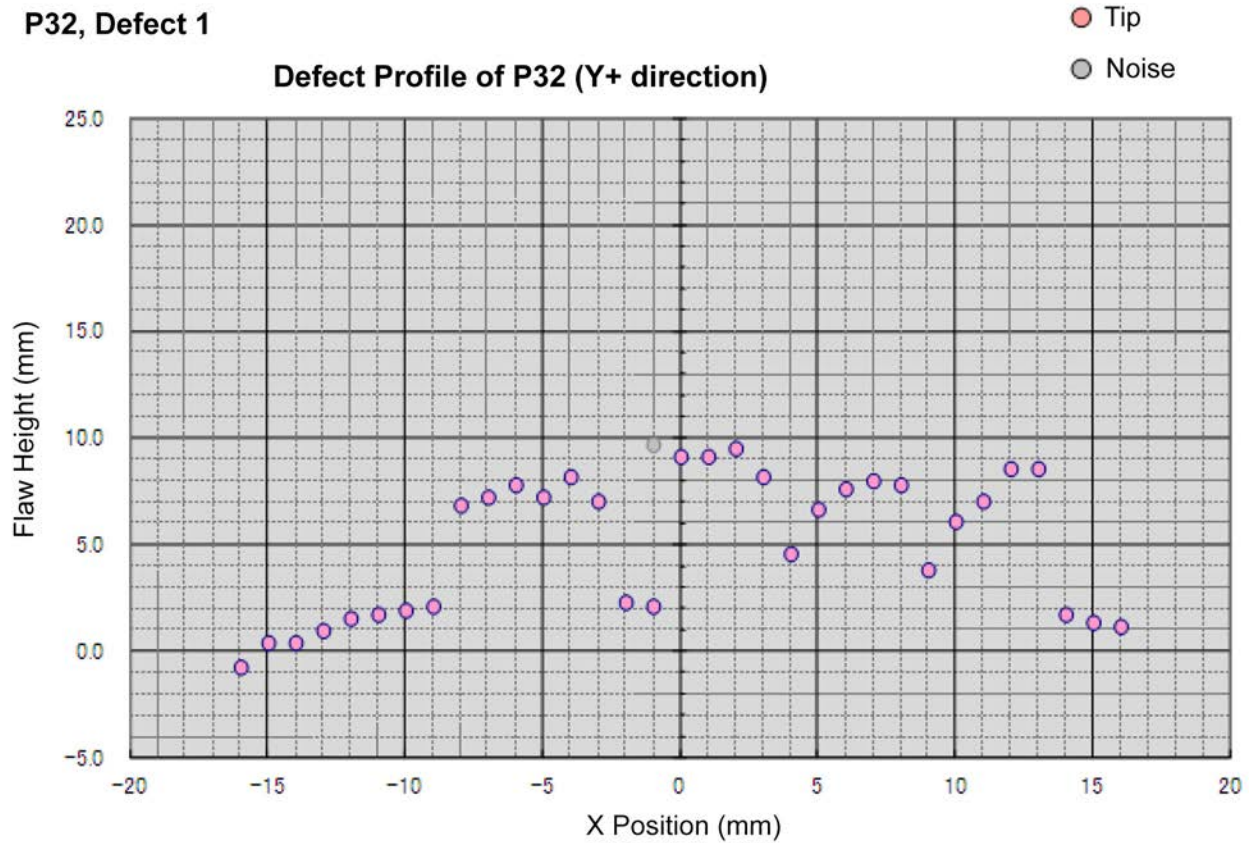


Figure 6.32 Indication Depth Profile Obtained by SAFT-17 on Test Block P32 with SCC Flaw

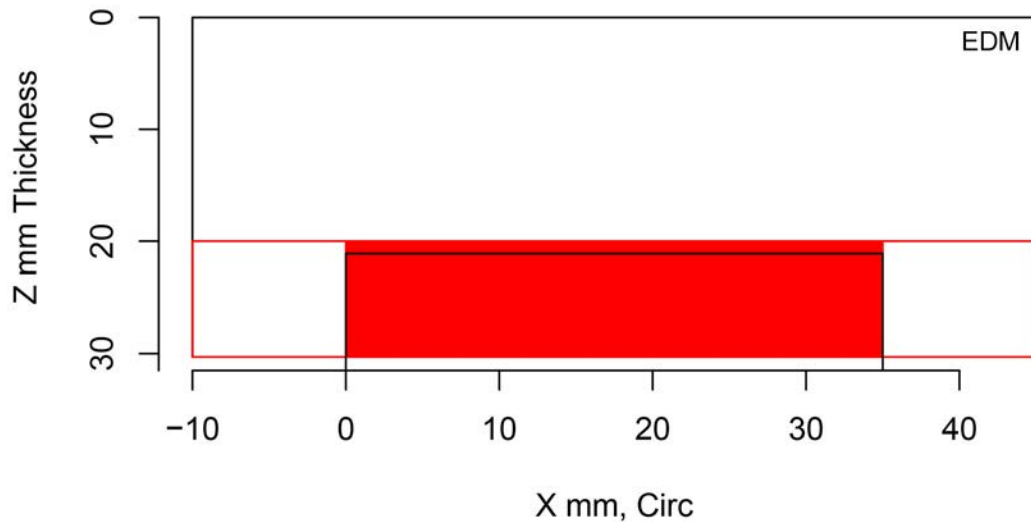
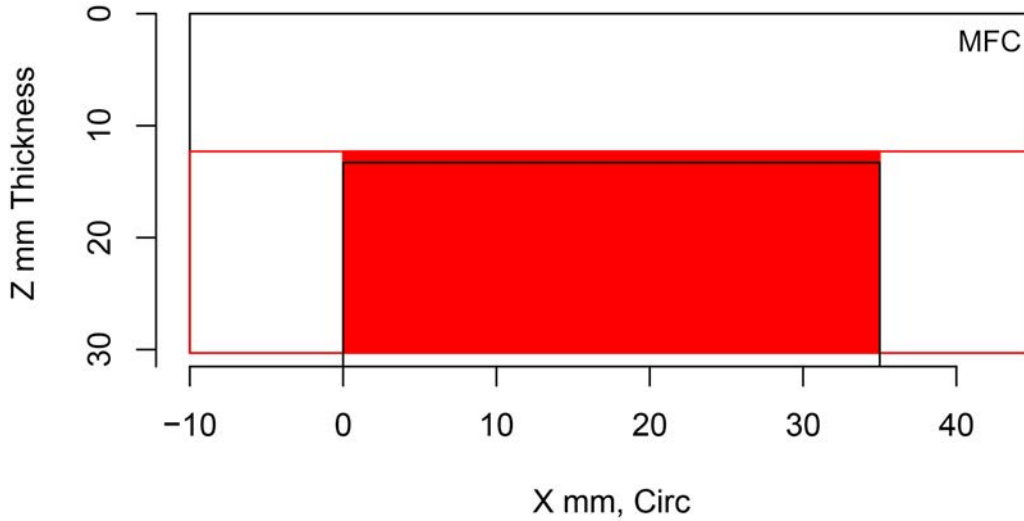
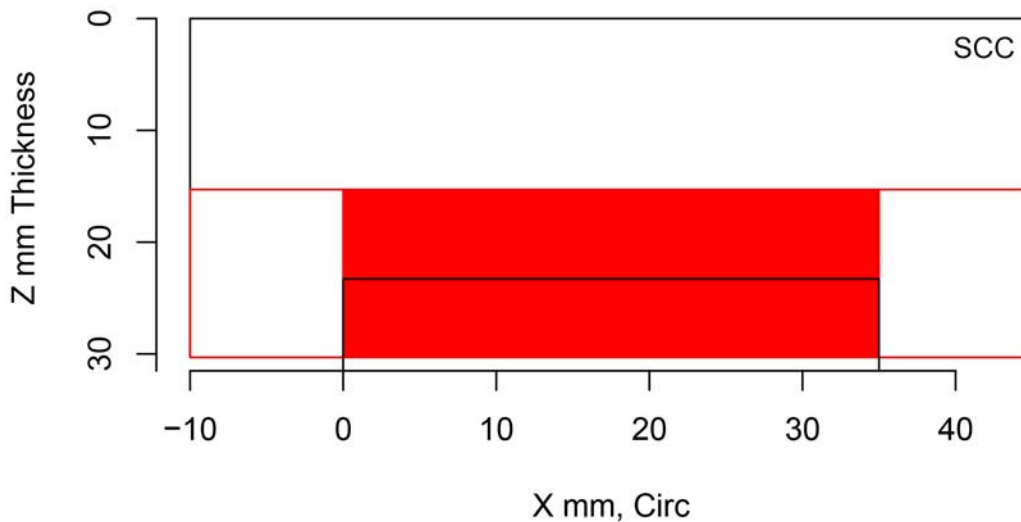


Figure 6.33 Indication Plot for Procedure SAFT.17 Applied to Test Block P42 in PARENT Open Testing (X - Z view)



**Figure 6.34** Indication Plot for Procedure SAFT.17 Applied to Test Block P30 in PARENT Open Testing (X – Z view)



**Figure 6.35** Indication Plot for Procedure SAFT.17 Applied to Test Block P32 in PARENT Open Testing (X – Z view)

### 6.7.3 PAUT.122.1 Responses from SCC Flaws

Data image responses from PAUT.122.1 are provided in this section from inspections of SCC flaws in P28 and P32 and inspections of MFC and EDM notch flaws in P30 and P42, respectively. PAUT.122.1 is a linear scan PAUT method applied with multiple refraction angles. Data images obtained for 60° and 50° angles applied to P28 from the right side of the weld are provided in Figure 6.36 and Figure 6.37, respectively. Figure 6.36 includes two arrows to highlight two weak signals that are considered possible crack tip responses. In Figure 6.37, a much stronger crack tip response is identified and used as the depth sizing basis for the inspection of P28.

Data images obtained from P32 are also included in Figure 6.38, Figure 6.39, and Figure 6.40. Figure 6.38 was obtained from the right side of the crack at a refraction angle of 50°. In this image, it is difficult to identify the response from the crack tip because of noise. Figure 6.39 and Figure 6.40 show data responses obtained from the left side of the weld in P32 at angles of 50° and 55°, respectively. In these figures, postulated crack tip responses are highlighted. Finally, Figure 6.41 and Figure 6.42 show data responses obtained from an MFC flaw in P30 and an EDM notch in P42, respectively.

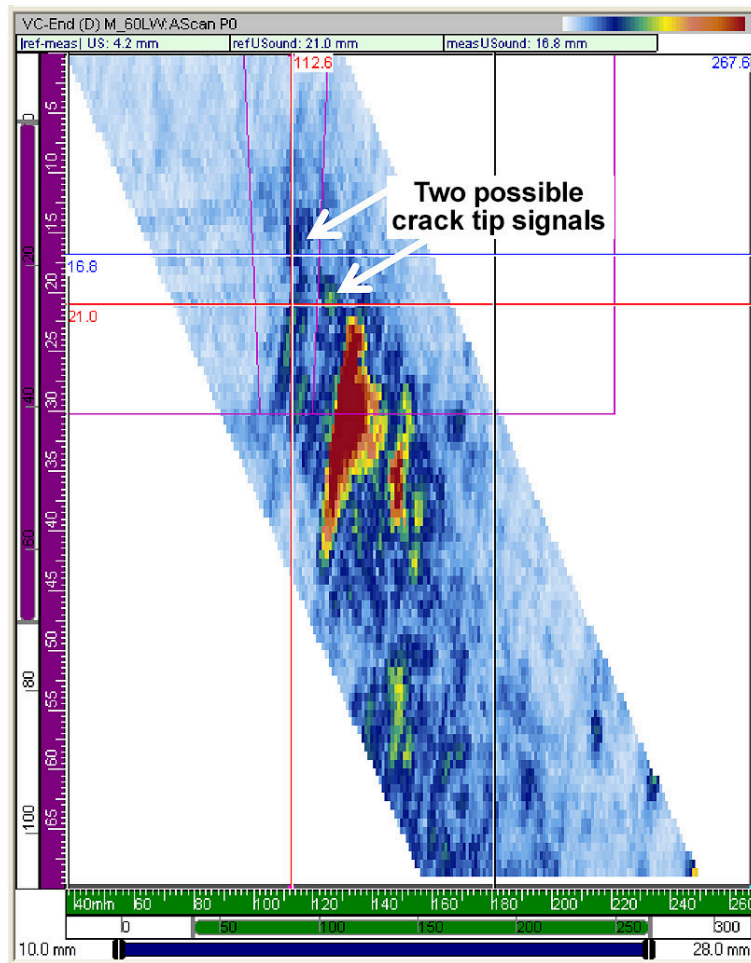


**Figure 6.36** Data Image Response for PAUT.122.1 Inspection of SCC Flaw in P28 Viewed from the Right Side of Weld. The Inspection was performed by linear scanning with longitudinal wave modes from TRL probe at 60°. Two possible crack tip signals are highlighted by arrows in the image.

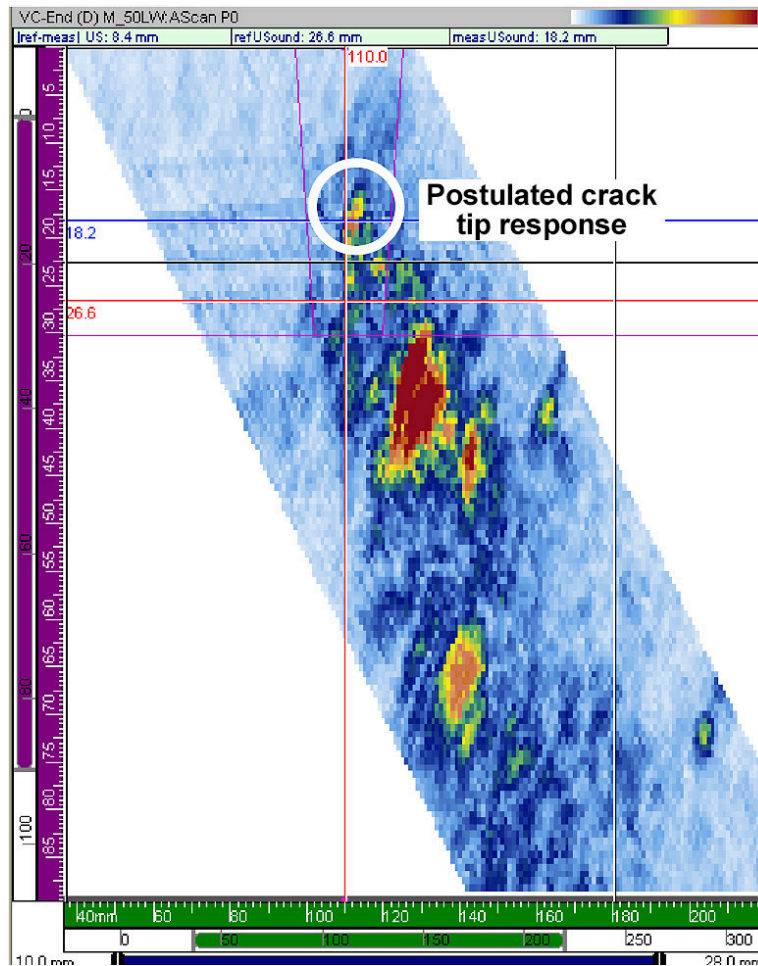


**Figure 6.37** Data Image Response for PAUT.122.1 Inspection of SCC Flaw in P28 Viewed from the Right Side of Weld. The Inspection was performed by linear scanning with longitudinal wave modes from TRL probe at 50°. The likely crack tip signal is identified with the white circle.

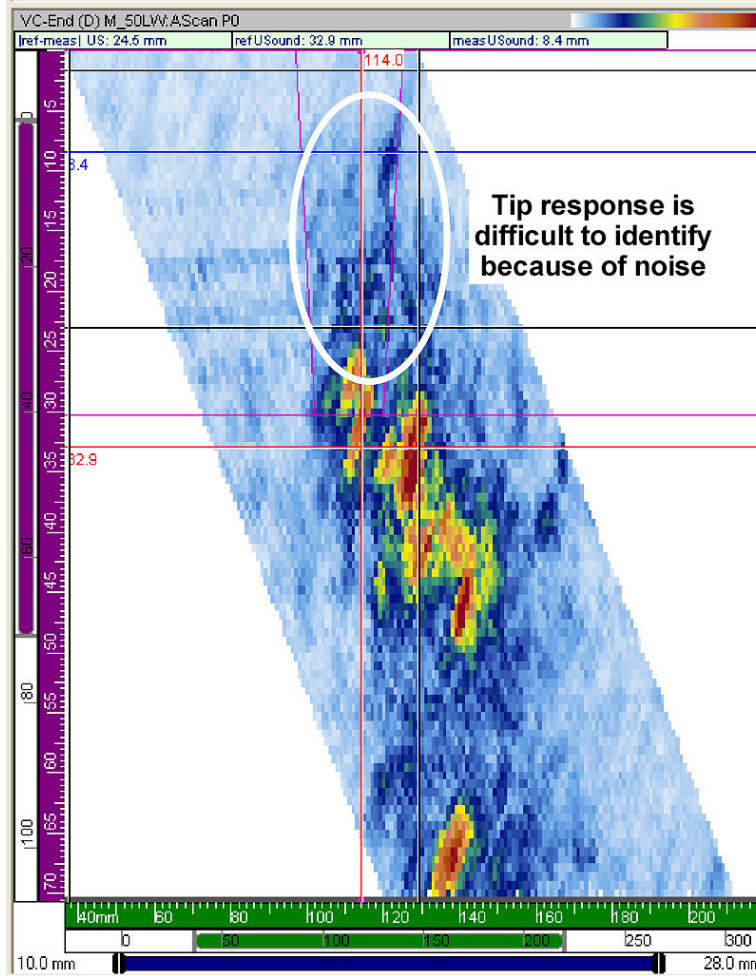


**Figure 6.38** Data Image Response for PAUT.122.1 Inspection of SCC Flaw in P32 Viewed from the Right Side of Weld. The inspection was performed by linear scanning with longitudinal wave modes from TRL probe at 50°. The white circle indicates that it is difficult to separate the tip response from noise.



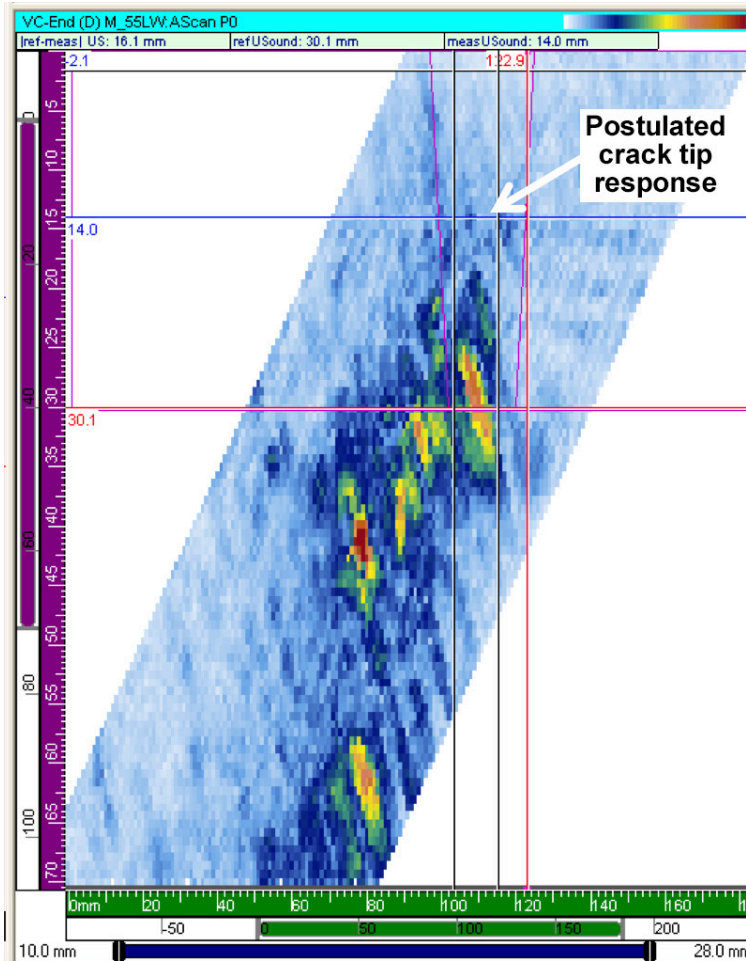


**Figure 6.39** Data Image Response for PAUT.122.1 Inspection of SCC Flaw in P32 Viewed from the Left Side of Weld. The inspection was performed by linear scanning with longitudinal wave modes from TRL probe at 55°. The white arrow highlights a weak signal considered to be the crack tip response.

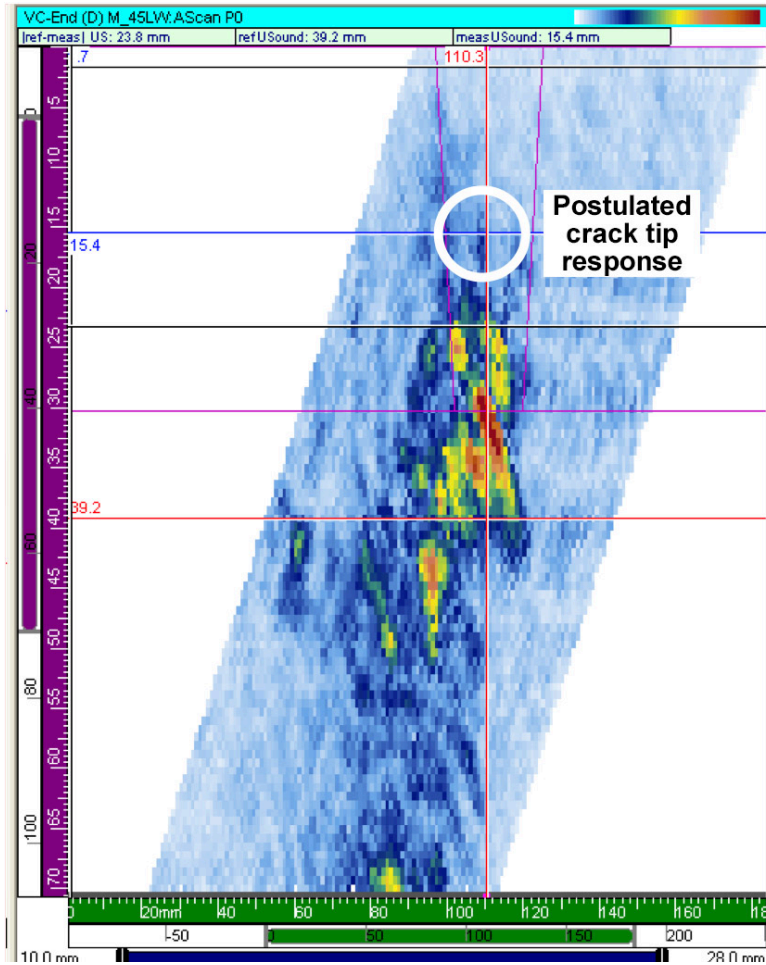


**Figure 6.40** Data Image Response for PAUT.122.1 Inspection of SCC Flaw in P32 Viewed from the Left Side of Weld. The inspection was performed by linear scanning with longitudinal wave modes from TRL probe at 45°. The white circle highlights the signal considered to be the crack tip response.

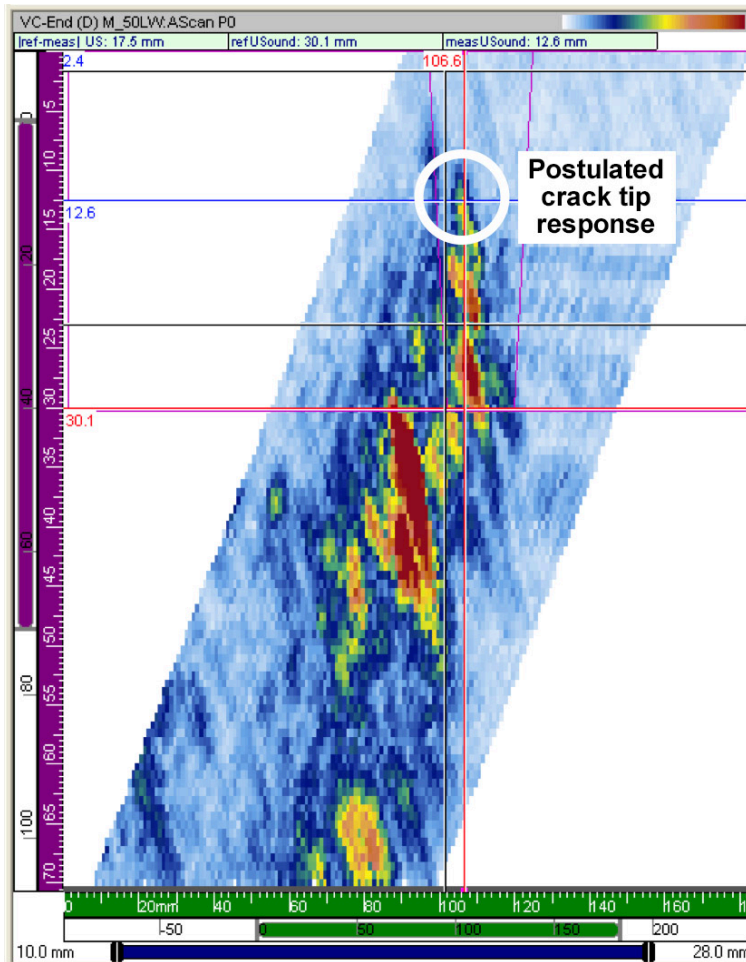


**Figure 6.41** Data Image Response for PAUT.122.1 Inspection of MFC Flaw in P30 Viewed from the Left Side of Weld. The inspection was performed by linear scanning with longitudinal wave modes from TRL Probe at 50°. The white circle highlights the signal considered to be the tip response.

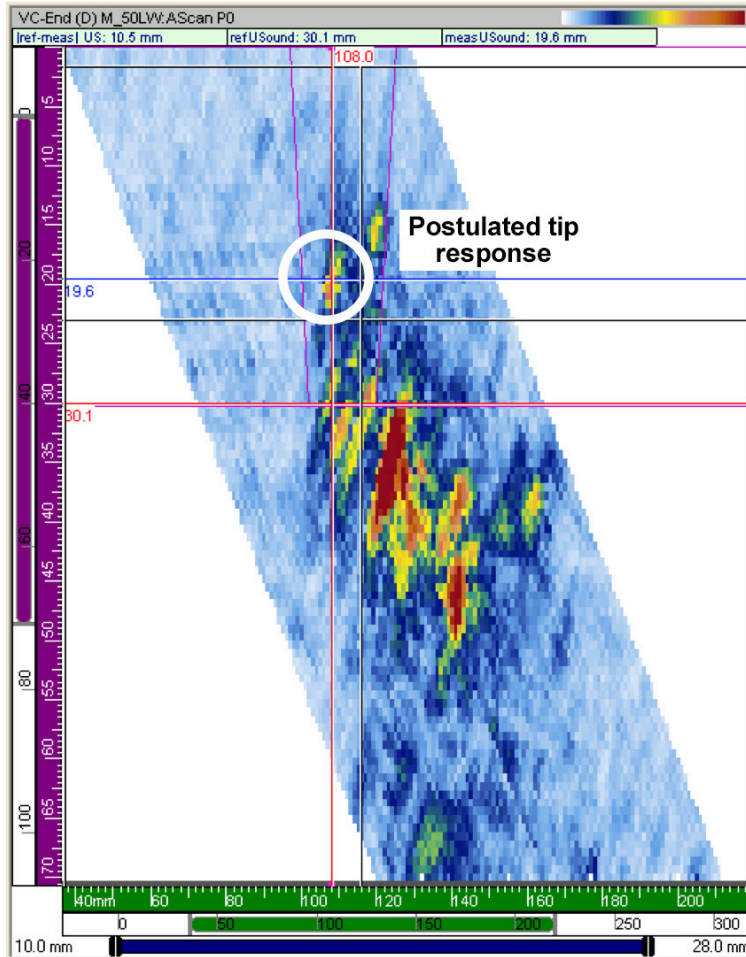


**Figure 6.42 Data Image Response for PAUT.122.1 Inspection of EDM Notch in P42 Viewed from the Right Side of Weld. The inspection was performed by linear scanning with longitudinal wave modes from TRL probe at 50°. The white circle highlights the signal considered to be the tip response.**

#### **6.7.4 Team 22 SAFT and PATRT Responses from P29**

Images of team 22 responses obtained on FB test block P29 are included in Figures 6.43 through 6.46. The flaw in FB test block is a laboratory-grown SCC flaw. The responses are obtained for a synthetic aperture focusing technique (SAFT) and phased array time reversal technique (PATRT) using longitudinal (L-mode) and shear (S-mode) waves. The A-scan in the left of Figure 6.43 indicates a sharp response at the potential location of the crack tip; however, the back-wall signal is not observable. Figures 6.44 and 6.46, which represent responses for S-mode waves using SAFT and PATRT, respectively, illustrate that although the crack tip signal may be discernable, the SNR does not appear to be large. Finally, the image in Figure 6.45 for L-mode waves using PATRT appears to provide the clearest crack tip and back-wall signals.

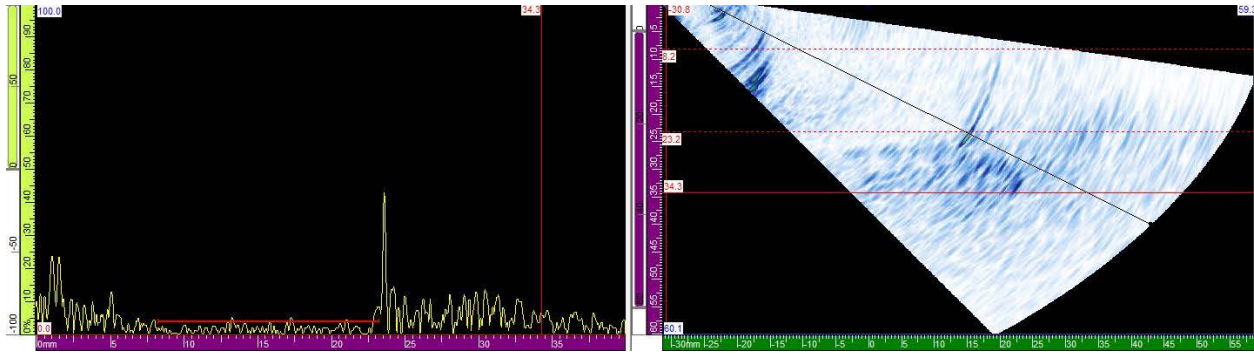


**Figure 6.43 Image of Response for Team 22 SAFT Response with L-waves**

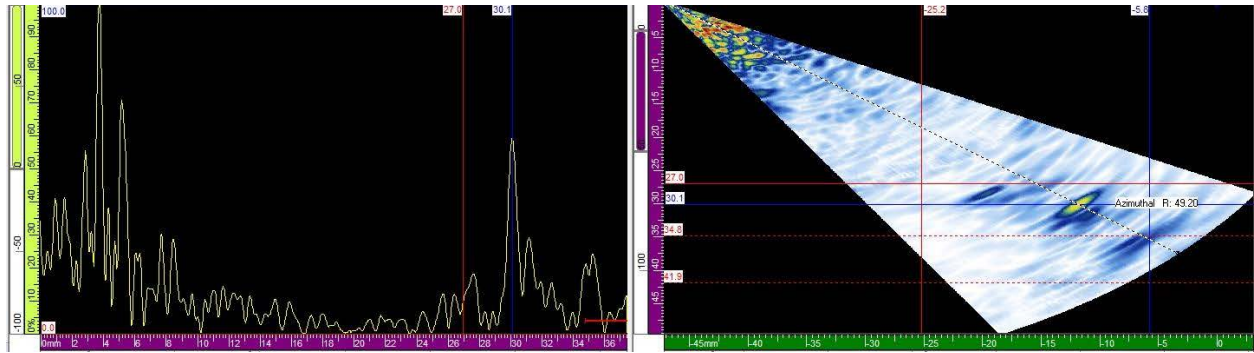


**Figure 6.44 Image of Response for Team 22 SAFT Response with S-waves**

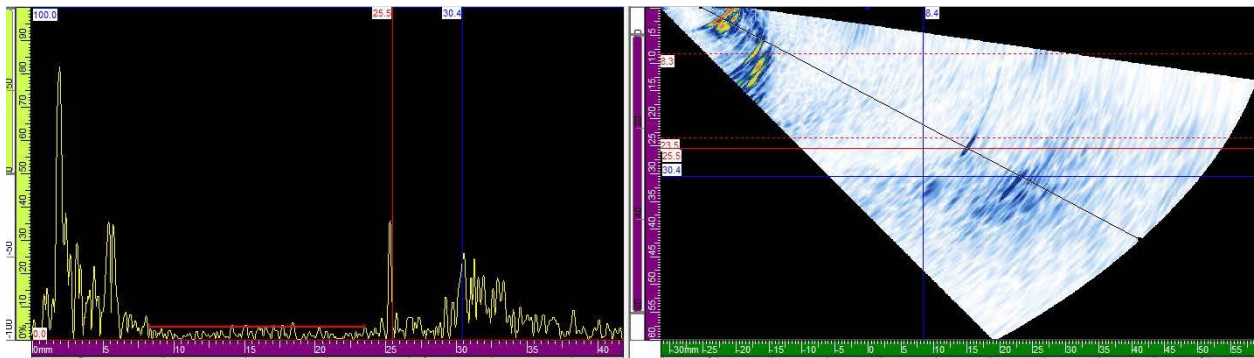


**Figure 6.45 Image of Response for Team 22 PATRT Response with L-waves**

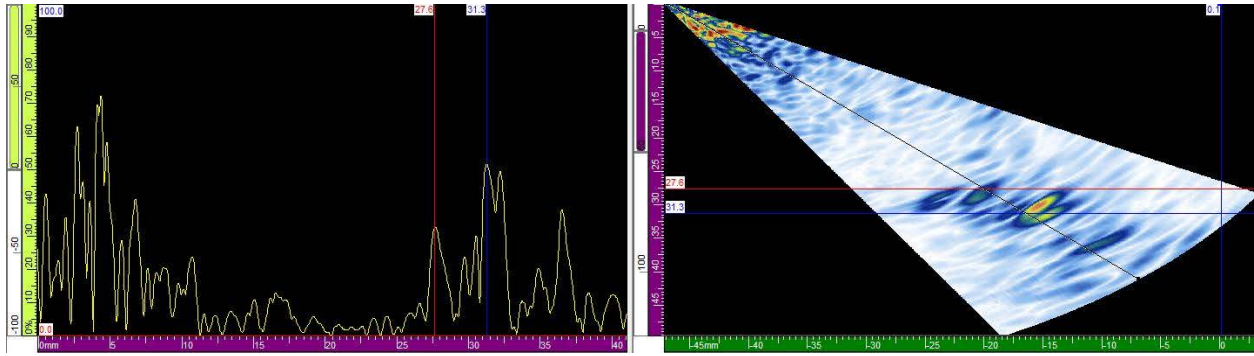


**Figure 6.46 Image of Response for Team 22 PATRT Response with S-waves**

### 6.7.5 SAFT.17 Depth Measurement on P46

Test data collected by SAFT.17 on FB test block P46 is interesting because P46 is blank and a depth measurement was reported. An illustration of P46 geometry and dimensions are provided in Figure 6.47. In this case, measurements were made on both sides of the center of P46 where a flaw would be expected (at  $y = 110$ ) and access was from the O.D. surface. Data images of the response from SAFT.17 obtained at  $y = 103.6$  mm are provided in Figure 6.48 and a profile of the measured indication depth along  $x$  is provided in Figure 6.49. Similarly, data images of the response from SAFT.17 obtained at  $y = 120$  mm are provided in Figure 6.50 and a profile of the measured indication depth along  $x$  is provided in Figure 6.51. These measurements indicate that the level of noise in blank test block P46 is sufficient to be mistaken for an actual defect.

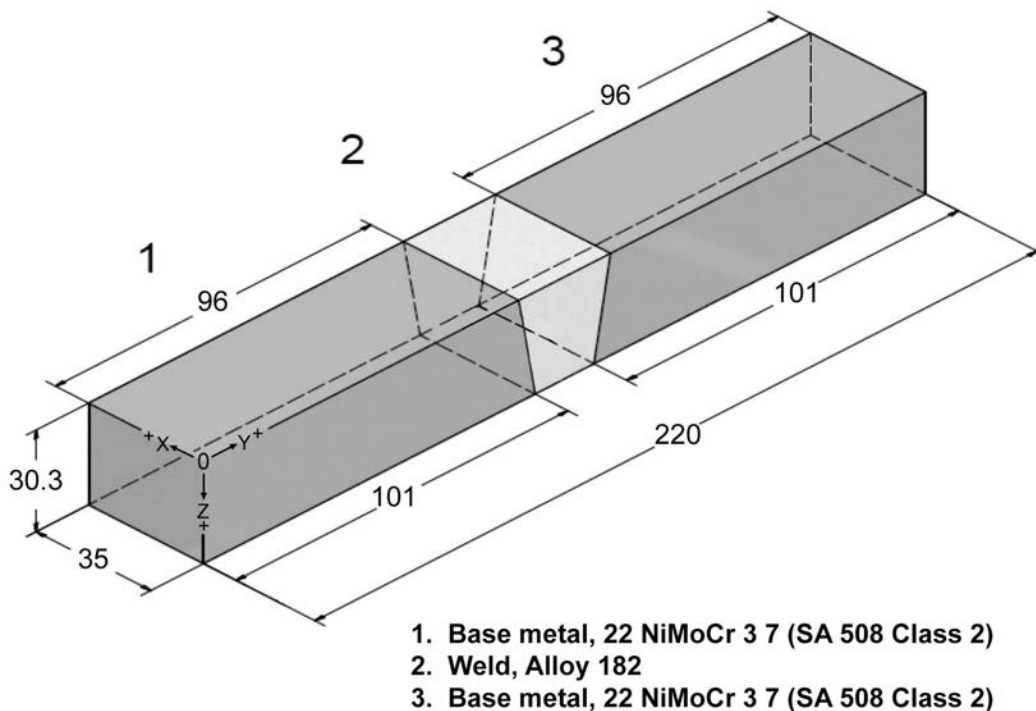


**Figure 6.47 Coordinate System Definition, Dimensions, and Illustrations of FB Test Block P46**

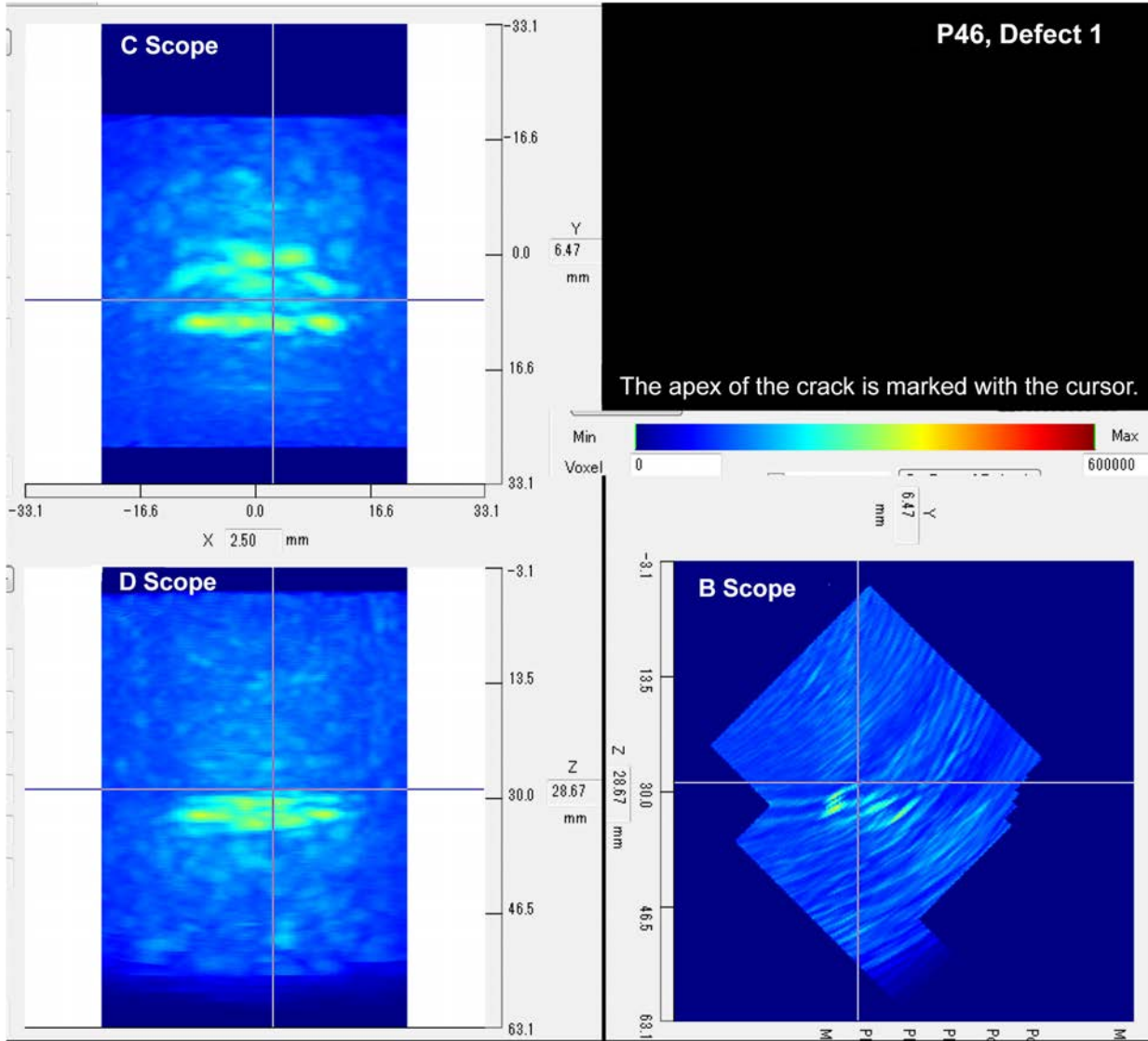
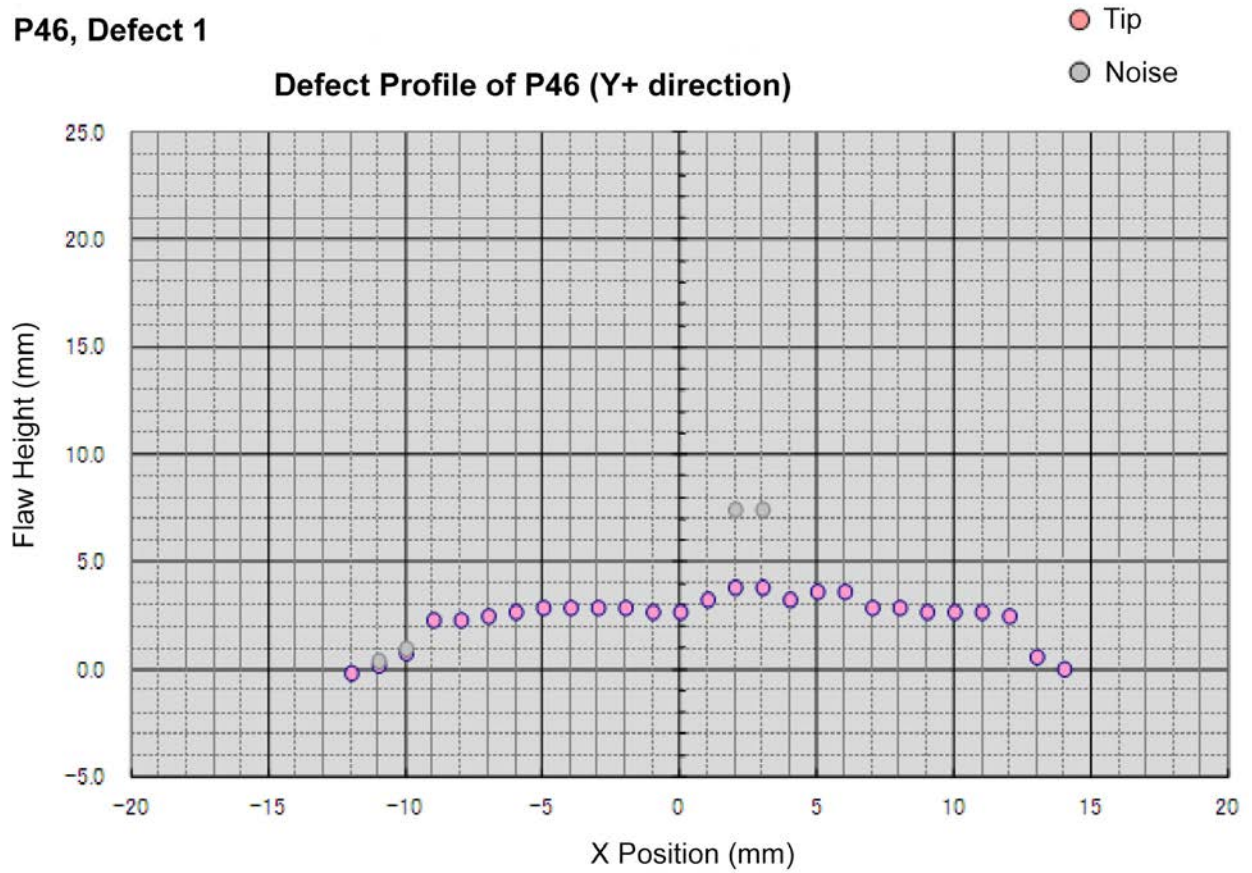


Figure 6.48 Data Images of Responses Obtained by SAFT-17 on Test Block P46 from y-position 103.6 mm

P46, Defect 1



**Figure 6.49** Indication Depth Profile Obtained by SAFT-17 on Test Block P46 from y-position 103.6 mm



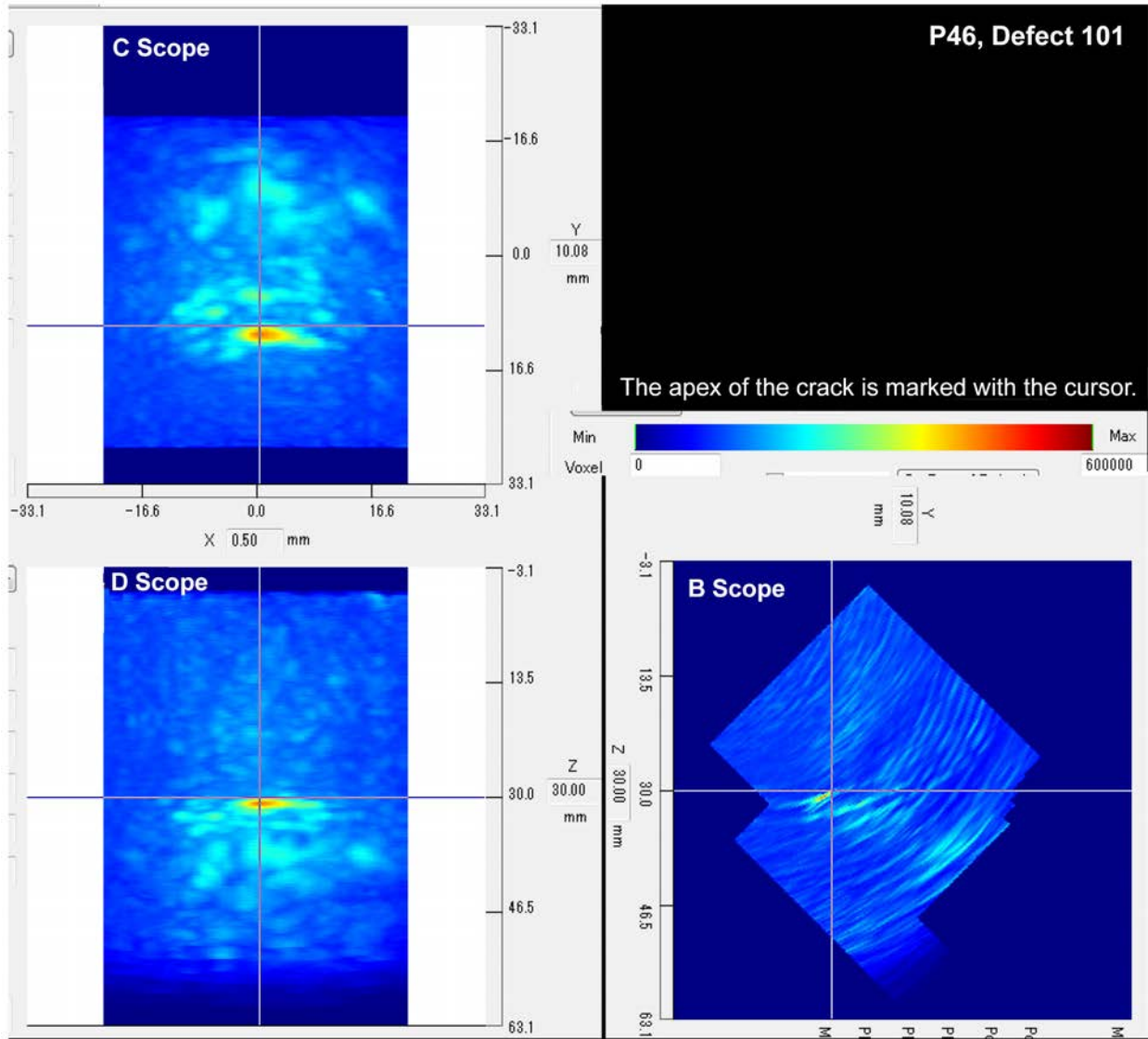


**Figure 6.50** Data Images of Responses Obtained by SAFT-17 on Test Block P46 from y-position 120 mm

**P46, Defect 101**

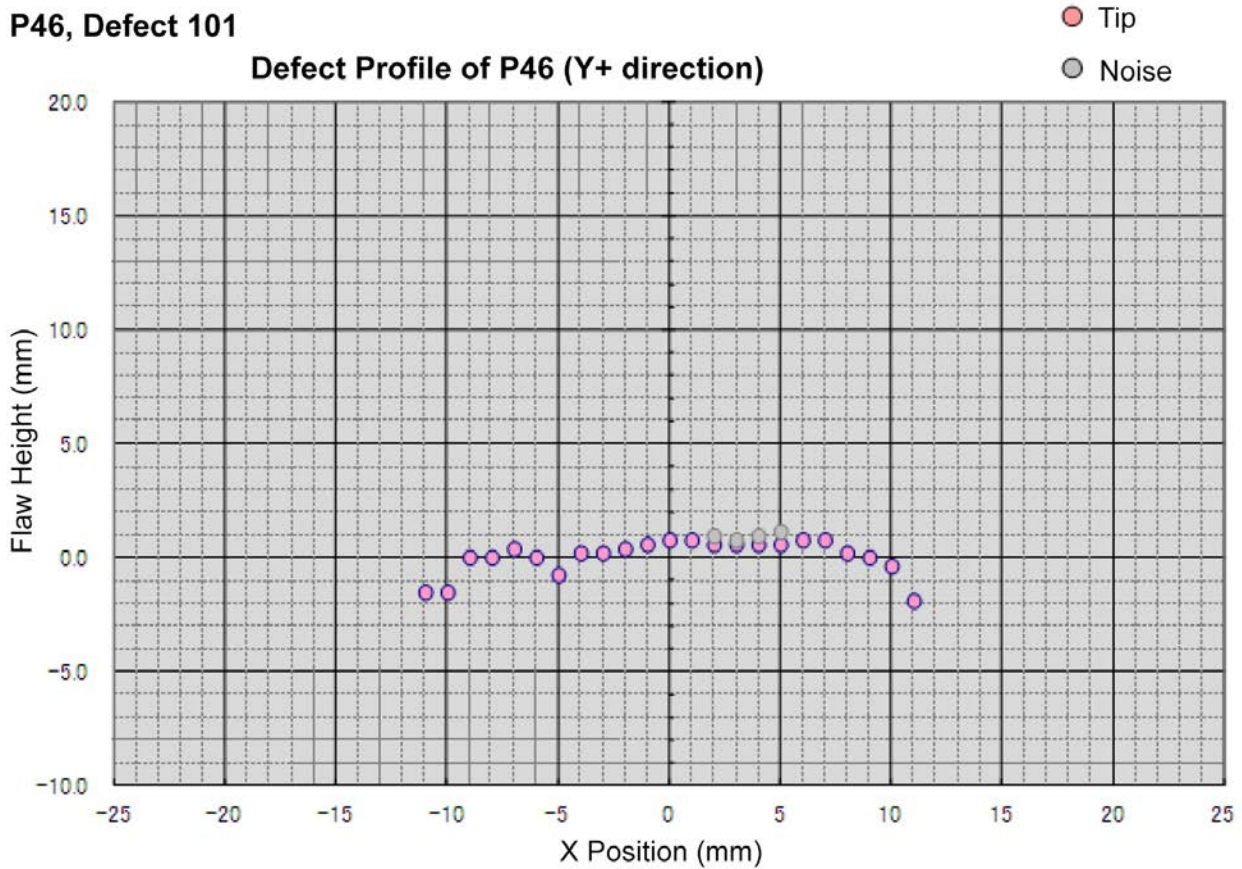


**Figure 6.51 Indication Depth Profile Obtained by SAFT-17 on Test Block P46 from y-position 120 mm**

**6.8 Procedures with Sparsely Populated Datasheets**

Datasheets for several procedures were submitted with most of the X, Y, and Z coordinate fields for indications populated with non-numerical entries. This indicates that X, Y, and Z coordinate information for flaws could not be identified with the applied procedure, despite having knowledge of the true state. This situation applied to procedures MM.28.1, MM.28.2, GUW.21, NRUS.11, and PECT.11. An example of a sparsely populated sheet submitted for MM.28.1 and MM.28.2 is provided in Figure 6.52. Similar examples are provided for GUW.21, PECT.11, and NRUS.11 in Figures 6.53, 6.54, and 6.55, respectively. In the case of MM.28.1, MM.28.2, and GUW.21, some datasheets were submitted with numerical data in some of the X, Y, and Z coordinate fields, indicating that flaw detection was possible in some instances. All of the datasheets for PECT.11 and NRUS.11 were submitted with non-numerical data in the X, Y, and Z coordinate fields. This data indicates that the techniques applied in these procedures are relatively insensitive to detect flaws or that more development is required for applying the techniques for this application.

DMW Summary Sheet

### PARENT RRT -- DMW INSPECTION SUMMARY Data Sheet

Inspection ID:  Procedure ID:   
TeamID.BlockID.SeqNo TeamID.SeqNo

Test Block ID:  Access:   
p<number>

Team ID:  Start Date:    
number yyyy/mm/dd

Detection:  End Date:    
number yyyy/mm/dd (optional)

Length Sizing:   
 Depth Sizing:

Technique Data Sheets  
 New  
 28.p4.1-2

Comments

Weld Volume Inspected  
 X1:  mm X2:  mm  
 Y1:  mm Y2:  mm  
 Z1:  mm Z2:  mm

Defect No	X1 mm	X2 mm	Y1 mm	Y2 mm	Z1 mm	Z2 mm	Ymax mm	Amp db	sbreak	Comments
1	na	na	na	na	na	na	na	na	no	
2	na	na	na	na	na	na	na	na	no	
3	na	na	na	na	na	na	na	na	no	
4	na	na	na	na	na	na	na	na	no	

Procedure Sheets  
 New  
 ProcedureSheet\_28.1

**Figure 6.52 Example of Datasheet Submission for Procedures MM.28.1 and MM.28.2 with Non-Numerical Data in X, Y, and Z Fields for Indications**

DMW Summary Sheet

### PARENT RRT -- DMW INSPECTION SUMMARY Data Sheet

Inspection ID:  TeamID.BlockID.SeqNo  
 Test Block ID:  p<number>  
 Team ID:  number  
 Detection:   
 Length Sizing:   
 Depth Sizing:

Procedure ID:  TeamID.SeqNo  
 Access:   
 Start Date:    
 End Date:   yyyy/mm/dd (optional)

Technique Data Sheets  
    
 New  
 21.p4.1-1

Comments  
 Specimen, p4, is relatively thick, but short to inspect by guided wave. The guided wave signal bounce back in the short specimen. For the short distance specimen, we need to carefully tuned guided wave mode and frequency. It is still possible to detect defects approaching from OD.

Weld Volume Inspected  
 X1:  mm X2:  mm  
 Y1:  mm Y2:  mm  
 Z1:  mm Z2:  mm

Procedure Sheets  
    
 New  
 Procedure Sheet

Defect No	X1 mm	X2 mm	Y1 mm	Y2 mm	Z1 mm	Z2 mm	Ymax mm	Amp db	SBreak	Comments

Coordinates must be numeric or "na", defect number must be an integer.

**Figure 6.53 Example of Datasheet Submission for Procedure GUW.21 with Blank X, Y, and Z Fields for Indications**

DMW Summary Sheet

### PARENT RRT -- DMW INSPECTION SUMMARY Data Sheet

Inspection ID: 11.p28.2  
TeamID.BlockID.SeqNo

Test Block ID: p28  
p<number>

Team ID: 11  
number

Detection: Yes

Length Sizing: No

Depth Sizing: No

Procedure ID: 11.2  
TeamID.SeqNo

Access: OD

Start Date: 2013/03/15   
yyyy/mm/dd

End Date: 2013/03/16   
yyyy/mm/dd (optional)

**Technique Data Sheets**

New  
11.p28.2-5

**Weld Volume Inspected**

X1: 0 mm X2: 35 mm  
Y1: 0 mm Y2: 220 mm  
Z1: 0 mm Z2: 30 mm

**Comments**

At the ferromagnetic material region, the height of pulse amplitude is nearly constant, and minimum amplitude is observed at the defect position. But, considering that large pulse amplitude induces in the ferromagnetic region than the nonmagnetic region, it is hard to say that PEC can detect the defect in this specimen. (Refer to experimental results). The PECT signal shows minimum value at the de

Defect No	X1 mm	X2 mm	Y1 mm	Y2 mm	Z1 mm	Z2 mm	Ymax mm	Amp db	Sbreak	Comments
1	na	na	na	na	na	na	110	7.01972	yes	min PEC Amplitude at

**Procedure Sheets**

New  
PECT Procedure

Defect No X1 mm X2 mm Y1 mm Y2 mm Z1 mm Z2 mm Ymax mm Amp db Sbreak Comments

Coordinates must be numeric or "na", defect number must be an integer.

**Figure 6.54 Example of Datasheet Submission for Procedures PECT.11 with Non-Numerical Data in X, Y, and Z Fields for Indications**

DMW Summary Sheet

**PARENT RRT -- DMW INSPECTION SUMMARY Data Sheet**

Inspection ID: 11.p30.1  
TeamID.BlockID.SeqNo

Procedure ID: 11.1  
TeamID.SeqNo

Test Block ID: p30  
p<number>

Access: OD

Team ID: 11  
number

Start Date: 2013/03/25  
yyyy/mm/dd

End Date:   
yyyy/mm/dd (optional)

Detection: Yes

Length Sizing: No

Depth Sizing: No

**Comments**

acoustic nonlinearity is observed by NRUS As the exciting voltage increases, a resonance frequency shift is observed for some vibration modes of the specimen P28- This fact can be explained as an acoustic nonlinearity or a crack exists in the specimen- (Refer to an attached Image Data Sheet-)

**Weld Volume Inspected**

X1: 0 mm X2: 35 mm  
Y1: 0 mm Y2: 220 mm  
Z1: 0 mm Z2: 30 mm

**Technique Data Sheets**

New  
11.p30.1-4

New Edit Delete

Defect No	X1 mm	X2 mm	Y1 mm	Y2 mm	Z1 mm	Z2 mm	Ymax mm	Amp db	sbreak	Comments
0	na	na	na	na	na	na	na	na	yes	Linear Scanning

**Procedure Sheets**

New  
Procedure data sheet

New Edit Delete

Defect No X1 mm X2 mm Y1 mm Y2 mm Z1 mm Z2 mm Ymax mm Amp db sBreak Comments

Coordinates must be numeric or "na", defect number must be an integer.

Delete Selected Add Update Selected Import from Technique Sheet

Validate Save Save & Return to Main Return to Main Without Saving

**Figure 6.55 Example of Datasheet Submission for Procedures NRUS.11 with Non-Numerical Data in X, Y, and Z Fields for Indications**

## 6.9 Discussion of Test Block Appropriateness

As discussed in Section 6.8, datasheets for several procedures were sparsely populating, indicating difficulty in obtaining detectable signals from flaws in the inspected test blocks or difficulty in interpreting the responses. This may indicate that more development of the techniques employed in these procedures is required before practical applications are considered. For some techniques, however, the test blocks provided in PARENT were not adequate for performing a fair evaluation. For instance, testing by guided wave ultrasound (GUW) results in signals that travel significant distances in component materials. Boundaries and discontinuities cause reflections to appear in the signal, which greatly complicates signal analysis and interpretation. The test blocks in PARENT represent sectioned or cut-out portions of reactor components. As a result, the test blocks have boundaries that do not represent actual field conditions, but have an adverse influence on testing by GUW techniques. Team 21 makes note of this difficulty in comments entered into the example datasheet in Figure 6.53 for procedure GUW.21.

The test blocks used in PARENT open testing were also not ideal for evaluating testing by non-linear ultrasound techniques (NLUT). NLUT techniques such as NRUS and HHUT are being researched by the community primarily for detecting degradation in metals at early stages, or

before macro-discontinuities form. All of the flaws intentionally inserted into PARENT test blocks are macro-discontinuities including various forms of cracks that are described in Section 2.6. Future efforts to evaluate NLUT techniques should include test blocks with flaws intentionally inserted to represent earlier stages of degradation, prior to the formation of macro-discontinuities.

## **6.10 Techniques to Consider for Blind Testing**

The results of open testing indicate that several techniques demonstrate a capability of detecting simulated PWSCC/IDSCC flaws. However, a reliable measure of detection performance cannot be obtained under open conditions. To obtain a measure of detection performance, a blind test could be performed on techniques that exhibit sufficient capability under the open test. Further criteria should be applied in choosing open techniques for blind test evaluation such as the ability to deploy the technique for a measurement in the field. Further, although several conventional UT and PAUT techniques were included in the open test study, these techniques were also evaluated in the PARENT blind test, and thus, additional blind testing is not deemed useful. Applying these criteria, the list of open techniques for which further blind testing is recommended include:

- ADVPAUT
  - PAATOFD.29.0
  - PAATOFD.29.1
  - PAATOFD.29.2
  - PAATOFD.29.3
  - PATP.29
  - PATRT.22
  - SAFT.17
  
- NLUT
  - SHPA.6.1
  - SHPA.6.2
  - SHPA.6.3
  - LASH.18
  - HHUT.27.1
  - HHUT.27.2
  - HHUT.30
  
- ECT
  - ECT.7
  - AECT.33
  - ECT.16

It is noted that while certain techniques such as UIR.20 and LUV.170 demonstrated a capability for detection of flaws, both techniques required access to the surface that the cracks intersect with. It is not clear that these techniques could be useful for detection of I.D.-connected flaws with access to the O.D. surface or if I.D. access in the field is feasible for the two techniques.





## 7 CONCLUSIONS AND FUTURE WORK

This report documents the results of the Open RRT portion of PARENT. Data were collected for procedures incorporating novel NDE techniques on SBDMW, FB, LBDMW, and BMI test blocks. This analysis has been restricted to depth sizing and length sizing analysis because of the open nature of the test. The objective of open testing is in establishing basic capability of techniques to justify further development and more detailed assessments of performance. Thus, only approximate measures of depth and length sizing performance were sought in open testing. To obtain a more complete picture of performance, some data response images provided by test participants were qualitatively analyzed to supplement the sizing analysis. Relative comparisons within open testing are emphasized over absolute values obtained by sizing analyses. Data was collected using established PAUT techniques to provide a benchmark for comparison. Readers are cautioned against directly comparing the sizing results from open testing with sizing results from blind testing because of the different conditions associated with each test.

Some significant conclusions drawn for the results documented in this report include:

- A general trend is observed for oversizing shallow flaws and undersizing deep flaws with the exception of ADVPAUT procedure types and NLUT procedures based on sub-harmonic techniques, which exhibit a more consistent error over the range of flaw depths considered.
- NLUT procedures based on sub-harmonic techniques exhibit better depth sizing performance than NLUT procedures based on higher harmonic techniques based on overall RMSE and regression fits.
- ADVPAUT procedure types do not exhibit better overall depth sizing accuracy than PAUT procedure types in this study based on RMSE.
- Overall, NLUT procedure types do not exhibit better overall depth sizing accuracy in comparison to ADVPAUT and PAUT procedure types based on RMSE.
- PAUT procedures exhibit a more consistent length sizing error over the range of flaw lengths considered for SBDMW test blocks in comparison to ADVPAUT, which tend to oversize short flaws and undersize long flaws.
- Better depth sizing performance is observed on FB test blocks (most with laboratory-grown SCC flaws) for ADVPAUT, NLUT, and UT procedure types in comparison to SBDMW test blocks (with SC flaws). PAUT procedure types exhibit better depth sizing performance on SBDMW test blocks in comparison to FB test blocks.
- ECT.16 exhibits a more consistent length sizing error over the range of flaw lengths considered for SBDMW test blocks in comparison to “Advanced” ECT procedures (AECT.33), which tend to oversize short flaws and undersize long flaws.
- Depth sizing data for UIR.20 was obtained in a way that would not be practical in a field environment. However, the results indicate a capability for flaw detection and flaw length sizing.
- Data response images for PAATOFD.29.2 and SAFT.17 in Sections 6.7.1 and 6.7.2 illustrate that SCC flaws result in weaker crack tip responses in comparison to MFC and EDM notch flaws.

- Data response images for PAUT technique PAUT.122.1 in Section 6.7.3 illustrate that identifying crack tip signals with established PAUT can be difficult and that crack tip signal identification by image pattern analysis is, in part, a subjective determination.
- Data response images for SAFT.17 obtained from blank test block P46 in Section 6.7.5 and PAUT.122.1 in Section 6.7.3 illustrate difficulty in distinguishing noise from crack tip responses.
- Tip diffraction signals with low SNR are easier to detect under open testing conditions with flaw information provided to test participants. Detecting tip diffraction signals with low SNR under blind test conditions will be more challenging.

Based on the results documented in this report and the conclusions outlined above, the following recommendations can be made:

- Blind testing of some of the open test procedures described in this report could be conducted based on the open testing results to obtain an estimate of detection performance and more realistic estimates of sizing performance. The specific techniques for which blind testing is recommended are summarized in Section 6.8 and included here for convenience:
  - ADVPAUT
    - PAATOFD.29.0
    - PAATOFD.29.1
    - PAATOFD.29.2
    - PAATOFD.29.3
    - PATP.29
    - PATRT.22
    - SAFT.17
  - NLUT
    - SHPA.6.1
    - SHPA.6.2
    - SHPA.6.3
    - LASH.18
    - HHUT.27.1
    - HHUT.27.2
    - HHUT.30
  - ECT
    - ECT.7
    - AECT.33
    - ECT.16
- Procedures UIR.20 and LUV.170 incorporate stand-off inspection techniques that have the potential for deployment during reactor operation. Evaluation of these procedures should be based on test pieces subject to relevant field conditions.

- NLUT procedure types, which incorporate techniques that are sensitive to degradation in early stages, should be evaluated using test blocks with simulated early degradation to better evaluate their potential.
- Procedure G UW.21 had difficulty detecting flaws due to the geometrical limitations of the test blocks used in PARENT. Future efforts to evaluate G UW testing should ensure the dimensions of the test blocks are sufficient so that boundaries do not significantly influence the response.



## 8 REFERENCES

- Abeelee K and F Windels. 2006. "Characterization and Imaging of Microdamage Using Nonlinear Resonance Ultrasound Spectroscopy (NRUS): An Analytical Model." In *Universality of Nonclassical Nonlinearity*, Ch. 23, pp. 369-388. ed: P Delsanto. Springer, New York.
- Abidin IZ, C Mandache, GY Tian and M Morozov. 2009. "Pulsed Eddy Current Testing with Variable Duty Cycle on Rivet Joints." *NDT & E International* 42:599-605.
- Biwa S, S Hiraiwa and E Matsumoto. 2006. "Experimental and Theoretical Study of Harmonic Generation at Contacting Interface." *Ultrasonics* 44, Supplement:e1319-e1322.
- Buck O, WL Morris and JM Richardson. 1978. "Acoustic Harmonic Generation at Unbonded Interfaces and Fatigue Cracks." *Applied Physics Letters* 33(5):371-373.
- Cartz L. 1995. *Nondestructive Testing*. ASM International, Materials Park, Ohio.
- Cheong YM, JH Kim, JW Hong and HK Jung. 2000. "Measurement of Dynamic Elastic Constants of RPV Steel Weld due to Localized Microstructural Variation." *Journal of Korean Society of Nondestructive Testing* 20(5):390-396.
- Cumblidge SE, SR Doctor, PG Heasler and TT Taylor. 2010. *Results of the Program for the Inspection of Nickel Alloy Components*. NUREG/CR-7019; PNNL-18713, Rev. 1, U.S. Nuclear Regulatory Commission, Washington, D.C.
- Dillenz A, D Wu, K Breitruck and G Busse. 2000. "Lock-in Thermography for Depth Resolved Defect Characterisation." In *15th World Conference on Nondestructive Testing*. October 15-21, 2000, Rome, Italy. The Italian Society for Nondestructive Testing and Monitoring Diagnostics.
- Elbern AW and L Guimaraes. 1999. "Synthetic Aperture Focusing Technique for Image Resaturation." In *International Symposium on NDT Contribution to the Infrastructure Safety Systems (NDTISS'99)*. November 22-26, 1999, Torres, Brazil. UFSM, Santa Maria, RS, Brazil.
- EPRI. 2008. *Recommendations for an Effective Program to Control the Degradation of Buried Pipe*. Report No. 1016456, Electric Power Research Institute (EPRI), Palo Alto, California.
- Ewert U, G-R Jaenisch, K Osterloh, U Zscherpel, C Bathias, M Hentschel, A Erhard, J Goebbels, H Hanselka, J Nuffer and W Daum. 2007. "Performance Control and Condition Monitoring." In *Springer Handbook of Materials Measurement Methods*, Ch. 16 eds: H Czichos, T Saito and L Smith.
- Fink M. 1992. "Time Reversal of Ultrasonic Fields. I. Basic Principles." *IEEE Transactions on Ultrasonics, Ferroelectrics and Frequency Control* 39(5):555-566.
- Fink M. 1999. "Time-Reversed Acoustics." *Scientific American* November:91-97.
- Halmshaw R. 1987. "X-ray Real-Time Imaging for Weld Inspection: IIW 3rd Progress Report." *British Journal of Nondestructive Testing* 29(6):426-428.

Hirse Korn S, M Hirse Korn and PP Delsanto. 2006. "Nonlinear Ultrasonic Transmission Through Thin Bonded Interfaces: Theoretical Background and Numerical Simulations." In *Universality of Nonclassical Nonlinearity*, Ch. 15, pp. 231-250. ed: P Delsanto. Springer, New York.

Ishida H and J Kitasaka. 2013. "Development of a Phased Array TOFD UT Method to Measure the Depth of SCCs in Dissimilar Metal Weld." In *9th International Conference on NDE in Relation to Structural Integrity for Nuclear and Pressurized Components*, pp. 754-762. May 22-24, 2012, Seattle, Washington. NDT.net, Rheintalstr, Germany.

Jhang K-Y. 2000. "Applications of Nonlinear Ultrasonics to the NDE of Material Degradation." *IEEE Transactions on Ultrasonics, Ferroelectrics and Frequency Control* 47(3):540-548.

Karasawa H, T Ikeda, S Matsumoto, T Hamajima and H Isobe. 2009. "3D-SAFT Ultrasonic Inspection Equipment "Matrixeye™". In *Proceedings of the Seventh International Conference on NDE in Relation to Structural Integrity for Nuclear and Pressurised Components*, pp. 669-683. May 12-14, 2009, Yokohama, Japan. European Commission Joint Research Centre, Luxembourg.

Kim J-Y, A Baltazar, JW Hu and SI Rokhlin. 2006. "Hysteretic Linear and Nonlinear Acoustic Responses from Pressed Interfaces." *International Journal of Solids and Structures* 43(21):6436-6452.

Komura I and T Furukawa. 2010. "Improvement of SCC Depth Sizing Capability by 3D-SAFT UT Method in Ni Alloy Weld." In *Proceedings of the Eighth International Conference on NDE in Relation to Structural Integrity for Nuclear and Pressurised Components*, pp. 831-837. September 29-October 1, 2010, Berlin, Germany. European Commission Joint Research Centre, Luxembourg.

Lebrun B, Y Jayet and J-C Baboux. 1997. "Pulsed Eddy Current Signal Analysis: Application to the Experimental Detection and Characterization of Deep Flaws in Highly Conductive Materials." *NDT & E International* 30:163-170.

Lee KH, MK Baek and IH Park. 2012. "Estimation of Deep Defect in Ferromagnetic Material by Low Frequency Eddy Current Method." *IEEE Transactions on Magnetics* 48:3965-3968.

Lowe MJS, DN Alleyne and P Cawley. 1998. "Defect Detection in Pipes Using Guided Waves." *Ultrasonics* 36(1-5):147-154.

Maldague X. 2001. *Theory and Practice of Infrared Technology for Nondestructive Testing*. John Wiley and Sons, New York.

Meyer RM. 2014. *NDE Techniques Used in PARENT Open Round Robin Testing*. PNNL-23387, Pacific Northwest National Laboratory, Richland, Washington.

Meyer RM and PG Heasler. 2017. *Results of Blind Testing for the Program to Assess the Reliability of Emerging Nondestructive Techniques*. NUREG/CR-7235, PNNL-24196, U.S. Nuclear Regulatory Commission, Washington, D.C.

Murfin AS, RAJ Soden, D Hatrick and RJ Dewhurts. 2000. "Laser-Ultrasound Detection Systems: A Comparative Study with Rayleigh Waves." *Measurement Science and Technology* 11:1208-1219.

- Murray TW and JW Wagner. 1999. "Laser Generation of Acoustic Waves in the Ablative Regime." *Journal of Applied Physics* 85(4):2031.
- Ohara Y, K Kawashima, M Murase and N Hirose. 2003. "Identification of Sintered Irons with Ultrasonic Nonlinearity." In *Review of Progress in Quantitative Nondestructive Evaluation, Vol. 22*, pp. 1257-1264. July 14-19, 2002, Bellingham, Washington. American Institute of Physics, Melville, New York.
- Ohara Y, S Yamamoto, T Mihara and K Yamanaka. 2008. "Ultrasonic Evaluation of Closed Cracks Using Subharmonic Phased Array." *Japanese Journal of Applied Physics* 47(5):3908-3915.
- Prada C, S Manneville, D Spoliansky and M Fink. 1996. "Decomposition of the Time Reversal Operator: Detection and Selective Focusing on Two Scatterers." *The Journal of the Acoustical Society of America* 99(4):2067-2076.
- Rose JL. 1999. *Ultrasonic Waves in Solid Media*. Cambridge University Press, Cambridge, United Kingdom.
- Rose LRF. 1984. "Point-source Representation for Laser-generated Ultrasound." *Journal of the Acoustical Society of America* 75(3):723-732.
- Solodov I, K Pfeleiderer and G Busse. 2006. "Nonlinear Acoustic NDE: Inherent Potential of Complete Nonclassical Spectra." In *Universality of Nonclassical Nonlinearity*, Ch. 29, pp. 467-486. ed: P Delsanto. Springer, New York.
- Solodov IY. 1998. "Ultrasonics of Non-linear Contacts: Propagation, Reflection and NDE-applications." *Ultrasonics* 36(1-5):383-390.
- Ulrich TJ, AM Sutin, RA Guyer and PA Johnson. 2008. "Time Reversal and Non-linear Elastic Wave Spectroscopy (TR NEWS) Techniques." *International Journal of Non-Linear Mechanics* 43(2):209-216.
- Yusa N, Y Sakai and H Hashizume. 2011. "An Eddy Current Probe Suitable to Gain Information about the Depth of Near-side Flaws Much Deeper than the Depth of Penetration." *NDT & E International* 44:121-130.
- Zoughi R and S Kharkovsky. 2008. "Microwave and Millimetre Wave Sensors for Crack Detection." *Fatigue & Fracture of Engineering Materials & Structures* 31:695-713.





## **APPENDIX A**

### **11<sup>TH</sup> ICNDE PAPERS**



# APPENDIX A

## 11<sup>TH</sup> ICNDE PAPERS

<b>A.1</b>	<b>Simulation of Inspection for Dissimilar Metal Welds by Phased Array UT with Focusing Techniques .....</b>	<b>A-2</b>
<b>A.2</b>	<b>Challenge for the Detection of Crack in Dissimilar Weld Region Using PECT (Pulsed Eddy Current Technology) .....</b>	<b>A-7</b>
<b>A.3</b>	<b>Manufacturing of a New Type of NDE Test Samples with Laboratory-Grown Intergranular SCC Cracks in a Nickel-Base Weld – Comparison of Various NDE-Techniques Applied to a Challenging Crack Morphology.....</b>	<b>A-15</b>
<b>A.4</b>	<b>Integrity Evaluation Case Subject to Replacement &amp; Preventive Maintenance for NPP Ni-alloy Components .....</b>	<b>A-29</b>

## **A.1 Simulation of Inspection for Dissimilar Metal Welds by Phased Array UT with Focusing Techniques**

### **Simulation of inspection for dissimilar metal welds by phased array UT with focusing techniques**

Young-In Hwang<sup>1</sup>, Jae-Hyun Bae<sup>1</sup>, Hak-Joon Kim<sup>1</sup>, Sung-Jin Song<sup>1</sup>, Kyung-Cho Kim<sup>2</sup>, Yong-Buem Kim<sup>2</sup> and Hun-Hee Kim<sup>3</sup>

<sup>1</sup>Sungkyunkwan University, Republic of Korea

<sup>2</sup>Korea Institute of Nuclear Safety, Republic of Korea

<sup>3</sup>Doosan Heavy Industries & Construction, Republic of Korea

#### **Abstract**

Dissimilar metal welds (DMWs) are widely used as nozzles of major components in nuclear power plants, for example, control rod drive mechanism (CRDM), bottom-mounted instrumentation (BMI) and large bore pipe connecting reactor vessel and steam generator. These welds have caused significant reliability problem; leakage in the small bore piping, Primary Water Stress Corrosion Cracking (PWSCC) associated with safe end welds and etc. Especially, PWSCC is critical to the potential for large loss of coolant inventory or control rod ejection and loss of coolant accident. Inspection of dissimilar metal welds can be performed with ultrasonic testing. However, ultrasonic inspection of nickel-based dissimilar metal welds is difficult due to anisotropic and dendrite structure of DMWs and attenuation phenomena which propagates dendrite structure. So, phased array ultrasound is widely used to inspect surface break cracks and stress corrosion cracks in DMWs. Nevertheless, the inspection of dissimilar metal weld using phased array ultrasound has relatively low probability of detection of cracks due to high attenuation and noise caused by coarse grains and beam skewing due to anisotropy in material properties. Therefore, advanced focusing techniques of phased array ultrasound are needed for improvement in the probability of detection of flaws in DMWs. In this study, we had investigated focusing and steering phased array ultrasound in dissimilar metal welds with modeling crystalline structure and determination of time delays. And, compared focusing techniques to enhance SNR of phased array ultrasonic signals for optimal inspection setup of testing systems in DMWs.

**Keywords :** Dissimilar Metal Weld, Phased array ultrasonic testing, Adaptive focusing technique, Time Reversal Technique

#### **1. Introduction**

In nuclear power plants, PWSCC in dissimilar metal welds is critical as there is high potential for a serious loss of control rod ejection and coolant inventory. By tension residual stress and etc., corrosion damage can occur in nuclear power plant at BMI Nozzle RCS hot leg and CRDM, especially. Ultrasonic Testing of Dissimilar Metal Welds is a very difficult task due to grain noise and splitting by anisotropic / inhomogeneous structure and coarse grain. From those figures, we can see grain noise and splitting effect at austenitic weld area.

Phased array ultrasonic techniques are increasingly adapted as those can focus beams at desired locations. However, inspection of dissimilar metal welds using phased array ultrasound has relatively low probability of detection of cracks due to beam skewing in dissimilar metal welds and high attenuation and noise caused by coarse grain. So, advanced focusing techniques of phased array ultrasound are needed for improvement in the probability of detection of flaws in DMWs.

#### **2. Objectives**

Modeling crystalline structures of dissimilar metal welds, Determination of time delays for focusing and/or steering ultrasonic beams at desired position in the austenitic steel welds, Comparison of focusing techniques such as time reversal technique, adaptive focusing technique, and conventional focusing techniques to enhance SNR of phased array ultrasonic signals were performed to investigate a focusing techniques for optimal inspection setup of phased array ultrasonic testing systems in dissimilar metal welds.

### 3. Modeling of DMWs

Even though Ogilvy's model [1] is widely used in the austenitic stainless steel welds, it can describe just symmetric welds. In this study, we adopted the modified Ogilvy's model [2] that can describe asymmetric weld structures using Eqs. (1) and (2).

$$F(y, z) = \tan \theta_1 = \frac{(T_1(D_1 + z \tan \alpha_1))}{y^\eta} \quad y > 0 \quad (1)$$

$$F(y, z) = \tan \theta_2 = \frac{(T_2 |(D_2 + z \tan \alpha_2)|)}{|y^\eta|} \quad y < 0 \quad (2)$$

$T_1$  and  $T_2$  are proportional to the tangents of the grain axes at the sloping edges.  $\eta$  is a parameter for determination of how fast the grain orientation falls with an increase in  $y$ . Figure 1. shows result of grain orientation in dissimilar metal welds based on the modified Ogilvy's model.

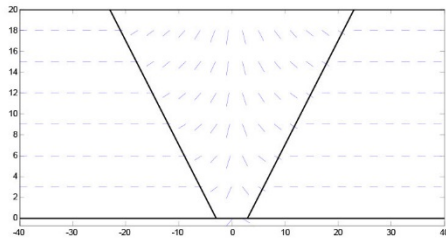


Figure 1. Grain orientation in dissimilar metal welds based on the modified Ogilvy's model

We applied rotation matrix to elastic constant of transversely isotropic austenitic weld metal, then we calculate applied elastic constant using this matrix. The center frequency of transducer 2.25 MHz and 16 elements of phased array transducer were used. The width and spacing of phased array transducer are 0.8mm and 1mm and bush shaped flaw image was extracted [3] and imported for the application of DMWs. Figure 2. shows the simulation setup for ultrasonic propagation in DMW. The calculations were carried out by a finite element modeling software, COMSOL Multiphysics.

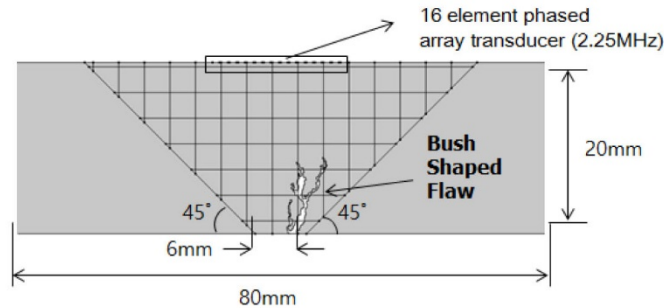


Figure 2. Simulation setup for ultrasonic propagation in DMW

To investigate the performance of three focusing techniques for phased array ultrasonic testing in dissimilar metal welds, firstly, we simulate the ultrasonic beam propagation without any time delay. As shown in Figure 3., due to the

complexity of grain orientation in weldments, there occurred beam distortion and skewing during ultrasonic beam propagation. One can see low signal-noise ratio from crack in weldments due to beam distortion and skewing. It is hard to discriminate flaw from the signals. For that reason, it is necessary to have enhanced focusing techniques to improve signal-noise ratio. So, we applied focusing techniques such as time reversal technique and adaptive focusing technique.

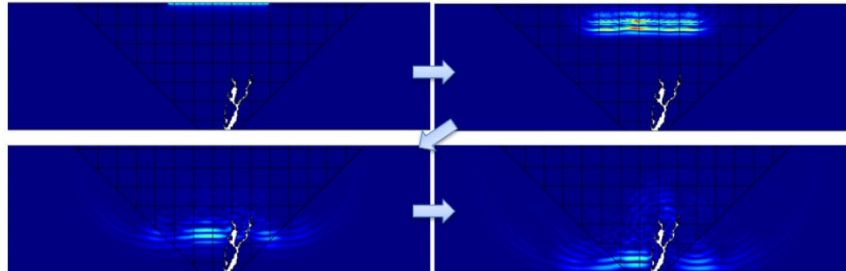


Figure 3. Simulation of phased array ultrasonic beam without time delay

#### 4. Comparison of flaw signals with different ultrasonic focusing methods

We compared the performances of three focusing techniques to improve the probability of detection of flaws in the DMWs; phase matching method, adaptive focusing method and time reversal method.

To focus the phased array ultrasonic beam, time delays should be applied to the array elements. In order to determine the time delay to be applied, the distances of between individual elements to the focal point should be identified. Then, the time delay can be determined. For phase matching at focal point, we matched radiated sound pressure. Then, we matched radiated sound pressure. The adaptive focusing technique is a time delay estimation method based on the cross correlation. Time delay can be rapidly detected and quantified using a cross-correlation between each received signals. Time reversal technique was time delay estimation method that can be used in ultrasonic testing to improve flaw detection through anisotropy and inhomogeneous material such as dissimilar metal weld. Among the techniques, we applied DORT method.

Figure 4. shows simulation of ultrasonic beam propagation using phase matching method. Using the phase matching methods, the reflected beam from crack was weak and it still caused beam distortion and skewing during the ultrasonic beam propagation.

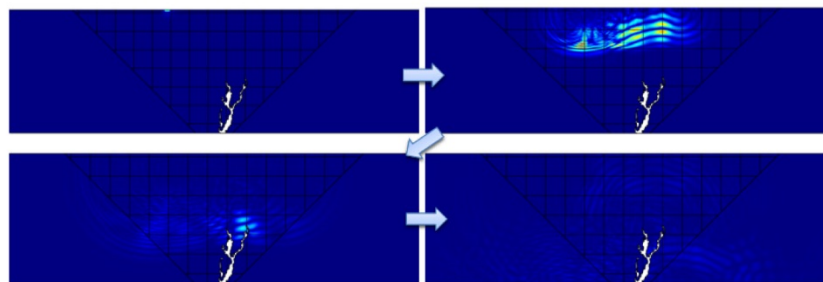


Figure 4. Simulation of phased array ultrasonic beam with time delay

For calculating the cross-correlation between each received signals, the maximum of the cross-correlation function indicates the point in time where the signals are best aligned[4]. Figure 5. shows the calculated time delay using adaptive focusing techniques. This figure shows the simulation results using the adaptive focusing method. The reflected beam from crack using adaptive focusing method was stronger than reflected beam using phase matching method. And, the beam distortion and skewing during ultrasonic beam propagation noticeably decreased, compared to phase matching method.

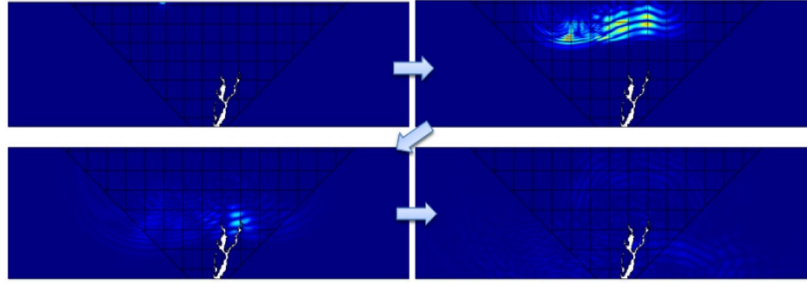


Figure 5. Simulation of phased array ultrasonic beam with adaptive focusing technique

For time reversal method, first, Acquired inter-element waveforms from crack without time-delay are measured by each of the elements. Then, we have converted from time-domain to frequency-domain. We used singular value decomposition (SVD) of the transfer matrix to obtain eigenvalue and eigenvector of acquired inter-element waveforms[5]. The number of significant eigenvalues is equal to the number of well resolved scatters. Each eigenvector provides phase and amplitude information that should be applied to the transducer array in order to focus on each scatterer. One high eigenvalue means that there is only one scatter exist in the sector. Figure 6. shows simulation of ultrasonic beam propagation using time reversal techniques. The reflected beam from crack using time reversal techniques was strongest among the focusing techniques. Using the time reversal technique, the beam distortion and skewing during the ultrasonic beam propagation noticeably decreased compared to the phase matching technique and the adaptive focusing technique.

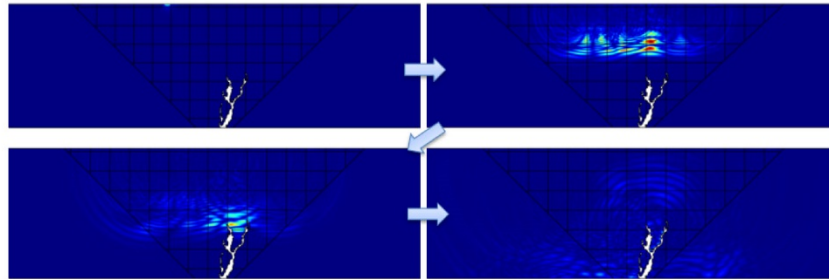


Figure 6. Simulation of phased array ultrasonic beam with time reversal technique

Figure 7. shows the comparison of A-scan signals obtained by using three different focusing techniques. When the time delay determined by the time reversal techniques, the signal amplitude is the highest, showing higher than that by the phase matching method. Time reversal techniques enhanced SNR of phased array ultrasonic signals most effectively compared to other techniques.

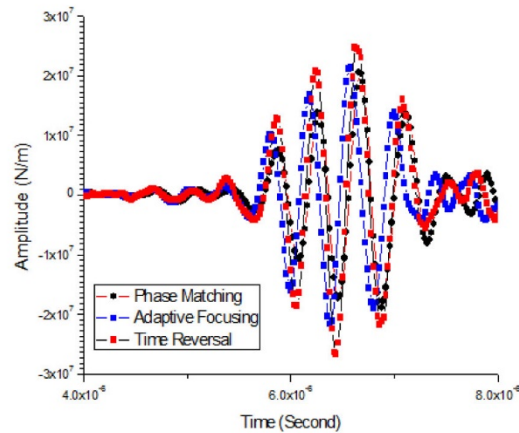


Figure 7. Comparison of A-scan signals obtained by using three different focusing techniques

## 5. Conclusion

Modeling crystalline structures of the austenitic steel welds was performed using Ogilvy's crystalline structure model. Time delays were calculated for focusing and/or steering ultrasonic beams at desired position in the austenitic steel welds, for phase matching focusing techniques, adaptive focusing techniques and time reversal technique. Comparison of focusing techniques such as time reversal technique, adaptive focusing technique, and etc. to enhance SNR of phased array ultrasonic signals were performed. Time reversal techniques enhanced SNR of phased array ultrasonic signals more than other techniques. However, in practical field, adaptive focusing techniques could be one of alternative method to improve SNR.

## Acknowledgements

This work was supported by the National Research Foundation of Korea (NRF) grant funded by the Korea government (MEST) (No. 2012R1A1A2044423)

## References

- [1] JA Ogilvy, Computerized ultrasonic ray tracing in austenitic steel, NDT international, 18 pp. 66-67 (1985)
- [2] J. Ye, H. J. Kim, S. J. Song, S. S. Kang, K. C. Kim, M. H. Song, Model-based simulation of focused beam fields produced by a phased array ultrasonic transducer in dissimilar metal welds, NDE&E International, 44, 3, pp. 290-296, 2011
- [3] Heloisa CunhaFurtado, Iain Le May, High Temperature Degradation in Power Plants and Refineries, Materials Research, Vol. 7, No. 1, pp. 103-110, 2004
- [4] Noor Shafiza Mohd Tamim, Farid Ghani, "Techniques for Optimization in Time Delay Estimation from Cross Correlation Function", International Journal of Engineering & Technology IJET-IJENS, Vol. 10, No.02
- [5] C. Prada, etc, "Time reversal techniques in ultrasonic nondestructive testing of scattering media", Inverse Problems, Vol. 18, pp. 1761-1773, 2002.



## **A.2 Challenge for the Detection of Crack in Dissimilar Weld Region Using PECT (Pulsed Eddy Current Technology)**

### **Challenge for the Detection of Crack in Dissimilar Weld Region Using PECT (Pulsed Eddy Current Technology)**

Duck-Gun Park<sup>1</sup>, M.B Kishore

*Nuclear Materials Safety Research Division, Korea Atomic Energy Research Institute, Daejeon,  
South Korea -305-353*

#### **Abstract**

Pulsed Eddy Current (PEC) technique uses multiple frequency current pulse to drive the excitation coil of PEC probes unlike conventional single frequency eddy current methods. In the present study, we make an effort to detect the crack in dissimilar weld region using PEC technique. The test samples were prepared by welding two base metals, the composition of base metal is SA508 cl.2 and that of welding metal is alloy 182. The defect region was positioned in the weld metal, and the types of defect are stress corrosion cracking, fatigue cracks having the width of several micrometers. A rectangular pulse having 10ms pulse width and 15A current is applied to the exciting coil of PEC probe to inspect the sample cracks. The peak amplitude of the detected PEC pulse was chosen as a measure to estimate the cracks under the sample surface. The PEC signal amplitude detected in the defect region (welded part) showed lower value than that of base material. The crack is positioned in the middle of dissimilar weld region, which shows the minimum PEC signal amplitude. In time domain analysis, the peak amplitude of the detected pulse is decreased, with an increase in the crack depth. The experimental results indicated that the proposed system using PEC technique has the potential to detect the sub surface cracks in dissimilar weld region.

Keywords— pulsed eddy current, dissimilar weld, crack, PEC probe, hall sensor, peak amplitude

#### **1. Introduction**

Eddy current testing is a non destructive testing (NDT) method used for metals and includes the detecting and sizing of defects, identifying composition, structure and measuring thicknesses. Among the available conventional NDT methods, eddy current testing (ECT) is the most promising technique to detect flaws in conductive materials. The conventional ECT uses a single-frequency sinusoidal excitation for the detection of defects or flaws as a function of changes in voltage, impedance, or phase. Because of limited depths of penetration and complexity in signal analysis ECT was confined to limited applications [1]. Unlike a conventional ECT, PEC uses a multiple frequency sinusoidal excitation of the electric current resulting from the broad band nature of the pulse; hence it has the ability to penetrate different depths in a conductive material and provides the depth information of the defects [2, 3] located at different depths. PEC testing has been demonstrated to be one of the most effective methods, and is capable of performing different inspection tasks, such as sub-surface defect detection in complex structures, wall thinning detection, crack detection, coating thickness detection etc. [4,5]. Moreover, PEC is more economical than other NDT methods such as low power consumption owing to short pulse excitation and it doesn't need any complex electronic circuitry. Even though the use of PEC has long been considered for the testing of materials, in recent decades, PEC testing has become the subject of wide spread interests in NDT because of its advancement in technologies such as computer data acquisition and digital signal processing. Because of the potential advantages of the PEC, prevalent investigations on this technique have been made, such as for detection of wall thinning and corrosion in aircraft multilayer structures [9, 10]. Especially, it is efficient to detect the subsurface crack of thick plate often used in the nuclear industry. The thickness of tubes and nozzle used in the nuclear power plant is up to

several tenth of millimeter, which is made of stainless steel and/or Inconel alloy to protect the corrosion. The crack detecting sensitivity using PEC probes depends on several parameters such as pulse width, coil size, coil diameter. To achieve this, it is necessary to increase the flux through the circular coil, which can be described by the following equation.

$$\Phi = B\pi r^2$$

Where B is the magnitude of the magnetic flux density perpendicular to the surface defined by the coil of radius (r). Therefore, if larger size coil is used for the detection purposes, a low resolution and sensitivity would be achieved. The reason is that they respond to all magnetic flux line passing through the coil winding, regardless of their spatial direction and orientation. This characteristic together with the size of the coil can impact the sensitivity of this sensor. Using smaller coil would provide a better sensitivity but would limit eddy current penetration within the test object. Therefore, in order to detect the deep crack buried under thick sample, we have to design PEC probe considering many parameters such as skin depth, coil inductance, and detection sensor. In the present study, a new PEC probe to detect a very thin cracks made by stress corrosion cracking phenomena in the dissimilar weld region was made by considering special resolution and sensitivity of detecting element. For this purpose, specially designed probe was used, and the performance of the new designed probe was tested with a PEC system designed and developed for this purpose

## 2. Experimental Setup

The block diagram of the PEC system design is shown in Figure 1. The system consists of a rectangular waveform generator, a probe integrated with an excitation coil and a pickup Hall-sensor to detect the induced field from test specimen, an amplifier to process the signal obtained from Hall-sensor for further steps as the sensor output is too low in magnitude, a data acquisition card connected to PC using signal processing software to digitize the obtained data and to record the PEC data. The operational flow of the PEC system is as follows; the waveform generator produces a rectangular pulse with variable frequency and duty cycle. The pulse is fed to a coil driver circuit which excites the driving coil of the PEC probe. When the probe is mounted on the metal structure, the pick-up hall sensor will measure the vertical resultant magnetic field, which is the vector sum of the field generated by the excitation coil and the opposing magnetic field generated by the induced eddy currents in the test sample (Primary flux  $\Phi_1$  created by driving coil induces EC in the conducting medium, induced EC produces counter flux  $\Phi_2$ . Now pick-up sensor measures total flux  $\Phi = \Phi_1 + \Phi_2$ .) The signal obtained from the pick-up sensor is amplified by a voltage amplifier with variable gain. The A/D card will convert the analog input signal into digital data which can be used for further signal analysis by the end user. A software program is used to Signal pre-processing, feature extraction, defect categorization, and the presentation of the results on the PC monitor.

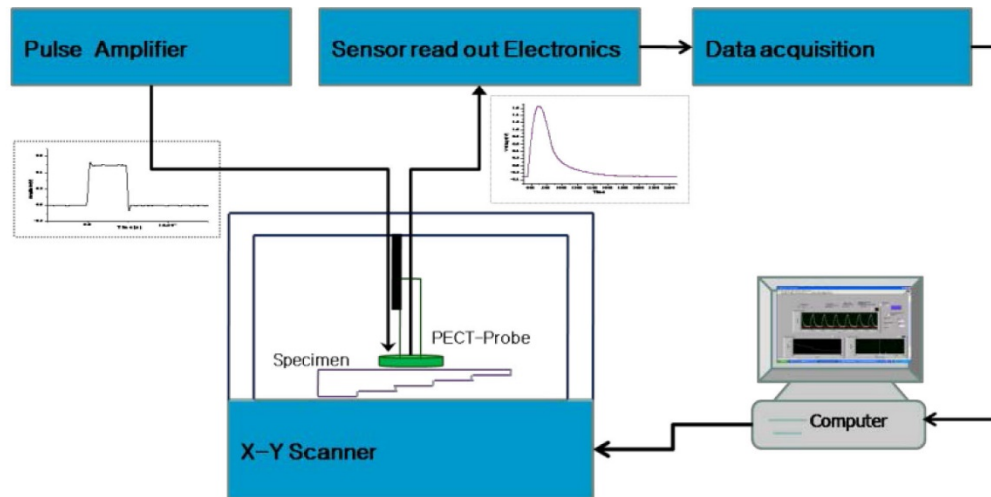


Figure 1. The block diagram of the PEC system.

The pulse amplifier supplies a high current pulse to the Driving Coil or exciting coil. The pulse width, pulse amplitude and duty cycle can be controlled and selected by considering the skin depth of sample. The excitation coil is a 1x3 mm rectangular cross sectional copper wire wound on the cylindrical ferrite core, the number of turns are made to be 132 turns having total resistance 0.192  $\Omega$ . To obtain good special resolution, the probe has a 60mm height and 9mm inner diameter, and the Hall-sensor was positioned in the center of probe to detect the induced signal from defects. The cylindrical type ferrite core not only reduces the magnetic leakage but also improves the detection sensitivity by sustaining adequate excitation intensity. The Hall-sensor gives the frequency independent sensitivity from DC to 100 KHz, high spatial resolution, less power consumption with increased sensitivity and simple readout circuitry. When the probe was placed in close proximity to the conducting plate, the steep exciting pulse induces eddy currents and its associated magnetic field dissipates exponentially to approach its steady state. The induced eddy current field flow is in the opposite direction to primary exciting field, hence when the probe is placed on the conducting plate, the detected field rises slowly to the maximum peak value.

### 3. PEC signal measurement and Tested Sample

A 10ms pulse width and 15A excitation current is applied to exciting coil of the probe to test the sample. figure 2(a) shows the experimental setup, The PEC probe is fixed to the X-Y scanner to perform the manual scanning on the defect free side of the tested sample. Initially the probe is placed on the sample such that the hall sensor positions at the center in vertical direction i.e. about x axis and continued to be at its center position as the scanning process continues along the y axis i.e. along the length of the test sample, the probe used in this experiment and the test specimen can be observed in figure 2(b) . A LabView based data acquisition program shown in figure 2(c) was developed to continuously monitor the variation in the thickness of the sample and is observed on the computer screen. The time domain feature, peak amplitude of the detected pulse is used to detect the sub-surface cracks in the tested sample. in order to reduce the experimental error, average of 5 pulses is considered as the resultant PEC pulse. The three kinds of test blocks with ID 28, 29, and 30 provided by ENSI were tested. the flaw types of these test blocks are BWR/NWC SCC Crack, Fatigue Crack, and PWR SCC crack, respectively. The samples were composed by the welding of two base metals, and the composition of base metal is SA508 cl.2, and the welding metal is alloy 182 as shown in the figure 2(d).

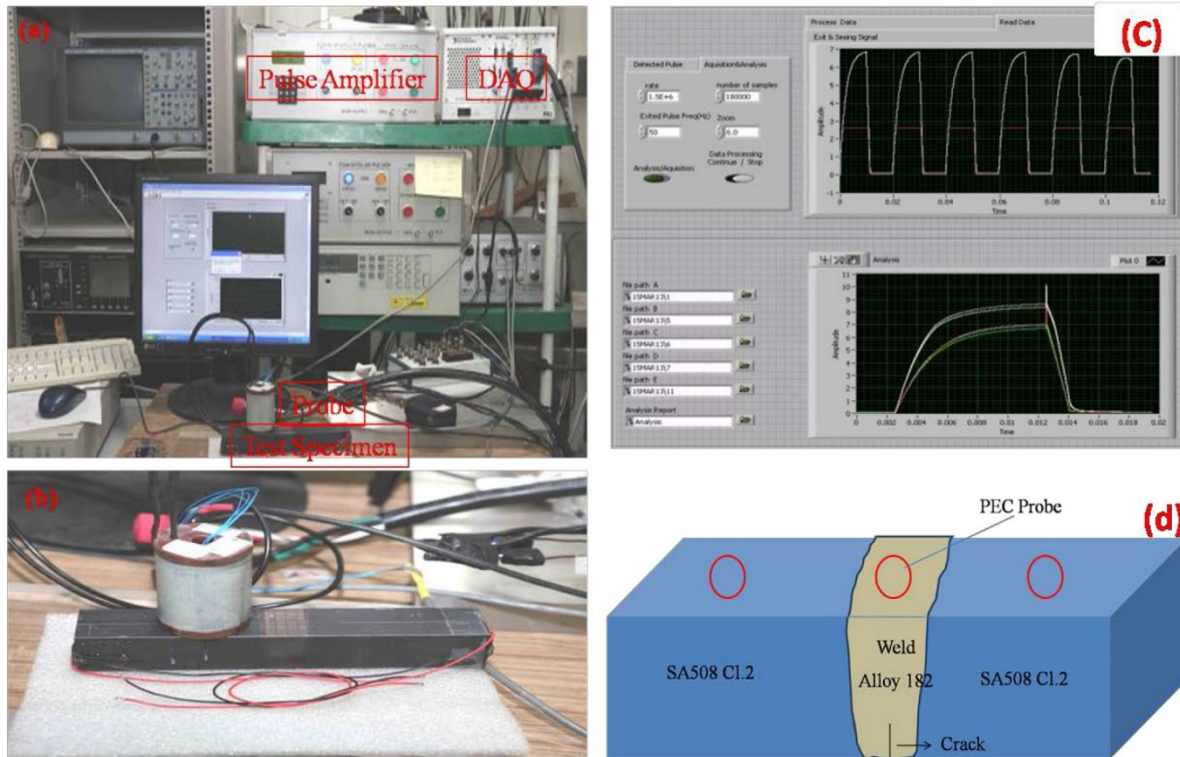


Figure 2(a).Experimental Setup. (b) closed view of Probe and Test specimen. (c) Lab VIEW based application to read and process PEC data. (d) Schematic of PARENT Test Specimen, PECT probe is located on the opposite side of crack surface

## 5. Experimental results and feature extraction

When the probe is placed on the test specimen, the excitation pulse will generate a primary magnetic field which can penetrate into the test sample resulting into eddy currents to generate and pass through the sample, these small eddy currents will generate secondary magnetic field which can oppose the primary magnetic field will be detected by the hall element. Since the secondary field is opposite to the primary magnetic field, the detected pulse tends to change depending on the test specimen and portrayed as the defect information. A typical response signal from PEC probe when placed on the test sample in such a position is shown in Fig. 3. Calibration of PEC signal with standard specimen is essential to obtain a reliable experimental result. Because of no calibration sample is prepared, the validity of experiment was verified using the difference of the PEC peak amplitude obtained in the crack and opposite side (Fig. 4). The base metal of sample block SA508 Cl.2 is ferromagnetic and welding material alloy 182 which is nonmagnetic material. Therefore, the PEC amplitude measured in the ferromagnetic part is higher than that of the nonmagnetic part. The y coordinate 10 and 12 cm neighborhood is the interface region between ferromagnetic and nonmagnetic material. The crack is positioned in the neighborhood of y coordinate 11 cm, which shows the minimum PEC signal amplitude.

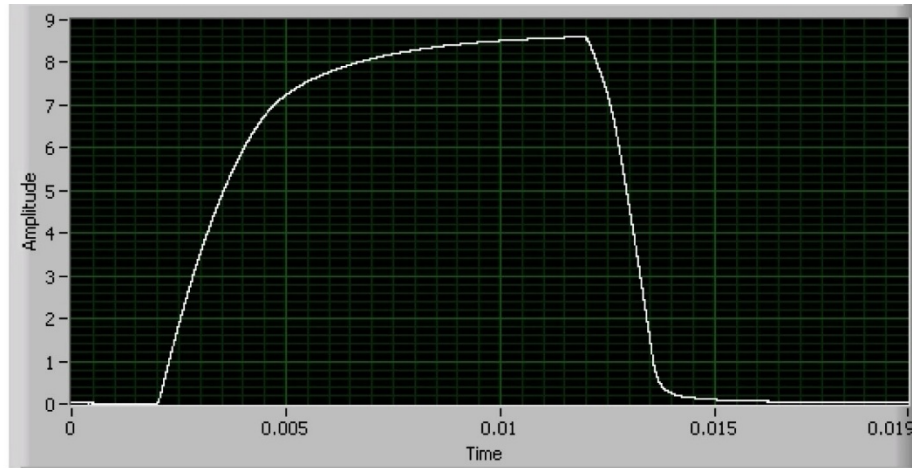
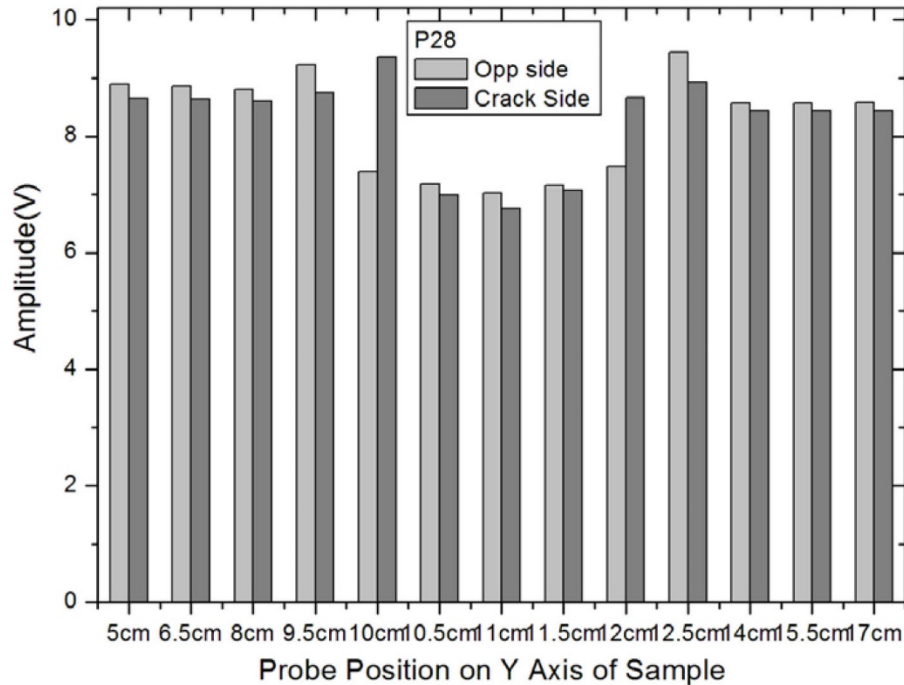


Figure 3. Typical PEC signal induced in the Hall-sensor from the test block.

The important characteristic of detected signal to interpret the results is the peak value of the pulse. The measuring points were selected as a x-y coordinate, the x points were fixed at the center of transverse direction and y points were selected along the longitudinal direction.

Fig. 5 shows the change of PEC peak amplitude along the coordinate and shows minimum value at the defect position.



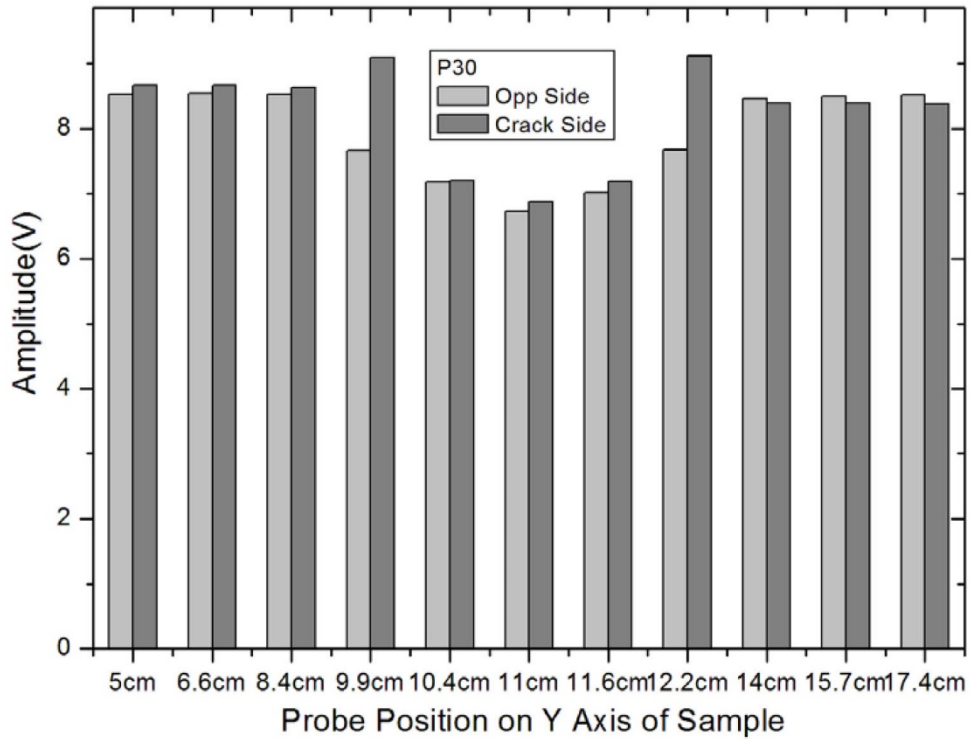
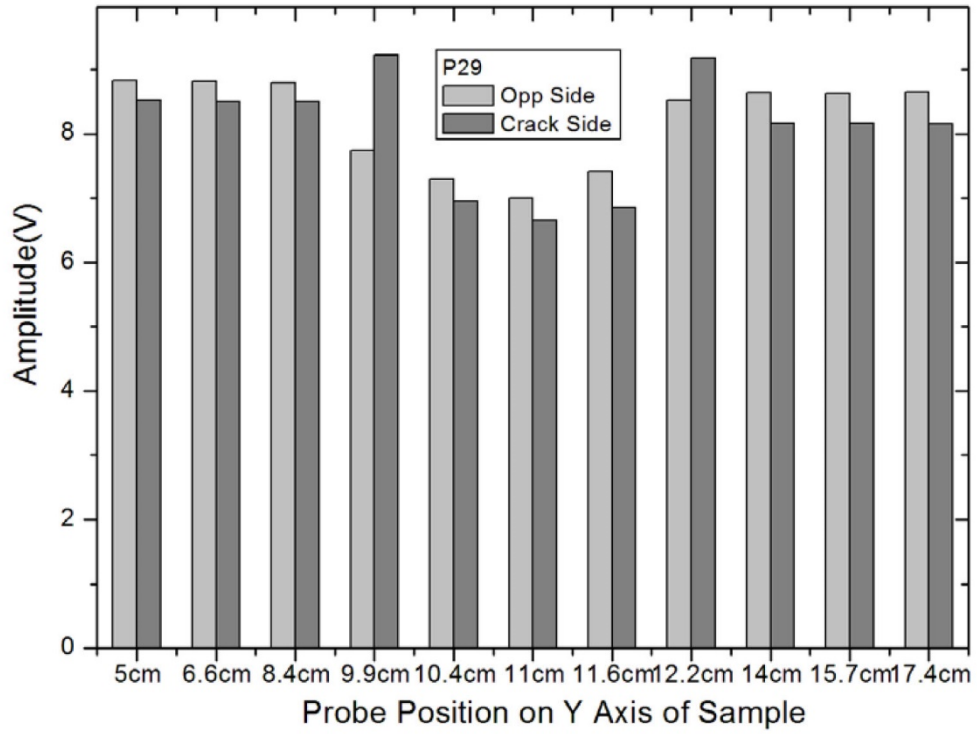


Figure 4. The difference of the PEC peak amplitude obtained in the crack and opposite side for P28, P29 and P30.

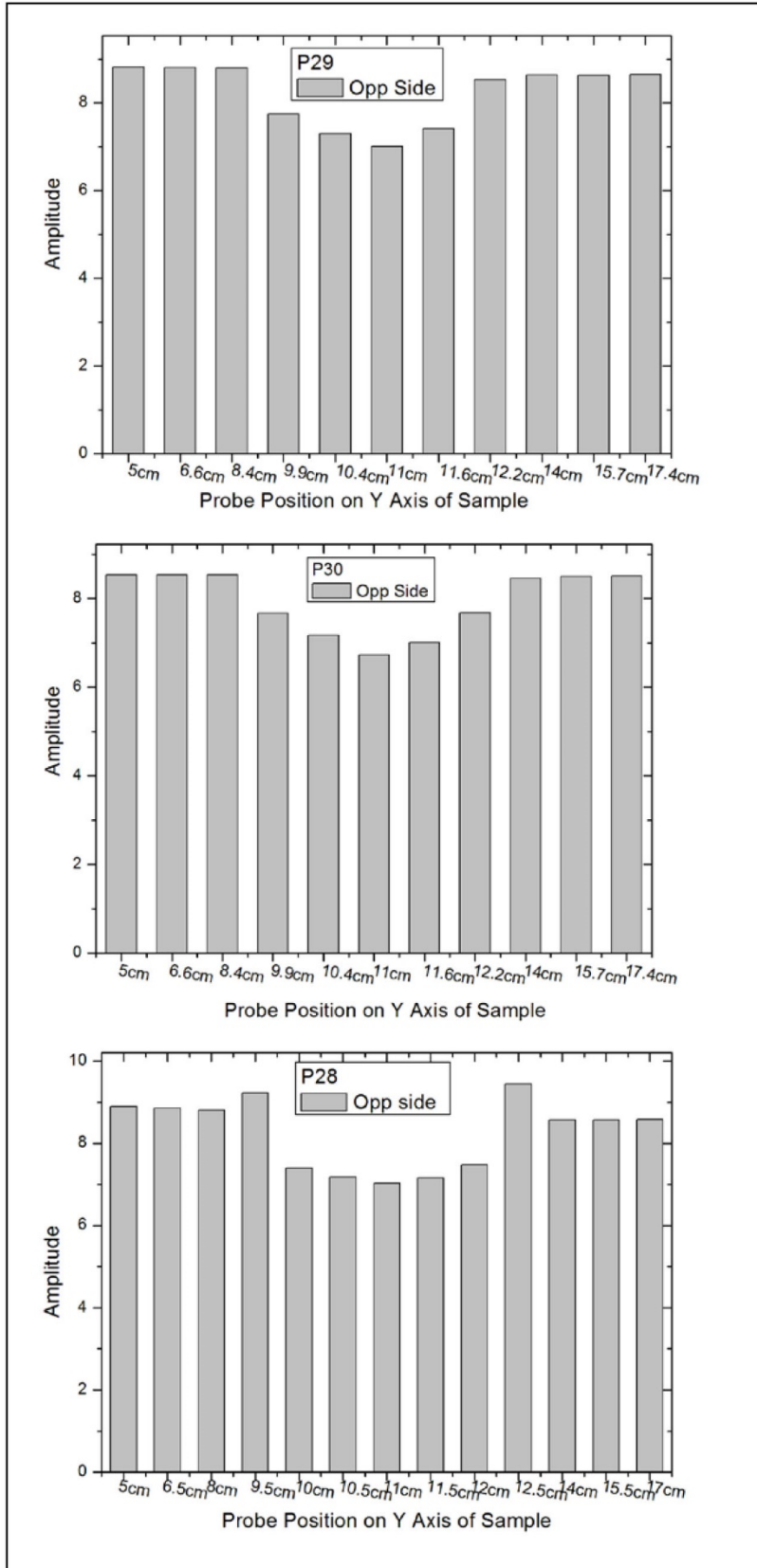


Figure 7. The difference of the PEC peak amplitude obtained in the crack and opposite side for P28, P29 and P30

## 6. Summary

1) The nondestructive evaluation (NDE) using PECT to detect the sub surface crack under the thick plate has been performed on the PARENT round robin sample. Three classes of round robin sample for P28, P29 and P30 have been tested, each class has dissimilar weld region between two ferromagnetic base materials.

2) The PEC amplitude detected in the defect region (welded part) showed lower value than that of base material. The y coordinate 10 and 12 cm neighborhood is the interface region between ferromagnetic and nonmagnetic material. The crack is positioned in the neighborhood of y coordinate 11 cm, which shows the minimum PEC signal amplitude.

3) The base material is made of ferromagnetic materials, and dissimilar weld region is made of nonmagnetic materials. Considering the ferromagnetic materials induce a high magnetic signal, it is not certain that the decrements of amplitude are attributed to the defects or nonmagnetic part.

4) The PEC technology showed potential possibility detecting the subsurface crack in the nonmagnetic stainless steel plate, but the signals are largely depend on the appearance of ferromagnetic substance. Therefore the PECT technique requires further assessment and improvement in order to apply in the dissimilar weld region.

## References

- [1] G. Y. Tian, Z. X. Zhao, and R. W. Baines, "The research of inhomogeneity in eddy current sensors", *Sens. Act. A.*, vol. 69, pp 148–151, 1998.
- [2] E. E. Kriezis, Theodoros D. Tsiboukis, Stavros M. Panas and John A. Tegopoulos, "Eddy currents: Theory and applications", *Proceedings of IEEE*, Vol. 80, No. 10, pp 1559- 1589, Oct 1992.
- [3] B.P.C. Rao, B. Raj, T. Jayakumar and P. Kalyanasundaram, "An Artificial neural network for eddy current testing of austenitic stainless steel welds", *NDT&E International*, Vol. 35,pp 393-398, 2002.
- [4] Y. He, F. Luo, M. Pan, "Defect characterisation based on pulsed eddy current imaging technique", *Sensors and Actuators A*, Vol 164, pp 1-7, 2010.
- [5] J.C. Moulder, J.A. Bieber, W.W. Ward III, J.H. Rose, "Scanned pulsed eddy current instrument for non-destructive inspection of aging aircraft", *SPIE 2945*, pp 2–13,1996.
- [6] B.P.C. Rao, B. Raj, T. Jayakumar and P. Kalyanasundaram, "An Artificial neural network for eddy current testing of austenitic stainless steel welds", *NDT&E International*, Vol. 35,pp 393-398, 2002.
- [7] Y. He, M. Pan, F. Luo, G.Ti, "Pulsed eddy current imaging and frequency spectrum analysis for hidden defect nondestructive testing and evaluation", *NDT& Int.*, Vol 44, pp 344-352, 2011.
- [8] H. C. Yang, C.C. Tai, "Pulsed eddy current measurement of a conducting coating on a magnetic metal plate", *Meas Sci Technol*, Vol 13, pp 1259-1265, 2002.
- [9] M. A. Robers, R. Scottini, "Pulsed eddy current in corrosion detection", *NDT.net The e-Journal of Nondestructive Testing*, Vol.7, Oct. 2002.
- [10] A. Smith, G. R. Hugo, "Transient Eddy-current NDE for aging aircraft capabilities and limitations", *Insight: Non-Des. Testing and Condition Monitoring*, Vol.43, pp. 14-25, Jan. 2001.



### **A.3 Manufacturing of a New Type of NDE Test Samples with Laboratory-Grown Intergranular SCC Cracks in a Nickel-Base Weld – Comparison of Various NDE-Techniques Applied to a Challenging Crack Morphology**

#### **Manufacturing of a new type of NDE test samples with laboratory-grown intergranular SCC cracks in a nickel-base weld – Comparison of various NDE-techniques applied to a challenging crack morphology**

Klaus GERMERDONK<sup>1</sup>, Hans-Peter SEIFERT<sup>2</sup>, Hardy ERNST<sup>3</sup>, Alexander FLISCH<sup>4</sup>,  
Dominik NUSSBAUM<sup>5</sup> and Stefan RITTER<sup>2</sup>

<sup>1</sup>ENSI – Swiss Federal Nuclear Safety Inspectorate, Industriestrasse 19, Brugg, Switzerland

<sup>2</sup>PSI – Paul Scherrer Institute (PSI), Nuclear Energy and Safety Research Department, Laboratory for Nuclear Materials, Villigen, Switzerland

<sup>3</sup>SVTI – Swiss Association for Technical Inspections – Nuclear Inspectorate, Wallisellen; and  
QuANDT GmbH, Switzerland

<sup>4</sup>EMPA – Swiss Federal Laboratories for Materials Science and Technology, Dübendorf, Switzerland

<sup>5</sup>ALSTOM – ALSTOM Thermal Power, NDT METHODOLOGIES, Baden, Switzerland

#### **Abstract**

In order to produce NDE test samples with a crack morphology close to PWSCC/IDSCC cracks found in the field, a modified fracture mechanic specimen was designed. Several test samples were produced containing different crack morphologies (PWSCC/IDSCC cracks as well as fatigue cracks and EDM notches for comparison purposes).

The specimen fit into the autoclave test facilities at PSI. The specimens were loaded under typical PWR und BWR water chemistry conditions at 290 and 320°C. It took several months until sufficient IDSCC crack growth was achieved, afterwards the NDE specimen were machined to the final geometry for later NDE testing.

In order to validate the new test samples for further utilization, several organizations in Switzerland performed evaluations by advanced NDE-techniques on those test samples including X-ray testing as well as UT-techniques. Furthermore, metallographic analysis of a laboratory grown IDSCC crack completed the investigations.

The UT measurements seem to indicate that the existing tip diffraction technique reaches its limit for the challenging crack morphology ensuing from the newly developed NDE test samples.

**Keywords:** laboratory-grown SCC, PWSCC/IDSCC, tip diffraction technique

## 1. Introduction

Alloy 182 has been widely used as a weld filler and attachment pad metal to join the low-alloy steel (LAS) reactor pressure vessel (RPV) and pressure vessel (steam generator, pressurizer) nozzles to both wrought nickel-base alloys (Alloy 600) and austenitic stainless steel (304L, 316L, 316NG) components in light water reactors by manual shielded metal arc welding (SMAW). In recent years, incidents of stress corrosion cracking (SCC) in Alloy 182 in both boiling water (BWR) [1, 2] and pressurized water reactors (PWR) [2, 3] were reported in some countries and seriously challenged the integrity of the primary coolant circuit in some cases. The cracking was interdendritic/intergranular and usually confined to the weld metal [1-6].

These Alloy 182 DMW usually have a complex weld configuration with a reduced accessibility for NDE in some important cases (Figure 1). A very heterogeneous and anisotropic weld microstructure with a lot of interfaces and different microstructural zones and the presence of high residual stresses/plastic weld shrinkage strains or potential welding defects (e.g. hot cracking) are characteristic for such welds [2]. The SCC cracks in Alloy 182 are usually very tight (small crack openings, in particular during shut-down periods with in-service inspection) and the crack flanks covered by a corrosion-grown conducting oxide film. They usually reveal a high surface roughness, crack branching, many un-cracked ligaments or a very inhomogeneous crack growth (finger-like cracking). For all these reasons, the detection and, in particular, sizing of such SCC defects in DMW represent a challenge and are related to relevant uncertainties and errors [10]. As shown by service experience, the crack depth may be significantly underestimated by currently used NDE methods.

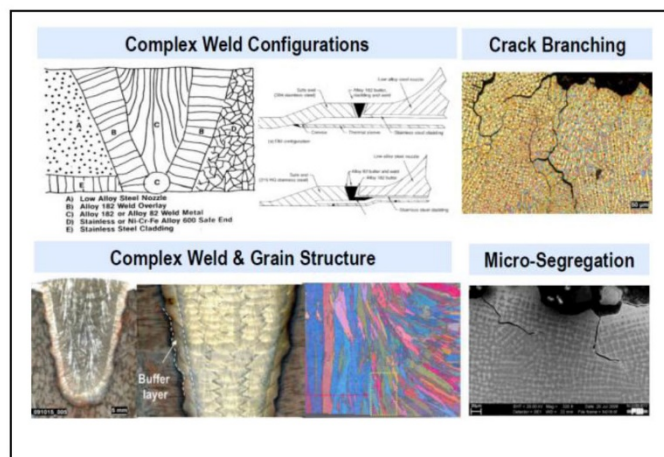


Figure 1. Complex DMW configurations and weld microstructures

The international PARENT program is therefore dealing with the assessment of established and new emerging NDE-techniques to detect and assess flaws in such DMW [11]. This multinational program is led by the US NRC and includes regulators, industrial groups and research institutions and was initiated in 2012. A Swiss consortium formed by ENSI, PSI, ALSTOM, EMPA and SVTI is participating in this program. One of the main Swiss contribution was the fabrication (by PSI) of test samples with different realistic SCC (laboratory grown) crack configurations for a systematic evaluation of various emerging NDE-techniques within the PARENT project. As a new type of NDE test samples was developed, advanced NDE measurements (by ALSTOM, SVTI and EMPA) were initially performed to validate and characterize these test samples.

## 2. Fabrication of NDE test samples with laboratory grown SCC cracks

NDE test samples with different “circumferential” SCC crack configurations and crack depth to wall thickness ratios in an Alloy 182-RPV steel DMW were generated in high-temperature water loop autoclave systems at PSI under simulated BWR/normal water chemistry (NWC) and primary PWR conditions at 274°C and 290 & 320°C, respectively. In total, nine test bodies having SCC and fatigue cracks or a semi-elliptical EDM notch were fabricated. The generation of NDT test samples with SCC cracks was extremely time consuming and expensive - in particular in PWR environment - and involved test durations of up to six months!

### 2.1 Test welds

The DMW test weld was fabricated according to GE welding procedures by Sulzer Innotec (Winterthur, Switzerland) by qualified welders with welder approval test certificates. The DMW was manufactured by filling a 100 mm deep U-shaped groove in a large (1300 × 850 × 220 mm) forged 22 NiMoCr 3 7 (= SA 508 Cl. 2) plate by SMAW with Alloy 182 weld metal (AWS A5.11: E NiCrFe-3, Trade name: Böhler UTP 7015) (Figure 2). The RPV steel was from the forged lower cylindrical shell of a German PWR RPV, which was not commissioned (Biblis C) and revealed a moderate and low susceptibility to environmentally-assisted cracking (EAC) and dynamic strain ageing (DSA). In a first step, a weld butter layer (double layer at the groove root, single layer on the groove flanks) was produced by SMAW, which was then grinded and post-weld heat treated at 620 °C for 9 h 15 min. The groove was then filled by multipass SMAW without subsequent PWHT. The bulk weld metal is thus in the as-welded condition, in contrast to the buffer layer that is sensitized with chromium carbide precipitation on the grain boundaries

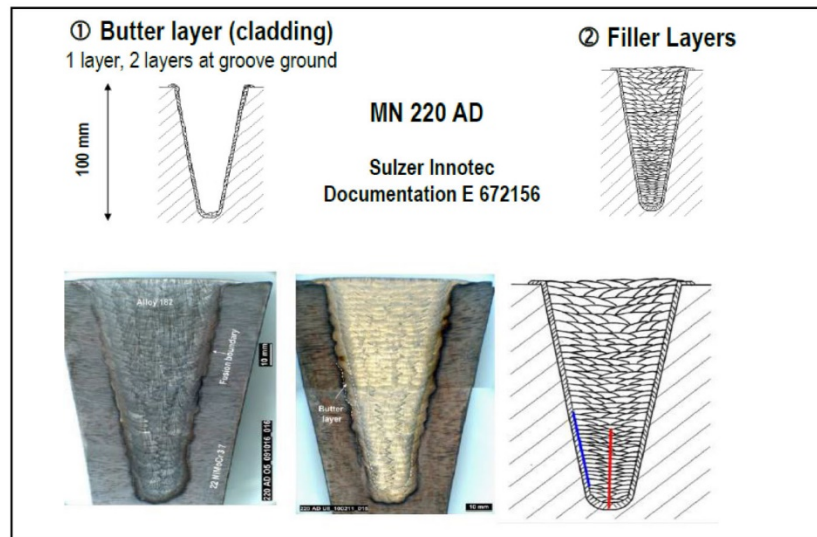


Figure 2. Welding specification for buffer and filler layers; Macro-etching of weld and schematic of crack configurations.

The chemical composition of the Alloy 182 weld metal and LAS base metal measured by inductively coupled plasma atomic emission spectroscopy (ICP-AES) and hot gas extraction (C, S, N) are summarized in Table 1. The Vickers micro hardness in the bulk weld metal (as-welded) and peak hardness in the LAS HAZ were in the range of 280 to 340 HV0.1 and 350 to 410 HV0.1, respectively. The hardness in the buffer layer (PWHT) was slightly lower than in the bulk weld metal. The thickness of the weld HAZ in the LAS varied between 1.5 to 4.5 mm and the peak hardness in the LAS HAZ was usually close to the fusion line. The dilution zone (DLZ) in the Alloy 182 weld metal close to the fusion line with a different chemical composition than the bulk weld metal (BWM) had a thickness of 1.5 to 2.5 mm and, besides the chromium precipitation, a similar microstructure as the bulk weld metal.

Table 1. Chemical composition of weld metal and low-alloy RPV steel

Material		C	Ni	Cr	Fe	P	S	Mn	Mo	Si	Ti	Nb+Ta	Al	Co	Cu
DMW	Alloy 182	0.026	69.3	16.1	5.3	0.002	0.005	6.19	0.18	0.57	0.068	2.31	0.024	0.013	0.007
	22 NiMoCr 3 7	0.215	0.88	0.42	96.8	0.008	0.007	0.91	0.53	0.2	-	-	0.018	-	0.04

## 2.2 Geometry of NDT test samples

For the SCC tests a modified 35 mm thick 1.4 T C(T) fracture mechanics specimen with a 80 mm ligament with T-shape was used (Figure 3). This specific specimen geometry was selected due to space and load capacity limitations in the autoclave. After SCC testing, the load arms were cut from the specimen, which resulted in a rectangular NDT block (220 × 35 × 30 mm) with the weld metal and SCC crack in its middle. For the calculation of the stress intensity factors a 2-D finite element calibration curve was developed for this specific specimen geometry. Prior to the test, the specimen were fatigue pre-cracked in air at a load ratio of 0.3 and a frequency of 60 Hz with a final  $K_I$ -value at a maximum load of about  $20 \text{ MP}\cdot\text{m}^{1/2}$  and the fatigue pre-crack tip in the Alloy 182 weld metal.

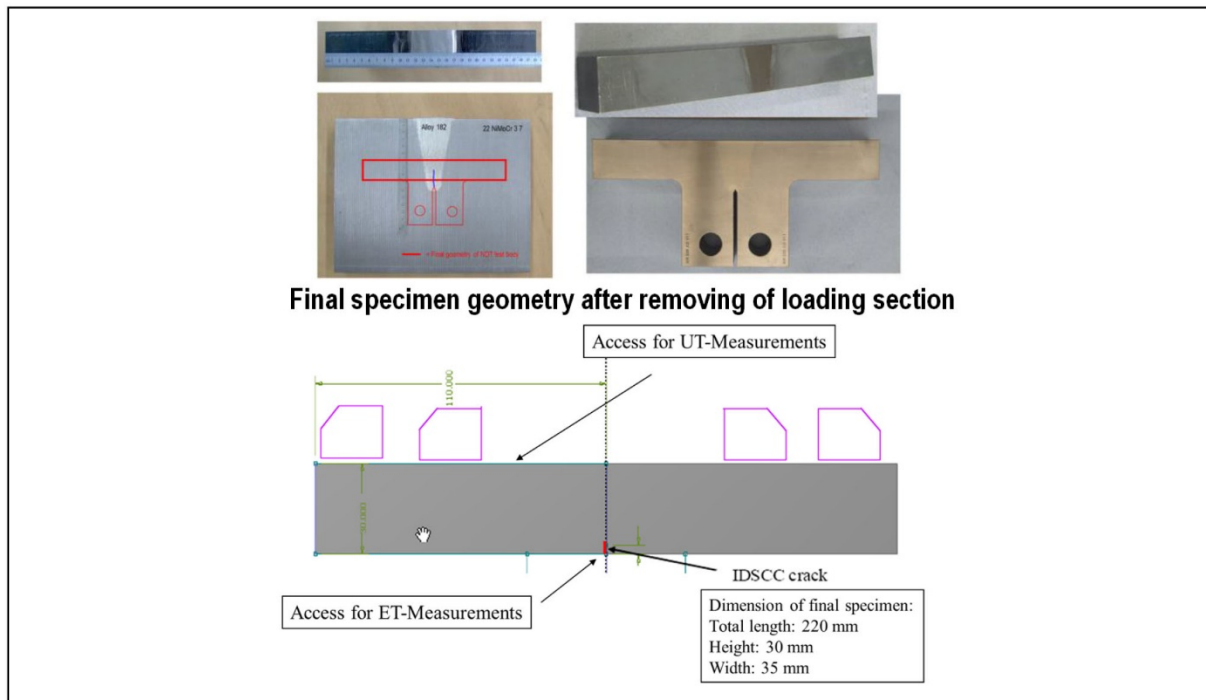


Figure 3. Geometry of SCC specimen and final NDT test body

## 2.3 Experimental set-up for manufacturing of laboratory grown SCC cracks

The SCC tests were performed under simulated BWR/NWC and PWR conditions in stainless steel autoclaves with integrated electromechanical loading systems, which were attached to sophisticated refreshing high-temperature water loops (Figure 4). During the experiments the crack growth and all important mechanical and environmental parameters at the inlet and outlet were recorded continuously. The specimens were electrically isolated from the autoclave using zirconia sleeves/spacers. The electrochemical corrosion potential (ECP) of the specimens and the redox potential (platinum probe) were continuously monitored with Cu/Cu<sub>2</sub>O ZrO<sub>2</sub>-membrane reference electrodes.

Ionic impurities of the water (collected at the inlet and outlet) were analyzed by Inductive Coupled Plasma-Atomic Emission Spectroscopy (ICP-AES) and Ion Chromatography (IC) once or twice during each test.

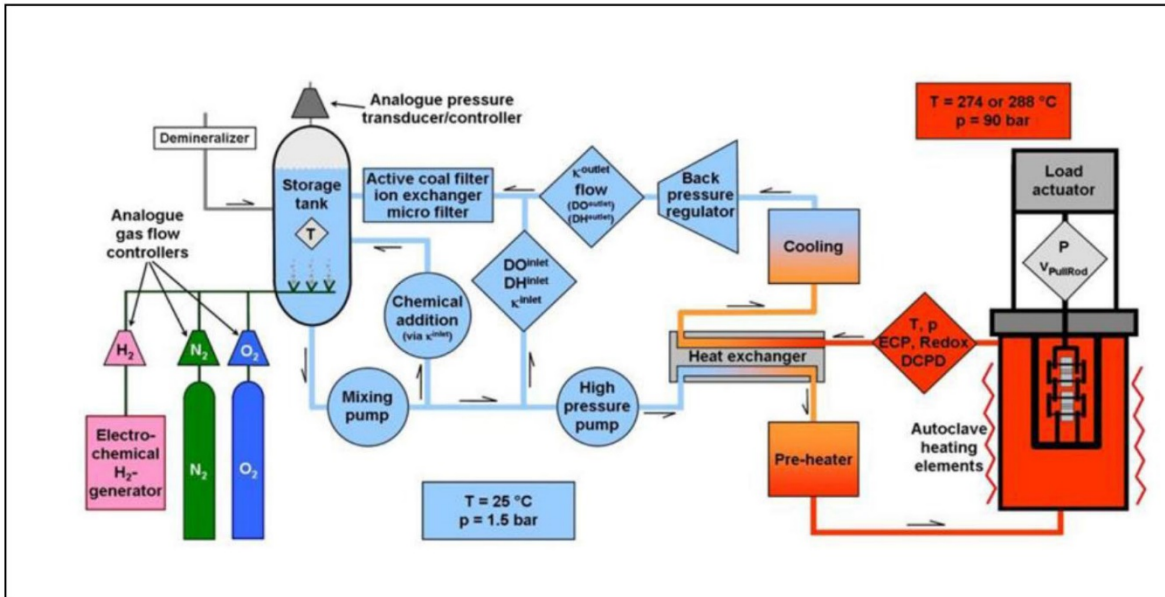


Figure 4. Schematic of high-temperature water loop autoclave system for SCC tests

**BWR/NWC environment:** The SCC tests in simulated BWR/NWC environment were performed in neutral ( $\text{pH}_{274}^{\circ\text{C}} = 5.65$ ) high-purity, oxygenated high-temperature water at 274 °C under low-flow conditions (5 autoclave exchanges per hour, local flow rate of some few mm/s) with a dissolved oxygen content of 2 ppm and 5 or 20 ppb of chloride. The increased dissolved oxygen content was used to simulate a realistic ECP at Alloy 182 attachment welds within the RPV of BWR and was in the range of +160 to +180  $\text{mV}_{\text{SHE}}$ . The corresponding redox potentials of the environment were +290 to +310  $\text{mV}_{\text{SHE}}$ . The chloride was added to accelerate SCC to reach larger crack depths in a reasonable time frame.

**Primary PWR environment:** Corresponding SCC tests in simulated PWR primary water environment were performed in boric and lithiated, slightly alkaline hydrogenated high-temperature water at 320 °C or 290 °C under low-flow conditions (5 autoclave exchanges per hour, local flow rate of some few mm/s) with  $\text{H}_3\text{BO}_3$  (850 to 900 ppm B) and LiOH (2.2 to 2.3 ppm Li) and a dissolved hydrogen content of 2.2 ppm, thus slightly above the Ni/NiO boundary. The  $\text{pH}_T$  and ECP at temperature were 7.3 or 7 and -800  $\text{mV}_{\text{SHE}}$  or -750  $\text{mV}_{\text{SHE}}$ , respectively.

**Mechanical loading procedure:** Before applying the different loading sequences, the specimens were pre-oxidised in the test environment at a small constant pre-load of 2 kN for at least one week in order to achieve stable environmental and electrochemical conditions.

Thereafter, a complex initial loading procedure was applied to achieve a complete transitioning from the transdendritic fatigue to an interdendritic SCC crack in the Alloy 182 weld metal along the whole crack front and to evolve a plastic zone, which is characteristic for a growing SCC crack. This involved cyclic loading with a stepwise increase of load ratio  $R$  from 0.3 to 0.7 and decrease of loading frequency before switching to periodic partial unloading ( $R = 0.7$ ,  $\Delta t_{\text{hold}} = 9000$  s). When the expected SCC crack growth rates were achieved, pure constant load was applied in the BWR/NWC tests, whereas periodical partial unloading was generally used in the PWR tests. Depending on the observed SCC growth rates and target crack depths, the load level was further stepwise increased to accelerate or sustain SCC crack growth and reduce the necessary testing time. The final  $K_I$  values of the SCC cracks at the end of the tests calculated by the mean crack depths varied between 28 and 63  $\text{MPa}\cdot\text{m}^{1/2}$ . Because of the very irregular and thumb-nail shape of crack front with massive tunneling in some cases, the local maximum  $K_I$ -values could be up to a factor of 2 higher. The high  $K_I$ -levels are characteristic for cracks in many dissimilar metal welds in the field (e.g. J-groove welds) [9].

Crack growth monitoring: The crack advance in the SCC tests was continuously monitored using the reversed direct current potential drop method (DCPD). The DCPD crack growth results were linearly corrected after the test with the average SCC crack increment measured on the side surfaces and an correction factor that is based on intensive testing experience at PSI with this and other Alloy 182 DMW under identical or similar conditions. The observed SCC cracking behavior was furthermore compared with that of similar other SCC tests in Alloy 182 at PSI and with literature data.

As shown in Figures 5 and 6, the observed SCC crack growth rates in the NDT test bodies were within the typical range of BWR/NWC and PWR conditions. For illustration also other PSI data representing relevant parameter studies on SCC growth, as well as selected SCC disposition lines, are included.

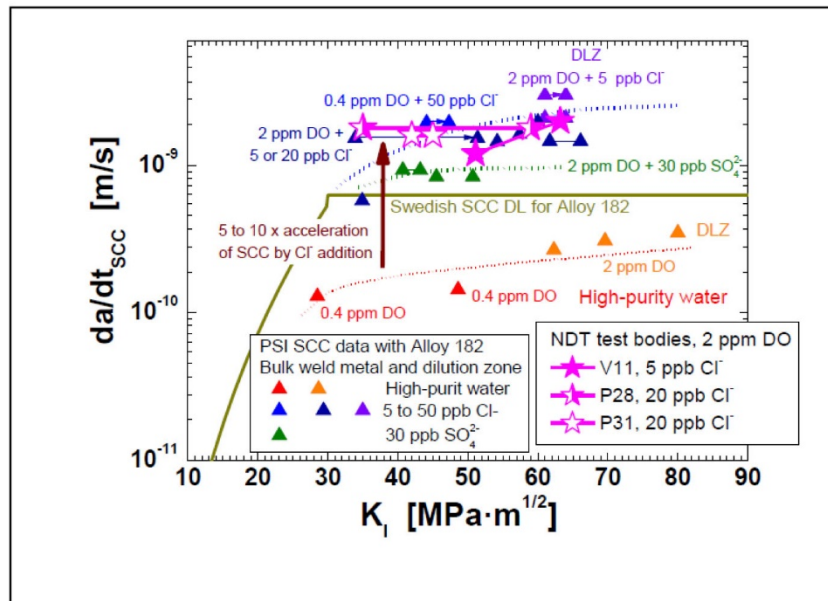


Figure 5. Comparison of BWR/NWC crack growth rates in NDT test samples with other PSI data [9], as well as with Swedish SCC disposition lines for Alloy 182 in BWR/NWC and PWR environment

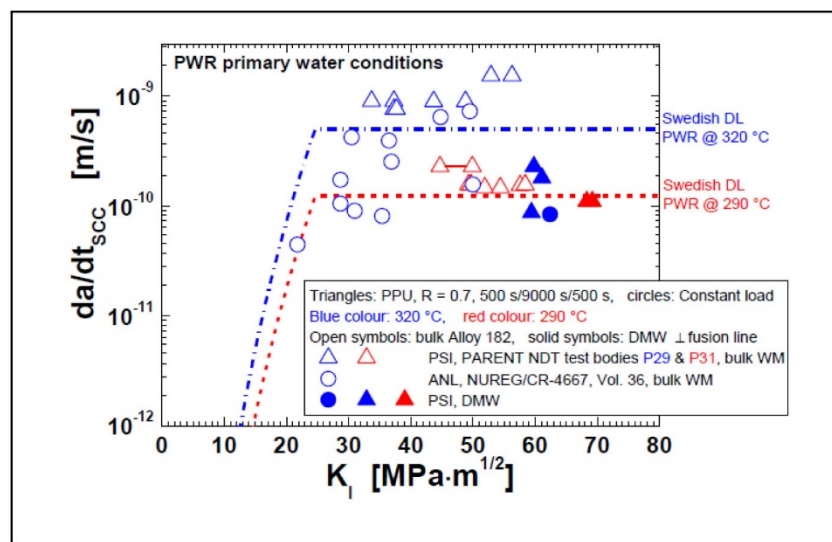


Figure 6. Comparison of PWR SCC crack growth rates in NDT test samples with other PSI and literature data [9], as well as with Swedish SCC disposition lines for Alloy 182 and PWR environment

## 2.4 Overview on NDE test samples

Table 2 gives an overview of the fabricated NDT test samples. They contain “circumferential” shallow or deep BWR SCC, PWR SCC and mechanical air fatigue cracks or a semi-elliptical EDM notch in the middle of the bulk weld metal. Additionally, one specimen contained a PWR SCC crack in the interface region between the weld butter and bulk weld metal parallel to the fusion boundary. The cracks had an approximately semi-elliptical global shape with the highest crack depth in the centre of the specimen. Due to size/geometry constraints in the autoclave, no “axial” cracks could be generated.

The SCC crack growth in BWR/NWC environment is usually more homogenous than in the PWR environment, where cracking can be very uneven with highly localized finger-like crack growth and higher frequency of un-cracked ligaments. The SCC cracks have a significantly higher surface roughness than the mechanical fatigue crack in air that does not contain any larger un-cracked ligaments. The roughness of the fracture surface usually increases with increasing SCC crack growth rate, the applied  $K_I$  and crack depth. Moderate out-of mid-plane cracking is not unusual and, in combination with the fracture surface roughness, results in mixed mode loading of the crack-tip and thus significant local crack closure even in the loaded conditions. The crack openings increase with applied  $K_I$ . In the unloaded conditions large parts of the crack area can be closed.

Table 2. NDE test samples

Specimen designation	V11	P28	P32	P29	P31	P38	P30
Type of crack	SCC	SCC	SCC	SCC	SCC	SCC	Mechanical fatigue
Environment	BWR/NWC 274 °C	BWR/NWC 274 °C	BWR/NWC 274 °C	PWR 320 °C	PWR 290 °C	PWR 290 °C	Air 25 °C
Location of crack plane	Middle of bulk WM	Middle of bulk WM	Middle of bulk WM	Middle of bulk WM	Middle of bulk WM	WB/WM-Interface parallel to FB	Middle of bulk WM
Estimated max. crack depth [%]	39	40	51 *	35	13	15	60
Estimated $\Delta a_{max}$ [mm]	11.9	12	15.3 *	11	4	4.7	18
Estimated $\langle \Delta a \rangle$ [mm]	7.6	9.4	9.2 *	6.8	1.9	2.6	16
Final $K_I$ [ $MPa \cdot m^{1/2}$ ]	63	60	45	56	50	58	28
Crack configurations							

\* Some hints indicate a possible deeper local maximum crack depth

WM: Weld metal

WB: Weld butter

FB: Fusion boundary

### 3. Characterization of SCC test samples

All SCC cracks in the NDE test samples were initially characterized by different UT-techniques and an advanced X-ray tomography system (Figure 7).

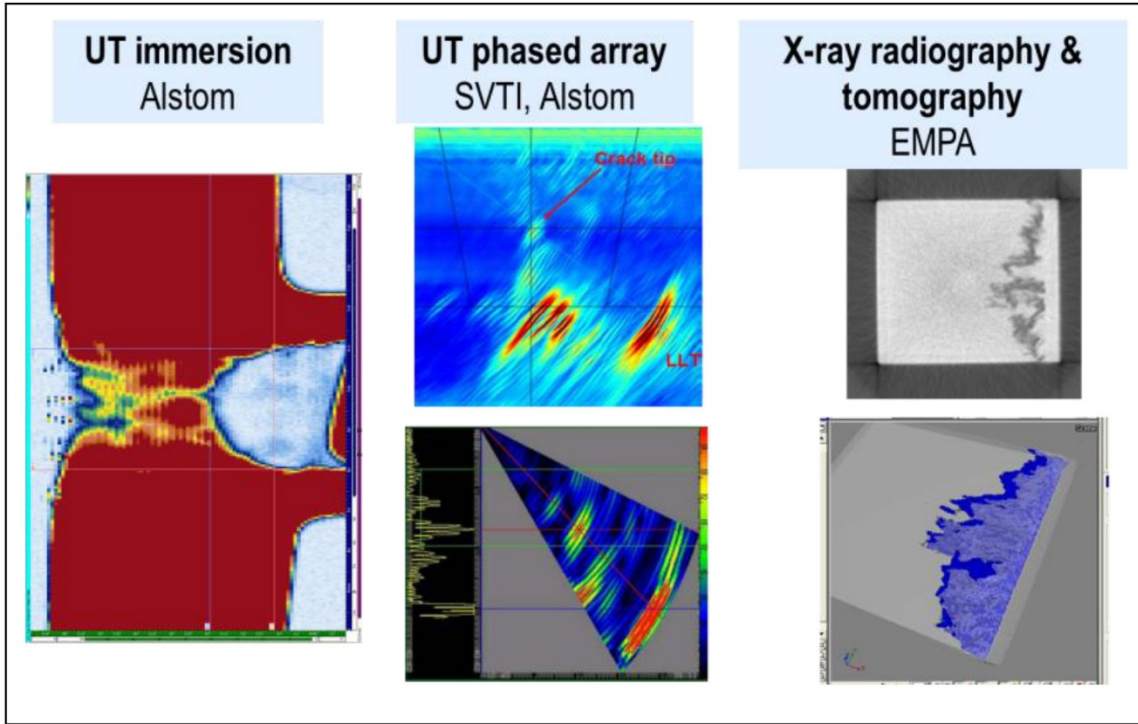


Figure 7. Overview on the applied NDT-techniques (broken up specimen V11)

A special high resolution mechanized UT immersion technique based on a pitch/catch-type transducer arrangement for transmission and reception of longitudinal waves was performed (transmission mode with strongly focused 10 MHz probes) (Figure 8). Furthermore, manual phased array ultrasonic examinations were performed to depth size the surface breaking PWSCC using state-of-the-art UT-techniques. Depth sizing with all the applied UT-techniques was challenging on the produced NDE test samples. Especially difficult were measurements on a sample with a rather deep crack (P32). It cannot be excluded that the actual maximum local depth (finger type) might be deeper than stated, probably due to significant amounts of un-cracked ligaments and local crack closure with contact of crack flanks. A more detailed explanation of the applied NDE-techniques will be included in the final Open testing report of the PARENT projects.

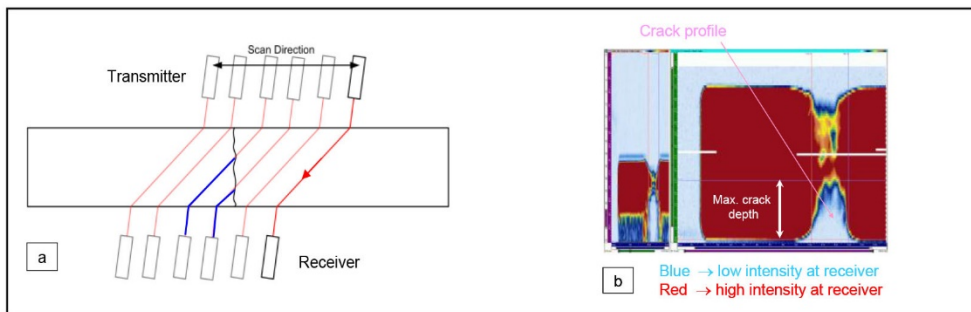


Figure 8. Schematic of applied UT transmission technique for characterization of crack profile (a) and resulting UT picture of PWR SCC crack in specimen (b)



### 3.1 Validation of manufacturing process of NDE test samples and the initially applied NDE-techniques

For the validation of the laboratory manufacturing process techniques and the applied initial NDE-techniques the test sample V11 (BWR/NWC SCC, crack in the bulk weld metal) was used. This sample was unintended significantly overloaded during optical measurement of surface crack length after finishing the SCC experiment and showed therefore a significant larger crack opening displacement than the remaining NDE test samples. A fairly good correlation between the UT (based on transmission mode) and DCPD results with only minimal underestimation of the real crack depths was observed (Figure 9). A clear identification of the crack-tip signal by standard UT-techniques was difficult in spite of perfect lab and surface conditions. X-ray tomography, on the other hand underestimated slightly the maximum crack depths and was only able to detect areas with clear crack flank separation (Figure 9).

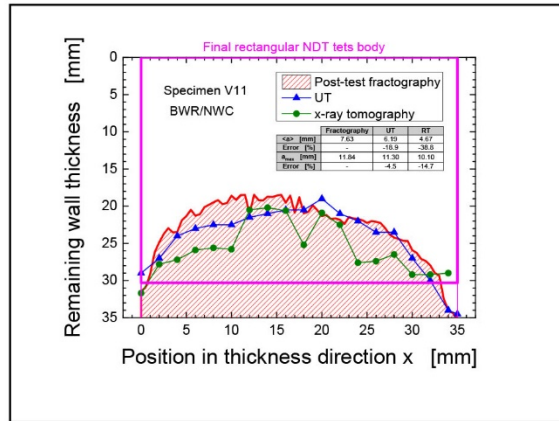


Figure 9. Comparison applied NDT-techniques with post-test fractography for a specimen V11

Figures 10 to 12 show some typical characteristic features of SCC in Alloy 182 in the specimen V11 like, e.g. high surface roughness, secondary cracking/crack branching, un-cracked ligaments or an inhomogeneous crack growth (finger-like cracking).

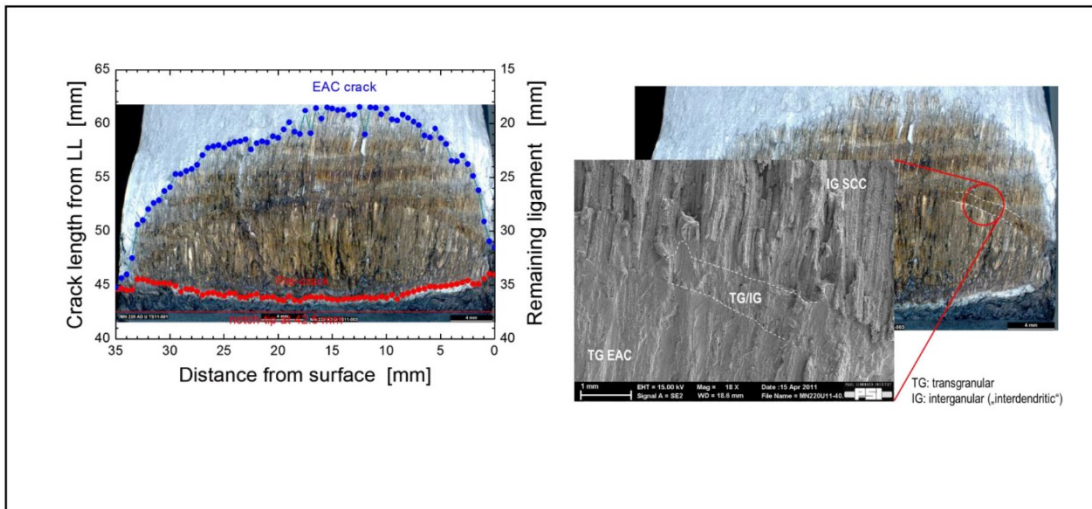


Figure 10. Overview on fracture surface in specimen V11 with deep BWR/NWC SCC crack. Higher surface roughness of the interdendritic IG SCC in comparison to the transgranular (TG) corrosion fatigue (TG EAC)

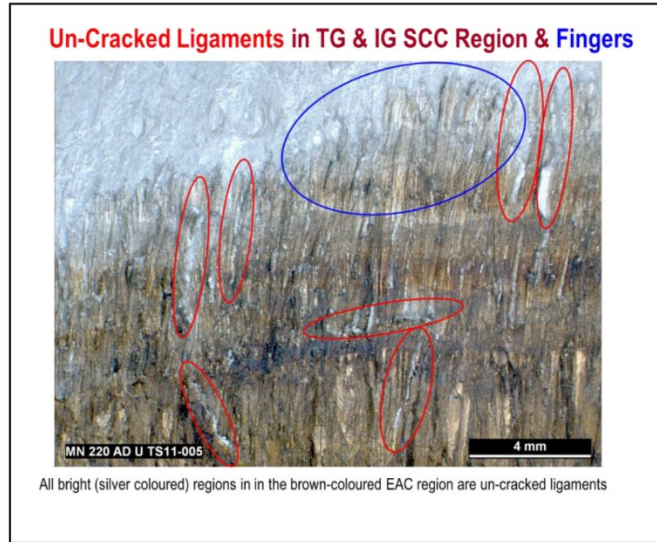


Figure 11. Un-cracked ligaments and finger-like local IG/ID SCC crack growth in V11

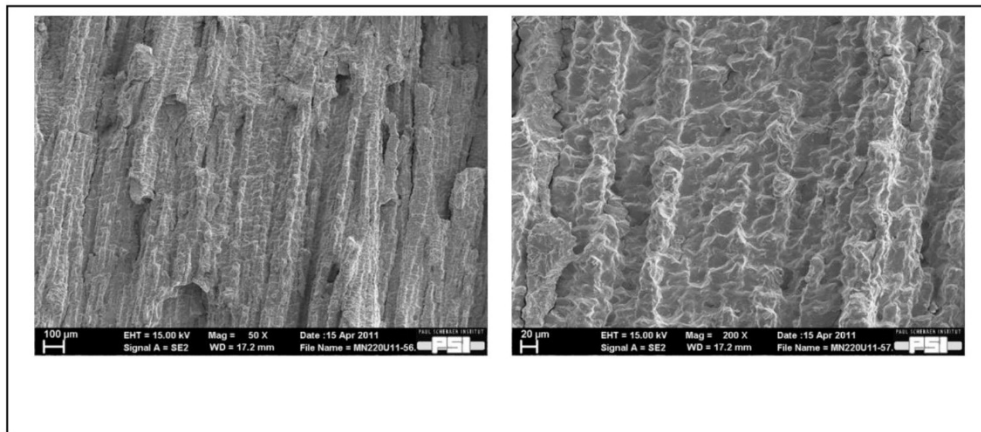


Figure 12. Typical micro-fractographic appearance “interdendritic” IG SCC

### 3.2 Detailed manual phased array measurements on NDE test sample P32

Manual phased array ultrasonic examinations were performed to depth size the surface breaking PWSCC crack in the P32 test sample.

For flaw depth sizing the Absolut Arrival Time Technique was applied. The technique relies upon obtaining a direct signal response from the flaw tip using a material depth calibration. From the crack tip response the amount of uncracked material or remaining ligament can be read directly from the sector or A-scan. Crack depth is calculated by subtracting the remaining ligament from the actual material thickness.

#### Equipment, delay laws and calibration

For the measurements the OmniScan MX ultrasonic instrument with an OMNI-M-PA3218PR-PG modul was used. The 2.0 MHz dual matrix array GEIT 115-000-485 with 2×16 elements and the GEIT wedge 360-151-056 were utilized for the measurements.

The Zetec Advanced PA Calculator 1.2R4 was used for delay law computation. Longitudinal waves in an angle range

from 25° to 70° with a step width of 1° were applied. The focal type was half path and the focal depth was 15 mm.

Calibration (exit point, wedge delay and beam angle) were performed utilizing a austenitic K2 calibration block, examination sensitivity was established using the 45° beam ID role response as reference.



Figure 13. Set-up for manual phased array measurements

Measurements

Figure 14 illustrates the measurement configurations. The measurements were performed from both sides of the weld from the ID and the OD of test sample P32.

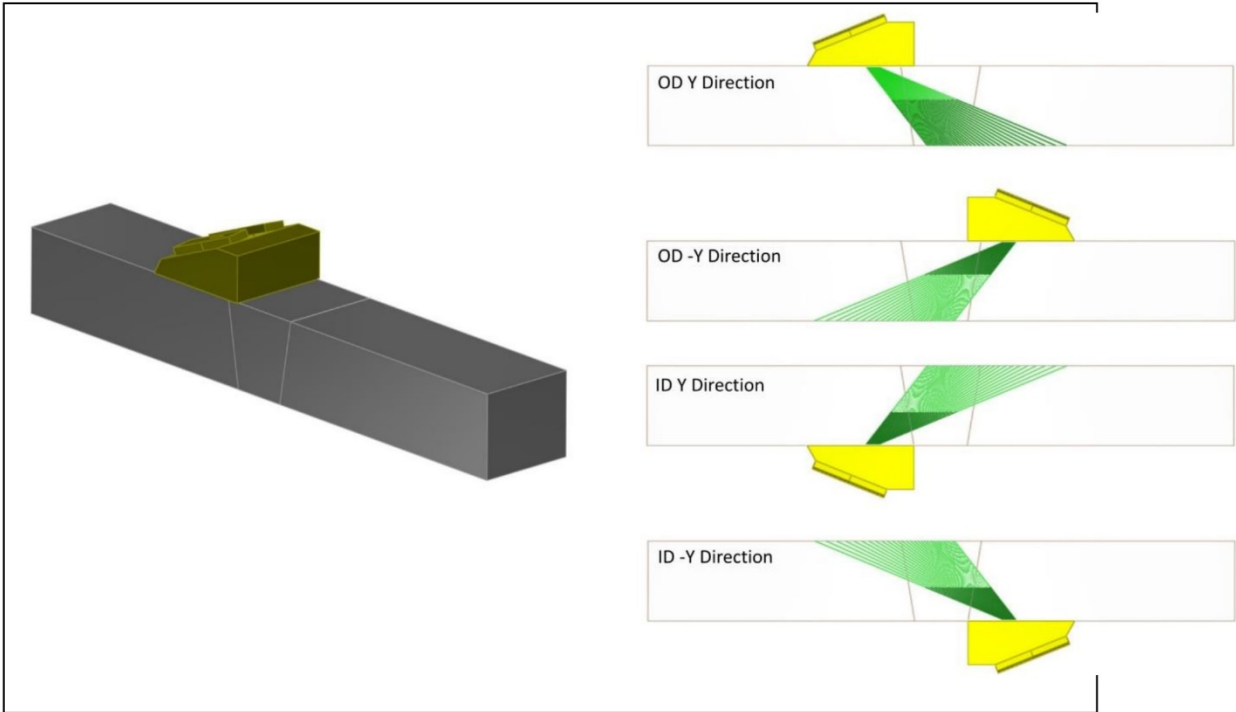


Figure 14. Measurement configuration for manual phased array measurements

## Results

Figure 15 shows the results. It can be assessed that depth sizing from the ID is possible (probe position on the same side as crack initiation). Responses from the flaw face and the flaw end are clearly detectable with good signal to noise ratio. However, from the OD (probe position on the opposite side of crack initiation) depth sizing is not reliably possible. The responses from the flaw face and the flaw end are not clearly resolvable from the noise induced by the anisotropic heterogeneous weld structure. The reason for the difference in the depth sizing performance between ID and OD measurements may be, that the sound propagation is affected by different grain columnar orientation with respect to the propagation direction.

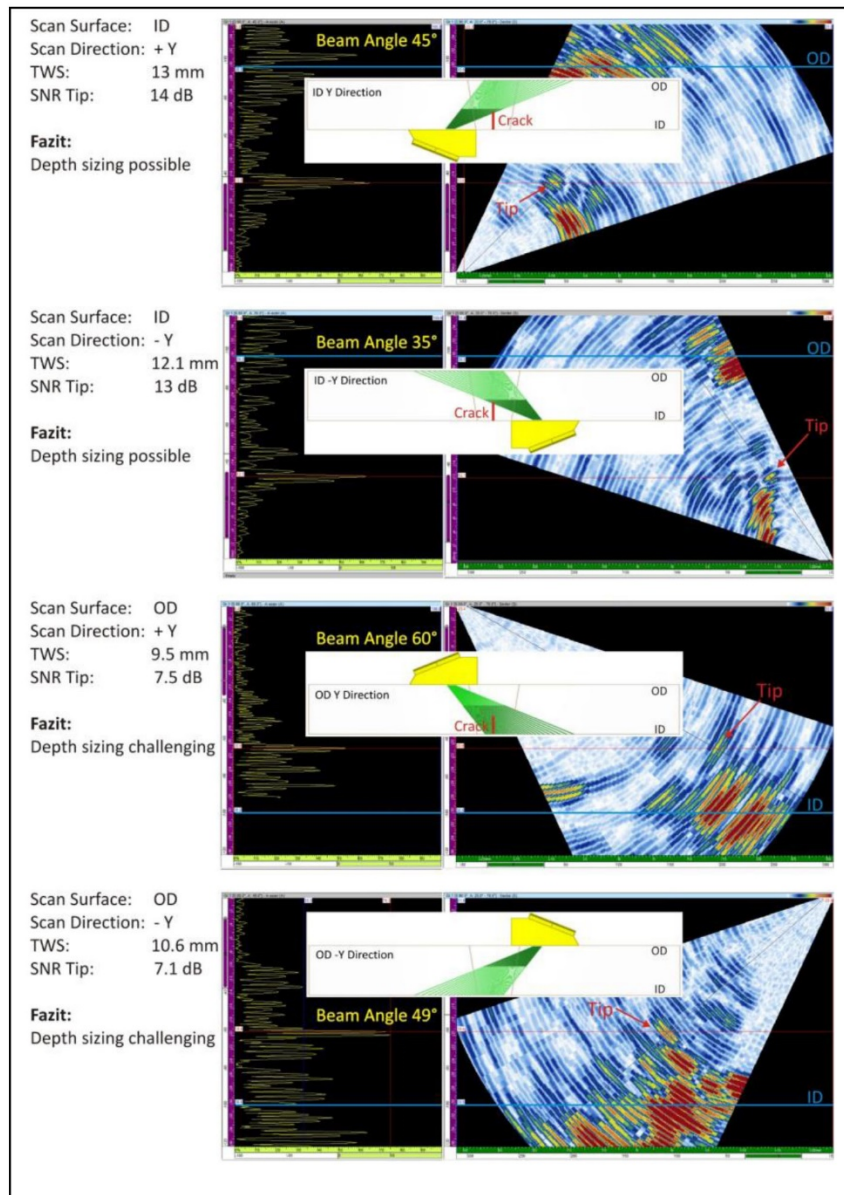


Figure 15. Sectorial scans of P32

#### 4. Summary

Several NDE test samples with laboratory grown SCC were produced. A metallographic analysis of a broken up specimen confirmed the typical interdendritic (ID SCC) crack morphology with pronounced surface roughness, crack branching and many un-cracked ligaments (finger type cracking) in the NDE test samples.

The performed initial NDE measurements were challenging, nevertheless it was possible to estimate the achieved crack depth in the NDE-test samples based on a combination of various NDE-techniques.

Summing up, it has to be assessed that the manual phased array measurements based on a state-of-the-art technique under perfect laboratory conditions gave evidence that the tip diffraction technique reaches the limit when the sound has to propagate through the anisotropic heterogeneous weld material and the flaw morphology is more complex and causes only weak ultrasonic responses. These effects could be enforced due to tight cracks, significant amounts of un-cracked ligaments and local crack closure with contact of crack flanks as expected to be present especially in sample P32.

It can be concluded that in cases of more challenging conditions, e.g. PWSCC in DMW in co-occurrence with field coupling surface conditions, the depth sizing using scattered flaw tip signals is not always possible. This result has to be further discussed and the practical implication on NDE-techniques applied in Swiss power plants to be evaluated by the Swiss Federal Nuclear Safety Inspectorate and the Swiss Qualification Body.

#### Acknowledgements

The results of this paper were generated with the financial support of the Swiss Federal Nuclear Safety Inspectorate (ENSI) within the research programs SAFE and PARENT. Thanks are also expressed to B. Baumgartner, L. Nue, and R. Schwenold (all PSI) for their experimental contribution.

#### References

- [1] R.M. Horn, P. L. Andresen, J. Hickling, "BWR Alloy 182 stress corrosion cracking experience", Proc. of the 5th Int. Symp. on Contribution of Materials Investigation to the Resolution of Problems Encountered in Pressurized Water Reactors (Fontevraud 5), pp. 55-67, CD-ROM, Fontevraud, France, September 23-27, 2002.
- [2] H. Hänninen et al., "Dissimilar metal weld joints and their performance in nuclear power plant and oil refinery conditions", VTT Research Notes 2347, VTT, Espoo, Finland, 2006 (available on <http://www.vtt.fi/inf/pdf/tiedotteet/2006/T2347.pdf>).
- [3] R.S. Pathania, A.R. McIlree, J. Hickling, "Overview of primary water cracking of Alloys 182/82 in PWRs", Proc. of the 5th Int. Symp. on Contribution of Materials Investigation to the Resolution of Problems Encountered in Pressurized Water Reactors (Fontevraud 5), pp. 13-27, CD-ROM, Fontevraud, France, September 23-27, 2002.
- [4] T. Matsunaga, K. Matsunaga, "Stress corrosion cracking of CRD stub tube joint and repair at Hamaoka Unit 1", Proc. 11th Int. Conference on Nuclear Engineering, Paper ICONE11-36056, Shinjuku, Tokyo, Japan, April 20-23, 2003.
- [5] A. Yamashita, K. Takeuchi, W. Sagawa, F. Manabe, "The stress corrosion cracking at shroud support Tsuruga Unit 1", Proc. 9th Int. Conference on Nuclear Engineering, Paper ICONE 9-66, April 8-12, 2001, Nice, France.
- [6] G. Rao, G. Moffatt, A. McIlree, "Metallurgical Investigation of Cracking in the Reactor Vessel Alpha Loop Hot Leg Nozzle to Pipe Weld and the V. C. Summer Station", Proceedings of Fontevraud 5, Contribution of Material Investigation to the Resolution of Problems Encountered in Pressurized Water Reactors, SFEN, pp. 29-41, Fontevraud, France, 23-27 September 2002.
- [7] H.P. Seifert, S. Ritter, Journal of Nuclear Materials, 372(1), pp. 114-131, 2008.

- [8] H.P. Seifert, S. Ritter, "Research and service experience with environmentally-assisted cracking of carbon and low-alloy steels in high-temperature water", SKI-Report 2005:60, Stockholm, Sweden, 2006 (available on [www.ssm.se](http://www.ssm.se)).
- [9] H.-P. Seifert, S. Ritter, H.J. Leber, S. Roychowdhury, "Stress Corrosion Cracking Behavior in the Transition Region of Alloy 182/Low-Alloy Reactor Pressure Vessel Steel Dissimilar Metal Weld Joints in Light Water Reactor Environments", *Corrosion*, 71 (4), 2015, pp. 433-454.
- [10] H. Ernst, D. Algernon, K. Dressler, K. Germerdonk, "Depth Sizing of Safety Relevant Defects with Ultrasonic Phased Array Techniques and Reconstruction Algorithms", 9 International Conference on NDE in Relation to Structural Integrity for Nuclear and Pressurized Components, Seattle, Washington, USA, May 22-24, 2012
- [11] B.G. Braatz, S.E. Cumblidge, S.R. Doctor, I.G. Prokofiev, "Primary water stress corrosion cracks in nickel alloy dissimilar metal welds: Detection and sizing using established and emerging nondestructive examination techniques", Third Int'l Conf. on NPP Life Management (PLiM) for Long Term Operations, (LTO) (Proc. Conf. Salt Lake City, UT, 2012), (2012). IAEA-CN-194-025

**A.4 Integrity Evaluation Case Subject to Replacement & Preventive Maintenance for NPP Ni-alloy Components**



Doosan Heavy Industries & Construction

**Integrity evaluation case subject to replacement & preventive maintenance for NPP Ni-alloy components**

**11<sup>th</sup> ICNDE**



2015. 05. 20.

QA) NDE Team

Chang Kuen Kim, Joo Youl Hong, Dong Jin Lee

# Contents

1. PARENT Activity of DHIC
2. Ni-Alloy material Replacement & Inspection
3. DMW Mitigation & Inspection
4. Summary



1

## 1. PARENT Activity of DHIC

✓ DHIC provided total 27 data sets for PARENT RRT consisting 14 Ni-Alloy components and 4 NDE Techniques.

Data build date	Specimen ID		Technique			
			UT	PA	ECT	TOFD
			Outside surface access	Outside surface access	Outside J-weld access	Tube bore Access(include ECT)
2011.7	LB DMW (Large Bore)	A	Manual	Manual	-	-
		B	Manual	Manual	-	-
		C	Manual	Manual	-	-
		D	Manual	Manual	-	-
2012.7	LB DMW	E	Manual	Manual	-	-
		F	Manual	Manual	-	-
	SB DMW (Small Bore)	G	Manual	Manual	-	-
		H	Manual	Manual	-	-
	WOL(Weld Overlay)	I		Manual	-	-
	BMI (Bottom Mounted Instrument)	J	-	-	Manual	Encoded
		K	-	-	Manual	Encoded
		L	-	-	Manual	Encoded
M		-	-	Manual	Encoded	
		N	-	-	Manual	Encoded

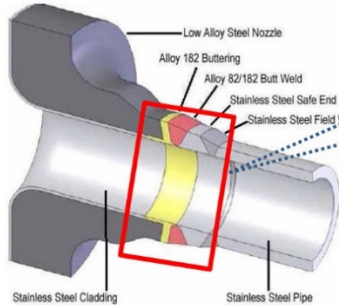


2



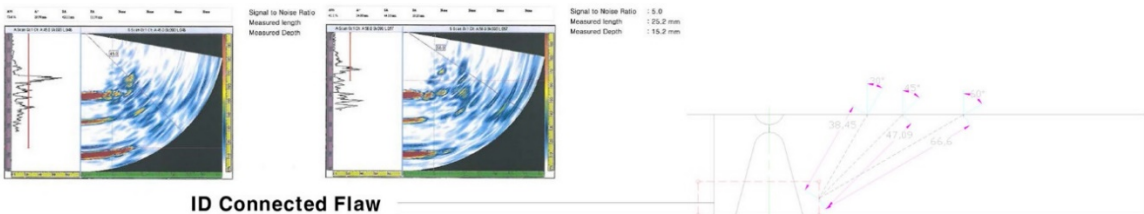
# 1. PARENT Activity of DHIC

✓ DHIC applied PE & PAUT for development of Emerging NDE Technique.



**Large/Small bore Dissimilar Metal Weld**  
 1. Conventional PE – Using Dual element focusing Transducers  
 2. Phased Array Technique – Using Pitch catch 2D Transducers

➤ Set-up the essential parameter for testing  
 ➤ Establish the best-fit testing procedure



ID Connected Flaw



# 1. PARENT Activity of DHIC

- ✓ Apply TOFD (Time Of Flight Diffraction) for Inconel 600 material of BMI.
  - TOFD method has a high POD (Probability Of Detection) to detect diffraction signal from crack tips.
- ✓ Simultaneously, Make to data set using PE & ECT method.

**On Bore side of Penetration tube**

1. Angle PE – Axial & Circum
2. TOFD – Axial & Circum
3. ECT – X coil type

➤ Get the possibility to evaluate SCC in material using ECT & TOFD.

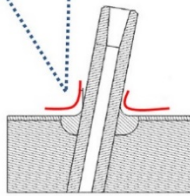
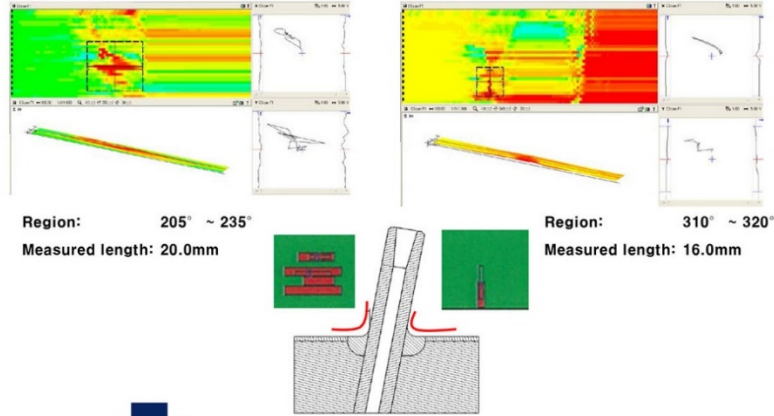


# 1. PARENT Activity of DHIC

✓ Especially, Flexible ECT Array Technique was applied for complex surface geometry.

About J-weld surface examination

1. ECT System
  - MS5800EU
  - 64 MUX
  - Umbilical Cable
  - Software : Multiview 6.1
2. ECT Probe
  - 32CH, pan-cake Type
  - Freq. : 100 KHz ~ 500 KHz
  - Size :  $\phi 4$  mm



- Investigate higher POD than rigid probes due to more accessibility.
- And higher resolution for adjacent flaws than other NDE method.



5

# 2. Ni-Alloy material Replacement & Inspection

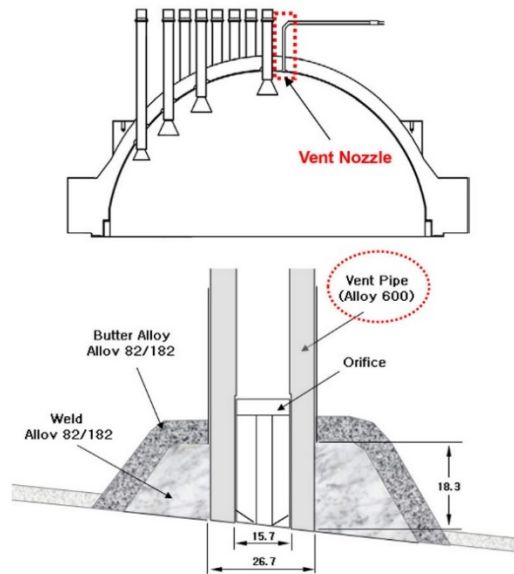
➢ I-600 is replace by I-690 for corrosion resistance

✓ Key technology

- Automatic machining and welding
- NDE(UT/ECT) using special scanner

✓ Field application (12 units)

- HANBIT #3, 4, 5, 6 reactor head vent pipe
- HANUL #3, 4, 5, 6 reactor head vent pipe
- SHIN KORI #1, 2 reactor head vent pipe
- SHIN WOLSONG #1, 2



Typical Vent Nozzle configuration

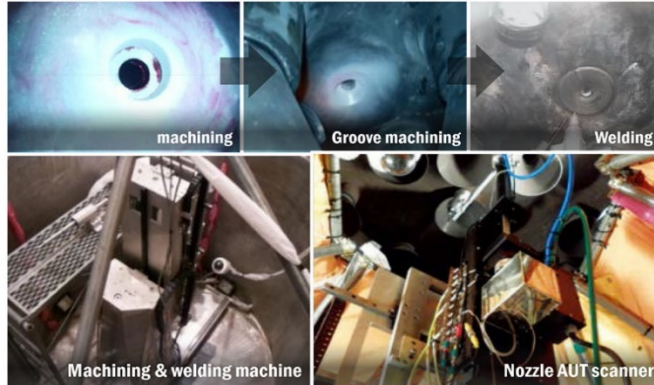


6

## 2. Ni-Alloy material Replacement & Inspection

### ✓ Activities

- Orifice removal and nozzle reinstatement
- Groove machining
- Welding
- UT/ECT using automatic scanner



7

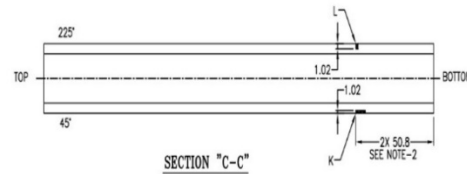
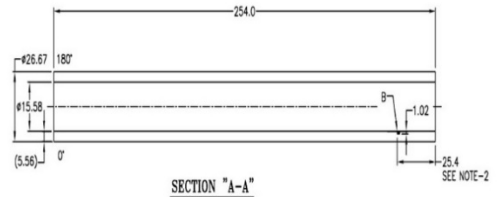
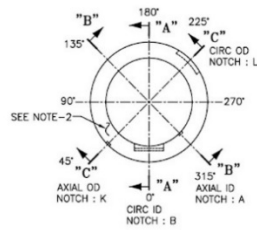
## 2. Ni-Alloy material Replacement & Inspection

### ➤ UT/ECT Techniques Demonstration for Vent nozzle

### ➤ Mock-up

- Axial/Circumferential EDM Notches with 18%T
- For UT, ID & OD position
- For ECT, ID position

EDM Notch	Description	Depth ±0.12	Length ±0.12	Width ±0.12
A	UT/ECT Axial ID	1.02mm	6.35mm	0.15mm
B	UT/ECT Circ ID	1.02mm	6.35mm	0.15mm
L	UT Axial ID	1.02mm	6.35mm	0.15mm
K	UT Circ ID	1.02mm	6.35mm	0.15mm



8

# 2. Ni-Alloy material Replacement & Inspection

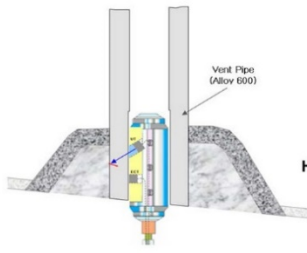
➤ Set-up for demonstration

✓ System

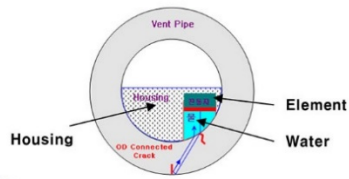
- H/W - Optimized Motorizing Scanner
- S/W - IntraSpect (Wesdyne)

✓ Probe

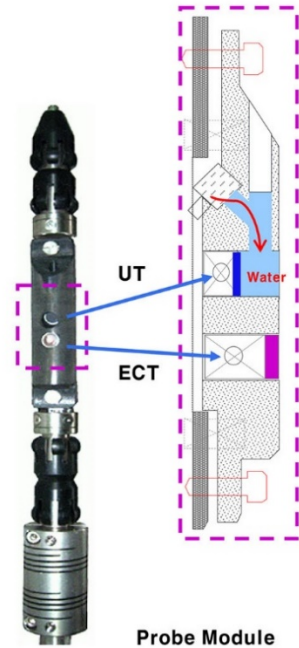
- UT : Immersion, Single, 10 MHz,  $\phi$  0.25"
- ECT : Driver Pickup X-Point Probe,  $\phi$  0.25"



Axial Scan



Circ. Scan

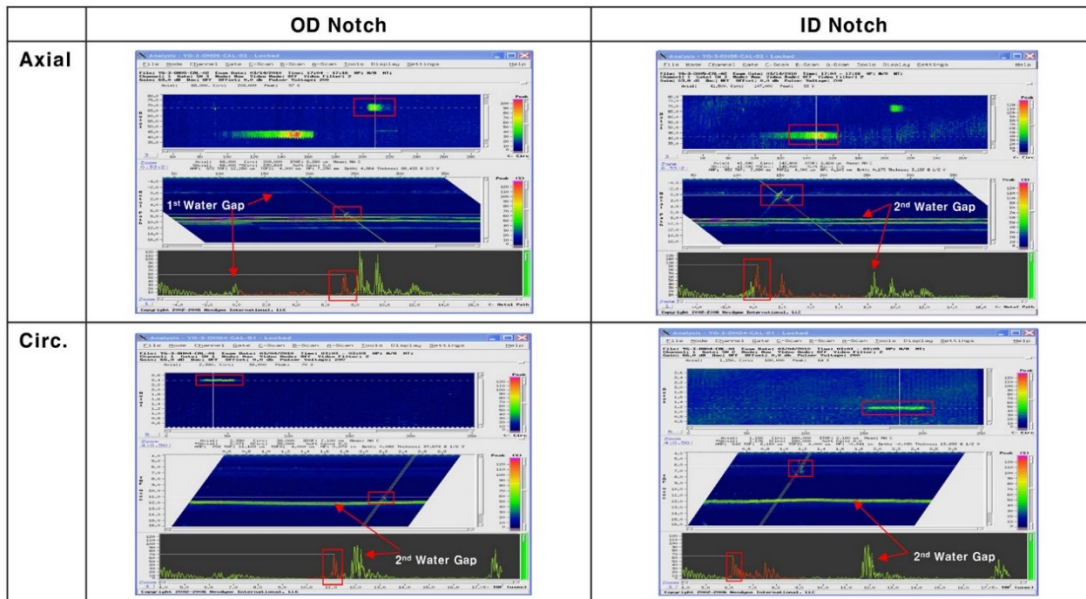


Probe Module



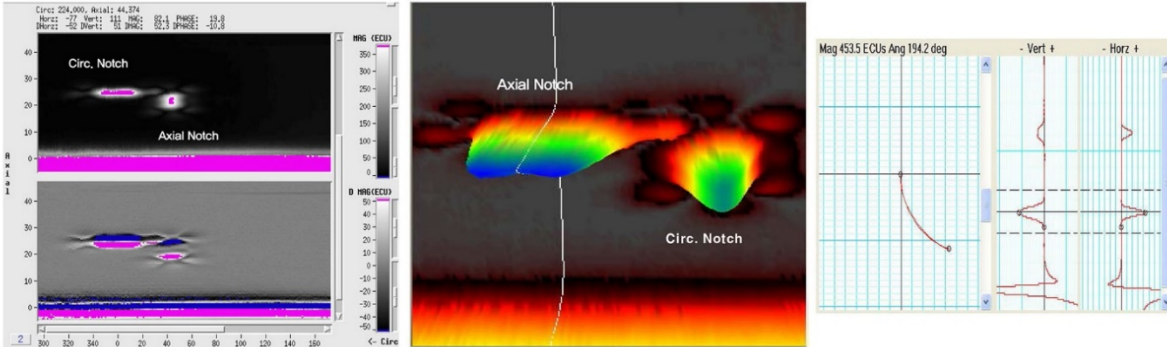
# 2. Ni-Alloy material Replacement & Inspection

➤ UT Results : All notches detect clearly & obtain very high S/N ratio.



## 2. Ni-Alloy material Replacement & Inspection

- ECT Results : All I/D notches detect clearly & obtain very high S/N ratio.



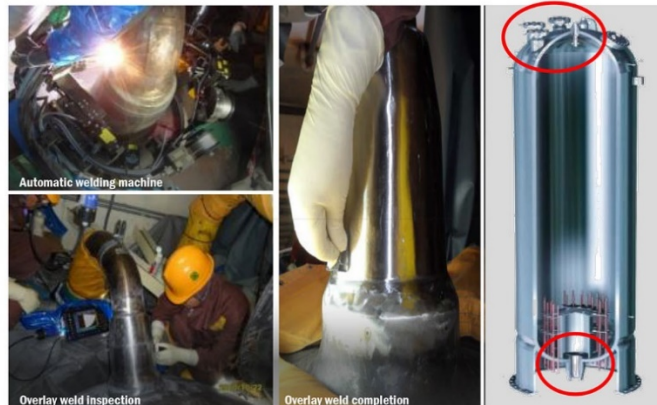
- Applied ECT & TOFD techniques to be demonstrated the SCC assessment in Ni-alloy material
- For NPP-ISI, Set-up the vent inspection & provide guideline of signal analysis thru experimental mock-up



11

## 3. DMW Mitigation & Inspection

- ✓ Another key maintenance of Ni-alloy components
  - Full Structural Weld Overlay & Inspection
    - Generally applied to repair & mitigate the defects embedded in dissimilar metal weld
    - In Korea, performed as PM (Preventive Maintenance) activity of pressurizer nozzles
- ✓ Key technology
  - Temper bead welding technology
  - Optimized welding system
  - Overlay design technology
  - Integrity assessment
- ✓ Field application (9 units)
  - KORI #2, 3, 4 pressurizer nozzles
  - HANBIT #1, 2, 5, 6 pressurizer nozzles
  - HANUL # 3,4 pressurizer nozzles

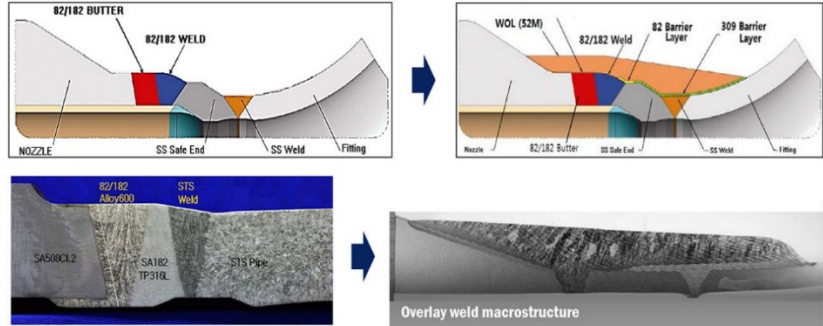


12

### 3. DMW Mitigation & Inspection

➤ PAUT Techniques Demonstration for DMW Integration

➤ Mock-up



➤ Set-up for demonstration

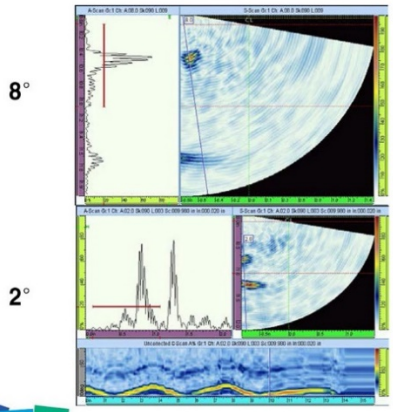
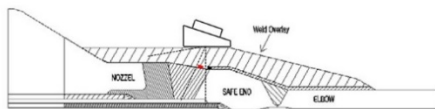
- UT detector : OmniScan 32/128PR
- Probe : 2-D Matrix Array Probe(115-000-485, GEIT, 2.0MHz, 2X16EL, 1.75X4mm)
- Wedge : 360-152-059, 360-152-058 (GEIT)



### 3. DMW Mitigation & Inspection

➤ Results of PAUT Techniques Demonstration

✓ Assessment of Laminar Flaw(LOB-Lack Of Bonding)



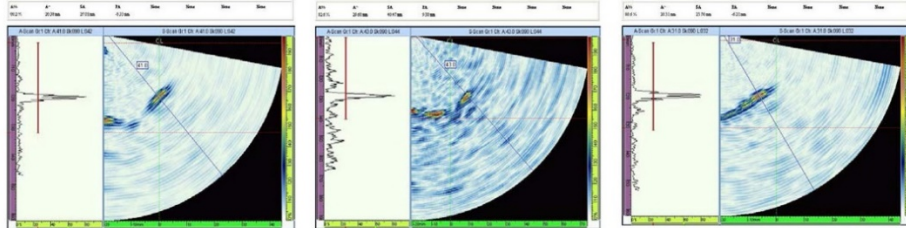
➤ Investigate signal patterns

- ✓ Have an image & a high amplitude similar to back wall
- ✓ Significant drop or disappear at above the 25° of testing angle
- ✓ Sometimes detect when circumferential scanning

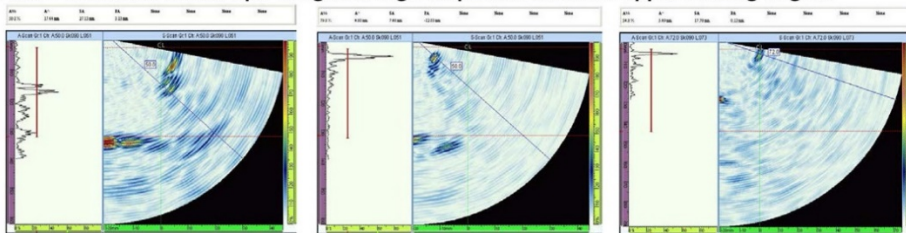
### 3. DMW Mitigation & Inspection

✓ Assessment of Crack

- WBM (Weld Base Metal) Crack : ID connected image & high amplitude at some lower testing angles



- WOL Crack : Branched crack tips images & high amplitude at some upper testing angles

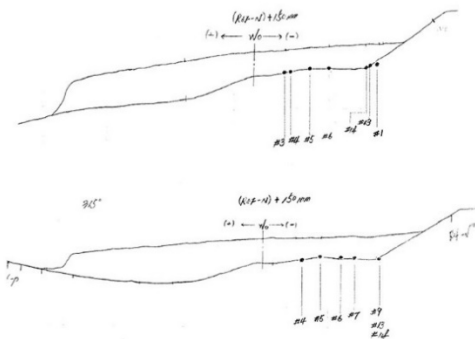


15

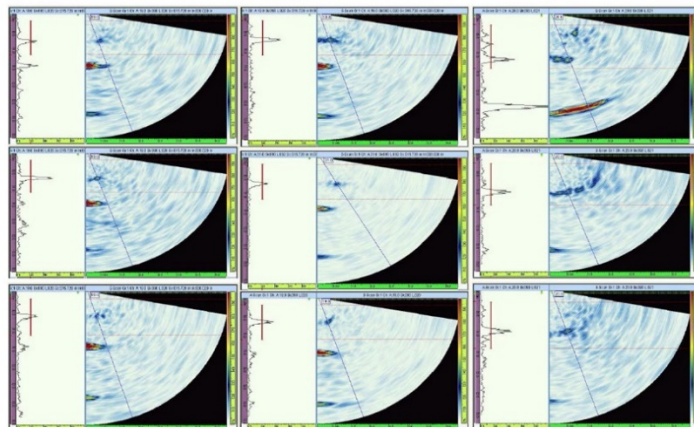
### 3. DMW Mitigation & Inspection

✓ Assessment of Non-relevant signal

- Especially, some signals can be confusing to analysis of the flaw signals
- These signals frequently acquired during site WOL work



Sectional Plots



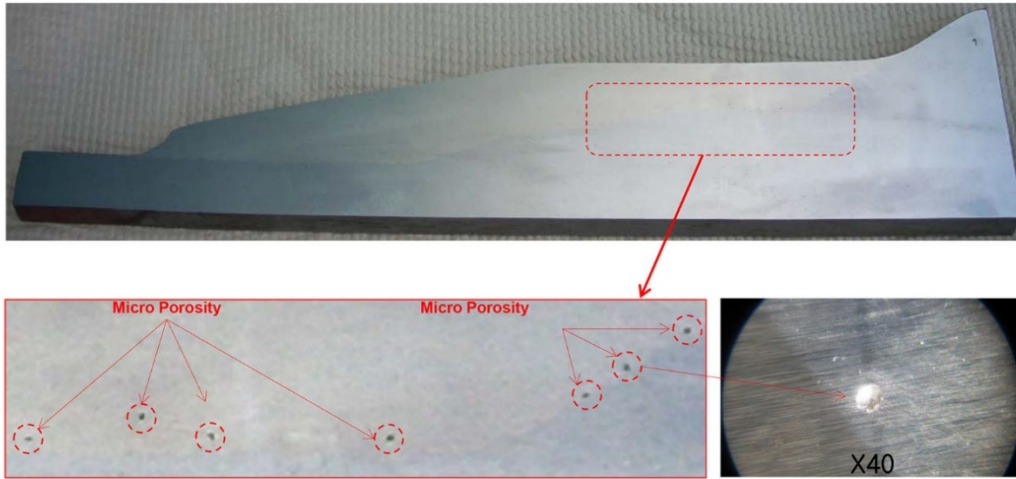
Acquired signals



16

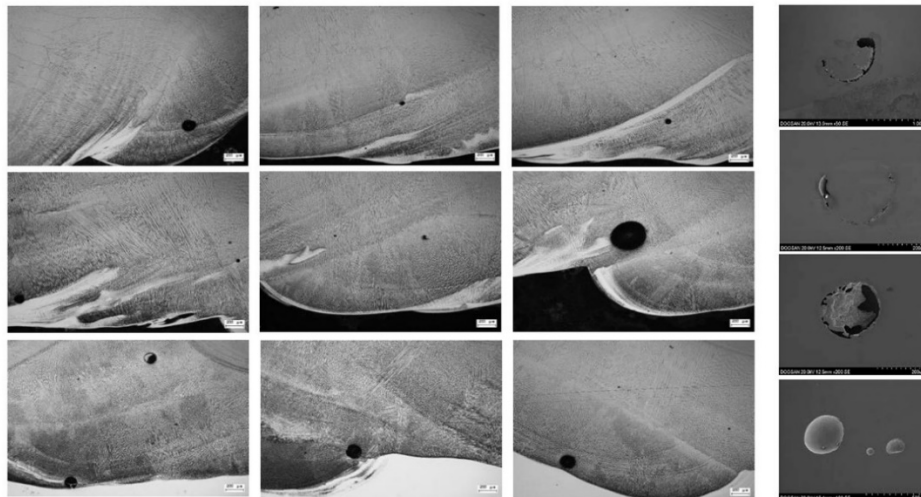
# 3. DMW Mitigation & Inspection

- ✓ Assessment of Non-relevant signal
  - Cut out Mock-up : Below 0.5 Dia. Micro Porosity



# 3. DMW Mitigation & Inspection

- ✓ Assessment of Non-relevant signal
  - Review of microstructure
    - position at 1<sup>st</sup> ~ 2<sup>nd</sup> layer of weld

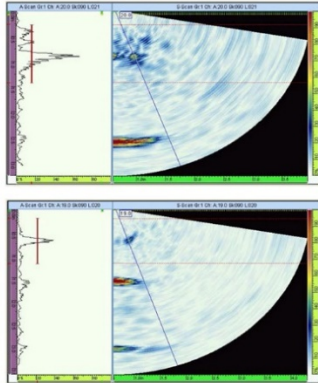




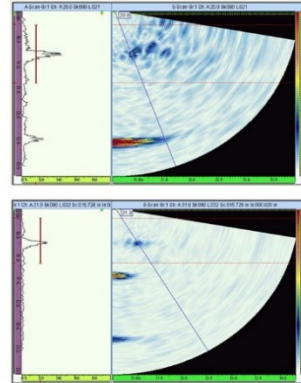
### 3. DMW Mitigation & Inspection

✓ Assessment of Non-relevant signal

Lower Testing Angles(0° ~25° )



Upper Testing Angles(Over 25° )



➤ Investigate signal patterns

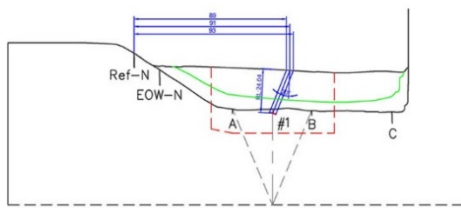
- ✓ Significant amplitude drop does not seen at above the 25 °
- ✓ When transducer move to the left or right, significant drop or appear new signal frequently
- ✓ About twice lower amplitude than LOB



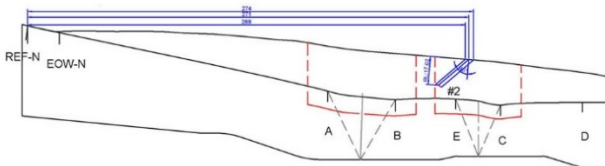
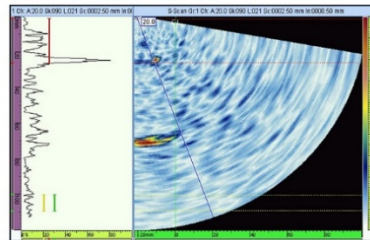
### 3. DMW Mitigation & Inspection

➤ Apply mock-up results to site work

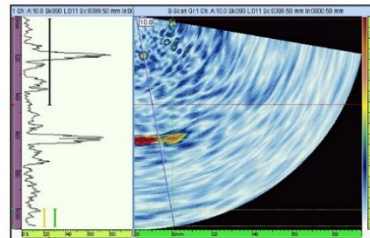
→ Decide to Non-relevant signal



Safety Nozzle



Surge Nozzle



## 4. Summary

➤ DHIC provided total 27 data sets for PARENT RRT consisting 14 Ni-Alloy components and 4 NDE Techniques

✓ Especially, Flexible ECT Array Technique was applied for complex surface geometry.

▪ Investigate higher POD than rigid probes due to more accessibility.

▪ And higher resolution for adjacent flaws than other NDE method.

➤ Ni-Alloy material Replacement & Inspection(Vent)

✓ For NPP-ISI, Set-up the vent inspection & provide guideline of signal analysis thru experimental mock-up

➤ Another key maintenance of Ni-alloy components(WOL)

✓ For assessment of the non-relevant signals, capture the signal patterns

and discriminate the site work signals



## **APPENDIX B**

### **SUMMARY TABLE OF OPEN NDE TECHNIQUES**



## APPENDIX B

### SUMMARY TABLE OF OPEN NDE TECHNIQUES

B.1	Summary of Techniques Applied to Flat Bar Test Blocks .....	B-2
B.2	Summary of Techniques Applied to SBDMW Test Blocks.....	B-7
B.3	Summary of Techniques Applied to LBDMW Test Blocks.....	B-15
B.4	Summary of Techniques Applied to BMI Test Blocks.....	B-21

## B.1 Summary of Techniques Applied to Flat Bar Test Blocks

NDE											
Team #	Technique Description (from Test Block Master)	Form Procedure ID	Procedure Used in Documentation	Technique ID	Test Blocks Applied To	Manual or Automated	Encoded (Y/N)	Exam Surface	Comment	Function	
11	Nonlinear Resonant Ultrasound Spectroscopy	11.1	NRUS.11	11-NRUT0	P28, P29, P30	Manual	N	O.D.	Wide-band piezo-electric element. Resonance frequencies and vibration modes are specified from prior vibration mode analysis for the specimen.	Detection	
	Pulsed Eddy Current	11.2	PECT.11	11-PECT0	P28, P29, P30	Manual	N	O.D.	10 ms (pulse width), 0.5 (duty ratio)	Detection	
20	Phased Array UT	20.1	PAUT.20	20-PA1	P31, P32, P38	Manual	N	O.D.	Shear wave	Location, Length, Depth Sizing	
				20-PA2	P28, P29, P30	Manual	N	O.D.	Longitudinal wave		
	Ultrasound Infrared Thermography	20.2	UIR.20	20-UIR0	P28, P29, P30, P31, P32, P38	Manual	N	Side	Excitor Frequency 20 (kHz)/Inspection Angle 90 (Deg.)/Detector 20 mk (NETD) Access ID: label side, opposite label side, bottom Access O.D.: Top	Location, Length, Depth Sizing	
22	Phased Array UT	22.1	PATRT.22	22-PA-SAFT1	P29	Manual	N	O.D.	5 MHZ/45° SAFT, P-Wave OLYMPUS 5L64-A2	Location, Length, Depth Sizing	
				22-PA-SAFT2	P29	Manual	N	O.D.	5 MHZ/55° SAFT, S-Wave OLYMPUS 5L64-A2		

Team #	Technique Description (from Test Block Master)	Form Procedure ID	Procedure Used in Documentation	Form ID	Procedure ID	Technique ID	Test Blocks Applied To	Manual or Automated	Encoded (Y/N)	Exam Surface	Comment	Function
	NDE											
						22-PA-TRT1	P29	Manual	N	O.D.	5 MHz/45° Time Reversal Technique P-Wave OLYMPUS 5L64-A2	
						22-PA-TRT2	P29	Manual	N	O.D.	5 MHz/55° Time Reversal Technique S-Wave OLYMPUS 5L64-A2	
30	Higher Harmonic UT	30.1	HHUT.30			30-HHUT0	P28, P29, P30	Automated Manual	N	I.D. O.D.	3 MHz vertical beam T: 2 MHz, R: 4 MHz 45° Access: Auto: PE(Z-axis), Manual: PE(X-axis) and VS Olympus V126 Krautkramer MWB45-2, MWB45-4	Location/Depth Sizing
						30-HHUT1	P28, P29, P30	Automated Manual	N	I.D. O.D.	3 MHz vertical beam T: 2 MHz, R: 4 MHz 45° Access: Auto: PE(Z-axis), Manual: PE(X-axis) and VS Olympus V126 Krautkramer MWB45-2, MWB45-4	
27	Higher Harmonic UT	27.1	HHUT.27.2			27-HHUT3	P28, P29, P30, P31, P32, P38, P42, P46	Automated	Y	O.D.	5 MHz/Immersion/2°Angular Focal depth: 76 mm/3.5 MHz excitation	Detection, Depth Sizing, Characterization, Length Sizing and Positioning
6	Subharmonic Phased Array for Crack Evaluation (SPACE)	6.1	SHPA.6.1			6-SHPA1	P28	Manual	N	O.D.	5 MHz-Bulk-Space	Detection, Characterization, Depth Sizing
						6-SHPA4	P28	Manual	N	I.D.	3.5 MHz-SAW-Space	Detection, Characterization,

Team #	Technique Description (from Test Block Master)	Form Procedure ID	Procedure Used in Formal Documentation	Technique ID	Test Blocks Applied To	Manual or Automated	Encoded (Y/N)	Exam Surface	Comment	Function
		6.3	SHPA.6.3	6-SHPA2	P29, P30, P31, P32	Manual	N	O.D.	2 MHz-Bulk-Space	Detection, Characterization, Depth Sizing
				6-SHPA4	P29, P30, P31, P32	Manual	N	I.D.	3.5 MHz-SAW-Space	Detection, Characterization, Length Sizing, Positioning
17	3 Dimensional Synthetic Aperture Focusing Technique	17.1	SAFT.17	17-SAFT1	P28, P29, P30, P31, P32, P38, P42, P46	Manual	N	O.D.	2 MHz, 16x16ch, 45° 16x16ch Matrix array SAFT	Detection, Characterization, Depth Sizing, Positioning
18	Large Amplitude Excitation Subharmonic UT	18.1	LASH.18	18-LASH1	P28, P29, P30, P31, P32			O.D.	B-scan image by aperture synthesis 5 MHz ultrasound	Detection, Depth Sizing, Characterization
				18-LASH2	P28, P29, P30, P31, P32			O.D.	Large Amp. Excitation SPACE Input 5 MHz ( $\omega$ ) burst 1. Amplitude of subharmonic echo at crack 2. Imaging of high voltage 3. Imaging by $\omega$ and $\omega/2$ 4. Detectability of crack tip diffraction echo	



NDE

Team #	Technique Description (from Test Block Master)	Form Procedure ID	Procedure ID Used in Formal Documentation	Technique ID	Test Blocks Applied To	Manual or Automated	Encoded (Y/N)	Exam Surface	Comment	Function
29	Phased Array Asymmetrical Beam TOFD	29.3	PAATOFD.29.1	29-PAATOFD1	P28, P29, P30, P31, P32, P38, P42, P46	Automated	Y	I.D.	Phased array asymmetrical beam TOFD method with 2x16 probe Frequency: 2.25 MHz Inspection angle: -32 ~ +32 at 1° 1. Detection of tip echo on B, C, D-scan images 2. Determine the X position of the tip echo for the MA method 3. MA synthesis of scanning data 4. Depth sizing of the tip echo on the MA B-scan image	Depth Sizing
29.4			PAATOFD.29.2	29-PAATOFD2	P28, P29, P30, P31, P32, P38, P42, P46	Automated	Y	I.D.	Phased array asymmetrical beam TOFD method with 4x8 probe Frequency: 2.25 MHz Inspection angle: -28 ~ +28 at 1° 1. Detection of tip echo on B, C, D-scan images 2. Determine the X position of the tip echo for the MA method 3. MA synthesis of scanning data 4. Depth sizing of the tip echo on the MA B-scan image	Depth Sizing
33	Advanced ECT	33.1	AECT.33	33-AECT1	P28, P29, P30, P31, P32, P38, P42, P46	Automated	Y	I.D.	100 kHz/Pancake-4ch-TR probe Pancake-4ch-TR-probe, 100 kHz	Detection, Characterization, Length Sizing, Positioning

Team #	Technique Description (from Test Block Master)	Form Procedure ID	Procedure Used in Formal Documentation	Technique ID	Test Blocks Applied To	Manual or Automated	Encoded (Y/N)	Exam Surface	Comment	Function
16	Eddy Current	16.1	ECT.16	16-ECT1	P28, P29, P30, P31, P32, P38, P42, P46	Automated	Y	I.D.: DMW O.D.: BMI	20 k-1 MHz/3 mm-12x2ch CrossCoil-Array-24ch-200 kHz	Detection, Characterization, Length Sizing, Positioning
28	Microwave Near-field Microscope	28.2	MM.28.2	28-MM12	P28, P29, P30, P31, P32	Automated	Y	I.D.	Open-ended coaxial line sensor, 110 GHz Open-ended coaxial line sensor, 110 GHz	Detection, Characterization, Length Sizing, Depth Sizing, Positioning
104	Mechanized UT Through Transmission Pitch-Catch	104.1	UT.104	104-UT-P/C0	P28, P29, P30, P31, P32, P38, P42, P46	Automated	Y	O.D.	1 MHz (10 mm aperture) 2.25 MHz (6 mm aperture) Through transmission, sound beam perpendicular to weld	Detection, Characterization, Length, Depth, Positioning
131	Manual Linear TR UT-PA;	131.1	PAUT.131.1	131-PA0	P28, P29, P30, P31, P32, P38, P42	Manual	N	O.D.	2.33 MHz/24 Elements; TRL40-70 UT PA Long 40-70; MultiX Contact Pulse Echo	Detection, Characterization, Length, Depth, Positioning
122	TRL Linear UT-PA Encoded	122.1	PAUT.122.1	122-PA1	P28, P29, P30, P31, P32, P38, P42	Automated	Y	O.D.	1.5 MHz, beam steering with fixed refraction angles	Detection, Characterization, Length, Depth, Positioning
114	Encoded Linear TR UT-PA	114.1	PAUT.114	114-PA1	P28, P29, P30, P31, P32, P38, P42	Automated	Y	O.D.	1.5 MHz, beam steering with fixed refraction angles	Detection, Characterization, Length, Depth, Positioning
122	TRL Sectorial Phased Array	122.2	PAUT.122.2	122-PA2	P28, P29, P30, P31, P32, P38, P42	Automated	Y	O.D.	1.5 MHz, sectorial scan 40-70 CIRCU-TRL-270/40-70LW CIRCD-TRL-90/40-70LW	Detection, Characterization, Length, Depth, Positioning

NDE											
Team #	Technique Description (from Test Block Master)	Form Procedure ID	Procedure Used in Documentation	Procedure ID	Technique ID	Test Blocks Applied To	Manual or Automated	Encoded (Y/N)	Exam Surface	Comment	Function
109	X-Ray Computed Tomography	109.1	RT.109	109-X-Ray CT	P29, P30, P31, P32, P38, P42	Automated	Not Specified	O.D.	Surface	Source: 450 kV /3.3 mA /1.0 mm focal spot; Detector: Single collimated (W) line detector (CdWO4) with 125 detector channels	Detection, Depth Sizing
112	X-Ray Digital Radiography	112.1	RT.112	112-X-Ray CT	P28, P29, P30	Automated	Not Specified	O.D.	Surface	Source: 300 to 450 kV; 1.5 to 2.25 mA; 0.4 mm focus; detector: CCD with scintillating faceplate with fiber optic lens; the projection angle is from -10° to +10°, with increments of 2°.	Detection, Depth Sizing

TRL = transmit-receive longitudinal

## **B.2 Summary of Techniques Applied to SBDMW Test Blocks**

NDE											
Team #	Technique Description (from Test Block Master)	Form Procedure ID	Procedure Used in Documentation	Procedure ID	Technique ID	Test Blocks Applied To	Manual or Automated	Encoded (Y/N)	Exam Surface	Probe Frequency (MHz)/ Inspection Angle (Deg.)/ Skew (Deg.)	Function
6	Subharmonic Phased Array for Crack Evaluation (SPACE)	6.1	SHPA.6.1	6-SHPA1	P1	Manual	N	O.D.	Surface	5 MHz-Bulk-Space	Detection, Characterization, Depth Sizing
				6-SHPA4	P1	Manual	N	I.D.	Surface	3.5 MHz-SAW-Space	Detection, Characterization, Length Sizing, Positioning

NDE

Team #	Technique Description (from Test Block Master)	Form Procedure ID	Procedure Used in Formal Documentation	Technique ID	Test Blocks Applied To	Technique	Manual or Automated	Encoded (Y/N)	Exam Surface	Probe Frequency (MHz)/ Inspection Angle (Deg.)/ Skew (Deg.)	Function
		6.2	SHPA.6.2	6-SHPA1	P4	Manual	Manual	N	O.D.	5 MHz-Bulk-Space	Detection, Characterization, Depth Sizing
				6-SHPA3	P4	Manual	Manual	N	O.D.	7 MHz-Bulk-Space	Detection, Characterization, Length Sizing, Positioning
				6-SHPA4	P4	Manual	Manual	N	I.D.	3.5 MHz-SAW-Space	Detection, Characterization, Length Sizing, Positioning
17	3 Dimensional Synthetic Aperture Focusing Technique	17.1	SAFT.17	17-SAFT1	P1, P41	Manual	Manual	N	O.D.	2 MHz, 16x16ch, 45° 16x16ch Matrix array SAFT	Detection, Characterization, Length Sizing, Depth Sizing, Positioning
18	Large Amplitude Excitation	18.1	LASH.18	18-LASH1	P1				O.D.	B-scan image by aperture synthesis 5 MHz ultrasound	Detection, Depth Sizing, Characterization

Team #	Technique Description (from Test Block Master)	Form ID	Procedure Used in Documentation	Procedure ID	Technique ID	Test Blocks		Exam Surface	Probe Frequency (MHz)/ Inspection Angle (Deg.)/ Skew (Deg.)	Function
						Applied To	Manual or Automated			
	Subharmonic UT			18-LASH2	P1	O.D.			Large Amp. Excitation SPACE Input 5 MHz ( $\omega$ ) burst 1. Amplitude of subharmonic echo at crack 2. Imaging of high voltage 3. Imaging by $\omega$ and $\omega/2$ 4. Detectability of crack tip diffraction echo	Detection, Depth Sizing, Characterization
20	Phased Array UT	20.1	PAUT.20	20-PA1	P1	Manual	N	O.D.	PAUT (Shear wave)	Location, Length, Depth Sizing
33	Advanced ECT	33.1	AECT.33	33-AECT1	P41	Automated	Y	I.D.	100 kHz/Pancake-4ch-TR-probe Pancake-4ch-TR probe, 100 kHz	Detection, Characterization, Length Sizing, Positioning
16	Eddy Current	16.1	ECT.16	16-ECT1	P1, P4, P41	Automated	Y	I.D.: DMW O.D.: BMI	20 k-1 MHz/3 mm-12x2ch CrossColi-Array-24ch-200 kHz	Detection, Characterization, Length Sizing, Positioning
104	Mechanized UT Through Transmission Pitch-Catch	104.1	UT.104	104-UT-P/C0	P41	Automated	Y	O.D.	1 MHz (10 mm aperture) 2.25 MHz (6 mm aperture) Through transmission, sound beam perpendicular to weld	Detection, Characterization, Length, Depth, Positioning
114	Encoded Linear TR UT-PA	114.1	PAUT.114	114-PA1	P1, P4, P41	Automated	Y	O.D.	1.5 MHz, beam steering with fixed refraction angles	Detection, Characterization, Length, Depth, Positioning

NDE

Team #	Technique Description (from Test Block Master)	Form Procedure ID	Procedure Used in Formal Documentation	Technique ID	Test Blocks Applied To	Manual or Automated	Encoded (Y/N)	Exam Surface	Probe Frequency (MHz)/ Inspection Angle (Deg.)/ Skew (Deg.)	Function
112	X-Ray Digital Radiography	112.1	RT.112	112-X-Ray CT	P41	Automated	Not Specified	O.D.	Source: 300 to 450 kV; 1.5 to 2.25 mA; 0.4 mm focus; Detector: CCD with scintillating faceplate with fiber optic lens; The projection angle is from -10° to +10°, with increments of 2°.	Detection, Depth Sizing
21	Guided Wave UT	21.1	G UW.21	21-GUW1	P4	Manual	N	O.D.	0.5/42/Yes GUW (L-wave mode)	Location
27	Higher Harmonic UT	27.1	HHUT.27.1	27-HHUT1	P1, P41	Automated	Y	O.D.	5 MHz/Immersion/Normal/Focal depth: 76 mm/4 MHz excitation Immersion-Normal-Incidence	Detection, Depth Sizing, Characterization, Length Sizing, and Positioning
<hr/>										
			HHUT.27.2	27-HHUT2	P1, P41	Automated	Y	O.D.	5 MHz/Immersion/5° Angular/ Focal depth: 76 mm/4 MHz excitation Immersion-5° Angular-Incidence	Detection, Depth Sizing, Characterization, Length Sizing, and Positioning

NDE

Team #	Technique Description (from Test Block Master)	Form Procedure ID	Procedure Used in Formal Documentation	Technique ID	Test Blocks Applied To	Manual or Automated	Encoded (Y/N)	Exam Surface	Probe Frequency (MHz)/ Inspection Angle (Deg.)/ Skew (Deg.)	Function
5	Controlled Excitation ECT	5.1	CEECT.5.1	5-CEECT1	P1, P4	Manual		I.D.	Eddy current inspection using a probe that enables to evaluate the depth of deep flaws more quantitatively than conventional eddy current testing. The distance between the exciters was 12 mm so that the probe could approach the inner surface of the specimen.  The probe was positioned at Y=-7.57 mm, and scanned the inner surface of the specimen in the circumferential direction (i.e., parallel to the flaws). The scanning was conducted manually, and the length of a scanning line to measure each flaw is approximately 200 mm. No scanning in axial direction was conducted because of the difficulty in positioning the probe. The probe was positioned so that the axes of the exciters were parallel to the flaws.	Detection, Length Sizing, Depth Sizing, Characterization and Positioning
28	Microwave Near-field Microscope	28.1	MM.28.1	28-MM1	P1, P4, P41	Manual	N	I.D.	Open-ended coaxial line sensor, 67 GHz	Detection, Characterization, Length Sizing, Depth Sizing, Positioning

NDE													
Team #	Technique Description (from Test Block Master)	29.2	Form Procedure ID	Procedure Used in Documentation	Form ID	Procedure ID	Technique ID	Test Blocks Applied To	Manual or Automated	Encoded (Y/N)	Exam Surface	Probe Frequency (MHz)/ Inspection Angle (Deg.)/ Skew (Deg.)	Function
29	Phased Array Twin Probe		PATP.29	29-PATP0	P1, P41	Manual	N	O.D.			Phased Array Twin Probe Method with 10x25 probe	Depth Sizing	
												Frequency: 1.5 MHz	
												Inspection angle: -45 ~ +45 at 1°	
												1. Detection of tip echo on B, C, D-scan images	
												2. Determine the X position of the tip echo for the MA method	
												3. MA synthesis of scanning data	
												4. Depth sizing of the tip echo on the MA B-scan image	



NDE										
Team #	Technique Description (from Test Block Master)	Form Procedure ID	Procedure Used in Documentation	Technique ID	Test Blocks Applied To	Manual or Automated	Encoded (Y/N)	Exam Surface	Probe Frequency (MHz)/ Inspection Angle (Deg.)/ Skew (Deg.)	Function
29	Phased Array Asymmetrical Beam TOFD	29.1	PAATOFD.29.0	29-PAATOFD0	P1, P41	Manual	N	O.D.	Phased array asymmetrical beam TOFD method with 10x25 probe	Depth Sizing
									Frequency: 1.5 MHz	
									Inspection angle: -35 ~ +35 at 1°	
									1. Detection of tip echo on B, C, D-scan images	
									2. Determine the X position of the tip echo for the MA method	
									3. MA synthesis of scanning data	
									4. Depth sizing of the tip echo on the MA B-scan image	

NDE											
Team #	Technique Description (from Test Block Master)	Form Procedure ID	Procedure Used in Formal Documentation	Technique ID	Test Blocks Applied To	Manual or Automated	Encoded (Y/N)	Exam Surface	Probe Frequency (MHz)/ Inspection Angle (Deg.)/ Skew (Deg.)	Function	
131	Manual Linear TR UT-PA; Manual UT-PA; Probe: GEIT; Equipment MultiX	131.2	PAUT.131.2	131-PA1	P1, P41	Manual	N	O.D.	2 MHz/2x16 Elements; TRL25-65 UT PA Long: Probe GEIT 16x2:Equip.: MultiX	Detection, Characterization, Length, Depth, Positioning	
	Manual Encoded Linear UT-PA; Probe: Sonaxis; Equipment: MultiX	131.2	PAUT.131.2	131-PA2	P4	Manual	N	O.D.	2 MHz/2x16 Elements; TRL45-75 UT PA Long 45-75L PE Probe: Sonaxis: MultiX	Detection, Characterization, Length, Depth, Positioning	
	Manual Matrix Unisequential UT-PA; Probe: GEIT; Equipment Phasor XS	131.4	PAUT.131.4	131-PA3	P41	Manual	N	O.D.	1.5 MHz/2x(5x3) Element; TRL40-70 UT PA Long/Probe: GEIT 16x2/Equipment Phasor XS	Detection, Characterization, Length, Depth, Positioning	
170	Laser Ultrasound Visualization	170.1	LUV.170	170-LUV	P1	Automated	Not Specified	O.D.	PZT excitation w/laser detection	Detection, Length Sizing	

### B.3 Summary of Techniques Applied to LBDMW Test Blocks

Team #	Technique Description (from Test Block Master)	Form Procedure ID	Procedure ID Used in Formal Documentation	Technique ID	Test Blocks Applied To	Manual or Automated	Encoded (Y/N)	Exam Surface	Probe Frequency (MHz)/ Inspection Angle (Deg.)/ Skew (Deg.)	Function
17	3 Dimensional Synthetic Aperture Focusing Technique	17.1	SAFT.17	17-SAFT1	P12, P23, P24, P37	Manual	N	O.D.	2 MHz, 16x16ch, 45° 16x16ch Matrix array SAFT	Detection, Characterization, Length Sizing, Depth Sizing, Positioning
18	Large Amplitude Excitation Subharmonic UT	18.1	LASH.18	18-LASH1	P12			O.D.	B-scan image by aperture synthesis 5 MHz ultrasound	Detection, Depth Sizing, Characterization
				18-LASH2	P12			O.D.	Large Amp. Excitation SPACE Input 5 MHz ( $\omega$ ) burst 1. Amplitude of subharmonic echo at crack 2. Imaging of high voltage 3. Imaging by $\omega$ and $\omega/2$ 4. Detectability of crack tip diffraction echo	Detection, Depth Sizing, Characterization

NDE

Team #	Technique Description (from Test Block Master)	Form Procedure ID	Procedure Used in Documentation	Technique ID	Test Blocks Applied To	Manual or Automated	Encoded (Y/N)	Exam Surface	Probe Frequency (MHz)/ Inspection Angle (Deg.)/ Skew (Deg.)	Function
29	Phased Array Twin Probe	29.2	PATP.29	29-PATP0	P12, P23, P24, P37	Manual	N	O.D.	Phased Array Twin Probe Method with 10x25 probe	Depth Sizing
									Frequency: 1.5 MHz	
									Inspection angle: -45 ~ +45 at 1°	
									1. Detection of tip echo on B, C, D-scan images	
									2. Determine the X position of the tip echo for the MA method	
									3. MA synthesis of scanning data	
									4. Depth sizing of the tip echo on the MA B-scan image	

NDE

Team #	Technique Description (from Test Block Master)	Form Procedure ID	Procedure Used in Documentation	Technique ID	Test Blocks Applied To	Manual or Automated	Encoded (Y/N)	Exam Surface	Probe Frequency (MHz)/ Inspection Angle (Deg.)/ Skew (Deg.)	Function
29	Phased Array Asymmetrical Beam TOFD	29.1	PAATOFD.29.0	29-PAATOFD0	P12, P23, P24, P37	Manual	N	O.D.	Phased array asymmetrical beam TOFD method with 10x25probe	Depth Sizing
									Frequency: 1.5 MHz	
									Inspection angle: -35 ~ +35 at 1°	
									1. Detection of tip echo on B, C, D-scan images	
									2. Determine the X position of the tip echo for the MA method	
									3. MA synthesis of scanning data	
									4. Depth sizing of the tip echo on the MA B-scan image	

NDE										
Team #	Technique Description (from Test Block Master)	Form Procedure ID	Procedure Used in Formal Documentation	Technique ID	Test Blocks Applied To	Manual or Automated	Encoded (Y/N)	Exam Surface	Probe Frequency (MHz)/ Inspection Angle (Deg.)/ Skew (Deg.)	Function
29	Phased Array Asymmetrical Beam TOFD	29.3	PAATOFD.29.1	29-PAATOFD1	P12, P23, P24, P37	Automated	Y	I.D.	Phased array asymmetrical beam TOFD method with 2x16probe Frequency: 2.25 MHz Inspection angle: -32 ~ +32 at 1° 1. Detection of tip echo on B, C, D-scan images  2. Determine the X position of the tip echo for the MA method  3. MA synthesis of scanning data  4. Depth sizing of the tip echo on the MA B-scan image	Depth Sizing
29.4			PAATOFD.29.2	29-PAATOFD2	P12	Automated	Y	I.D.	Phased array asymmetrical beam TOFD method with 4x8probe Frequency: 2.25 MHz Inspection angle: -28 ~ +28 at 1° 1. Detection of tip echo on B, C, D-scan images  2. Determine the X position of the tip echo for the MA method  3. MA synthesis of scanning data  4. Depth sizing of the tip echo on the MA B-scan image	Depth Sizing

NDE

Team #	Technique Description (from Test Block Master)	Form Procedure ID	Procedure Used in Documentation	Technique ID	Test Blocks Applied To	Manual or Automated	Encoded (Y/N)	Exam Surface	Probe Frequency (MHz)/ Inspection Angle (Deg.)/ Skew (Deg.)	Function
33	Advanced ECT	33.1	AECT.33	33-AECT1	P12, P37	Automated	Y	I.D.	100 kHz/Pancake 4ch-TR-probe Pancake 4ch-TR probe, 100 kHz	Detection, Characterization, Length Sizing, Positioning
16	Eddy Current	16.1	ECT.16	16-ECT1	P12	Automated	Y	I.D.: DMW O.D.: BMI	20 k-1 MHz/3 mm-12x2ch CrossColi-Array-24ch-200 kHz	Detection, Characterization, Length Sizing, Positioning

NDE

Team #	Technique Description (from Test Block Master)	Form Procedure ID	Procedure Used in Formal Documentation	Technique ID	Test Blocks Applied To	Manual or Automated	Encoded (Y/N)	Exam Surface	Probe Frequency (MHz)/ Inspection Angle (Deg.)/ Skew (Deg.)	Function
28	Microwave Near-field Microscope	28.1	MM.28.1	28-MM1	P12, P23, P24	Manual	N	I.D.	Open-ended coaxial line sensor, 67 GHz	Detection, Characterization, Length Sizing, Depth Sizing, Positioning
150	Phased Array UT	150.1	PAUT.150	150-PA1	P12, P37	Automated	Encoded	O.D.	MHz 2x(10x5) element matrix array Azimuthal PA angle sweeps from 20–80; 0, ±10 degree skew angles 1.0 MHz Imasonic TRL array probe	Detection, Characterization, Length Sizing, Depth Sizing, Positioning
7	Phased Array UT	7.2	PAUT.7	7-PA1	P12, P37	Automated	Encoded	I.D.	1.5 MHz electronic sweeping of the examination angle from 60° to 88° at 2° increments A Zetec Tomoscan-III PA 32/128 UT instrument was used for data acquisition	Detection, Characterization, Length Sizing, Depth Sizing, Positioning



## B.4 Summary of Techniques Applied to BMI Test Blocks

Team #	Technique Description (from Test Block Master)	Form Procedure ID	Procedure Used in Documentation	Form ID	Technique ID	Test Blocks Applied To	Manual or Automated	Encoded (Y/N)	Exam Surface	Probe Frequency (MHz)/ Inspection Angle (Deg.)/ Skew (Deg.)	Function
16	Eddy Current	16.1	ECT.16	16-ECT1	P5, P7	Automated	Y	I.D.: DMW O.D.: BMI	20 k-1 MHz/3 mm-12.2ch CrossCoil-Array-24ch-200 kHz	Detection, Characterization, Length Sizing, Positioning	
33	Advanced ECT	33.1	AECT.33	33-AECT1	P5, P7	Automated	Y	I.D.	100 kHz/Pancake-4ch-TR- probe Pancake-4ch-TR probe, 100 kHz	Detection, Characterization, Length Sizing, Positioning	
5	Controlled Excitation ECT	5.1	CEECT.5.1	5-CEECT1	P7	Manual		I.D.	Eddy current inspection using a probe that enables to evaluate the depth of deep flaws more quantitatively than conventional eddy current testing. The distance between the exciters was 12 mm so that the probe could approach the inner surface of the specimen.  The probe was positioned at Y=-7.57 mm, and scanned the inner surface of the specimen in the circumferential direction (i.e., parallel to the flaws). The scanning was conducted manually, and the length of a scanning line to measure each flaw is approximately 200 mm. No scanning in axial direction was conducted because of the difficulty in positioning the probe. The probe was positioned so that the axes of the exciters were parallel to the flaws.	Detection, Length Sizing, Depth Sizing, Characterization and Positioning	

NDE												
Team #	Technique Description (from Test Block Master)	Form Procedure ID	Procedure Used in Formal Documentation	Technique ID	Test Blocks Technique Applied To	Manual or Automated	Encoded (Y/N)	Exam Surface	Probe Frequency (MHz)/ Inspection Angle (Deg.)/ Skew (Deg.)	Function		
170	Laser Ultrasound Visualization	170.1	LUV.170	170-LUV	P5, P7	Automated	Not Specified	O.D.	PZT excitation w/laser detection	Detection, Length Sizing		
7	Eddy Current	7.1	ECT.7	7-ECT1	P5, P7, P21, P22	Manual	Not Specified	O.D.	50 kHz flexible eddy current array probe 3x3	Detection, Length Sizing		
28	Microwave Near-field Microscope	28.1	MM.28.1	28-MM1	P21	Manual	N	I.D.	Open-ended coaxial line sensor, 67 GHz	Detection, Characterization, Length Sizing, Depth Sizing, Positioning		
21	Guided Wave UT	G UW	21.1	21-GUW2	P5	Manual	N	O.D.	2/65/Yes G UW (Surface wave)	Location		

## **APPENDIX C**

### **SUMMARIES OF OPEN NDE TECHNIQUES**



# APPENDIX C

## SUMMARIES OF OPEN NDE TECHNIQUES

C.1	Technique Summaries.....	C-1
C.2	Europe Detailed Technique Descriptions.....	C-60
C.3	Korea Detailed Technique Descriptions.....	C-215
C.4	USA Detailed Technique Descriptions .....	C-271
C.5	Japanese Detailed Technique Descriptions.....	C-291

### C.1 Technique Summaries

#### C.1.1 Korean Techniques

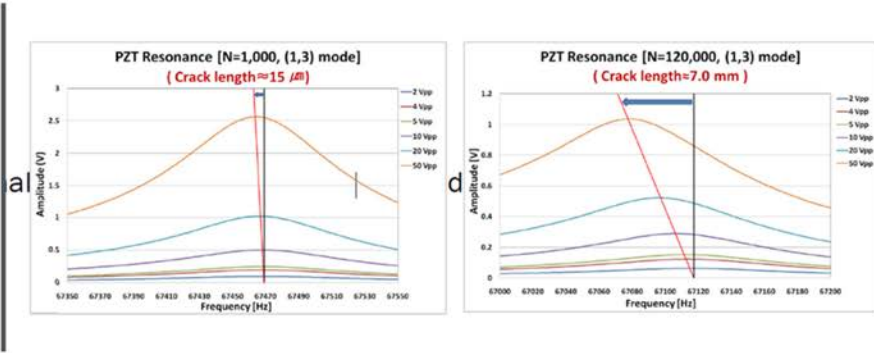
## **Korean Emerging NDE Technique**

*Slide - 2/116-*

# 11.1 NRUT

## □ Nonlinear Resonance Frequency Shift

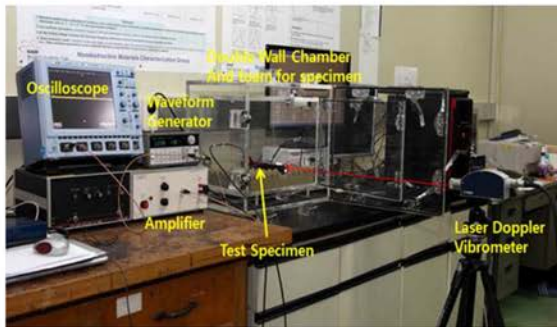
Resonance frequency shifts downward and the normalized amplitude decreases as the driving voltage increases for the case of cracked specimen.



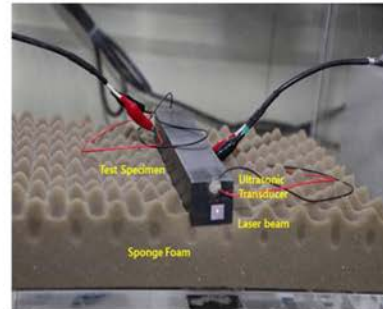
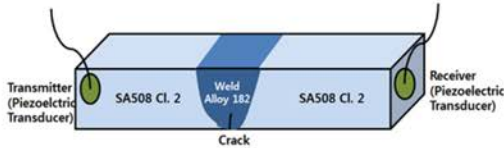
Slide - 3/116-

# 11.1 NRUT

## □ Nonlinear Resonance Ultrasonic Spectroscopy



Configuration No. 1 for PARENT TEST SPECIMEN (P28, P29, P30)  
(Both piezoelectric Transducers are located on the end of the specimen)



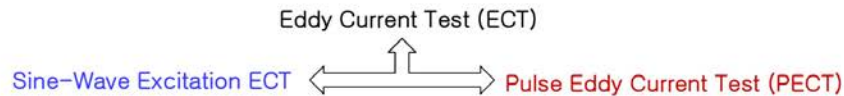
Slide - 4/116-

## Overview

- Test Blocks Types Examined: ENSI Blocks
- NDE Technique: Nonlinear Resonance Ultrasonic Spectroscopy
- Measures: Detection of Surface Breaking Flaws
- Data Acquisition: Both Piezoelectric Transducer are located on the end of specimen
- Access: Outside and Side Surface of Blocks
- Measurement Instrument: Oscilloscope, Waveform Generator, Amplifier
- Probe: Piezoelectric transducer
- Signal Analysis/Interpretation: Manual

Slide - 5/116-

## 11.2 PECT

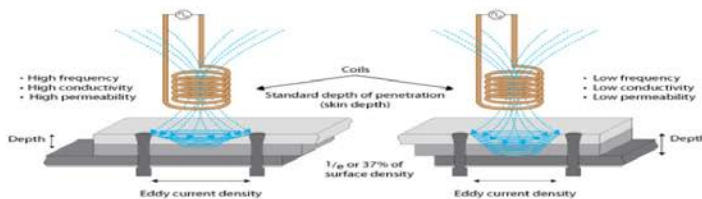


Sine-Wave EC testing methods have served as the primary NDE method in the Nuclear and air-craft industry for more than 50 years.

- Single frequency , continuous excitation.
- Limited by the depth of penetration of fields or skin depth.

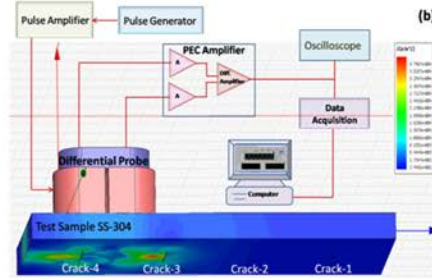
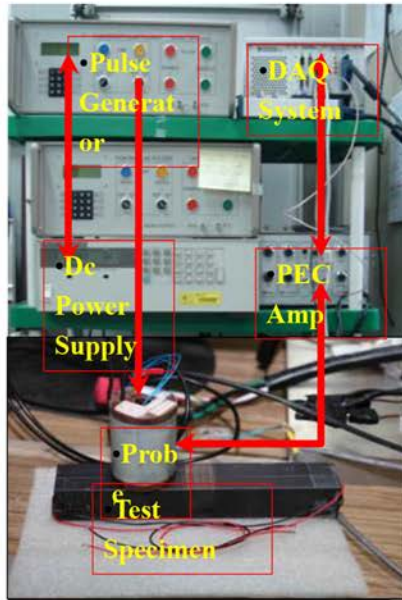
PECT is emerging technological approach which is principally developed for the detection of surface and sub surface defects.

- Large bandwidth.
- Information at low frequencies relevant for detecting deeper defects.



Slide - 6/116-

## 11.2 PECT

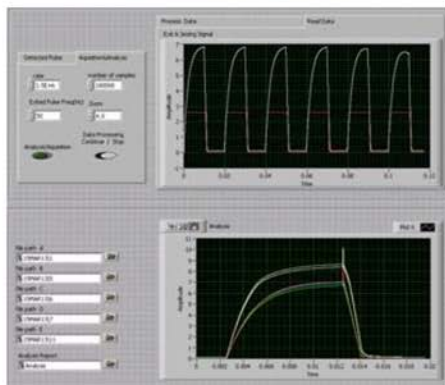


➤ PECT testing is one of the most effective methods, which has been demonstrated to be capable of tackling different inspection tasks, such as sub-surface defect detection in complex structures.

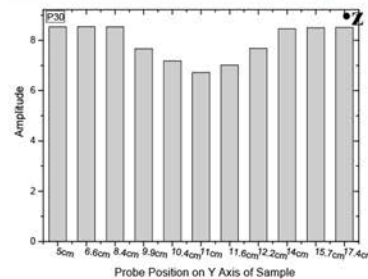
➤ The PECT system consists of a pulse amplifier, the probe having a driving coil and magnetic field detecting sensor, a sensitive PEC differential amplifier, and a computer with signal processing software.

Slide - 7/116-

## 11.2 PECT



- A short duration high current Pulse is applied to Excitation Coil, corresponding e response from the sample is detected by the hall sensor and is recorded in the computer.
- If the probe placed on the sample in such a position that the Hall-sensor comes above the crack, then typical response signal like above figure is induced in the Hall-sensor from the test block.



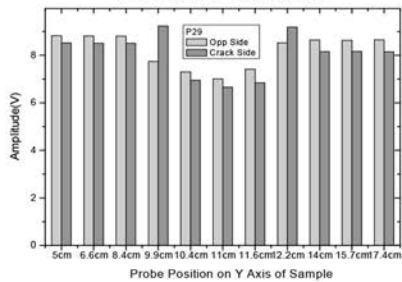
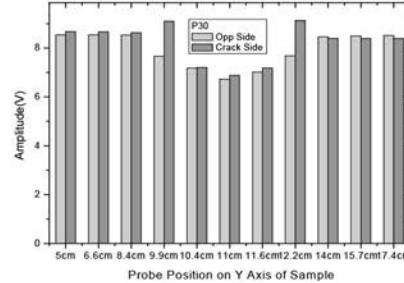
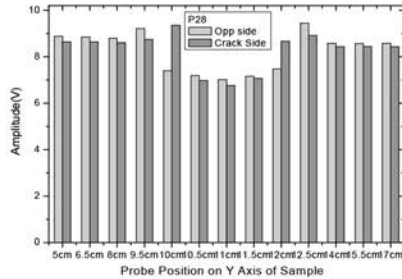
• At the ferromagnetic material region, the height of pulse amplitude is nearly constant, and minimum amplitude is observed at the defect position. The crack is positioned in the neighborhood of y coordinate 11 cm, which shows the minimum PEC signal amplitude.

Slide - 8/116-



## 11.2 PECT

- **PEC amplitude change with different sample and sample position. The data is obtained in the ide and opposite side of crack**



- The nondestructive evaluation (NDE) to detect the sub surface crack using PEC under the thick plate using the PARENT round robin sample has been tried. The PEC amplitude measured in the ferromagnetic part is higher than that of the nonmagnetic part.
- The crack is positioned in the neighborhood of y coordinate 11 cm, which shows the minimum PEC signal amplitude.

Slide - 9/116-

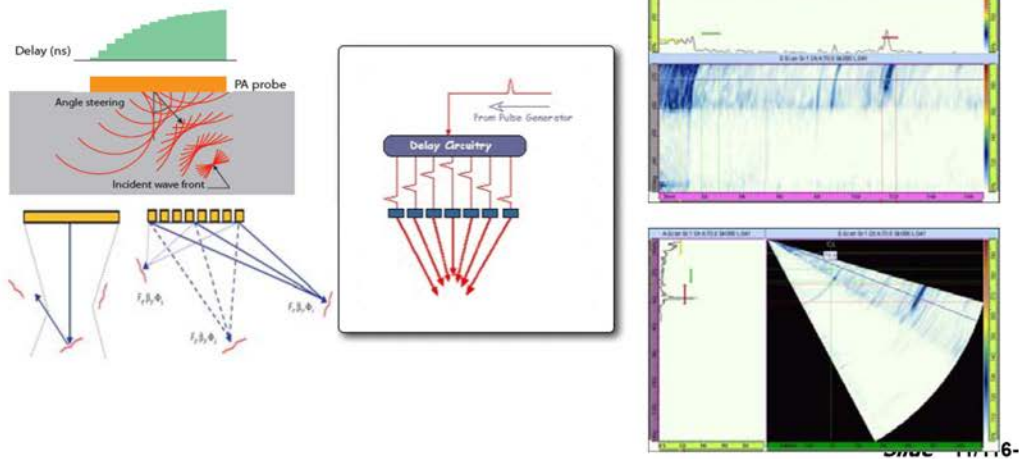
## Overview

- **Test Blocks Types Examined: ENSI Blocks**
- **NDE Technique: Pulsed Eddy Current**
- **Measures: Location of Surface Breaking Flaws**
- **Data Acquisition: X-Y Scanners**
- **Access: Outside Surface of Blocks**
- **Measurement Instrument: Pulse Generator, PEC Amplifier, DAQ**
- **Signal Analysis/Interpretation: Manual**

Slide - 10/116-

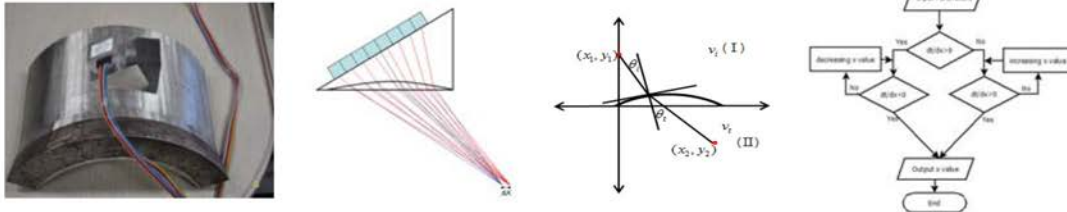
## 20.1 PAUT

- PAUT (Phased Array Ultrasonic Testing)
- Ultrasonic beam can be focused dynamically or steered by controlling the time delay for individual element of phased array ultrasonic transducer
- The position and size of defect can be visualized

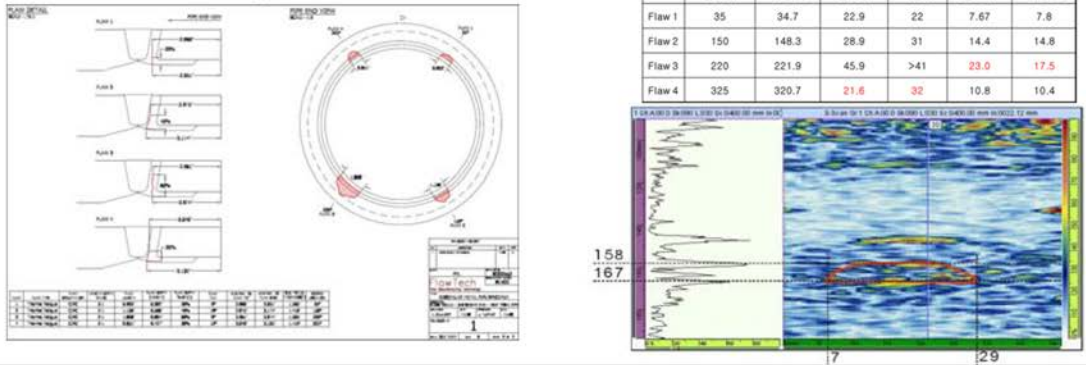


## 20.1 PAUT

- The curved wedge for pipe and compensation algorithm for its focal point



- Test results for DMW specimen



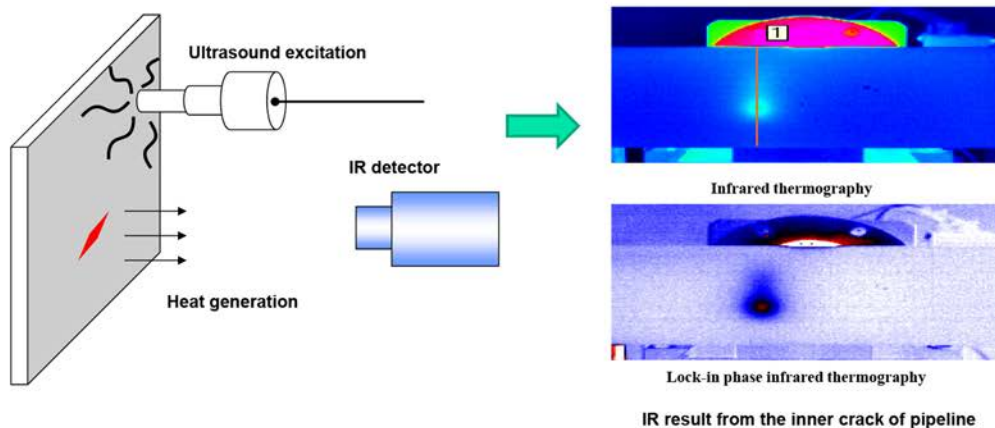
## Overview

- Test Blocks Types Examined: DWM and ENSI Blocks
- NDE Technique: Phased Array UT
- Measures: Location/Length /Depth of Surface Breaking Flaws
- Data Acquisition: Manual Scans
- Access: Outside Surface of Blocks
- Measurement Instrument: Olympus-OmniScan MXU
- Probe:
  - Phased Array Probe, 64 elements, 2.25 MHz, and 53/29/35 (mm) (Length/Width/Pitch)
- Signal Analysis/Interpretation: Manual

Slide - 13/116-

## 20.2 UIRT

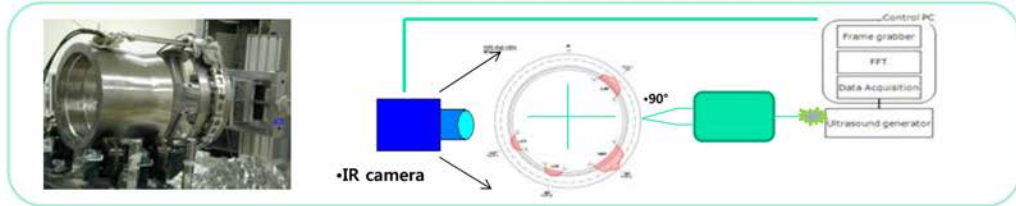
- UIRT (Ultrasound Infrared Thermography)
- Heat energy is generated from the crack when the external excitation (20-100 kHz) is applied into the test specimen
- Heat source is measured by the infrared thermography camera to detect defects.



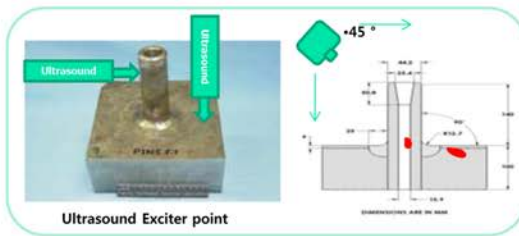
Slide - 14/116-

## 20.2 UIRT

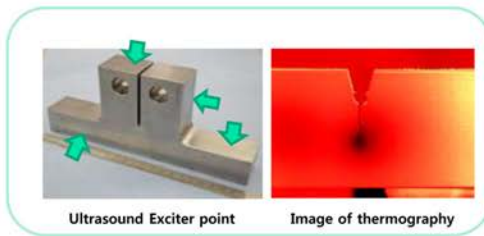
- The angle of  $0^\circ$  up to  $270^\circ$  was rotated by  $90^\circ$  step respectively



- Infrared camera rotates  $360^\circ$  with  $45^\circ$  angle of inclination



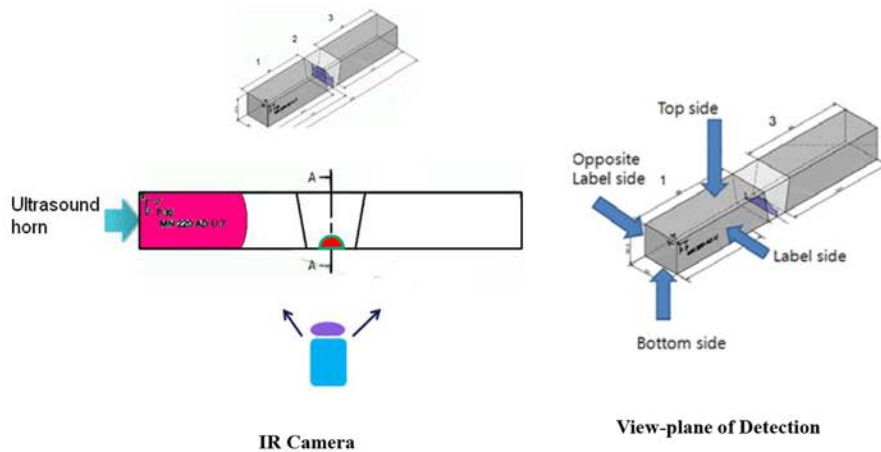
- Contact with the ultrasound horn on each side



Slide - 15/116-

## 20.2 UIRT

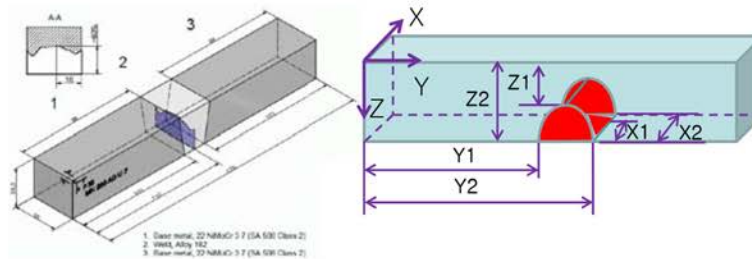
- ❖ Specimen : SBDMW Reference block P28,29,30,31,32,38
- ❖ Technical ID : UIR (Ultrasound Infrared Thermography)



Slide - 16/116-

## 20.2 UIRT

❖ Specimen : P30



Defect No:	X1	X2	Y1	Y2	Z1	Z2	Defect max Tem(°C)	Defect min Tem(°C)	Surface breaking	Comments
	(mm)	(mm)	(mm)	(mm)	(mm)	(mm)				
1	0.00	35.02	98.56	115.72	10.12	30.32	44.97	18.77	Yes	UIR



Label : Front side (Y,Z)



Bottom side(X,Y)



Label: Back side (Y,Z)



Top side (X,Y)

Slide - 17/116-

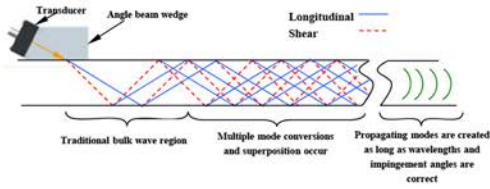
## Overview

- Test Blocks Types Examined: ENSI Blocks
- NDE Technique: Ultrasound Infrared Thermography
- Measures: Location/Length/Depth of Surface Breaking Flaws
- Data Acquisition: Manual Scans
- Access: Top side, Label Side, Opposite Label Side, Bottom Side of Blocks
- Measurement Instrument :
  - Ultrasound generator by UITec-SEE2 Sonic
  - Infrared thermography by FlirCedip siver480
- Signal Analysis/Interpretation: Manual

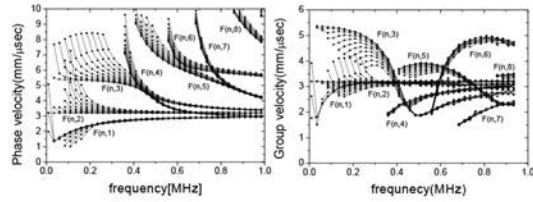
Slide - 18/116-

# 21 GW

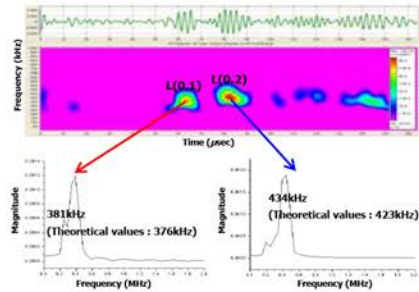
## □ Guided wave



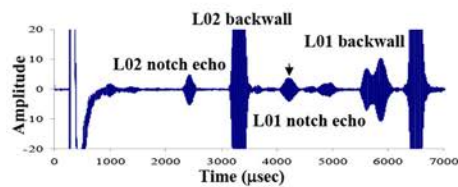
## • Guided wave dispersion curve



## • Guided wave mode identification



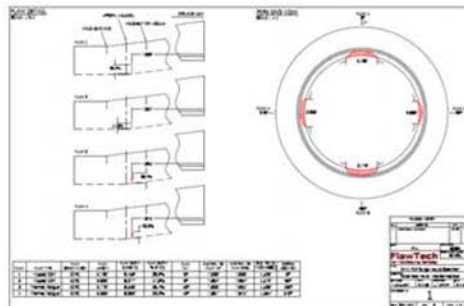
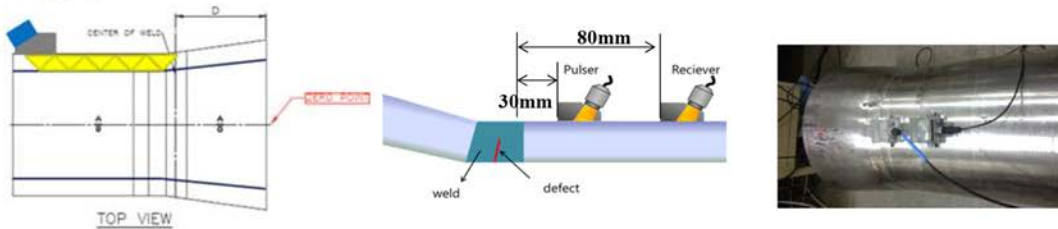
## • Guided wave long distance inspection signal



Slide - 19/116-

# 21 GW

## □ P4



## ➤ Guided wave inspection method

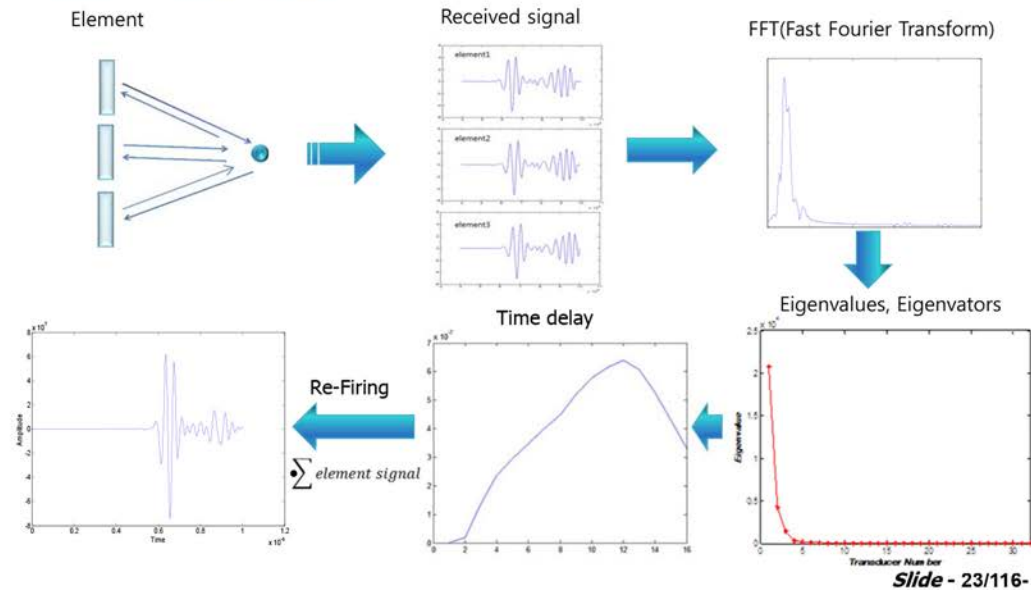
1. P4: At the distance of defect, guided waves propagate axial direction of specimen and receive the signal from the defects.
2. With volume coverage, it is possible to detect ID defects access from OD.

Slide - 20/116-



## 22 Time Reversal Technique

### □ Time reversal technique



## 22 Time Reversal Technique

### • Inspection Equipment

- Name : R/D TECH TomoScan FOCUS LT
- S/N : FLJ-1026



❖ Transducer : OLYMPUS 5L64-A2

❖ Wedge : P-45, SV-55 Wedge

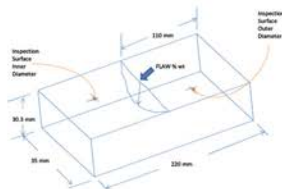
❖ References Block

- 명칭 : ASTM E164 FTW TYPE CALIBRATION BLOCK
- S/N : No. A14457



### • Specimens for OPEN RRT

- P29 specimen : fatigue crack



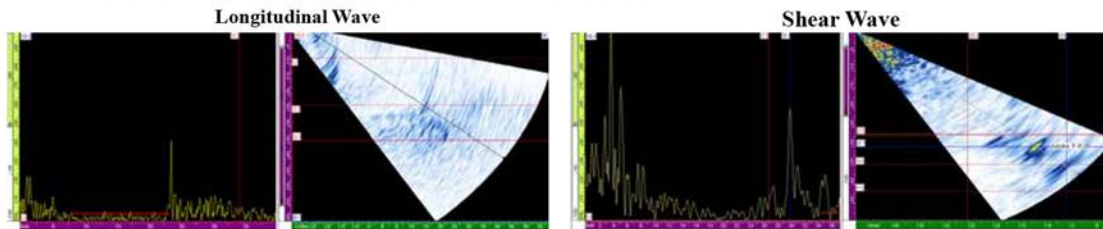
Flaw Position Relative to Weld	Center
End Reference to Flaw Base (Y)	110 mm
End Reference to Flaw Tip (Y)	110 mm
Flaw Depth (Absolute)	10 mm
Flaw Depth (Relative)	35%
X-Position at max. Flaw Depth	12 mm

Slide - 24/116-

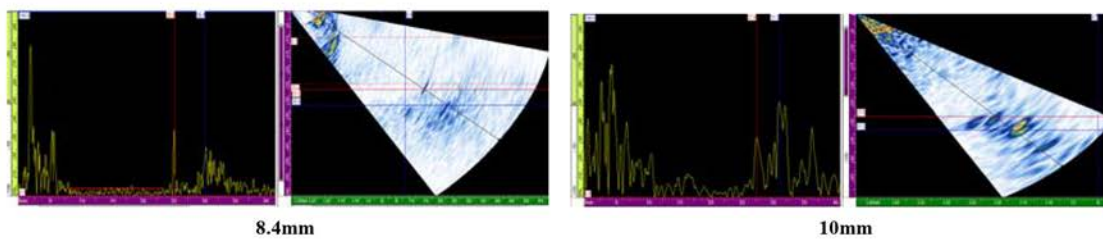


## 22 Time Reversal Technique

### • Synthetic Aperture Focusing Technique Results



### • Time Reversal Technique



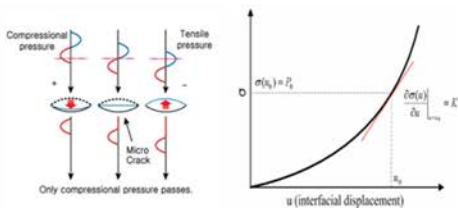
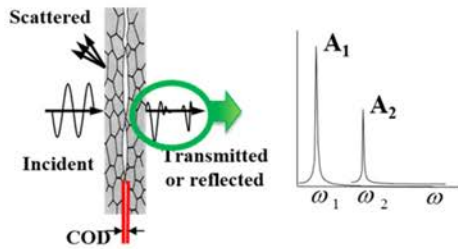
Slide - 25/116-

## Overview

- Test Blocks Types Examined: ENSI Blocks
- NDE Technique: Phased Array UT
- Measures: Location/Length/Depth of Surface Breaking Flaws
- Data Acquisition: Manual Scanner
- Access: Outside Surface of Blocks
- Measurement Instrument: Olympus TomoScan Focus LT
- Probe:
  - 5MHz 32Channel Olympus Phased array Ultrasonic Probes
- Signal Analysis/Interpretation: Manual

Slide - 26/116-

## 30 HHUT



Basic principle of contact acoustic nonlinearity

- The basic principle of the crack inspection by using higher harmonic UT (HHUT) is **the contact acoustic nonlinearity (CAN)**
- **CAN effect** is the phenomenon that generates harmonic component, which is caused by mainly two reasons as follows:

- **the waveform distortion** when the crack is temporarily clamping
- **the nonlinear relationship between pressure and displacement** at the contact interface

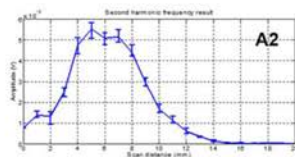
- The relative nonlinear parameter ( $\beta'$ )

$$\beta' = \frac{A_2}{A_1^2} \quad \begin{array}{l} A_1: \text{fundamental freq.} \\ A_2: \text{second harmonic freq.} \end{array}$$

Slide - 27/116-

## 30 HHUT

- CT Specimen (Al6061 fatigue crack) measurement using HHUT

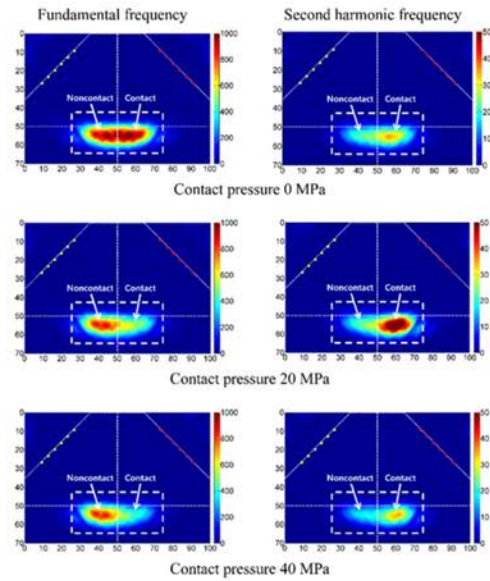
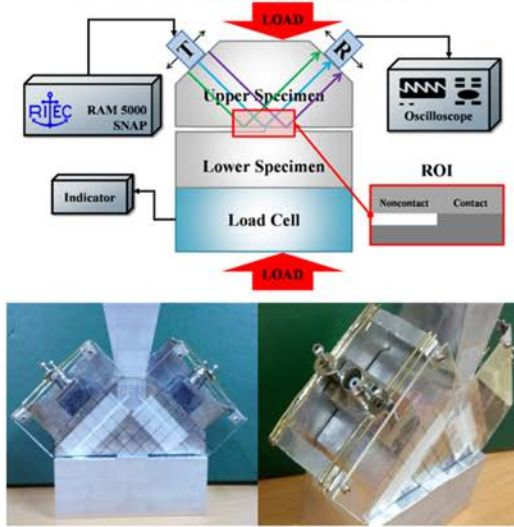


- The magnitudes of the fundamental frequency (A1) and the second harmonic frequency (A2) at different measuring positions along the crack direction from notch
- The maximum magnitude of the A1 appears at 4 mm, and the crack length was measured by **6.5 mm with 6dB drop (only open portion was detected)**
- A2 shows the maximum value at 5 mm as well as has **large value until 9 mm, which is close to the real size of the crack**
- HHUT is able to detect the closed crack and it can **improve the performance of crack sizing**

Slide - 28/116-

# 30 HHUT

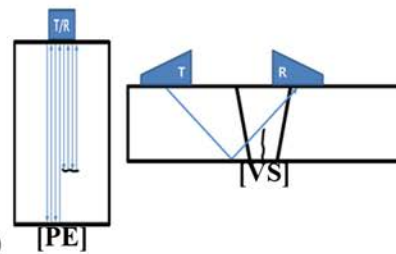
- Contact Acoustic Nonlinearity Imaging
- at Solid-Solid Contact Specimen



Slide - 29/116-

# Overview

- Test Blocks Types Examined: ENSI Blocks
- NDE Technique: Higher Harmonic Ultrasonic Technique
- Measures: Location/Depth of Surface Breaking Flaws
- Data Acquisition:
  - Manual : PE(X-axis), VS
  - Auto : PE(Z-axis)
- Access: Outside Surface of Blocks
- Measurement Instrument:
  - High power pulser-receiver (RAM-5000 SNAP)
  - Pulser-receiver (5077PR)
- Probe:
  - 5MHz 0.375 Ultrasonic Transducer
  - 45° 2MHz, MBW 45-2/ 45° 4MHz, MBW 45-4
- Signal Analysis/Interpretation: Manual



Slide - 30/116-

## C.1.2 Japanese Techniques

### Emerging Techniques Applied to Open RRT by Teams in Japan

#### ◆ UT techniques

- 1) Higher harmonic UT : (HHUT)
- 2) Sub-harmonic Phased Array for Crack Evaluation, SPACE : (SHPA) \*
- 3) Large Amplitude Excitation Sub-harmonic UT : (LASH)
- 4) 3 Dimensional Synthetic Aperture Focussing Technique : (SAFT) \*
- 5) Phased Array Asymmetrical beam TOFD : (PA-ATOFD)
- 6) Phased Array Twin Probe method : (PA-TP)

#### ◆ ECT technique

- 7) Advanced ECT technique : (AECT) \*
- 8) Controlled Excitation ECT technique : (CEECT) \*
- 9) Orthogonal coil (T/R Mode and Impedance Mode) array ECT : (ECT) \*

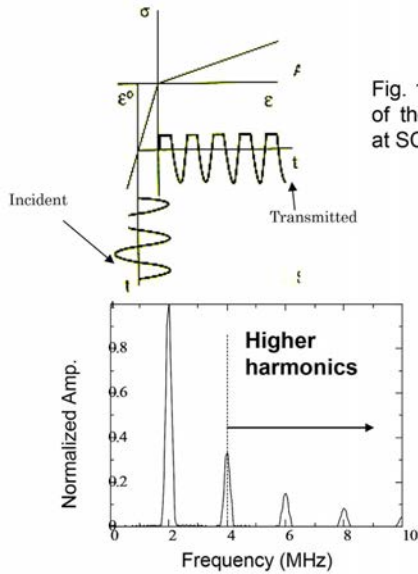
#### ◆ Microwave Near-field Microscope

- 10) Microwave Near-field Microscope : (MM)

\* : This study was performed as a part of "Japan Aging Management Program for System Safety", supported by Nuclear Regulation Authority, Japan.

## ◆ Higher Harmonic UT: HHUT (1)

### Basic concept of nonlinear ultrasonics (higher harmonic imaging)



- 1 Stress strain response of SCC with narrow gap exhibits nonlinearity as shown in Fig.1.
- 2 Lower stiffness in tensile phase result in severe waveform distortion of incident sinusoidal tone-burst wave shown in Fig. 1.
- 3 This waveform distortion is expressed by higher harmonics in frequency domain as shown in Fig. 2.
- 4 Higher harmonics are extracted by analog high-pass filter.
- 5 Higher harmonic amplitude is mapped for scanned area.

2

## ◆ Higher Harmonic UT: HHUT (2)

### Immersion higher harmonic imaging. Experimental set-up.

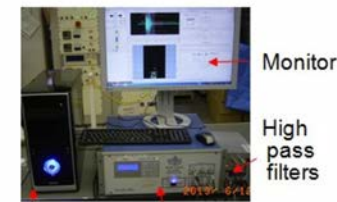


Fig.3 Higher harmonic imaging system.

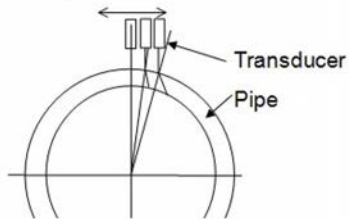


Fig. 4 Measurement set-up for normal incidence.

Fig. 6 Malfunction of in-plane scanning for pipes. Ultrasonic beam is deflected outwards at off-centered incidence.

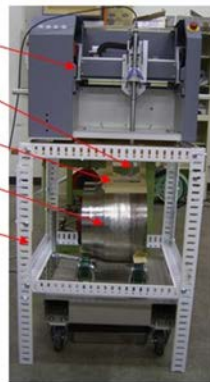


Fig. 5 Measurement set-up for angular incidence.

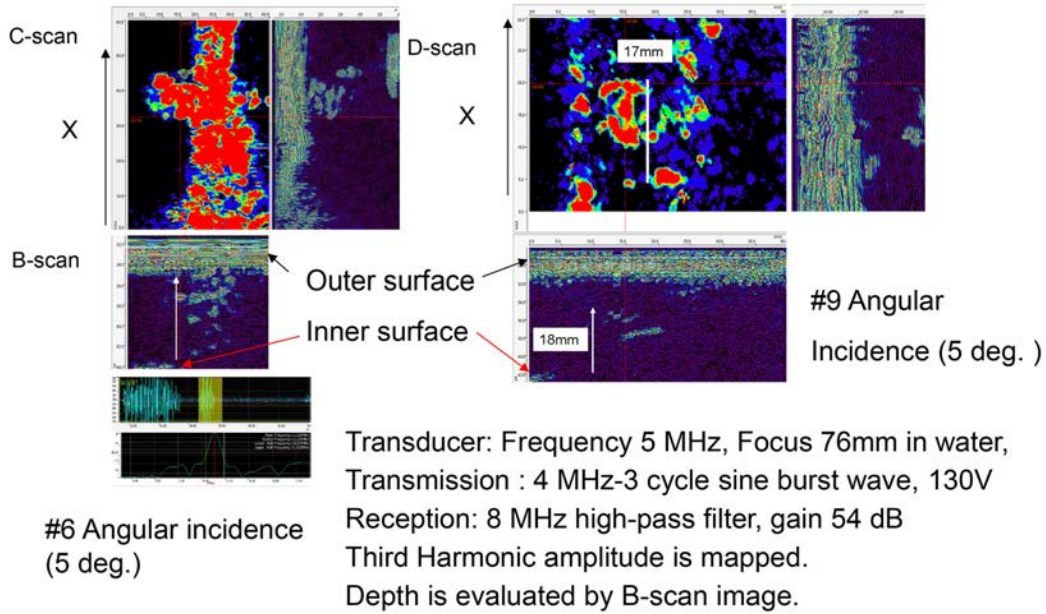


Fig. 7 Experimental set-up for P28~P32, P38, P42 and P46

3

### ◆ Higher Harmonic UT: HHUT (3)

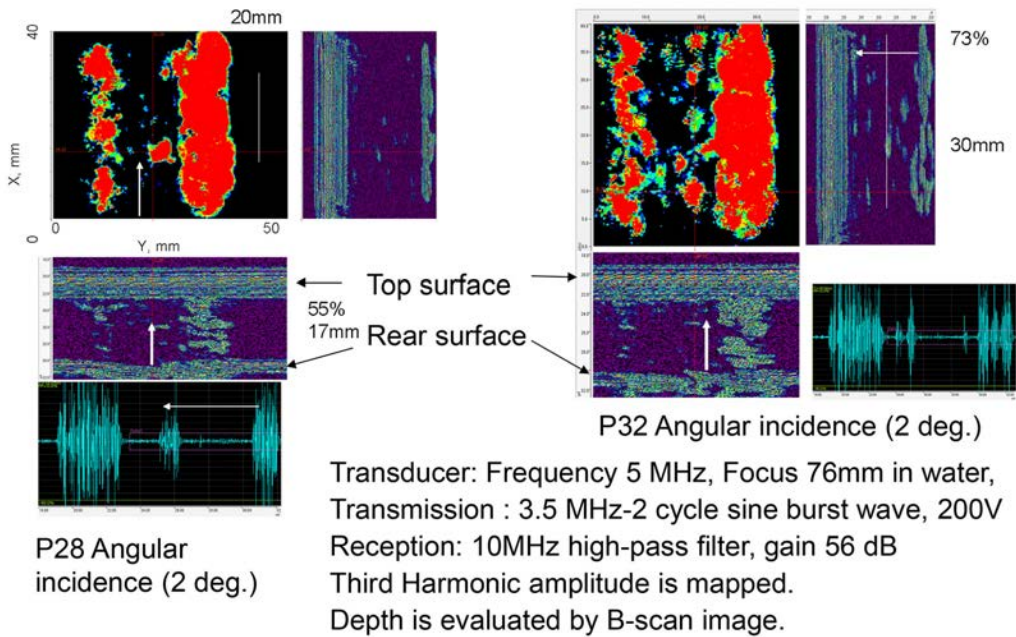
Higher harmonic images for P41.



4

### ◆ Higher Harmonic UT: HHUT (4)

Higher harmonic images for P28 & 32.



5

◆ Subharmonic Phased Array for Crack Evaluation(SPACE) : SHPA (1)

**SPACE** is a novel imaging method using the subharmonic generation by short-burst waves and a phased algorithm with frequency filtering.

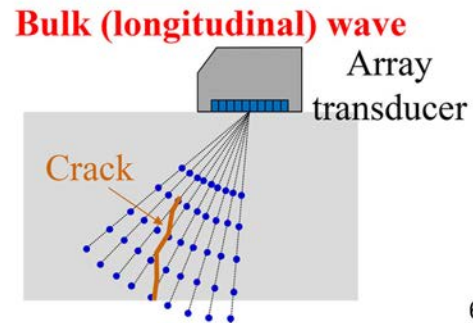
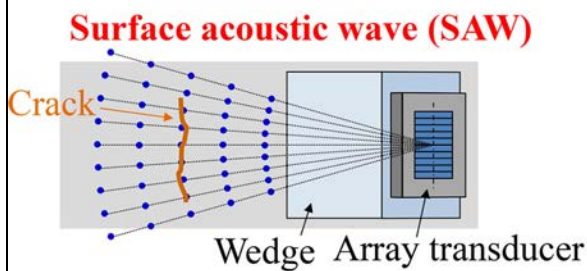
**SPACE** provides fundamental array (FA) images at frequency  $f$  and subharmonic array (SA) images at the frequency  $f/2$ , visualizing the open and closed parts of cracks, respectively.

Detection, Crack Length

Crack Depth

**SAW SPACE**

**Bulk SPACE**

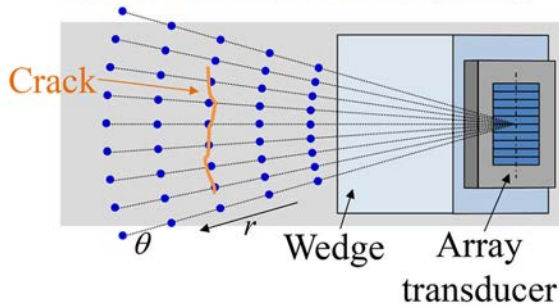


6

◆ Subharmonic Phased Array for Crack Evaluation(SPACE) : SHPA (2)

**SAW SPACE: Detection, Crack Length**

**Surface acoustic wave (SAW)**



**Specimen**

SCC(SUS304, HAZ, High temperature pressurized water)

**Array transducer**

5 MHz, 32 elements, 0.5 mm pitch

**Input condition**

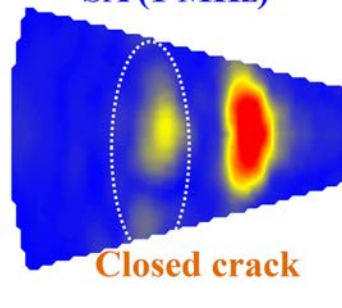
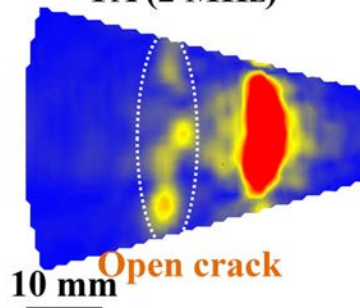
2 MHz, 3 cycle

$\theta = -14^\circ \sim 15^\circ$  ( $1^\circ$  step)

$r = 39.5$  mm,  $44.5$  mm

**FA (2 MHz)**

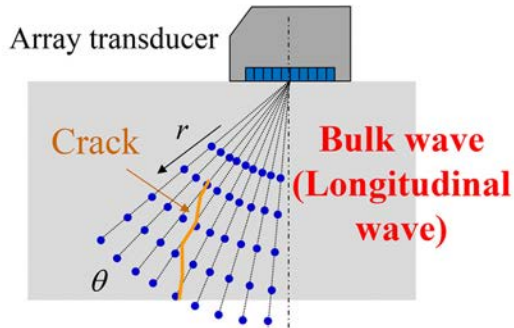
**SA (1 MHz)**



7

◆ Subharmonic Phased Array for Crack Evaluation(SPACE) : SHPA (3)

**Bulk SPACE : Crack Depth**



**Specimen**

SCC(SUS304, HAZ, High temperature pressurized water)

**Array transducer**

5 MHz, 32 elements, 0.5 mm pitch

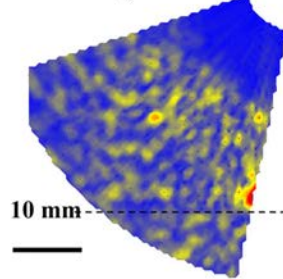
**Input condition**

7 MHz, 3 cycle

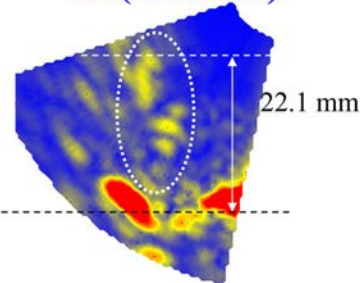
$\theta = 12^\circ \sim 71^\circ$  ( $1^\circ$  step)

$r = 12 \text{ mm} \sim 42 \text{ mm}$  (7.5 mm step)

FA (7 MHz)



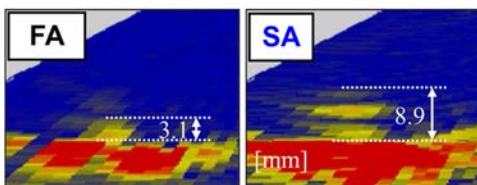
SA (3.5 MHz)



8

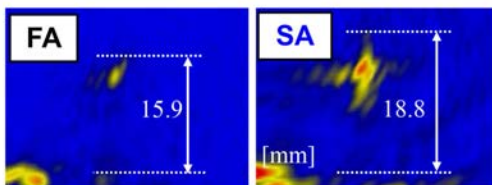
◆ Sub-harmonic Phased Array for Crack Evaluation(SPACE) : SHPA (4)

**Fatigue Crack (SUS316L)**

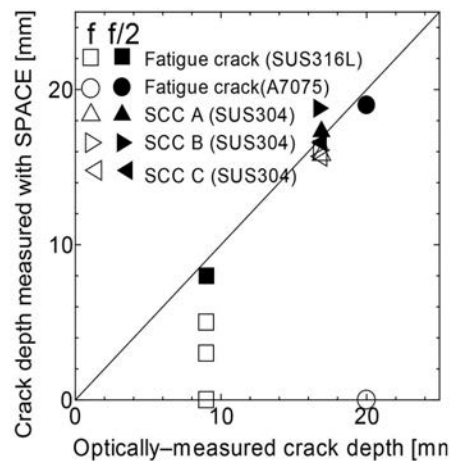


(a)Fundamental array (b)Subharmonic array

**SCC (Sensitized SUS304)**



(a)Fundamental array (b)Subharmonic array



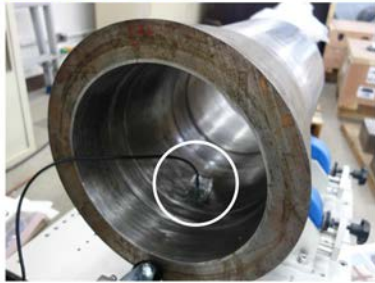
Depth of closed crack is precisely evaluated by the (b) subharmonic array (SA) images at frequency  $f/2$ .

9



## ◆ Subharmonic Phased Array for Crack Evaluation (SPACE) : SHPA (5)

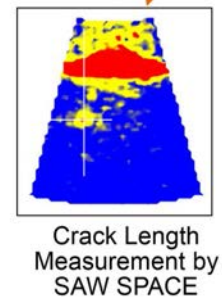
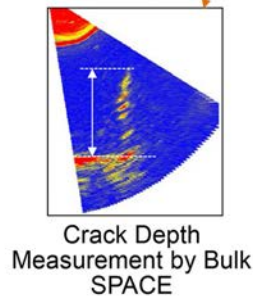
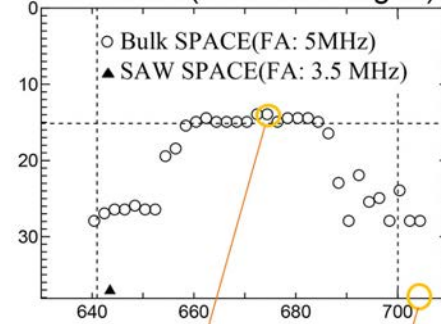
### SAW SPACE



### Bulk SPACE



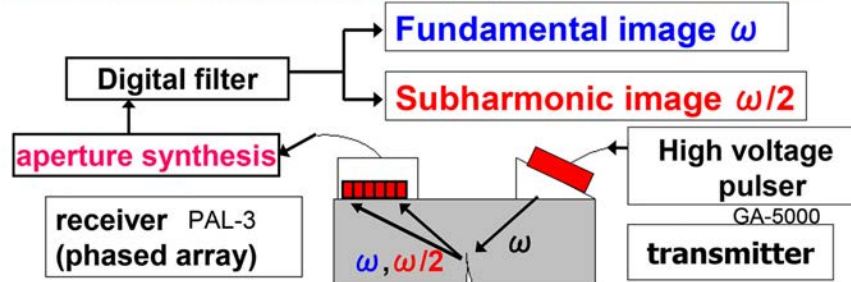
P1 Flaw3 (Thermal Fatigue)



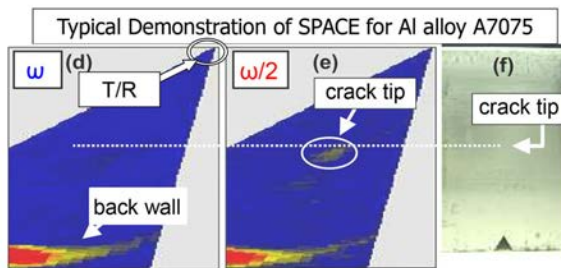
This study was performed as a part of "Japan Aging Management Program for System Safety", supported by Nuclear Regulation Authority, Japan. 10

## ◆ Large Amplitude Excitation Sub-harmonic UT : LASH (1)

Conventional Subharmonic imaging system called SPACE



Advantage of Subharmonic Imaging system



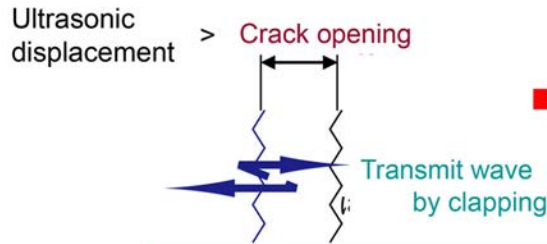
However,

Limitation of present SPACE

- Subharmonic wave generate only at closed cracks
- SPACE is not effective for most of the industrial open cracks

## ◆ Large Amplitude Excitation Subharmonic UT : LASH (2)

### Mechanism of Subharmonic Wave Generation



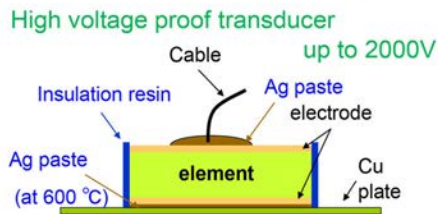
Present SPACE

Opening of Industrial crack will be larger than incident ultrasonic displacement.

Large Amplitude Ultrasound

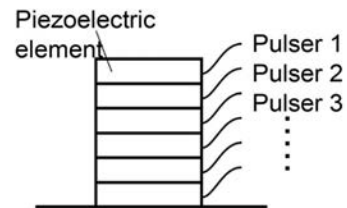
### Our Techniques of Large Amplitude Ultrasound

- 1) High voltage ultrasonic pulser with high voltage proof transducer (Special transform coil system)



We applied this technique here

- 2) Laminated transducer with delayed multi pulser system



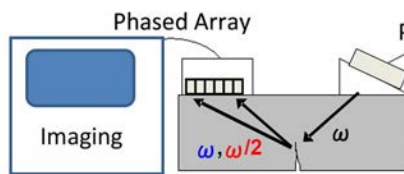
This will be used in future

12

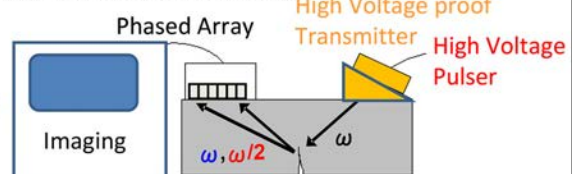
## ◆ Large Amplitude Excitation Subharmonic UT : LASH (3)

### Application of LASH for Industrial Inspection

○ SHPA (SPACE)



○ LASH (Large amplitude SPACE)



Example of round robin specimen : P29

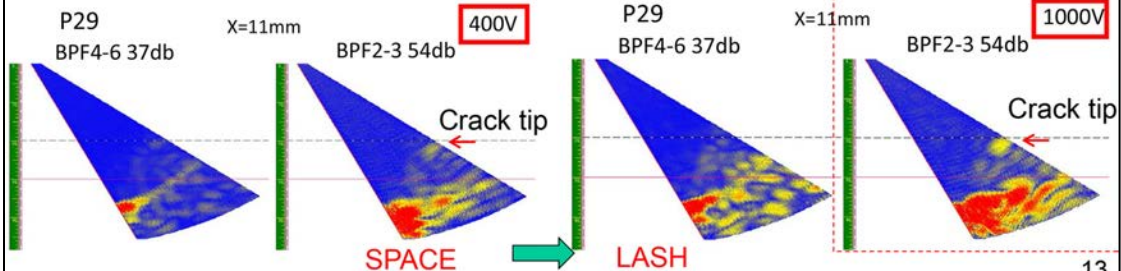
B-Scope image measurements at given crack positions

Fundamental image

Subharmonic image

Fundamental image

Subharmonic image

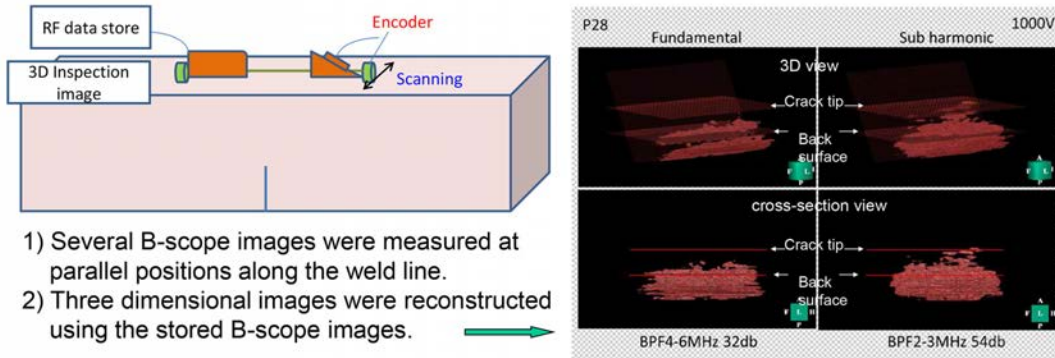


13

## ◆ Large Amplitude Excitation Subharmonic UT : LASH (4)

Only for the cracks in which crack tips can be observed in subharmonic B-scope images, three dimensional B-scope image were applied using the encoder system.

### Three Dimensional B-Scope Image Measurement (Optional measurement)

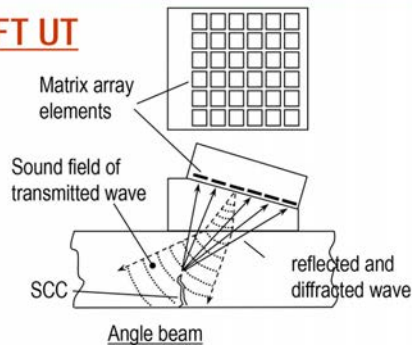


LASH technique could be improved S/N ratio of crack tip echo especially in subharmonic image for P-28, P-29 and Flaw-2 in P1.

14

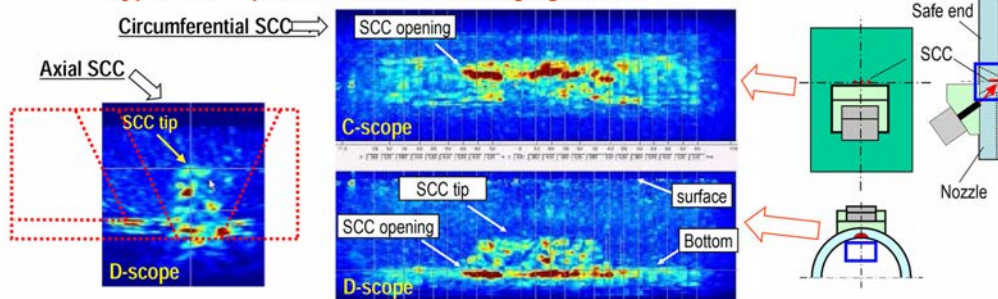
## ◆ 3 Dimensional Synthetic Aperture Focussing Technique: SAFT (1)

### 3D-SAFT UT



UT beams from many matrix array elements are transmitted into the objectives, and the reflected or diffracted waves from different directions are used for the SAFT processing

### Typical examples of 3D-SAFT UT imaging of SCC

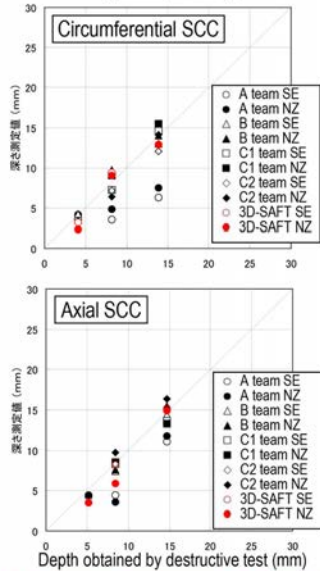


15

### ◆ 3 Dimensional Synthetic Aperture Focussing Technique: SAFT (2)

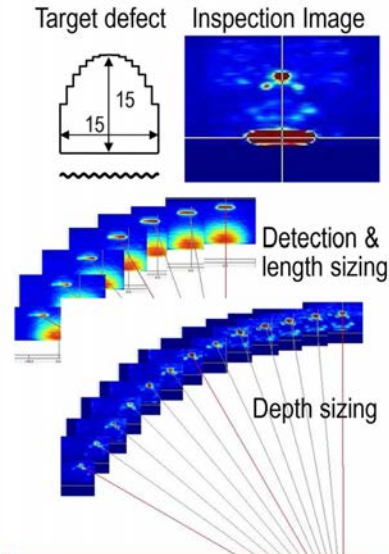
#### Application to Ni alloy weld inspection

##### Accuracy of SCC depth sizing (safety valve)



3D-SAFT has good accuracy of depth sizing.

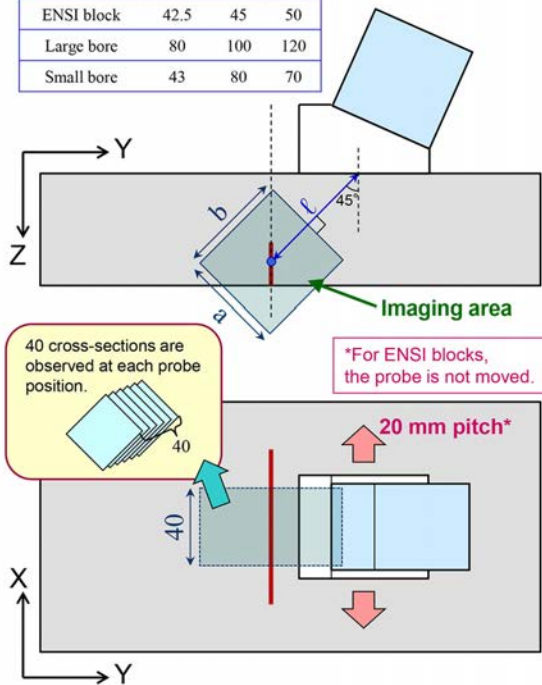
##### Inspection capability from offset position



Good result of length & depth sizing are obtained between 0~60° offset direction.

### ◆ 3 Dimensional Synthetic Aperture Focussing Technique: SAFT (3)

	$l$	$a$	$b$
ENSI block	42.5	45	50
Large bore	80	100	120
Small bore	43	80	70



##### Probe

Frequency: 2 MHz

Channel: 256ch (16 × 16)

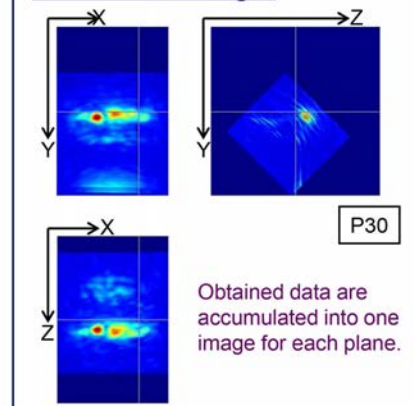
##### Probe wedge

Refracted angle (longitudinal wave): 45°

The contact surface is respectively contoured

- to match the curvature of both axial and circumferential inspection of SBDMW
- to match the curvature of both axial and circumferential inspection of LBDMW

##### Accumulated images



### ◆ 3 Dimensional Synthetic Aperture Focussing Technique: SAFT (4)

#### Measurement



ENSI block

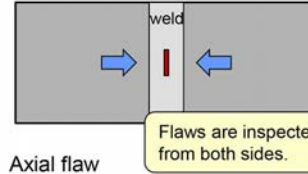


Small bore

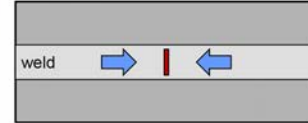


Large bore

#### Circumferential flaw

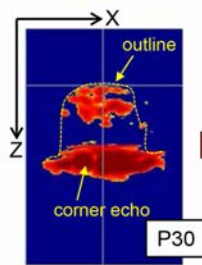


#### Axial flaw

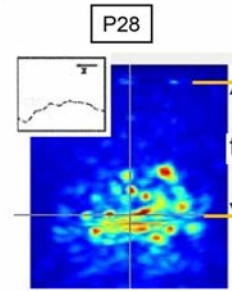
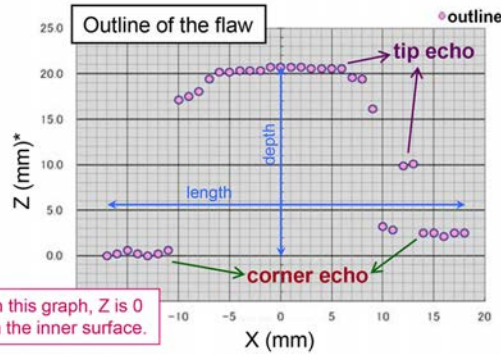


#### Sizing method

##### Binarized image



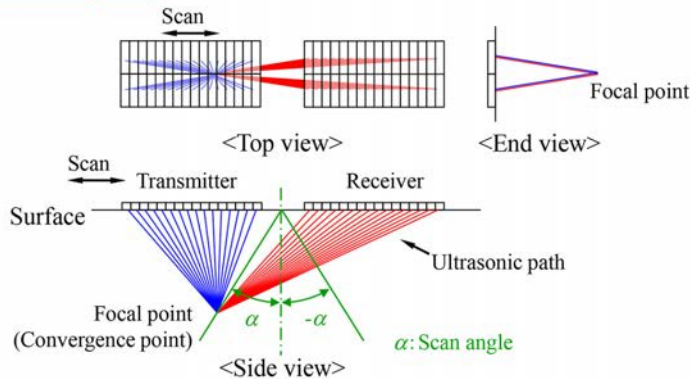
The threshold for binarization is the noise level.



This study was performed as a part of "Japan Aging Management Program for System Safety", supported by Nuclear Regulation Authority, Japan. 18

### ◆ Phased Array Asymmetrical Beam TOFD : PA-ATOFD (1)

#### ➤ Schematic diagram



Two array probes for transmitter and receiver parallel to the scan direction

Ultrasonic beams with different scan angles and path lengths of the transmitter and receiver



Acquire the tip echo of the flaw with different scan angles

## ◆ Phased Array Asymmetrical Beam TOFD : PA-ATOFD (2)

### Array probe

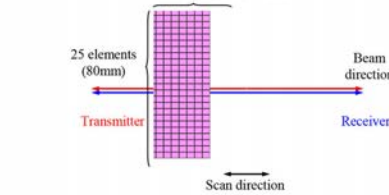
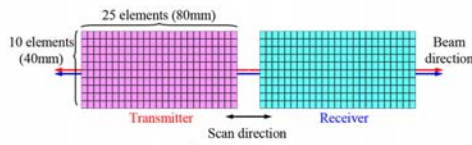
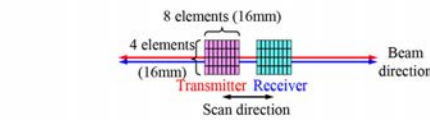
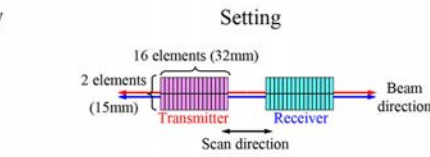
2.25MHz, 2x16 matrix array



2.25MHz, 4x8 matrix array



2MHz, 10x25 matrix array



Apply to the inner surface  
(near crack side)

LB  
P12, P23, P24, P37  
Test block  
P28, 29, 30, 31, 32, 38, 42, 46

Example of array probes  
and wedge



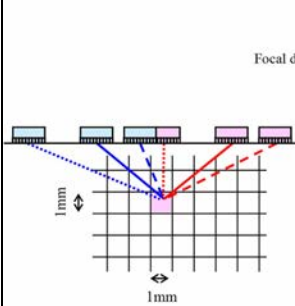
Apply to the outer surface  
(far crack side)

LB  
P12, P23, P24, P37  
SB  
P1, 41

20

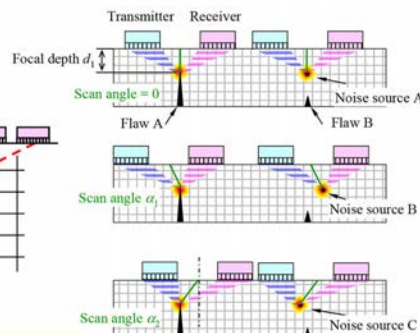
## ◆ Phased Array Asymmetrical Beam TOFD : PA-ATOFD (3)

### ➤ Data synthesis method

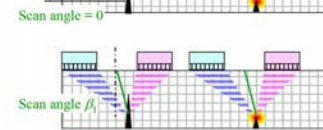
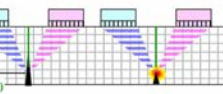


Scanning data are synthesized with different refraction angles and/or different depths of focus point.

This synthesis is expected to enable us to distinguish easily the tip echo and noise.



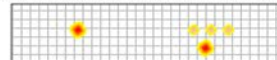
Synthesis (averaging) of the different scan angle data in focal depth  $d_1$



Synthesis (averaging) of the different scan angle data in focal depth  $d_2$



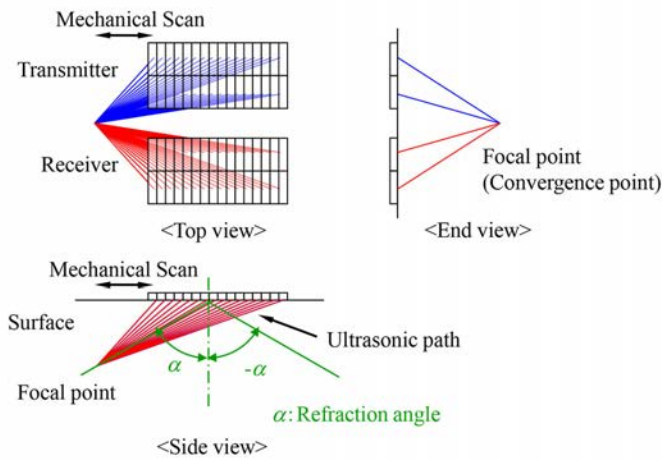
Synthesis (choosing maximum) of the different scan angle data in focal depth  $d_1, d_2$



21

## ◆ Phased Array Twin Probe Method : PA-TP (1)

### ➤ Schematic diagram

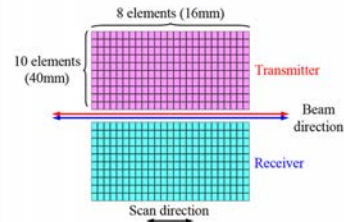


Two array probes for transmitter and receiver perpendicular to the scan direction  
 Ultrasonic beams with different scan angles on the both side of the normal

Acquire the tip echo of the flaw with different scan angles

### Array probe

2MHz, 10x25 matrix array



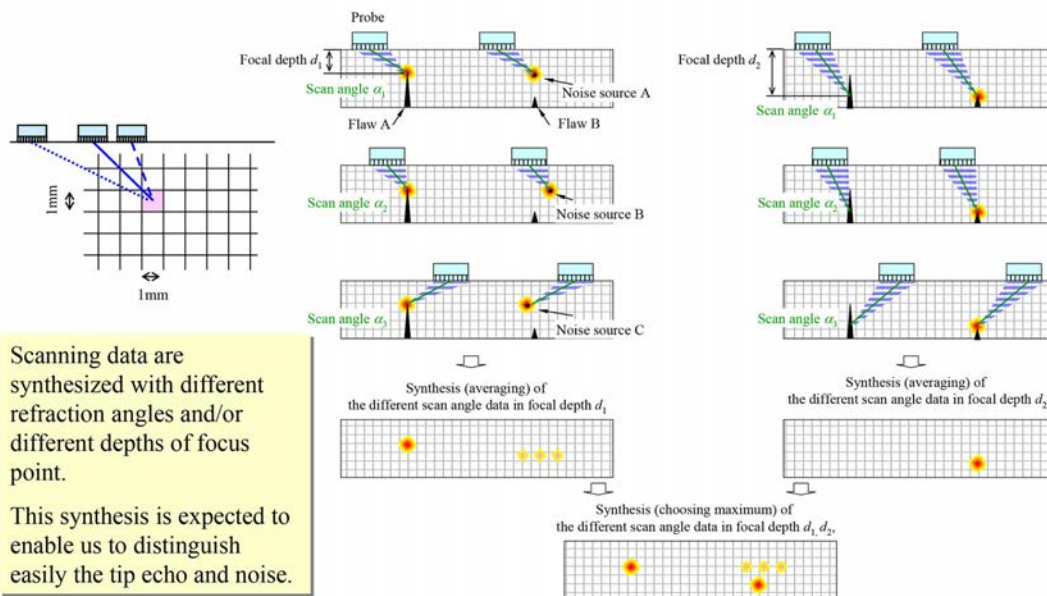
Apply to the outer surface (far crack side)

LB  
 P12, P23, P24, P37  
 SB  
 P1, 41

22

## ◆ Phased Array Twin Probe Method : PA-TP (2)

### ➤ Data synthesis method



Scanning data are synthesized with different refraction angles and/or different depths of focus point.

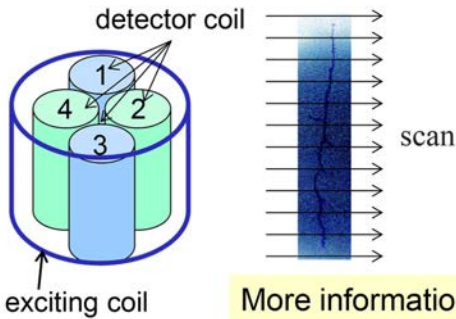
This synthesis is expected to enable us to distinguish easily the tip echo and noise.

23

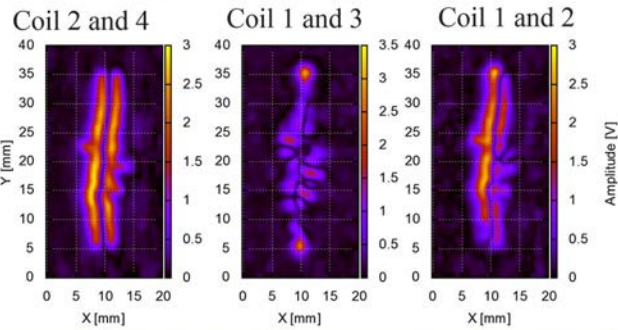
## ◆ Advanced ECT: AECT (1) : Multi coil probe

Multi coil probe

Four detector coils in exciting coil



Differential signal

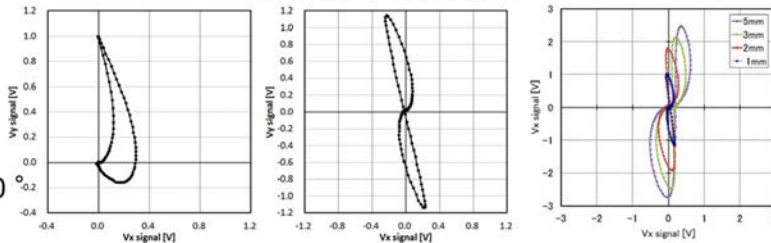


More information can be obtained at the same scan direction

Calibration of each coil

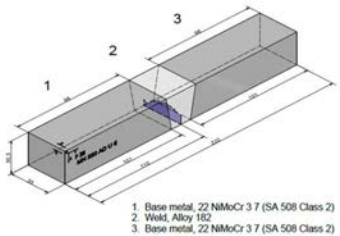
Standard specimen  
slit size  
depth 1, width 0.5mm

ETC signal  
amplitude: 1V, phase: 90°

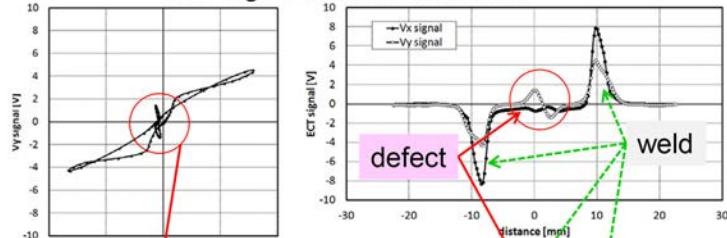


## ◆ Advanced ECT: AECT (2) : Signal processing

Result of Test block P28



ECT signal of center of defect



Phase is about 100° on defect

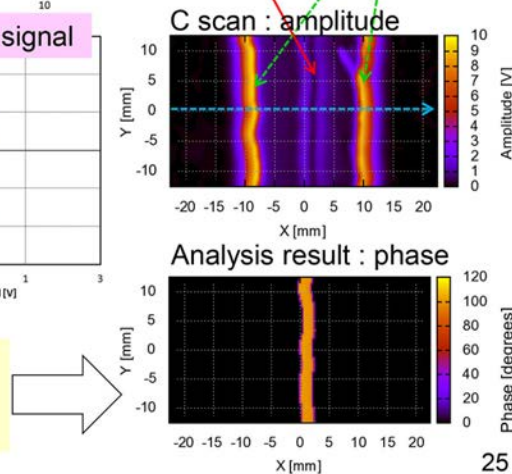
Phase is calculated as the  
inclination of changing signal  
between steps of the scan.

$$\theta = \text{ATAN} \left[ \frac{Vy_{(n+1)} - Vy_{(n)}}{Vx_{(n+1)} - Vx_{(n)}} \right]$$

$\theta$  : phase,  $Vx_{(n)}$  :  $Vx$  of  $n^{\text{th}}$

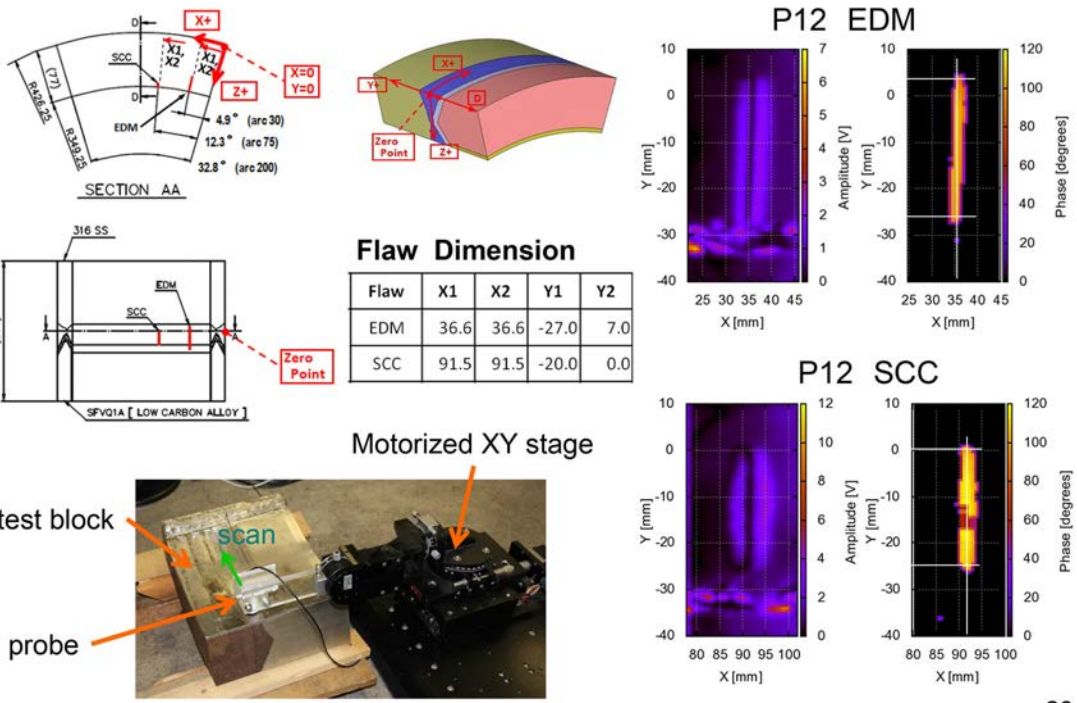
Filtering

Threshold of phase : 80-110 degrees  
Changing amplitude of  $Vy$  : 0.1[V] or more  
Number of continuous : 3 or more



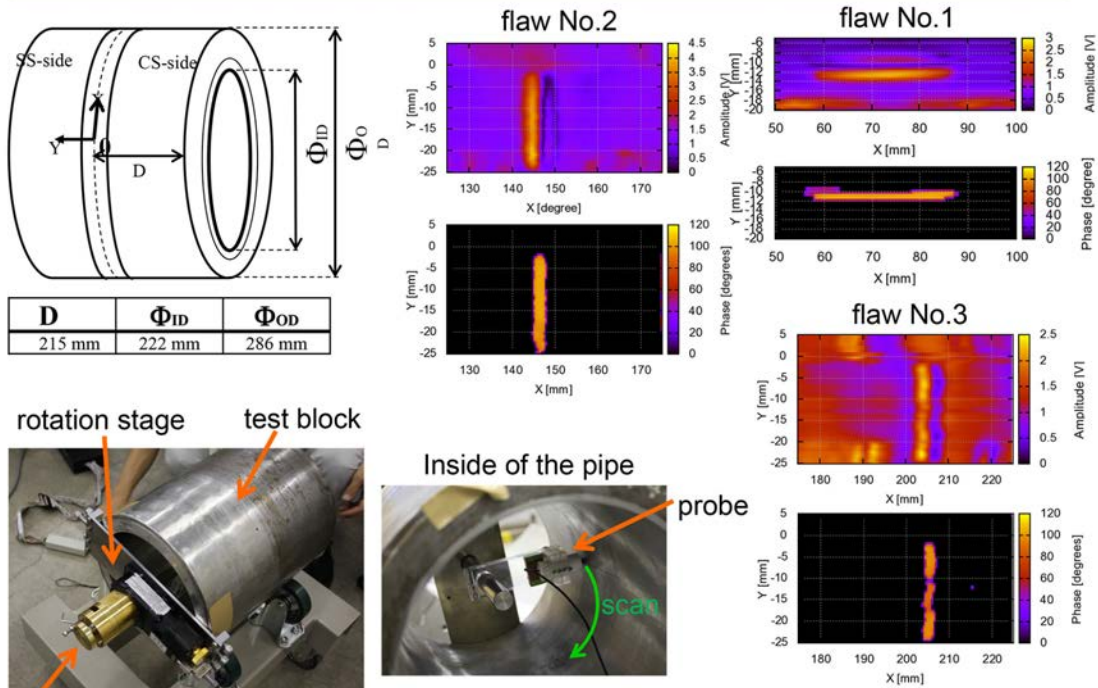


## ◆ Advanced ECT: AECT (3) : Results of test block P12



26

## ◆ Advanced ECT: AECT (4) : Results of test block P41



This study was performed as a part of "Japan Aging Management Program for System Safety", supported by Nuclear Regulation Authority, Japan.

27

## ◆ Controlled Excitation ECT: CEECT (1)

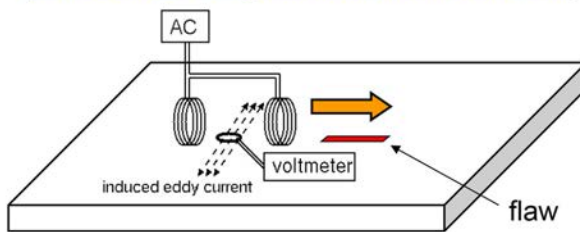
### Problem of Conventional Eddy Current Testing

It is difficult to evaluate the depth of a flaw by ECT because the depth of a flaw does not provide a big difference in the ECT signal when the depth of a flaw is more than a certain value (In other words, the ECT signal saturates).

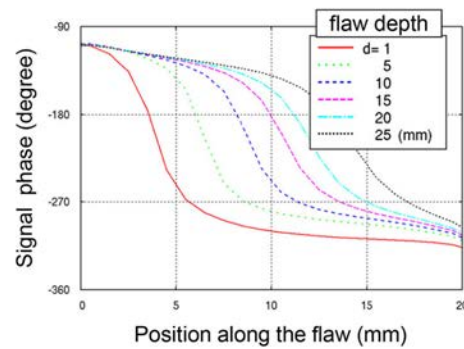


**CEECT shows a difference in the signal phase even if the depth of a flaw is big.**

### Probe Configuration of CEECT



Two vertical exciters and one horizontal detector located away from the exciters.

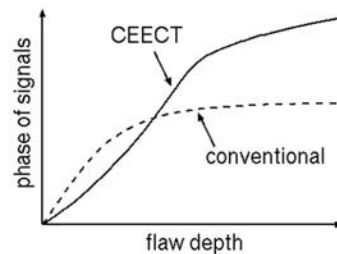
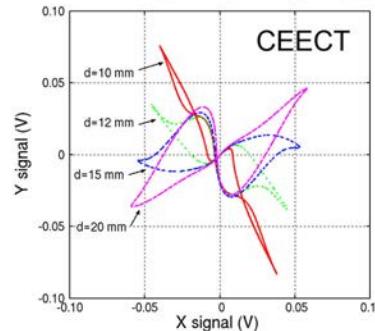
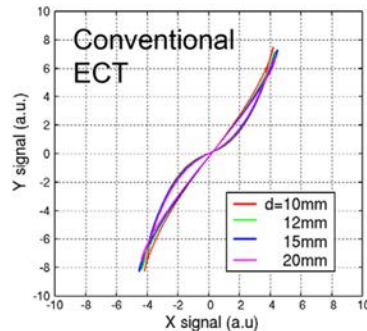


28

## ◆ Controlled Excitation ECT: CEECT (2)

### Experimental results

Signals due to rectangular artificial slits of 40 mm in length on 316L austenitic stainless steel. Measured from near-side with an exciting frequency of 100 kHz.



**CEECT shows a difference in the signal phase even if the depth of a flaw is big.**

29

## ◆ Controlled Excitation ECT: CEECT (3)

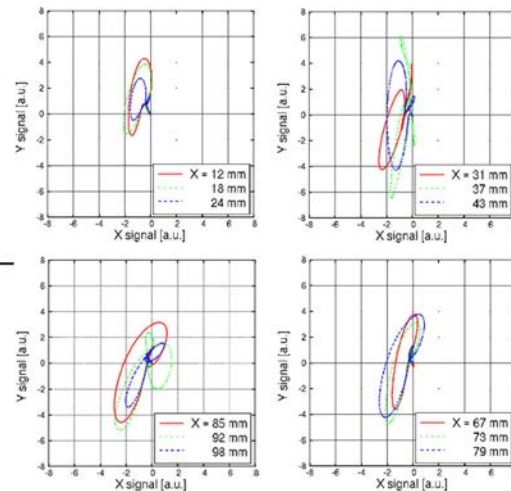
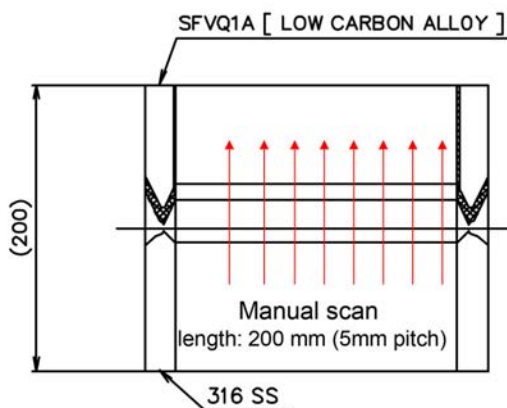
### Disadvantages of CEECT

- Obtained signals have a complicated dependency on flaw parameters. Not only the depth but also the length (probably cross-sectional profile and electrical resistance as well) has a large effect on signals, which has not been quantitatively revealed yet.
- If the length of a flaw is shorter than approximately 20 mm, the change in signals with respect to the depth of a flaw becomes quite similar to that of conventional ECT (no superiority over conventional ECT).
- Since the detector needs to be located away from the exciters, the probe becomes quite large.

30

## ◆ Controlled Excitation ECT: CEECT (4)

### Results of P12 inspection:



An 8-shaped loop: Flaw signal  
Non 8-shaped loop: Noise



Flaw indications were confirmed at X=37 and 92 mm (same with the specification).

This study was performed as a part of "Japan Aging Management Program for System Safety", supported by Nuclear Regulation Authority, Japan. 31

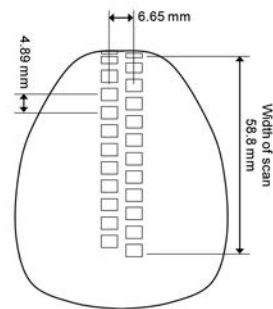
## ◆ Eddy Current : ECT (1)

The system is commercially available.



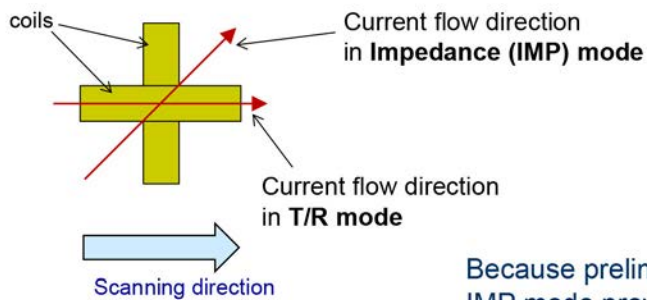
Instrument: R/D Tech MS5800  
 Probe: BMI probe (E342024D)  
 Coil: Ortho 3 mm  
 Number of coils: 24  
 Frequency: 200 kHz

### Probe



## ◆ Eddy Current : ECT (2)

### Orthogonal coil (T/R Mode and Impedance Mode)



Because preliminary experiments showed IMP mode provided better results than TR mode, only IMP mode is used.

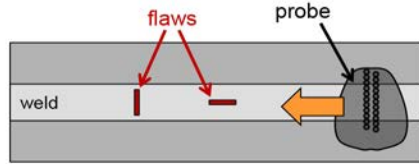
#### Advantages

- Orthogonal coils offer directional sensitivity
- Clear separation of circumferential and axial indications by 180° phase change
- Self compensation configuration (less sensitive to lift-off and conductive change)

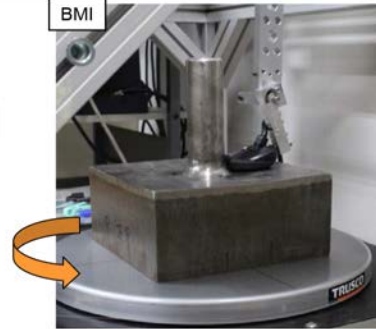
#### Limitations

- Low sensitivity to defects parallel to current flow
- Complex signal interpretation is required for multidirectional cracks

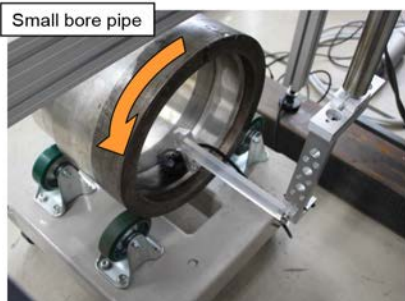
### ◆ Eddy Current : ECT (3)



Only one path is scanned for each test block.

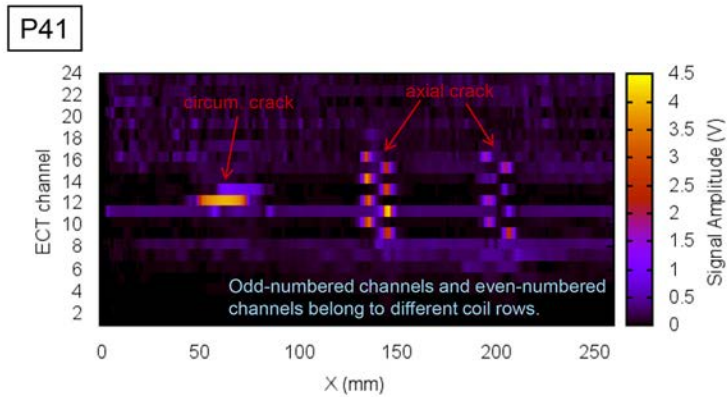


The wire end is attached to the outer surface.



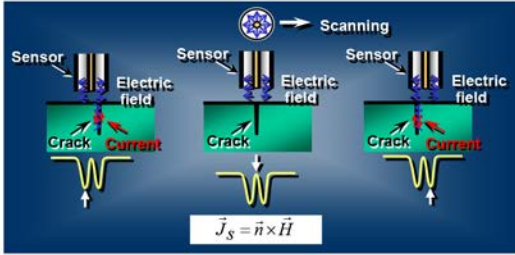
### ◆ Eddy Current : ECT (4)

Example of signal distribution

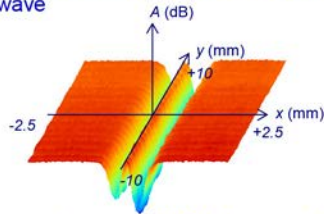


## ◆ Microwave Near-field Microscope : MM (1)

### Quantitative evaluation of fatigue crack

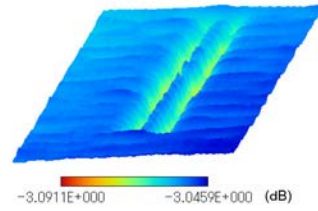


Mechanism of the detection of small crack using microwave



Microwave image of a 2-D fatigue crack

$$d = \frac{\Delta A(f_1) - \frac{G(f_1)}{G(f_2)} \Delta A(f_2)}{S(f_1) - \frac{G(f_1)}{G(f_2)} S(f_2)} \quad (1)$$



Microwave image of a 3-D fatigue crack

$$I = \Delta I'(f_1, y_1) - \frac{G'(f_1, y_1)}{G'(f_2, y_2)} \Delta I'(f_2, y_2) \quad (2) \quad [1]$$

$$\left. \begin{aligned} I_s(y_s) &= C_1 + C_2 \log \sqrt{\alpha^2 + \beta^2} \\ \alpha &= \frac{1}{M} \sum_{r=1}^M \frac{1}{\sqrt{kr}} \cos \left\{ 2kr \left( i \frac{\pi}{M} \right) \right\} \\ \beta &= \frac{1}{M} \sum_{r=1}^M \frac{1}{\sqrt{kr}} \sin \left\{ 2kr \left( i \frac{\pi}{M} \right) \right\} \end{aligned} \right\} \quad (3)$$

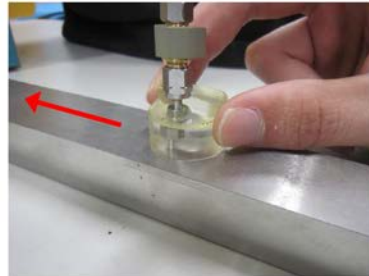
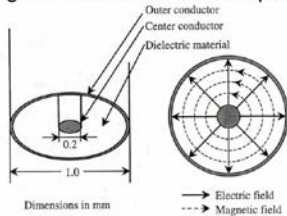
[1] Y. Ju et al., *NDT & E Int.*, 38, 726, (2005)

1

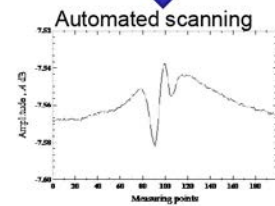
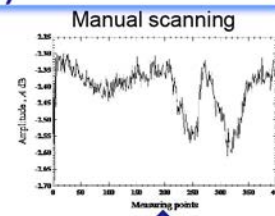
## ◆ Microwave Near-field Microscope : MM (2)

### Measurement by manual scanning

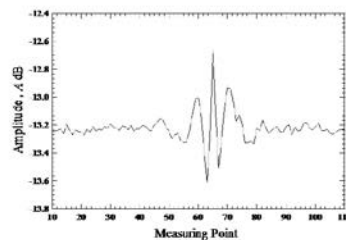
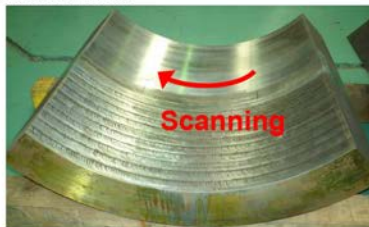
Distribution of the electric and magnetic field at the sensor aperture



Detection of closed fatigue crack (Frequency: 67 GHz)



detection result of P23



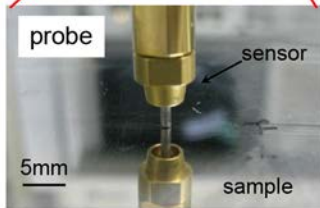
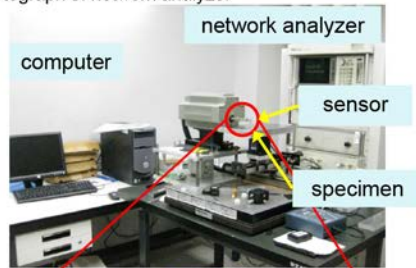
EDM slits on the curved surface were detected.

2

## ◆ Microwave Near-field Microscope : MM (3)

### Measurement by automated scanning

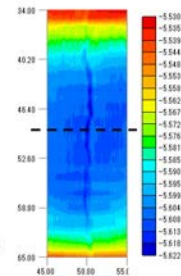
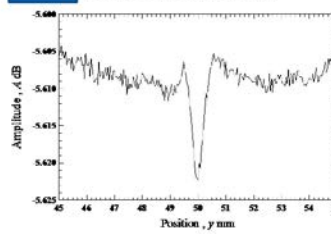
Photograph of network analyzer



#### Test parameters

Frequency: 110GHz  
 Standoff distance : 60 mm  
 Scan direction pitch : 0.04 mm  
 Step direction pitch : 1 mm

#### P28 Detection result



Visualization of crack  
 by two-dimensional imaging

Evaluation equation for crack depth sizing

$$d = \frac{\Delta A}{\eta_0 \eta_1 (40 \log_{10} e) \alpha}$$

$d$ : crack depth

$\Delta A$ : amplitude difference

$\alpha$ : Attenuation constant

$\eta_0, \eta_1$ : Constants of loss and irradiation of microwave

3

### C.1.3 European Techniques

## Technique Descriptions for 114-PA1, 122-PA1 & 122-PA2

PARENT-8, 20 December 2013

Esa Leskelä

VTT Technical Research Centre of Finland

### VTT's Open Test Teams and Test Blocks

#### Team 1: 114-PA1

P1, P4, P41,  
P28, P29 }  
P29, P31 } ENSI  
P32, P38 } Block  
P42, P46 } s

#### Team 3: 122-PA1 & 122-PA2

P28, P29 }  
P29, P31 } ENSI  
P32, P38 } Block  
P42, P46 } s



## **Techniques 114-PA1, 122-PA1 & 122-PA2**

- Phased array ultrasonic technique
- All the techniques use the same 1.5 MHz probes
  - Dedicated probes for circumferential flaw inspection
  - Dedicated probes for axial flaw inspection (only 114-PA1)
- Shear wave (SW) and longitudinal wave (LW)
- T/R configuration
- OD access, manual encoded scanning from both sides of the weld

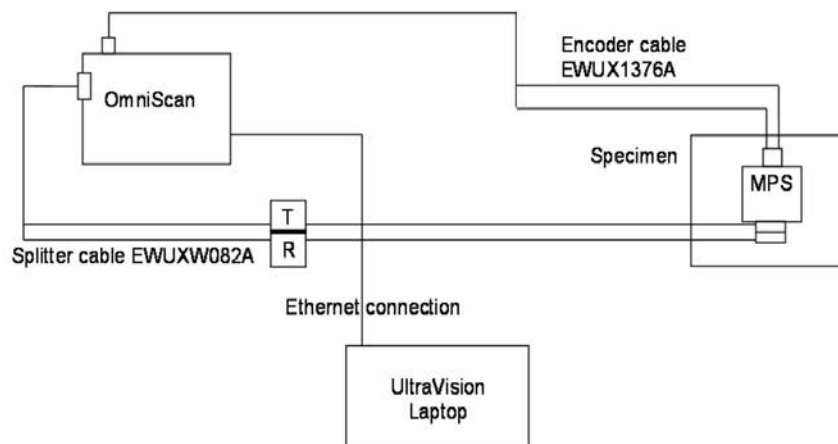
## **Technique 114-PA1**

- Circumferential flaws:
  - Detection, characterization and length and height sizing of inner surface breaking circumferential flaws
- Axial flaws:
  - Detection, characterization and height sizing of inner surface breaking axial flaws but no length sizing

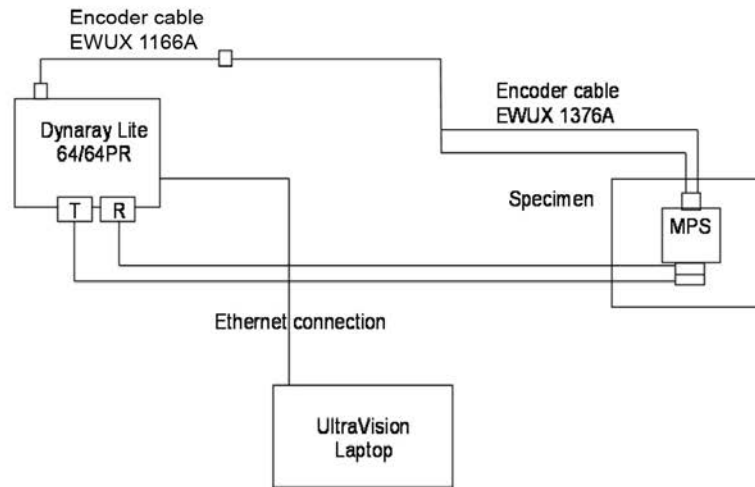
## Techniques 122-PA1 & 122-PA2

- Techniques were developed for more accurate height sizing of flaws in the ENSI blocks but are easily applicable to real piping inspections.
- Goal was also to compare the performance of linear and sectorial scan in flaw height sizing and crack tip detection.
- Manual encoded scanning was used because of practical reasons (large probe in relation to small ENSI test blocks) – otherwise an automated scanner is used.

## Equipment 114-PA1 & 122-PA1



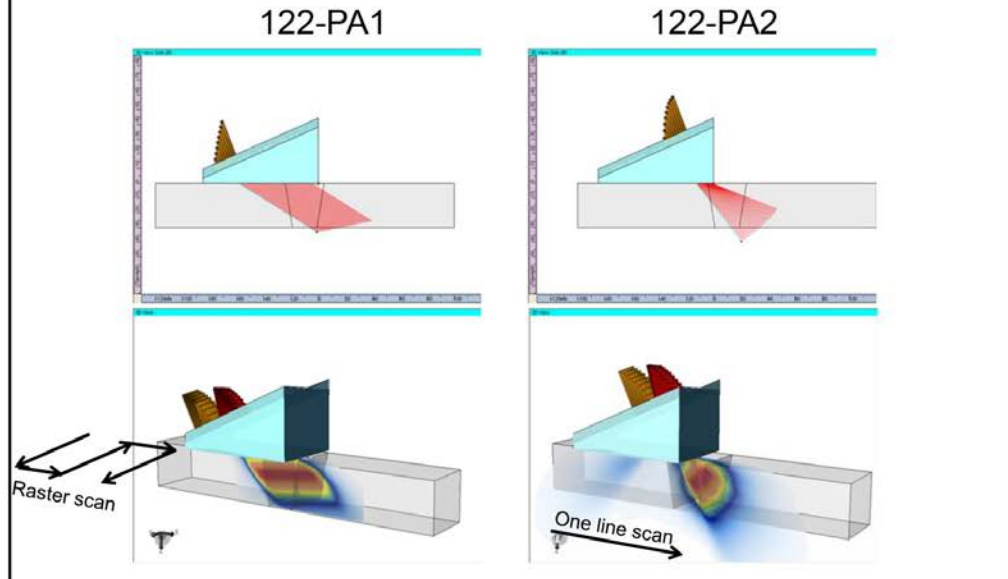
## Equipment 122-PA2



## Techniques 114-PA1, 122-PA1 & 122-PA2

Technique	Technology	Access	Scanning Mode	Wave Mode	Frequency	Equipment	Scan Type	Flaw Type	Array Configuration	Refracted Angles	Skew Angles	Length Sizing	Height Sizing		
114-PA1	PAUT, commercial procedure	OD	Manual encoded scanning	LW+SW	1.5 MHz	OmniScan & UltraVision	Linear T/R raster scan	CIRC + AXIAL	1D linear for circ. flaws, 2D matrix for axial flaws	LW for circ. flaws: 30°, 45°, 60°, 70°	Only for axial flaws -22.5° ... +22.5°, step 2.5°	Full amplitude drop	Crack tip or conservative measurement using the upper extent of the flaw image		
122-PA1	PAUT, non-commercial procedure									LW 45°, 50°, 55°, 60°, 65°				N/A	N/A
122-PA2	Dynaray Lite Sectorial T/R one line scan									Sectorial 40° – 70°, step 1°					

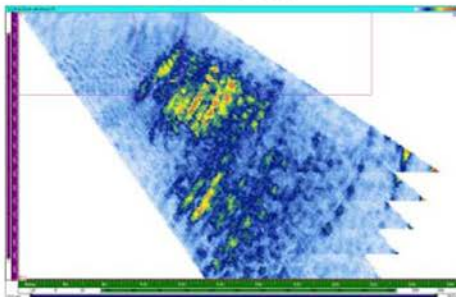
## Techniques 122-PA1 and 122-PA2



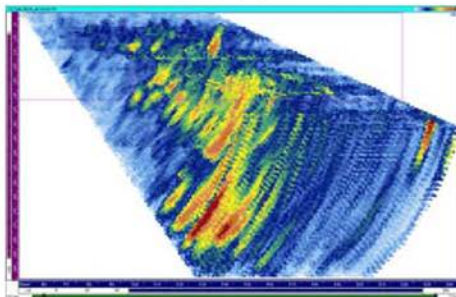
## Techniques 122-PA1 and 122-PA2

- End views of test block P46 without flaw
- Linear scan with 122-PA1: high resolution, good SNR  
→ good sizing performance expected
- Sectorial scan with 122-PA2: lower resolution, stronger metallurgical and mode converted signals

122-PA1



122-PA2



## **Self-assessment**

- Advantages:
  - Techniques are easy to set up for site inspection as well as for laboratory work.
  - The phased array probes are versatile and the search unit (probes+wedge) enables the use of multiple angles and both longitudinal and shear wave modes.
  - The interchangeable wedges enable a large variety of components to be inspected with the same probes.
  - Rather fast data acquisition.
  - Effective data handling because the data can be collected on the same hard disk of the laptop which is used for analysis so no data transfer is required.
  - Data processing prior to data analysis is simple and fast.

## **Self-assessment**

- Disadvantages:
  - Skewing of ultrasonic wave is not possible with the linear probes used for circumferential flaws. Same probe and wedge is used for both shear and longitudinal wave modes so focusing capability is limited.
  - Data analysis requires a lot of effort because of the multiple data merge groups which are analysed separately.
  - Data analysis requires a skilled person.

# Overview of the open PARENT RRT in Switzerland

December 2013

PARENT Consortium – Switzerland represented by

K. Germerdonk <sup>1</sup>, Hans-Peter Seifert <sup>2</sup>, Dominik Nussbaum <sup>3</sup>, Hardy Ernst <sup>4</sup>, Alex Flisch <sup>5</sup>

<sup>1</sup> Swiss Federal Nuclear Safety Inspectorate – ENSI, Brugg, Switzerland

<sup>2</sup> Paul Scherrer Institute (PSI), Nuclear Energy and Safety Research Department, Laboratory for Nuclear Materials, Villigen, Switzerland

<sup>3</sup> ALSTOM Power Products, NDT METHODOLOGIES, Baden, Switzerland

<sup>4</sup> Swiss Association for Technical Inspections – Nuclear Inspectorate, Wallisellen, Switzerland

<sup>5</sup> EMPA, Swiss Federal Laboratories for Materials Science and Technology, Dübendorf, Switzerland

## Open RRT NDE summary presentation

- X-ray computed tomography
- Phased array applications
- Through transmission

# X-ray computed tomography

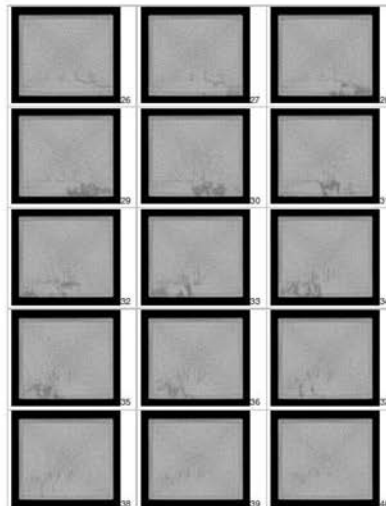
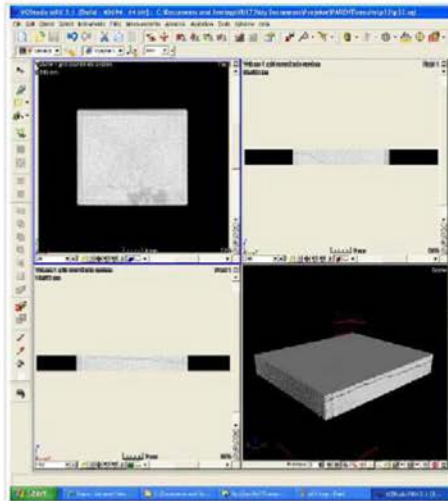
CT-Scanner	CITA 101 B+ (Cita Systems)
Beam geometry	Fan beam
X-ray source	X-ray system MG452 (YTU450-D09)
Parameters of X-ray source	450 kV / 3.3 mA / 1.0 mm focal spot
External X-ray filtration	1.5 mm Brass
Detector	Single collimated (W) line detector (CdWO4) with 125 detector channels
Detector aperture [mm]	0.35 x 0.15
Manipulator position	16
Pixel size of CT-slice [mm]	0.12 x 0.12
Slice distance [mm]	0.12
Object diameter [mm]	60
Ray Spacing [mm]	0.18
Integration time [ms]	100
Beam hardening correction	1.5

Photo of test object on CT-scanner:



Fig. 1:  
Test Block ID: P32 (N 220 AD U TS 5),  
view from X-ray source towards the line  
detector. The sample is oriented such that  
the crack opening is located on the side of  
the X-ray source.

# X-ray data



## X-ray data - depth sizing

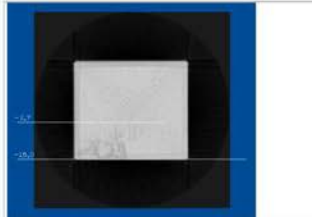


Fig. 26: CT-slice #34 (z=112.30 mm) of test block P20 (N 220 AD U TS 5), crack depth: 11.3 mm (= 2 pixel = 0.24 mm), 37.2% of weld thickness



Fig. 26: CT-slice #50 (z=107.40 mm) of test block P30 (N 220 AD U 7), crack depth: 17.6 mm (= 2 pixel = 0.24 mm), 66.7% of weld thickness

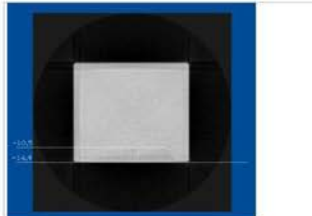


Fig. 26: CT-slice #29 (z=110.18 mm) of test block P28 (N 220 AD U TS 3), crack depth: 4.4 mm (= 2 pixel = 0.24 mm), 14.9% of weld thickness

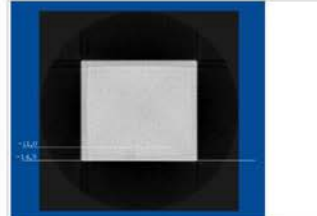


Fig. 26: CT-slice #17 (z=108.72 mm) of test block P31 (MN 220 AD U 1), crack depth: 3.9 mm (= 2 pixel = 0.24 mm), 12.9% of weld thickness

5

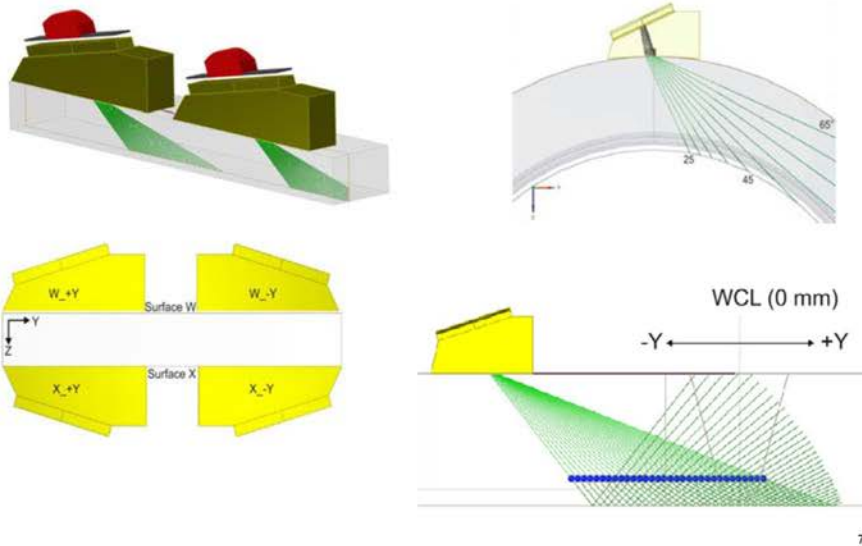
## Phased array applications using commercial probes

Method	Phased Array Ultrasonic Testing
Array / Technique	Dual / Matrix / Transmit - Receive
Wave Mode	Longitudinal
Angle Range	40° - 70°
Frequency	1.5 MHz
Scan Plan	Manual scanning perpendicular to weld both directions
Scanning Surface	OD
Method	Phased Array Ultrasonic Testing
Array / Technique	Single / Linear / Puls Echo
Wave Mode	Longitudinal
Angle Range	40° - 70°
Frequency	2.33 MHz
Scan Plan	Encoded in +Y and - Y direction
Scanning Surface	W & X
Method	Phased Array Ultrasonic Testing
Array / Technique	Dual / Linear / Transmit - Receive
Wave Mode	Longitudinal
Angle Range	25° - 65°
Frequency	2 MHz
Scan Plan	Manual scanning perpendicular to weld in +Y direction
Scanning Surface	OD

6



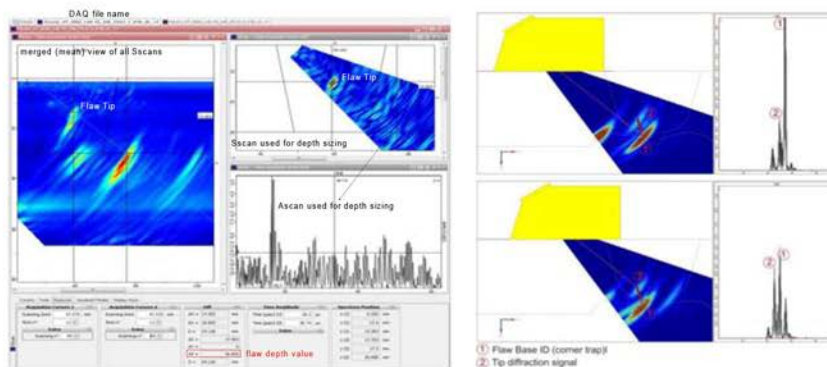
## Phased array applications for DMW



7

## Depth sizing - commercial probes

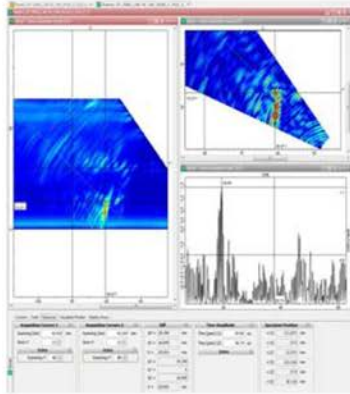
- Absolute Arrival Time Technique (AATT) was used
- Direct signal response from the flaw required
- Flaw depth is calculated by subtracting the remaining ligament from the actual material thickness



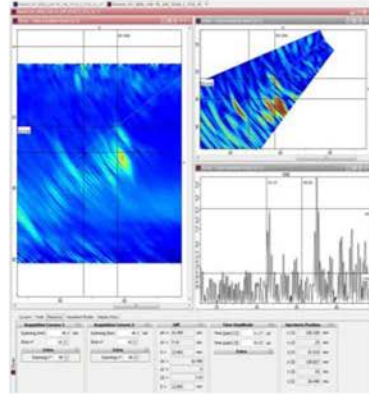
8

## Challenges of depth sizing on DMW

Images on specimen P32 (laboratory grown SCC) using same conventional PA-probe



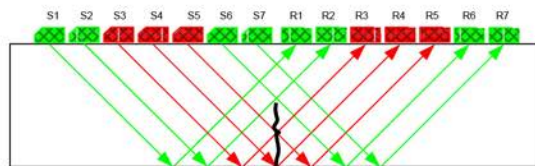
ID – measurement – estimated depth 13.4 mm



OD – measurement – estimated depth 7.5 mm

9

## Through transmission with reflection on back wall



### A very simple approach

- Sound is sent from S1 via back wall to R1, from S2 to R2 etc.
- As long as there is no discontinuity of the sound path the receiver will detect high amplitude (green). In case the sound is blocked by discontinuity (red) the receiver will detect much lower amplitude.
- The received amplitude can then be displayed on a C-scan representation

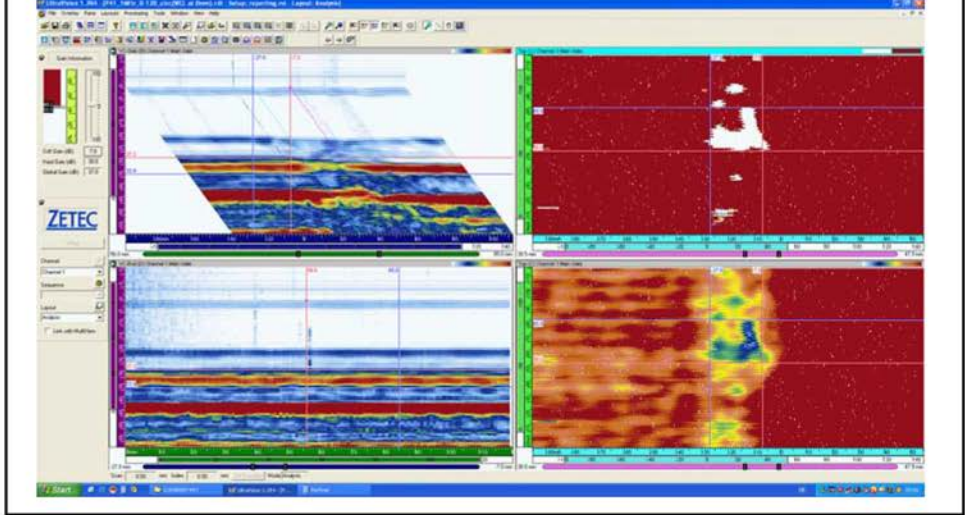
### Advantage

- No influence of flaw surface roughness
- Orientation of flaw doesn't influence detectability, but parallel inner surface is necessary
- Very low noise from scattered sound (grain boundaries...) therefore, higher frequencies can be used

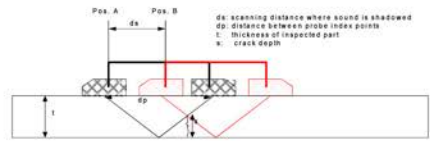
Parent consortium - Switzerland, PARENT  
Project Update, December 2013

10

# Through transmission data

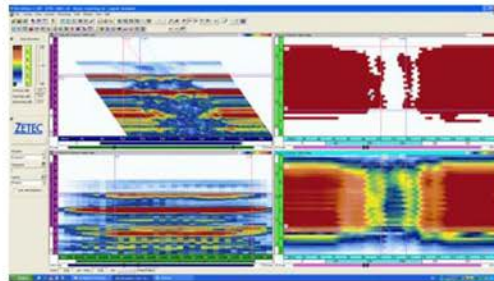
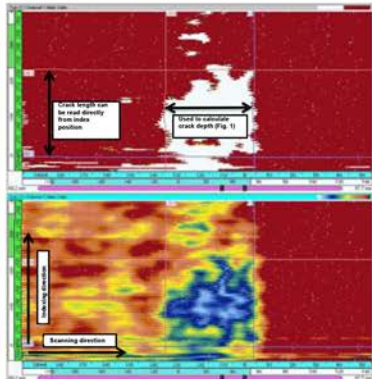


# Depth sizing



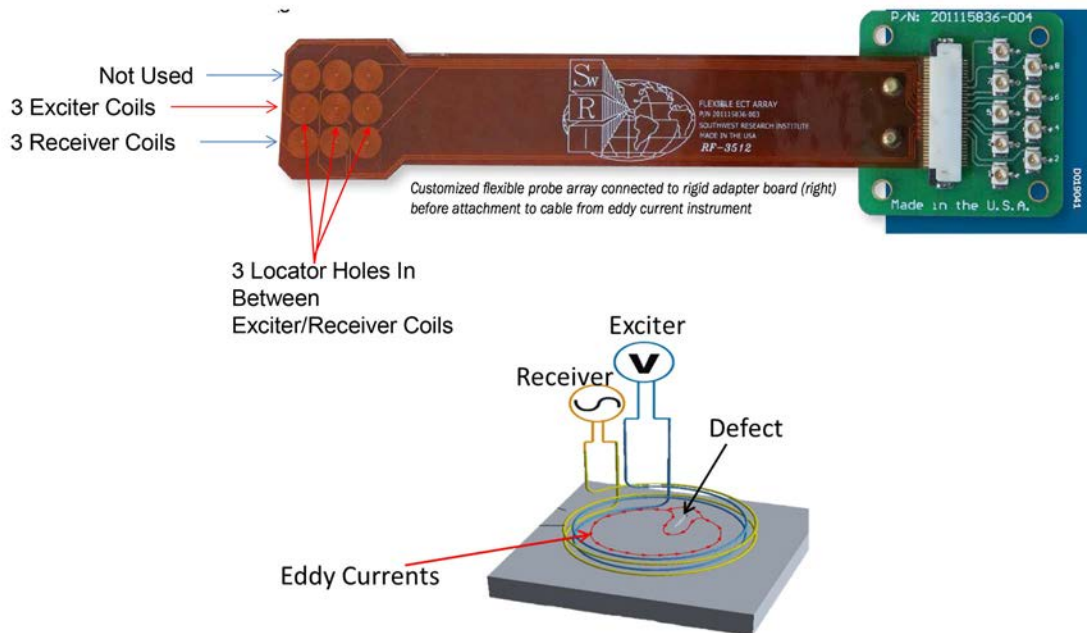
Setup:  
 - Two identical probes (aperture, frequency, angle) with an angle of about 40° to 45° (long), fixed in a probe holder.  
 - Distance between probe index points is optimized to receive the reflected longitudinal wave from the backwall (LL).  
 - Probe holder is moved over the surface and the distance where sound is shadowed by the crack will be stored (B-scan of the received signal).

Crack depth is given by the following formula:  
 $x = d_s \cdot t / d_p$



# Technical Description for Technique 7-ECT1

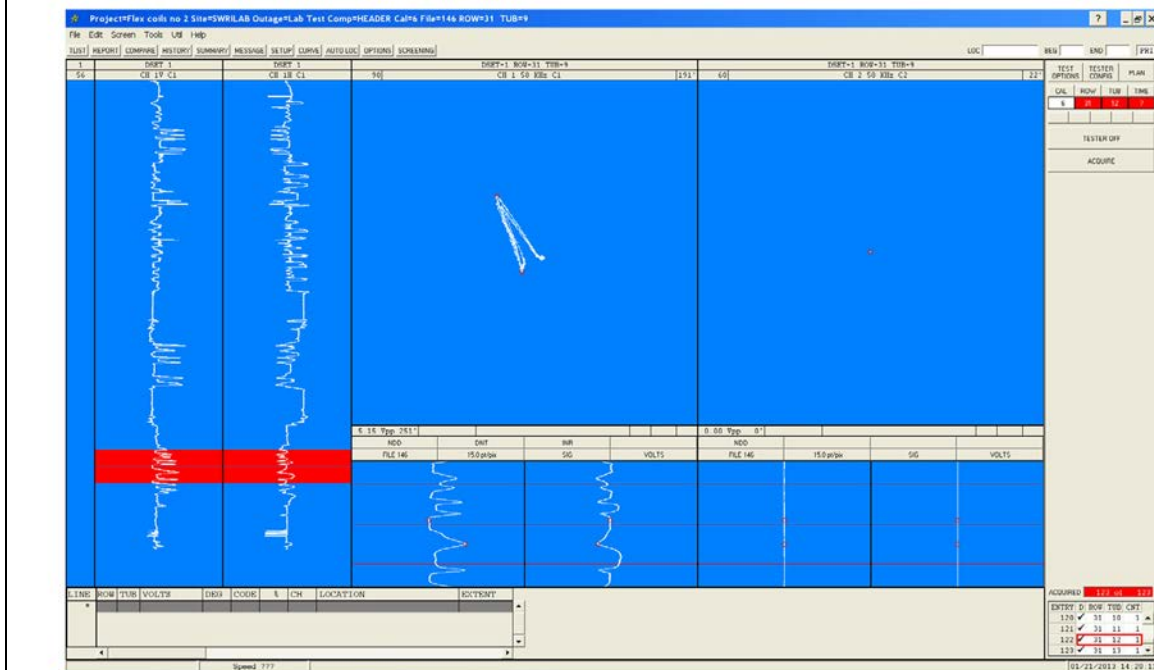
## Eddy Current Probe Functionality and Configuration



# Sample Flaw



# Corresponding Screen Shot



## Overview

- Test Blocks Types Examined: BMIs
- NDE Technique: Eddy Current
- Measures: Location/Length of Surface Breaking Flaws
- Data Acquisition: Manual Scans [Measurements & Probe Translation/Rotation]
- Access: J-Groove Weld Surface
- Measurement Instrument: CoreStar Omni 200
- Probe:
  - $\geq 50$ kHz Flexible Array [Southwest Research Institute 201115836-003]
  - 9 coils arranged in a 3x3 square matrix configuration
  - Designed to detect relatively large flaws on rough welded surfaces
- Signal Processing: None
- Signal Analysis/Interpretation: Manual
  - Visually estimate locations of ends of flaws using 6dB drop from maximum amplitude.
  - Manually mark the location on the test block of the 6dB point through the hole in the probe centered between the exciter/receiver coils.
  - Use a Coordinate Measurement Machine (CMM) to determine the X,Y coordinates of the flaw end points with respect to the R, $\theta$ ,Z zero point as defined in the protocol
  - Translate X,Y coordinates to R, $\theta$ .

## Test Team's Assessment of the Technique

- Test Blocks Types Examined: BMIs
- NDE Technique: Eddy Current
- Measures: Location/Length of Surface Breaking Flaws
- Data Acquisition: Manual Scans [Measurements & Probe Translation/Rotation]
- Access: J-Groove Weld Surface
- Measurement Instrument: CoreStar Omni 200
- Probe:
  - $\geq 50$ kHz Flexible Array [Southwest Research Institute 201115836-003]
  - 9 coils arranged in a 3x3 square matrix configuration
  - Designed to detect relatively large flaws on rough welded surfaces
- Signal Processing: None
- Signal Analysis/Interpretation: Manual
  - Visually estimate locations of ends of flaws using 6dB drop from maximum amplitude.
  - Manually mark the location on the test block of the 6dB point through the hole in the probe centered between the exciter/receiver coils.
  - Use a Coordinate Measurement Machine (CMM) to determine the X,Y coordinates of the flaw end points with respect to the R, $\theta$ ,Z zero point as defined in the protocol
  - Translate X,Y coordinates to R, $\theta$ .

## Test Team's Assessment of the Technique

### Advantages:

- Low cost for the part of the probe that will be subject to wear
- Possibility of manufacturing with even greater number of coils to ensure 100% coverage with a single scan
- Fabrication technique ensures accurate manufacturing repeatability
- Probe flexibility greatly simplifies the motions required of a mechanized scanner, especially in the case of penetrations that are not normal to the vessel surface

### Disadvantages:

- The use of single layer flexible printed circuit material (used to provide great flexibility) limits the number of turns of the coil; hence the spatial resolution is limited and the operating frequency had to be kept at 50 kHz or greater

## C.1.5 USA Technique 7-PA1

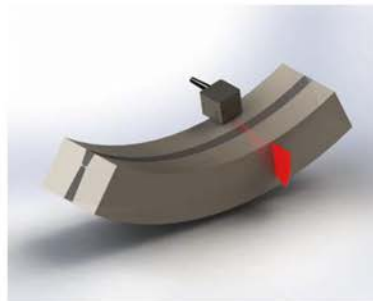
### Technical Description for Technique 7-PA1 & 7-PA2

#### Overview

- Technique 7-PA1: Detection, Characterization, Length Sizing, Positioning
- Technique 7-PA2: Depth Sizing

#### Common to Both Techniques:

- Test Block Type Examined: DMWs
- NDE Technique: Ultrasonic Phased Array
- Data Acquisition: Automated, Encoded
- Access: Inner Diameter
- Equipment: Zetec Tomoscan-III 32/128 [128 Phased Array Channels]
- Data Analysis Software: Ultravision 1
- Examination Directions: Upstream, Downstream, Clockwise, Counter-clockwise
- Probe Frequency: 1.5MHz





## Technique Specifics

### Common to Technique 7-PA1:

- Focal Law Gain: 14dB
- Examination Angles:
  - Circumferential & Axial Flaws: 60-88°, 2° Increments
- Maximum Increment Resolution: 0.05" (axial flaws), 0.15" (circumferential flaws)
- Detection: C-scan indications that exhibit echo-dynamics in the B-scan are considered to be flaws
- Characterization: Surface breaking if A-scan shows flaw signal at 0 inches.
- Length Sizing: Determined by measuring the ¼ maximum amplitude in a full-merged C-Scan (top view) for axial and circumferential flaws

### Common to Technique 7-PA2:

- Focal Law Gain: 20 dB
- Examination Angles:
  - Circumferential Flaws: 30-70°, 1° Increments
  - Axial Flaws: 60-82° & 40-46°, 2° Increments
  - Maximum Increment Resolution: 0.10" (axial & circumferential flaws)
  - Depth Sizing: Employs a methodology that uses information from merged and unmerged B-scans and D-scans.

## Test Team's Assessment of the Procedure/Technique

### Advantages:

- The use of multiple inspection angles increases the probability of detection.
- Allows for sectorial scanning and simplification of DMW's with complex geometry.
- A separate detection procedure allows larger indexing for a quicker detection examination.

### Disadvantages:

- A more complex examination technique which requires personnel with proper training and /or experience to implement it.
- A separate depth sizing examination at smaller indexing is required after flaw detection is completed.

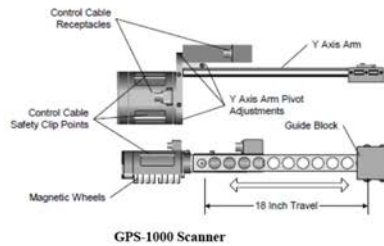
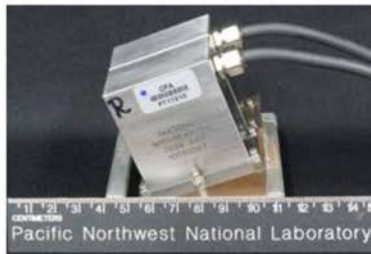
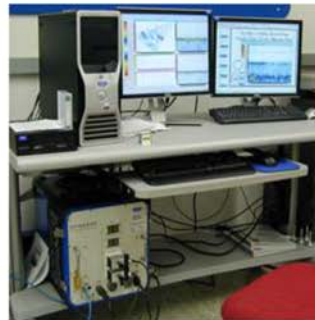
## C.1.6 ISA Technique 150-PA0

# Technical Description for Technique 150-PA0

## Phased Array Data Acquisition Equipment



0.2 – 20 MHz  
256 channels  
Ultravision® software

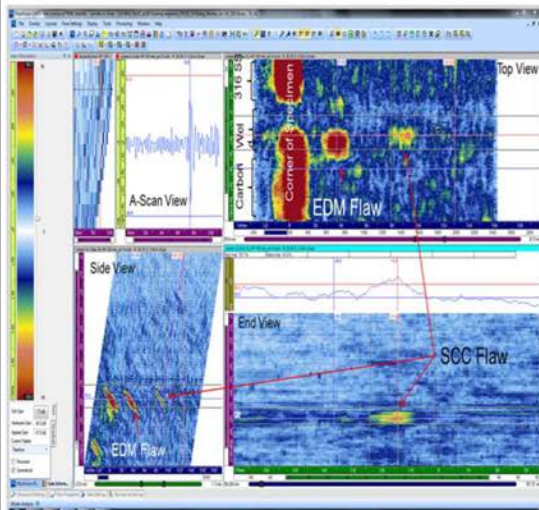


Probe and Scanner Configuration

## Pulsing and Scanning Parameters

- ▶ 1.0 MHz 2x(10x5) element matrix array [10 Elements in Primary]
  - Transmit-Receive Longitudinal
    - Each element pulsed with 500 ns negative 200V square wave excitation (Dynaray)
  - True Depth and Half Path focusing techniques
  - 20-60 degree azimuthal angle sweep, 3 degree increments
  - 0,±10 degree skew angles
  - OD inspection: Raster scan resolution: 1.0 mm scan, 1.0 mm index
- ▶ OD contoured Rexolite wedge
  - 15 degree wedge angle
- ▶ 0 pt., coordinates and scan conventions followed from test block information sheet
- ▶ Circumferential scans (looking for axial flaws)
  - Collect data in clockwise and counter clockwise directions
- ▶ Axial scans (looking for circumferential flaws)
  - Collect data from up stream and down stream locations
- ▶ Target Focus: Inner Diameter Regions
  - ID connected flaws (cracks)

## Data Imaging and Analysis

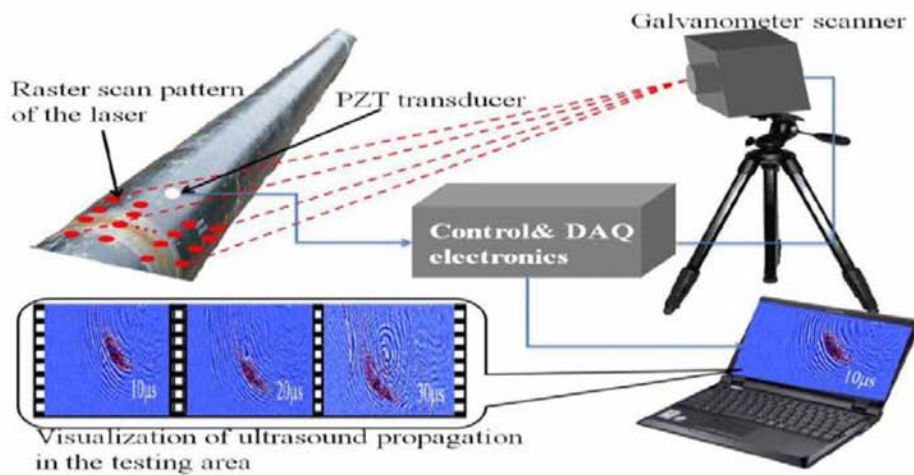


- ▶ Phased array image analysis
  - A-Scan (time-amplitude) along selected angles
  - C-Scan (Top View) scan vs. index axes – location and length of flaw
  - B-Scan (Side View) scan vs. ultrasound axes – depth of flaw
  - D-Scan (End View) index vs. ultrasound axes – length and depth of flaw
- ▶ Detection
  - Strong response signal(s) present in the ID region of component
    - Signal strength above background noise levels to be considered (greater than 6 dB above background)
- ▶ Characterization
  - Detected signals will be length sized using a -6 dB and loss of signal (LOS) method in the D-Scan view
  - Depth sizing will be assessed by measuring maximum flaw extent in the B and/or D Scan view(s)
  - Overall flaw circumferential and axial location assessed with C-Scan view

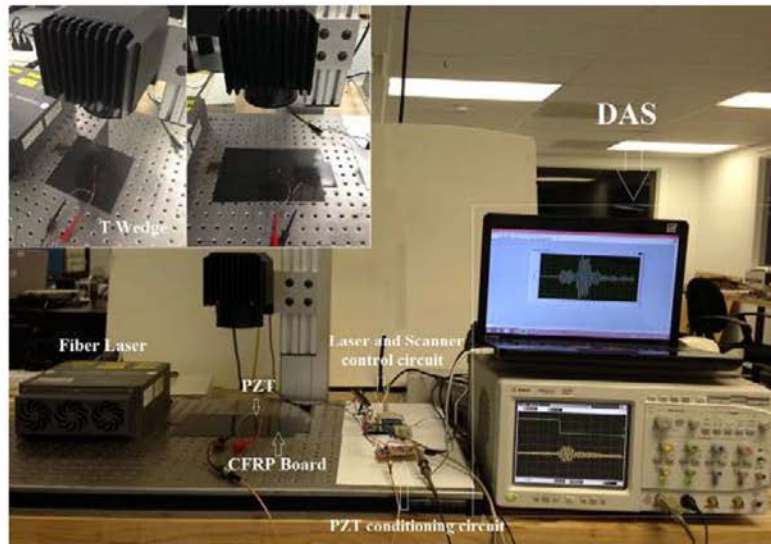
C.1.7 USA Technique 170-LUV0

**Technical Description for Technique  
170-LUV0**

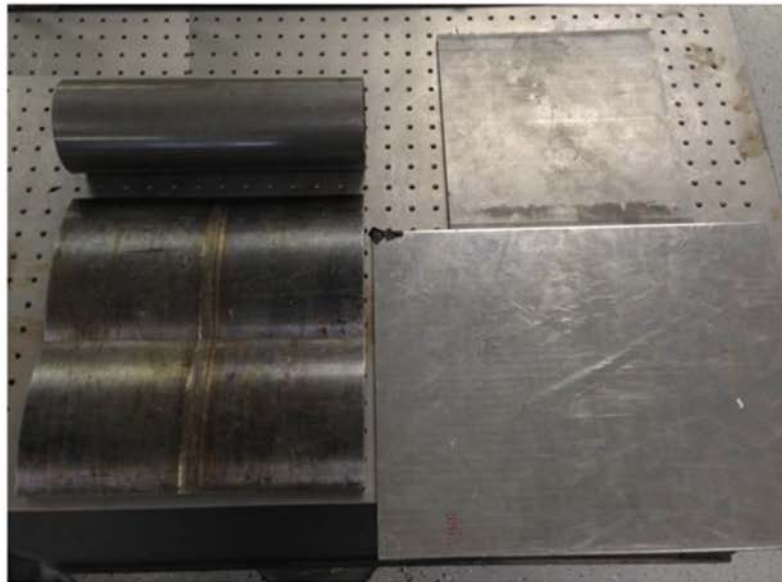
**Laser Ultrasound Visualization (LUV) Technique**



## Experimental System



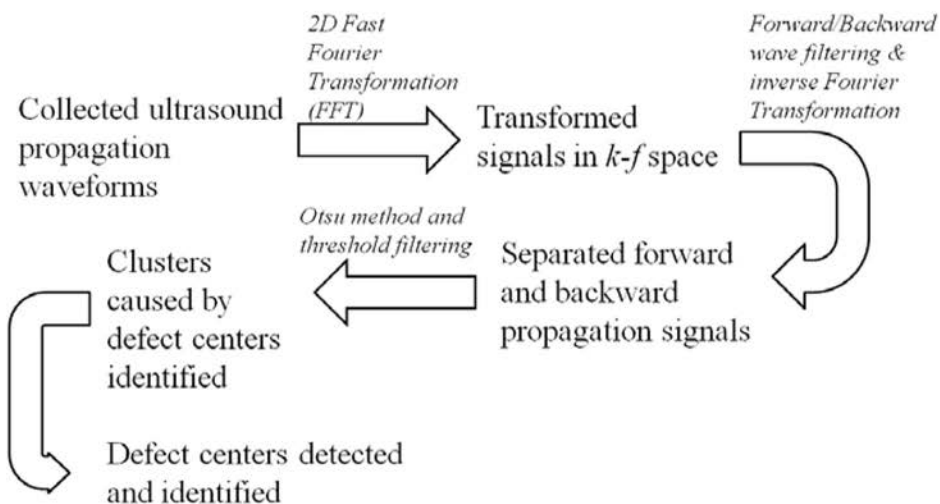
## Experimental Samples



## Overview

- Test Blocks Types Examined: BMIs & DMWs
- NDE Technique: Laser Ultrasound Visualization
- Measures:
  - Detects/Locates surface and sub-surface flaws (flaws within the material)
  - Depth/Length sizing capability is to be determined
- Data Acquisition: Automated
  - Spatial Sampling Step Size:  $\sim 1$ –several mm
  - Sampling Rate:  $5\text{-}20 \times 10^6$  samples/second
- Access: DMW – Outer Diameter, BMI – Surface of the J-Grove Weld
- Measurement Instrument: Commercial Off The Shelf (COTS) Components
  - Laser pulse energy delivery system (thermally induced ultrasound source)
  - Miniature piezoelectric transducer (detector of ultrasound placed on inspection surface)
  - Control and data acquisition electronics system (DAS)
  - Laptop computer
  - Power source - battery
- Signal Processing Approach for Automatic Defect Detection and Location
  - See following slide
- Signal Interpretation: Visual
  - Results are displayed as time based (micro-second scale) movie clips which permit operators to directly see/visualize the propagation of the ultrasound signals in time.
  - Cracks, voids, welding flaws, can easily be visualized by minimally trained personnel.

## Algorithm for Automatic Defect Detection & Location



## Test Team's Assessment of the Technique

### Advantages:

- Makes it possible to detect/identify flaws with a 2-dimensional image versus the 1-dimensional method of traditional ultrasound.
- Detection of flaws with 1-dimensional waveforms is confounded by the propagation modes, boundary reflections, and physical features that heavily convolute the ultrasonic waveforms propagating in real-world weld structures. Complicated modeling is often necessary to overcome these limitations. The LUV technique makes it possible to directly visualize flaws in complicated shapes and configurations.
- Compact, lightweight, portable
- Capable of detecting a wide variety of defects
- Compatible with complex shapes and configurations
- High sensitivity (excellent signal/noise ratio) and good spatial resolution (better than 1mm)
- High measurement throughput – 2m/second X/Y scan speed
- Safe to operators – involves no harmful radiation

### Disadvantages:

- Undetermined\*
  - \*The ability of this technique to accurately length size and depth size flaws in BMI/DMW configurations is under investigation, so is unknown at this time.

## C.2 Europe Detailed Technique Descriptions

### C.2.1 Through Transmission of Longitudinal Waves, Technique ID 104-UT-P/C0

#### C.2.1.1 Overview

Trough transmission of ultrasonic longitudinal waves is amongst others used for detection of delaminations in composites with difficult accoustic properties. Normally the delaminations are expected to be parallel to the inspection surface and sender and receiver probe are on oposite sides of the part to be inspected. In case of a delamiation the sound will be blocked and therefore the receiving probe will detect a reduced amplitude.

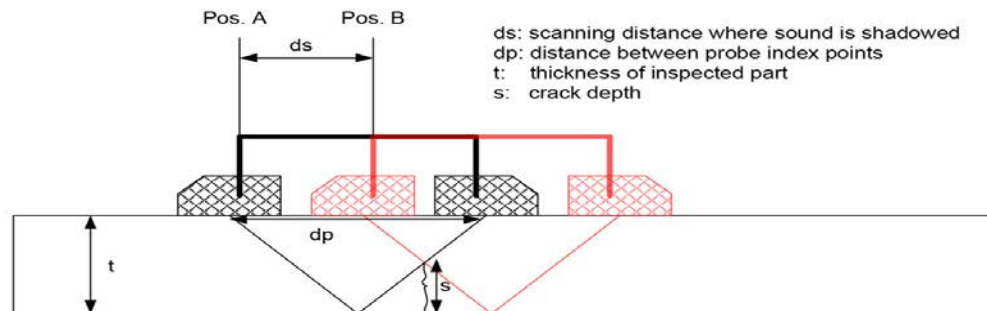
For this application there are mainly two things different:

1. The orientation of the crack is more or less perpendicular to the surface.
2. There is only access from one side

To get an interaction between crack and sound beam and to be able to measure the depth extension of the crack, through transmission with angle beam is necessary.

To overcome the problem with the not accessible back wall, the receiving probe will be placed on the same surface as the sending probe and one reflection on the back wall will be used.

With the set-up shown in Figure C.1, it is possible to detect and measure cracks perpendicular to the surface:



**Set-up:**

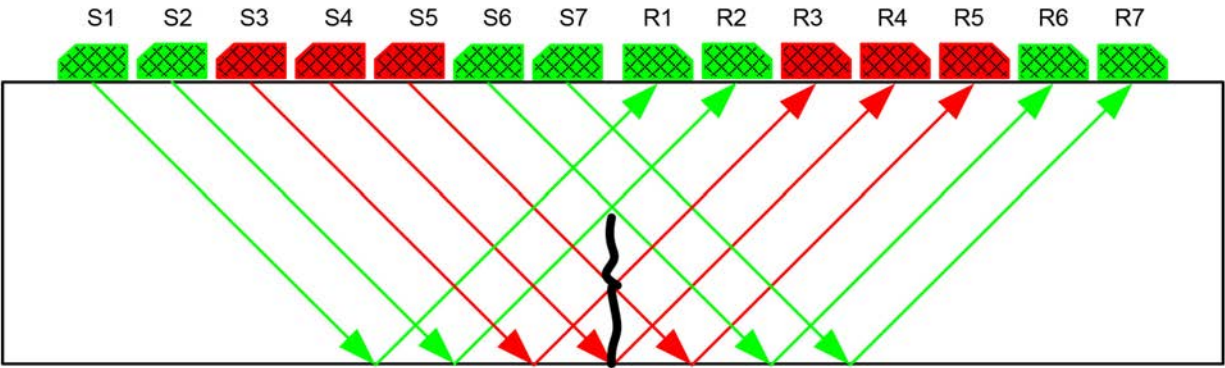
- Two identical probes (aperture, frequency, angle) with an angle of about 40° to 45° (long), fixed in a probe holder.
- Distance between probe index points is optimized to receive the reflected longitudinal wave from the backwall (LL)
- Probe holder is moved over the surface and the distance where sound is shadowed by the crack will be stored (B-scan of the received signal)

Crack depth is given by the following formula:

$$s = ds * t / dp$$

**Figure C.1 Illustration of Inspection Set-up and Calculation of Depth Extension of Crack**





Sound is sent from S1 via back wall to R1, from S2 to R2 etc. As long as there is no discontinuity on the sound path the receiver will detect high amplitude (green). In case sound is blocked by a discontinuity (red) the receiver will detect much lower amplitude. The received amplitude can then be displayed on a C-Scan representation and calculation described in Figure C.1 can be done using this C-Scan. Figure C.4 shows such a C-Scan.

**Figure C.2 Inspection Principle**

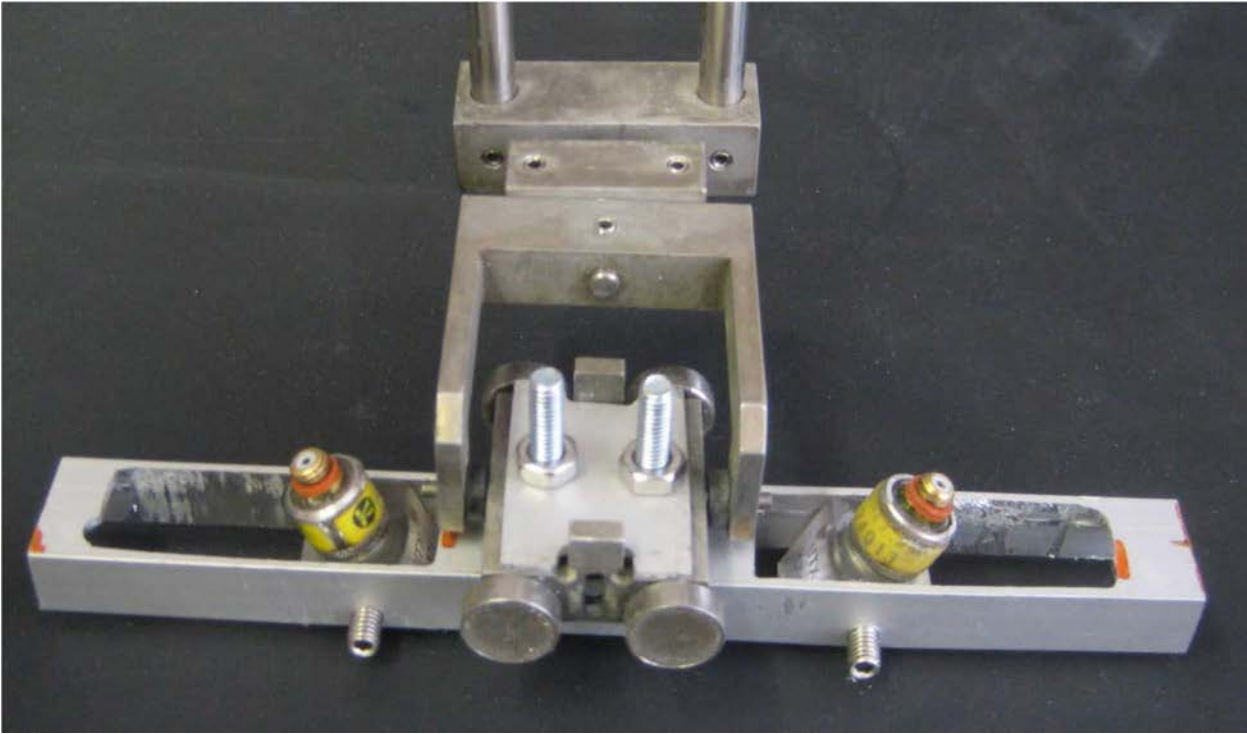
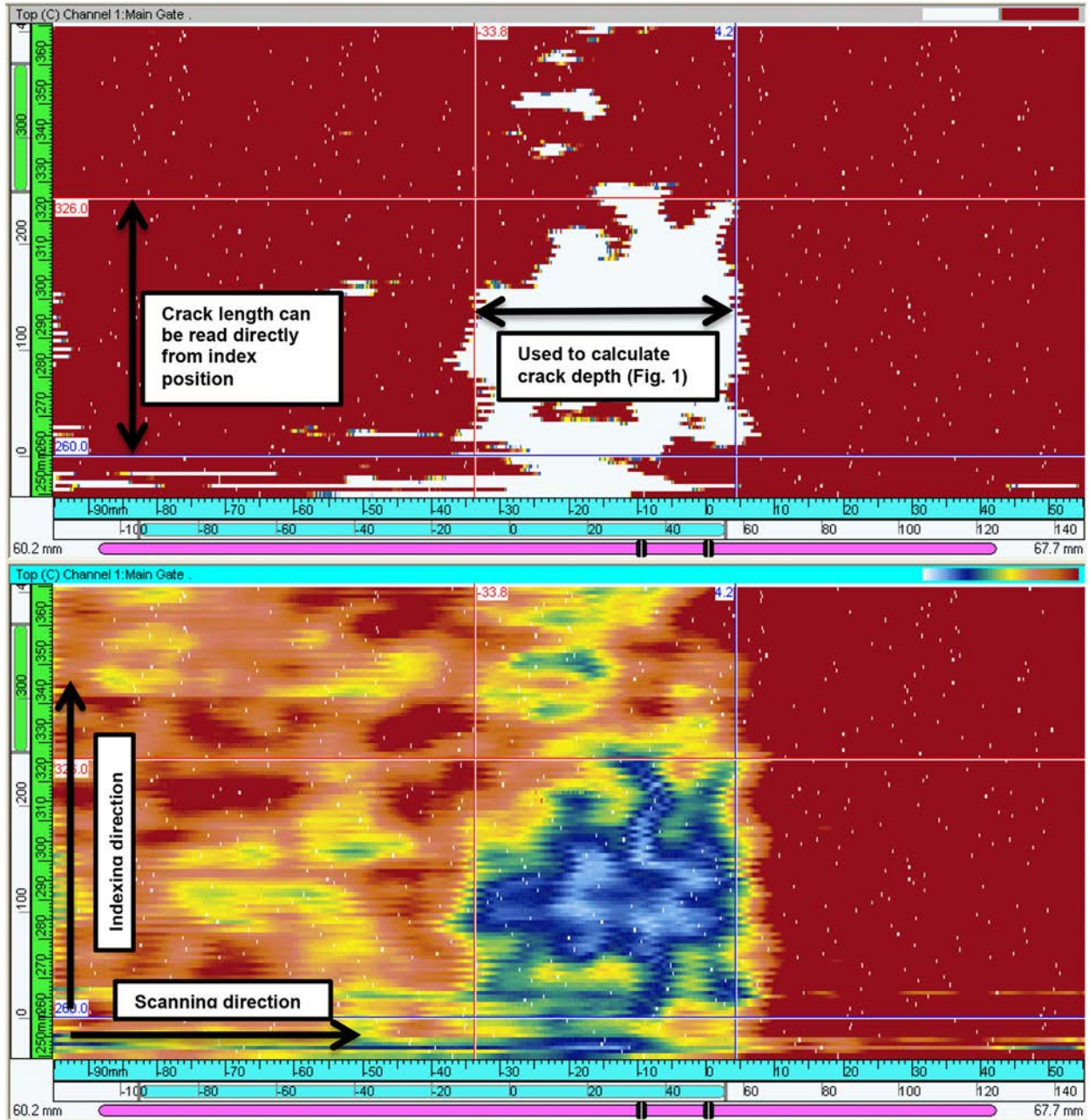


**Figure C.3 Probe Holder with Defined Distance between Sender and Receiver**

To allow offline evaluation of the data the full A-scan information needs to be stored together with position information (X and Y coordinates).



The lower C-Scan shows the received amplitude color coded (0% FSH [white] to 100% FSH [red]). The upper C-Scan shows the C-Scan after using a 6 dB drop filter (0% to 50 % FSH [white] and 50% to 100% FSH [red]). On the left side of the C-Scans the influence of the cladding is visible. The attenuation caused by the cladding is a limiting factor and if it's too high it can make inspection impossible.

**Figure C.4 Example of C-Scan Representation Used for Evaluation (circumferential flaw, open to inner surface)**

### **C.2.1.2 NDE Equipment**

A ZScan PA 64 (ZPA5022) from ZETEC together with Ultravision software was used for data acquisition. To facilitate coupling the part to be inspected was immersed in water. An XYZ-scanner was used to move the probe holder over the surface of the part. Encoder information from the scanner was provided to the ZScan to be stored together with A-scan data.

Two Panametrics probes were used:

- C548-SM with a diameter of 10 mm and a frequency of 1.0 MHz (sender)
- A548-SM with a diameter of 10 mm and a frequency of 1.5 MHz (receiver)

Rexolite wedges were used and their angle was machined to get an incident angle of 45° longitudinal wave in the test piece.

Distance between the probe indices is set to two times the wall thickness of the part to be inspected.

### **C.2.1.3 Data Acquisition Process (for defects with circumferential orientation)**

The probe holder was placed on the outer surface of the part to be inspected in a way that the direction from sender to receiver was parallel to the axial direction of the tube. This set-up is only valid for circumferential crack orientation.

After start of data acquisition in Ultravision the scanner was started as well. Scanning direction was in axial direction and the scanning length was set in a way that both probes were passing weld, buttering and HAZ. After one scan line the probe holder was shifted in circumferential direction (index) and a scan in opposite direction to the first one was performed.

Like this a certain circumferential range was tested. This range was limited due to the fact that it was not possible to rotate the part while scanning and the probe holder was only able to compensate a limited change of the surface orientation.

### **C.2.1.4 Data Analysis**

C-scan of 45° LL reflection of back wall was evaluated:

Where no (perpendicular) crack is present the back wall will be detected with high amplitude. At positions where the sound path from sender to receiver is affected by the crack the amplitude will drop. 6 dB drop compared to sound material will be used to define the extensions of the flaw. Additionally pattern recognition will be used.

A crack connected to the inner surface will result in a C-scan where the area with amplitude drop will be continuous whereas an inclusion or lack of fusion will result in two individual (mirrored) areas with amplitude drop).

Length of the crack corresponds to the scanning index distance where the crack will be detected.

Crack depth is calculated from the scanning distance where a drop of amplitude is detected. For calculation of crack depth compare sketch and formula in Figure C.1.

Sizing technique will be used for defect positioning. Centerline (perpendicular to scanning direction) of the area with amplitude drop will be used as defect position whereas the mechanical reference of the C-scan will be the center of the probe assembly.

### C.2.1.5 Self Assessment

Advantages of this UT inspection technique are:

- No influence of flaw surface roughness
- Orientation of flaw doesn't influence detectability
- Very low noise from scattered sound (grain boundaries...), therefore higher frequencies can be used

Disadvantage of this approach are:

- Cladding of the surface influences the amplitude of transmitted sound and therefore alters the inspection results
- A parallel inner surface is necessary. Otherwise Scanning becomes difficult (position dependent distance and/or inspection angle of sender and receiver probe).
- Altered microstructure influences the inspection result. This is mainly the problem when artificial flaws are produced by local heating or welding / brazing of a defective volume into the reference block.

## C.2.2 Phased Ultrasonic Array, Technique ID 131-PA0

### C.2.2.1 Overview

The techniques described in this report were utilized for the examination of the -specimens P28, P29, P30, P31, P32, P42 and P46.

Method	Phased Array Ultrasonic Testing
Array / Technique	Single / Linear / Pulse Echo
Wave Mode	Longitudinal
Angle Range	40° – 70°
Frequency	2.33 MHz
UT Instrument	M2M MultiX 64
Scan Plan	Encoded in +Y and – Y direction
Scanning Surface	W & X

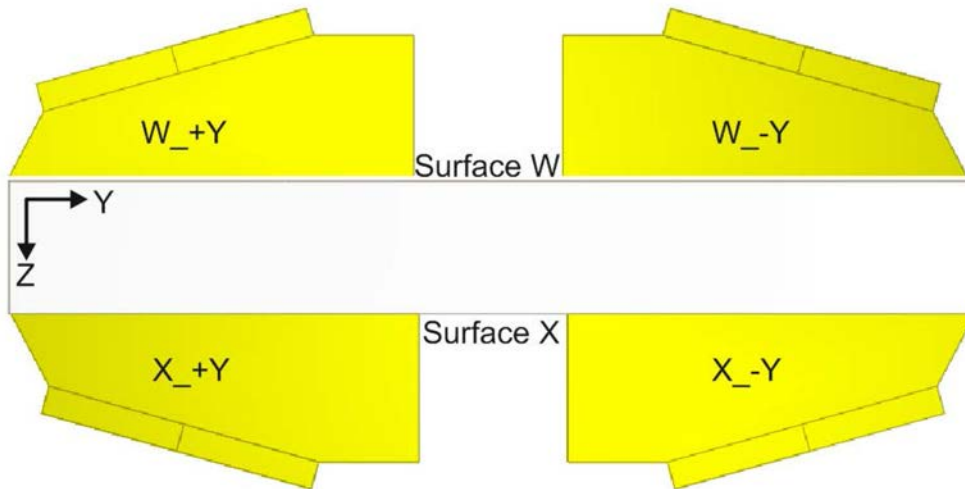
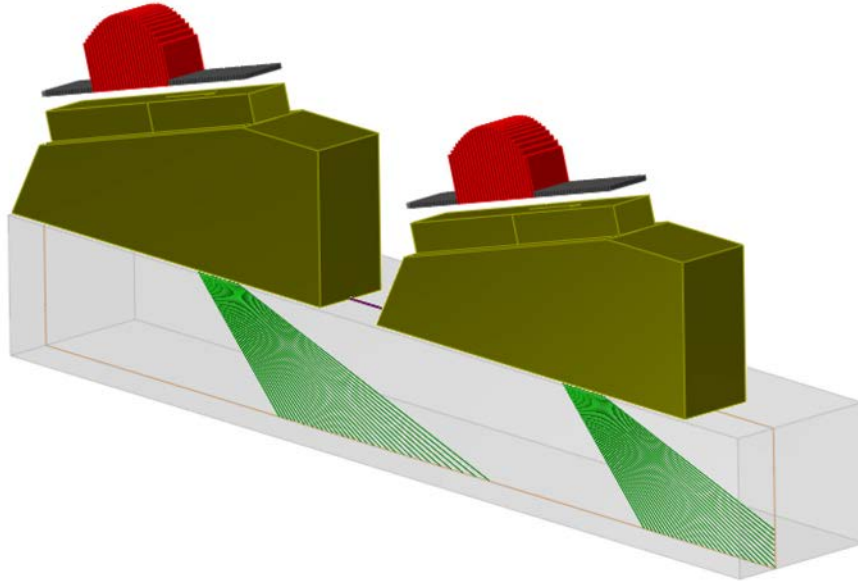


**Figure C.5 Technique Overview Illustrations**

**C.2.2.2 NDE Equipment / UT Settings**

**Search Unit**

For the measurement a sonaxis probe and wedge was used. The essential variables of the search unit are described below.

## Crystal Shape

Crystal shape **Focusing** Wedge Instrumentation Signal

Pattern Linear phased array

Phased array

Whole aperture

Incident dimension 63.9 mm

Orthogonal dimension 10 mm

Grid and gap

Number of elements 64

Gap between elements 0.1 mm

Dimensions and arrangement of elements

Element width 0.9 mm

Numbering

12 %  Top  0°  
 Bottom  +90°




Figure C.6

## Focusing

Crystal shape **Focusing** Wedge Instrumentation Signal

Surface type Flat

Focusing type  Shaped element

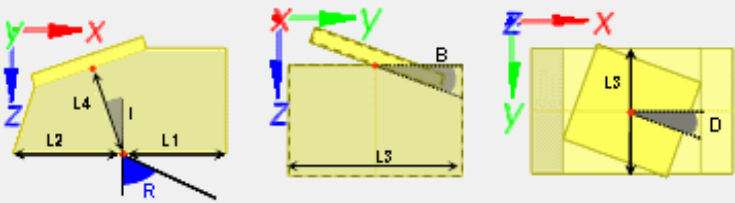
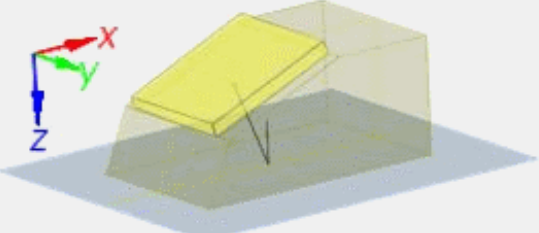
Figure C.7

## Wedge

Crystal shape Focusing Wedge Instrumentation Signal

Wedge Geometry (contact surface) ————

Wedge Geometry Flat



Front length (L1)  mm

Back length (L2)  mm

Width (L3)  mm

Height (L4)  mm

Crystal orientation ————

Refraction angle (R)  deg

Incidence angle (I)  deg

Other angles ————

Squint angle (B)  deg

Disorientation (D)  deg

Wave type ———— Propagation parameters ————

Wave type  Longitudinal  Transverse

Longitudinal wave velocity   $ms^{-1}$

Transverse wave velocity   $ms^{-1}$

Figure C.8

Signal

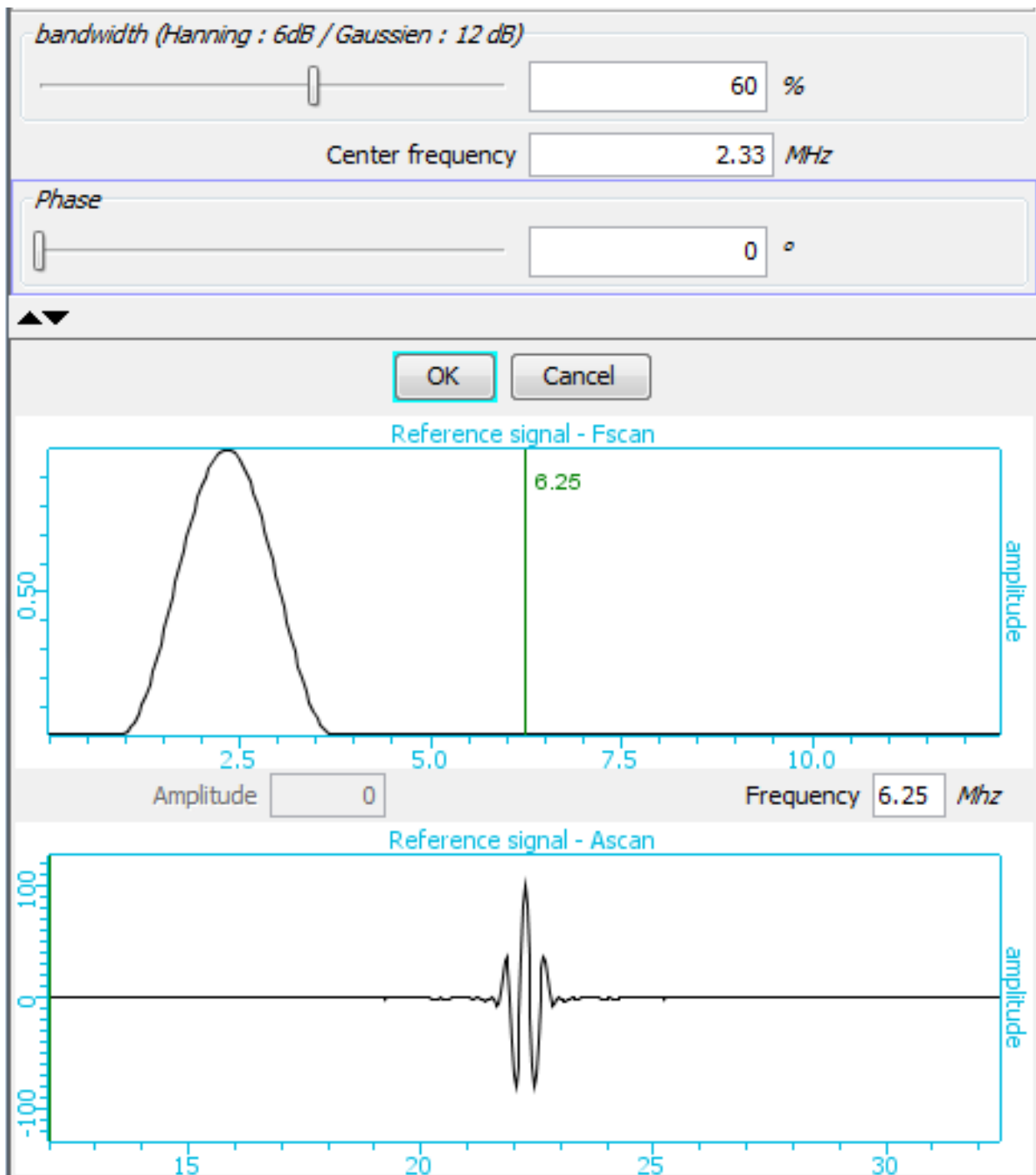
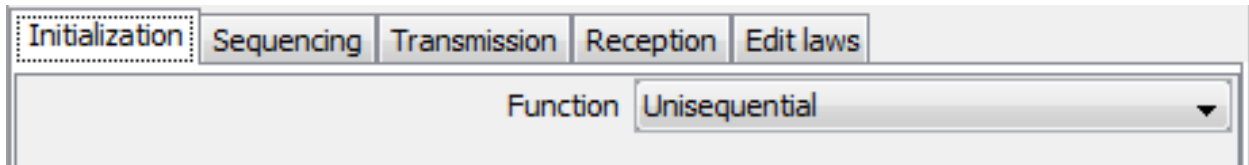


Figure C.9



## Phased Array Settings – Focal Law

### Initialization



**Figure C.10**

### Sequencing

The number and position of used elements was chosen to get good beam properties in the range of the expected flaw depth. The values are specified in the Cal and DAC Files of each specimen. The figure below shows an active aperture of 24 Elements (17 to 41).

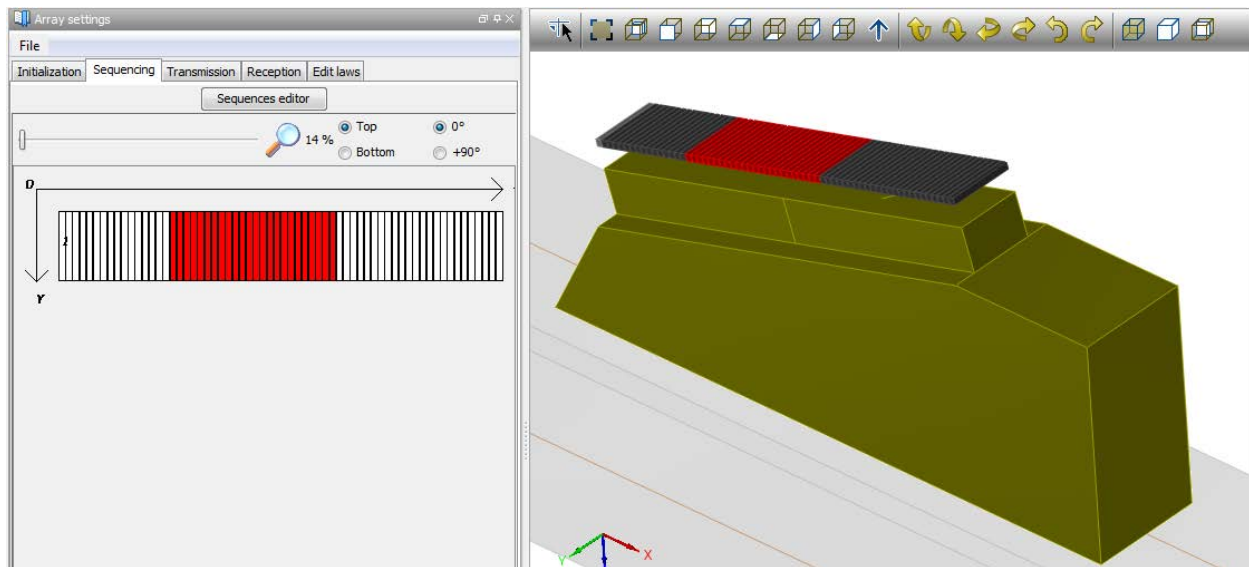
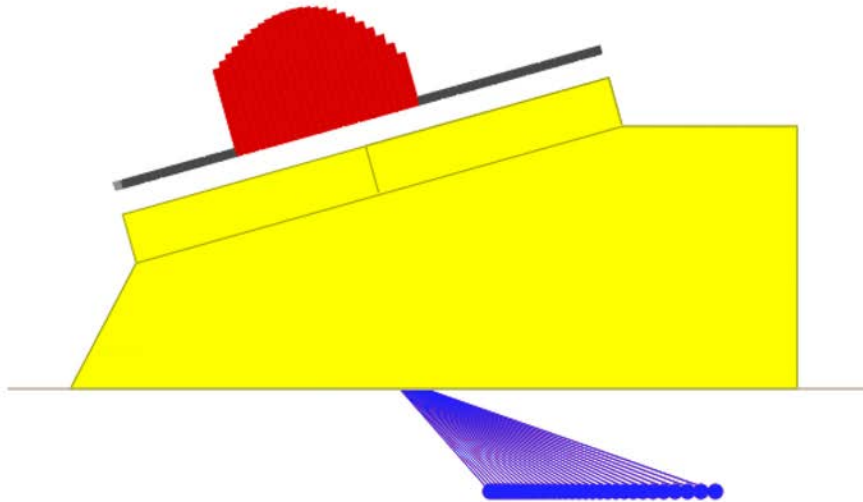


**Figure C.11**

### Transmission

The sector range goes for all measurements from 40° to 70° (Step 1°) Longwaves. The focal depth was chosen to get good beam properties in the range of the expected flaw depth. The values are specified in the Cal and DAC Files of each specimen. The figure below shows an example of the calculated focal points at 13 mm depth.



Initialization Sequencing **Transmission** Reception Edit laws

Transmission definition

Focusing type: Direction and depth scanning

Algorithm:  Optimized point  Geometrical point

Number of steps: 31

---

Extremity n°1

Angle	40	deg
Depth	13	mm
X	117.124	mm
Y	17.5	mm
Z	13	mm

Extremity n°2

Angle	70	deg
Depth	13	mm
X	145.642	mm
Y	17.5	mm
Z	13	mm

---

Delay law calculation

Wave type:  Longitudinal waves  Transversal waves

Figure C.12

## UT Equipment Settings - M2M MultiX 64

For the measurements a M2M MultiX UT System was used. MultiX system is a fully parallel architecture with 64 channels. In the following chapters the essential equipment settings are listed.

### General Settings

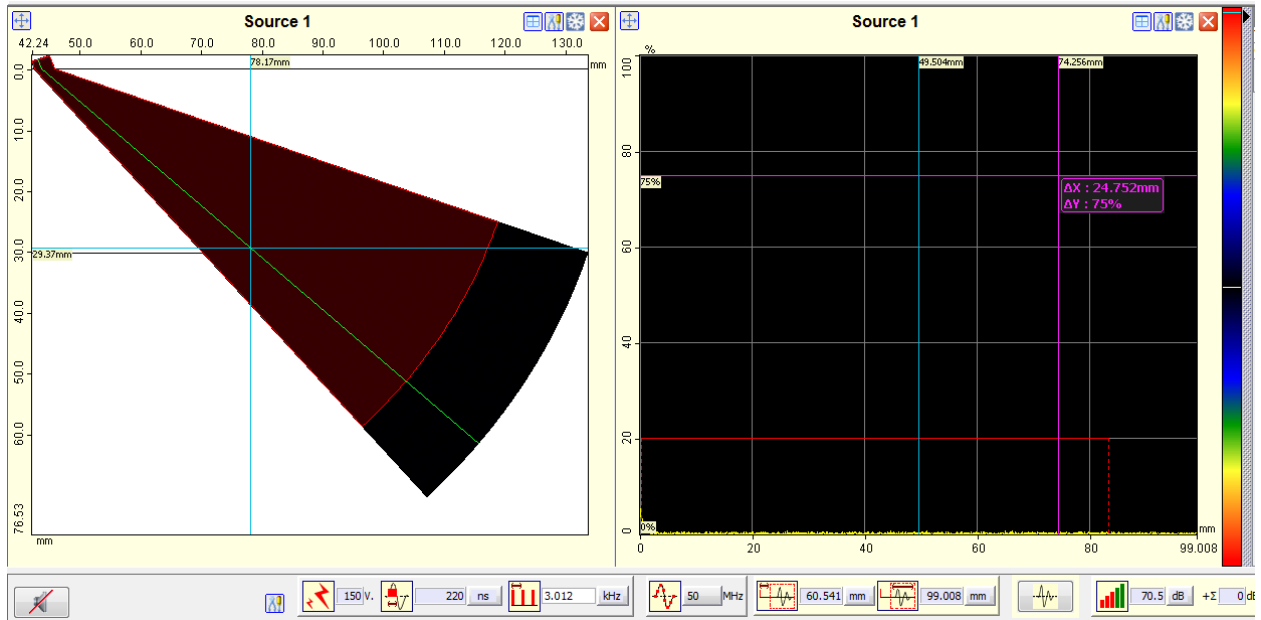


Figure C.13

### Gates

Identity		Acquisition-Storage			Position and size				Processing						
N°	Name	Color	State	Store Peaks-E-Elem	Threshold time gate	Setting mode	Start (mm)	Width (mm)	End (mm)	Height (%)	Detection Mode	No Echo	Delta Time (mm)	Synchro Start	Synchro End
1	Gate 1	Red	✓	Peaks+Σ	Always	Green	0.119	83.181	83.3	20.09	Echo Max (Abo)	1	0.744	Transmission	None

Figure C.14

### DAC

Calibration		
Analog		
DAC <input checked="" type="checkbox"/> Enable <input type="checkbox"/> Synchronized <input type="checkbox"/>		
Index_point	Position (mm)	Amplitude (db)

Figure C.15

## Coders

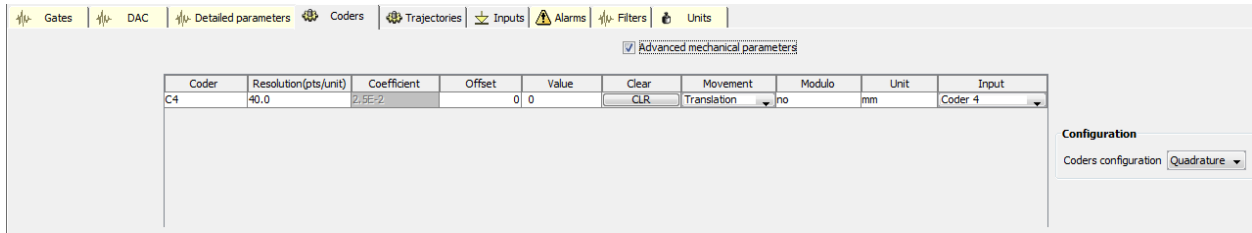


Figure C.16

## Trajectories

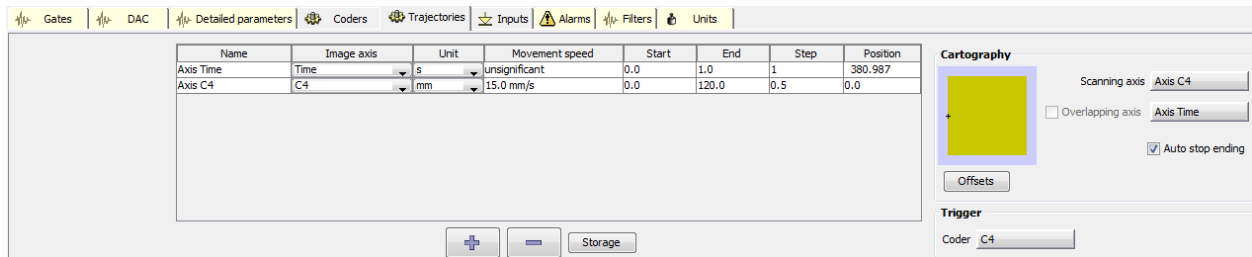


Figure C.17

## Filters

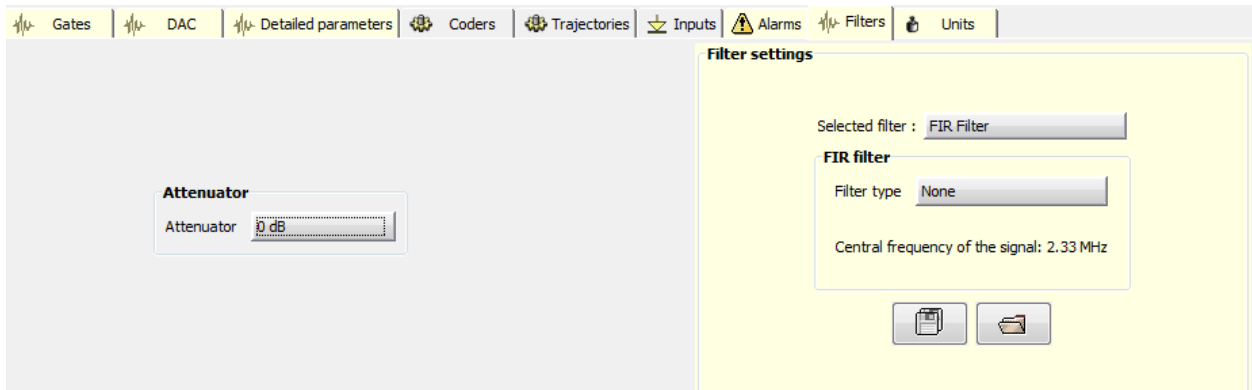


Figure C.18

## Units

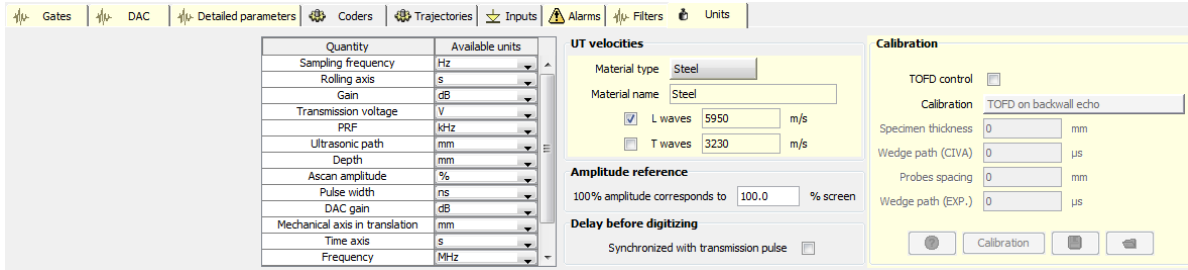


Figure C.19

### Calibration

The calibration of the measurement system were conducted direct before data acquisition. In the following sections the calibration process is described.

#### Probe Element Check (PEC)

- Load File: C:\Users\Multi2000\Desktop\PARENT\_L40-70 Contact\02 Default Cal Files\PEC\_Sonaxis\_64.m2K
- Perform PEC (configuration see figure below)
- Pass criterions: continuous slope - correct wiring, delta dB < 9dB
- Document PEC in Cal Sheet

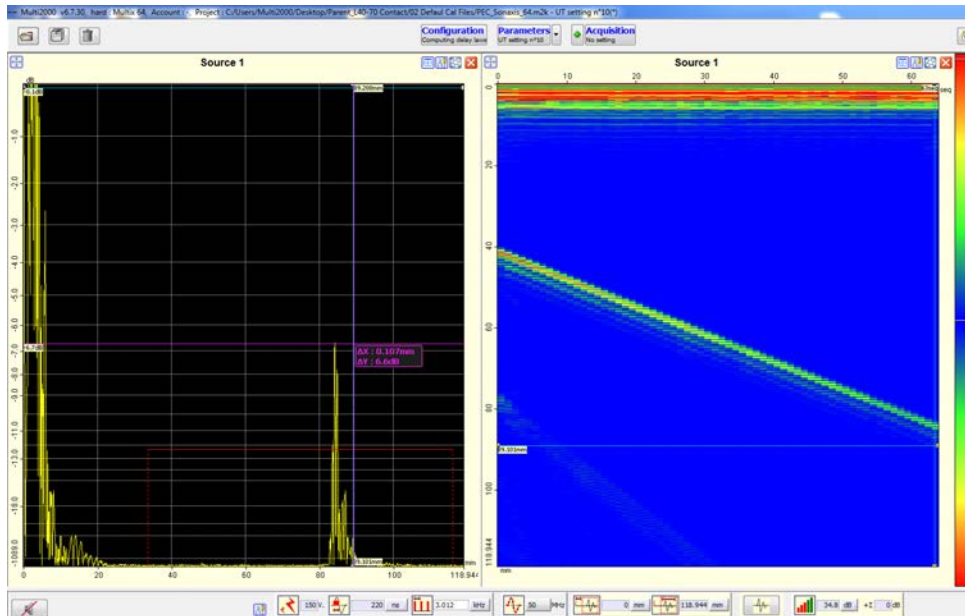


Figure C.20

### Wedge Calibration

- M2M > Parameters > Wedge Calibration
- Drag and Drop Bscan
- Set and adjust the gate on the wedge shoe echo
- Start wedge calibration
- Write values for Computed Angle and Computed Height on Cal Sheet

### Define Inspection Configuration

- Load Cal File: Cal\*\_\*Ele\_FD\*\*\_\*\_Notch.m2k
- M2M > Configuration > Probe > Wedge > Insert correct values for Computed Angle and Computed Height (see Cal Sheet)
- Array settings > Input Pattern > Safe
- Array settings > Transmission > Input Focal Depth, and compute Focal Laws
- Change to Parameters by clicking Apply

### Probe Exit Point

- Choose shot in Sscan with angle nearest to 50°
- Find Ascan maximum at 100mm radius of ferritic K1, mark the position with green ink on wedge (see picture below), document Reference Sensitivity (FSH) and Probe Index Point on Cal Sheet



**Figure C.21**

Refracted Angle

- Measure Refracted Angle  $50^\circ$  on ferritic K1, document the value in Cal Sheet (see picture below)



**Figure C.22**

### Depth Calibration

- Bring Cal Block **KKM\_24\_18\_12\_6** (see figure below) 18mm notch tip to 80% screen height using the 50° angle, document
  - gain/echo height
  - path length (PL) and TWS (Depth)
  - S/N

in Cal Sheet (in case of OD notch start with 6mm notch)



**Figure C.23**

- bring Cal Block **KKM\_24\_18\_12\_6** 12mm notch tip to maximum using the 50° angle, document echo height, path length/TWS and S/N in Cal Sheet
- bring Cal Block **KKM\_24\_18\_12\_6** 12mm notch tip to maximum using the 50° angle, document echo height, path length/TWS and S/N in Cal Sheet
- Save the Cal file
- Save the measurement file

PARENT\_OT\_ENSI\_L40-70\_AAE\_FDBB\_C\_PCC\_D\_+E.m2k

AA > Number of Elements

BB > Focal Depth

CC > Specimen Number



D > Scan surface according to figure coordinate system (W or X)  
E > Beam Direction (+Y or -Y)

### C.2.2.3 Data Acquisition

The figure below shows a picture of the measurement setup. A simple string encoder was used for encoded data acquisition.

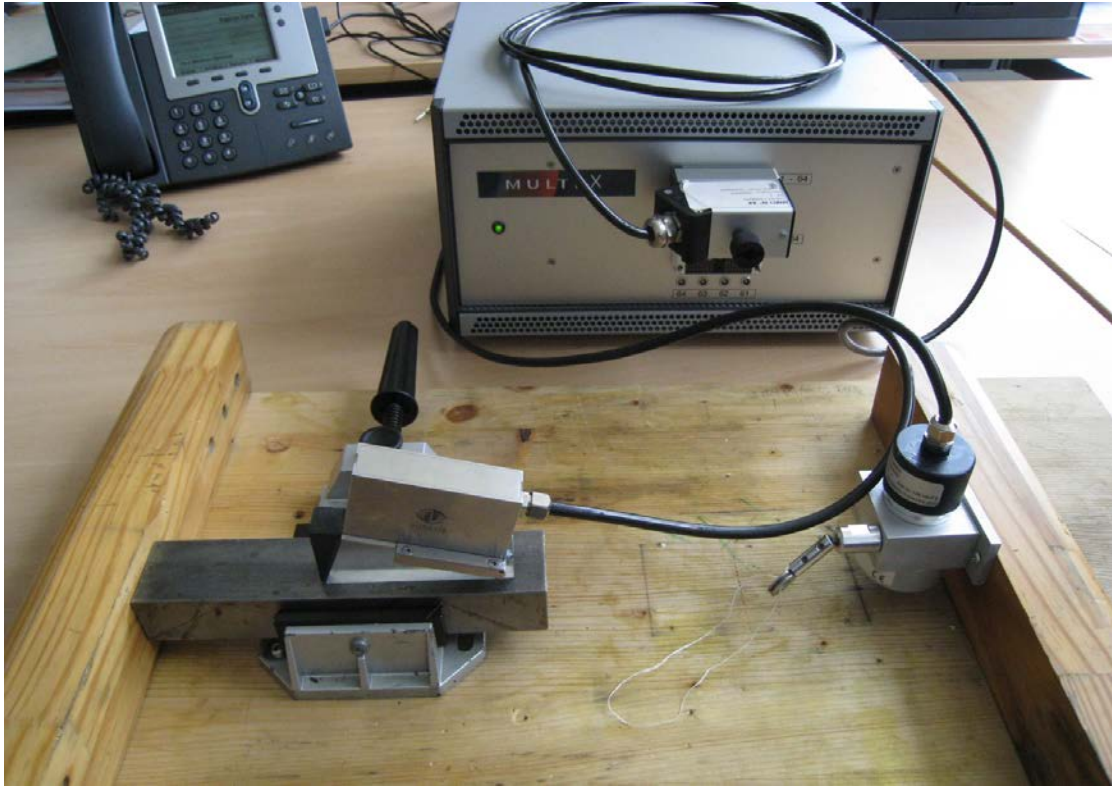


**Figure C.24**

The figures below show the scan plan. Data were just taken along one 120 mm long scan line in the center of the specimen with 0.5mm step width (240 steps).

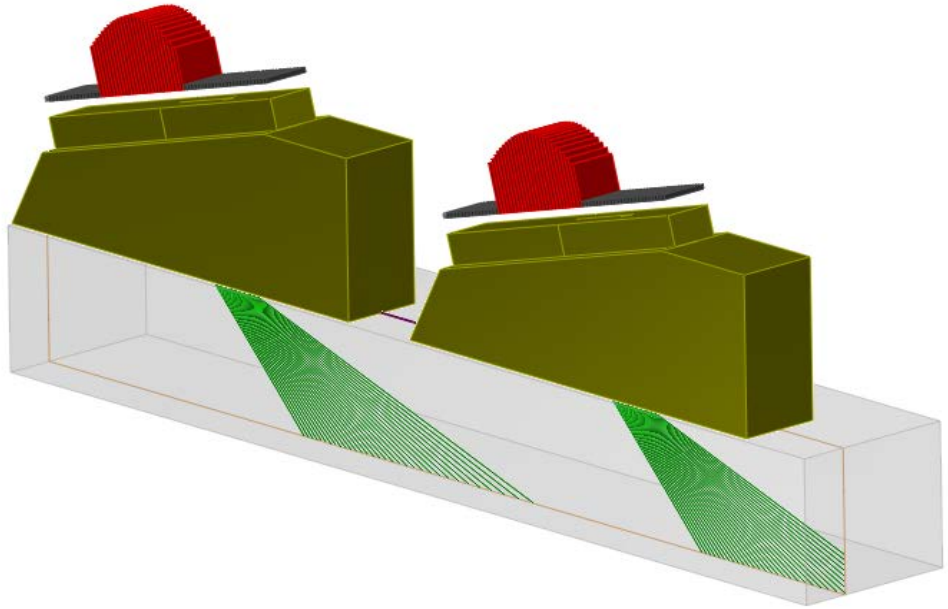


**Figure C.25**

The figure below shows the scan coordinate system and an example how it is defined in the data acquisition file name

PARENT\_OT\_ENSI\_L40-70\_24E\_FD13\_C\_P28\_W\_+Y

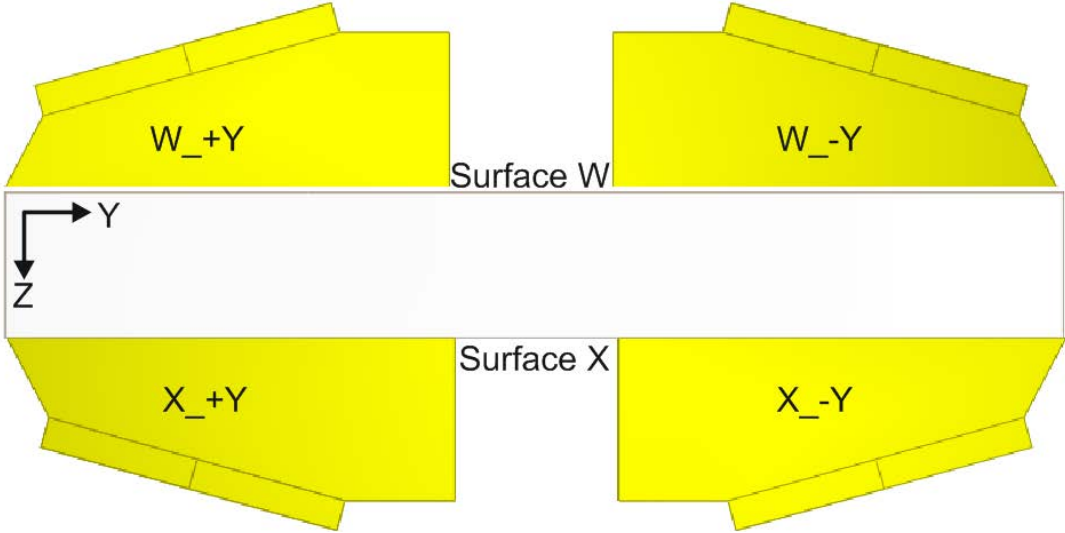


**Figure C.26**

**C.2.2.4 Data Analysis**

**Depth Sizing Technique**

For flaw depth sizing the Absolute Arrival Time Technique (AATT) is used. The technique relies upon obtaining a direct signal response from the flaw tip using a material depth calibration.

From the flaw tip response the amount of unflawed material or remaining ligament can be read directly from the Sscan. Flaw depth is calculated by subtracting the remaining ligament from the actual material thickness.

The figure below illustrates the technique.

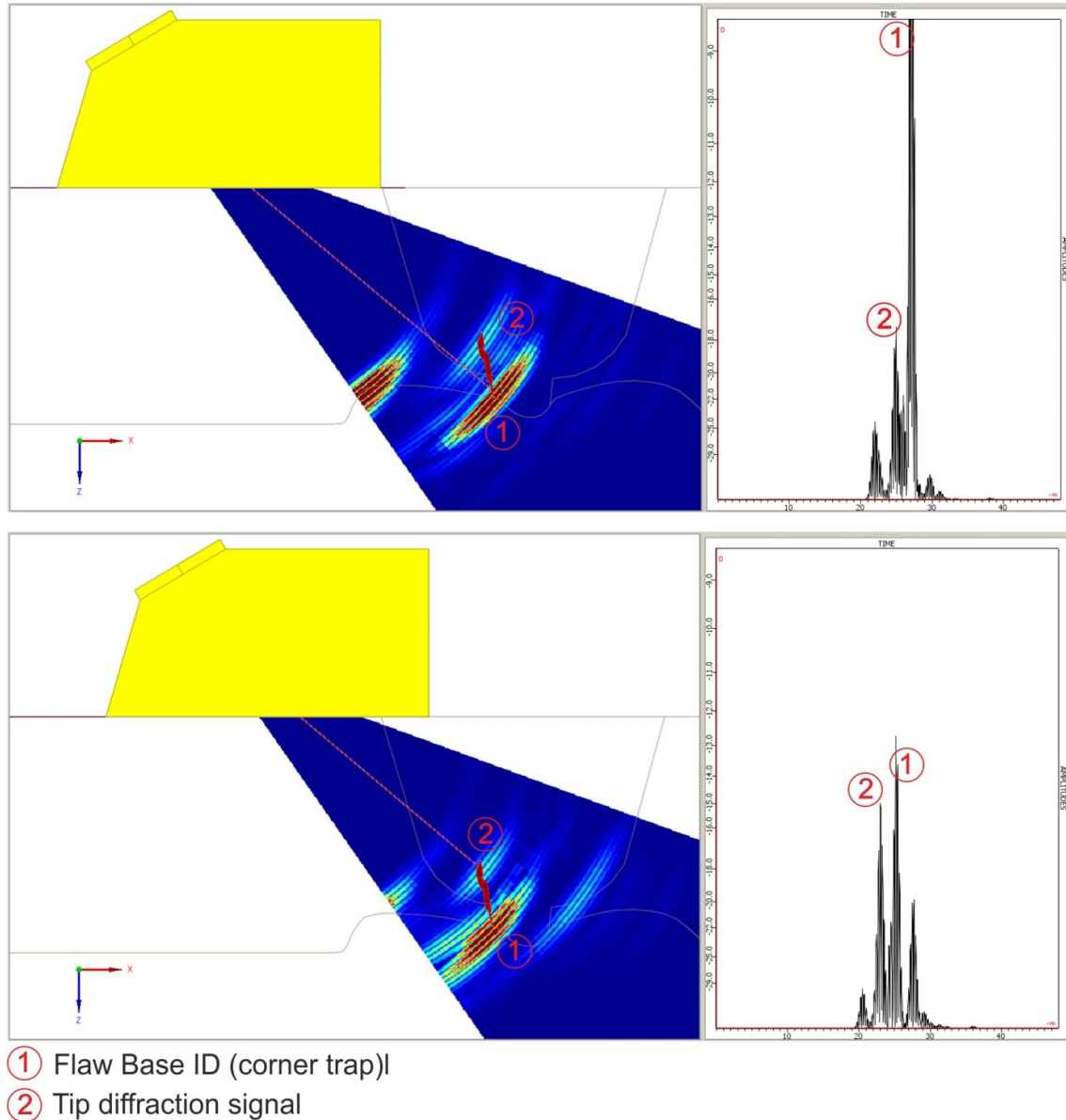


**Figure C.27**

**UT Depth Sizing Images**

The figure below shows a typical depth sizing print out used in the measurement report (2012\_Par\_OT\_ENSI Spec\_MeasReport\_L40-70C\_PE). The figure includes remarks for explanation of the UT images.

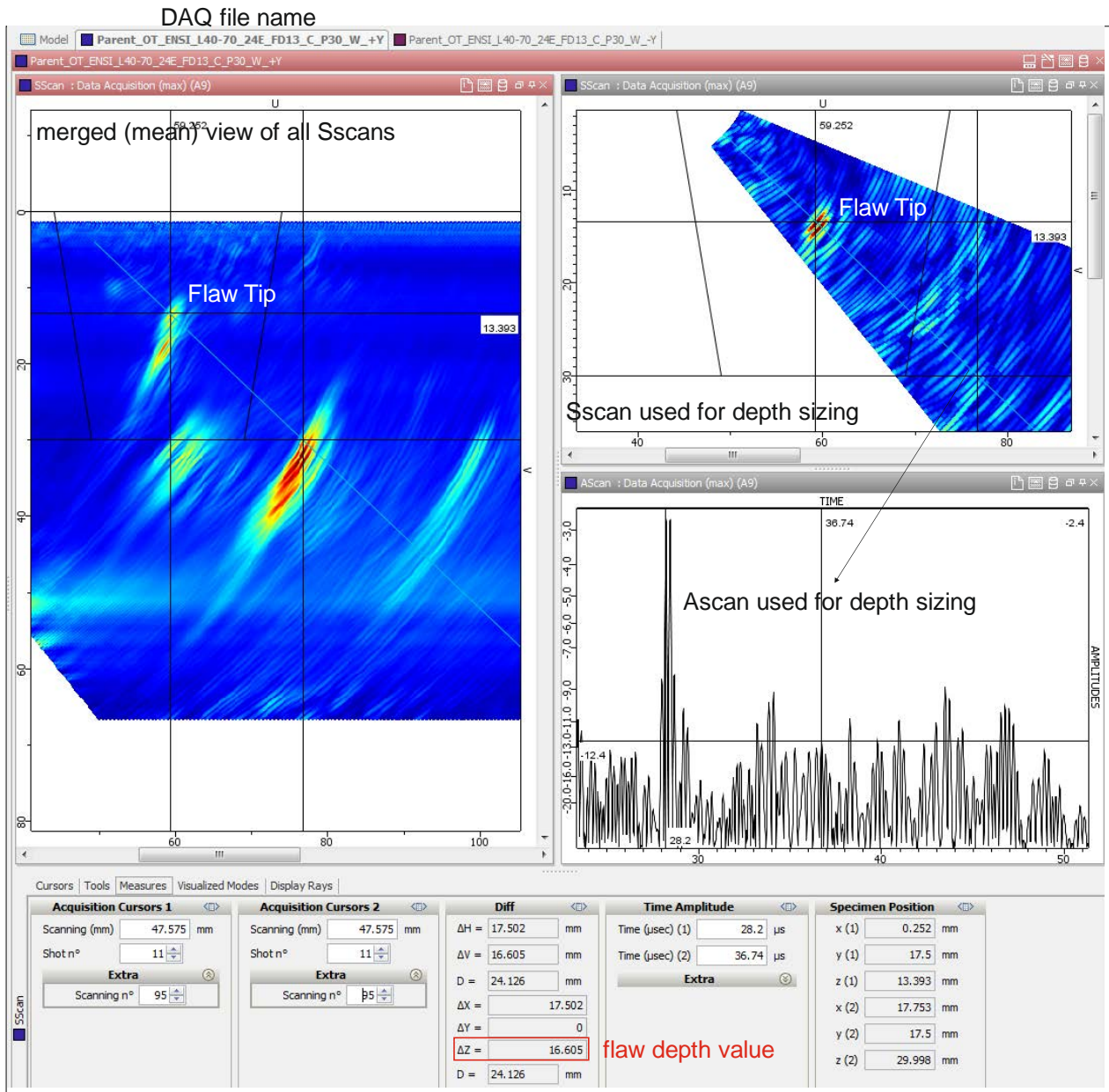


Figure C.28

### C.2.2.5 Results Specimens P28, P29, P30, P31, P32, P42 and P46

#### Specimen Information and Coordinate System

PARENT Sp. Designation	P28	P29	P30	P31	P32	P42	P46	P38
PSI Sp. Designation	6*	10*	*7	*1	*5	*12	*13	*3
Type of Crack	SCC	SCC	MF	SCC	SCC	EDM		SCC

\* MN 220 AD U, MF... Mech. Fatigue, SSC ... Stress Corrosion Crack

Coordinate System P28, P29, P30, P31, P32, P42 and P46

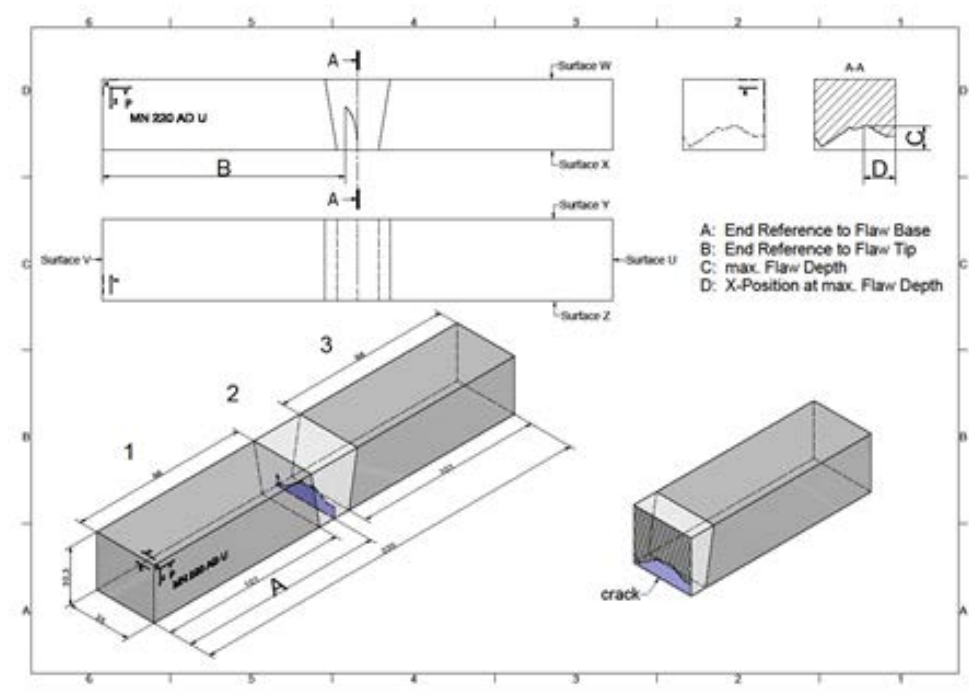


Figure C.29

Coordinate System P38

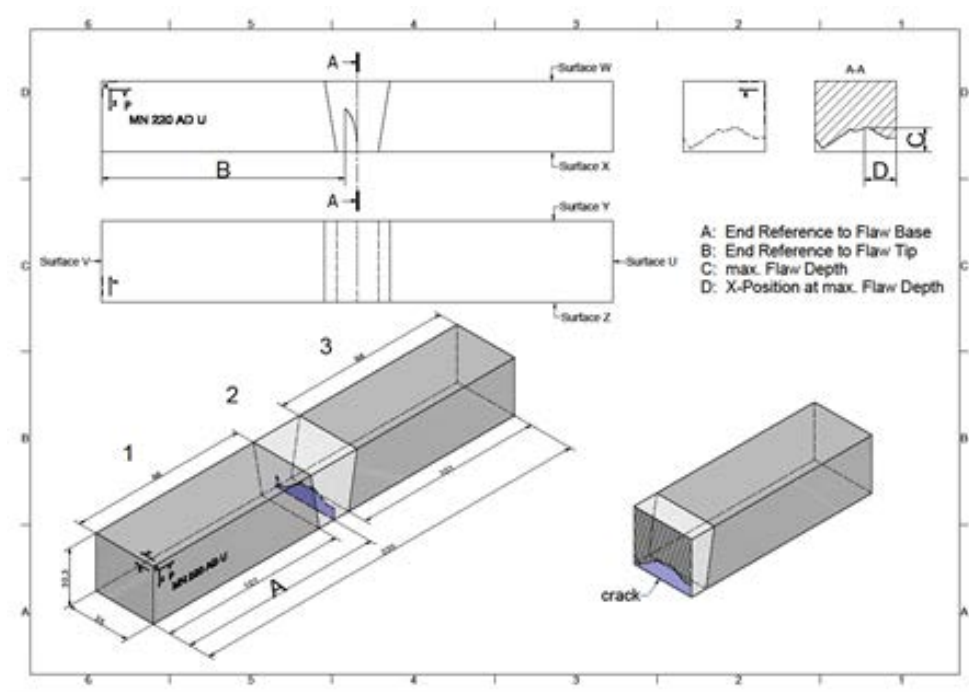


Figure C.30

### Flaw Depth Summary Table

Specimen	Scanning Surface	Beam Direction	DAQ File Name	Nb. of Elem.	Focal Depth	Flaw Depth*	UT Analysis / Images Chap.	Cal Sheet No.:
P28	W	+Y	PARENT_OT_ENSI_L40-70_24E_FD13_C_P28_W_+Y	24	13	<b>13.2</b>	3.1	1
	W	-Y	PARENT_OT_ENSI_L40-70_24E_FD13_C_P28_W_-Y	24	13	12.7	3.1	1
P29	W	+Y	PARENT_OT_ENSI_L40-70_24E_FD18_C_P29_W_+Y	24	18	<b>10.7</b>	3.2	6
	W	-Y	PARENT_OT_ENSI_L40-70_24E_FD18_C_P29_W_-Y	24	18	8.9	3.2	6
P30	W	+Y	PARENT_OT_ENSI_L40-70_24E_FD13_C_P30_W_+Y	24	13	16.6	3.3	1
	W	-Y	PARENT_OT_ENSI_L40-70_24E_FD13_C_P30_W_-Y	24	13	<b>17.8</b>	3.3	1
P31	W	+Y	PARENT_OT_ENSI_L40-70_32E_FD25_C_P31_W_+Y	32	25	2.7	3.4	3
	W	-Y	PARENT_OT_ENSI_L40-70_32E_FD25_C_P31_W_-Y	32	25	2.8	3.4	3
	X	+Y	PARENT_OT_ENSI_L40-70_24E_FD13_C_P31_X_+Y	24	13	4.3	3.4	4
	X	+Y	PARENT_OT_ENSI_L40-70_24E_FD13_C_P31_X_-Y	24	13	<b>4.6</b>	3.4	4
P32	W	+Y	PARENT_OT_ENSI_L40-70_24E_FD18_C_P32_W_+Y	24	18	9.5	3.5	6
	W	-Y	PARENT_OT_ENSI_L40-70_24E_FD18_C_P32_W_-Y	24	18	7.5	3.5	6
	X	+Y	PARENT_OT_ENSI_L40-70_32E_FD20_C_P32_X_+Y	32	20	12.4	3.5	5
	X	-Y	PARENT_OT_ENSI_L40-70_32E_FD20_C_P32_X_-Y	32	20	<b>13.4</b>	3.5	5
P42	W	+Y	PARENT_OT_ENSI_L40-70_24E_FD13_C_P42_W_+Y	24	13	9.3	3.6	1
	W	-Y	PARENT_OT_ENSI_L40-70_24E_FD13_C_P42_W_-Y	24	13	<b>9.7</b>	3.6	1
P38	W	+Y	PARENT_OT_ENSI_L40-70_24E_FD13_C_P38_W_+Y	24	13	6.6	3.7	1
	W	-Y	PARENT_OT_ENSI_L40-70_24E_FD13_C_P38_W_-Y	24	13	6.4	3.7	1
	X	+Y	PARENT_OT_ENSI_L40-70_24E_FD13_C_P38_X_+Y	24	13	5	3.7	4
	X	-Y	PARENT_OT_ENSI_L40-70_24E_FD13_C_P38_X_-Y	24	13	<b>5.7</b>	3.7	4

\* bolt values are final flaw depth calls

# UT Analysis Images

## Specimen 28

Specimen	Scanning Surface	Beam Direction	DAQ File Name	Nb. of Elem.	Focal Depth	Flaw Depth (mmm)	EVal. Angle (°)	S/N. (dB)
P28	W	+Y	PARENT_OT_ENSI_L40-70_24E_FD17_C_P28_W_+Y	24	13	13.2	44	7.5

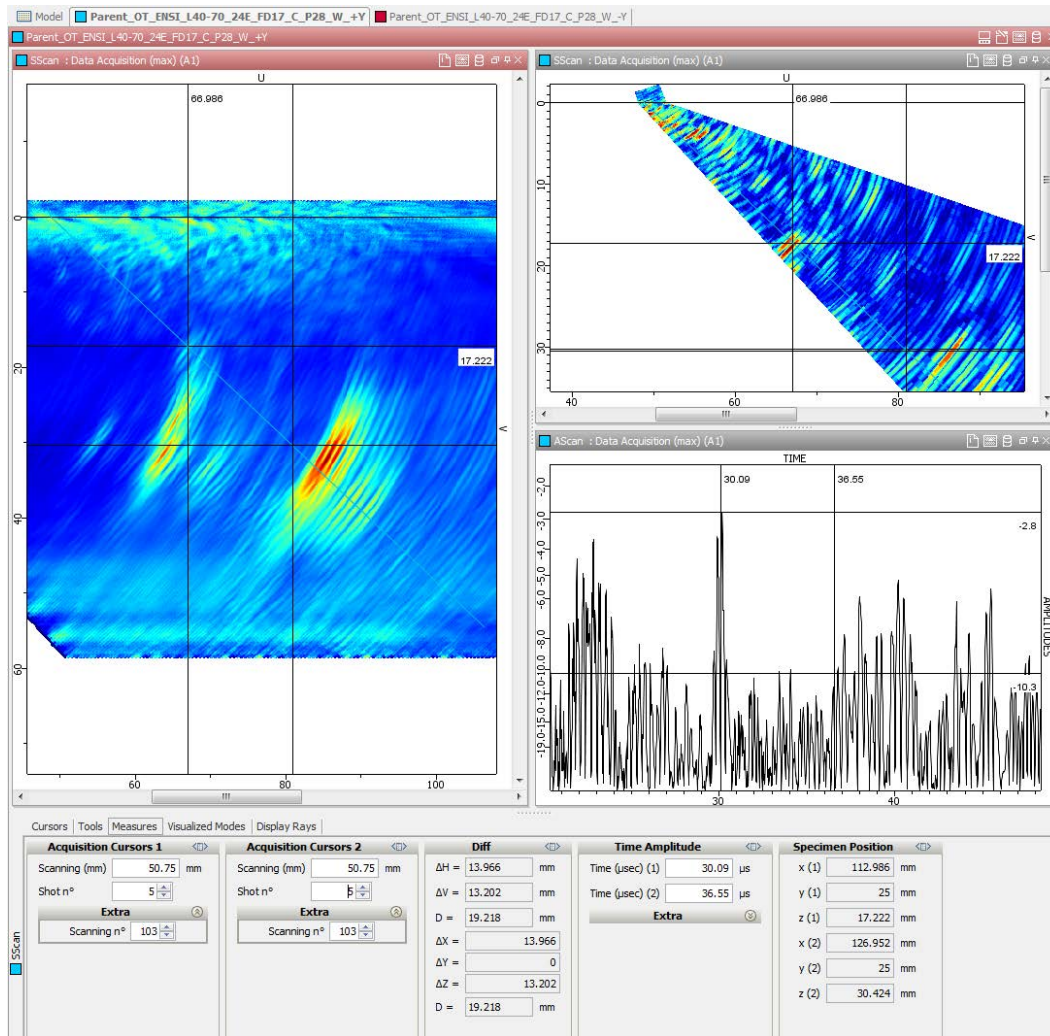


Figure C.31

Specimen	Scanning Surface	Beam Direction	DAQ File Name	Nb. of Elem.	Focal Depth	Flaw Depth (mmm)	EVal. Angle (°)	S/N. (dB)

P28	W	-Y	PARENT_OT_ENSI_L40-70_24E_FD17_C_P28_W_-Y	24	13	12.7	59	10
-----	---	----	---	----	----	------	----	----

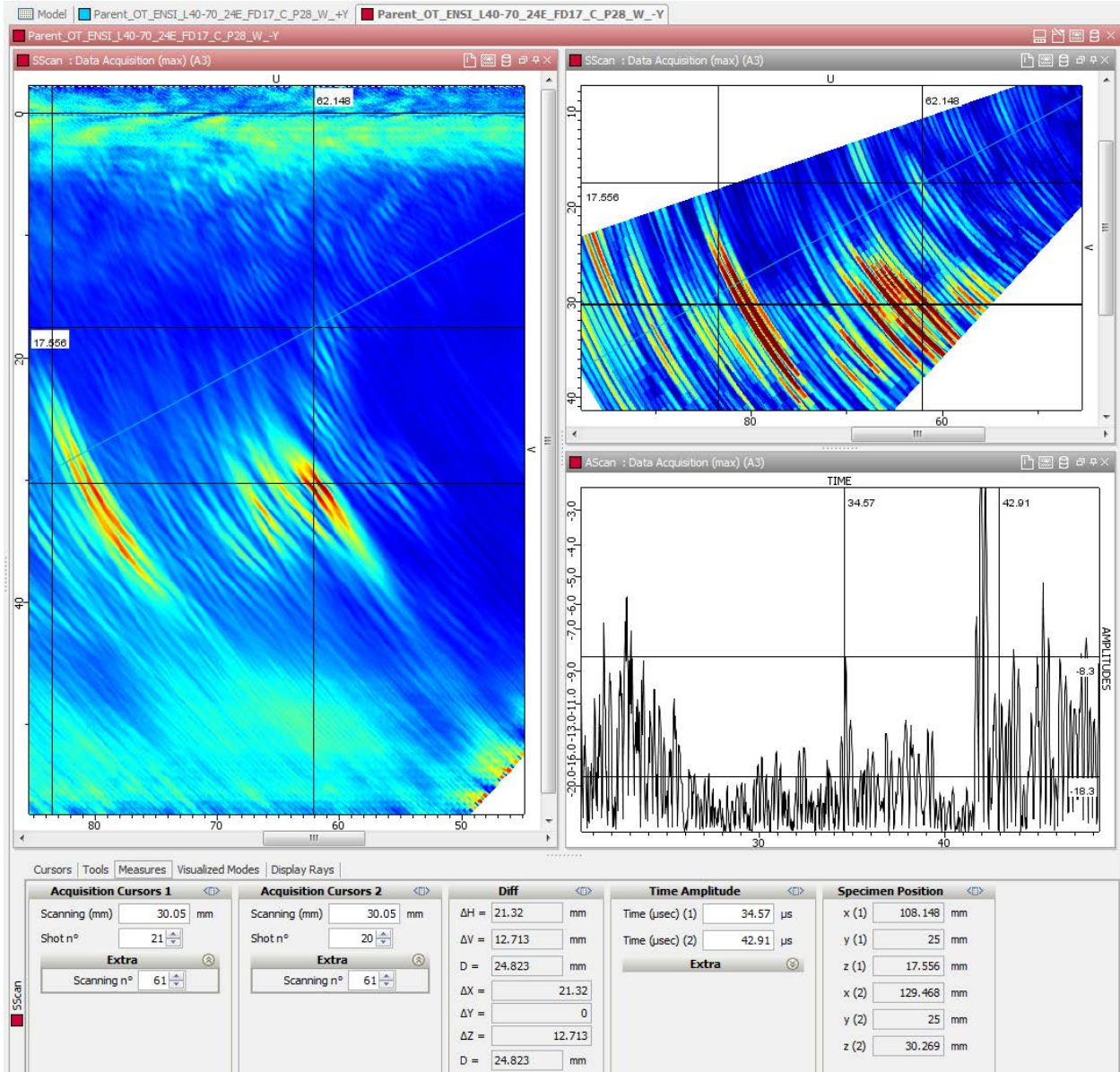


Figure C.32

Specimen P29

Specimen	Scanning Surface	Beam Direction	DAQ File Name	Nb. of Elem.	Focal Depth	Flaw Depth (mm)	Eval. Angle (°)	S/N. (dB)
P29	W	+Y	PARENT_OT_ENSI_L40-70_24E_FD18_C_P29_W_+Y	24	18	10.7	57	9



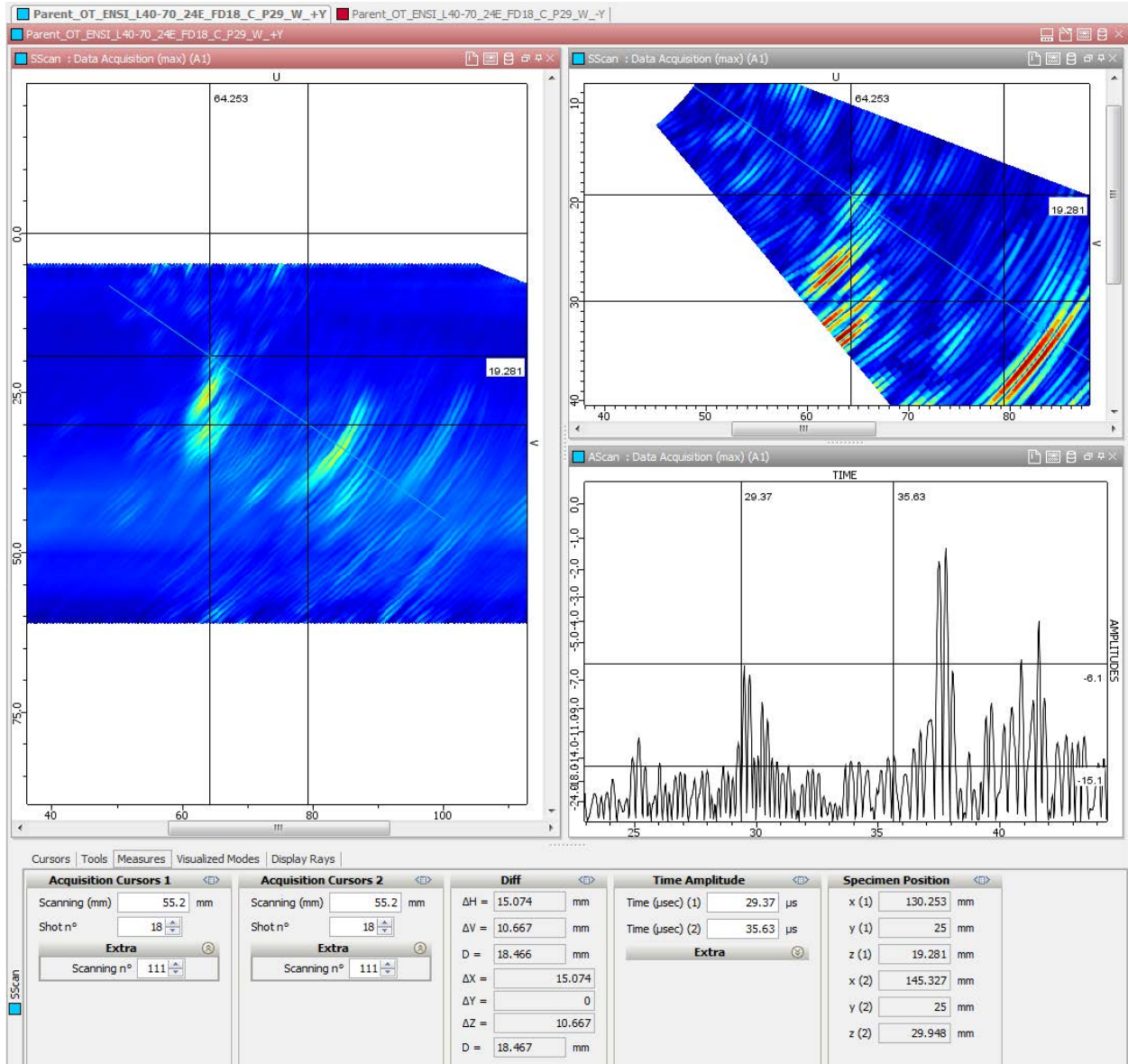


Figure C.33

Specimen	Scanning Surface	Beam Direction	DAQ File Name	Nb. of Elem.	Focal Depth	Flaw Depth (mm)	EVal. Angle (°)	S/N. (dB)
P29	W	-Y	PARENT_OT_ENSI_L40-70_24E_FD18_C_P29_W_+Y	24	18	8.9	61	3

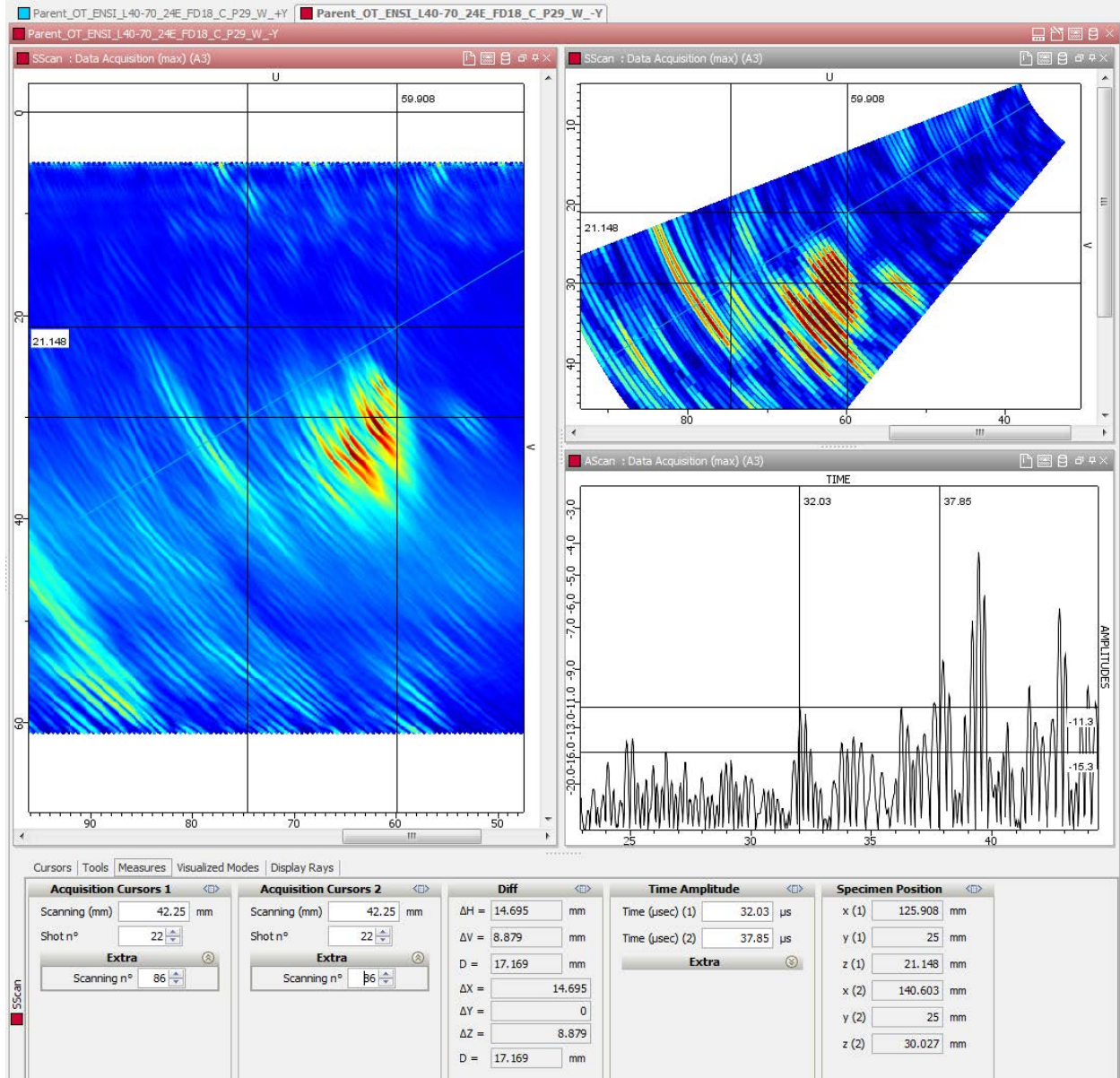


Figure C.34

Specimen P30

Specimen	Scanning Surface	Beam Direction	DAQ File Name	Nb. of Elem.	Focal Depth	Flaw Depth (mmm)	EVal. Angle (°)	S/N. (dB)
P30	W	+Y	PARENT_OT_ENSI_L40-70_24E_FD13_C_P30_W_+Y	24	13	16.6	50	10

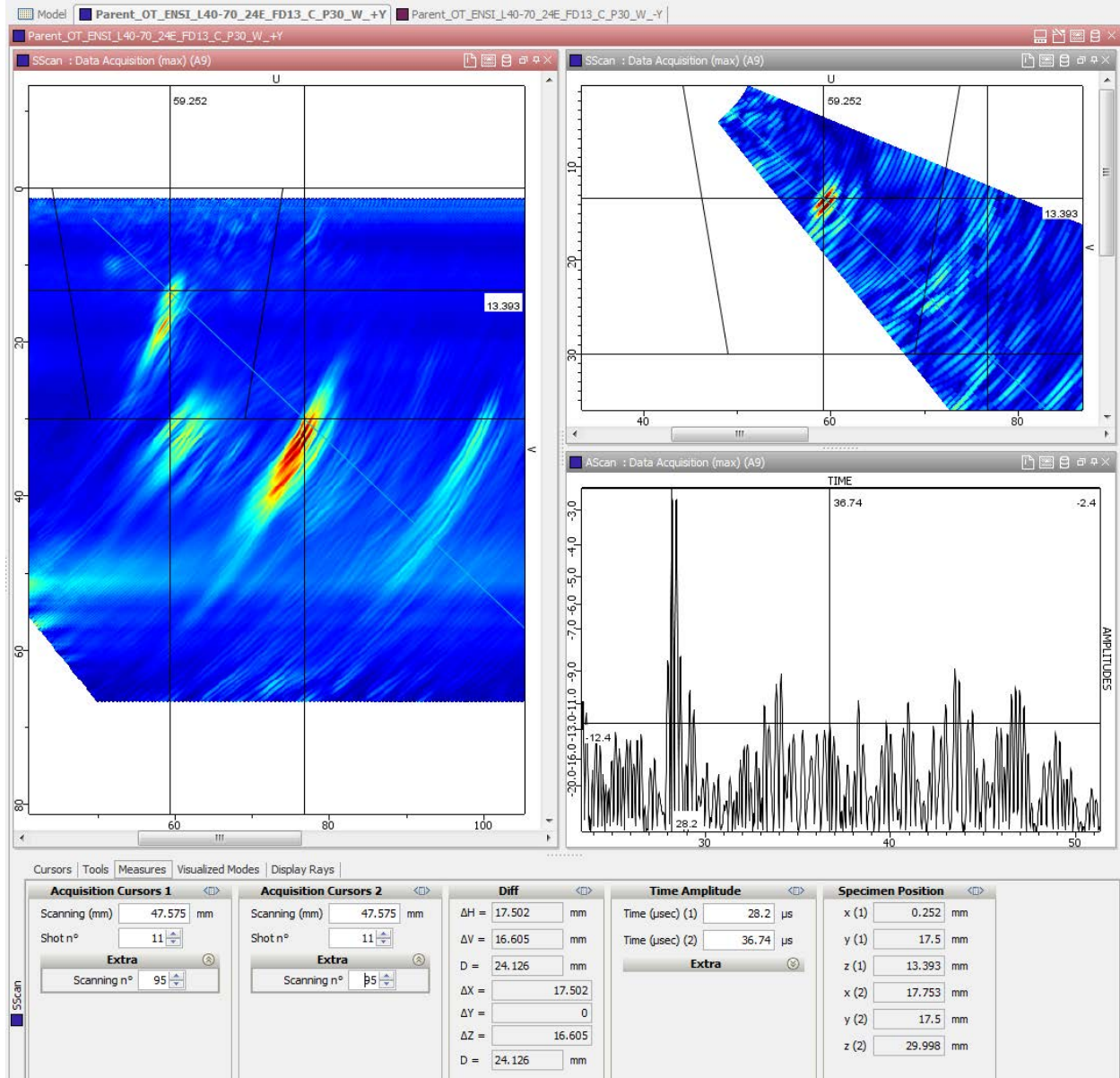


Figure C.35

Specimen	Scanning Surface	Beam Direction	DAQ File Name	Nb. of Elem.	Focal Depth	Flaw Depth (mmm)	EVal. Angle (°)	S/N. (dB)
P30	W	-Y	PARENT_OT_ENSI_L40-70_24E_FD13_C_P30_W_-Y	24	13	17.8	59	8

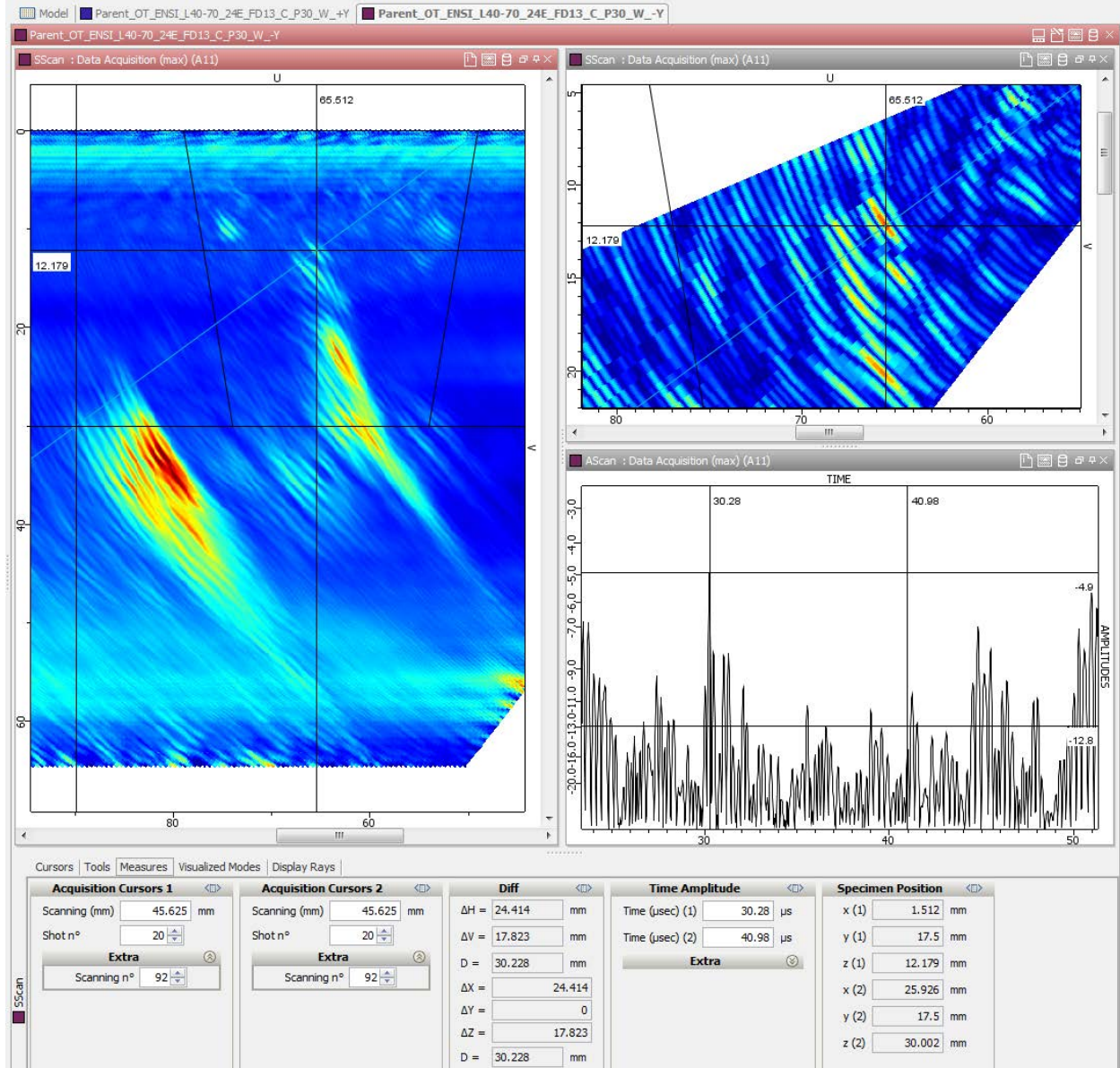


Figure C.36

Specimen P31

Specimen	Scanning Surface	Beam Direction	DAQ File Name	Nb. of Elem.	Focal Depth	Flaw Depth (mmm)	EVal. Angle (°)	S/N. (dB)
P31	W	+Y	PARENT_OT_ENSI_L40-70_32E_FD25_C_P31_W_+Y	32	25	2.7*	49	6

\* no mode converted TLL - shallow crack, tip weak, bad SN, only RATT

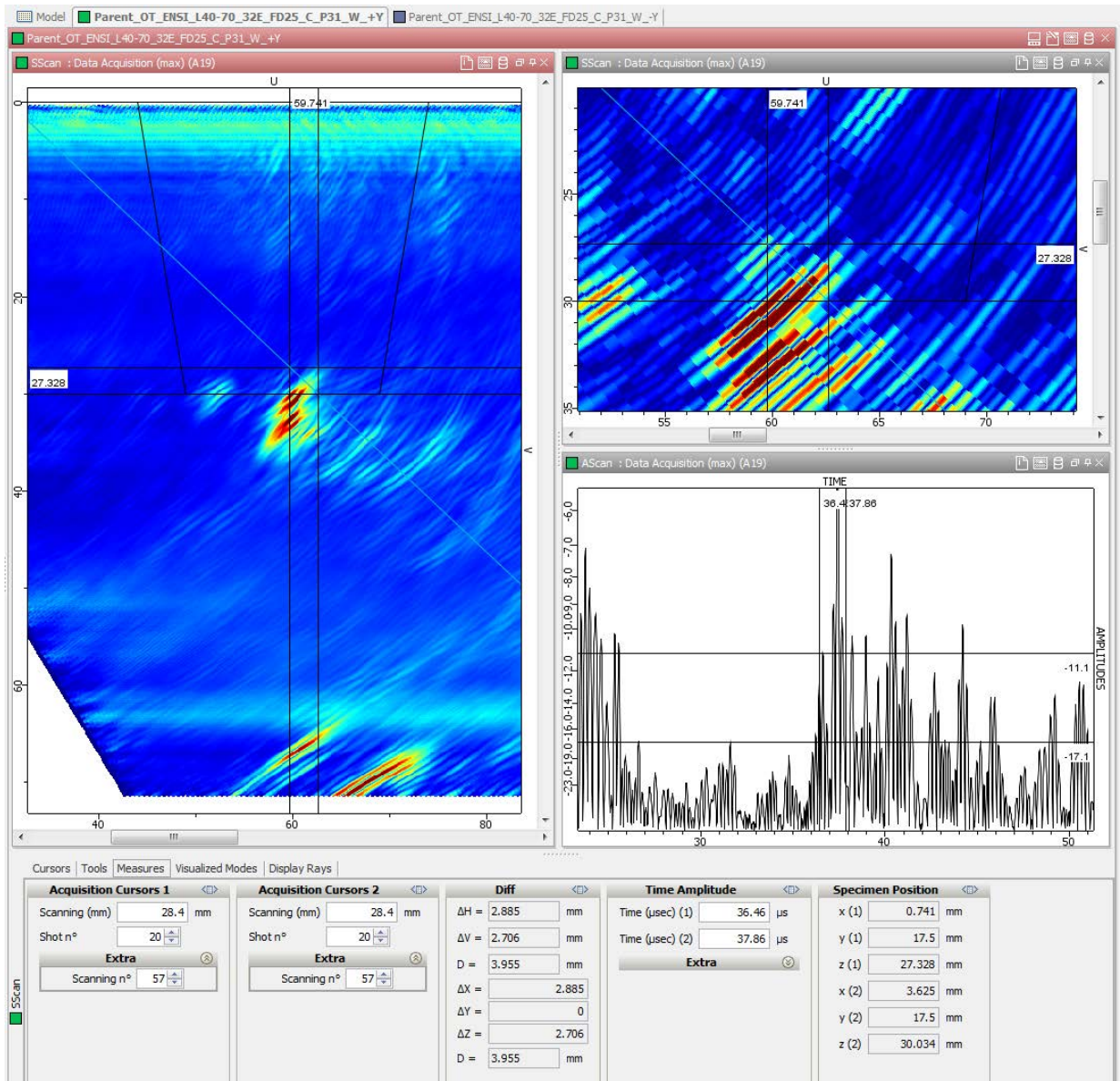


Figure C.37

Specimen	Scanning Surface	Beam Direction	DAQ File Name	Nb. of Elem.	Focal Depth	Flaw Depth (mmm)	Eval. Angle (°)	S/N. (dB)
P31	W	+Y	PARENT_OT_ENSI_L40-70_32E_FD25_C_P31_W_-Y	32	25	2.8*	45	3

\* no mode converted TLL - shallow crack, tip weak, bad SN, only RATT

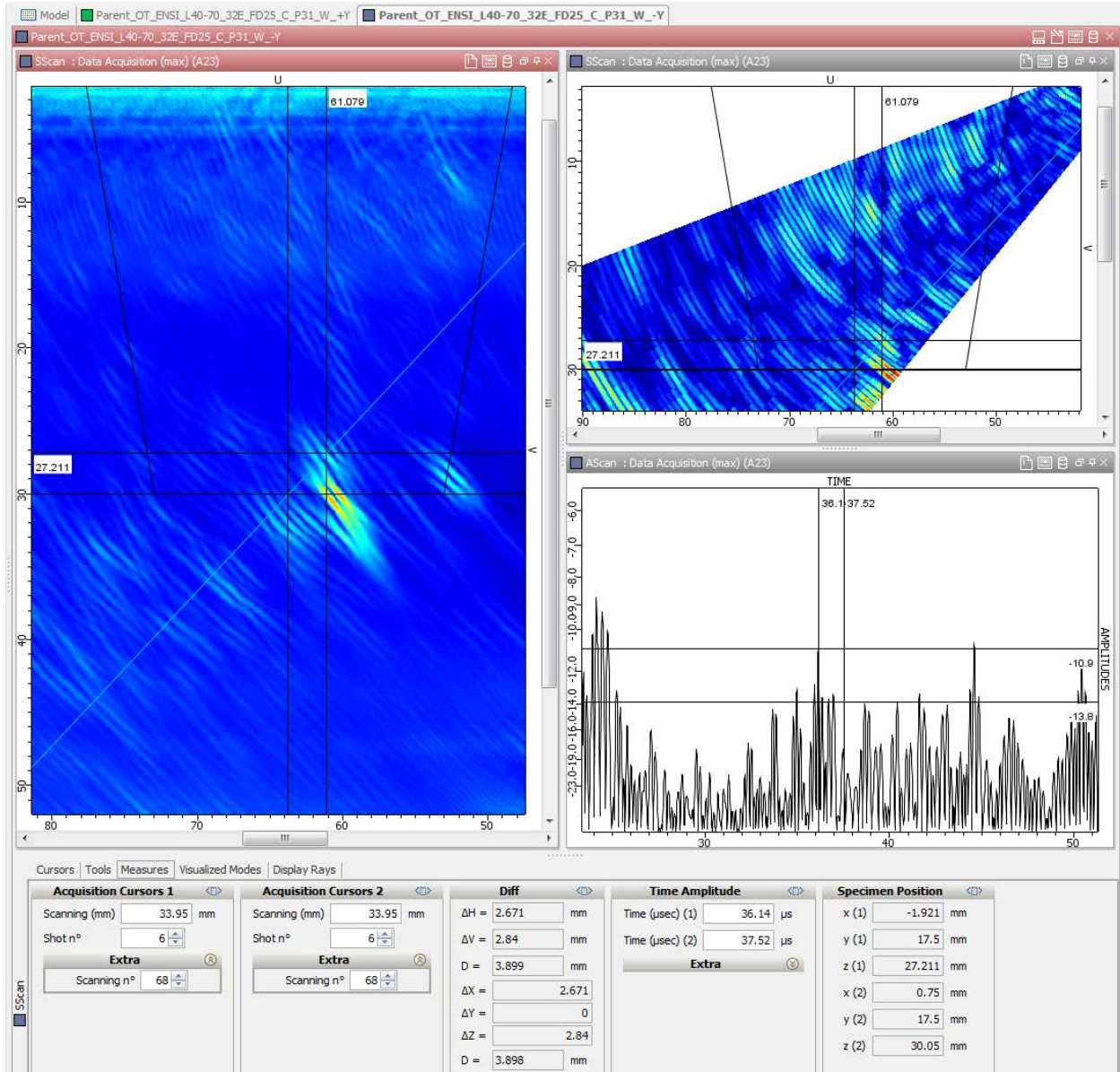


Figure C.38

Specimen	Scanning Surface	Beam Direction	DAQ File Name	Nb. of Elem.	Focal Depth	Flaw Depth (mmm)	EVal. Angle (°)	S/N. (dB)
P31	W	+Y	PARENT_OT_ENSI_L40-70_24E_FD13_C_P31_X+Y	24	13	4.3	63	10
* Remark. Weld drawing not correct.								

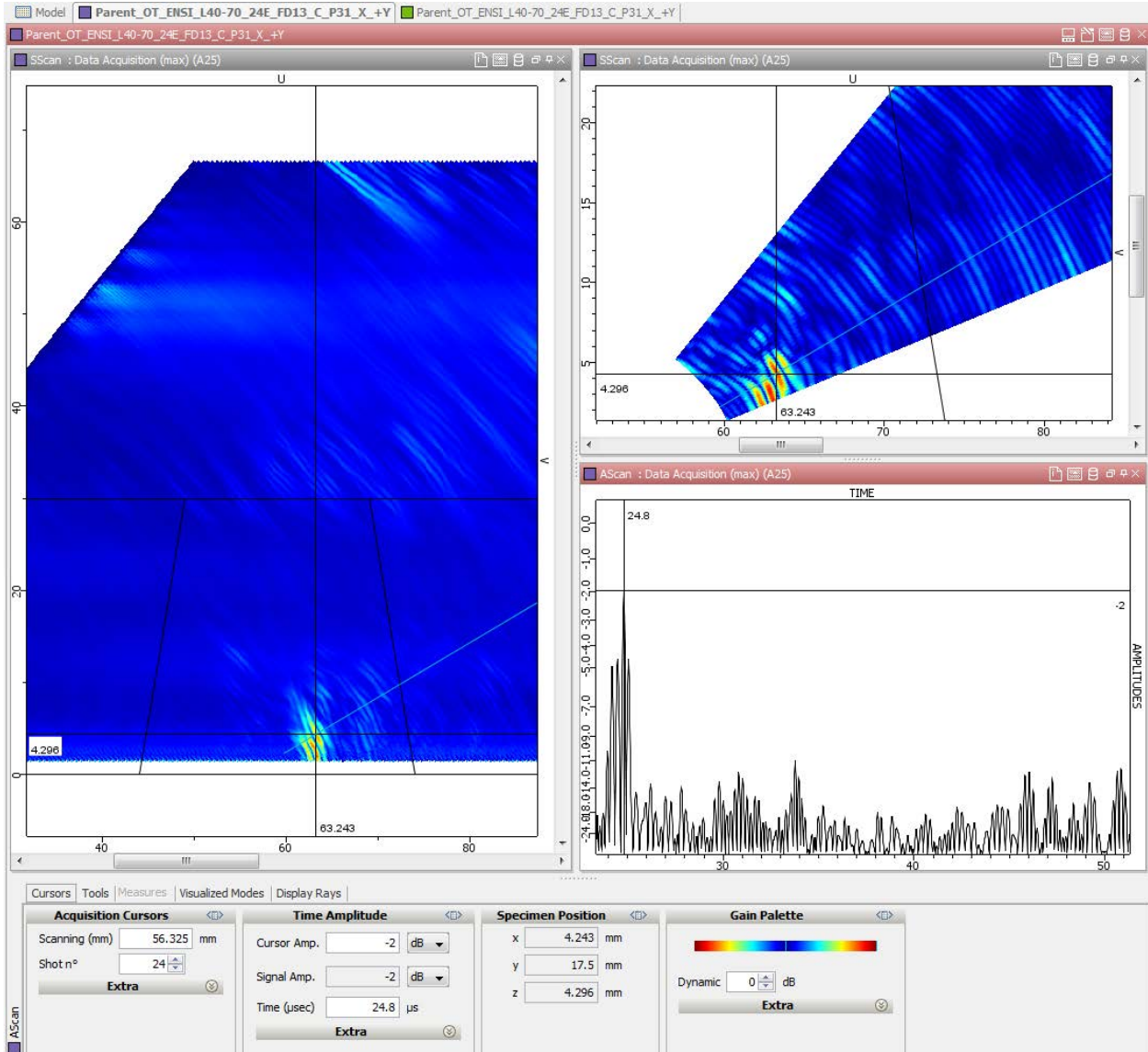


Figure C.39

Specimen	Scanning Surface	Beam Direction	DAQ File Name	Nb. of Elem.	Focal Depth	Flaw Depth (mmm)	EVal. Angle (°)	S/N. (dB)
P31	W	-Y	PARENT_OT_ENSI_L40-70_24E_FD13_C_P31_X-Y	24	13	4.6	50	5
* Remark. Weld drawing not correct.								

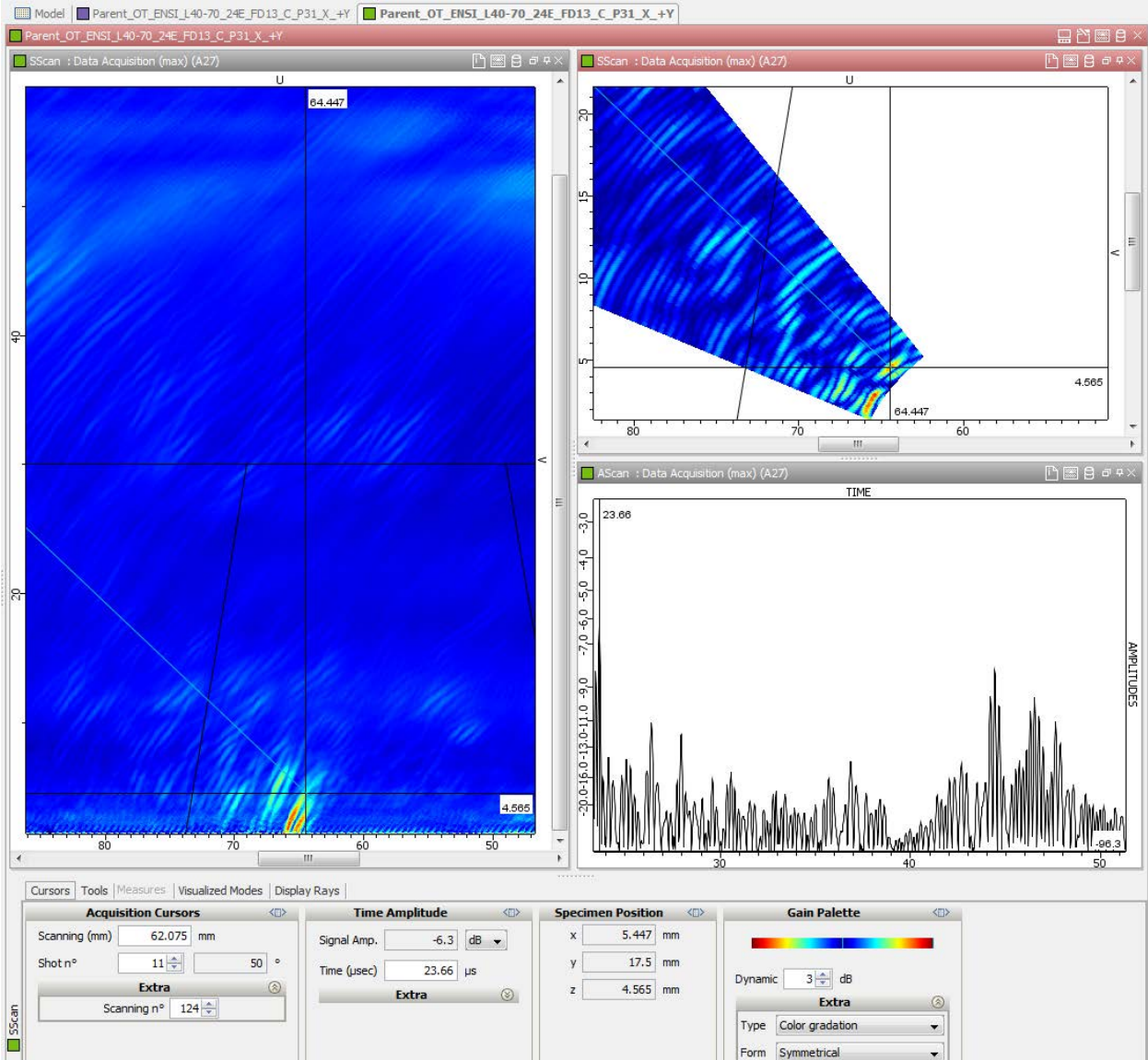


Figure C.40

Specimen P32

Specimen	Scanning Surface	Beam Direction	DAQ File Name	Nb. of Elem.	Focal Depth	Flaw Depth (mmm)	EVal. Angle (°)	S/N. (dB)
P32	W	+Y	PARENT_OT_ENSI_L40-70_24E_FD18_C_P32_W_+Y	24	18	9.5	63	6



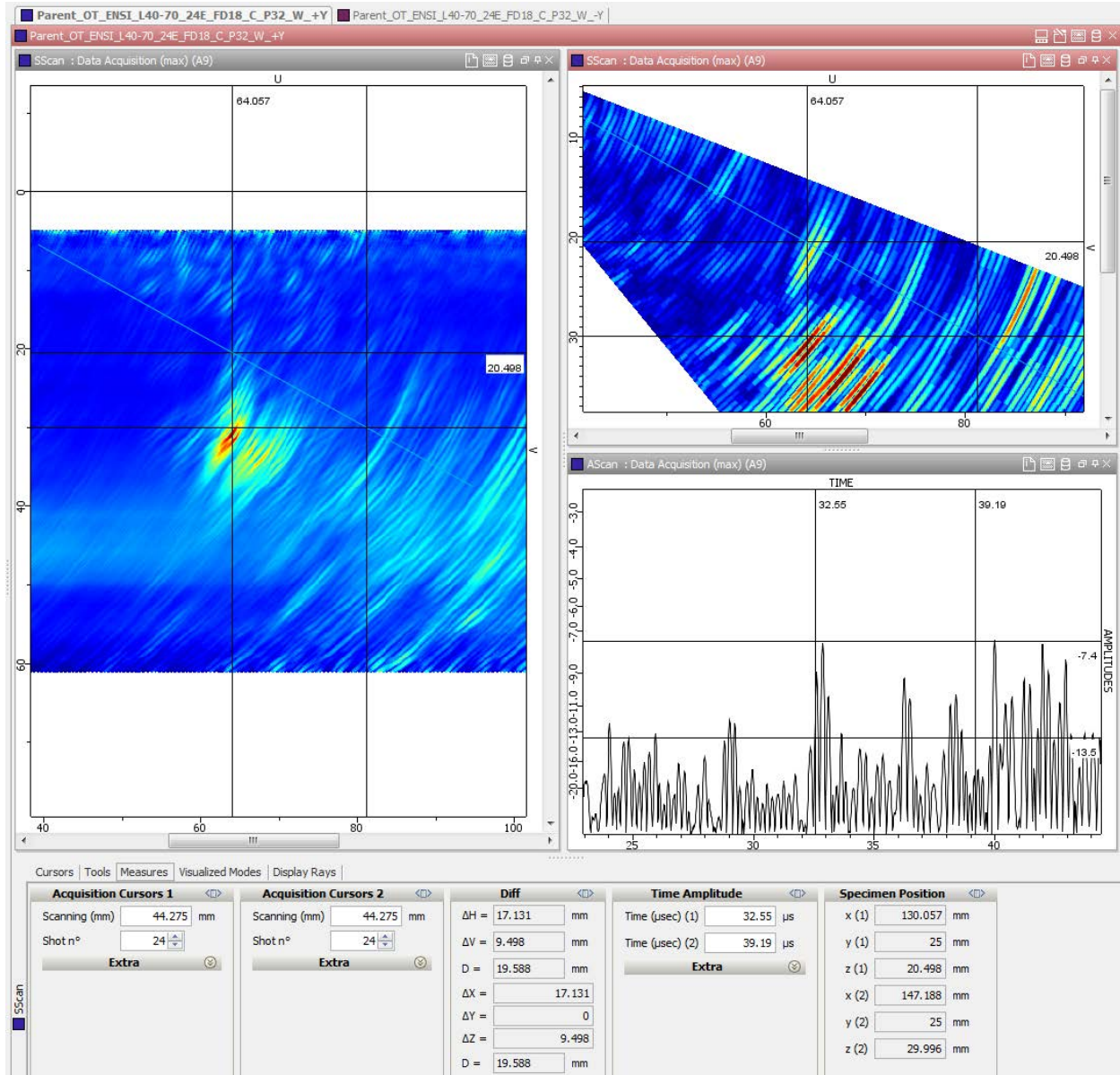


Figure C.41

Specimen	Scanning Surface	Beam Direction	DAQ File Name	Nb. of Elem.	Focal Depth	Flaw Depth (mmm)	Eval. Angle (°)	S/N. (dB)
P32	W	+Y	PARENT_OT_ENSI_L40-70_24E_FD13_C_P32_W_-Y	24	13	7.5	57	10

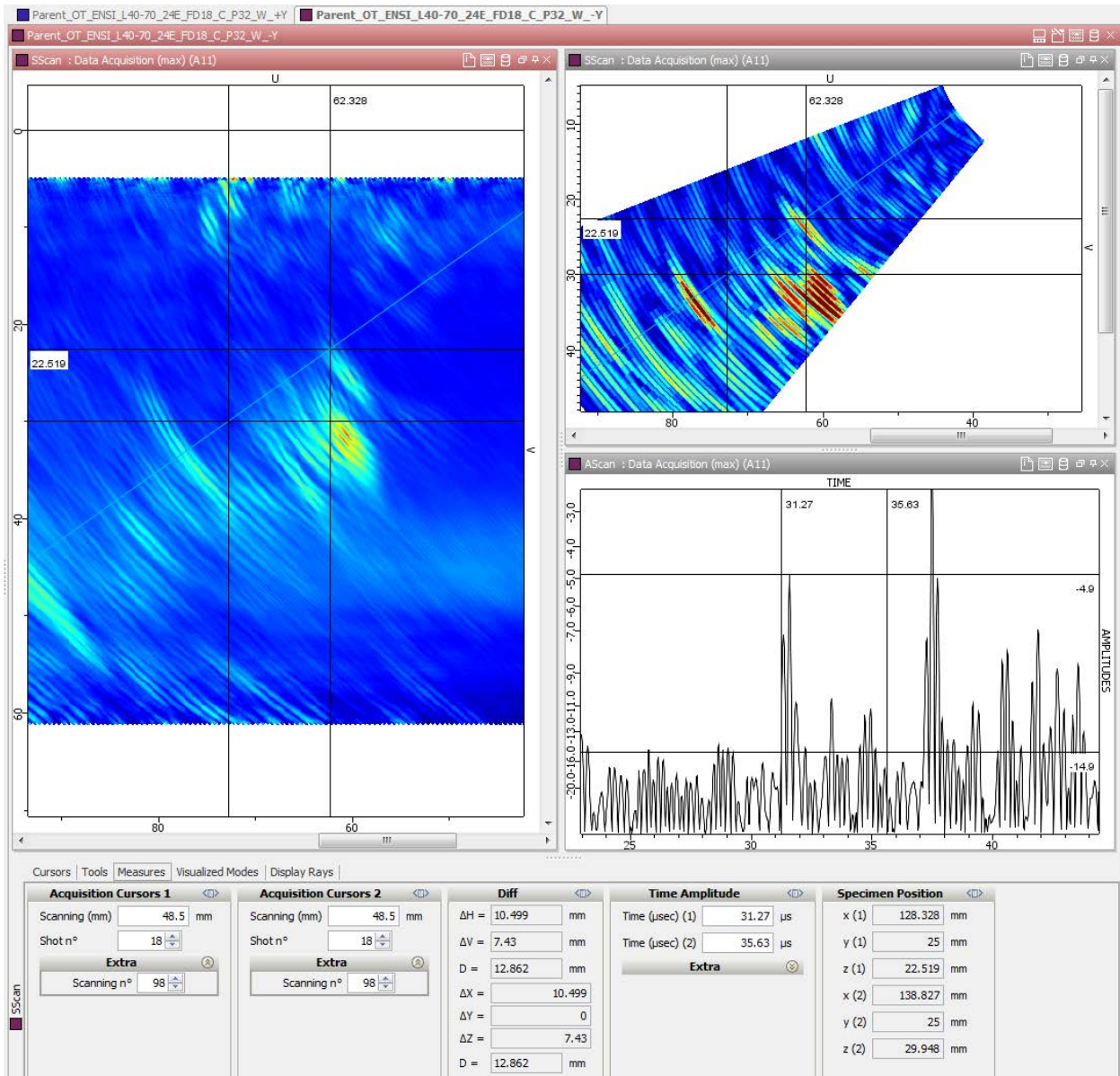


Figure C.42.

Specimen	Scanning Surface	Beam Direction	DAQ File Name	Nb. of Elem.	Focal Depth	Flaw Depth (mm)	EVal. Angle (°)	S/N. (dB)
P31	X	+Y	PARENT_OT_ENSI_L40-70_32E_FD20_C_P32_X+Y	32	20	12.4	61	13

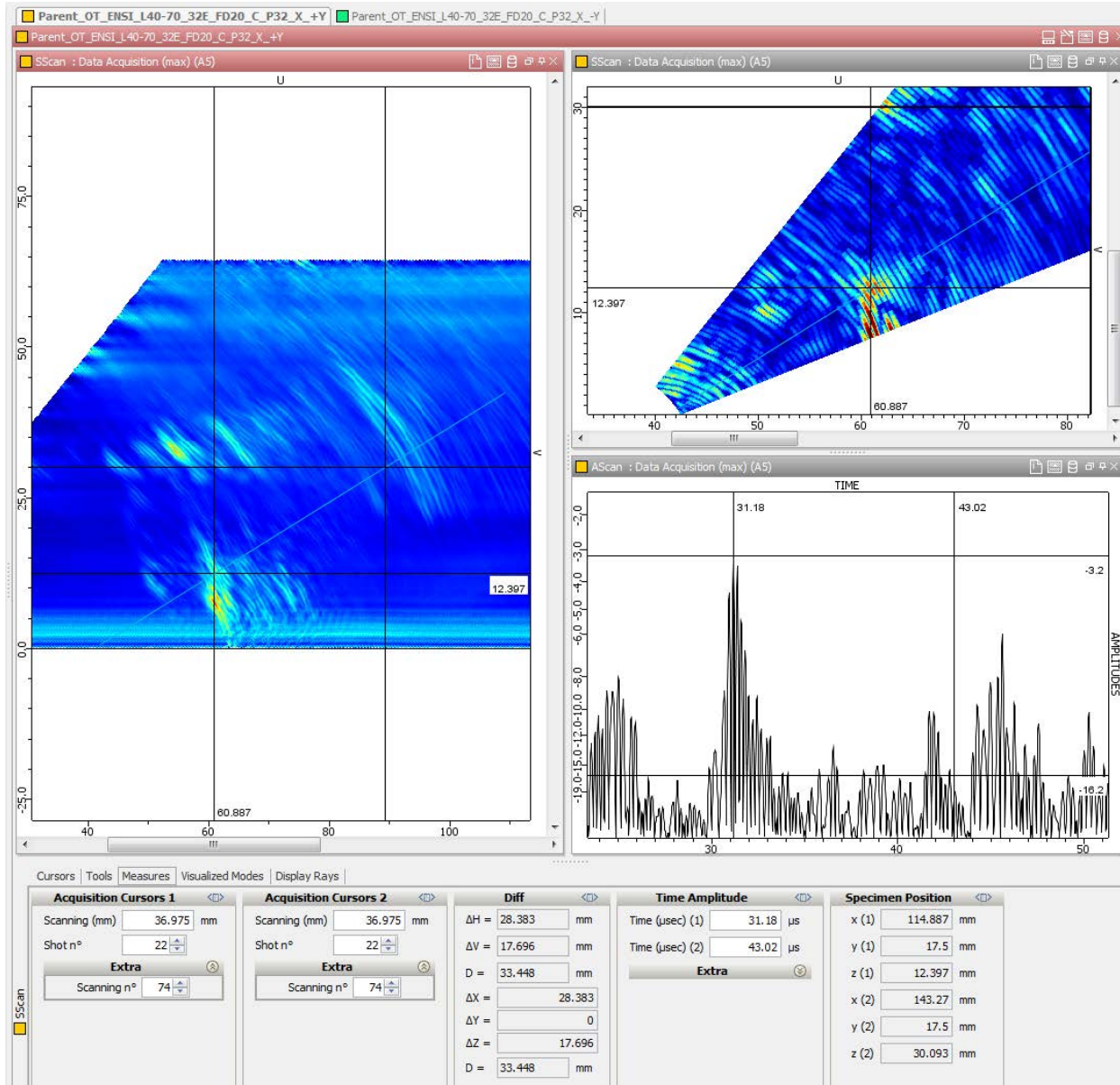


Figure C.43.

Specimen	Scanning Surface	Beam Direction	DAQ File Name	Nb. of Elem.	Focal Depth	Flaw Depth (mmm)	EVal. Angle (°)	S/N. (dB)
P32	X	-Y	PARENT_OT_ENSI_L40-70_32E_FD20_C_P32_X-Y	32	20	13.4	52	8

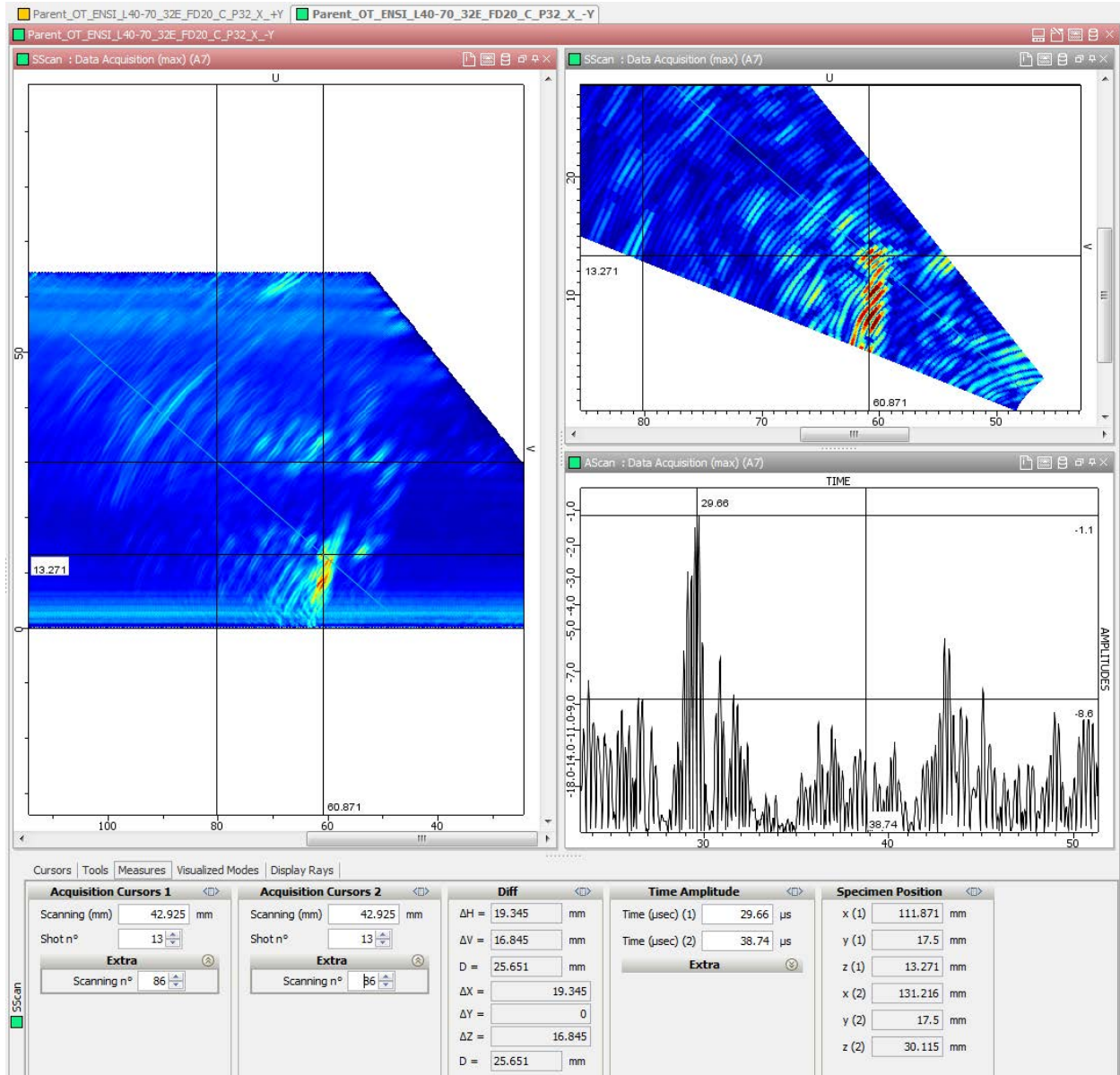


Figure C.44.

Specimen P42

Specimen	Scanning Surface	Beam Direction	DAQ File Name	Nb. of Elem.	Focal Depth	Flaw Depth (mmm)	EVal. Angle (°)	S/N. (dB)
P42	W	+Y	PARENT_OT_ENSI_L40-70_24E_FD13_C_P42_W_+Y	24	13	9.3	46	11

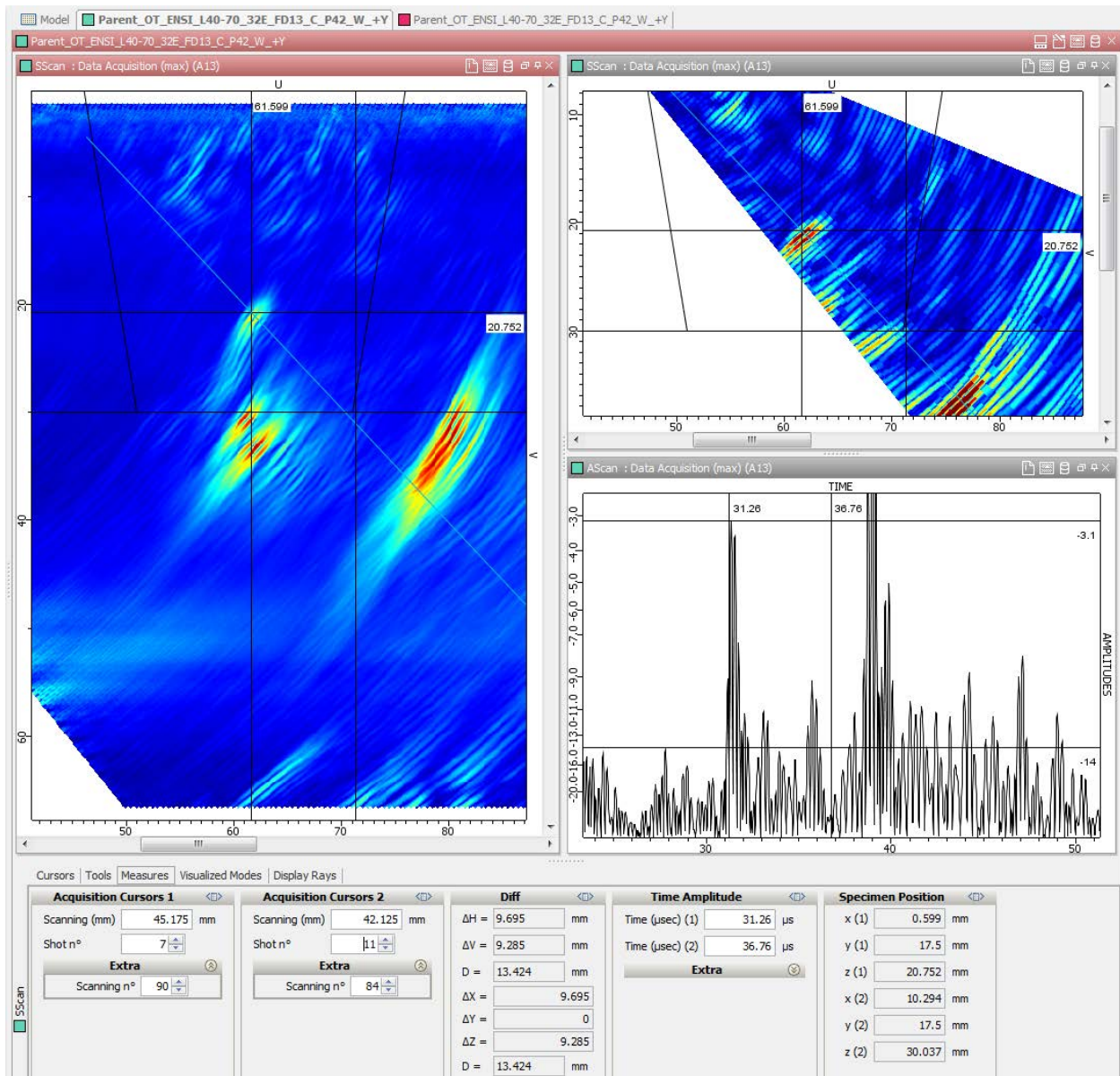


Figure C.45.

Specimen	Scanning Surface	Beam Direction	DAQ File Name	Nb. of Elem.	Focal Depth	Flaw Depth (mmm)	Eval. Angle (°)	S/N. (dB)
P31	W	-Y	PARENT_OT_ENSI_L40-70_24E_FD13_C_P42_W_-Y	24	13	9.7	48	8

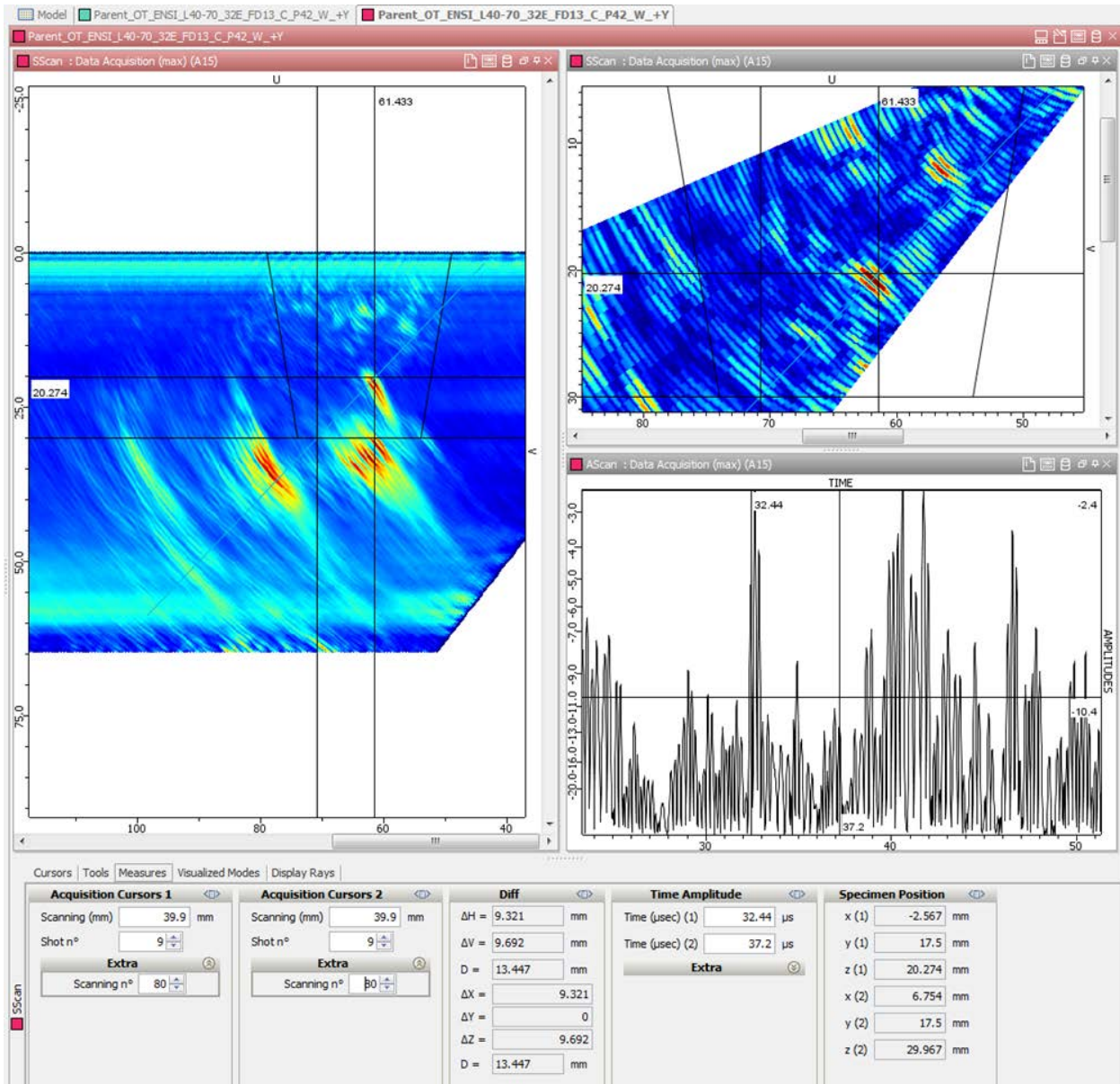


Figure C.46.

Specimen P38

Specimen	Scanning Surface	Beam Direction	DAQ File Name	Nb. of Elem.	Focal Depth	Flaw Depth (mm)	EVal. Angle (°)	S/N. (dB)
P38	W	+Y	PARENT_OT_ENSI_L40-70_24E_FD13_C_P38_W_+Y	24	13	6.6	59	4
*weak mode converted TLL - shallow crack, tip very weak, bad SN								

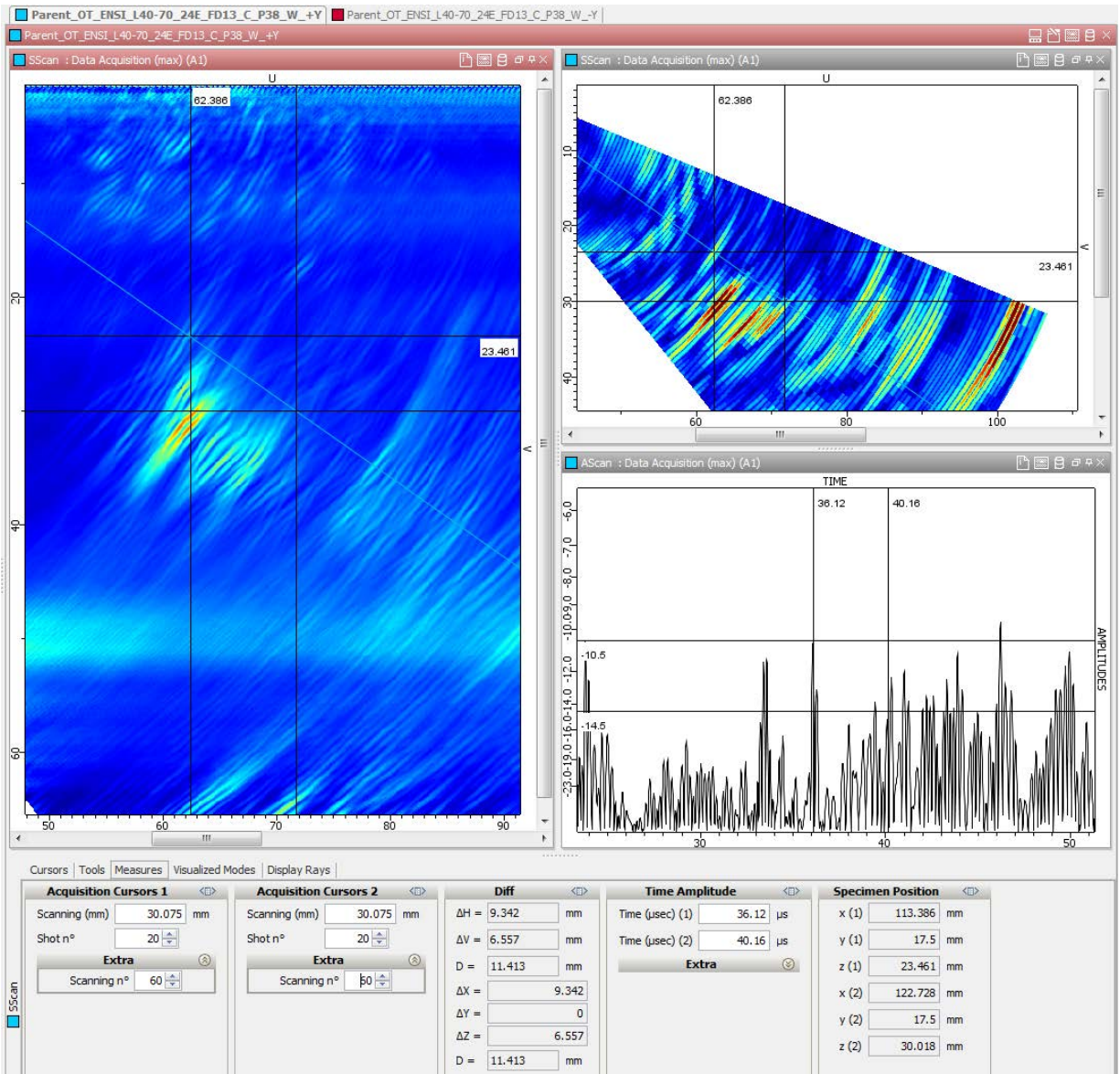


Figure C.47.

Specimen	Scanning Surface	Beam Direction	DAQ File Name	Nb. of Elem.	Focal Depth	Flaw Depth (mmm)	EVal. Angle (°)	S/N. (dB)
P38	W	-Y	PARENT_OT_ENSI_L40-70_24E_FD13_C_P38_W_-Y	24	13	6.4	59	5.3
*weak mode converted TLL - shallow crack, tip very weak, bad SN								

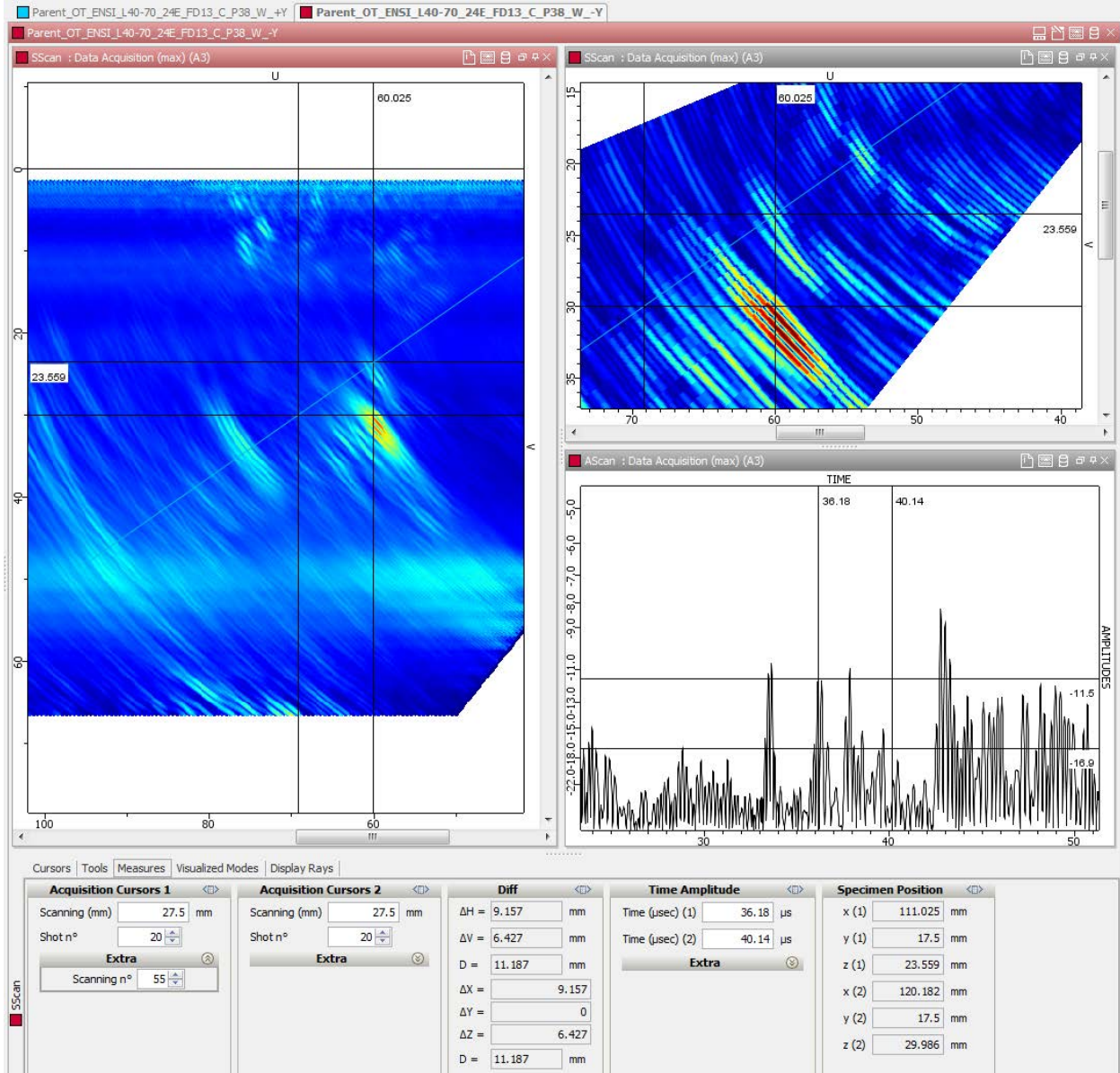


Figure C.48.

Specimen	Scanning Surface	Beam Direction	DAQ File Name	Nb. of Elem.	Focal Depth	Flaw Depth (mmm)	EVal. Angle (°)	S/N. (dB)
P38	X	+Y	PARENT_OT_ENSI_L40-70_24E_FD13_C_P38_X_+Y	24	13	5	50	11



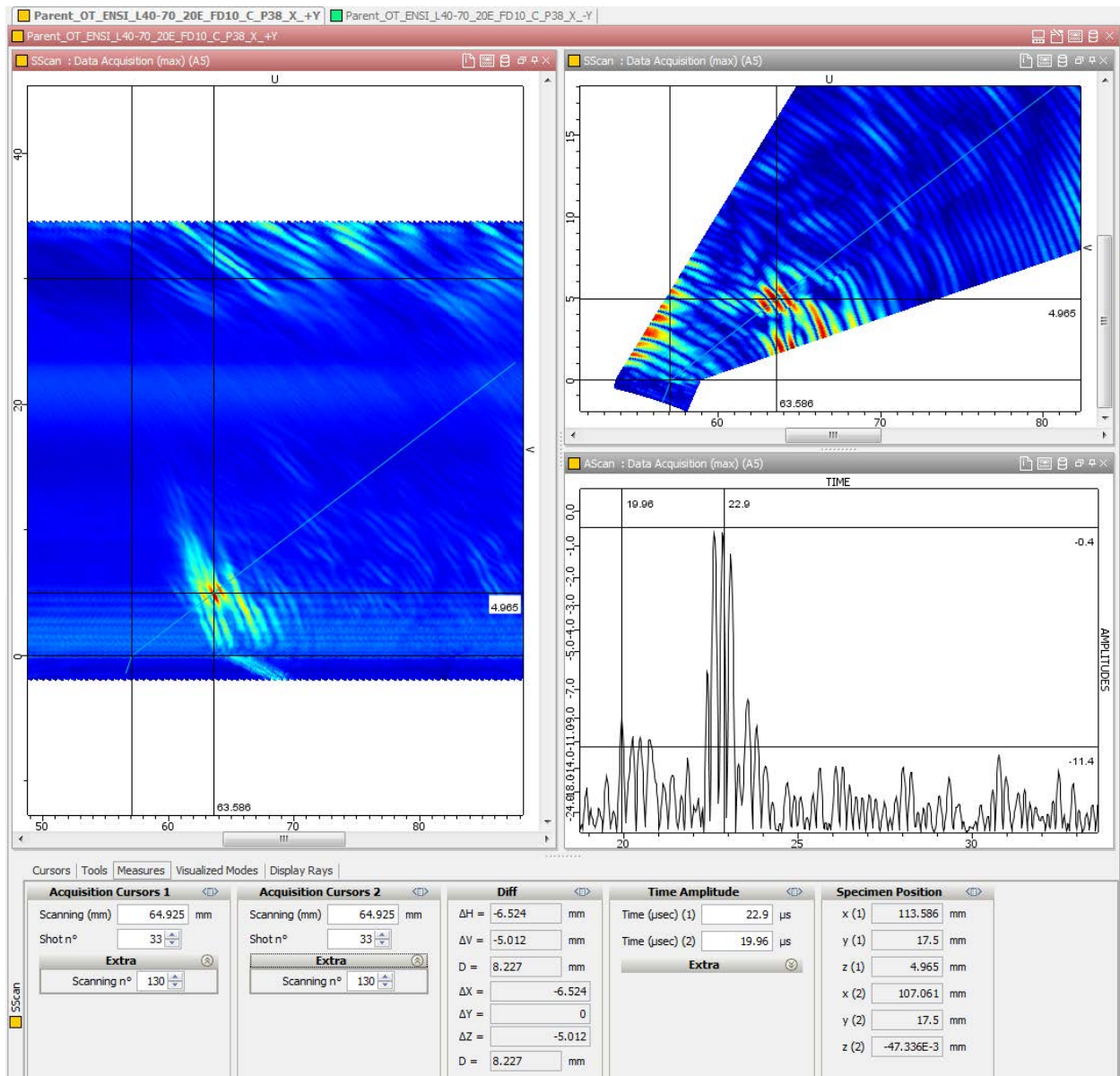


Figure C.49.

Specimen	Scanning Surface	Beam Direction	DAQ File Name	Nb. of Elem.	Focal Depth	Flaw Depth (mmm)	EVal. Angle (°)	S/N. (dB)
P38	X	-Y	PARENT_OT_ENSI_L40-70_24E_FD13_C_P38_X-Y	24	13	5.7	51	7

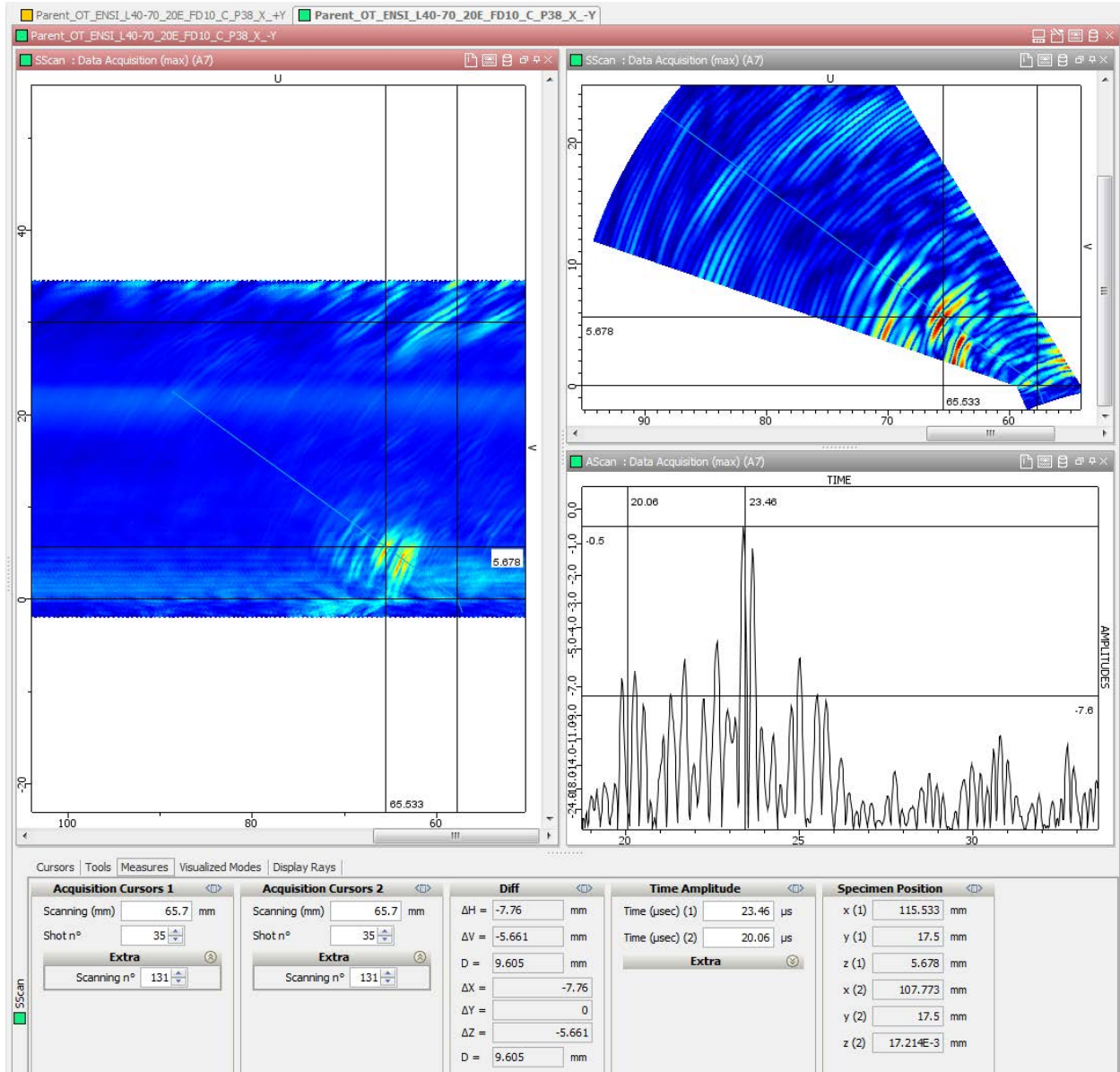


Figure C.50.

### C.2.2.6 Self Assessment

- Good TWS of EDM notch and mechanical fatigue crack, clear tip diffraction echo's from all examination directions visible
- TWS of stress corrosion cracks challenging, tip diffraction echo's not seen from all examination directions (Remark: TWS of specimen SCC under field conditions (surface conditions, access) very hard and sometimes not possible)

## C.2.3 Phased Ultrasonic Array, Technique ID 131-PA1

### C.2.3.1 Overview

The techniques described in this report were utilized for the examination of the PARENT specimens P1 and P41.

Method	Phased Array Ultrasonic Testing
Array / Technique	Dual / Linear / Transmit - Receive
Wave Mode	Longitudinal
Angle Range	25° – 65°
Frequency	2 MHz
UT Instrument	M2M MultiX 64
Scan Plan	Manual scanning parallel and perpendicular to weld from both directions
Scanning Surface	OD

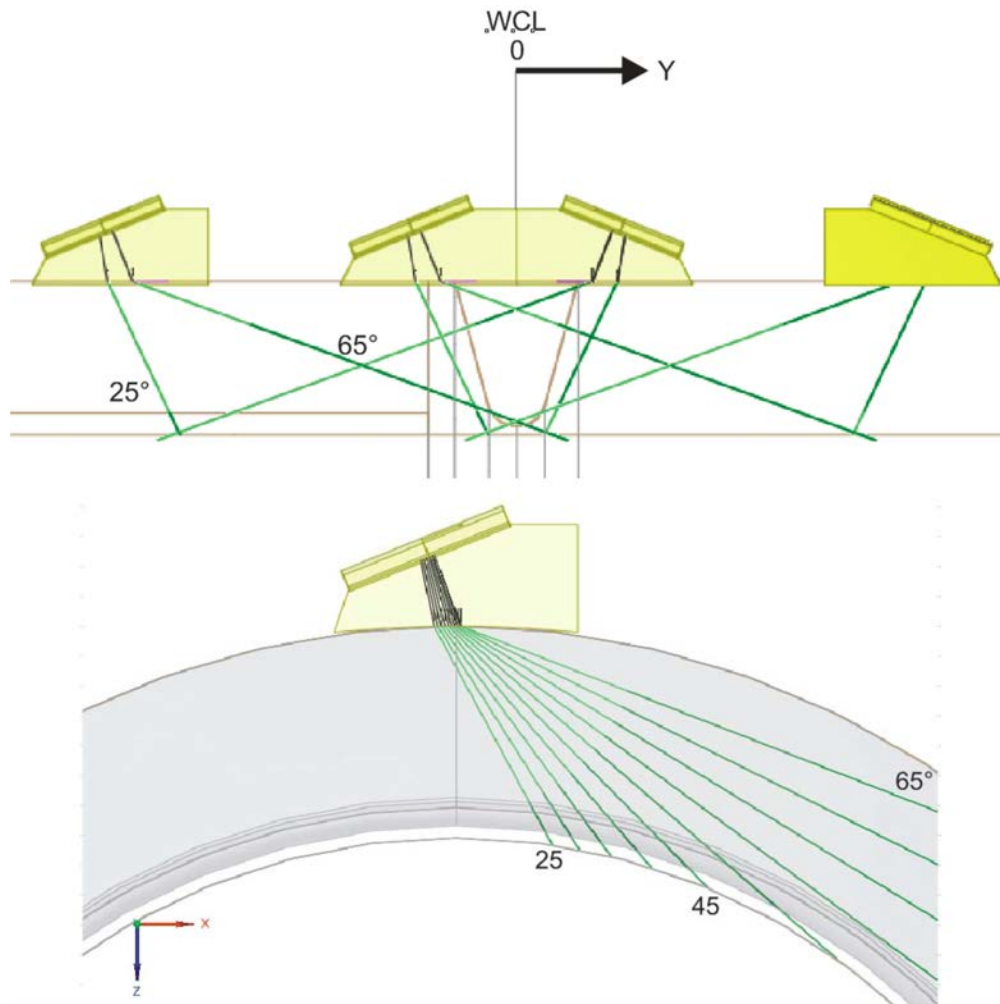


Figure C.51.

### C.2.3.2 NDE Equipment / UT Settings

#### Search Unit

For the measurement a GEIT probe and wedge was used. The essential variable of the search unit are described in the next chapters.

#### Crystal Shape

Probe type: Dual Element

Crystal shape: Focusing | Wedge | Instrumentation | Signal

Pattern: Linear phased array

Phased array

Whole aperture

Incident dimension: 28.75 mm

Orthogonal dimension: 8 mm

Grid and gap

Number of elements: 16

Gap between elements: 0.05 mm

Dimensions and arrangement of elements

Element width: 1.75 mm

Numbering

34 %

Top  0°

Bottom  +90°

D

X

Y

34	35	36	37	38	39	40	41	42	43	44	45	46	47	48	49
1	2	3	4	5	6	7	8	9	10	11	12	13	14	15	16

Figure C.52

## Focusing

Crystal shape	Focusing	Wedge	Instrumentation	Signal
Surface type		Flat ▼		
Focusing type		<input checked="" type="radio"/> Shaped element		

**Figure C.53**

## Wedge for Axial Scanning (Circ Flaws)

Crystal shape	Focusing	Wedge	Instrumentation	Signal
Geometry <span style="float:right">Material</span>				
Wedge Geometry (contact surface)				
Wedge Geometry		Cylindrical concave		
Axe (A)		parallel		
Radius (R)		203 mm		
Front length (L1)	19 mm	Width (L3)	36.47 mm	
Back length (L2)	21.04 mm	Height (L4)	12 mm	
Crystal orientation		Convergence point		
Refraction angle (R)	73.664 deg	Depth (L5)	9.098 mm	
Roof angle	6 deg	Distance (L6)	7.5 mm	
Incidence angle (I)	22 deg			
Other angles				
Rotation (A1)	0 deg			
Disorientation (A2)	0 deg			
Wave type		Propagation parameters		
Wave type	<input checked="" type="radio"/> Longitudinal	Longitudinal wave velocity	5900 ms <sup>-1</sup>	
	<input type="radio"/> Transverse	Transverse wave velocity	3230 ms <sup>-1</sup>	

Wedge material: Rexolite  $c_l=2237$  m/s

Figure C.54

## Wedge for Circumferential Scanning (Axial Flaws)

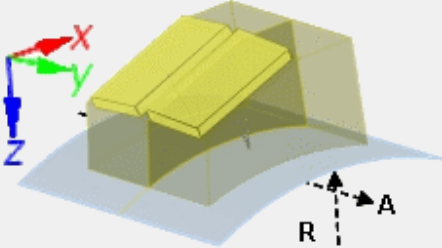
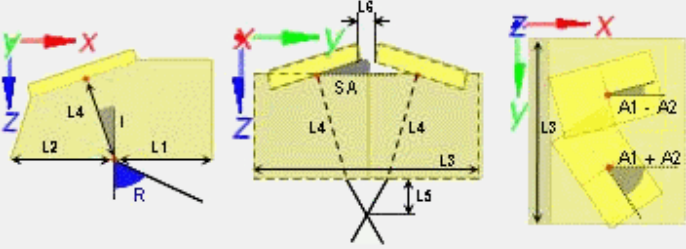
Crystal shape	Focusing	Wedge	Instrumentation	Signal
Geometry		Material		
Wedge Geometry (contact surface)				
Wedge Geometry		Cylindrical concave		
Axe (A)		perpendicular		
Radius (R)		203 mm		
				
				
Front length (L1)	20 mm	Width (L3)	36.47 mm	
Back length (L2)	20.4 mm	Height (L4)	12.5 mm	
Crystal orientation		Convergence point		
Refraction angle (R)	77.822 deg	Depth (L5)	3.627 mm	
Roof angle	6 deg	Distance (L6)	7.5 mm	
Incidence angle (I)	22 deg			
Other angles				
Rotation (A1)	0 deg			
Disorientation (A2)	0 deg			
Wave type		Propagation parameters		
Wave type	<input checked="" type="radio"/> Longitudinal <input type="radio"/> Transverse	Longitudinal wave velocity	5900 ms <sup>-1</sup>	
		Transverse wave velocity	3230 ms <sup>-1</sup>	

Figure C.55

Signal

*bandwidth (Hanning : 6dB / Gaussien : 12 dB)*

60 %

Center frequency  MHz

*Phase*

0 °

▲▼

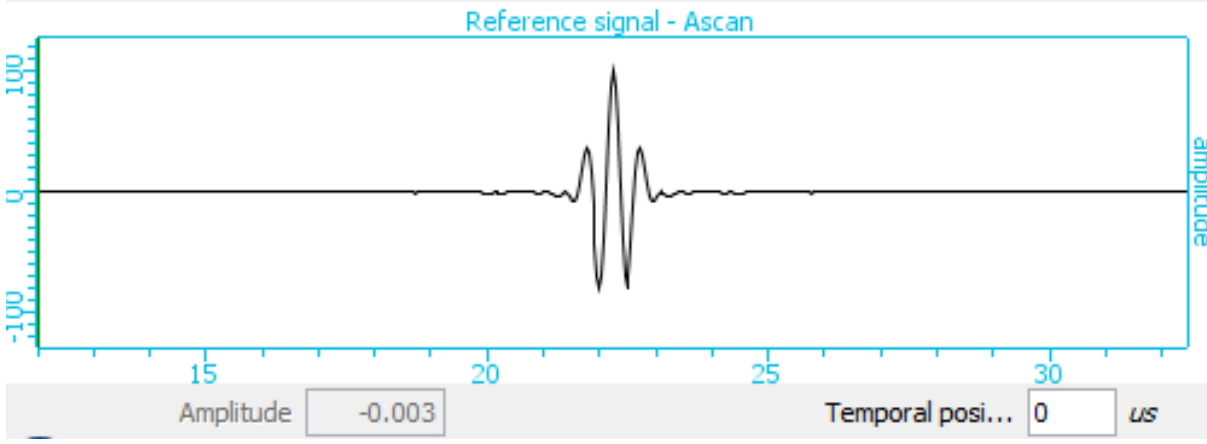
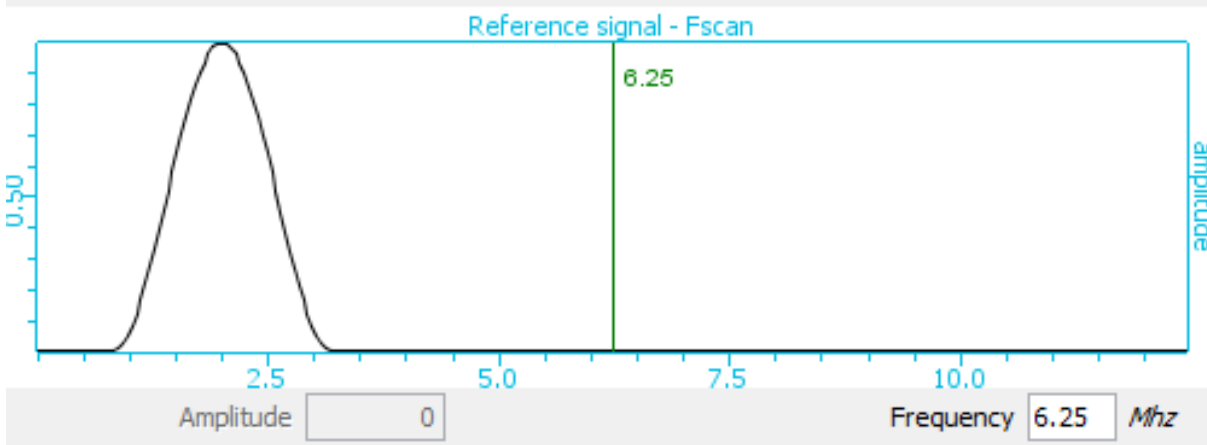


Figure C.56



## Phased Array Settings – Focal Laws

### Initialization

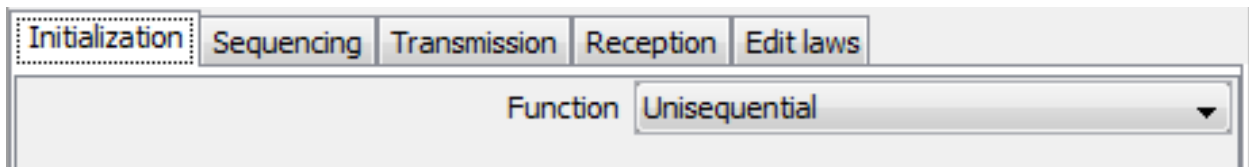


Figure C.57

### Sequencing

Transmission Element 1 (lower wedge end) to Element 14

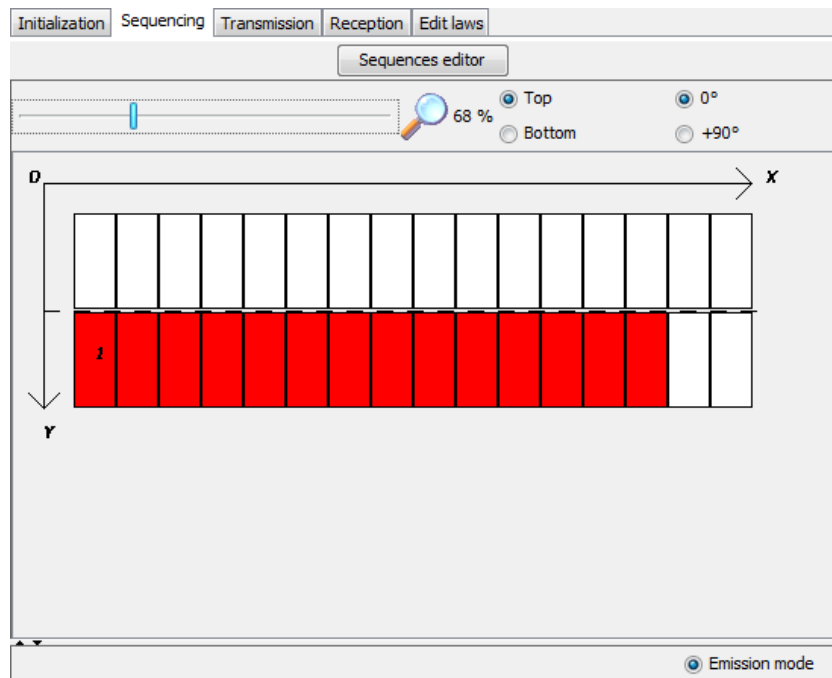
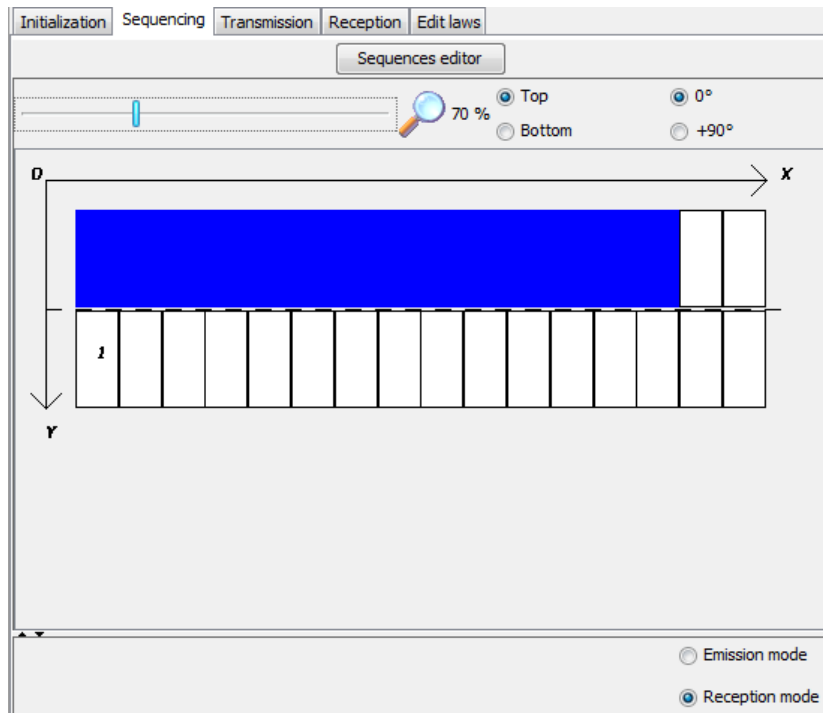


Figure C.58

Receiving Element 1 (lower wedge end) to Element 14



**Figure C.59**

Transmission

The focusing type is sectorial scanning. The sector range goes from 25° to 65° (Step 1°) longitudinal waves.

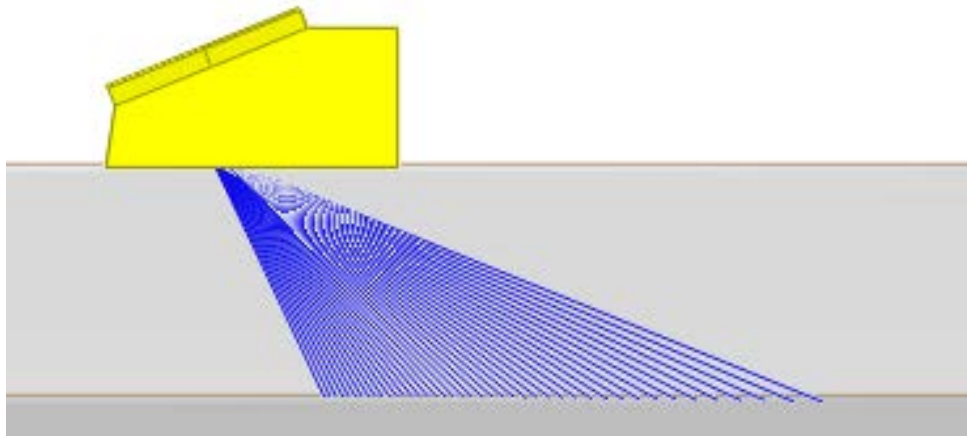


**Figure C.60**

Initialization	Sequencing	Transmission	Reception	Edit laws
Transmission definition				
Focusing type		Sectorial scanning		
Initial angle		25	deg	
Final angle		65	deg	
Number of steps		41		
Step size		0.976	deg	
Reference frame		Along normal		
Delay law calculation				
Wave type		<input checked="" type="radio"/> Longitudinal waves <input type="radio"/> Transversal waves <input type="checkbox"/> Backwall reflexion		
Amplitude law				
Amplitude law		Uniform		

**Figure C.61**

### UT Equipment Settings - M2M MultiX 64

For the measurements a M2M MultiX UT System was used. MultiX system is a fully parallel architecture with 64 channels. In the following chapters the essential equipment settings are listed.

## General Settings

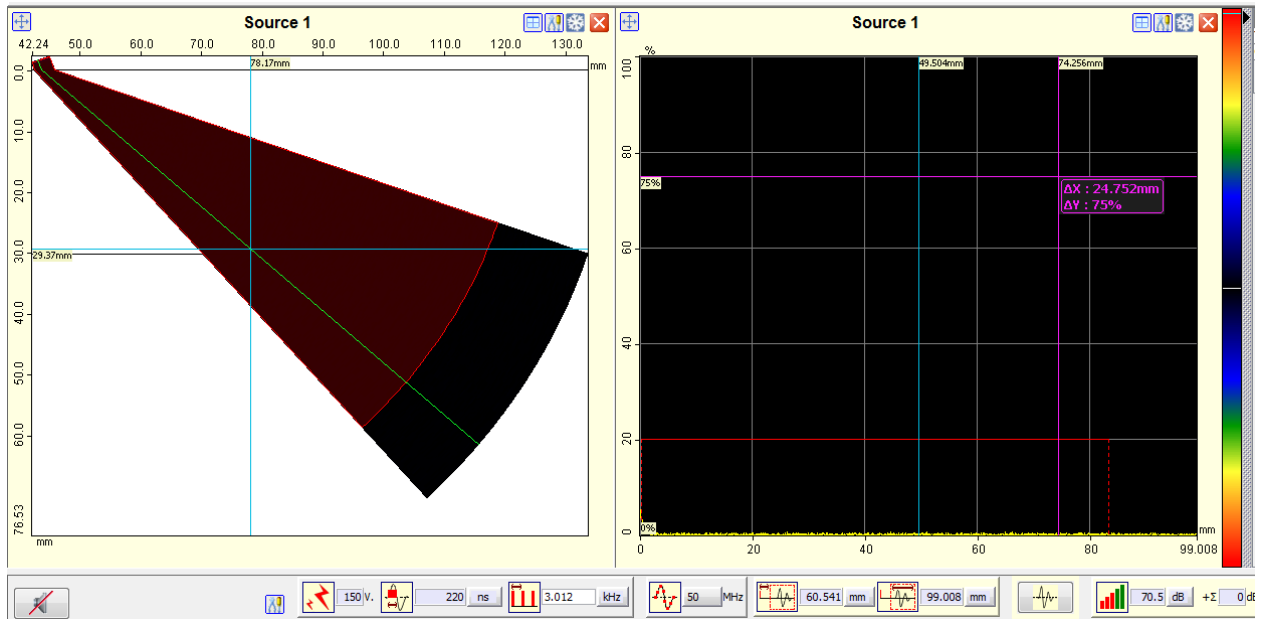


Figure C.62

## Gates

N°	Name	Color	State	Acquisition-Storage				Position and size				Processing			
				Store Peak+Z-Elm	Threshold time gate	Setting mode	Start (mm)	Width (mm)	End (mm)	Height (%)	Detection Mode	No Echo	Delta Time (mm)	Synchro Start	Synchro End
1	Gate 1	Red	<input checked="" type="checkbox"/>	Peak+Z	Always		0.119	83.181	83.3	20.09	Echo Max (Abs)	<input checked="" type="checkbox"/>	0.7757	Transmission	None

Figure C.63

## DAC

Index_point	Position (mm)	Amplitude (dB)

Figure C.64

## Coders

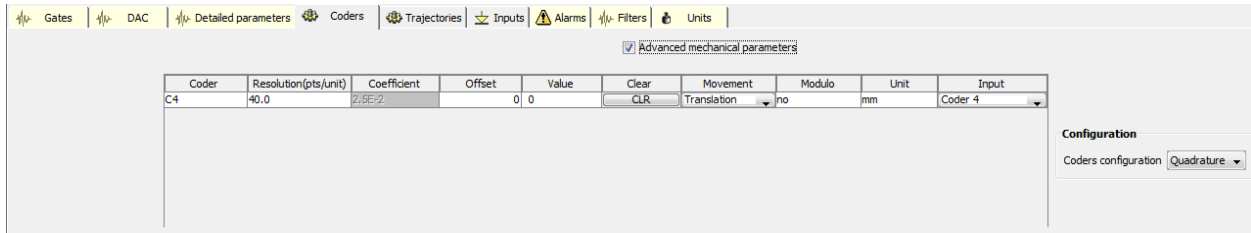


Figure C.65

## Trajectories

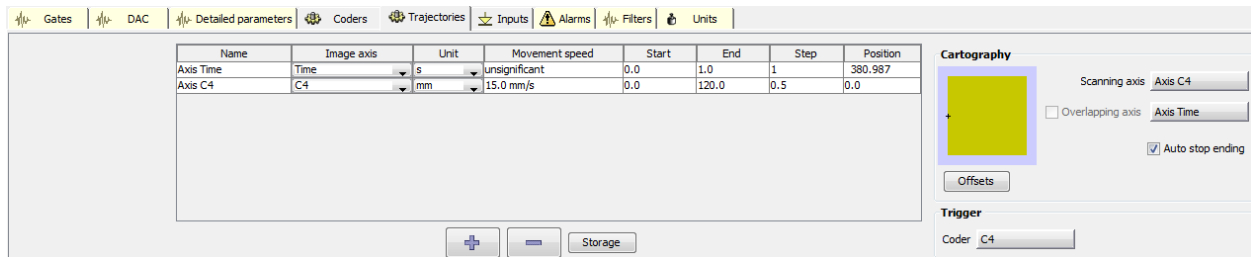


Figure C.66

## Units

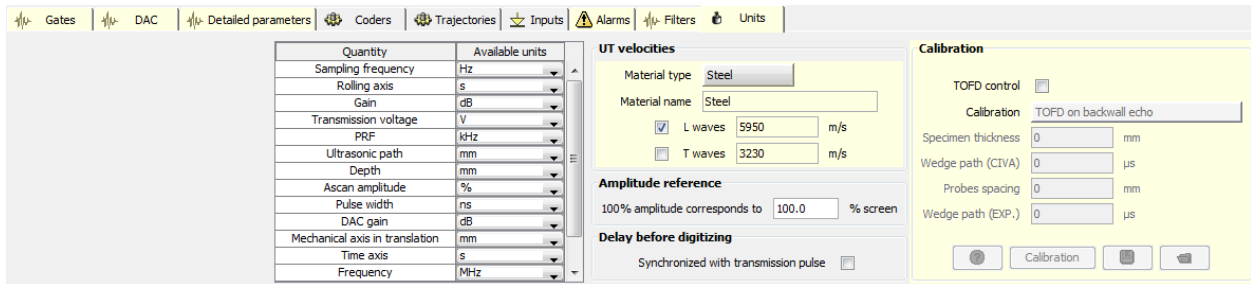


Figure C.67

### C.2.3.3 Data Acquisition (Scan Plan for Manual Examination)

#### Scanning for Circumferential Flaws

- Beam shall be directed essentially perpendicular to the weld axis from both directions

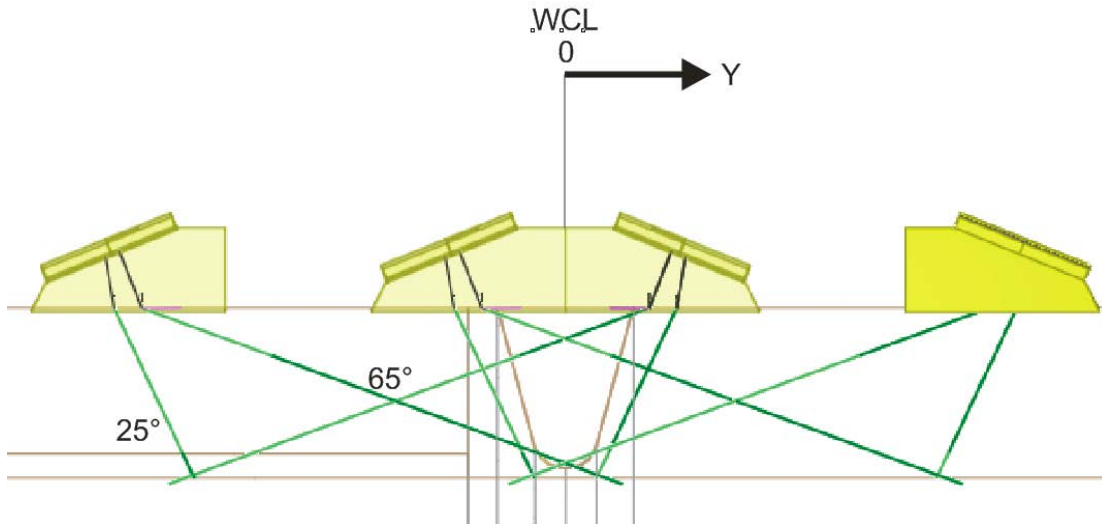


Figure C.68

#### Scanning for Axial Flaws

- Beam shall be directed essentially parallel to the weld in two opposing directions

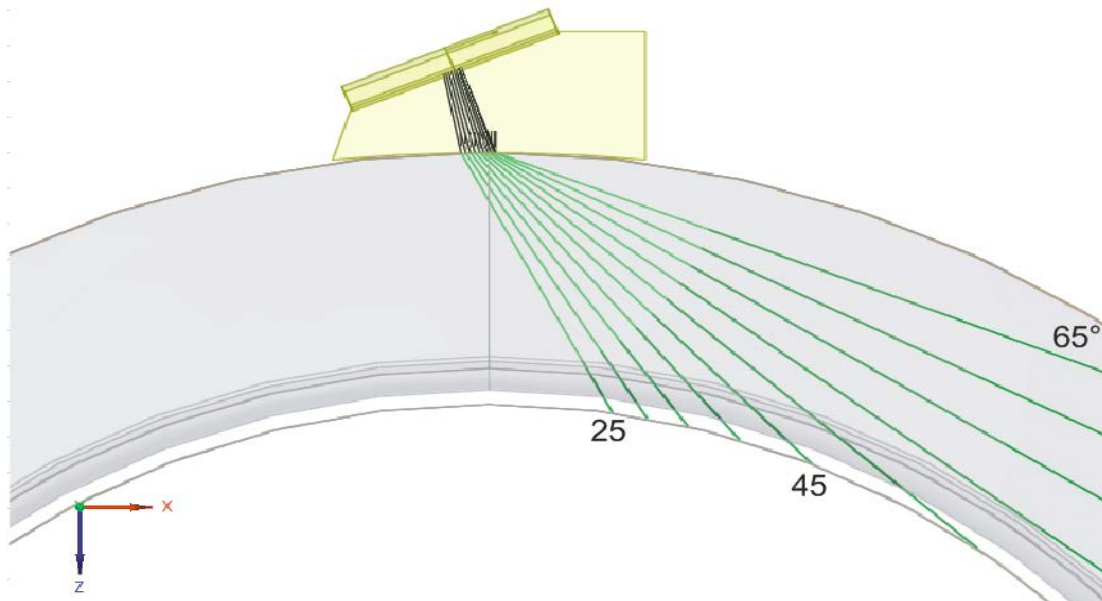


Figure C.69

#### **C.2.3.4 Analysis**

##### **Detection**

The detection of surface breaking ID flaws relies upon the corner response being observed.

##### **Characterization**

The characterization is based on the identification of flaw like indications which cannot be attributed to the component geometry based on the supplied as built drawings, manufacturing defects (reported during previous inspections) or indications due to reflection's or scattering on the anisotropic und heterogeneous weld structure.

Flaw discrimination criterions:

- Good signal to noise ratio (variations along the length)
- Plots to susceptible crack location
- Substantial echo dynamic travel
- Areas of unique amplitude
- Inconsistent time base positions
- Tip signals
- Conformation from the opposite direction
- Seen with many angles
- Mode converted shear signal (only circ flaws with substantial depth)
- Non relevant indications criterions:
- Near WCL or weld geometry
- Seen continuously
- Consistent time & amplitude
- Weak echo dynamic travel

##### **Length Sizing**

- Length of a flaw is determined by moving the probe along the flaw.
- on the same side of the weld as the indication

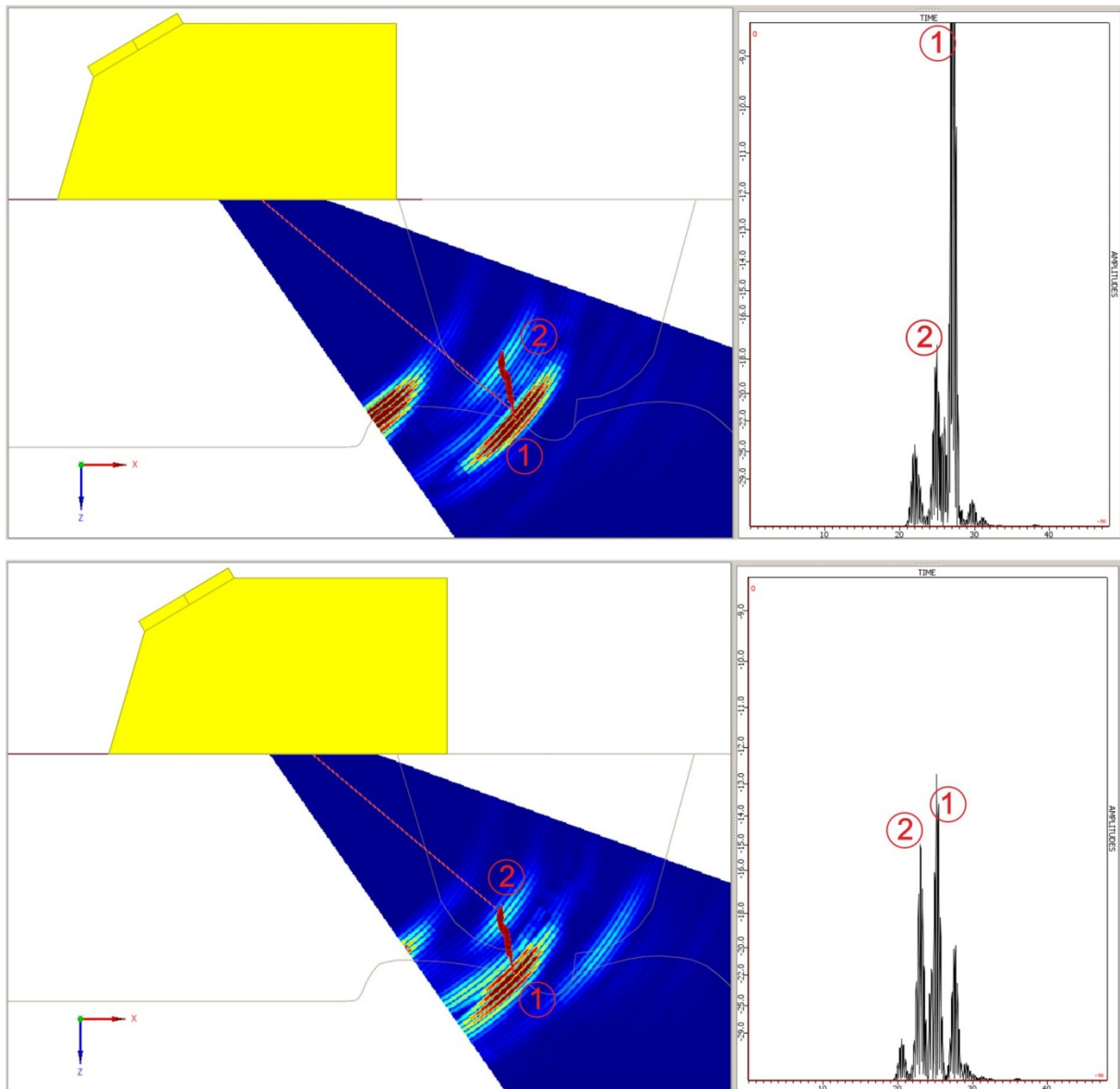
- optimize the signal from the flaw indication
- adjust the system gain until the response is ~ 80 % FSH
- scan along the length of the flaw in each direction until the signal response has been reduced to:
  - background noise for far side indication
  - 20% FSH (12 dB drop) for near side indication
- The length on outside diameter is longer than the actual inside diameter length. Calculate correct ID flaw length according to:  $(ID/OD) \times OD \text{ flaw length} = ID \text{ flaw length}$ .

### **Depth Sizing**

For flaw depth sizing the Absolut Arrival Time Technique (AATT) is used. The technique relies upon obtaining a direct signal response from the flaw tip using a material depth calibration. From the flaw tip response the amount of unflawed material or remaining ligament can be read directly from the Sscan. Flaw depth is calculated by subtracting the remaining ligament from the actual material thickness.

The figure below illustrates the technique.





- ① Flaw Base ID (corner trap)
- ② Tip diffraction signal

**Figure C.70**

### **Defect Positioning**

Due to uncertainties associated with sound propagation in anisotropic, heterogeneous austenitic weld material indication positioning require detailed evaluation. The information provided below may assist indication positioning.

- Perform thickness and surface contour recordings at the indication position.
- Evaluate the flaw signal amplitude responses from each side of the weld. Observe if the signal response appears reduced due to weld volume sound attenuation from one side or another.
- Identify standard benchmark responses (weld root, weld noise, acoustic interfaces) and flaw indication responses.
- Coordinate and plot the information on a cross sectional drawing of the weld.

### C.2.3.5 Self Assessment

The manual Phased Array Technique using a dual linear search unit and longitudinal waves in the range from 25° to 65° demonstrated good detection, length sizing and TWS performance of ID flaws with depth greater than 10% of the wall thickness.

## C.2.4 Phased Ultrasonic Array, Technique ID 131-PA2

### C.2.4.1 Overview

The techniques described in this report were utilized for the examination of the PARENT specimens P4. In case of P4 different techniques were used for examination in +Y and -Y direction.

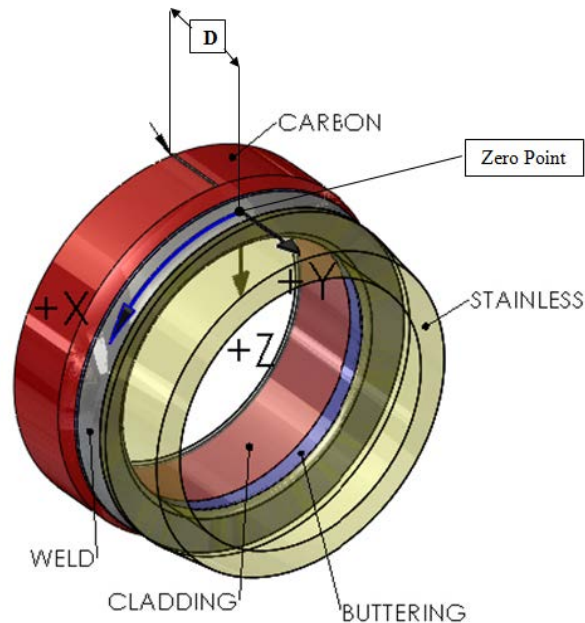


Figure C.71

### Scanning for Circumferential Flaws in +Y Direction

Method	Phased Array Ultrasonic Testing
Array / Technique	Dual / Linear / Transmit - Receive
Wave Mode	Longitudinal
Angle Range	25° – 65°
Frequency	2 MHz
UT Instrument	M2M MultiX 64
Scan Plan	Manual scanning perpendicular to weld in +Y direction
Scanning Surface	OD

### Scanning for Circumferential Flaws in -Y Direction

Method	Phased Array Ultrasonic Testing
Array / Technique	Single / Linear / Puls Echo
Wave Mode	Longitudinal
Angle Range	40° – 75°
Frequency	2.33 MHz
UT Instrument	M2M MultiX 64
Scan Plan	Manual scanning perpendicular to weld in -Y direction
Scanning Surface	OD

#### C.2.4.2 NDE Equipment / UT Settings / +Y Technique

##### Search Unit

For the measurement a GEIT probe and wedge was used. The essential variable of the search unit are described in the next chapters.

## Crystal Shape

Probe type: Dual Element

Crystal shape: Focusing | Wedge | Instrumentation | Signal

Pattern: Linear phased array

Phased array

Whole aperture

Incident dimension: 28.75 mm

Orthogonal dimension: 8 mm

Grid and gap

Number of elements: 16

Gap between elements: 0.05 mm

Dimensions and arrangement of elements

Element width: 1.75 mm

Numbering

34 %

Top  0°

Bottom  +90°

D

X

34 35 36 37 38 39 40 41 42 43 44 45 46 47 48 49

1 2 3 4 5 6 7 8 9 10 11 12 13 14 15 16

Y

Figure C.72

## Focusing

Crystal shape: Focusing | Wedge | Instrumentation | Signal

Surface type: Flat

Focusing type:  Shaped element

Figure C.73

## Wedge for Axial Scanning (Circ Flaws)

Crystal shape | Focusing | Wedge | Instrumentation | Signal

Geometry | Material

Wedge Geometry (contact surface)

Wedge Geometry: Cylindrical concave

Axe (A): parallel

Radius (R): 203 mm

Front length (L1): 19 mm

Back length (L2): 21.04 mm

Width (L3): 36.47 mm

Height (L4): 12 mm

Crystal orientation

Refraction angle (R): 73.664 deg

Roof angle: 6 deg

Incidence angle (I): 22 deg

Convergence point

Depth (L5): 9.098 mm

Distance (L6): 7.5 mm

Other angles

Rotation (A1): 0 deg

Disorientation (A2): 0 deg

Wave type

Wave type:  Longitudinal  Transverse

Propagation parameters

Longitudinal wave velocity: 5900 ms<sup>-1</sup>

Transverse wave velocity: 3230 ms<sup>-1</sup>

Wedge material: Rexolite  $c_l=2237$  m/s

Figure C.74

Signal

*bandwidth (Hanning : 6dB / Gaussien : 12 dB)*

60 %

Center frequency  MHz

*Phase*

0 °

▲▼

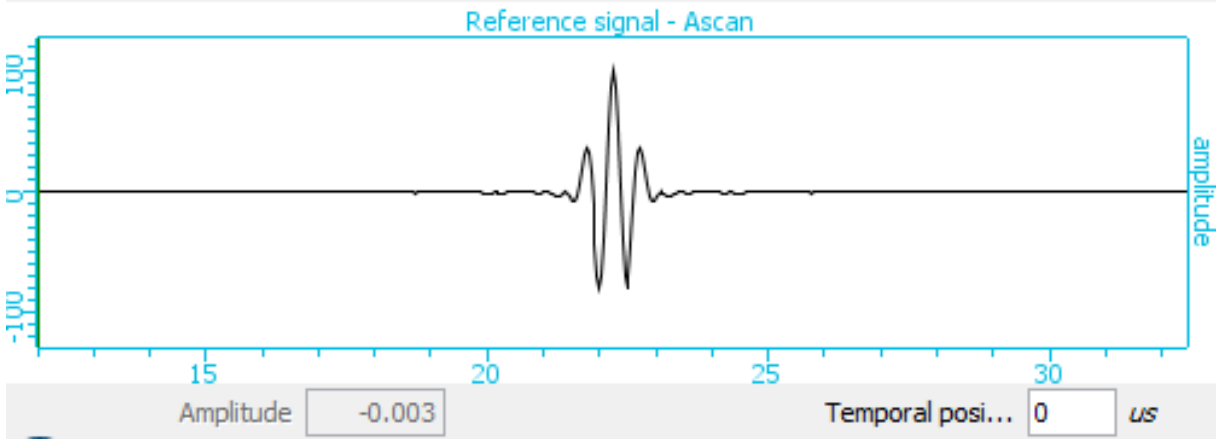
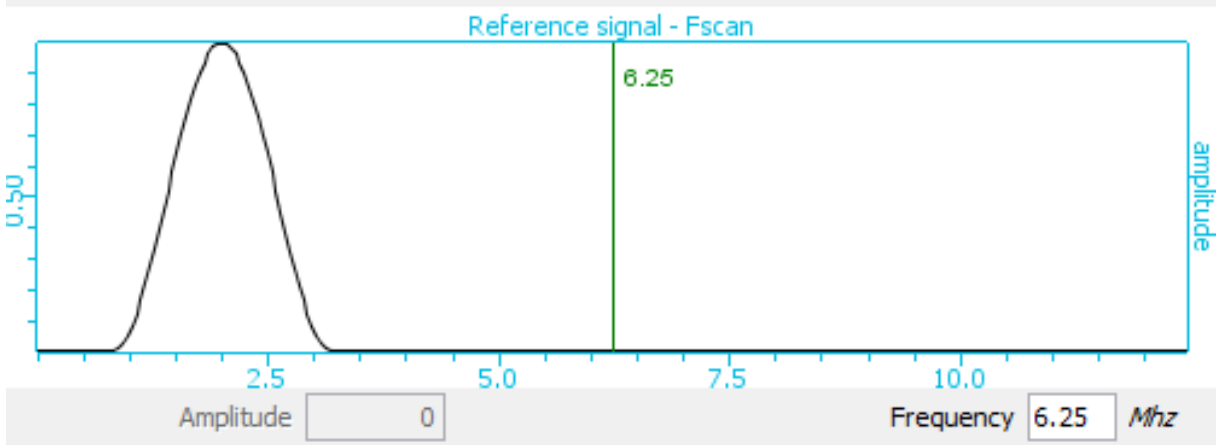


Figure C.75

## Phased Array Settings – Focal Laws

### Initialization

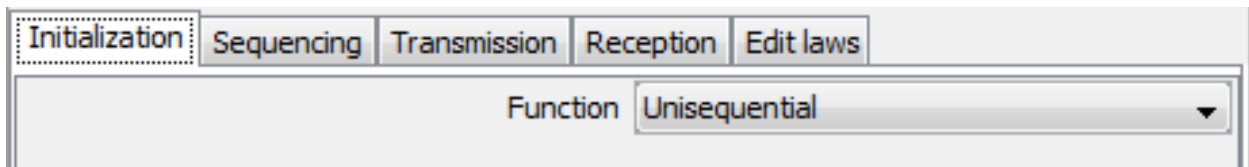


Figure C.76

### Sequencing

Transmission Element 1 (lower wedge end) to Element 14

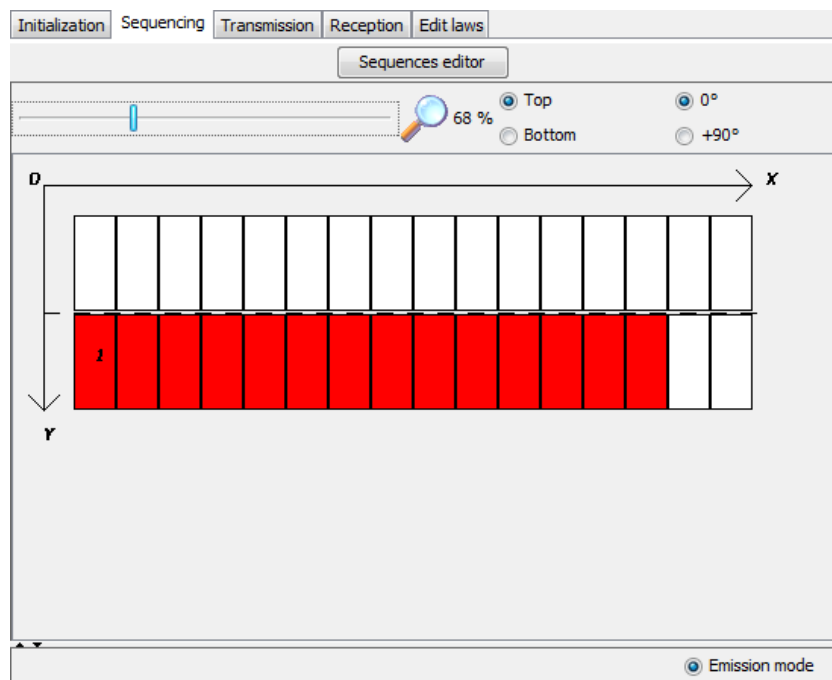
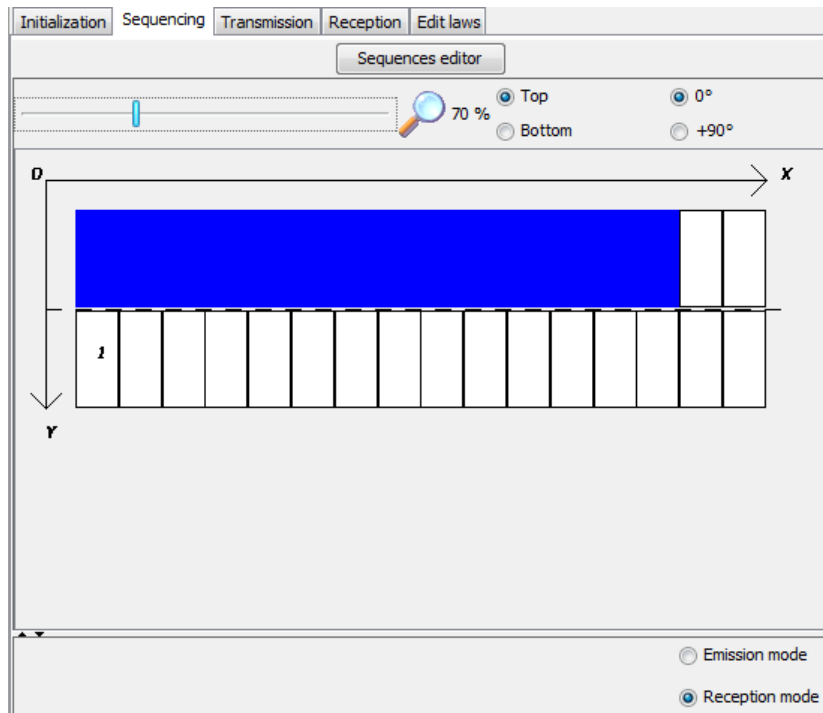


Figure C.77

Receiving Element 1 (lower wedge end) to Element 14



**Figure C.78**

Transmission

The focusing type is sectorial scanning. The sector range goes from 25° to 65° (Step 1°) longitudinal waves.

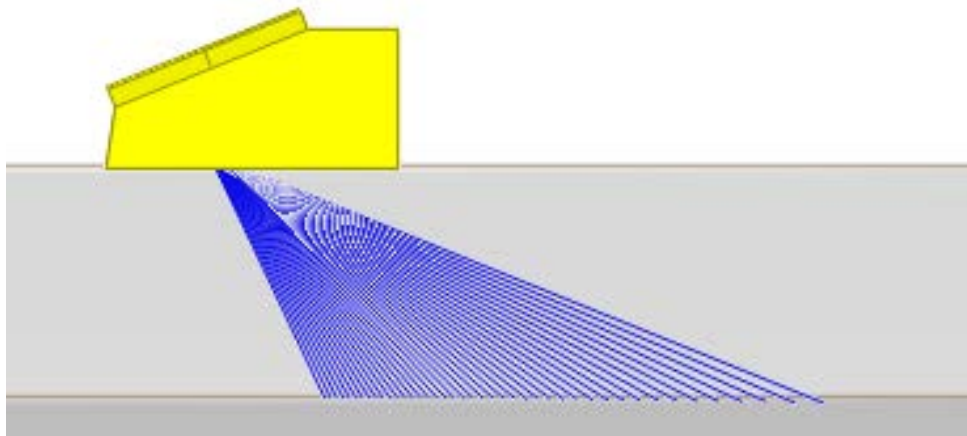


**Figure C.79**



Initialization	Sequencing	Transmission	Reception	Edit laws
Transmission definition				
Focusing type		Sectorial scanning		
Initial angle		25	deg	
Final angle		65	deg	
Number of steps		41		
Step size		0.976	deg	
Reference frame		Along normal		
Delay law calculation				
Wave type		<input checked="" type="radio"/> Longitudinal waves <input type="radio"/> Transversal waves <input type="checkbox"/> Backwall reflexion		
Amplitude law				
Amplitude law		Uniform		

**Figure C.80**

### UT Equipment Settings – M2M MultiX 64

For the measurements a M2M MultiX UT System was used. MultiX system is a fully parallel architecture with 64 channels. In the following chapters the essential equipment settings are listed.

## General Settings

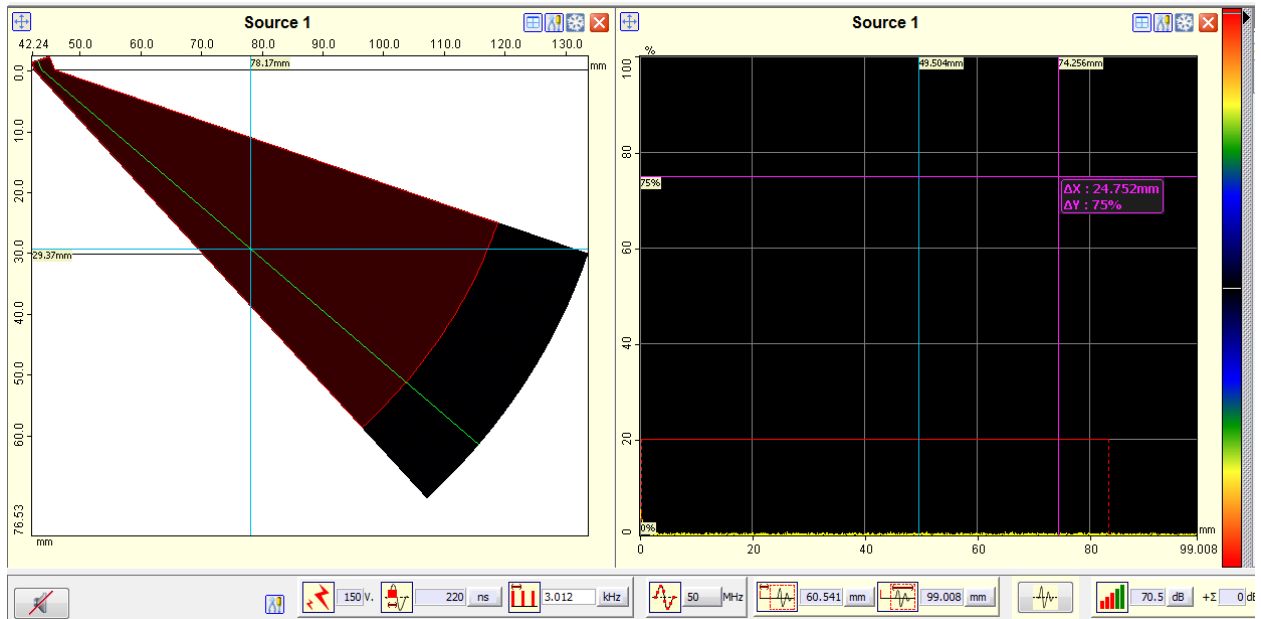


Figure C.81

## Gates

Identity		Acquisition-Storage				Position and size				Processing					
N°	Name	Color	State	Store Peak+Σ Elem	Threshold time gate	Setting mode	Start (mm)	Width (mm)	End (mm)	Height (%)	Detection Mode	No Echo	Delta Time (mm)	Synchro Start	Synchro End
1	Gate 1	Red	✓	Peak+Σ	Always		0.119	83.181	83.3	20.09	Echo Max (Abs)	✓	0.7757	Transmission	None

Figure C.82

## DAC

Index_point	Position (mm)	Amplitude (dB)

Figure C.83

## Coders

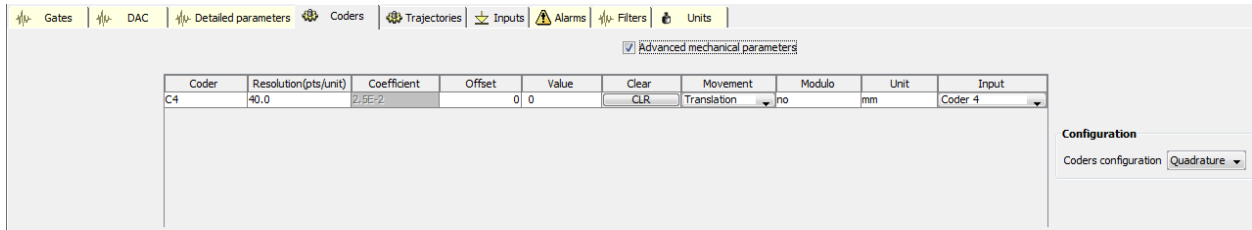


Figure C.84

## Trajectories

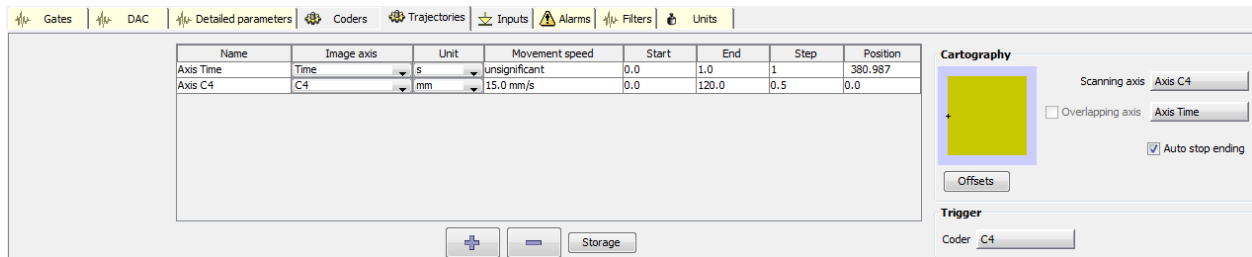


Figure C.85

## Units

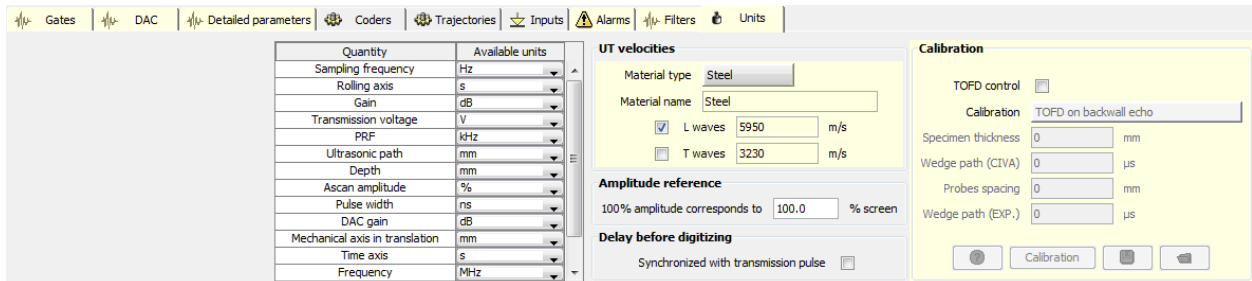


Figure C.86

### C.2.4.3 NDE Equipment / UT Settings / -Y Technique

#### Search Unit

For the measurement a Sonaxis probe and wedge was used. The essential variable of the search unit are described in the next chapters.

## Crystal Shape

Probe type Contact

Crystal shape Focusing Wedge Instrumentation Signal

Pattern Linear phased array

Phased array

Whole aperture

Incident dimension  mm

Orthogonal dimension  mm

Grid and gap

Number of elements

Gap between elements  mm

Dimensions and arrangement of elements

Element width  mm

Numbering

Top  0°

Bottom  +90°

10 %




Figure C.87

## Focusing

Crystal shape Focusing Wedge Instrumentation Signal

Surface type Flat

Focusing type  Shaped element

Figure C.88

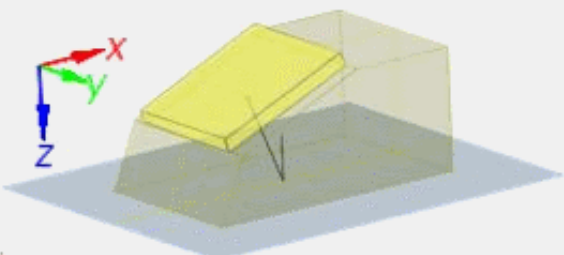
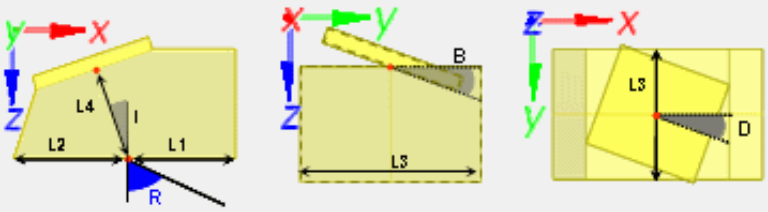
### Wedge for Axial Scanning (Circ Flaws)

Crystal shape Focusing Wedge Instrumentation Signal

Geometry Material

Wedge Geometry (contact surface) —————

Wedge Geometry Flat

Front length (L1)  mm

Back length (L2)  mm

Width (L3)  mm

Height (L4)  mm

Crystal orientation —————

Refraction angle (R)  deg

Incidence angle (I)  deg

Other angles —————

Squint angle (B)  deg

Disorientation (D)  deg

Figure C.89 Wedge Material: Rexolite  $c_l=2237$  m/s

Signal

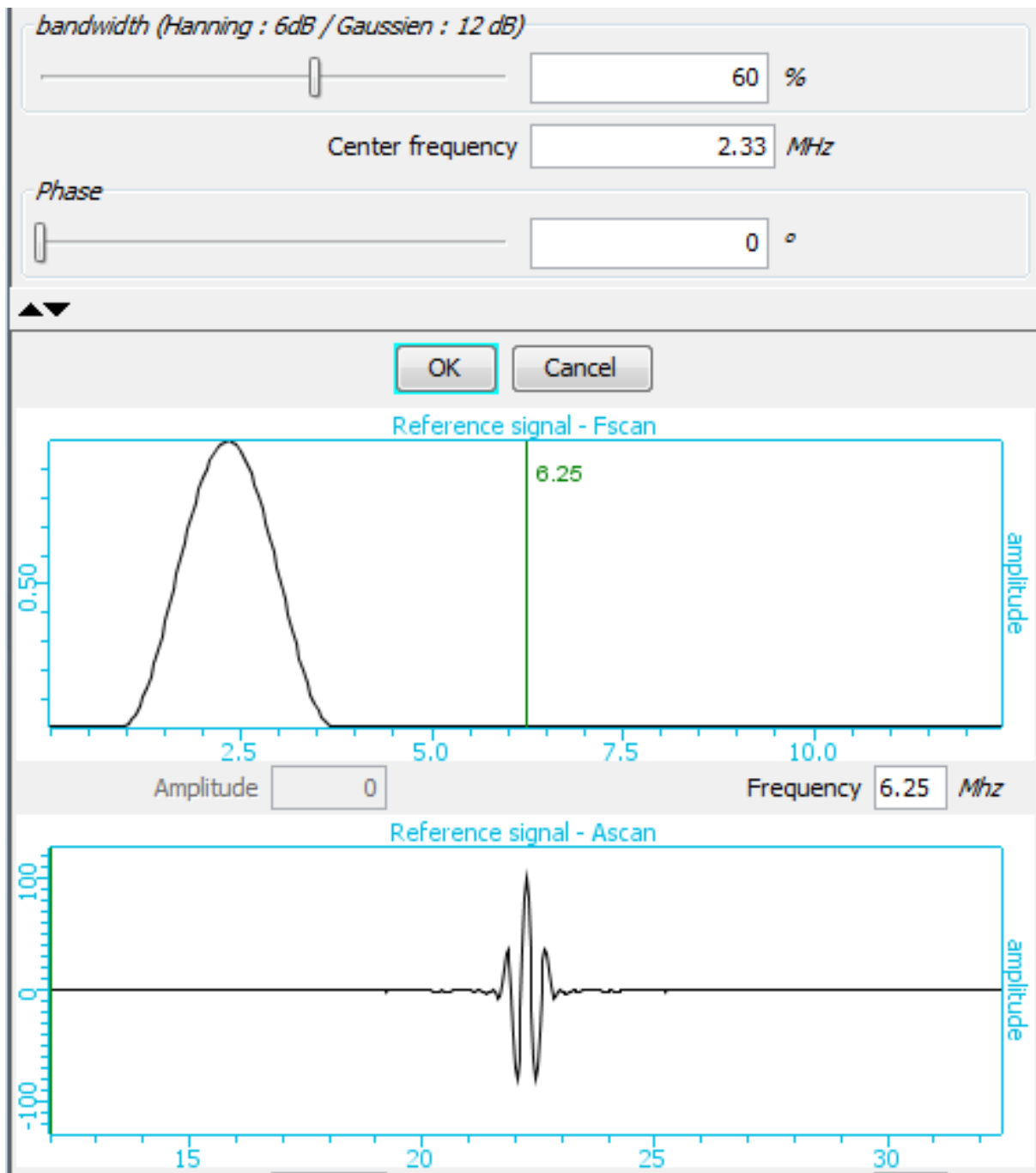


Figure C.90

## Phased Array Settings – Focal Laws

### Initialization

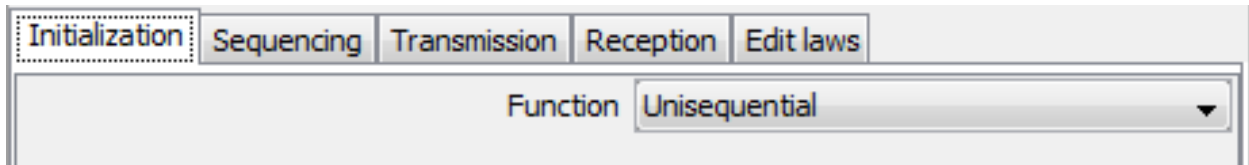


Figure C.91

### Sequencing

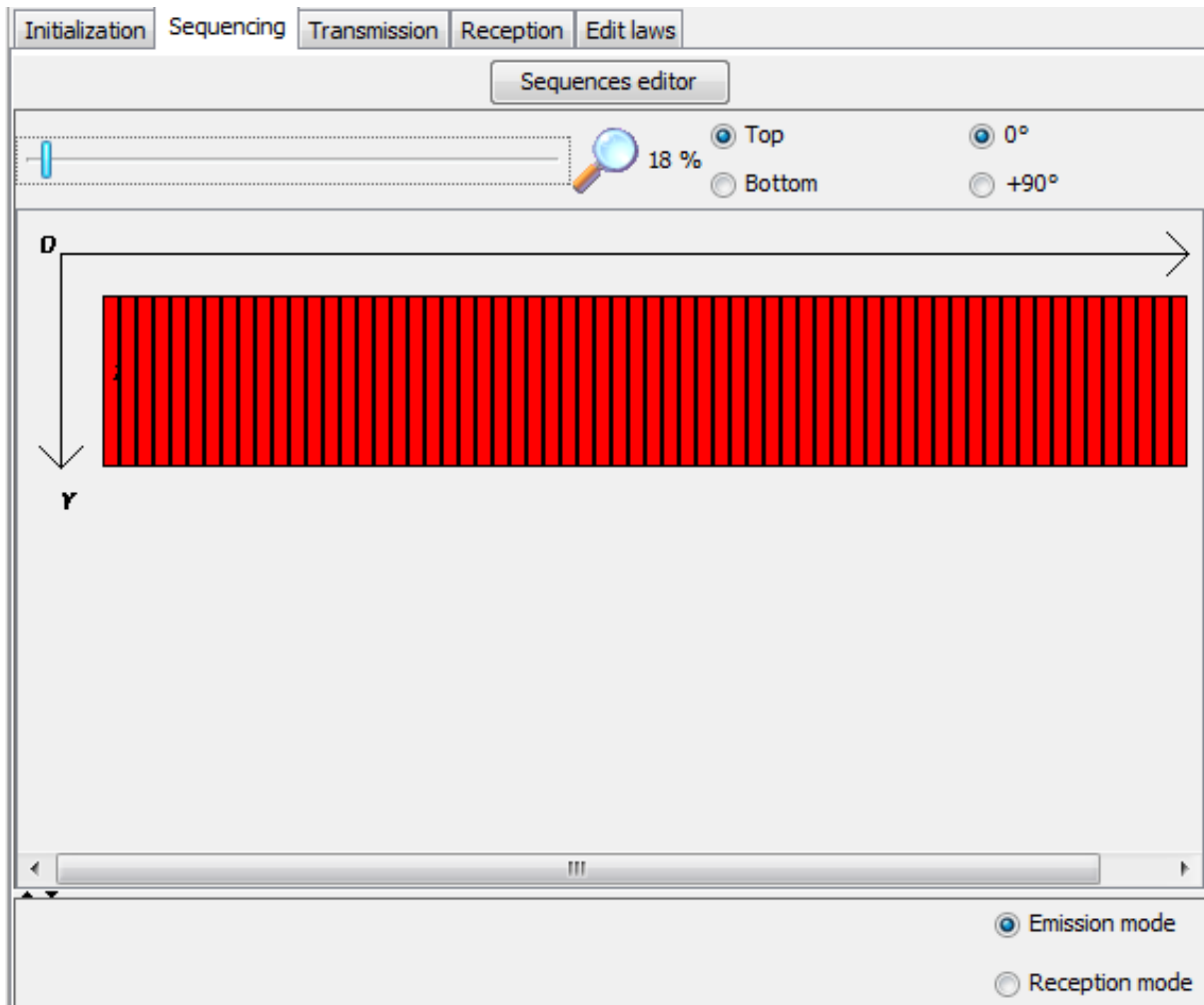


Figure C.92

### Transmission

The focusing type is sectorial scanning with constant focal depth at 35mm. The sector range goes from 45° to 75° (Step 1°) longitudinal waves.

Initialization	Sequencing	Transmission	Reception	Edit laws
Transmission definition				
Focusing type		Direction and depth scanning		
Algorithm		<input checked="" type="radio"/> Optimized point <input type="radio"/> Geometrical point		
Number of steps		61		
Extremity n°1		Extremity n°2		
Angle	45 deg	Angle	75 deg	
Depth	35 mm	Depth	35 mm	
Y	188.666 mm	Y	286.701 mm	
$\theta$	0 deg	$\theta$	0 deg	
R	126.5 mm	R	126.5 mm	
Delay law calculation				
Wave type		<input checked="" type="radio"/> Longitudinal waves <input type="radio"/> Transversal waves		
Amplitude law				
Amplitude law		Uniform		

**Figure C.93**

Sound Field Simulations for 65° Angle

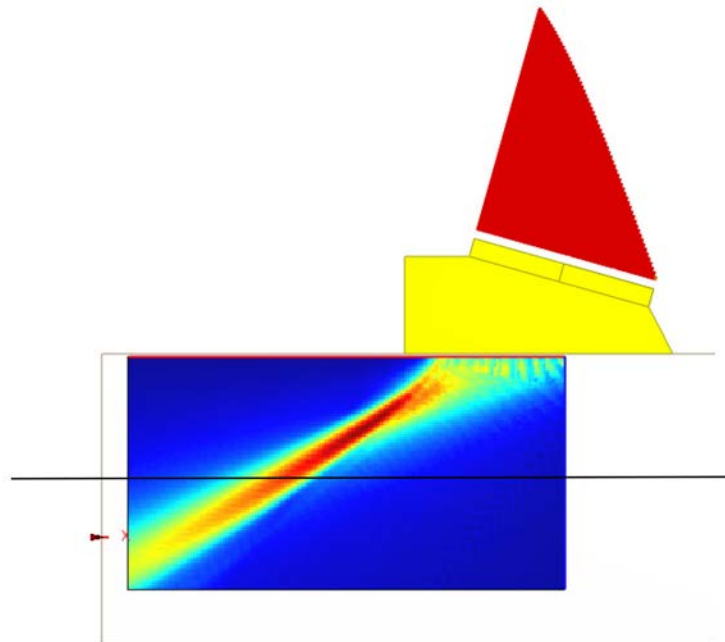


**Figure C.94** 65° Beam, Black Line: ID Position  $\approx$  38 mm



## UT Equipment Settings - M2M MultiX 64

For the measurements a M2M MultiX UT System was used. MultiX system is a fully parallel architecture with 64 channels. In the following chapters the essential equipment settings are listed.

### General Settings

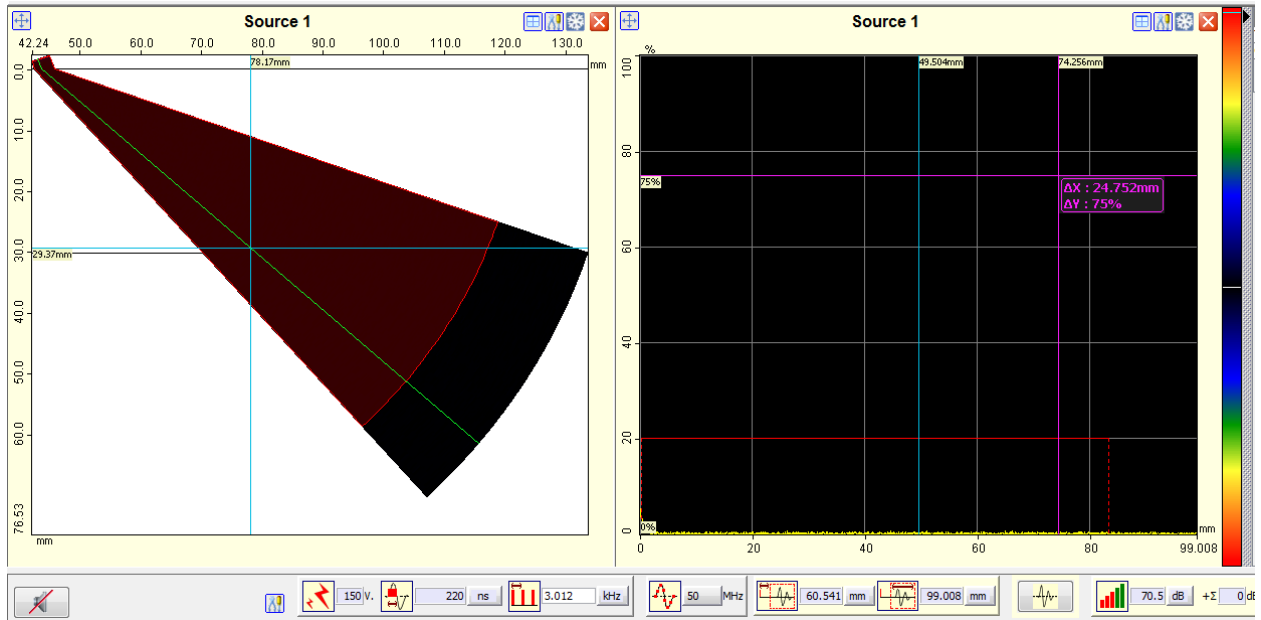


Figure C.95

### Gates

Identity		Acquisition-Storage				Position and size				Processing					
N°	Name	Color	State	Store Peaks-Elem	Threshold time gate	Setting mode	Start (mm)	Width (mm)	End (mm)	Height (%)	Detection Mode	No Echo	Delta Time (mm)	Synchro Start	Synchro End
1	Gate 1	Red	✓	Peaks+Σ	Always	Auto	0.119	83.181	83.3	20.09	Echo Max (Abs)	1	0.754	Transmission	None

Figure C.96

### DAC

Calibration		
Index_point	Position (mm)	Amplitude (dB)

DAC     Enable     Synchronized

Figure C.97

## Coders

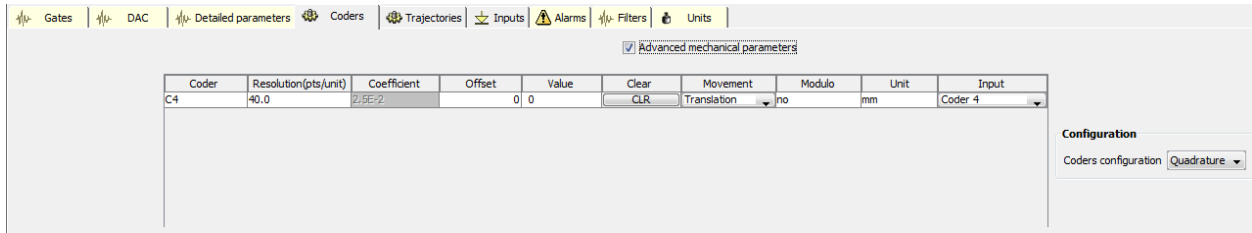


Figure C.98

## Trajectories

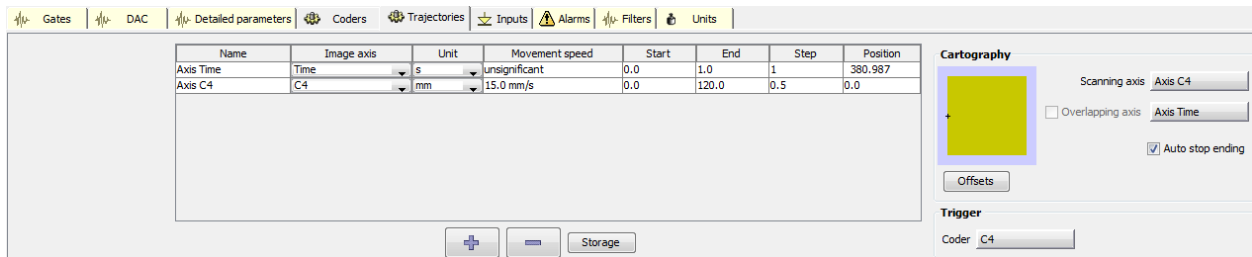


Figure C.99

## Filters

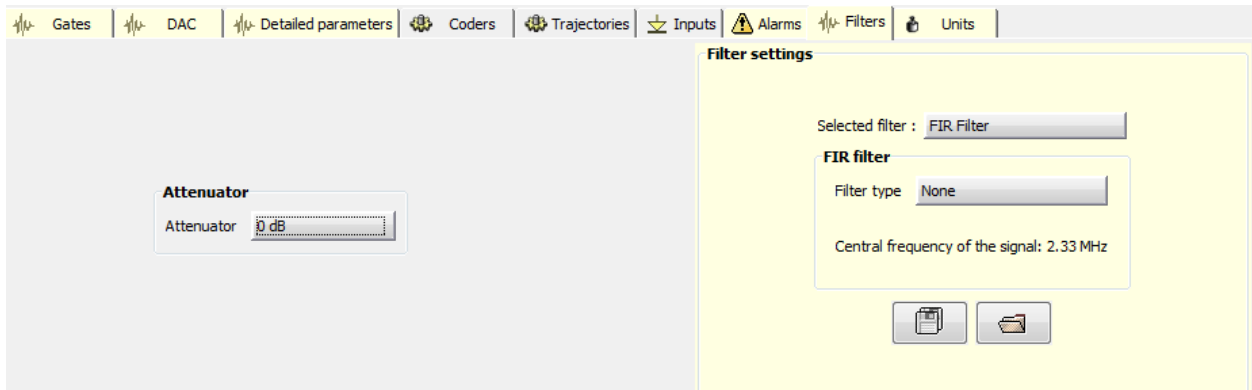


Figure C.100

## Units

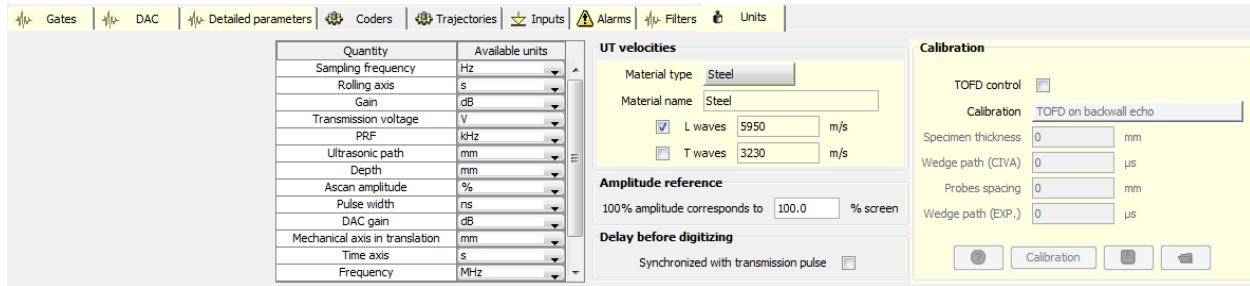


Figure C.101

### C.2.4.4 Data Acquisition (Scan Plan for Manual Examination)

#### Scanning for Circumferential Flaws

- Beam shall be directed essentially perpendicular to the weld axis from both directions.

### C.2.4.5 Analysis

#### Detection

The detection of surface breaking ID flaws relies upon the corner response being observed.

#### Characterization

The characterization is based on the identification of flaw like indications which cannot be attributed to the component geometry based on the supplied as built drawings, manufacturing defects (reported during previous inspections) or indications due to reflection's or scattering on the anisotropic und heterogeneous weld structure.

Flaw discrimination criterions:

- Good signal to noise ratio (variations along the length)
- Plots to susceptible crack location
- Substantial echo dynamic travel
- Areas of unique amplitude
- Inconsistent time base positions
- Tip signals
- Conformation from the opposite direction
- Seen with many angles

- Mode converted shear signal (only circ flaws with substantial depth)

Non relevant indications criterions:

- Near WCL or weld geometry
- Seen continuously
- Consistent time & amplitude
- Weak echo dynamic travel

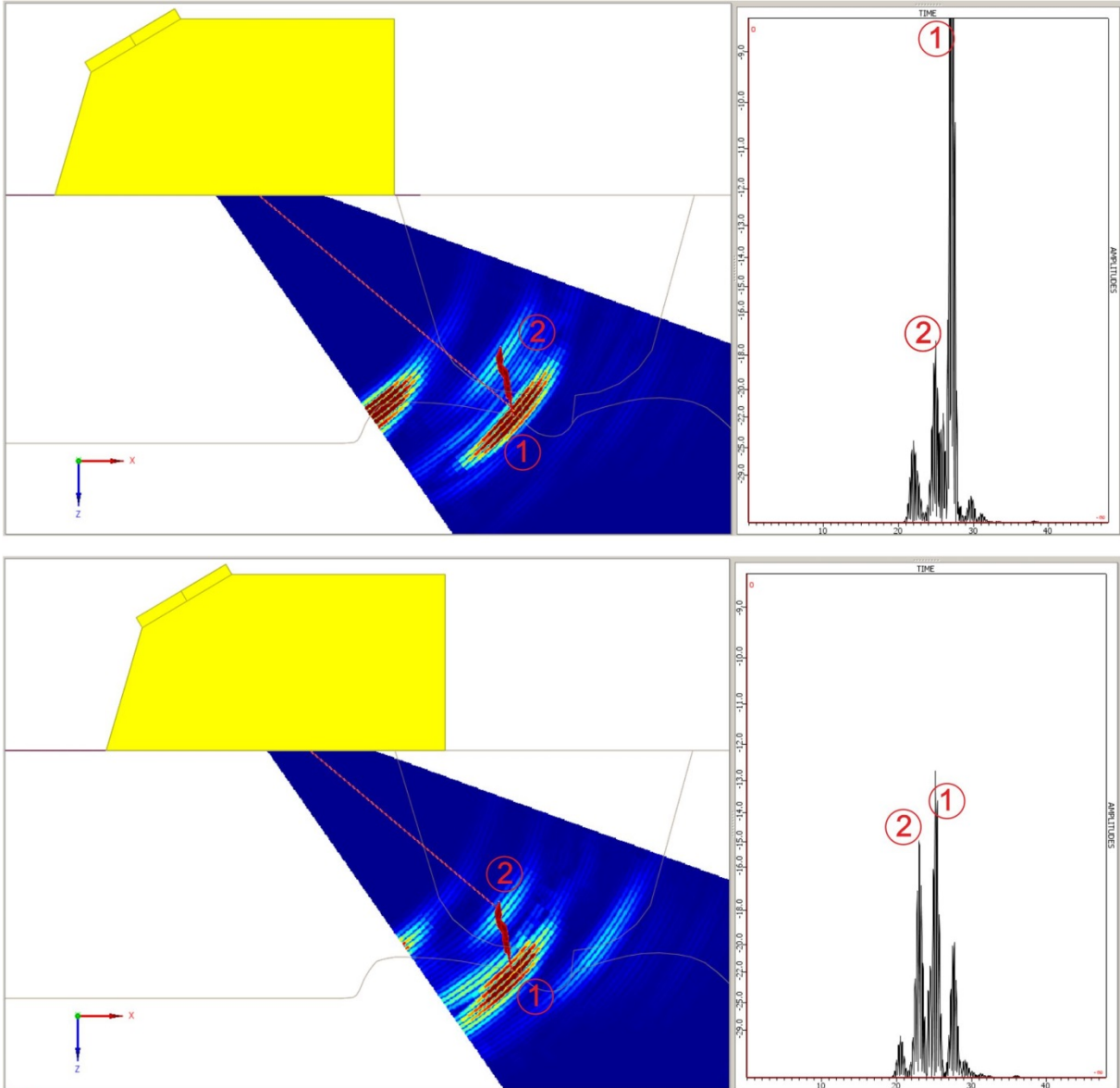
### **Length Sizing**

- Length of a flaw is determined by moving the probe along the flaw.
- on the same side of the weld as the indication
- optimize the signal from the flaw indication
- adjust the system gain until the response is ~ 80 % FSH
- scan along the length of the flaw in each direction until the signal response has been reduced to:
  - background noise for far side indication
  - 20% FSH (12 dB drop) for near side indication
- The length on outside diameter is longer than the actual inside diameter length. Calculate correct ID flaw length according to:  $(ID/OD) \times OD \text{ flaw length} = ID \text{ flaw length}$ .

### **Depth Sizing**

For flaw depth sizing the Absolut Arrival Time Technique (AATT) is used. The technique relies upon obtaining a direct signal response from the flaw tip using a material depth calibration. From the flaw tip response the amount of unflawed material or remaining ligament can be read directly from the Sscan. Flaw depth is calculated by subtracting the remaining ligament from the actual material thickness.

The figure below illustrates the technique.



- ① Flaw Base ID (corner trap)
- ② Tip diffraction signal

Figure C.102

## Defect Positioning

Due to uncertainties associated with sound propagation in anisotropic, heterogeneous austenitic weld material indication positioning require detailed evaluation. The information provided below may assist indication positioning.

- Perform thickness and surface contour recordings at the indication position.
- Evaluate the flaw signal amplitude responses from each side of the weld. Observe if the signal response appears reduced due to weld volume sound attenuation from one side or another.
- Identify standard benchmark responses (weld root, weld noise, acoustic interfaces) and flaw indication responses.
- Coordinate and plot the information on a cross sectional drawing of the weld.

### C.2.4.6 Self Assessment

#### Scanning for Circumferential Flaws in +Y Direction

The manual Phased Array Technique using a dual linear search unit and longitudinal waves in the range from 25° to 65° demonstrated good detection, length sizing and TWS performance of ID flaws with depth greater than 10% of the wall thickness.

#### Scanning for Circumferential Flaws in -Y Direction

Using the +Y direction technique the detection, length sizing and TWS of two flaws in P4 was challenging. Therefore a different search unit was for the -Y direction examinations. The performance of this search unit was better but TWS was still very challenging. It has to be mentioned, that the used linear array probe is due to its size (large footprint) not suitable for field inspections.

## C.2.5 Phased Ultrasonic Array, Technique ID 131-PA3

### C.2.5.1 Overview

The techniques described in this report were utilized for the examination of the PARENT specimen P41.

Method	Phased Array Ultrasonic Testing
Array / Technique	Dual / Matrix / Transmit - Receive
Wave Mode	Longitudinal
Angle Range	40° – 70°
Frequency	1.5 MHz
UT Instrument	Phasor XS
Scan Plan	Manual scanning perpendicular to weld both directions
Scanning Surface	OD

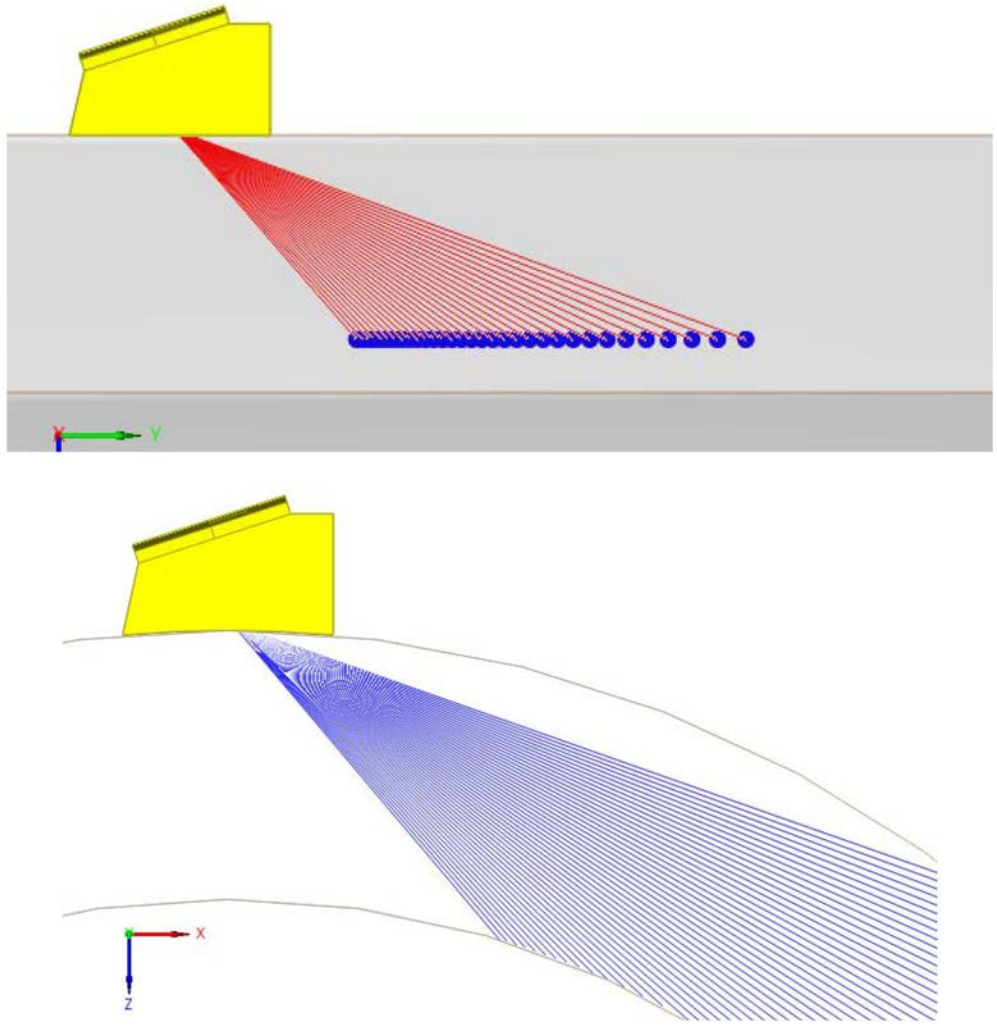


**Figure C.103**

**C.2.6 NDE Equipment / UT Settings**

**UT Instrument**

For the measurements a GEIT Phasor XS was used.

**Search Unit**

For the measurement a GEIT probe and wedge was used. The essential variable of the search unit are described in the next chapters.



Figure C.104



## Crystal Shape

Probe type: Dual Element

Crystal shape: Focusing | Wedge | Instrumentation | Signal

Pattern: Matrix phased array

Phased array

Whole aperture

Incident dimension: 19 mm

Orthogonal dimension: 12 mm

Grid and gap

Number of rows (incident plane): 5

Number of columns (orthogonal plane): 3

Gap between rows: 0 mm

Gap between columns: 0 mm

Dimensions and arrangement of elements

Width in incident plane: 3.8 mm

Width in orthogonal plane: 4 mm

Selected row: 2

Number of elements in selected row: 3

Numbering

134 %

Top  0°

Bottom  +90°

16	17	18	19	20
21	22	23	24	25
26	27	28	29	30
1	2	3	4	5
6	7	8	9	10
11	12	13	14	15

Figure C.105

Focusing

Crystal shape	Focusing	Wedge	Instrumentation	Signal
Surface type Flat				
Focusing type <input checked="" type="radio"/> Shaped element				

**Figure C.106**

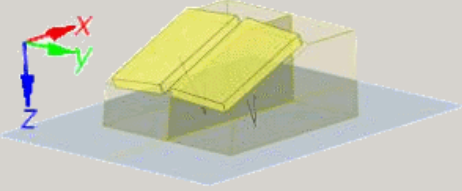
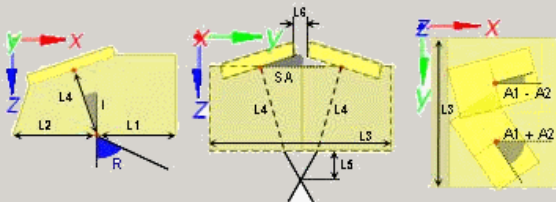
## Wedge for Axial Scanning (Circ Flaws)

Crystal shape | Focusing | **Wedge** | Instrumentation | Signal

Geometry | Material

Wedge Geometry (contact surface) —

Wedge Geometry Flat

Front length (L1)  mm

Back length (L2)  mm

Width (L3)  mm

Height (L4)  mm

Crystal orientation —

Refraction angle (R)  deg

Roof angle  deg

Incidence angle (I)  deg

Convergence point —

Depth (L5)  mm

Distance (L6)  mm

Other angles —

Rotation (A1)  deg

Disorientation (A2)  deg

Wave type —

Wave type  Longitudinal  Transverse

Propagation parameters —

Longitudinal wave velocity   $ms^{-1}$

Transverse wave velocity   $ms^{-1}$

Wedge material: Rexolite  $c_l=2237$  m/s

Figure C.107

### Wedge for Circumferential Scanning (Axial Flaws)

Probe type: Dual Element

Crystal shape: Focusing **Wedge** Instrumentation Signal

Wedge Geometry: Cylindrical concave  
 Axe (A): perpendicular  
 Radius (R): 406 mm

Front length (L1): 20.4 mm  
 Back length (L2): 20 mm  
 Width (L3): 36 mm  
 Height (L4): 14 mm

Crystal orientation ————— Convergence point —————

Refraction angle (R): 73.538 deg  
 Roof angle: 5.5 deg  
 Incidence angle (I): 22 deg  
 Depth (L5): 4.931 mm  
 Distance (L6): 8 mm

Other angles —————

Rotation (A1): 0 deg  
 Disorientation (A2): 0 deg

Figure C.108

# Signal

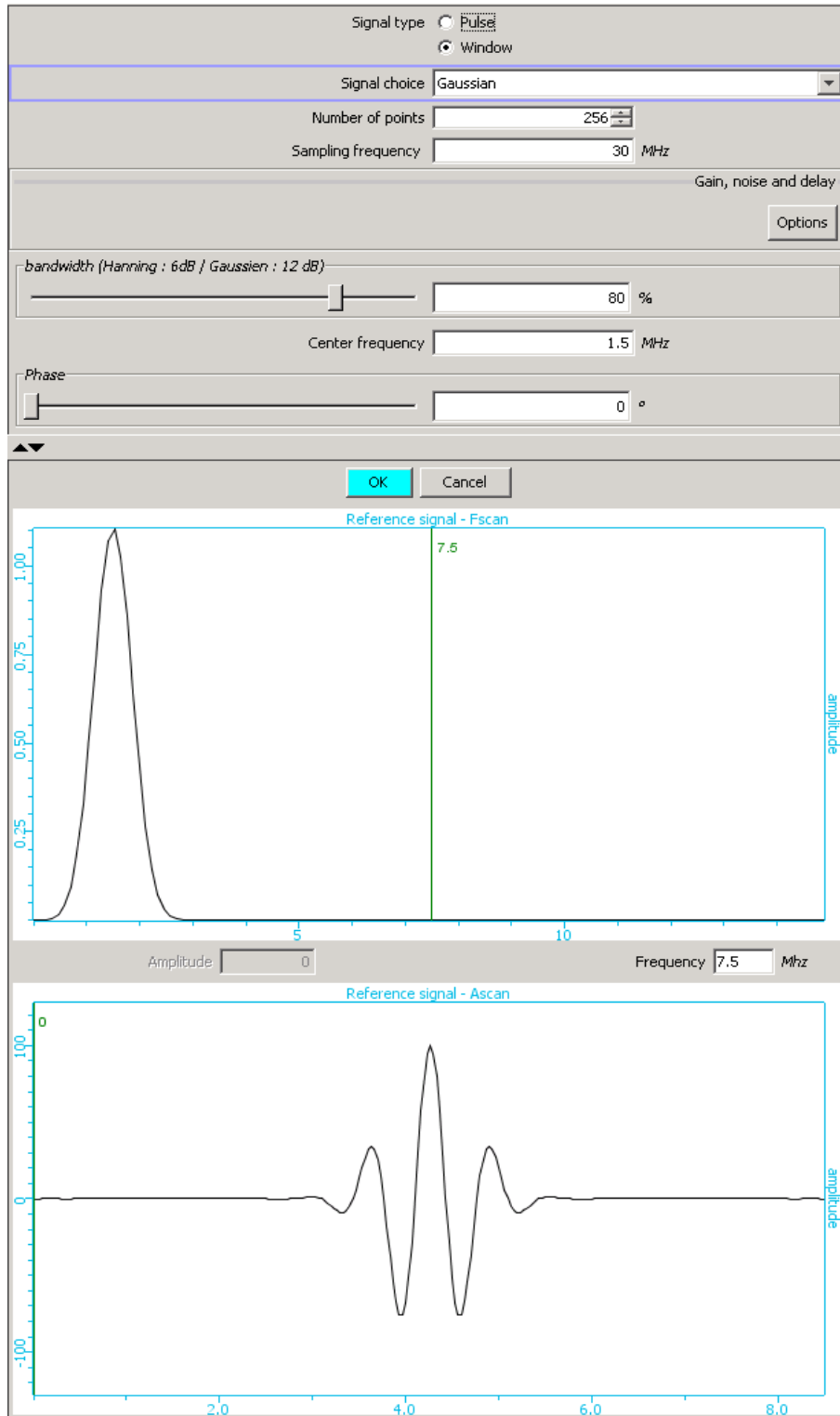


Figure C.109

## Phased Array Settings – Focal Laws

### Initialization

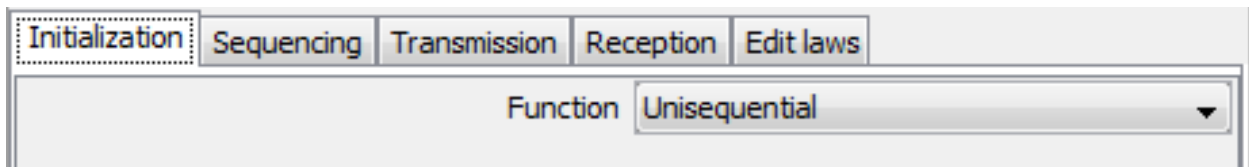


Figure C.110

### Sequencing

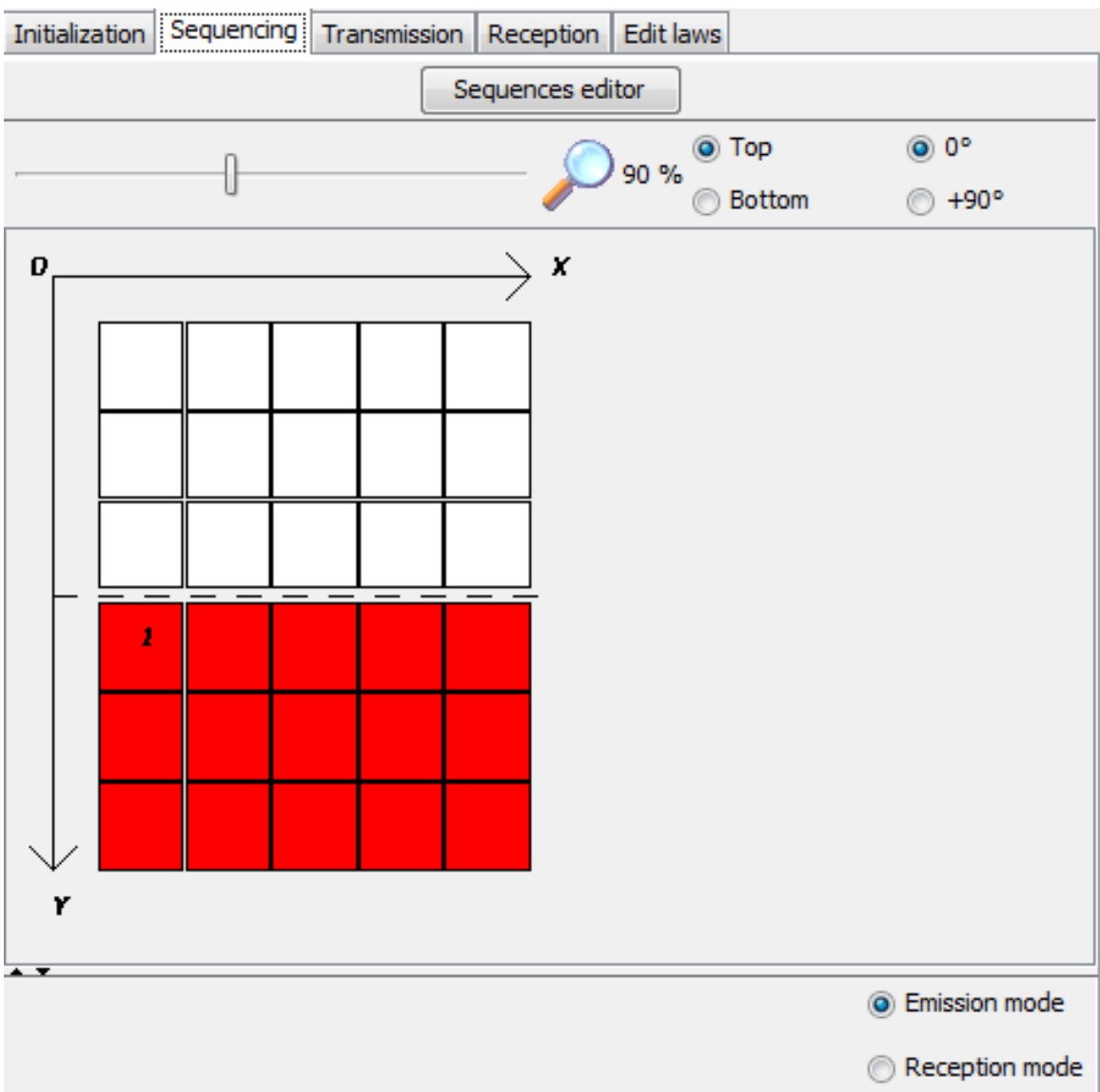


Figure C.111

## Transmission

The focusing type is sectorial scanning at a constant focal depth of 25.4 mm. The sector range goes from 40° to 70° (Step 1°) longitudinal waves.

Initialization Sequencing **Transmission** Reception Edit laws

Transmission definition

Focusing type: Direction and depth scanning

Algorithm:  Optimized point  Geometrical point

Number of steps: 31

Extremity n°1

Angle	40	deg
Depth	25.4	mm
Y	208.768	mm
θ	-0	deg
R	117.6	mm

Extremity n°2

Angle	70	deg
Depth	25.4	mm
Y	257.241	mm
θ	0	deg
R	117.6	mm

Orientation

Orientation type: Fixed

Squint	0	deg
Skew	0	deg

Delay law calculation

Wave type:  Longitudinal waves  Transversal waves

Amplitude law

Figure C.112

### C.2.6.1 Data Acquisition (Scan Plan for Manual Examination)

#### Scanning for Circumferential Flaws

- Beam shall be directed essentially perpendicular to the weld axis from both directions

#### Scanning for Axial Flaws

- Beam shall be directed essentially parallel to the weld in two opposing directions

## **C.2.6.2 Analysis**

### **Detection**

The detection of surface breaking ID flaws relies upon the corner response being observed.

### **Characterization**

The characterization is based on the identification of flaw like indications which cannot be attributed to the component geometry based on the supplied as built drawings, manufacturing defects (reported during previous inspections) or indications due to reflection's or scattering on the anisotropic und heterogeneous weld structure.

Flaw discrimination criterions:

- Good signal to noise ratio (variations along the length)
- Plots to susceptible crack location
- Substantial echo dynamic travel
- Areas of unique amplitude
- Inconsistent time base positions
- Tip signals
- Conformation from the opposite direction
- Seen with many angles
- Mode converted shear signal (only circ flaws with substantial depth)

Non relevant indications criterions:

- Near WCL or weld geometry
- Seen continuously
- Consistent time & amplitude
- Weak echo dynamic travel

### **Length Sizing**

- Length of a flaw is determined by moving the probe along the flaw.
- on the same side of the weld as the indication



- optimize the signal from the flaw indication
- adjust the system gain until the response is ~ 80 % FSH
- scan along the length of the flaw in each direction until the signal response has been reduced to:
  - background noise for far side indication
  - 20% FSH (12 dB drop) for near side indication
- The length on outside diameter is longer than the actual inside diameter length. Calculate correct ID flaw length according to:  $(ID/OD) \times OD \text{ flaw length} = ID \text{ flaw length}$

### **Depth Sizing**

For flaw depth sizing the Absolut Arrival Time Technique (AATT) is used. The technique relies upon obtaining a direct signal response from the flaw tip using a material depth calibration. From the flaw tip response the amount of unflawed material or remaining ligament can be read directly from the Sscan. Flaw depth is calculated by subtracting the remaining ligament from the actual material thickness.

The figure below illustrates the technique.

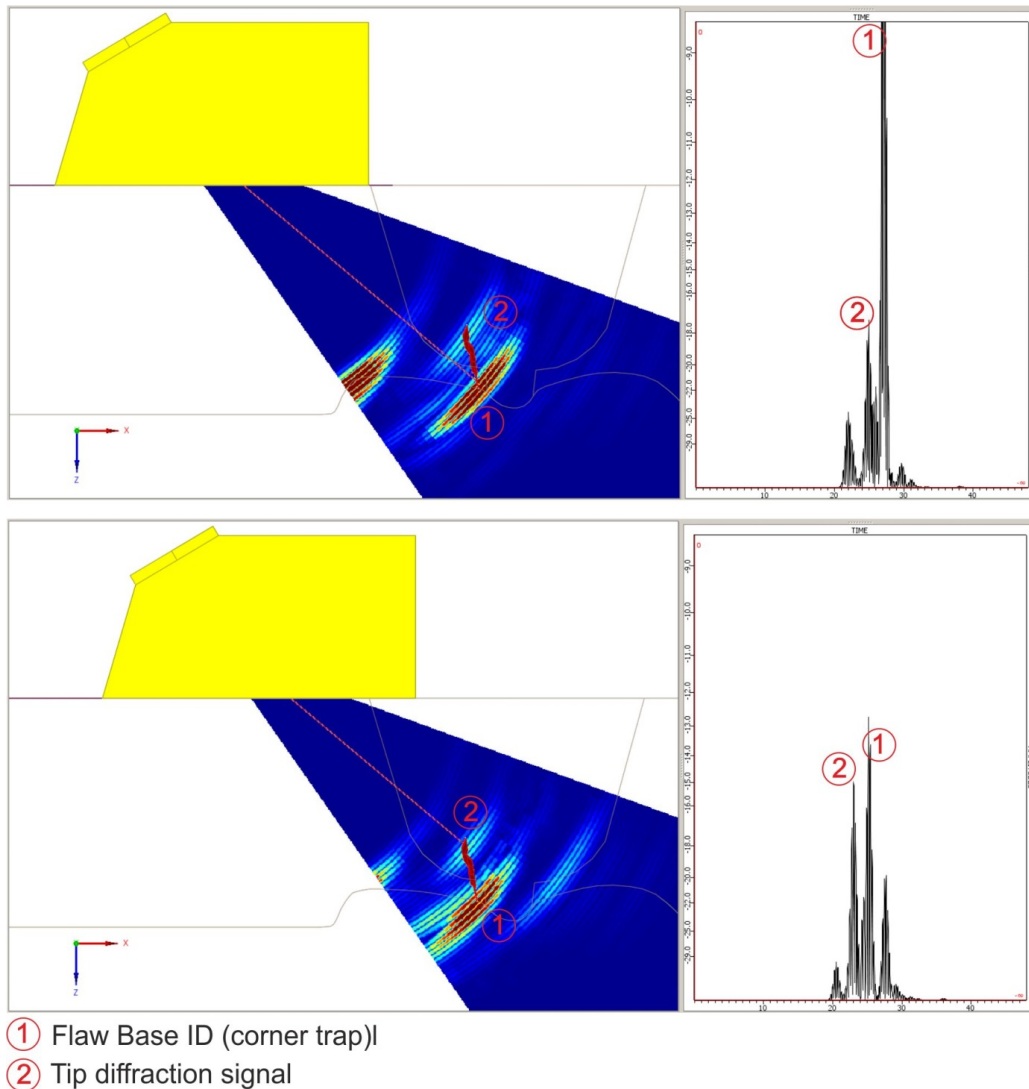


**Figure C.113**

### Defect Positioning

Due to uncertainties associated with sound propagation in anisotropic, heterogeneous austenitic weld material indication positioning require detailed evaluation. The information provided below may assist indication positioning.

- Perform thickness and surface contour recordings at the indication position.
- Evaluate the flaw signal amplitude responses from each side of the weld. Observe if the signal response appears reduced due to weld volume sound attenuation from one side or another.
- Identify standard benchmark responses (weld root, weld noise, acoustic interfaces) and flaw indication responses.

- Coordinate and plot the information on a cross sectional drawing of the weld.

### C.2.6.3 Results PARENT Specimen P41

#### Specimen Information and Coordinate System

##### Geometry

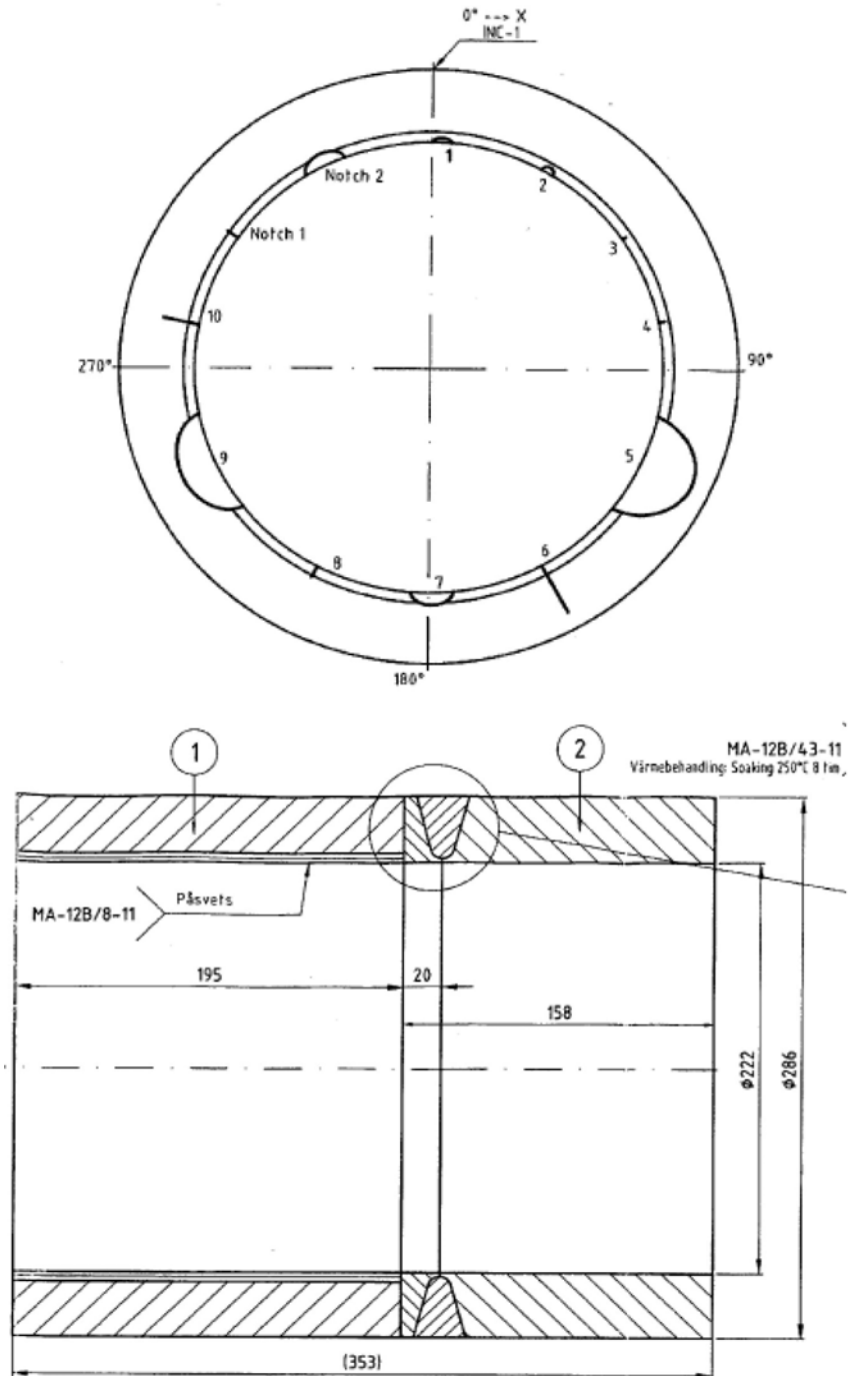


Figure C.114

Flaw Information

Burlat nr.	Repåka										Notch 1	Notch 2
	1	2	3	4	5	6	7	8	9	10		
Skala 1:51												
Höjd	2	3	2	3	28	26	6	6	17	17	6	6
Längd	19	6	10	5	50	20	20	20	20	20	20	20
Öppning, utmät	07/010 an	20/54/20 an	51/105/105 an	77/154/105 an	117/105/105 an	150/200/210 an	172/238/132 an	206/160/155 an	230/165/153 an	270/150/150 an	307/166/155 an	325/160/150 an
Z	Yttryande	Yttryande	Yttryande	Yttryande	Yttryande Lgn II	Yttryande Lgn II	Yttryande Lgn II	Yttryande Lgn II	Yttryande Lgn II	Yttryande Lgn II	Yttryande Lgn II	Yttryande
Skivning	0°	0°	0°	0°	0°	0°	0°	0°	0°	0°	0°	0°
Lutning	0°	0°	0°	0°	0°	0°	0°	0°	20°	0°	0°	0°
Detaljtyp	Stelningspöcka • WTD	Stelningspöcka • WTD	Stelningspöcka • WTD	Stelningspöcka • WTD	Stelningspöcka • WTD	Stelningspöcka • WTD	Stelningspöcka • WTD	Stelningspöcka • WTD	Stelningspöcka • WTD	Stelningspöcka • WTD	Stelningspöcka • WTD	EDM notch • WTD
Bremsning	Lågs svets	Lågs svets	Tvårs svets	Tvårs svets	Lågs svets	Tvårs svets	Lågs svets	Tvårs svets	Lågs svets	Tvårs svets	Tvårs svets	Lågs svets
Liggning					10, 4, 16, 7, 15	54 21 ovan	54 21 ovan	54 21 ovan	10, 4, 16, 4, 11, 3, 3	54 21 ovan	54 21 ovan	

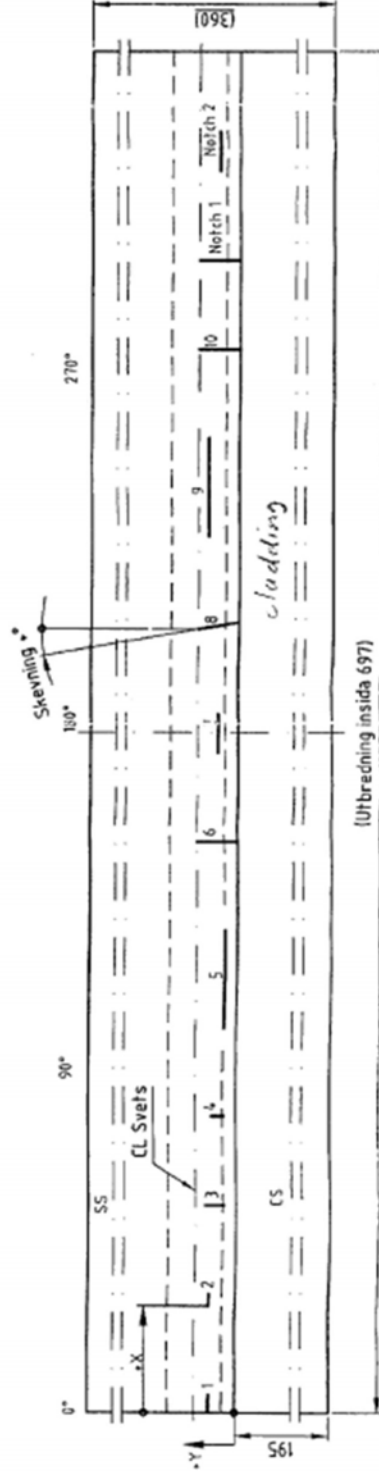


Figure C.115

## Coordinate System

The figure shows the PARENT Coordinate System. The X direction is opposite to the SQC drawing coordinate system. To allow direct comparison of the SQC drawing flaw positions to the measurements in this report the X direction were therefore defined in the opposite direction (see figure).

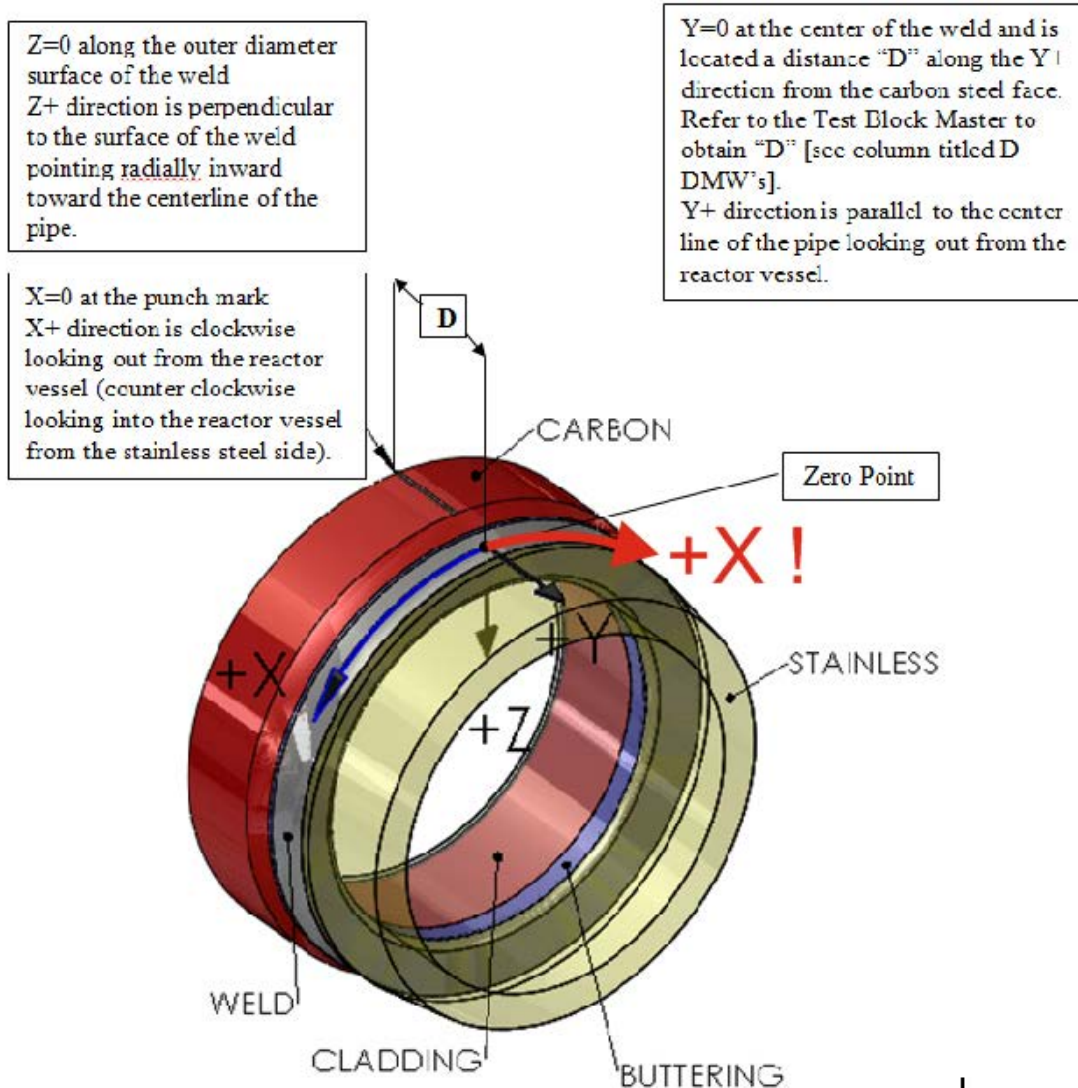
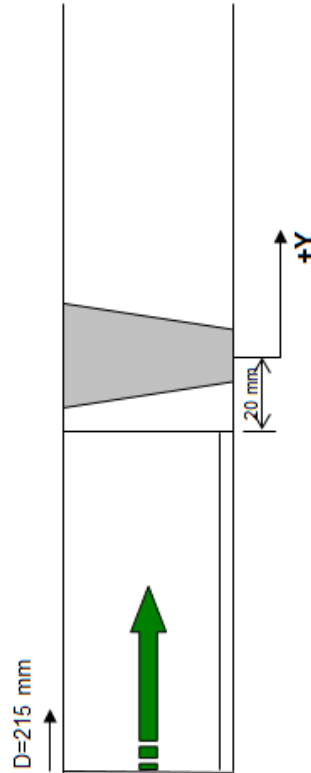


Figure C.116

Corrected Flaw Positions (PARENT coordinate system)

**P41**

ORIGINAL DRAWING						PARENT (Inside surface)				PARENT (Outside surface)			
Def. nr	Orient.	X deg	X mm	Y-pos	Length	Def. nr	Orient.	X deg	X mm	Y-pos	Length	X Start	Length
1	Circ	0	0	13	10	12	Circ	354	687	-7	10	885	13
2	Circ	28	54	11	6	11	Circ	328	637	-9	6	821	8
3	Axial	54	105	6/16	10	10	Axial	306	582	-14/-4	10	765	10
4	Axial	77	150	5/11	6	9	Axial	283	541	-15/-9	6	708	6
5	Circ	101	195	11	50	8	Circ	233	452	-9	50	582	64
6	Axial	150	290	1/21	20	7	Axial	210	387	-19/1	20	525	20
7	Circ	173	335	10	20	6	Circ	176	342	-10	20	441	26
8	Axial	206	400	0/20	20	5	Axial	154	277	-20/0	20	385	20
9	Circ	230	445	12	50	4	Circ	104	202	-8	50	260	64
10	Axial	279	540	0/20	20	3	Axial	81	137	-20/0	20	203	20
11	Axial	302	585	0/20	20	2	Axial	58	92	-20/0	20	145	20
12	Circ	325	630	10	20	1	Circ	24	47	-10	20	61	26



$D_1 = 222,0 \text{ mm}$ ,  $t = 32 \text{ mm}$

Inner circumference = 697,4 mm, which gives 1,94 mm/deg

Outer circumference = 898 mm, which gives 2,50 mm/deg

Figure C.117

## Flaw Indication Summary Tables

### Circumferential Flaws

Probe Position: Carbon Steel Side / Beam Direction: +Y

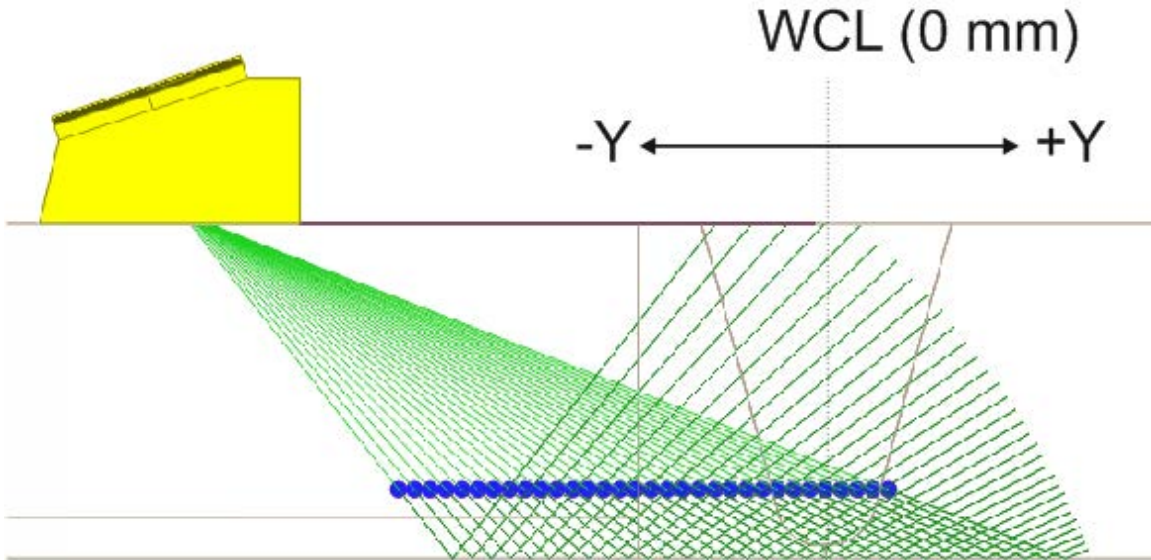


Figure C.118

Flaw No.:	As Built Information (SQC Drawing)					Measurement Results					Remarks	UT Analysis Section	Cal Sheet No:
	Flaw X Position OD			Flaw Depth	Flaw Y Pos.	Flaw X Position OD			Flaw Depth	Flaw Y Pos.			
	Start	Length	End			Start	Length	End					
	mm	mm	mm	mm	mm	mm	mm	mm					
1	0.0	12.9	12.9	2	CS* B**	895	15	8	3.2	-Y	1)	4.1	1
2	69.9	7.7	77.6	3	CS* B**	72	85	13	3.2	-Y	2)	4.2	1
5	252.1	64.4	316.5	26	CS* B**	250	72	322	26.1	-Y	3)	4.3	2
7	431.8	25.8	457.5	6	CS* B**	432	33	465	5.55	-Y	4)	4.4	3
9	574.0	64.4	638.5	17	CS* B**	578	67	645	14.7	-Y	5)	4.5	4
12	811.1	25.8	836.9	6	CS* B**	813	32	845	5.55	-Y	6)	4.6	3

\*Flaw on Carbon Steel (CS) / Buttering (B) Side in respect to weld center line  
See next page for Remarks!

Remarks:

- 1) No separation of tip diffraction from corner trap echo, no TLL echo indicates shallow flaw, flaw depth estimation procedure: if no separation of tip diffraction from corner trap and flaw seems to be shallow the flaw depth is defined per default to 10% pipe thickness at flaw position → 3.2 mm
- 2) No separation of tip diffraction from corner trap echo, no TLL echo indicates shallow flaw, flaw depth estimation procedure: if no separation of tip diffraction from corner trap and flaw seems to be shallow the flaw depth is defined per default to 10% pipe thickness at flaw position → 3.2 mm
- 3) For quantitative flaw depth sizing calibration at 24 mm deep notch of calibration block KKM\_24\_18\_12\_6 (RL = 6 mm)
- 4) For quantitative flaw depth sizing calibration at 6 mm deep notch of calibration block KKM\_24\_18\_12\_6 (RL = 24 mm)
- 5) For quantitative flaw depth sizing calibration at 12 mm deep notch of calibration block KKM\_24\_18\_12\_6 (RL = 18 mm)
- 6) For quantitative flaw depth sizing calibration at 6 mm deep notch of calibration block KKM\_24\_18\_12\_6 (RL = 24 mm)

Probe Position: Stainless Steel Side / Beam Direction: -Y

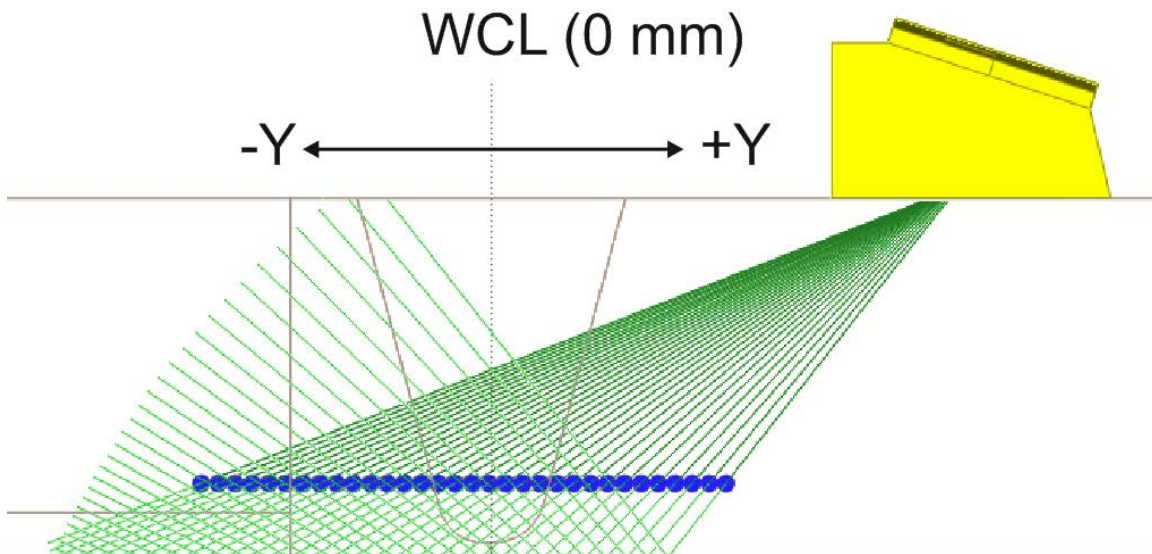


Figure C.119



Flaw No.:	As Built Information (SQC Drawing)					Measurement Results					Remarks	UT Analysis Section	Cal Sheet No:
	Flaw X Position OD			Flaw Depth	Flaw Y Pos.	Flaw X Position OD			Flaw Depth	Flaw Y Pos.			
	Start	Length	End			Start	Length	End					
	mm	mm	mm	mm	mm	mm	mm	mm					
1	0.0	12.9	12.9	2	CS* B**	no detection from fare side			-Y	-	-	1	
2	69.9	7.7	77.6	3	CS* B**	no detection from fare side			-Y	-	-	1	
5	252.1	64.4	316.5	26	CS* B**	252	60	312	25.89	-Y	1)	4.7	2
7	431.8	25.8	457.5	6	CS* B**	432	29	461	7.78	-Y	2)	4.8	3
9	574.0	64.4	638.5	17	CS* B**	578	67	645	14.7	-Y	3)	4.9	4
12	811.1	25.8	836.9	6	CS* B**	817	25	842	3.2	-Y	4)	4.10	1

\*Flaw on Carbon Steel (CS) / Buttering (B) Side in respect to weld center line  
See below for remarks!

- 1) For quantitative flaw depth sizing calibration at 24 mm deep notch of calibration block KKM\_24\_18\_12\_6 (RL = 6 mm)
- 2) Very hard to find the tip for depth sizing, only possible if inspector knows in witch depth region he has to look for tips; flaw depth estimation procedure: if flaw is seen with high angles of the S-scan and there is a quiet strong TLL reflection it indicates that flaw has at least some true wall extension (20-40%); delta to as built depth may result from beam redirection in heterogeneous anisotropic weld material
- 3) For quantitative flaw depth sizing calibration at 12 mm deep notch of calibration block KKM\_24\_18\_12\_6 (RL = 18 mm), delta to as built depth may result from beam redirection in heterogeneous anisotropic weld material
- 4) No separation of tip diffraction from corner trap echo, no TLL echo indicates shallow flaw, flaw depth estimation procedure: if no separation of tip diffraction from corner trap and flaw seems to be shallow the flaw depth is defined per default to 10% pipe thickness at flaw position → 3.2 mm

Axial Flaws

Scan Direction: + X

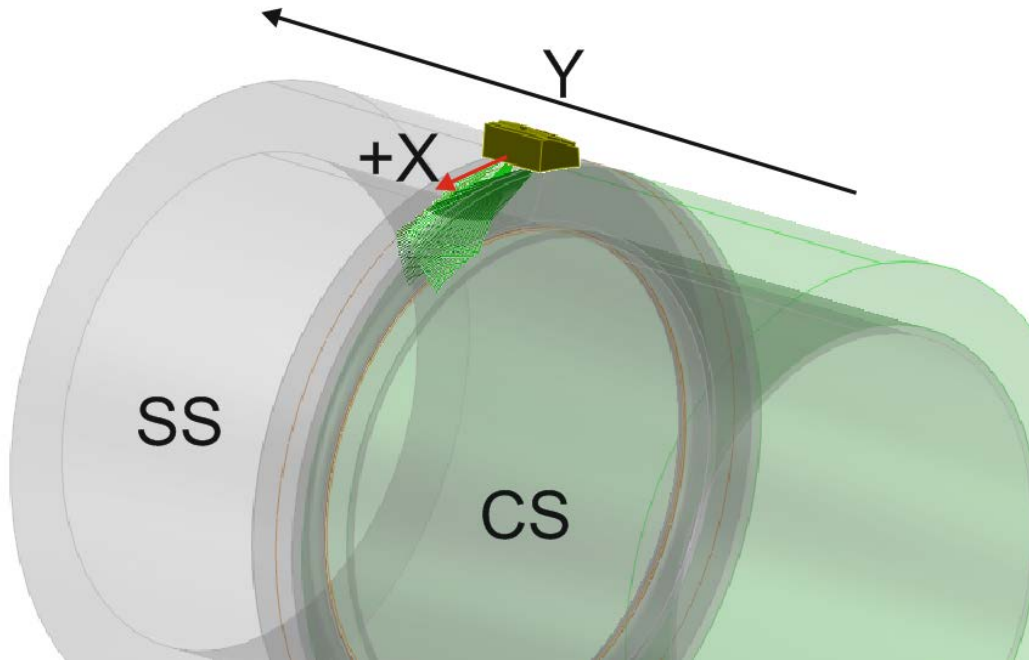


**Figure C.120**

Flaw No.:	As Built Information (SQC Drawing)				Measurement Results				Remarks	UT Analysis Section	Cal Sheet No:
	Flaw X Position OD	Length	Flaw Depth	Flaw Y Pos.	Flaw X Position OD	Length	Flaw Depth	Flaw Y Pos.			
	mm	mm	mm		mm	mm	mm				
<b>3</b>	135	10	2	CS* B**	135	≈ 10	3.2	-Y	1)	4.11	6
<b>4</b>	193	6	3	CS* B**	195	≈ 6	3.2	-Y	2)	4.12	6
<b>6</b>	374	20	26	CS* B**	370	≈ 30	26	-Y	3)	4.13	7
<b>8</b>	515	20	6	CS* B**	515	≈ 25	6.07	-Y	4)	4.14	8
<b>10</b>	696	20	17	CS* B**	698	20	16.74	-Y	5)	4.15	9
<b>11</b>	754	20	6	CS* B**	750	20	6.67	-Y	6)	4.16	8

\*Flaw on Carbon Steel (CS) / Buttering (B) Side in respect to weld center line  
See next page for remarks!

## Remarks

- 1) Very hard to detect with manual inspection; length sizing hard lots of noise from buttering; no separation of tip diffraction from corner trap echo, no TLL echo indicates shallow flaw, flaw depth estimation procedure: if no separation of tip diffraction from corner trap and flaw seems to be shallow the flaw depth is defined per default to 10% pipe thickness at flaw position → 3.2 mm
- 2) Hard to detect with manual inspection; length sizing hard lots of noise from buttering; no separation of tip diffraction from corner trap echo, no TLL echo indicates shallow flaw, flaw depth estimation procedure: if no separation of tip diffraction from corner trap and flaw seems to be shallow the flaw depth is defined per default to 10% pipe thickness at flaw position → 3.2 mm
- 3) Length sizing hard lots of noise from buttering; for quantitative flaw depth sizing calibration with 9 mm deep SDH (Ø 1,5 mm) of calibration block "SVTI AS\_D270\_T30"
- 4) Length sizing hard lots of noise from buttering; depth sizing only possible when probe is skewed (flaw skew angle 10°); for quantitative flaw depth sizing calibration with 26 mm deep SDH (Ø 1,5 mm) of calibration block "SVTI AS\_D270\_T30"
- 5) Quantitative flaw depth sizing calibration with 15 mm deep SDH (Ø 1,5 mm) of calibration block "SVTI AS\_D270\_T30"
- 6) Flaw depth sizing hard, very weak tip signal; quantitative flaw depth sizing calibration with 26 mm deep SDH (Ø 1,5 mm) of calibration block "SVTI AS\_D270\_T30"

Scan Direction: - X

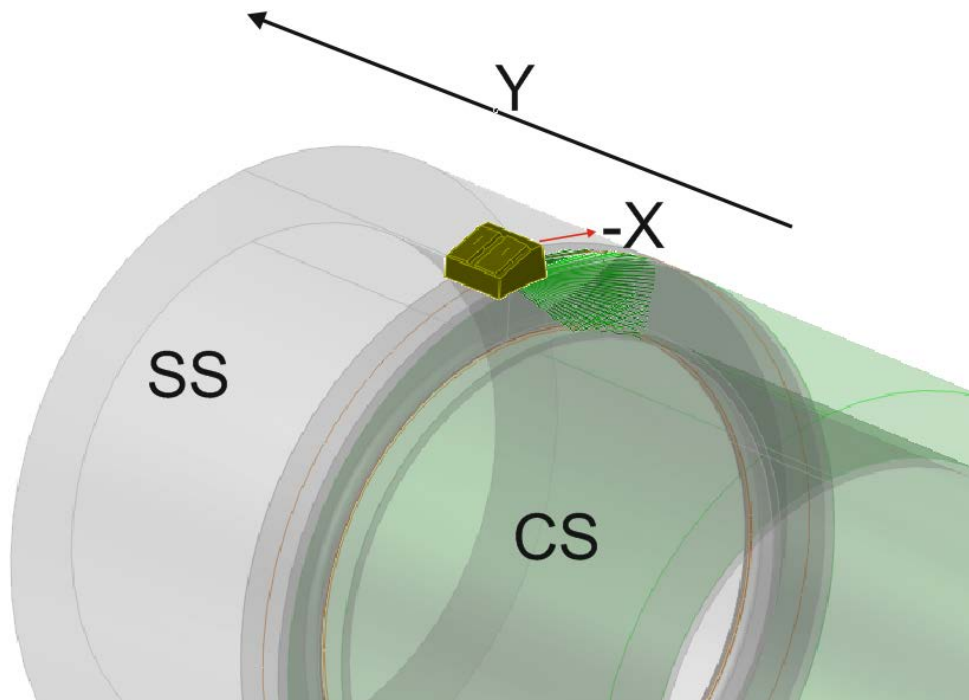


**Figure C.121**

Flaw No.:	As Built Information (SQC Drawing)				Measurement Results				Remarks	UT Analysis Section	Cal Sheet No:
	Flaw X Position OD	Length	Flaw Depth	Flaw Y Pos.	Flaw X Position OD	Length	Flaw Depth	Flaw Y Pos.			
	mm	mm	mm		mm	mm	mm				
3	135	10	2	CS* B**	135	≈ 10	3.2	-Y	1)	4.17	6
4	193	6	3	CS* B**	195	≈ 6	3.2	-Y	2)	4.18	6
6	374	20	26	CS* B**	370	≈ 20	26.48	-Y	3)	4.19	7
8	515	20	6	CS* B**	515	≈ 25	6.81	-Y	4)	4.20	8
10	696	20	17	CS* B**	698	≈ 25	16.74	-Y	5)	4.21	9
11	754	20	6	CS* B**	750	20	6.37	-Y	6)	4.22	8

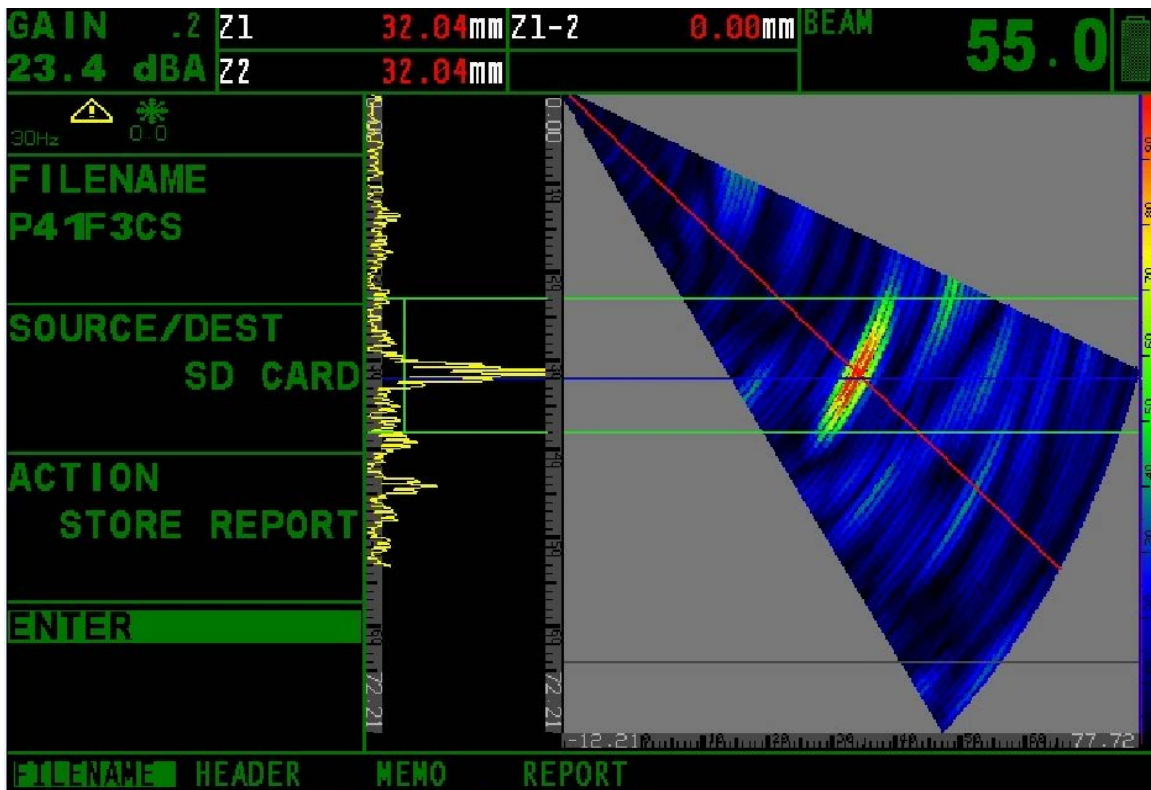
\*Flaw on Carbon Steel (CS) / Buttering (B) Side in respect to weld center line  
See below for remarks!

- 1) Very hard to detect with manual inspection; length sizing hard lots of noise from buttering; no separation of tip diffraction from corner trap echo, no TLL echo indicates shallow flaw, flaw depth estimation procedure: if no separation of tip diffraction from corner trap and flaw seems to be shallow the flaw depth is defined per default to 10% pipe thickness at flaw position → 3.2 mm
- 2) Hard to detect with manual inspection; length sizing hard lots of noise from buttering; no separation of tip diffraction from corner trap echo, no TLL echo indicates shallow flaw, flaw depth estimation procedure: if no separation of tip diffraction from corner trap and flaw seems to be shallow the flaw depth is defined per default to 10% pipe thickness at flaw position → 3.2 mm
- 3) Length sizing hard lots of noise from buttering; for quantitative flaw depth sizing calibration with 9 mm deep SDH (Ø 1,5 mm) of calibration block "SVTI AS\_D270\_T30"
- 4) Length sizing hard lots of noise from buttering; depth sizing hard only possible when probe is skewed (flaw skew angle 10°); for quantitative flaw depth sizing calibration with 26 mm deep SDH (Ø 1,5 mm) of calibration block "SVTI AS\_D270\_T30"
- 5) Quantitative flaw depth sizing calibration with 15 mm deep SDH (Ø 1,5 mm) of calibration block "SVTI AS\_D270\_T30"
- 6) Flaw depth sizing good, good tip signal; quantitative flaw depth sizing calibration with 26 mm deep SDH (Ø 1,5 mm) of calibration block "SVTI AS\_D270\_T30"

## UT Analysis Images

Flaw 1 / Probe Position: Carbon Steel Side / Beam Direction: -Y

Flaw No.:	As Built Information (SQC Drawing)					Measurement Results					Remarks	UT Analysis Section	Cal Sheet No.:
	Flaw X Position OD			Flaw Depth	Flaw Y Pos.	Flaw X Position OD			Flaw Depth	Flaw Y Pos.			
	Start	Length	End			Start	Length	End					
	mm	mm	mm	mm	mm	mm	mm	mm					
1	0.0	12.9	12.9	2	CS* B**	895	15	8	3.2	-Y	1)	3.1	1



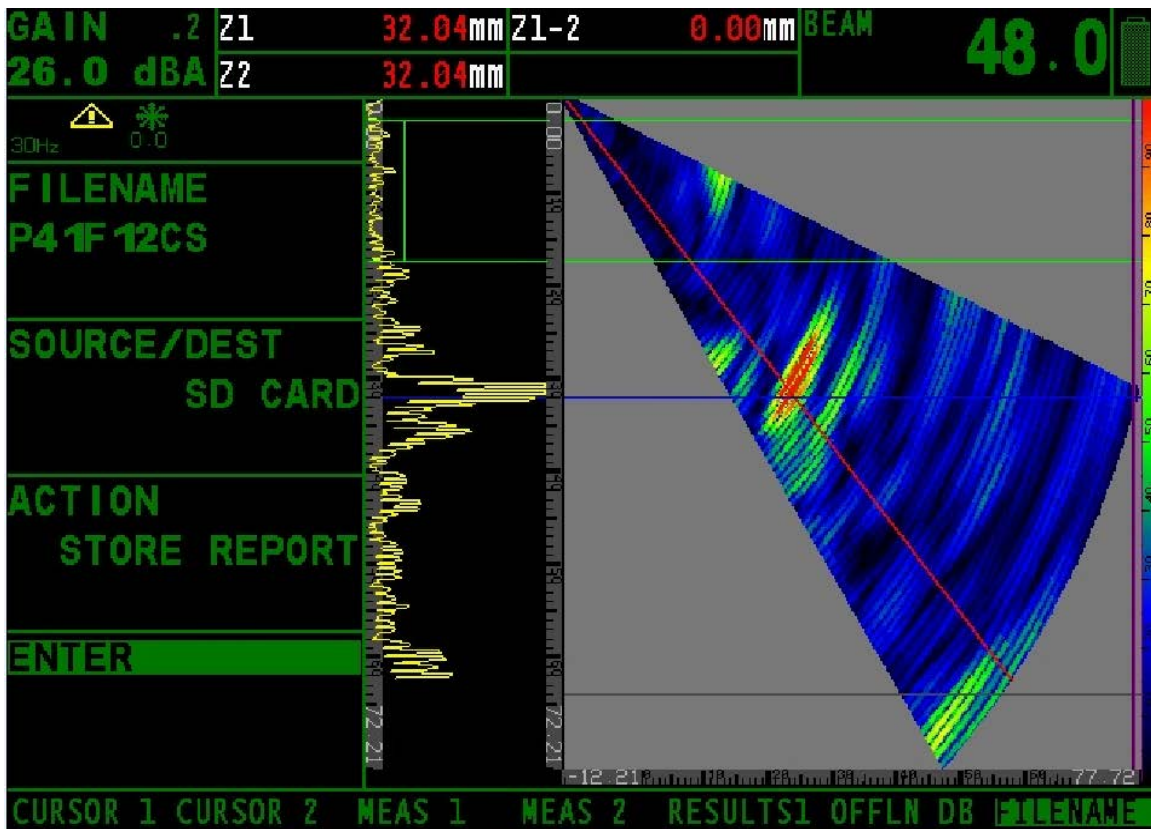
No separation of tip diffraction from corner trap echo, no TLL echo indicates shallow flaw, flaw depth estimation procedure: if no separation of tip diffraction from corner trap and flaw seems to be shallow the flaw depth is defined per default to 10% pipe thickness at flaw position → 3.2 mm

Remarks: File name in picture not correct (coordinate system problem), file name has been renamed correctly during analysis

Figure C.122

Flaw 2 / Probe Position: Carbon Steel Side / Beam Direction: -Y

Flaw No.:	As Built Information (SQC Drawing)					Measurement Results					Remarks	UT Analysis Section	Cal Sheet No:
	Flaw X Position OD			Flaw Depth	Flaw Y Pos.	Flaw X Position OD			Flaw Depth	Flaw Y Pos.			
	Start	Length	End			Start	Length	End					
	mm	mm	mm	mm	mm	mm	mm	mm					
2	69.9	7.7	77.6	3	CS* B**	72	85	13	3.2	-Y	2)	1	



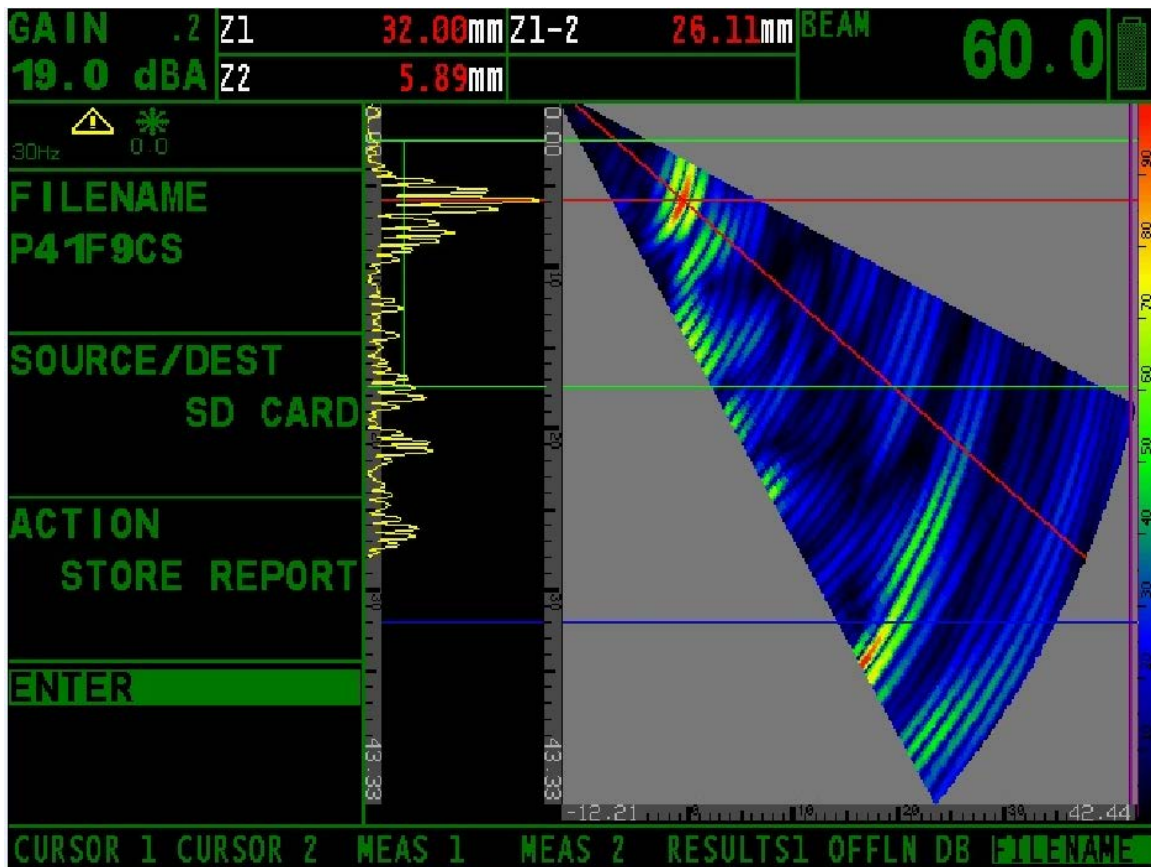
Hard to detect; no separation of tip diffraction from corner trap echo; no TLL echo indicates shallow flaw; flaw depth estimation procedure: if no separation of tip diffraction from corner trap and flaw seems to be shallow the flaw depth is defined per default to 10% pipe thickness at flaw position → 3.2 mm

Remarks: File name in picture not correct (coordinate system problem), file name has been renamed correctly during analysis

Figure C.123

Flaw 5 / Probe Position: Carbon Steel Side / Beam Direction: -Y

Flaw No.:	As Built Information (SQC Drawing)					Measurement Results					Remarks	UT Analysis Section	Cal Sheet No:
	Flaw X Position OD			Flaw Depth	Flaw Y Pos.	Flaw X Position OD			Flaw Depth	Flaw Y Pos.			
	Start	Length	End			Start	Length	End					
	mm	mm	mm	mm	mm	mm	mm	mm					
5	252.1	64.4	316.5	26	CS* B**	250	72	322	26.11	-Y	3)		2



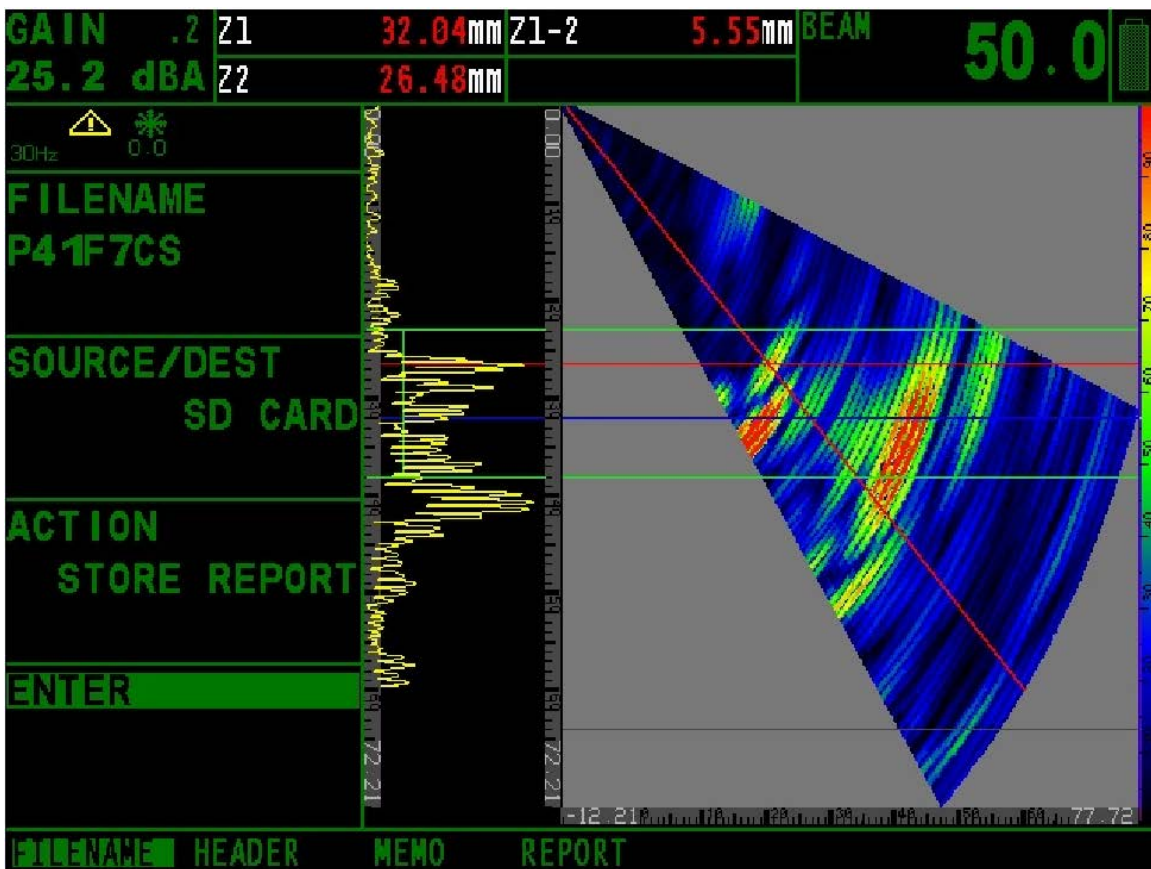
For quantitative flaw depth sizing calibration at 24 mm deep notch of calibration block KKM\_24\_18\_12\_6 (RL = 6 mm)

Remarks: File name in picture not correct (coordinate system problem), file name has been renamed correctly during analysis

Figure C.124

Flaw 7 / Probe Position: Carbon Steel Side / Beam Direction: -Y

Flaw No.:	As Built Information (SQC Drawing)					Measurement Results					Remarks	UT Analysis Section	Cal Sheet No:
	Flaw X Position OD			Flaw Depth	Flaw Y Pos.	Flaw X Position OD			Flaw Depth	Flaw Y Pos.			
	Start	Length	End			Start	Length	End					
	mm	mm	mm	mm	mm	mm	mm	mm					
7	431.8	25.8	457.5	6	CS* B**	432	33	465	5.55	-Y	4)	3	



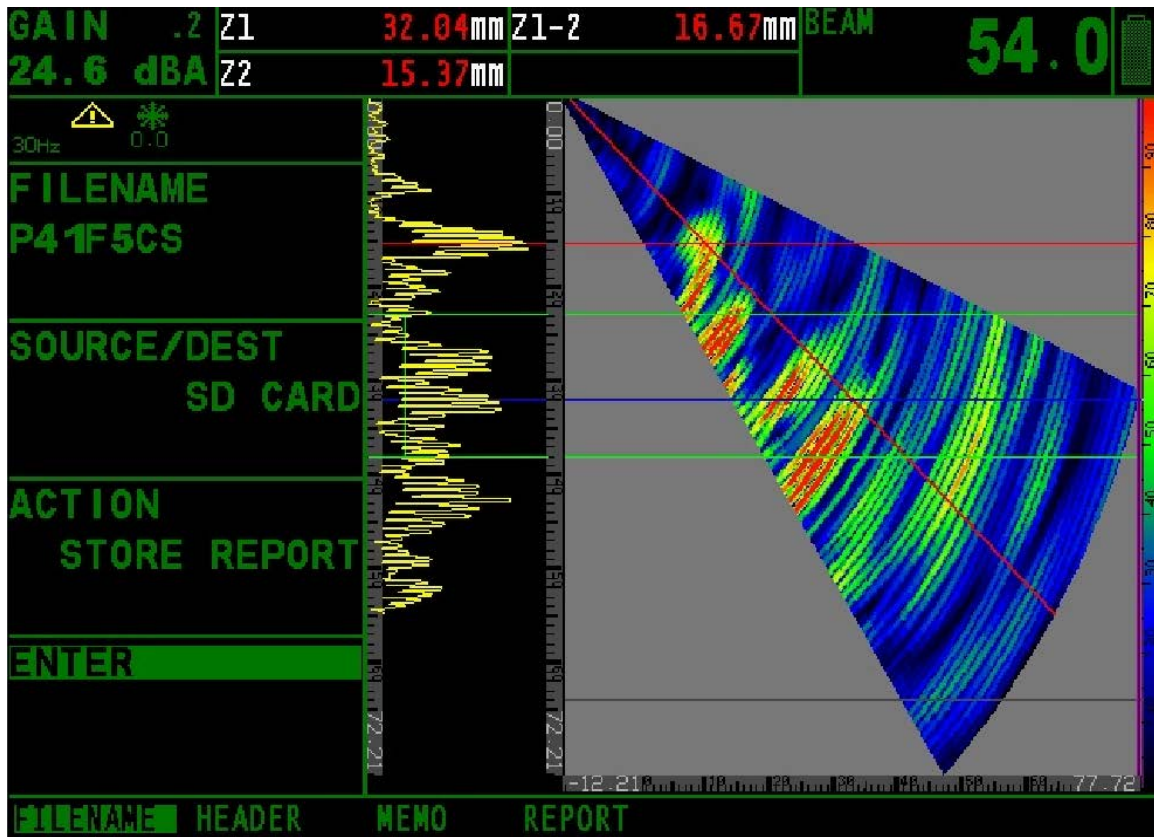
For quantitative flaw depth sizing calibration at 6 mm deep notch of calibration block KKM\_24\_18\_12\_6 (RL = 24 mm)

Figure C.125



Flaw 9 / Probe Position: Carbon Steel Side / Beam Direction: -Y

Flaw No.:	As Built Information (SQC Drawing)					Measurement Results					Remarks	UT Analysis Section	Cal Sheet No:
	Flaw X Position OD			Flaw Depth	Flaw Y Pos.	Flaw X Position OD			Flaw Depth	Flaw Y Pos.			
	Start	Length	End			Start	Length	End					
	mm	mm	mm	mm	mm	mm	mm	mm					
9	574.0	64.4	638.5	17	CS* B**	578	67	645	14.7	-Y	5)		4



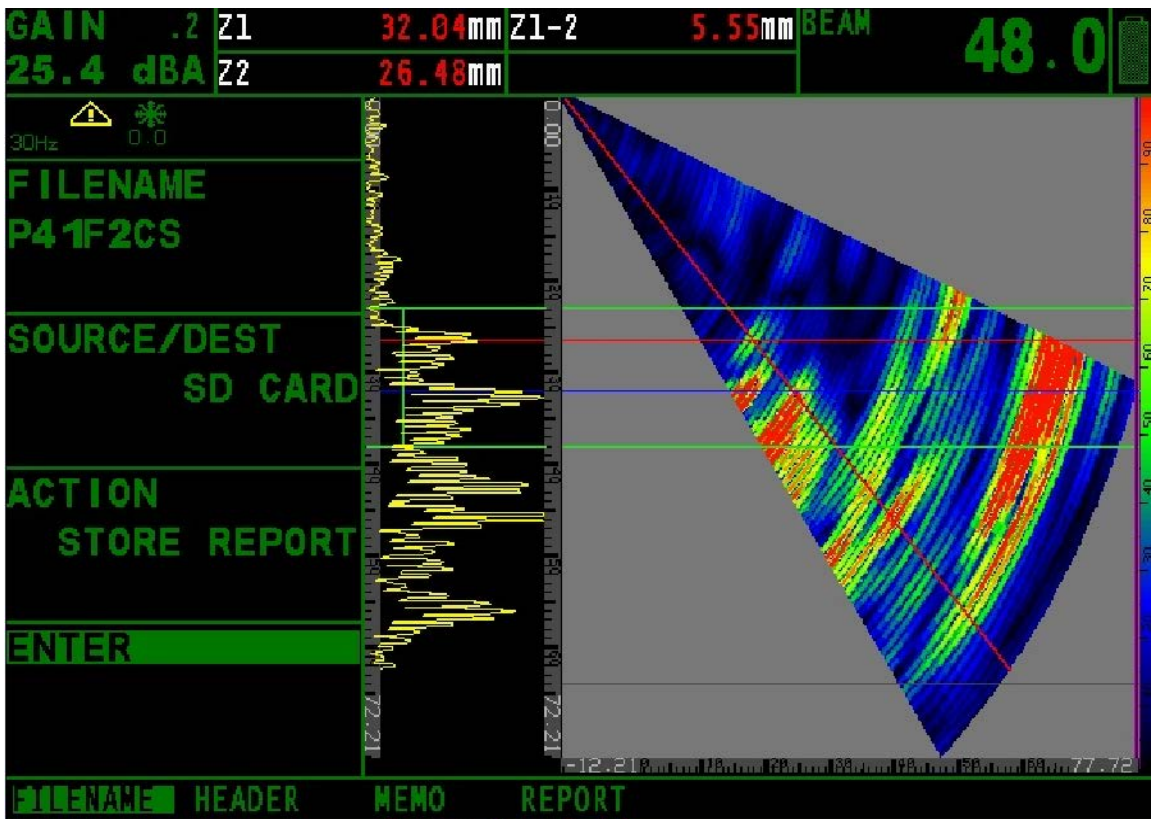
For quantitative flaw depth sizing calibration at 12 mm deep notch of calibration block KKM\_24\_18\_12\_6 (RL = 18 mm)

Remarks: File name in picture not correct (coordinate system problem), file name has been renamed correctly during analysis

Figure C.126

Flaw 12 / Probe Position: Carbon Steel Side / Beam Direction: -Y

Flaw No.:	As Built Information (SQC Drawing)					Measurement Results					Remarks	UT Analysis Section	Cal Sheet No:
	Flaw X Position OD			Flaw Depth	Flaw Y Pos.	Flaw X Position OD			Flaw Depth	Flaw Y Pos.			
	Start	Length	End			Start	Length	End					
	mm	mm	mm	mm	mm	mm	mm	mm					
12	811.1	25.8	836.9	6	CS* B**	813	32	845	5.55	-Y	6)		3



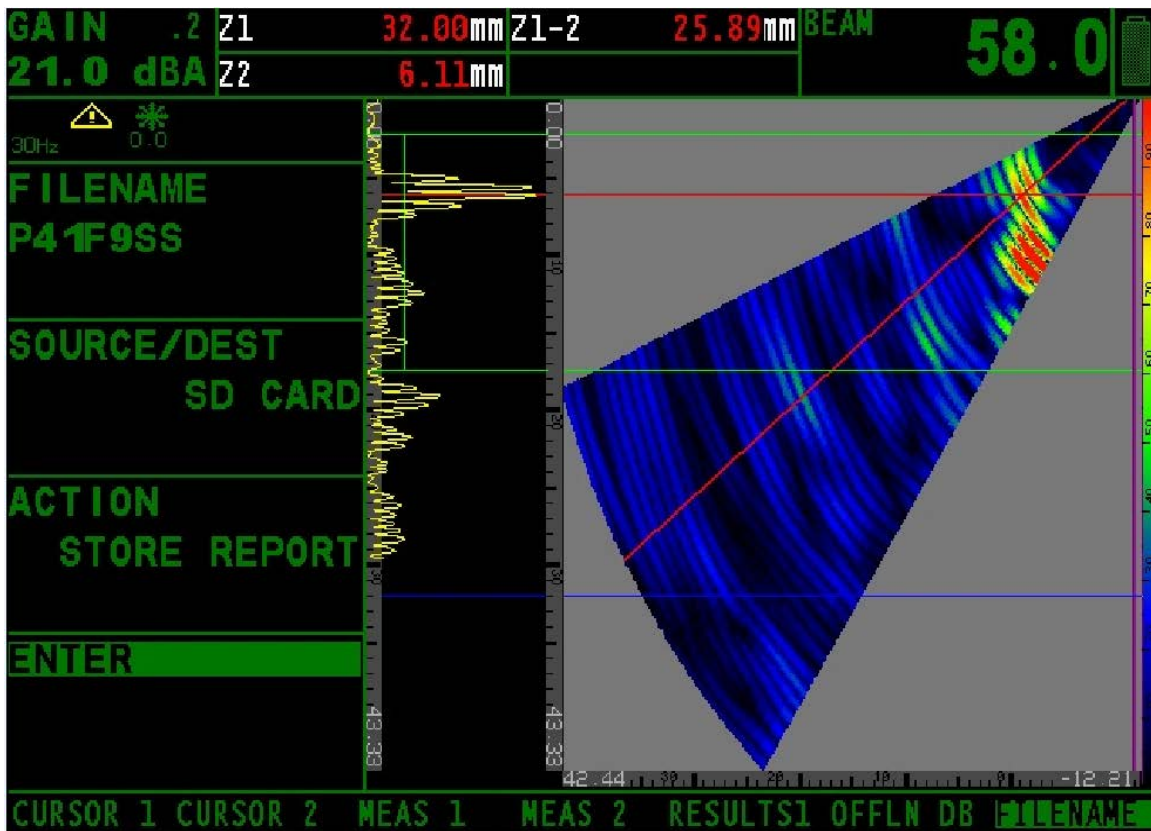
For quantitative flaw depth sizing calibration at 6 mm deep notch of calibration block KKM\_24\_18\_12\_6 (RL = 24 mm)

Remarks: File name in picture not correct (coordinate system problem), file name has been renamed correctly during analysis

Figure C.127

Flaw 5 / Probe Position: Stainless Side / Beam Direction: +Y

Flaw No.:	As Built Information (SQC Drawing)					Measurement Results					Remarks	UT Analysis Section	Cal Sheet No:
	Flaw X Position OD			Flaw Depth	Flaw Y Pos.	Flaw X Position OD			Flaw Depth	Flaw Y Pos.			
	Start	Length	End			Start	Length	End					
	mm	mm	mm	mm	mm	mm	mm	mm					
5	252.1	64.4	316.5	26	CS* B**	252	60	312	25.89	-Y	1)	4.7	2



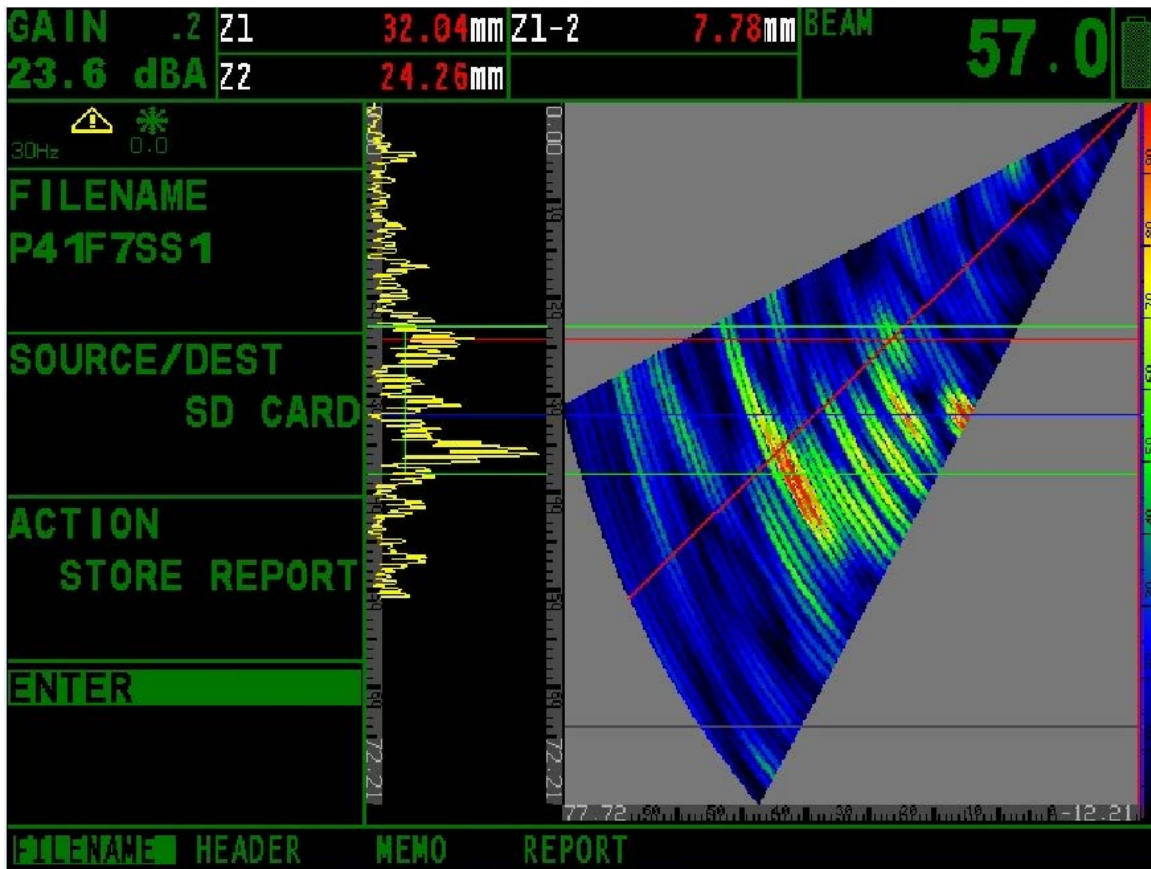
For quantitative flaw depth sizing calibration at 24 mm deep notch of calibration block KKM\_24\_18\_12\_6 (RL = 6 mm)

Remarks: File name in picture not correct (coordinate system problem), file name has been renamed correctly during analysis

Figure C.128

Flaw 7 / Probe Position: Stainless Side / Beam Direction: +Y

Flaw No.:	As Built Information (SQC Drawing)					Measurement Results					Remarks	UT Analysis Section	Cal Sheet No:
	Flaw X Position OD			Flaw Depth	Flaw Y Pos.	Flaw X Position OD			Flaw Depth	Flaw Y Pos.			
	Start	Length	End			Start	Length	End					
	mm	mm	mm	mm	mm	mm	mm	mm					
7	431.8	25.8	457.5	6	CS* B**	432	29	461	7.78	-Y	2)	4.8	3

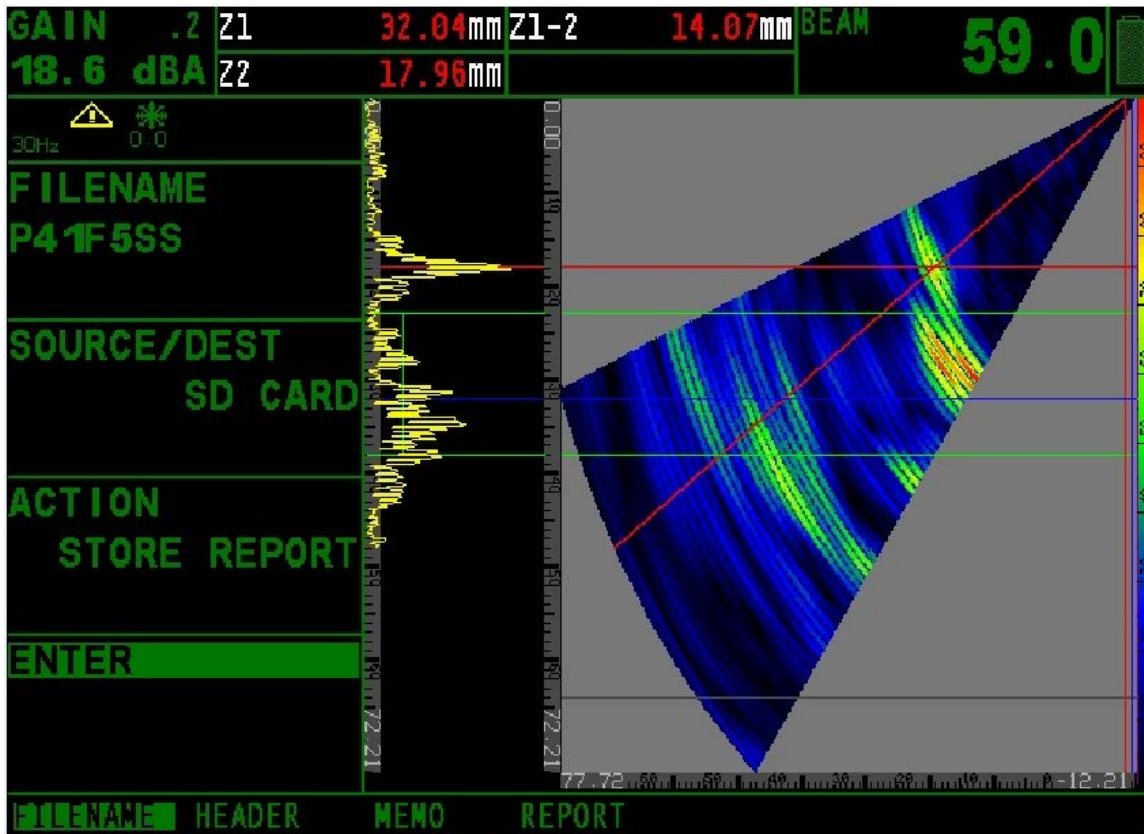


Very hard to find the tip for depth sizing, only possible if inspector knows in which depth region he has to look for tips; flaw depth estimation procedure: if flaw is seen with high angles in the S-scan and there is a quiet strong TLL reflection it indicates that flaw has at least some true wall extension (20-40%); delta to as built depth may result from beam redirection in heterogeneous anisotropic weld material.

Figure C.129

Flaw 9 / Probe Position: Stainless Side / Beam Direction: +Y

Flaw No.:	As Built Information (SQC Drawing)					Measurement Results					Remarks	UT Analysis Section	Cal Sheet No:
	Flaw X Position OD			Flaw Depth	Flaw Y Pos.	Flaw X Position OD			Flaw Depth	Flaw Y Pos.			
	Start	Length	End			Start	Length	End					
	mm	mm	mm	mm	mm	mm	mm	mm					
9	574.0	64.4	638.5	17	CS* B**	578	67	645	14.7	-Y	3)	4.9	4



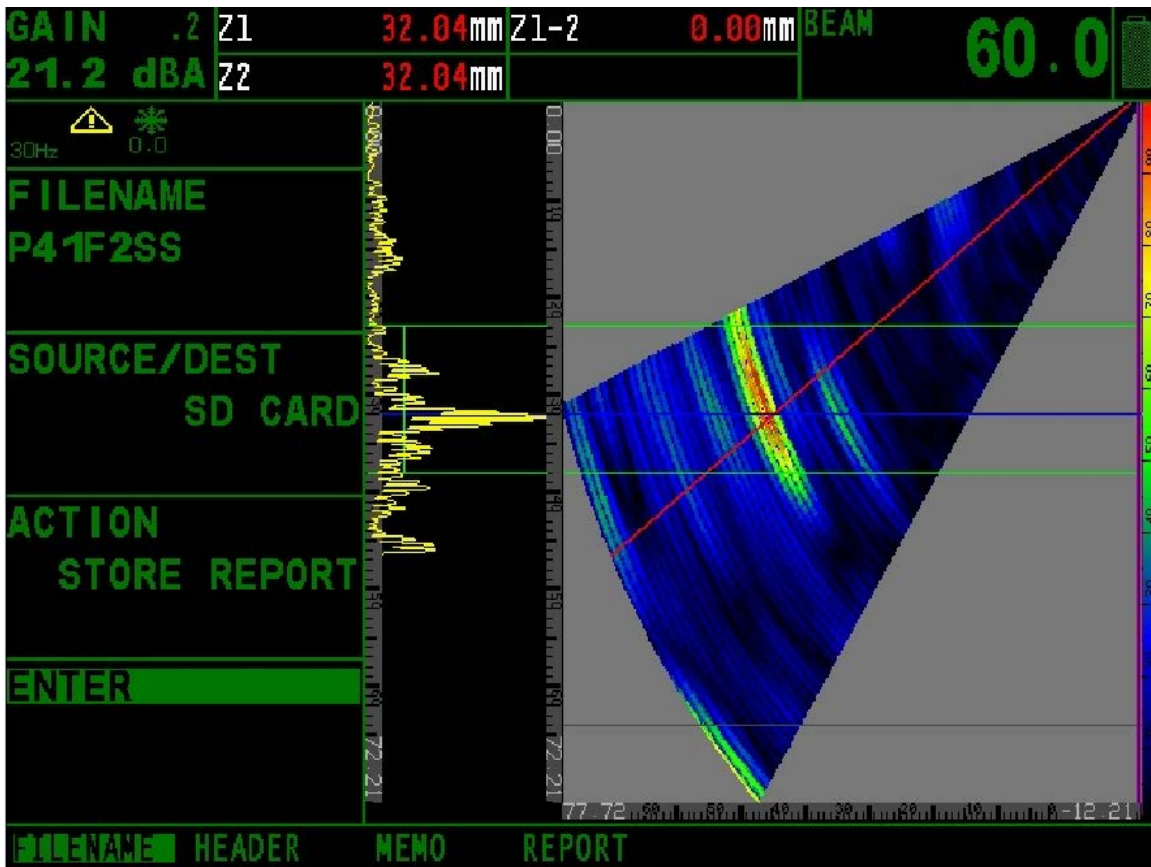
For quantitative flaw depth sizing calibration at 12 mm deep notch of calibration block KKM\_24\_18\_12\_6 (RL = 18 mm), delta to as built depth may result from beam redirection in heterogeneous anisotropic weld material

Remarks: File name in picture not correct (coordinate system problem), file name has been renamed correctly during analysis

Figure C.130

Flaw 12 / Probe Position: Stainless Side / Beam Direction: +Y

Flaw No.:	As Built Information (SQC Drawing)					Measurement Results					Remarks	UT Analysis Section	Cal Sheet No:
	Flaw X Position OD			Flaw Depth	Flaw Y Pos.	Flaw X Position OD			Flaw Depth	Flaw Y Pos.			
	Start	Length	End			Start	Length	End					
	mm	mm	mm	mm	mm	mm	mm	mm					
12	811.1	25.8	836.9	6	CS* B**	817	25	842	3.2	-Y	4)	4.10	3



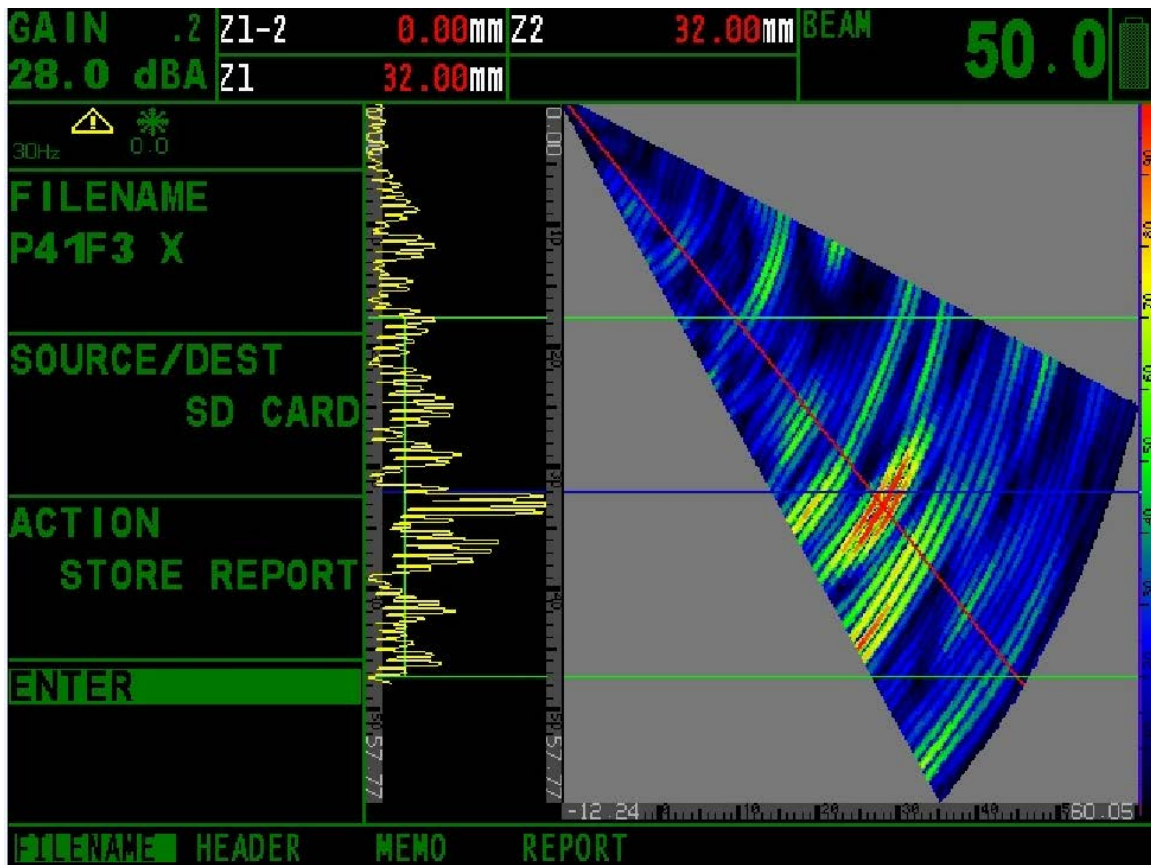
No separation of tip diffraction from corner trap echo, no TLL echo indicates shallow flaw, flaw depth estimation procedure: if no separation of tip diffraction from corner trap and flaw seems to be shallow the flaw depth is defined per default to 10% pipe thickness at flaw position → 3.2 mm

Remarks: File name in picture not correct (coordinate system problem), file name has been renamed correctly during analysis

Figure C.131

Flaw 3 / Scan Direction: + X

Flaw No.:	As Built Information (SQC Drawing)				Measurement Results				Remarks	UT Analysis Section	Cal Sheet No:
	Flaw X Position OD	Length	Flaw Depth	Flaw Y Pos.	Flaw X Position OD	Length	Flaw Depth	Flaw Y Pos.			
	mm	mm	mm		mm	mm	mm				
3	135	10	2	CS* B**	135	≈ 10	3.2	-Y	1)	4.9	

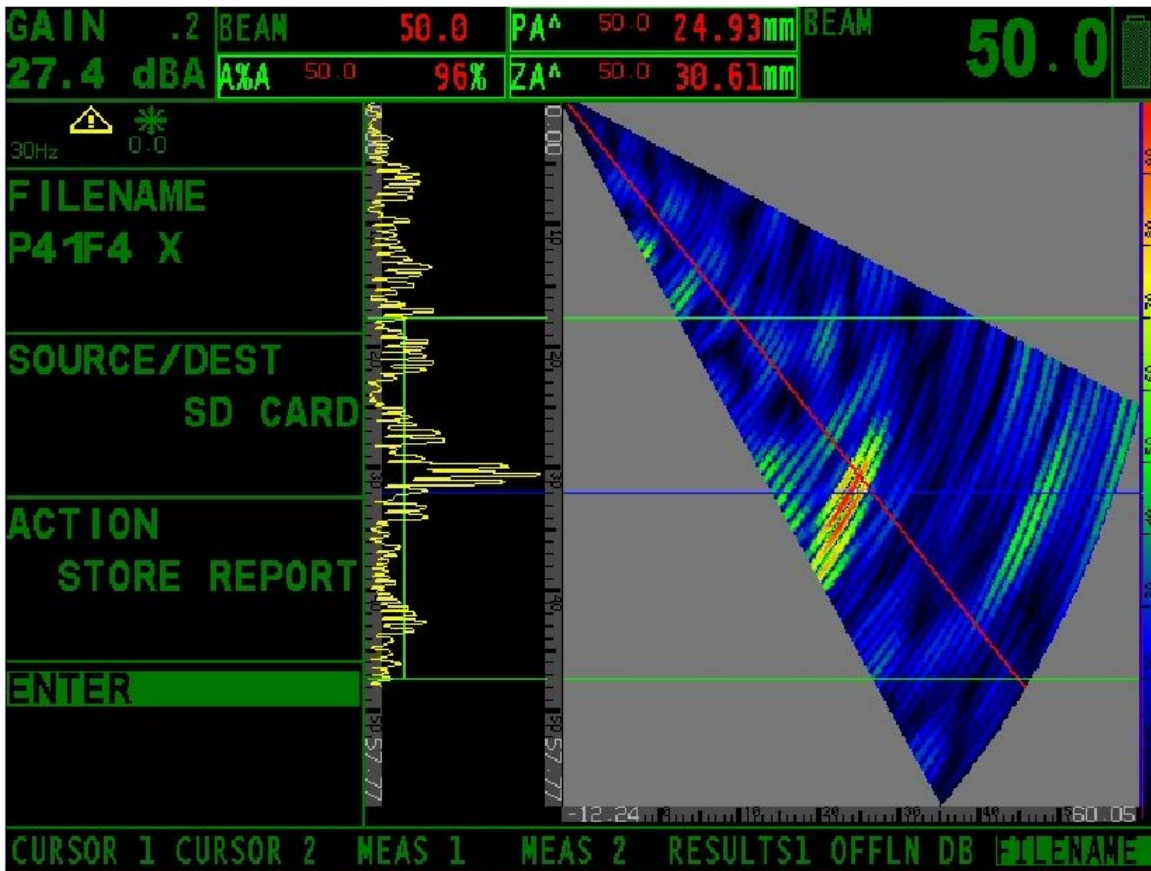


Very hard to detect with manual inspection; length sizing hard lots of noise from buttering; no separation of tip diffraction from corner trap echo, no TLL echo indicates shallow flaw, flaw depth estimation procedure: if no separation of tip diffraction from corner trap and flaw seems to be shallow the flaw depth is defined per default to 10% pipe thickness at flaw position → 3.2 mm.

Figure C.132

Flaw 4 / Scan Direction: + X

Flaw No.:	As Built Information (SQC Drawing)				Measurement Results				Remarks	UT Analysis Section	Cal Sheet No:
	Flaw X Position OD	Length	Flaw Depth	Flaw Y Pos.	Flaw X Position OD	Length	Flaw Depth	Flaw Y Pos.			
	mm	mm	mm		mm	mm	mm				
4	193	6	3	CS* B**	195	≈ 6		-Y	2)		



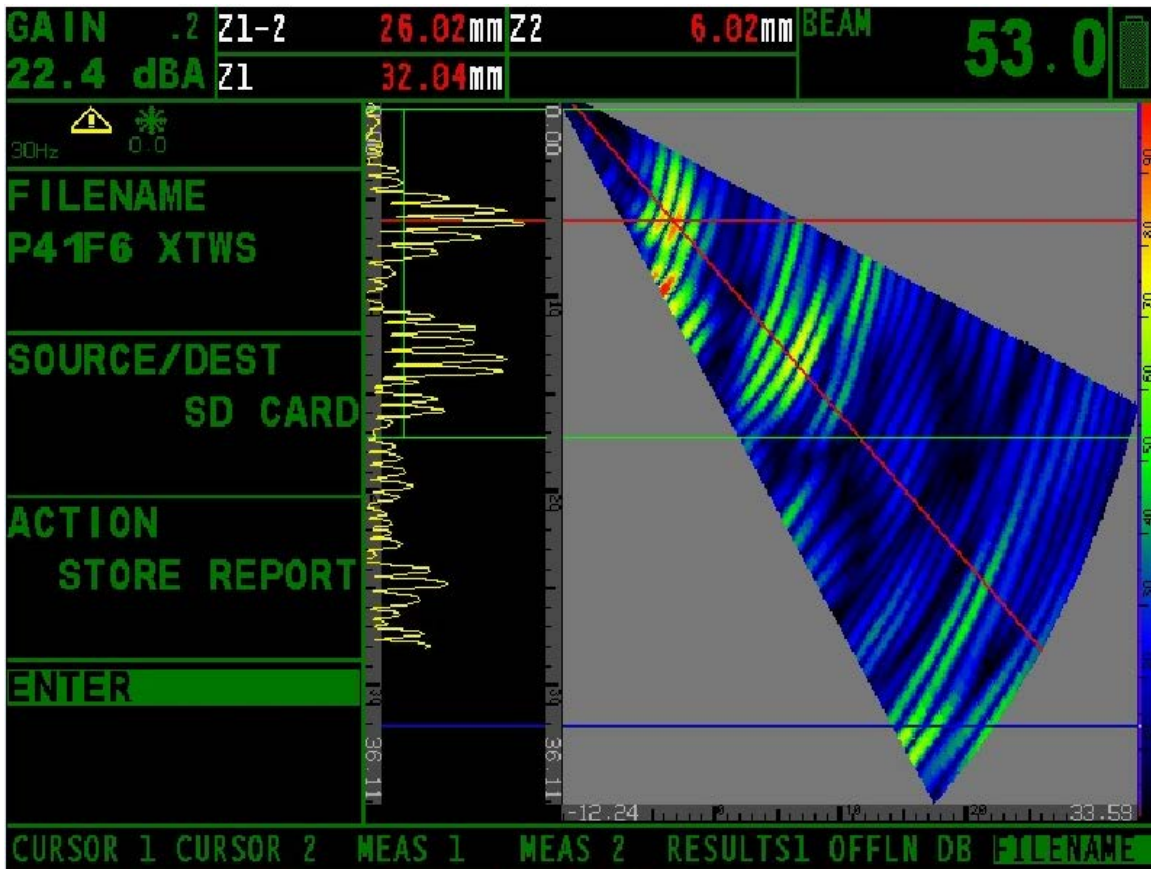
Hard to detect with manual inspection; length sizing hard lots of noise from buttering; no separation of tip diffraction from corner trap echo, no TLL echo indicates shallow flaw, flaw depth estimation procedure: if no separation of tip diffraction from corner trap and flaw seems to be shallow the flaw depth is defined per default to 10% pipe thickness at flaw position → 3.2 mm.

Figure C.133



Flaw 6 / Scan Direction: + X

Flaw No.:	As Built Information (SQC Drawing)				Measurement Results				Remarks	UT Analysis Section	Cal Sheet No:
	Flaw X Position OD	Length	Flaw Depth	Flaw Y Pos.	Flaw X Position OD	Length	Flaw Depth	Flaw Y Pos.			
	mm	mm	mm		mm	mm	mm				
6	374	20	26	CS* B**	370	≈ 30	26.02	-Y	3)	4.13	4

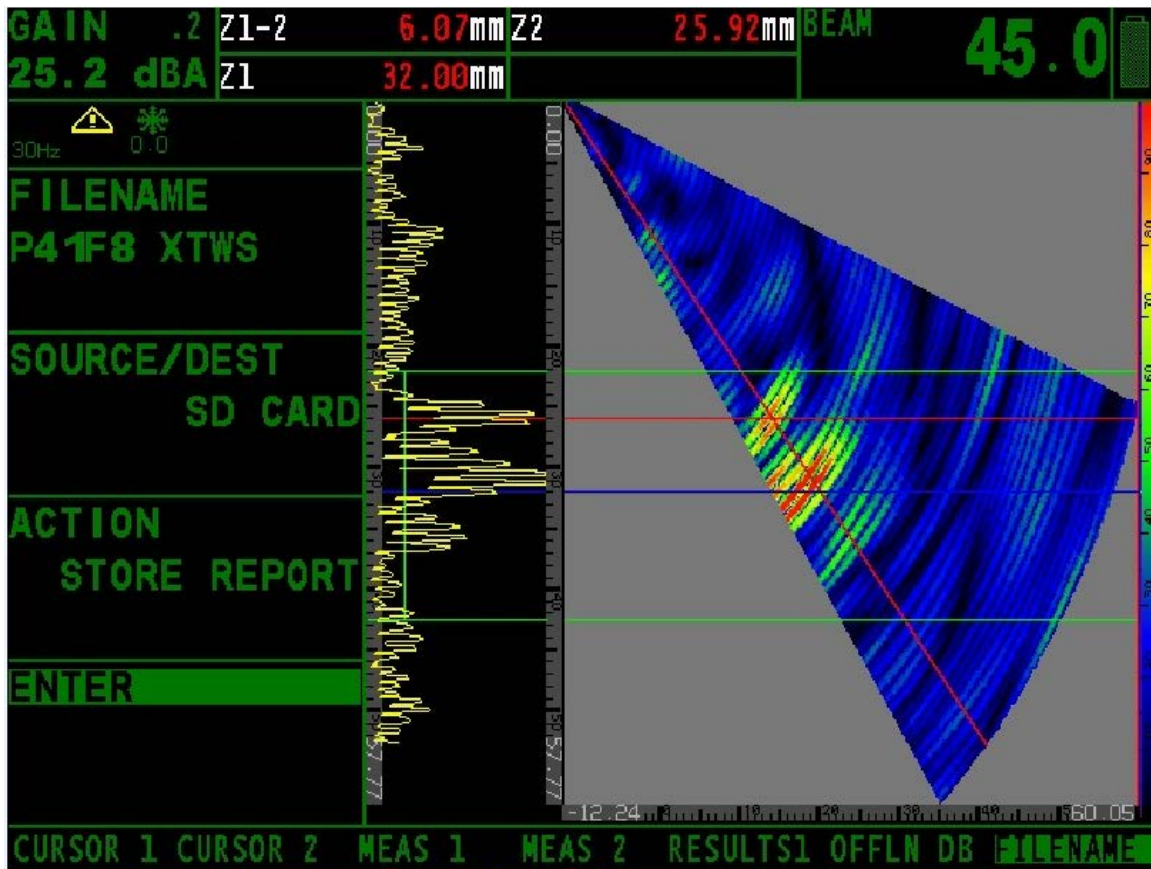


Length sizing hard lots of noise from buttering; for quantitative flaw depth sizing calibration with 9 mm deep SDH (Ø 1,5 mm) of calibration block "SVTI AS\_D270\_T30"

Figure C.134

Flaw 8 / Scan Direction: + X

Flaw No.:	As Built Information (SQC Drawing)				Measurement Results				Remarks	UT Analysis Section	Cal Sheet No:
	Flaw X Position OD	Length	Flaw Depth	Flaw Y Pos.	Flaw X Position OD	Length	Flaw Depth	Flaw Y Pos.			
	mm	mm	mm		mm	mm	mm				
8	515	20	6	CS* B**	515	≈ 25	6.07	-Y	4)	4.14	5

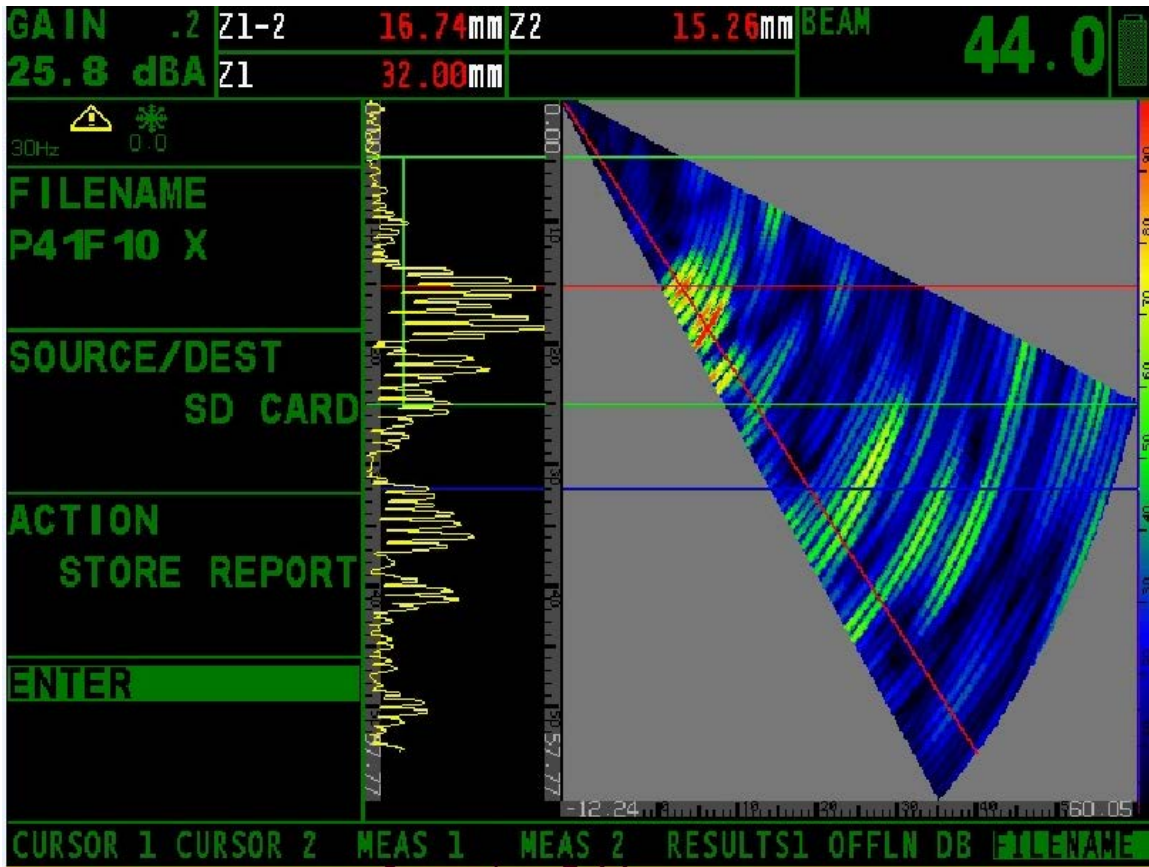


Length sizing hard lots of noise from buttering; depth sizing only possible when probe is skewed (flaw skew angle 10°); for quantitative flaw depth sizing calibration with 26 mm deep SDH (Ø 1,5 mm) of calibration block "SVTI AS\_D270\_T30"

Figure C.135

Flaw 10 / Scan Direction: + X

Flaw No.:	As Built Information (SQC Drawing)				Measurement Results				Remarks	UT Analysis Section	Cal Sheet No:
	Flaw X Position OD	Length	Flaw Depth	Flaw Y Pos.	Flaw X Position OD	Length	Flaw Depth	Flaw Y Pos.			
	mm	mm	mm		mm	mm	mm				
10	696	20	17	CS* B**	698	20	16.74	-Y	5)	4.15	6

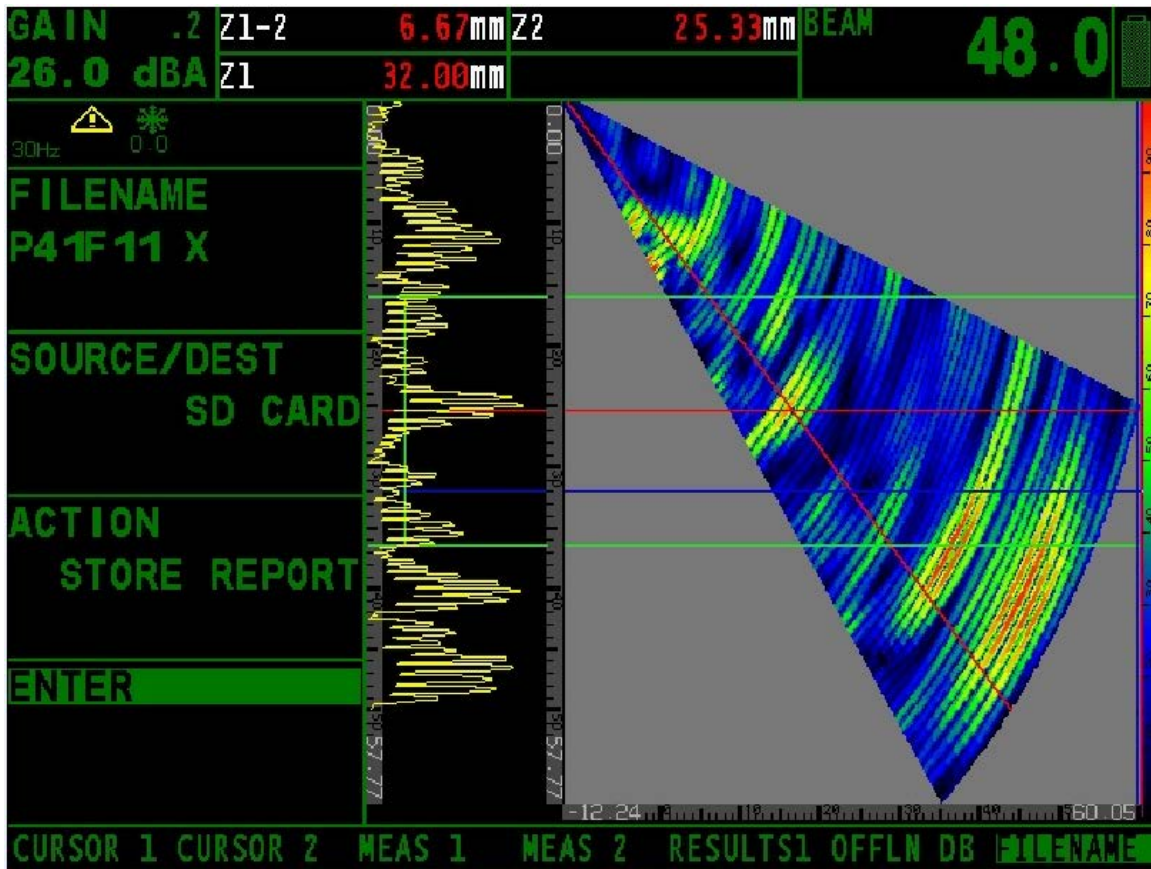


Quantitative flaw depth sizing calibration with 15 mm deep SDH (Ø 1,5 mm) of calibration block "SVTI AS\_D270\_T30"

Figure C.136

Flaw 11 / Scan Direction: + X

Flaw No.:	As Built Information (SQC Drawing)				Measurement Results				Remarks	UT Analysis Section	Cal Sheet No:
	Flaw X Position OD	Length	Flaw Depth	Flaw Y Pos.	Flaw X Position OD	Length	Flaw Depth	Flaw Y Pos.			
	mm	mm	mm		mm	mm	mm				
11	754	20	6	CS* B**	750	20	6.67	-Y	6)	4.16	5

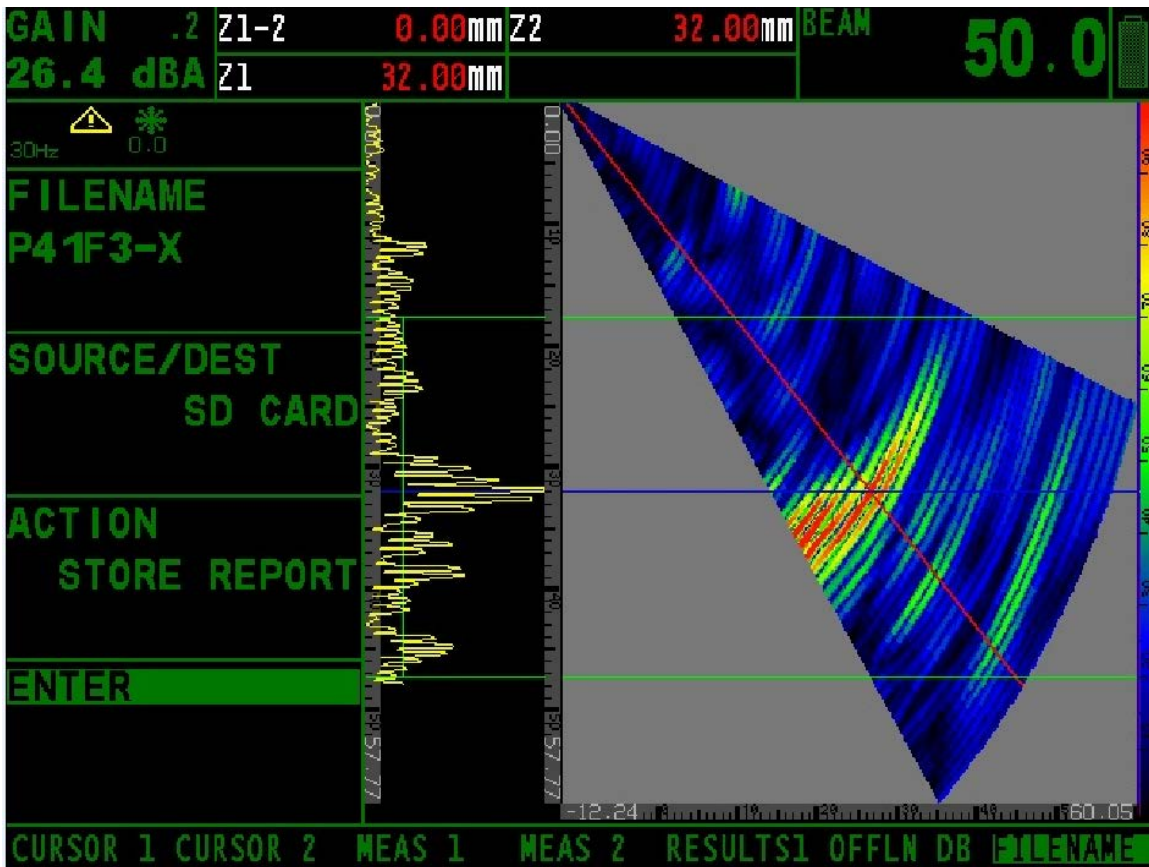


Flaw depth sizing hard, very weak tip signal; quantitative flaw depth sizing calibration with 26 mm deep SDH (Ø 1,5 mm) of calibration block "SVTI AS\_D270\_T30"

Figure C.137

Flaw 3 / Scan Direction: - X

Flaw No.:	As Built Information (SQC Drawing)				Measurement Results				Remarks	UT Analysis Section	Cal Sheet No:
	Flaw X Position OD	Length	Flaw Depth	Flaw Y Pos.	Flaw X Position OD	Length	Flaw Depth	Flaw Y Pos.			
	mm	mm	mm		mm	mm	mm				
3	135	10	2	CS* B**	135	≈ 10	3.2	-Y	1)		

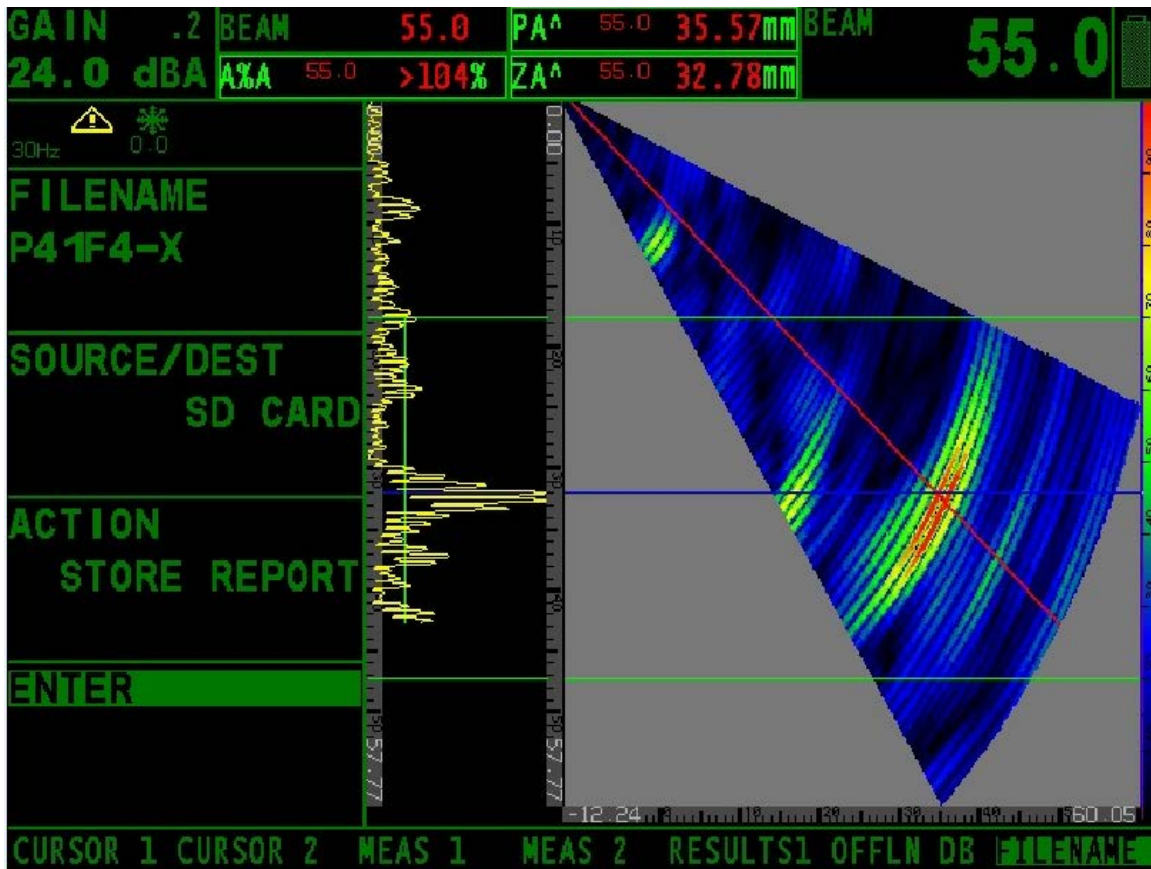


Very hard to detect with manual inspection; length sizing hard lots of noise from buttering; no separation of tip diffraction from corner trap echo, no TLL echo indicates shallow flaw, flaw depth estimation procedure: if no separation of tip diffraction from corner trap and flaw seems to be shallow the flaw depth is defined per default to 10% pipe thickness at flaw position → 3.2 mm

Figure C.138

Flaw 4 / Scan Direction: - X

Flaw No.:	As Built Information (SQC Drawing)				Measurement Results				Remarks	UT Analysis Section	Cal Sheet No:
	Flaw X Position OD	Length	Flaw Depth	Flaw Y Pos.	Flaw X Position OD	Length	Flaw Depth	Flaw Y Pos.			
	mm	mm	mm		mm	mm	mm				
4	193	6	3	CS* B**	195	≈ 6		-Y	2)		

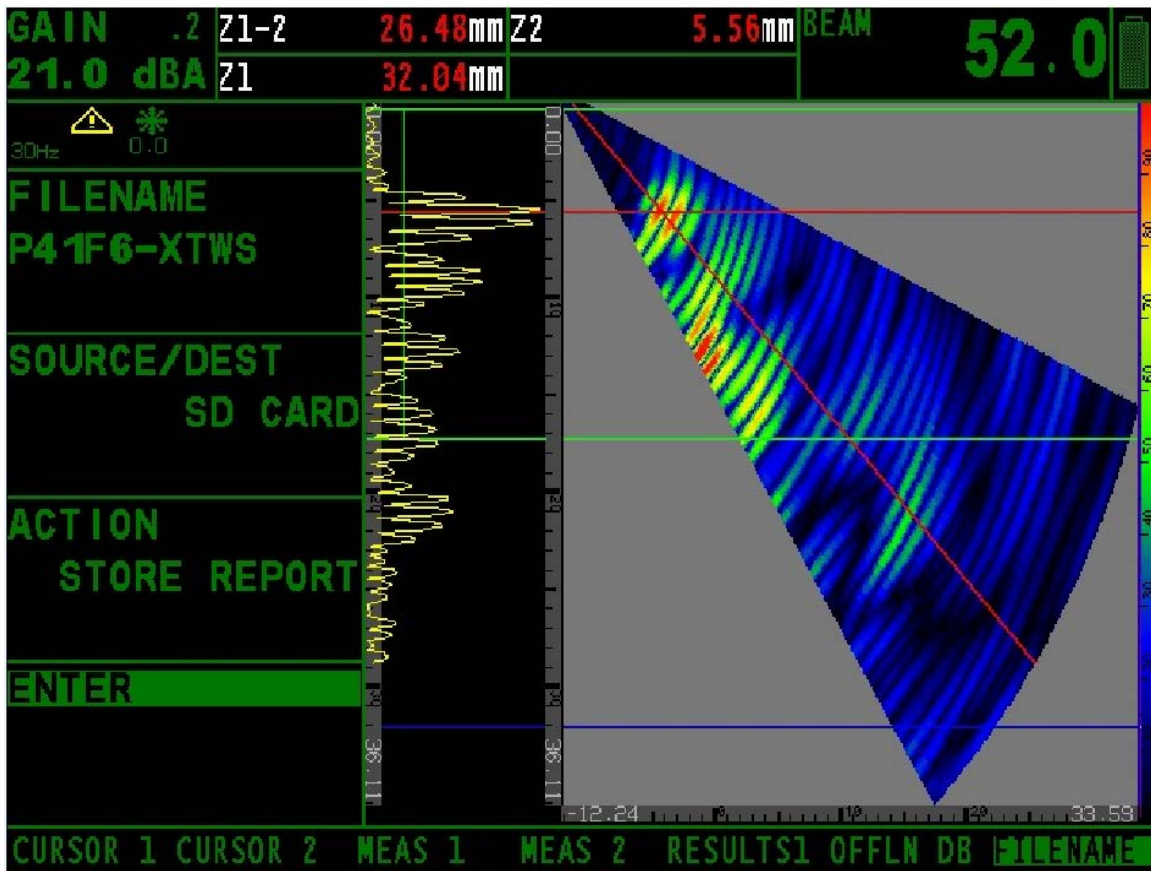


Hard to detect with manual inspection; length sizing hard lots of noise from buttering; no separation of tip diffraction from corner trap echo, no TLL echo indicates shallow flaw, flaw depth estimation procedure: if no separation of tip diffraction from corner trap and flaw seems to be shallow the flaw depth is defined per default to 10% pipe thickness at flaw position → 3.2 mm

Figure C.139

Flaw 6 / Scan Direction: - X

Flaw No.:	As Built Information (SQC Drawing)				Measurement Results				Remarks	UT Analysis Section	Cal Sheet No:
	Flaw X Position OD	Length	Flaw Depth	Flaw Y Pos.	Flaw X Position OD	Length	Flaw Depth	Flaw Y Pos.			
	mm	mm	mm		mm	mm	mm				
6	374	20	26	CS* B**	370	≈ 20	26.48	-Y	3)		4

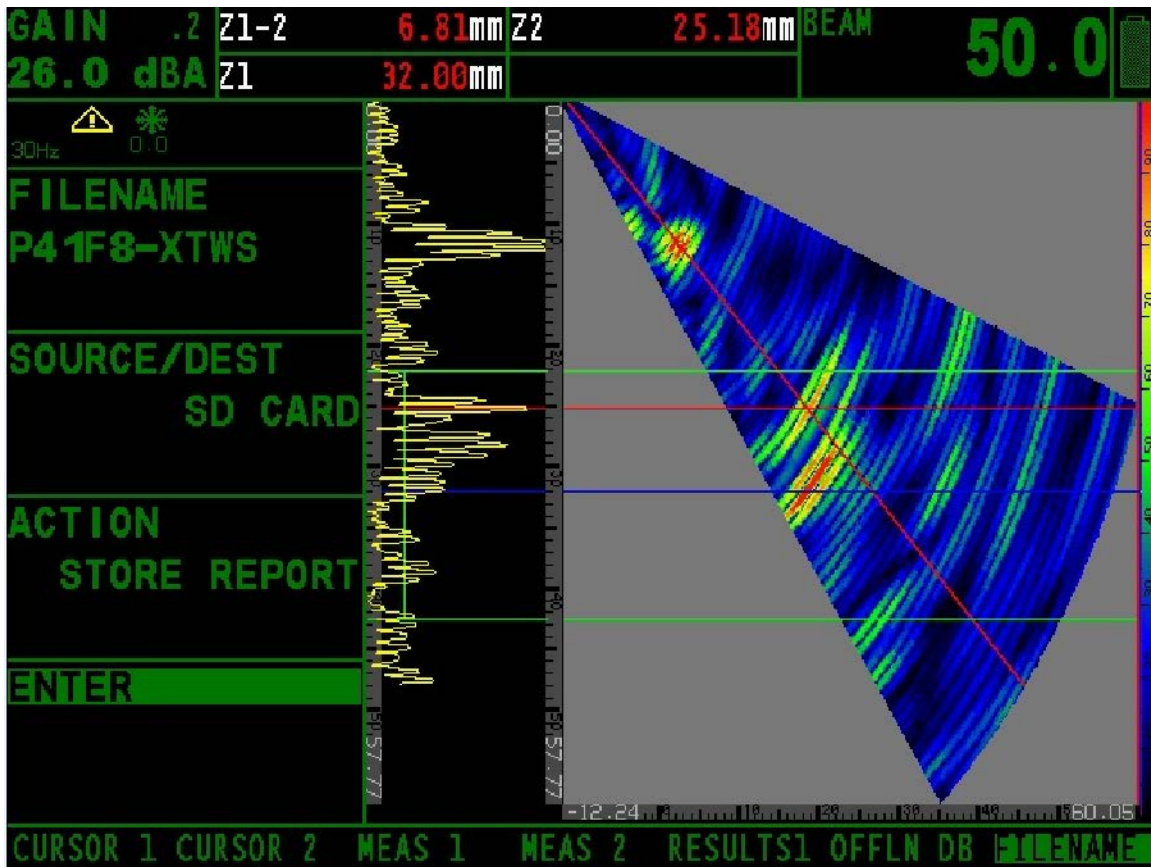


Length sizing hard lots of noise from buttering; for quantitative flaw depth sizing calibration with 9 mm deep SDH (Ø 1,5 mm) of calibration block "SVTI AS\_D270\_T30"

Figure C.140

Flaw 8 / Scan Direction: - X

Flaw No.:	As Built Information (SQC Drawing)				Measurement Results				Remarks	UT Analysis Section	Cal Sheet No:
	Flaw X Position OD	Length	Flaw Depth	Flaw Y Pos.	Flaw X Position OD	Length	Flaw Depth	Flaw Y Pos.			
	mm	mm	mm		mm	mm	mm				
8	515	20	6	CS* B**	515	≈ 25	6.81	-Y	4)		5



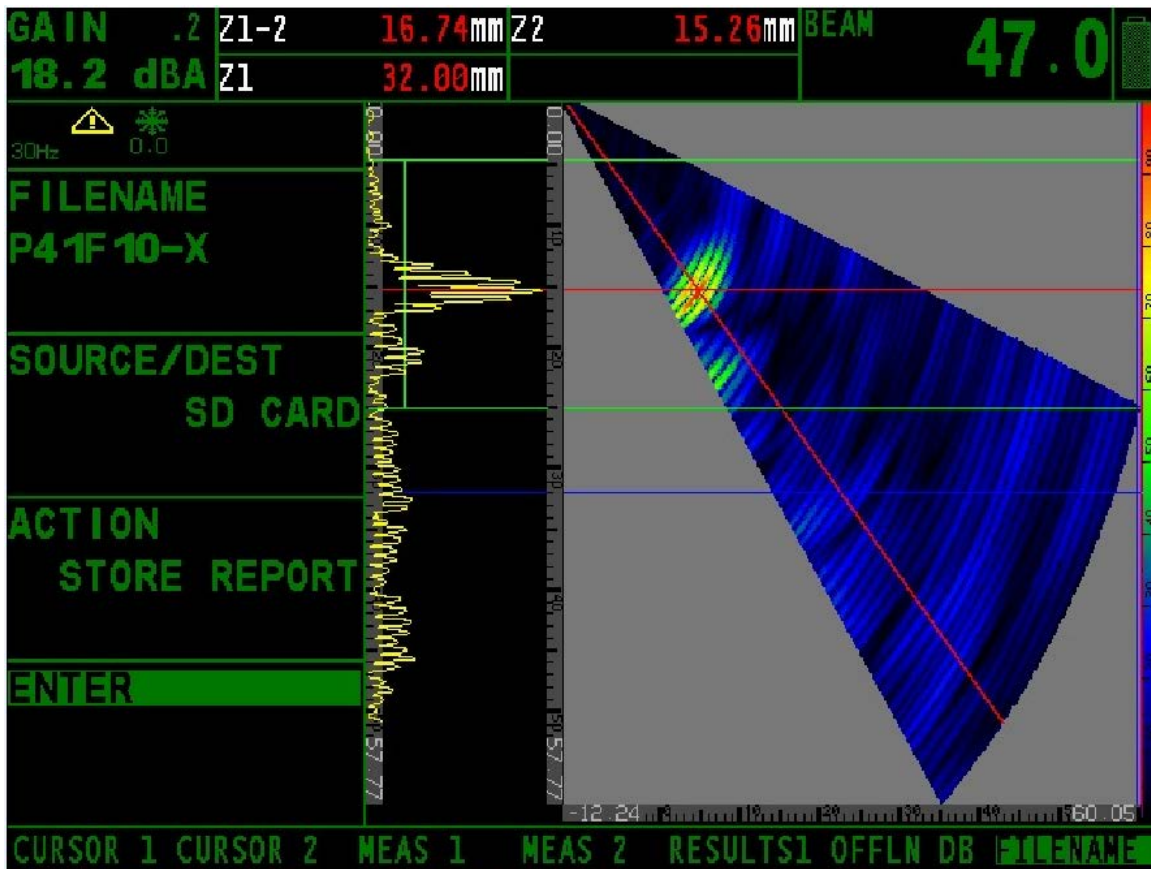
Length sizing hard lots of noise from buttering; depth sizing hard only possible when probe is skewed (flaw skew angle 10°); for quantitative flaw depth sizing calibration with 26 mm deep SDH (Ø 1,5 mm) of calibration block "SVTI AS\_D270\_T30"

Figure C.141



Flaw 10 / Scan Direction: - X

Flaw No.:	As Built Information (SQC Drawing)				Measurement Results				Remarks	UT Analysis Section	Cal Sheet No:
	Flaw X Position OD	Length	Flaw Depth	Flaw Y Pos.	Flaw X Position OD	Length	Flaw Depth	Flaw Y Pos.			
	mm	mm	mm		mm	mm	mm				
10	696	20	17	CS* B**	698	≈ 25	16.74	-Y	5)		

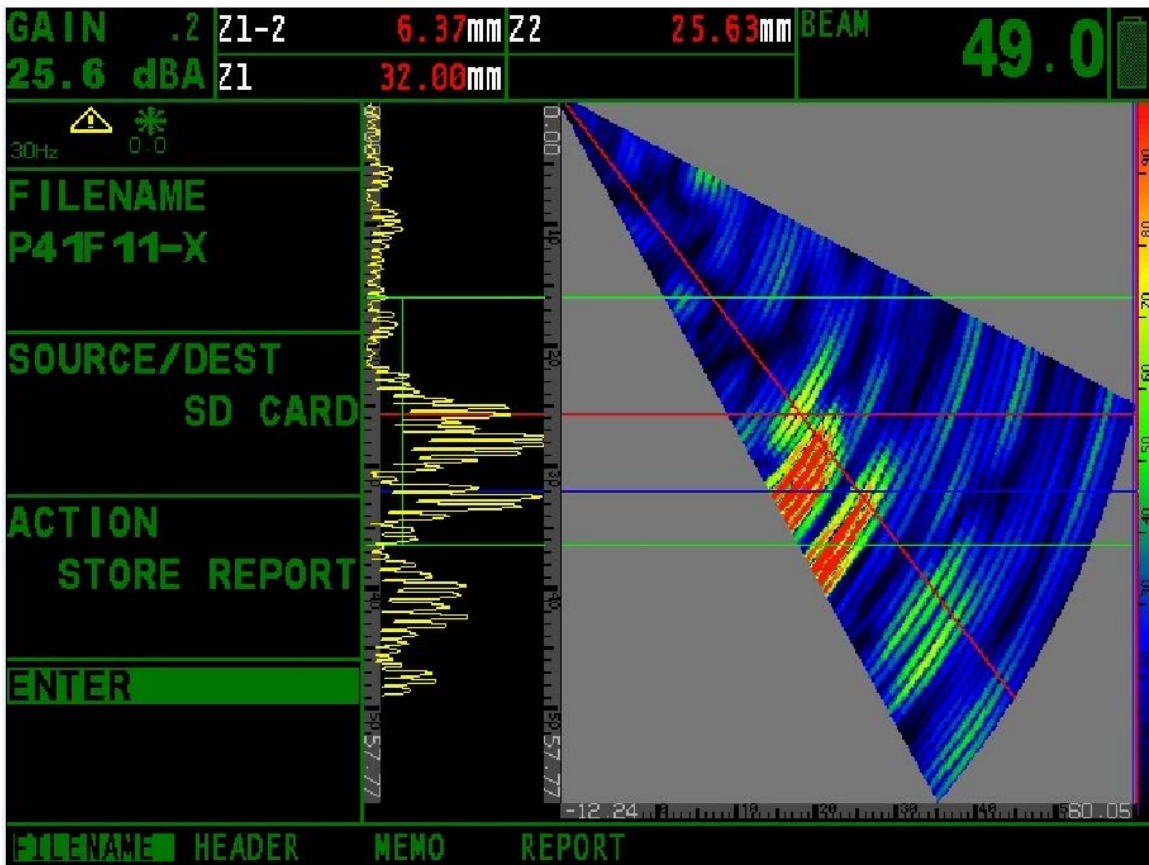


Quantitative flaw depth sizing calibration with 15 mm deep SDH (Ø 1,5 mm) of calibration block "SVTI AS\_D270\_T30"

Figure C.142

Flaw 11 / Scan Direction: - X

Flaw No.:	As Built Information (SQC Drawing)				Measurement Results				Remarks	UT Analysis Section	Cal Sheet No:
	Flaw X Position OD	Length	Flaw Depth	Flaw Y Pos.	Flaw X Position OD	Length	Flaw Depth	Flaw Y Pos.			
	mm	mm	mm		mm	mm	mm				
11	754	20	6	CS* B**	750	20	6.37	-Y	6)		



Flaw depth sizing good, good tip signal; quantitative flaw depth sizing calibration with 26 mm deep SDH (Ø 1,5 mm) of calibration block "SVTI AS\_D270\_T30"

Figure C.143

#### C.2.6.4 Self Assessment

The manual Phased Array Technique using a dual matrix search unit and longitudinal waves in the range from 40° to 70° demonstrated good detection, length sizing and TWS performance of ID flaws with depth greater than 10% of the wall thickness.

## C.2.7 Computer Tomography, Technique ID 109-CT0

### C.2.7.1 Assignment of Task

Analysis of crack depth in weld of PARENT Test Blocks by means of X-ray computed tomography according procedure elaborated for Sample P32.

### C.2.7.2 Test Objects

Test object	PARENT Test Block
Material	Base metal: 22 NiMoCr 3 7 (SA 508 Class 2) Weld: Alloy 182
Dimensions [mm]	ca. 35 x 30.3 x 220
Weight [kg]	1.84 kg
Fixation on CT-scanner	double sided adhesive tape

Photo of test object on CT-scanner:

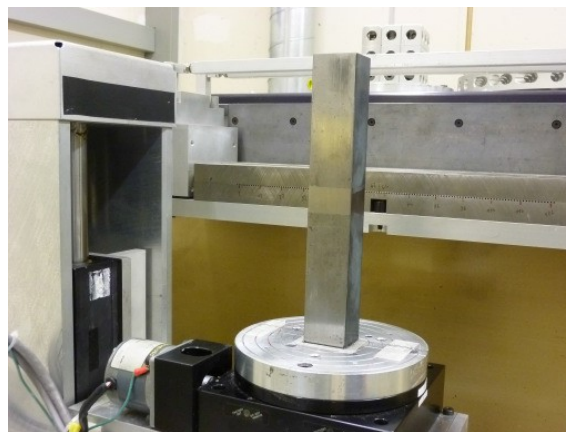


**Figure C.144** Test Block ID: P32 (N 220 AD U TS 5), view from X-ray source towards the line detector. The sample is oriented such that the crack opening is located on the side of the X-ray source.

### C.2.7.3 Parameters for Data Acquisition

CT-Scanner	CITA 101 B+ (Cita Systems)
Beam geometry	Fan beam
X-ray source	X-ray system MG452 (YTU450-D09)
Parameters of X-ray source	450 kV / 3.3 mA / 1.0 mm focal spot
External X-ray filtration	1.5 mm Brass
Detector	Single collimated (W) line detector (CdWO <sub>4</sub> ) with 125 detector channels
Detector aperture [mm]	0.35 x 0.15
Manipulator position	16
Pixel size of CT-slice [mm]	0.12 x 0.12
Slice distance [mm]	0.12
Object diameter [mm]	60
Ray Spacing [mm]	0.18
Integration time [ms]	100
Beam hardening correction	1.5

#### Specific Parameters

Test Block ID	P28	P29	P30	P31	P32	P38
Number of slices	39	32	25	30	41	40
Z position of 1st slice [mm]	109.68	110.64	106.80	106.80	108.36	106.80
Vertical scanning range [mm]	4.56	3.72	2.88	3.48	4.80	4.68

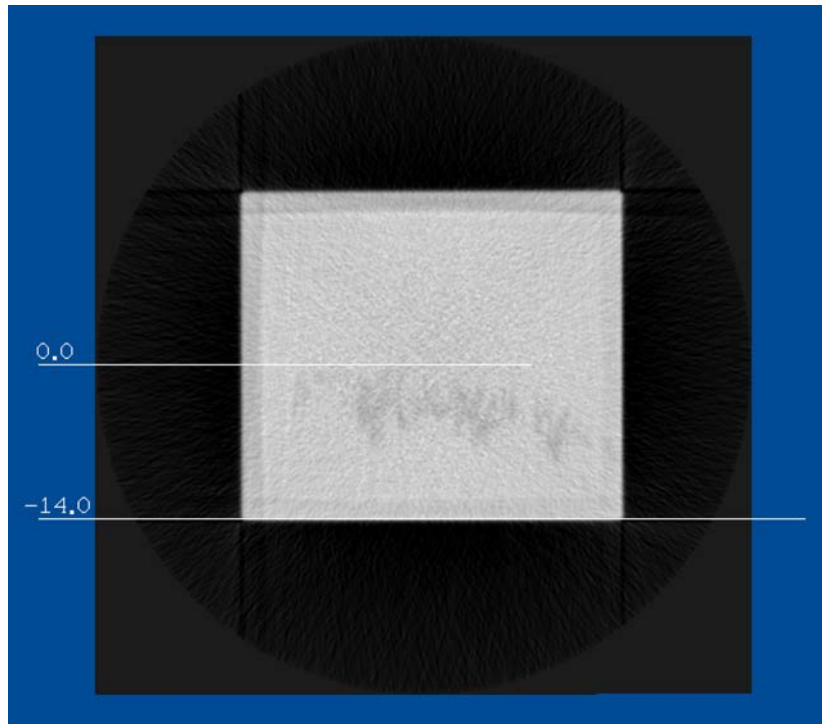
### C.2.7.4 Analysis of Crack Depth

Test Block ID	P28	P29	P30	P31	P32	P38
Slice # of max. crack depth	31	26	06	17	34	29
Z position of max. crack depth [mm]	113.28	113.64	107.40	108.72	112.32	110.16
Crack depth [mm]	14.0	13.0	17.8	3.9	11.3	4.4
Weld thickness [mm]	30.3	30.3	30.3	30.3	30.3	30.3
Crack depth in % of weld thickness	46.2	42.9	58.7	12.9	37.3	14.5

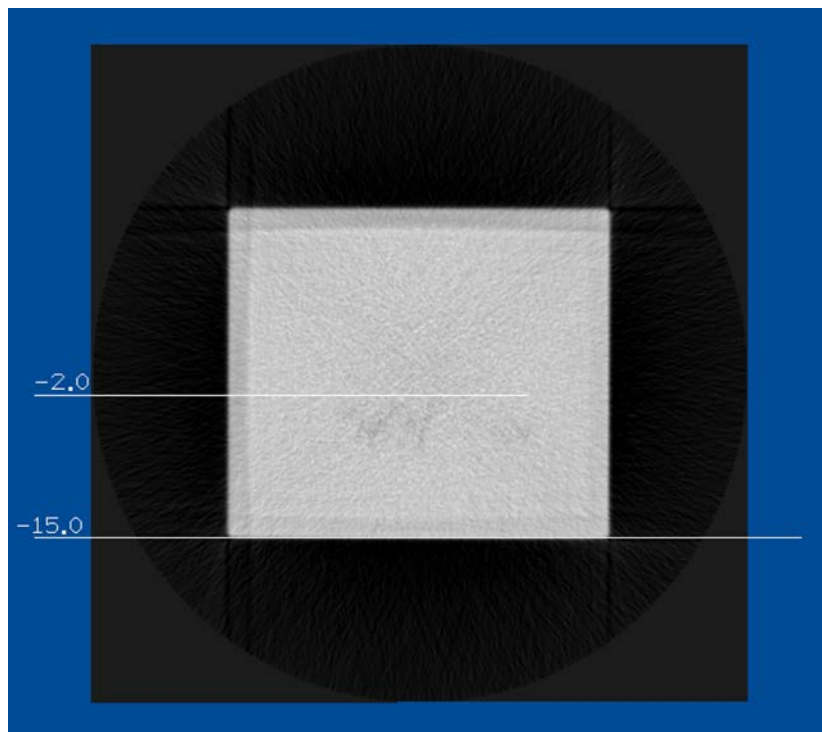
### C.2.7.5 CT Images

Figure C.145 shows the CT-slices of the six test blocks in which the maximum crack depth is assumed. The crack depth is measured from the sample surface and is indicated in the CT-images. Figure C.146 shows a stack of 15 CT-slices per test block. Figure C.147 shows the 3D-CT visualization of the six test blocks with VGStudioMax.

All CT-slices are available on the FTP server of EMPA as individual TIFF or 16 bit raw image files and as 3D-CT volumes in VGStudioMax format.



**Figure C.145a** CT-slice #31 (z=113.28 mm) of test block P28 (N 220 AD U 6), crack depth: 14.0 mm (+/- 2 pixel = 0.24 mm), 46.2% of weld thickness



**Figure C.145b** CT-slice #26 (z=113.64 mm) of test block P29 (N 220 AD U 10), crack depth: 13.0 mm (+/- 2 pixel = 0.24 mm), 42.9% of weld thickness

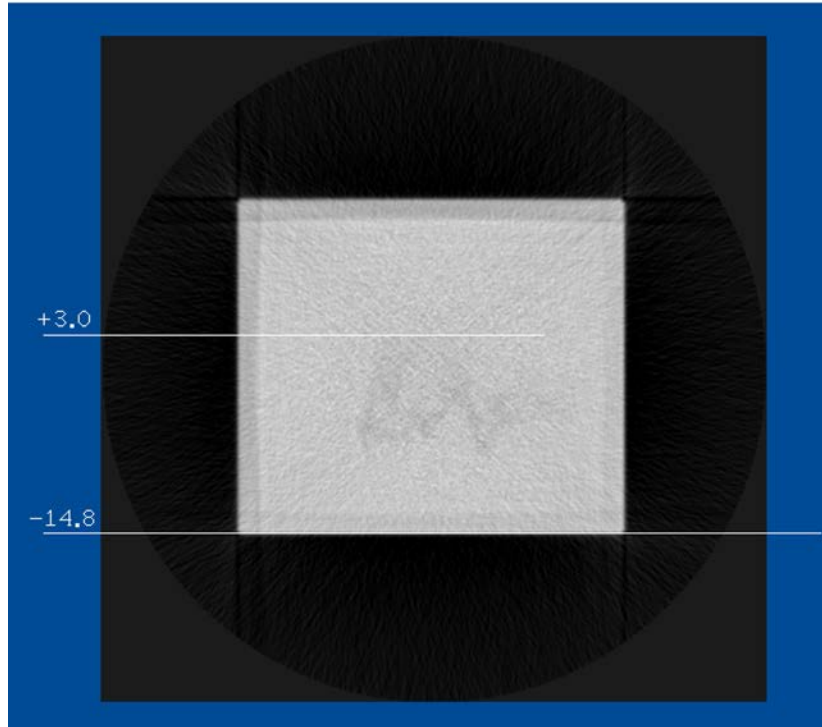


**Figure C.145c** CT-slice #06 (z=107.40 mm) of test block P30 (N 220 AD U 7), crack depth: 17.8 mm (+/- 2 pixel = 0.24 mm), 58.7% of weld thickness

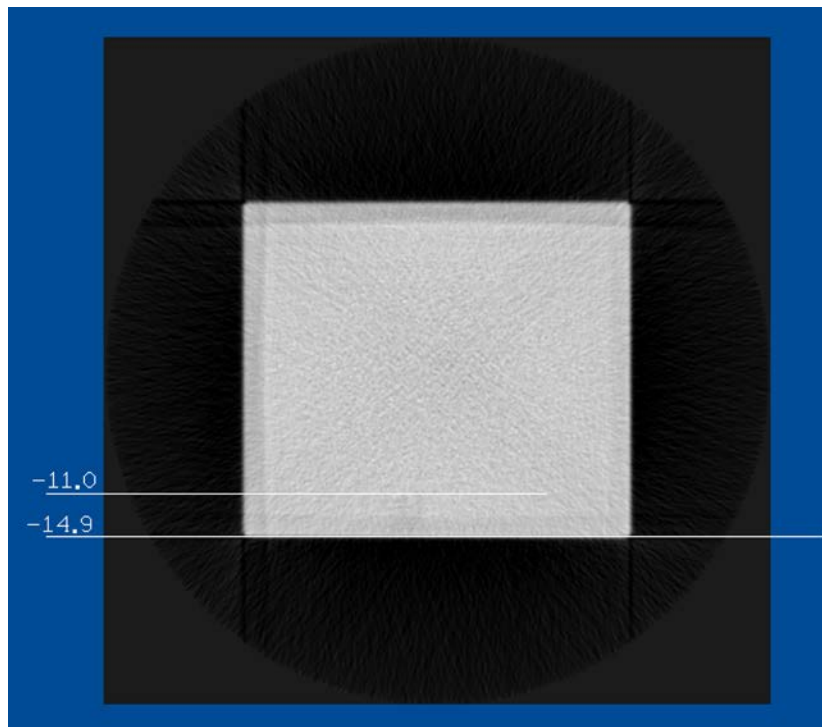


**Figure C.145d** CT-slice #17 (z=108.72 mm) of test block P31 (MN 220 AD U 1), crack depth: 3.9 mm (+/- 2 pixel = 0.24 mm), 12.9% of weld thickness

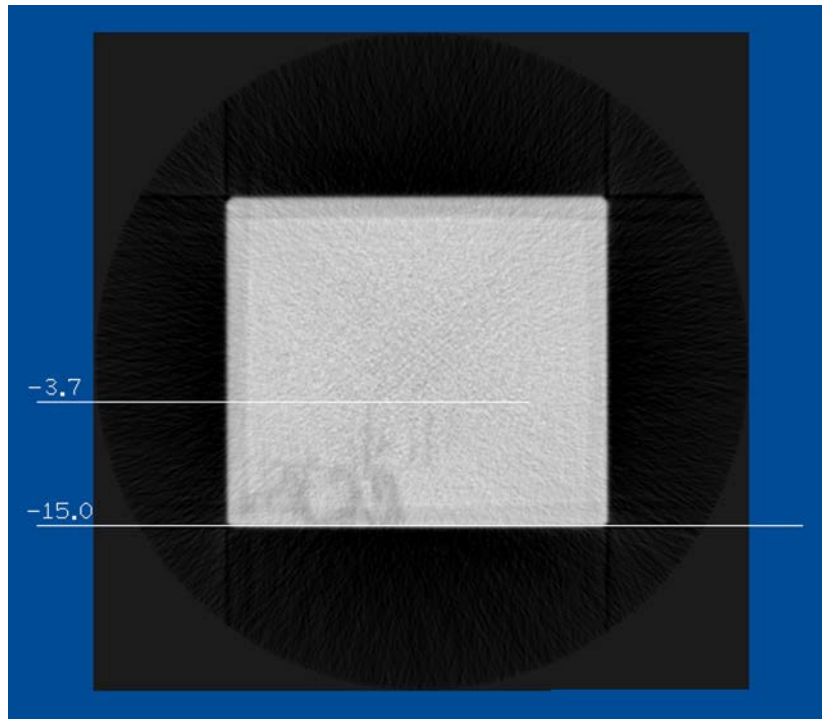


**Figure C.145e** CT-slice #34 ( $z=112.32$  mm) of test block P32 (N 220 AD U TS 5), crack depth: 11.3 mm ( $\pm 2$  pixel = 0.24 mm), 37.3% of weld thickness

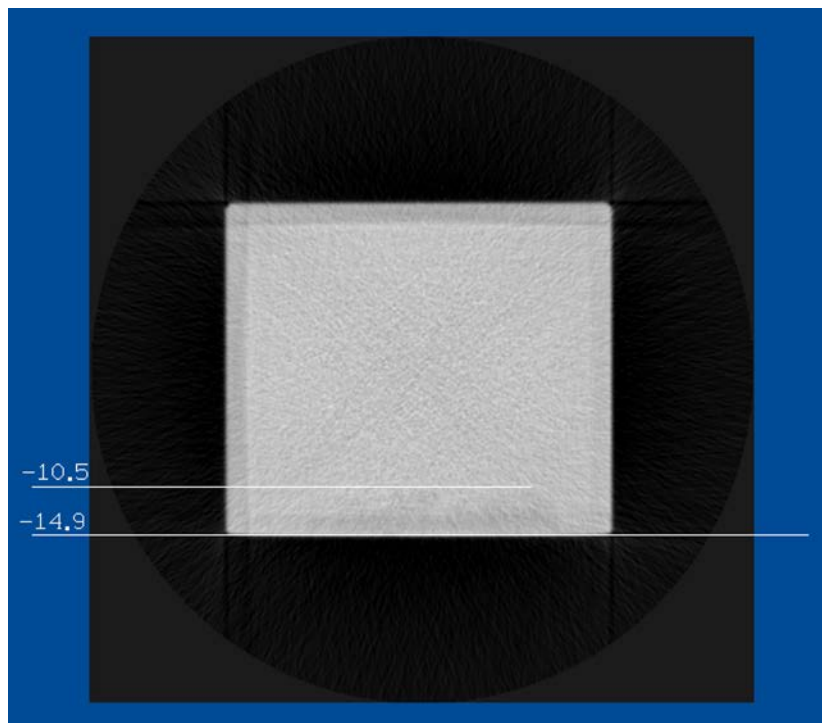


**Figure C.145f** CT-slice #29 ( $z=110.16$  mm) of test block P38 (N 220 AD U TS 3), crack depth: 4.4 mm ( $\pm 2$  pixel = 0.24 mm), 14.5% of weld thickness

**Test Block P28 (N 220 AD U 6)**

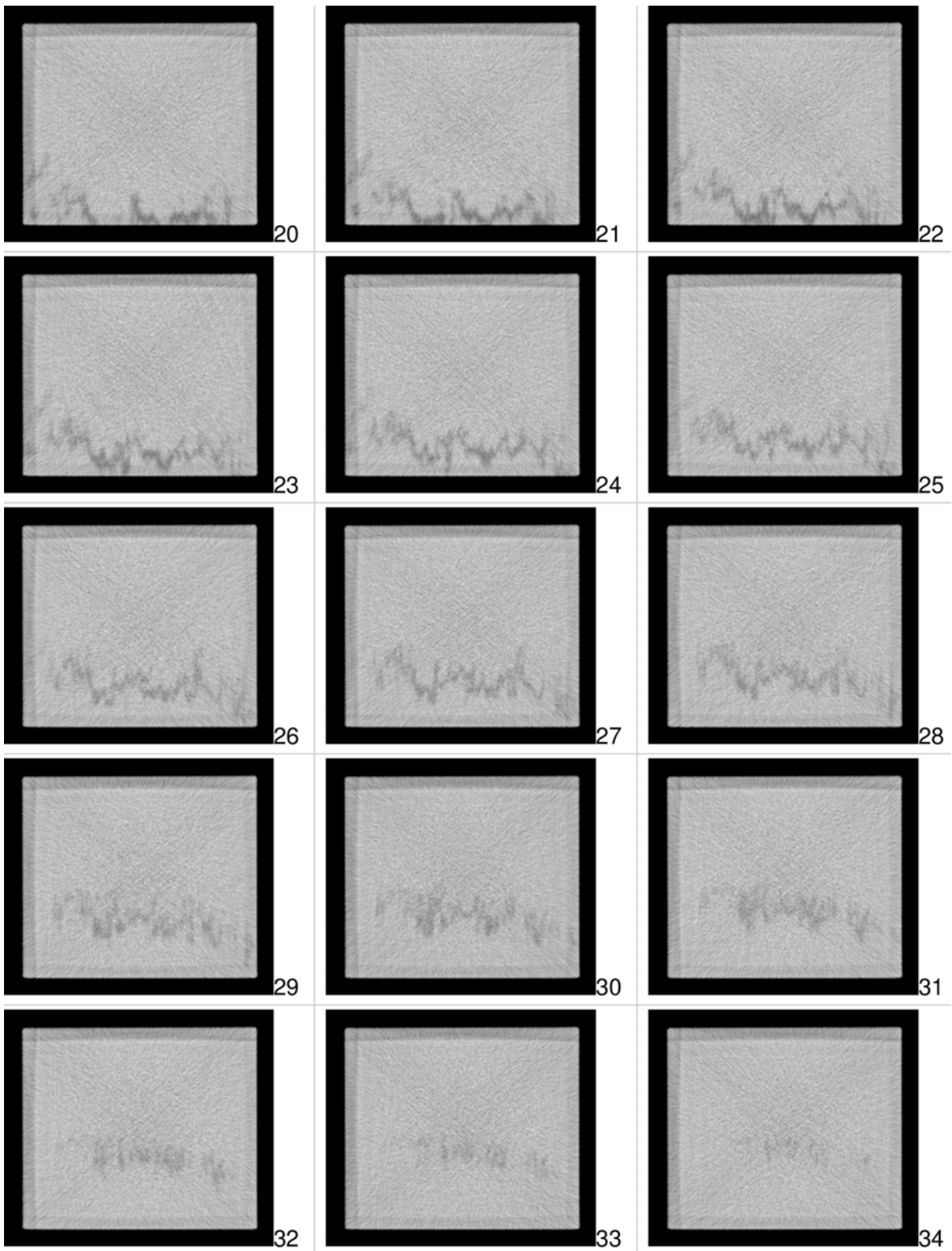


**Figure C.146a 15 CT-slices in stack of 39, starting with slice #20 and ending with #34**



Test Block ID P29 (N 220 AD U 10)

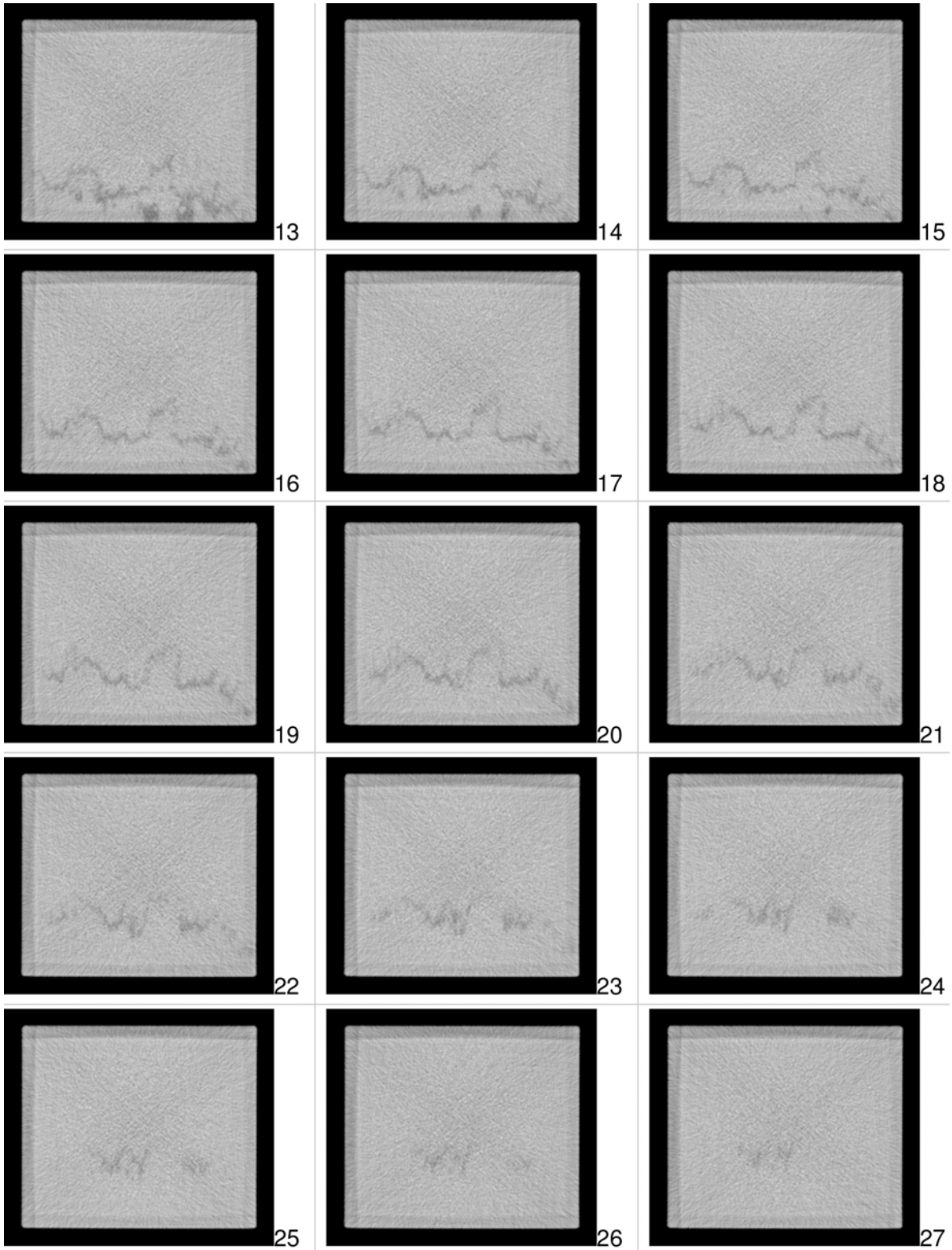


Figure C.146b 15 CT-slices in stack of 32, starting with slice #13 and ending with #27

Test Block ID P30 (N 220 AD U 7)

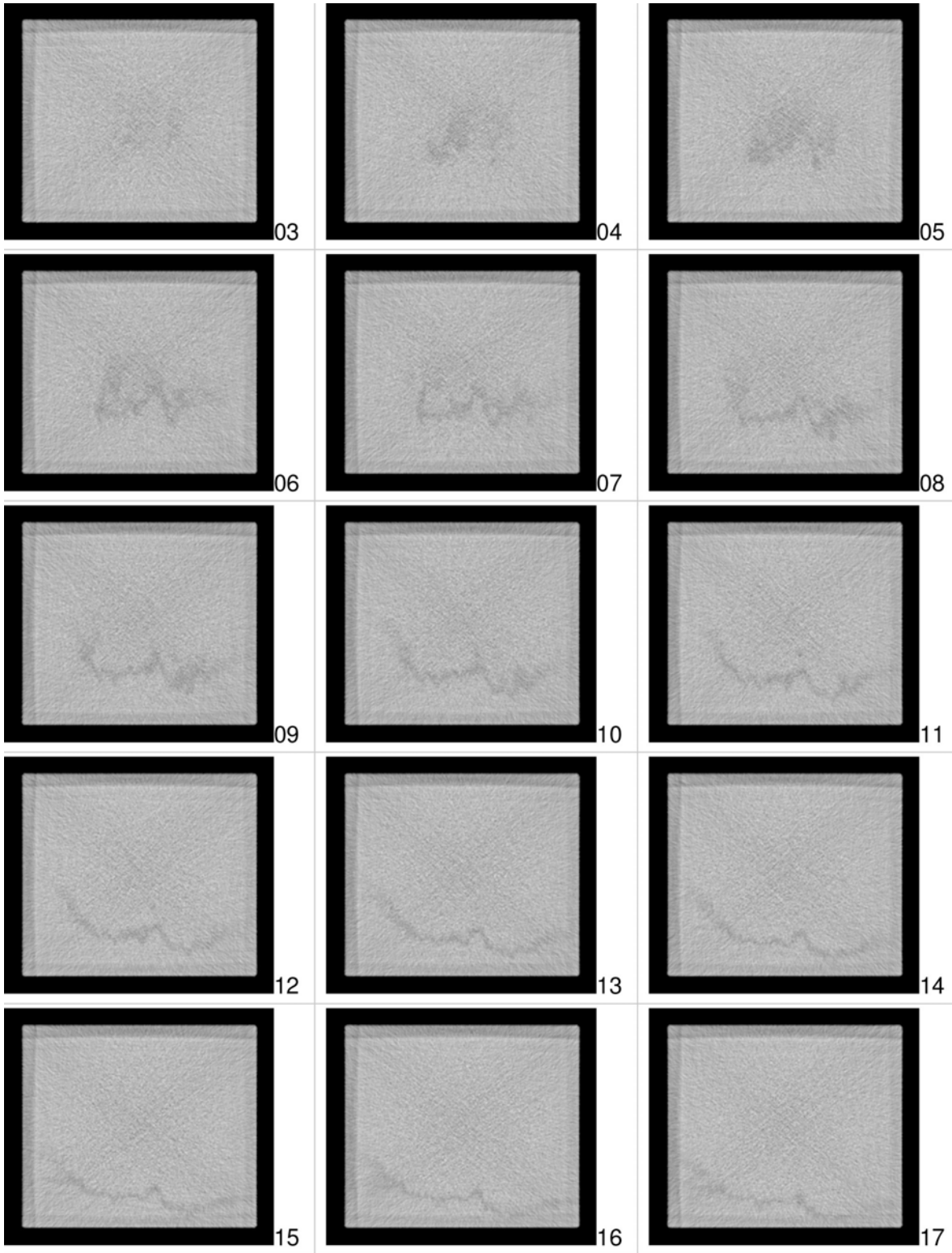


Figure C.146c 15 CT-slices in stack of 25, starting with slice #3 and ending with #17

Test Block ID P31 (MN 220 AD U 1)

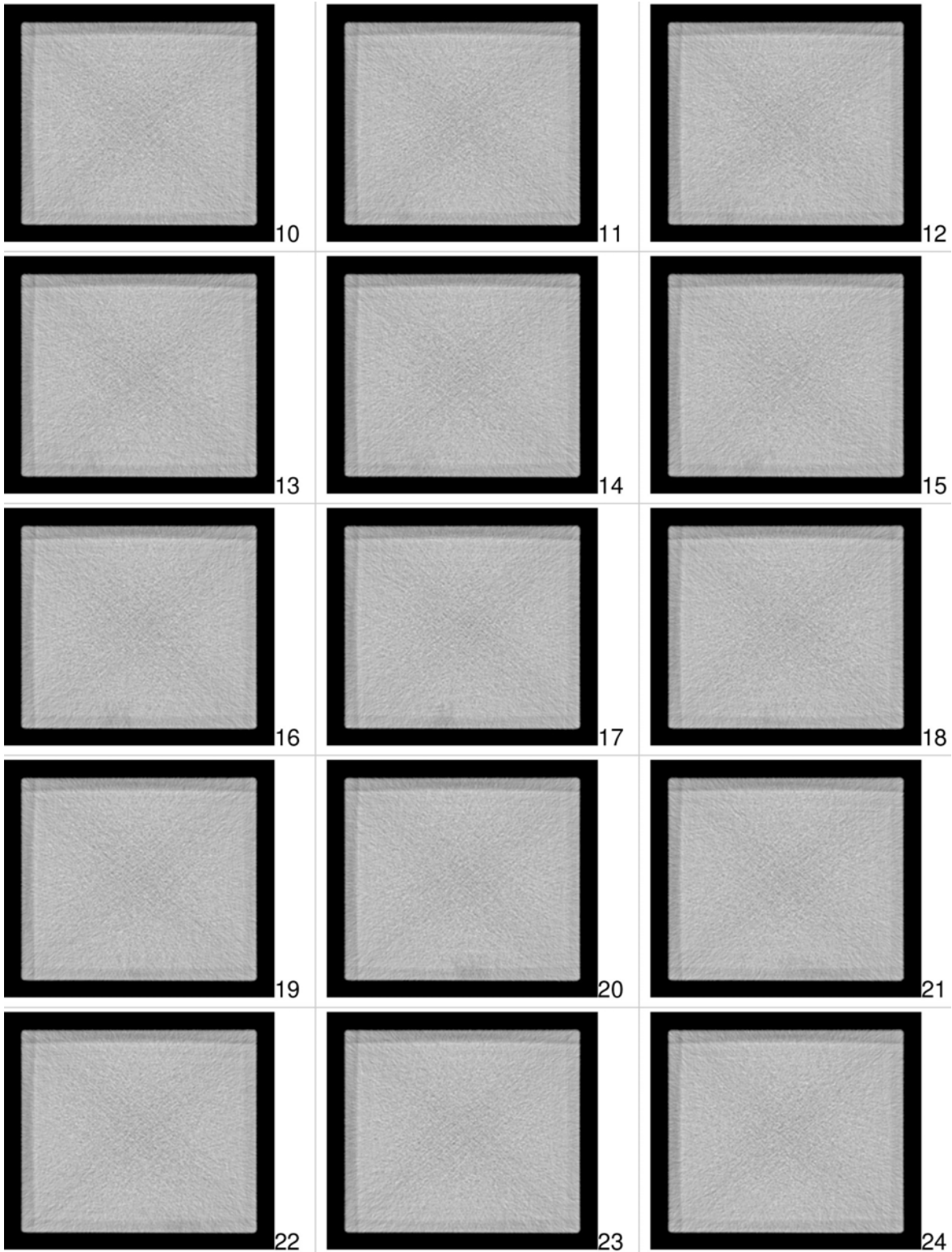


Figure C.146d 15 CT-slices in stack of 30, starting with slice #10 and ending with #24

Test Block ID P32 (N 220 AD U TS 5)

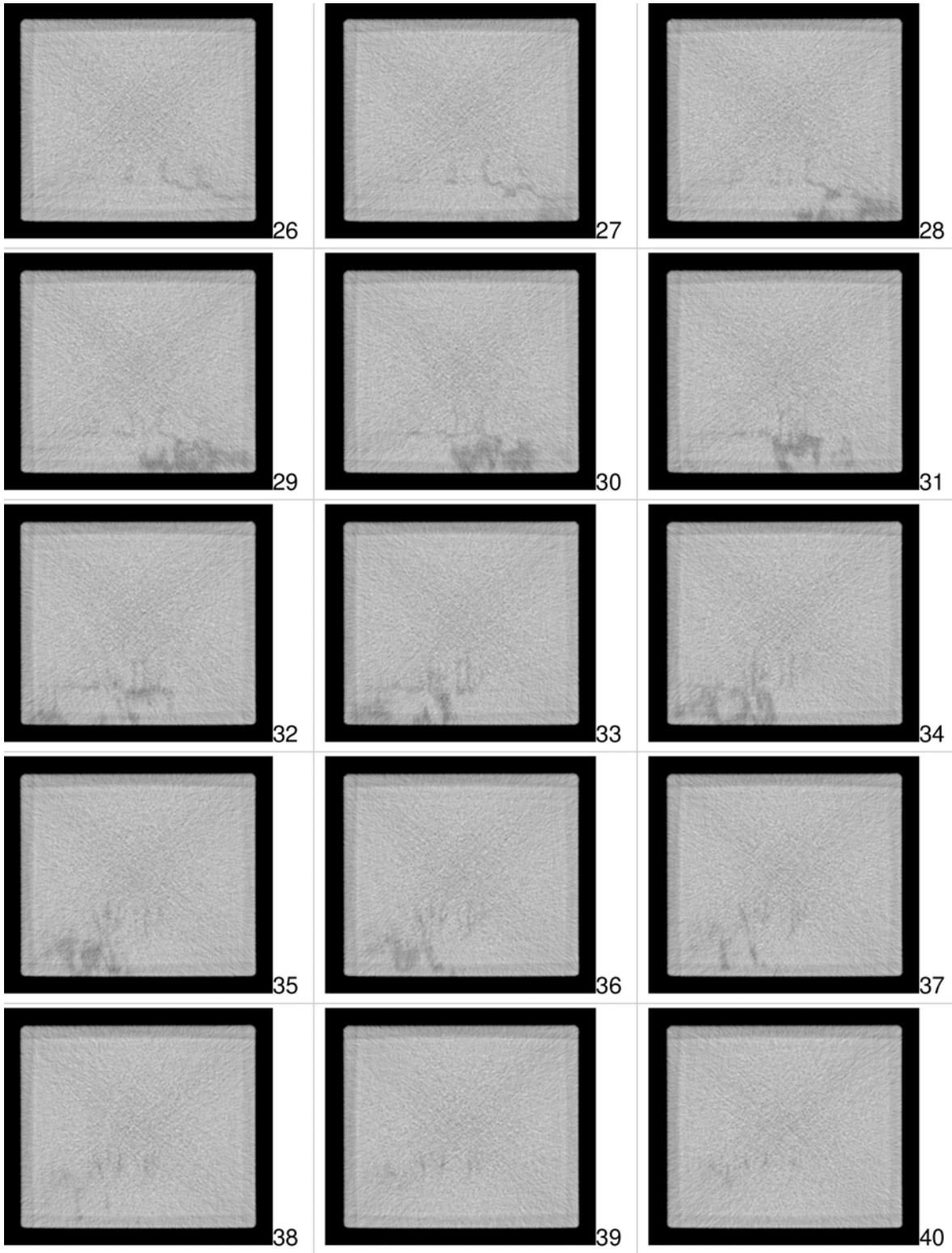
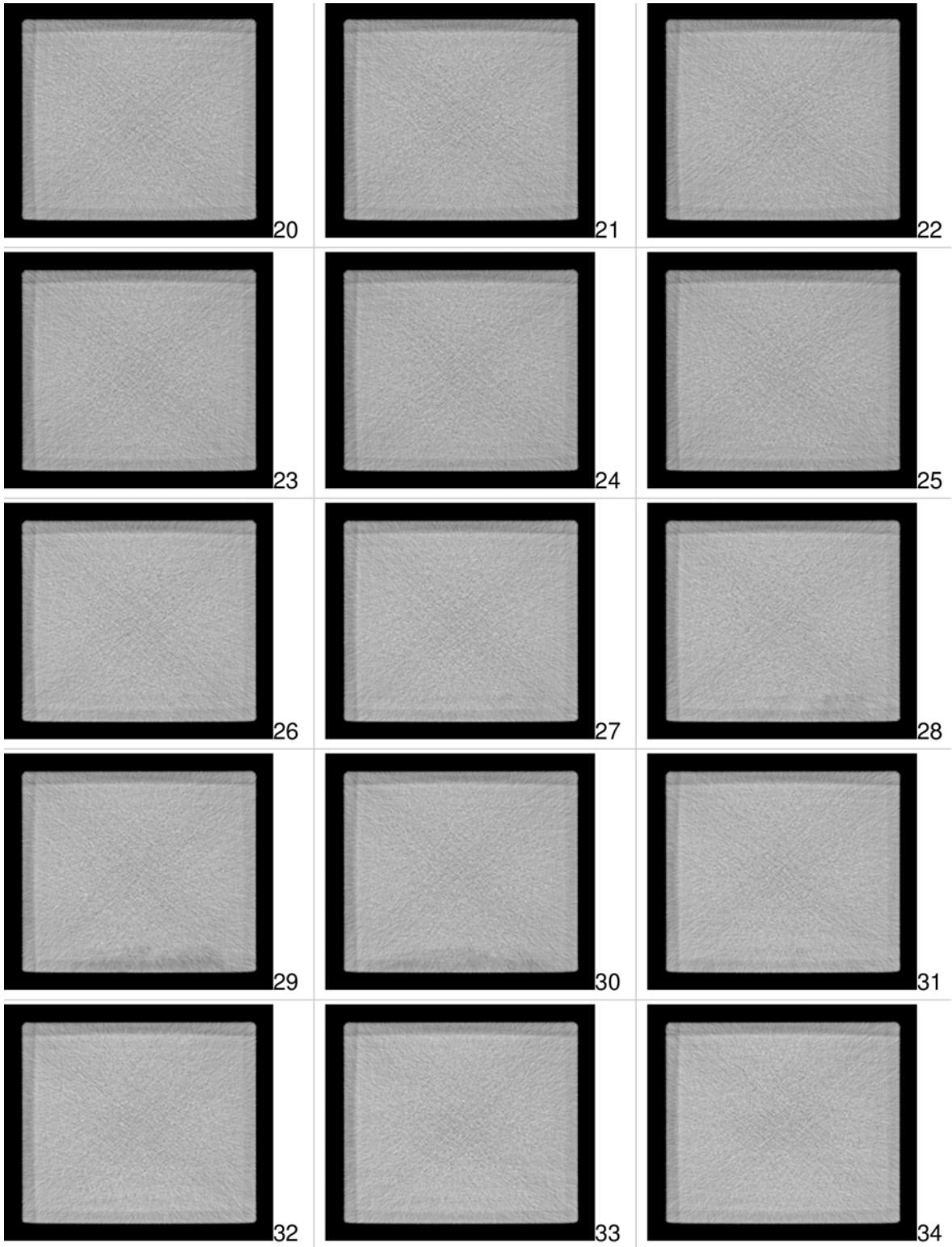


Figure C.146e 15 CT-slices in stack of 41, starting with slice #26 and ending with #40

**Test Block ID P38 (N 220 AD U TS 3)**



**Figure C.146f 15 CT-slices in stack of 40, starting with slice #20 and ending with #34**

## Test Block ID P28 (N 220 AD U 6)

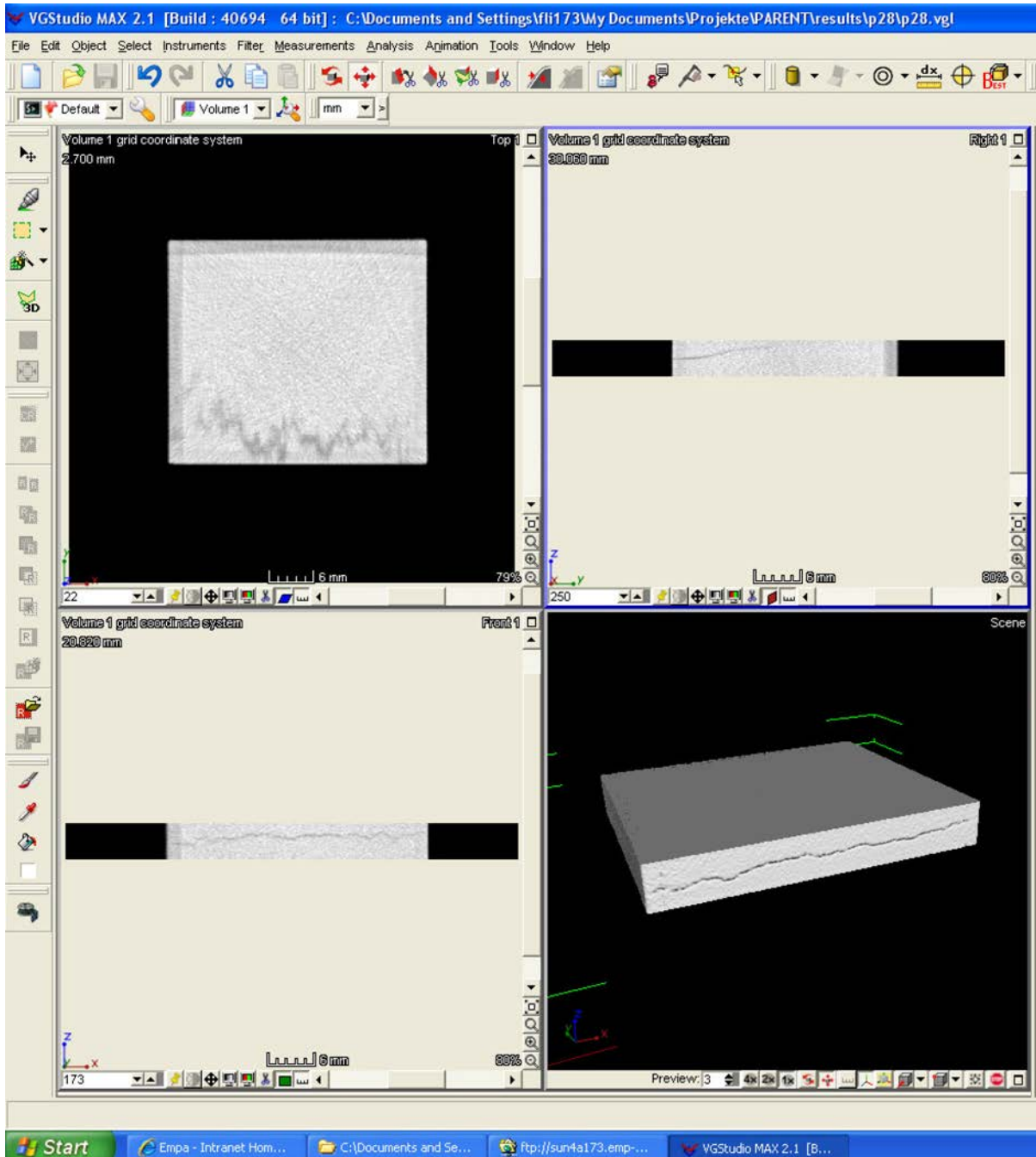


Figure C.147a Visualization of 3D-CT volume of test block P28 with VGStudioMax

Test Block ID P29 (N 220 AD U 10)

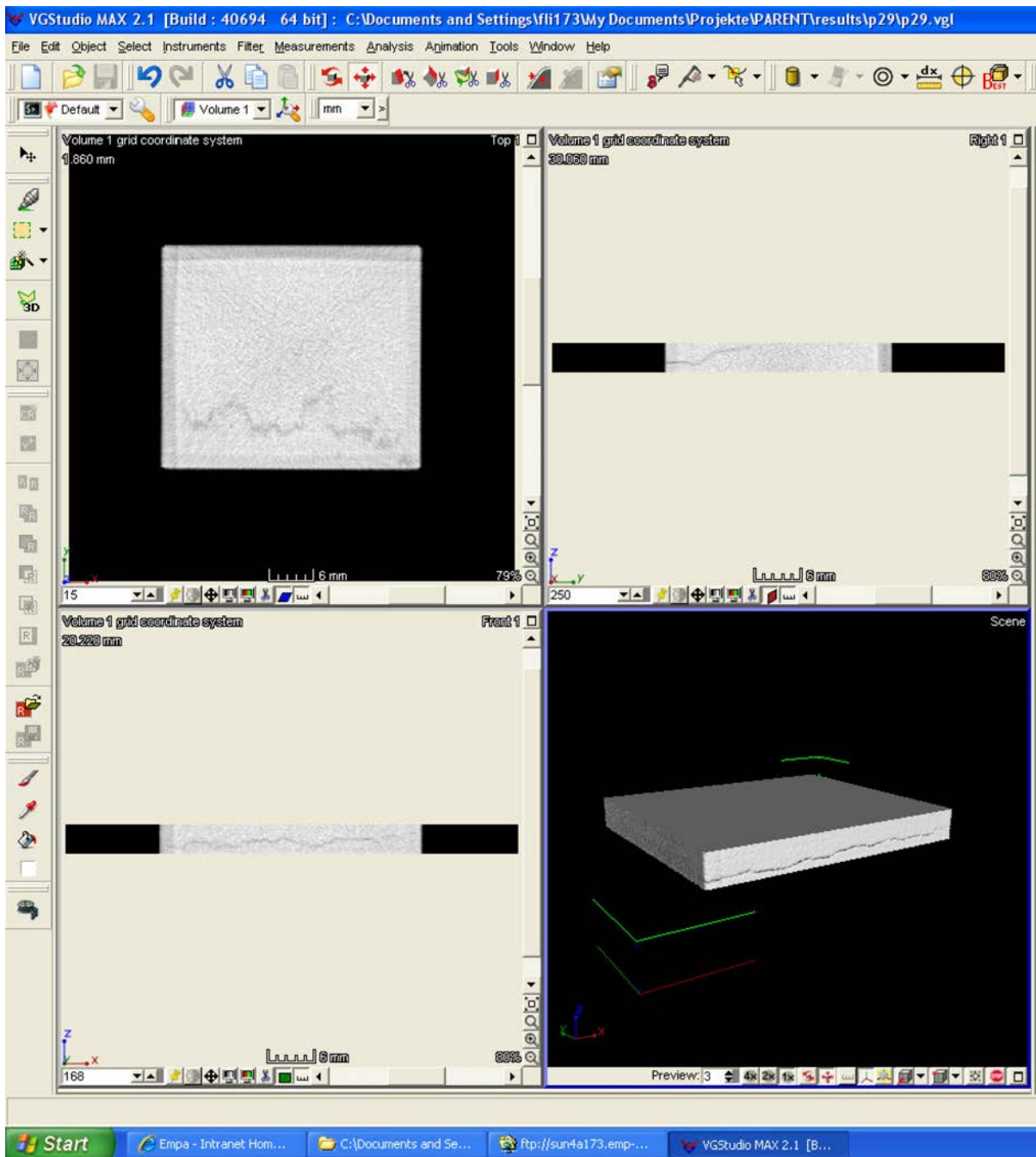


Figure C.147b Visualization of 3D-CT volume of test block P29 with VGStudioMax

### Test Block ID P30 (N 220 AD U 7)

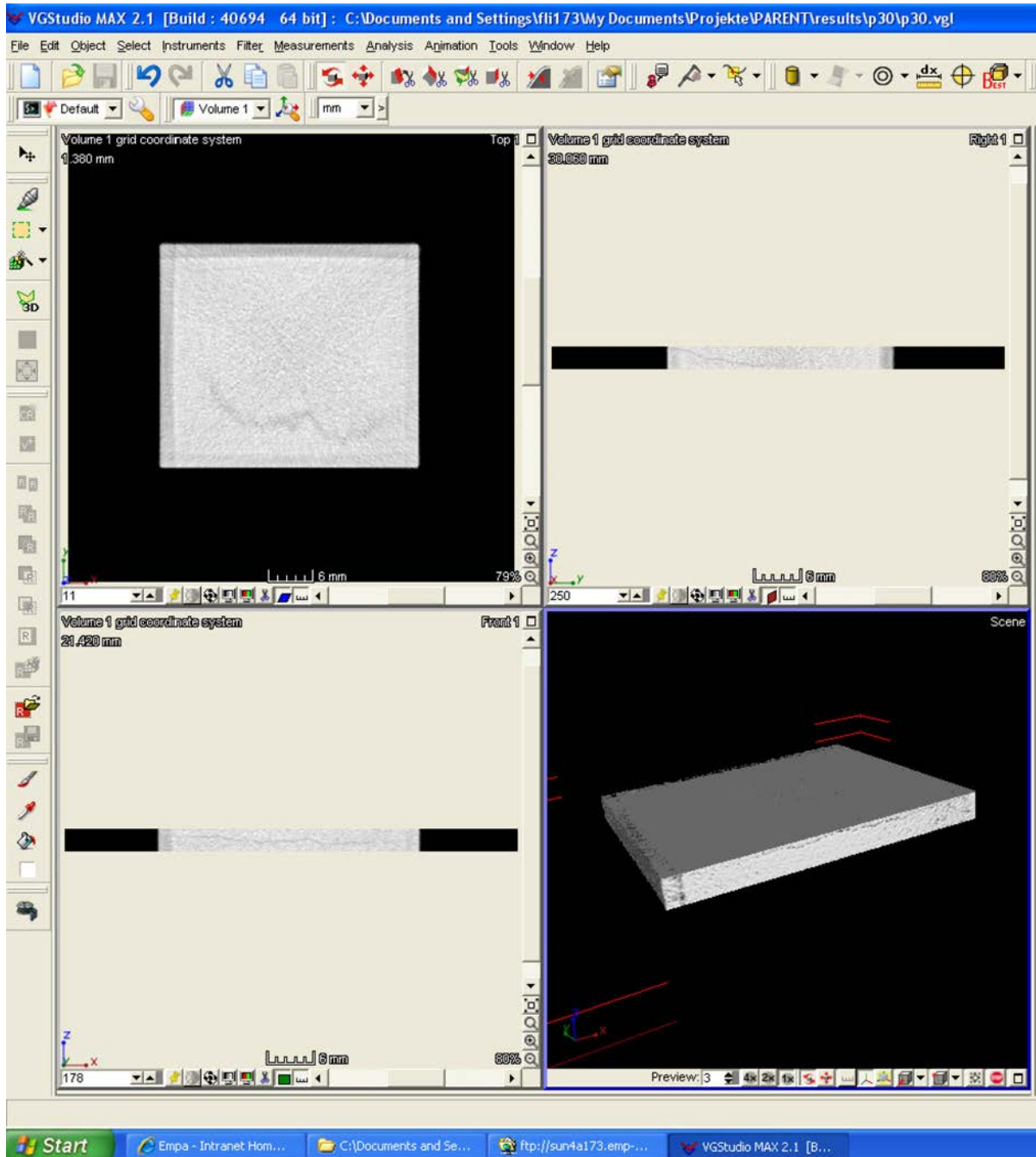


Figure C.147c Visualization of 3D-CT volume of test block P30 with VGStudioMax



## Test Block ID P31 (MN 220 AD U 1)

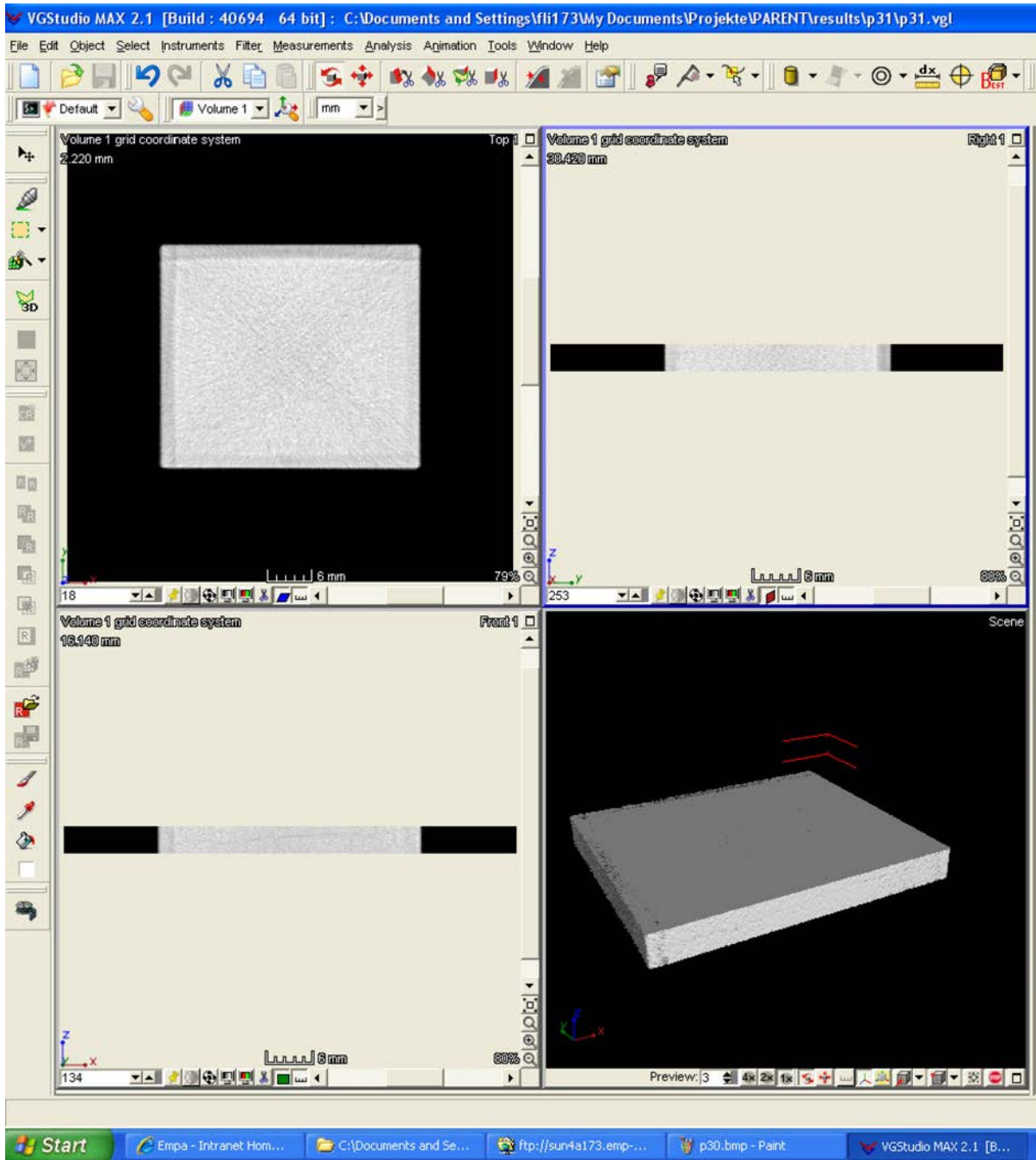


Figure C.147d Visualization of 3D-CT volume of test block P31 with VGStudioMax

## Test Block ID P32 (N 220 AD U TS 5)

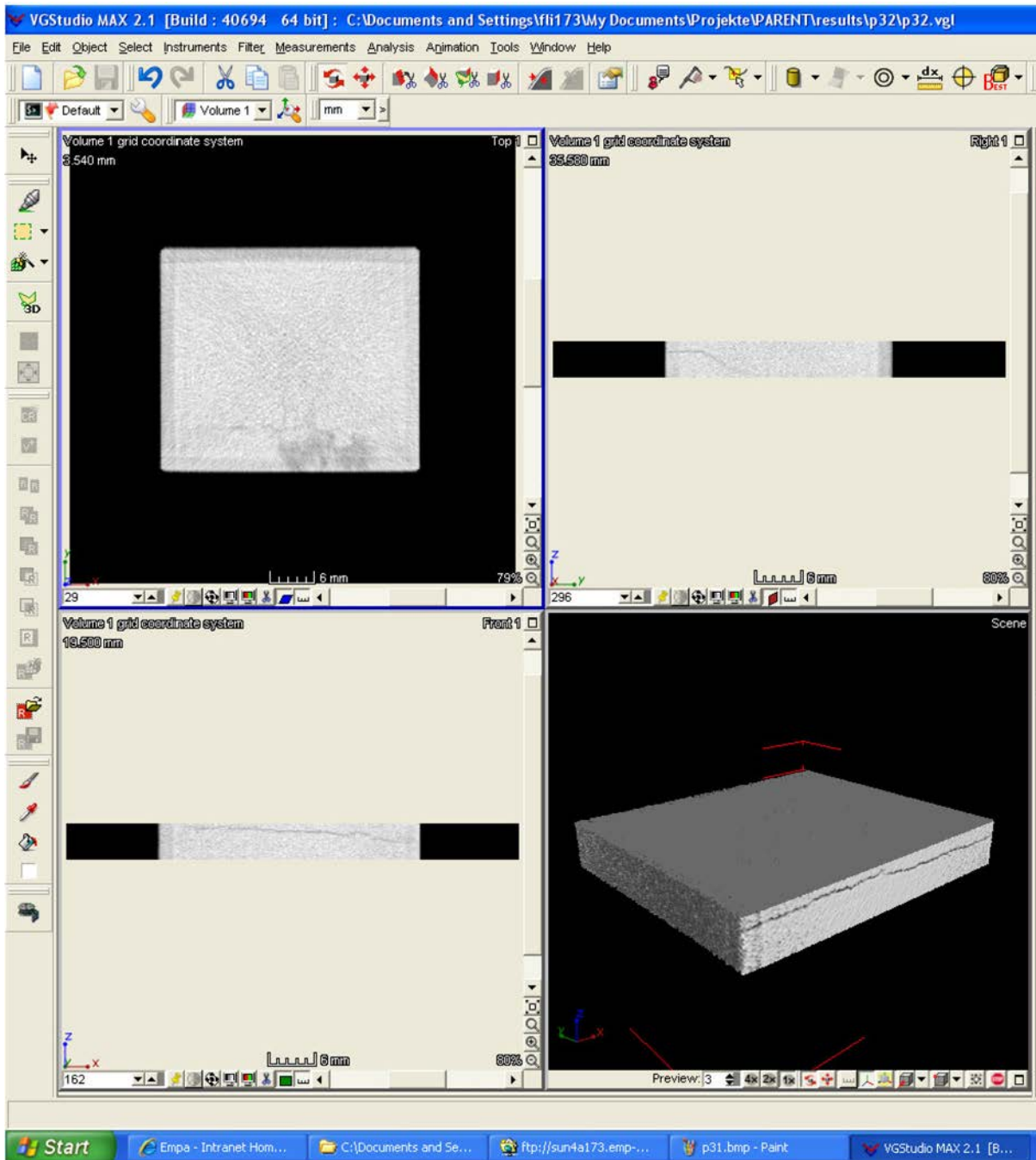


Figure C.147e Visualization of 3D-CT volume of test block P32 with VGStudioMax

### Test Block ID P38 (N 220 AD U TS 3)

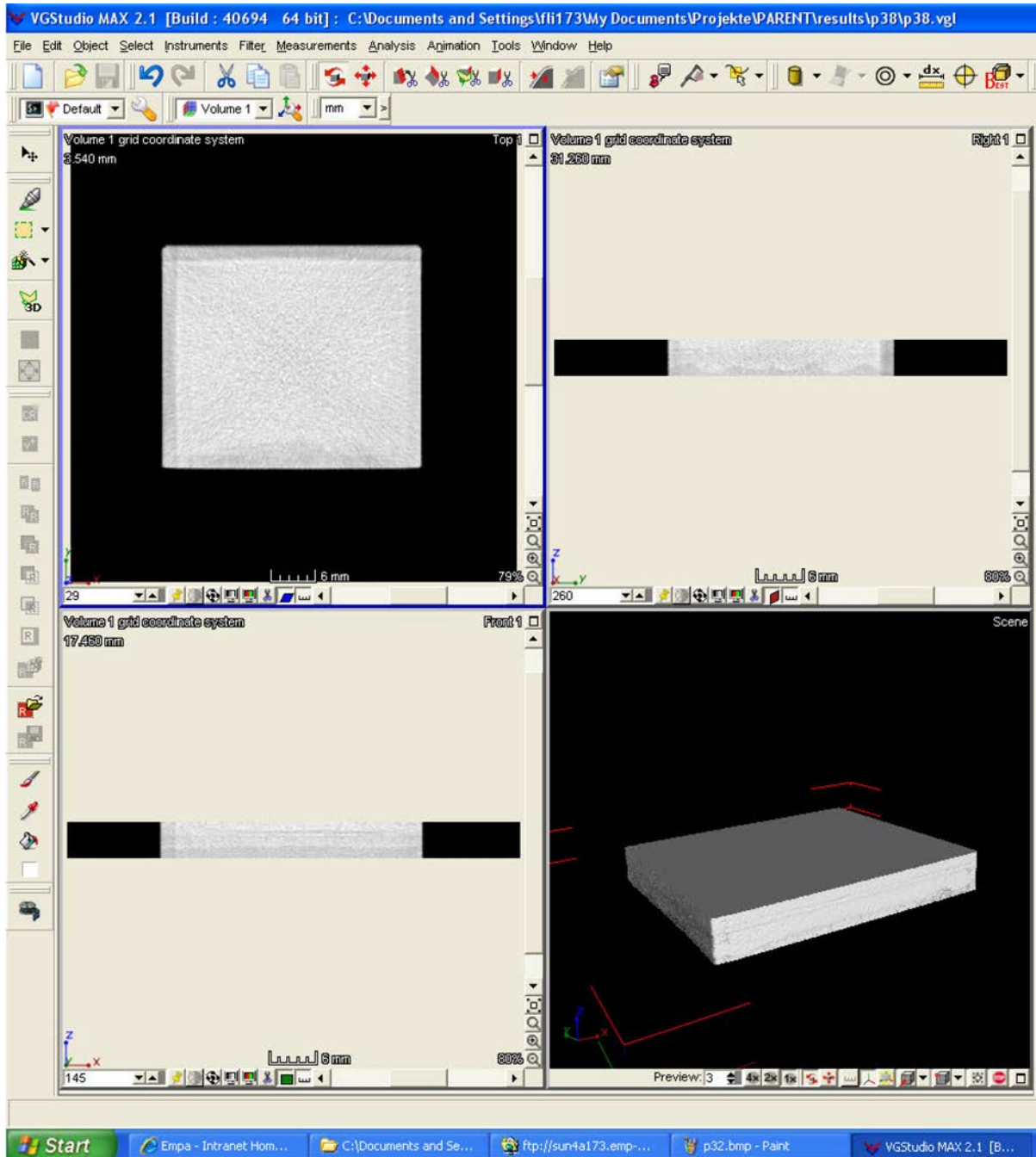


Figure C.147f Visualization of 3D-CT volume of test block P38 with VGStudioMax

## C.2.8 High Resolution X-ray, Technique ID 112-HRT0

### C.2.8.1 Introduction

This report describes an x-ray technique that has been developed for detection and characterization of service induced defects, e.g., intergranular stress corrosion cracking (IGSCC). The x-ray source is a 450 kV x-ray machine and the detector is CCD-based with fiber optic lens and glass fiber optic scintillation screen. The objects are positioned and rotated by a rotation unit which is stepper motor driven.

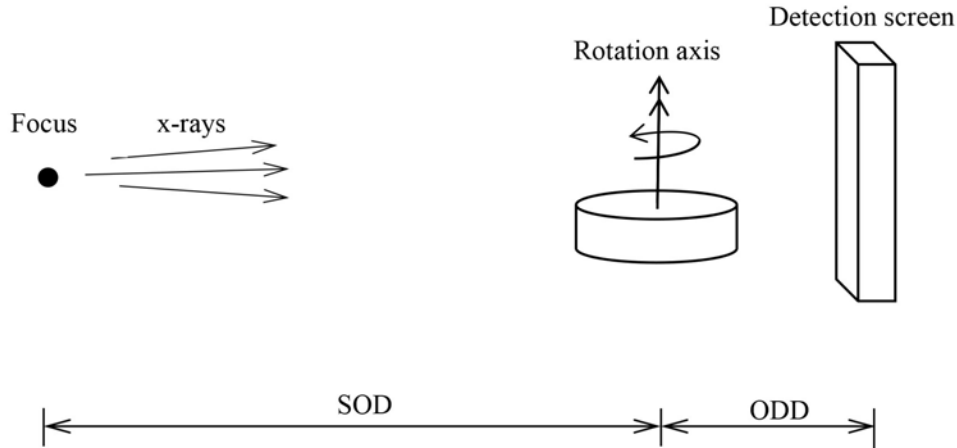


Figure C.148 Set Up

### C.2.8.2 X-ray Machine

The X-ray machine is a GE Titan 450 kV constant potential with ISOVOLT 450 M2/0.4-1.0HP tube. This is a high power tube with a small focus,  $f$ , of only 0,4 mm (25 % modulation).

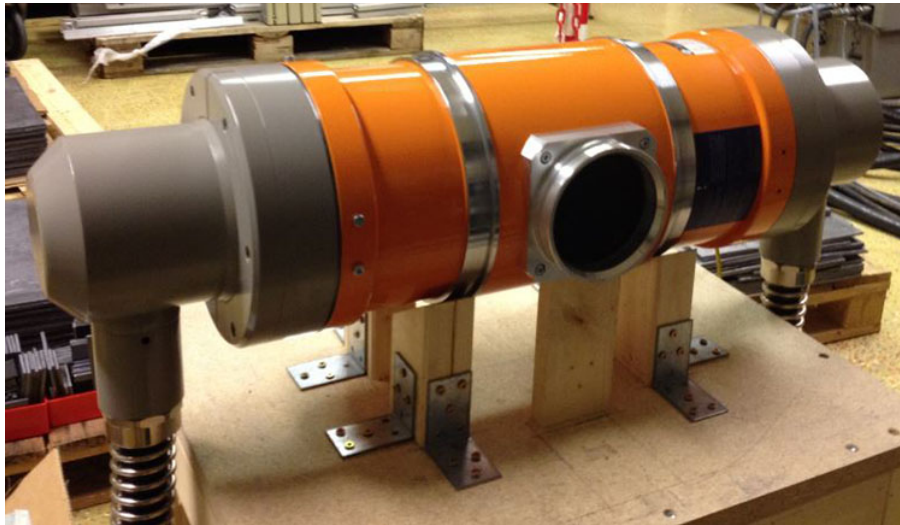


Figure C.149 X-ray Tube

The source to object distance (SOD) has been 650 mm and object to detector distance (ODD) was 50 mm. In this case the crack opening is defined as the object. The geometrical unsharpness is less than 0,04 mm.

$$U_g = \frac{f \cdot ODD}{SOD} \quad [\text{mm}] \quad (\text{C.1})$$

### C.2.8.3 Digital Detector

The x-ray camera is an imaging detector with a scintillating screen of glass fiber optics. It is a new design of a proven concept where the design issue was to minimize the amount radiation induced noise. This was done by bending the fiber optic lens (image conduit) which moved CCD-chip out of the primary beam. The spatial resolution is increased by using a new type of scintillating face plate. The new scintillating faceplate has unique properties which have eliminated the internal light spread and increased the spatial resolution.

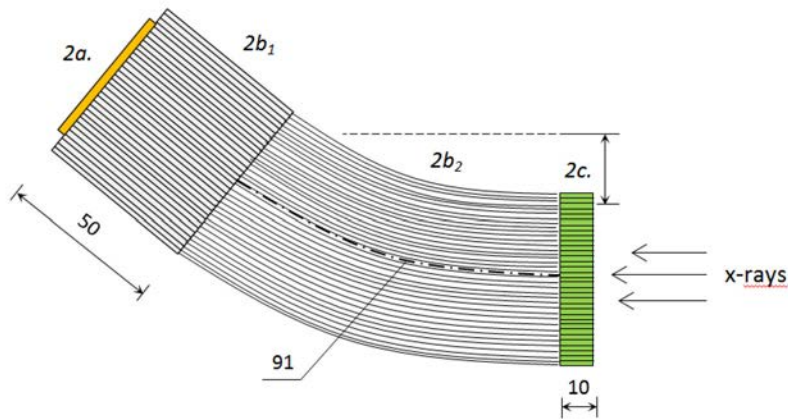


**Figure C.150 Fiber Optic Lenses and Scintillating Faceplate**

The new detector is based on a front illuminated full frame CCD camera (EEV CCD42-40) (2K x 2K) with pixel size of 13,5x13,5  $\mu\text{m}$ . It is Peltier cold down to  $-30^\circ\text{C}$  and is equipped with fiber optic input window. The input window is a fiber optic lens with fiber diameter of 4,5  $\mu\text{m}$  with a length of 50 mm (see Figure C.150). In the front of the camera, the bended fiber optic lens with the scintillating screen is mounted.

The imaging area is only 27 x 27 mm (see Figure C.151) but the spatial resolution is very high. The detector unsharpness is measured to be less than 0,08 mm. Better than 50% modulation of the 13:th wire pair with the EN462-5 double wire IQI.



**Figure C.151 The X-ray Detector with a Cu-filter in Front**

#### **C.2.8.4 Exposure Data**

For the test blocks P28-P30 the following data was applied:

- U= 300 kV; I= 2,25 mA; 30 mm Inconel
- Exposure time: 8 x 60 s (18 mAmin)

For the test block P41 is following data used:

- U= 450 kV; I= 1,5 mA, 64 mm Inconel
- Exposure time: 8 x 120 s (24 mAmin)

The reason to use such a long exposure time is that it corresponds to an optical density between 3,0-3,5 with Agfa D5 industrial x-ray film. We are using the cooled CCD to be able to integrate for long exposure times. In other word we have similar exposure time as film but much better image quality.

#### **C.2.8.5 Test Procedure**

The object coordinate system is placed so the crack opening is coincident to the axis of rotation in the object manipulator. The defects in test block P41 are orientated in two directions, axial and circumferential and P41 test block is thus in two different positions.

- The test block P28-P30 (square bars) is placed in such a way that its X-axis is parallel to the axis of rotation of the object manipulator in the coordinates Y=0 and Z=30,3 [mm] (see Figure C.152).
- In the position for testing axial defects in test block P41, the Y-axis of the test object coincident to the axis of rotation of the object manipulator in coordinate Z=0 [mm] and the polar coordinate X [degrees]of the defect (see Figure C.153).
- In the position for testing circumferential defects the tangent of the defects polar X-coordinate coincident with the axis of rotation of the object manipulator. The Y-coordinate is the value for the actual defect and Z=0 [mm].

X-ray radiography is a volumetric method and to be able to detect cracks or parts of cracks the orientation has to be reasonably parallel with the x-ray beams. Therefore each defect is radiographed in series of projections. The projection angle is from  $-10^{\circ}$  to  $+10^{\circ}$ , with increments of  $2^{\circ}$ .

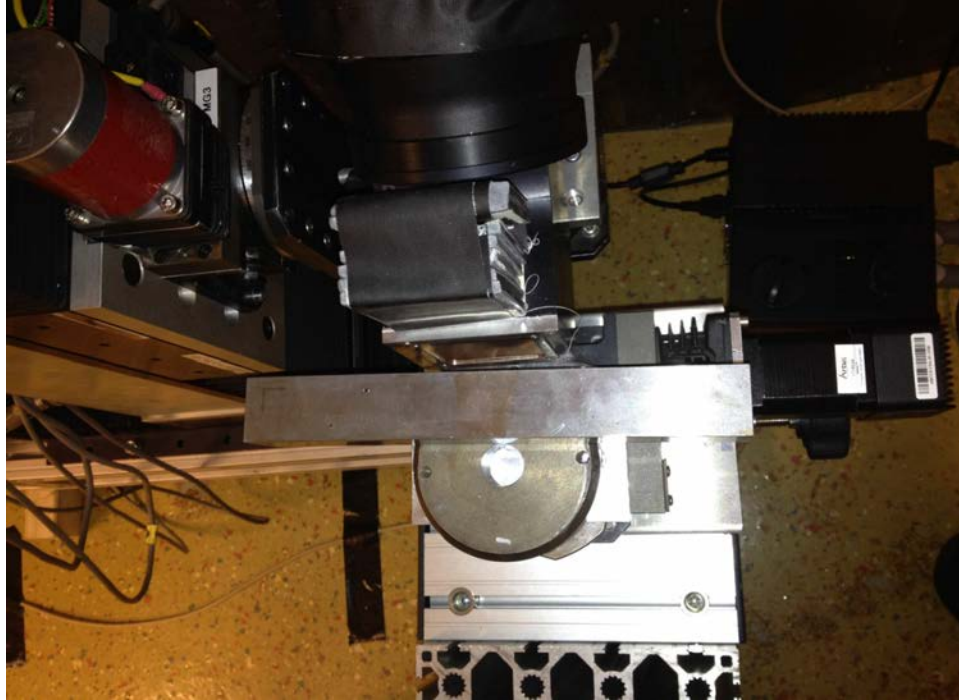


**Figure C.152 Test Block P28-P30**

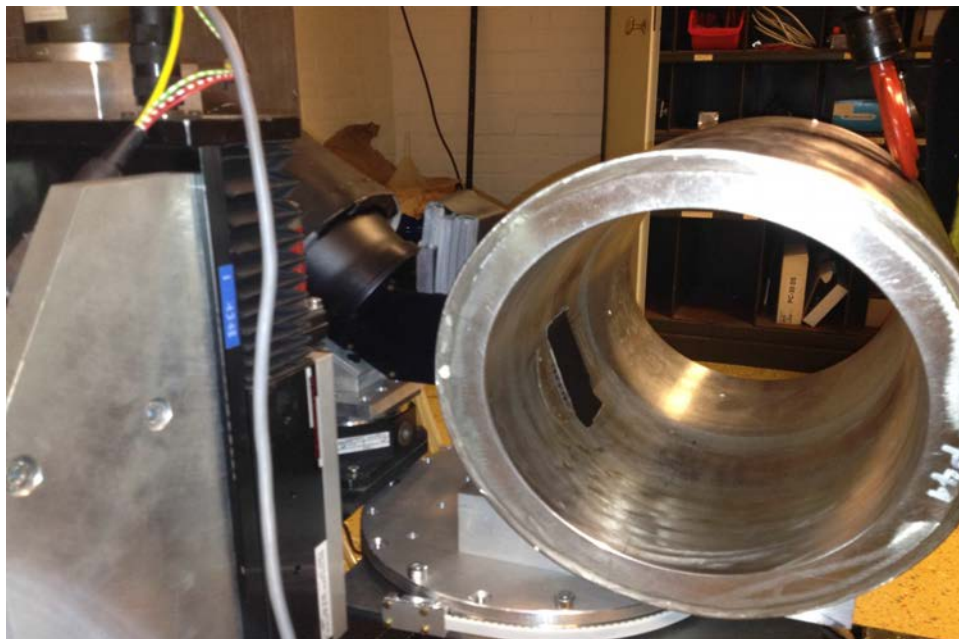


**Figure C.153 Test Block P41. Position for axial defects.**

### C.2.8.6 Image Processing

Each x-ray image is divided in eight exposures. They are then integrated to improve the signal-to-noise (SNR) ratio. As each image also can contain radiation induced noise they are compared statistically and the noise (white dots) are removed. Conventional background and flat field correction to remove the structural noise is done in the next step. Finally a “lifting”-operation is done by multiplying the corrected raw image with an interpolated surface based on curve fitting in the perpendicular direction of the cracks. The Fourier-series of third grade is used as function for curve fitting as it can adapt nearly any shape in a “smooth” way.

The images are presented in an animation (link below each image). By using animations the crack can be seen clearly and it is easy to characterize them.

### C.2.8.7 Size

To determine the size or the depth (z-coordinate) an expression (see Figure C.154) is developed which describes the depth,  $d$ , as function of the movement of the observed crack tip between the end positions in the series of exposures.

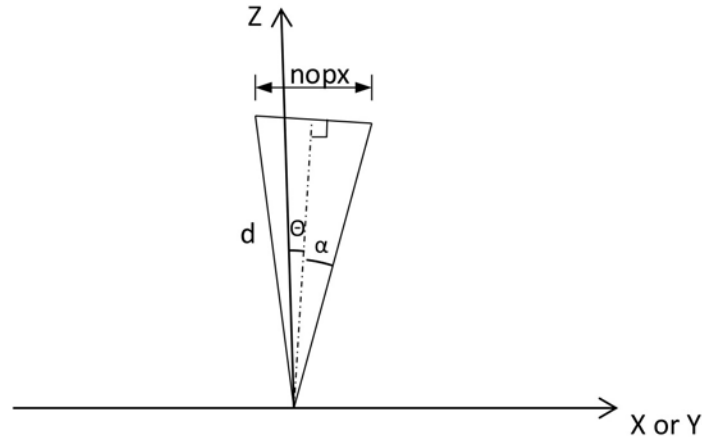


**Figure C.154 Crack Depth Calculation**

Where  $\Theta$ , is the projection angle of the crack tip in the center position of the projection series. The angle,  $\alpha$ , is half the angle between the end positions. The distance,  $nopx$ , is measured between the end positions of the crack tip. The pixel size is  $pxsize=0,0135$  [mm]. The geometrical enlargements is  $M=1,045$ . And finally,  $d$ , is the depth of the defect ( $Z_{max}$ -coordinate).

$$d = \frac{nopx \cdot pxsize}{2 \cdot M \cdot \cos \theta \cdot \tan \alpha} \quad [\text{mm}] \quad (\text{C.2})$$

The measured width ( $nopx$ ) can be seen in Figure C.155.



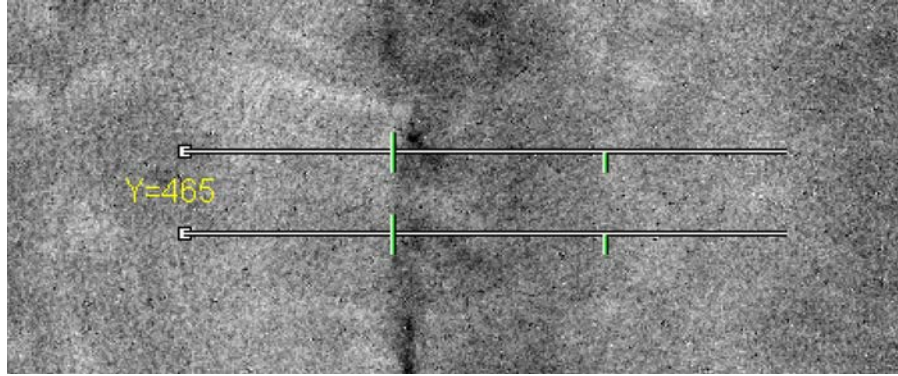


**Figure C.155 Measurement of the Distance, nopx**

Sizing of each defect is presented in a table with:

- X X-coordinate of the defect [mm or degrees].
- $X_1, X_2$  Coordinates of the line profile.
- nopx No. of pixels (projected width).
- $Z_{\max}^{(1)}$  Maximum Z-coordinate (=d, maximum depth of the defect).
- Length Real length in the image plane.

All images are of same size,  $26,45 \times 26,45 \text{ mm}^2$ , which is the real size in the image plane. The size in the detector plane is compensated by the geometrical enlargement, M.

---

(<sup>1</sup>) The  $Z_{\max}$  is systematically under estimated in the case of “real” defects such as SCC and fatigue in P28-P30. This is because the volume in the crack close to the crack tip goes to zero. Experience from earlier work with SCC gave an under estimation of about 1–2 mm.

In the test block P41 where the defects are artificially produced the  $Z_{\max}$  estimation is more correct.

## U6 (SCC)

$\alpha=10^\circ$  and  $\Theta=8^\circ$ ; From  $-10^\circ$  to  $+10^\circ$ ;  $2^\circ/\text{pos}$ ; 11 positions

X [mm]	X <sub>1</sub>	X <sub>2</sub>	nopx	Z <sub>max</sub> [mm]
27,8	85	341	256	9,5
22,7	71	323	252	9,3
17,5	93	329	236	8,7
12,3	93	381	288	10,6
7,2	97	358	261	9,7

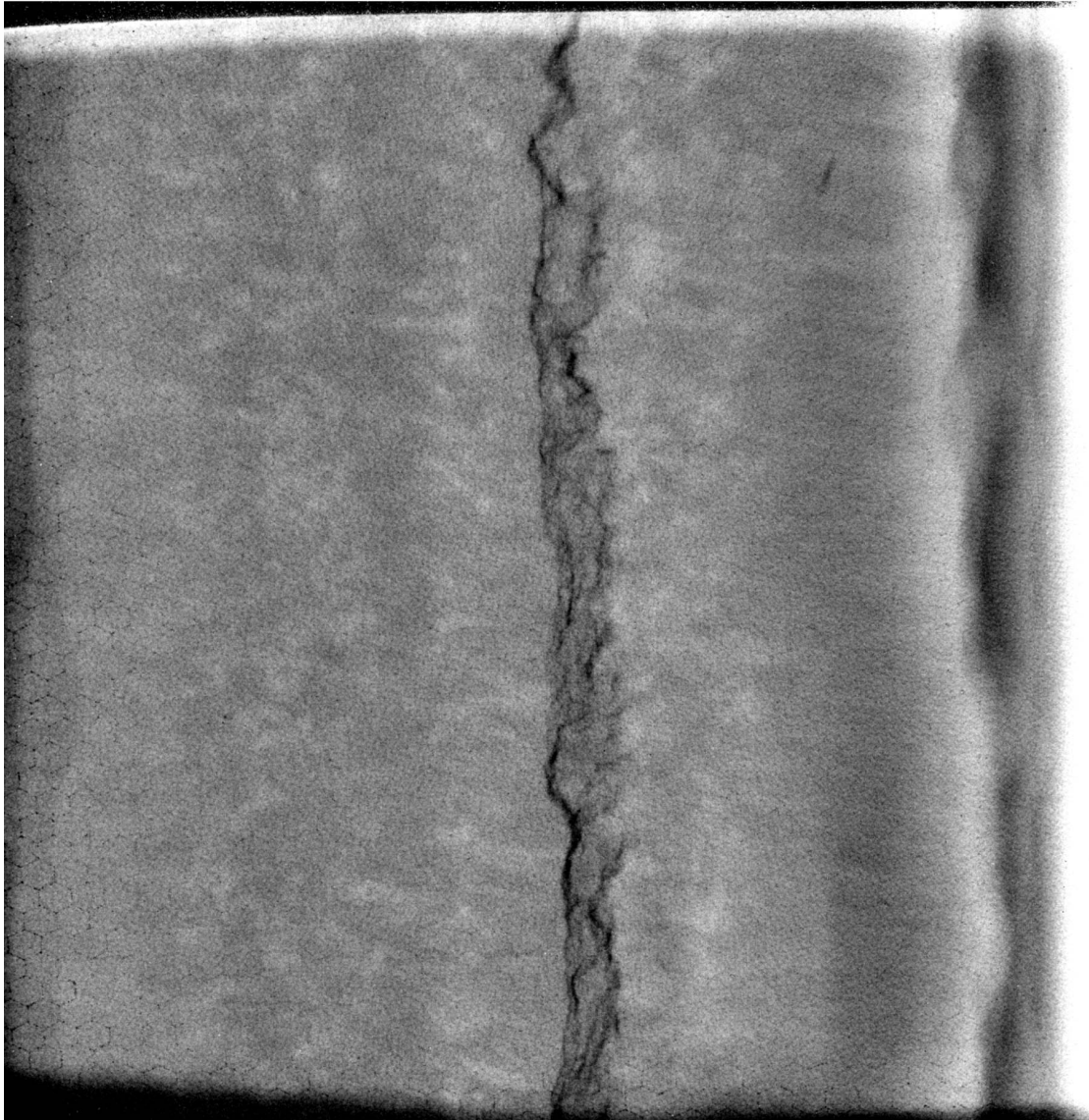


Figure C.156 U6, 6th position (Image size 26,45 x26,45 mm<sup>2</sup>)



P28 MN 220 AD U6 spline 8 bit 512 inv.avi

## U7 (Fatigue)

$\alpha=6^\circ$  and  $\Theta=5^\circ$ ; From  $+1^\circ$  to  $-11^\circ$ ;  $1^\circ/\text{pos}$ ; 13 positions

X [mm]	X <sub>1</sub>	X <sub>2</sub>	nopx	Z <sub>max</sub> [mm]
27,8	82	289	207	12,8
22,7	94	366	272	16,8
17,5	60	295	235	14,5
12,3	94	311	217	13,4
7,2	96	271	175	10,8

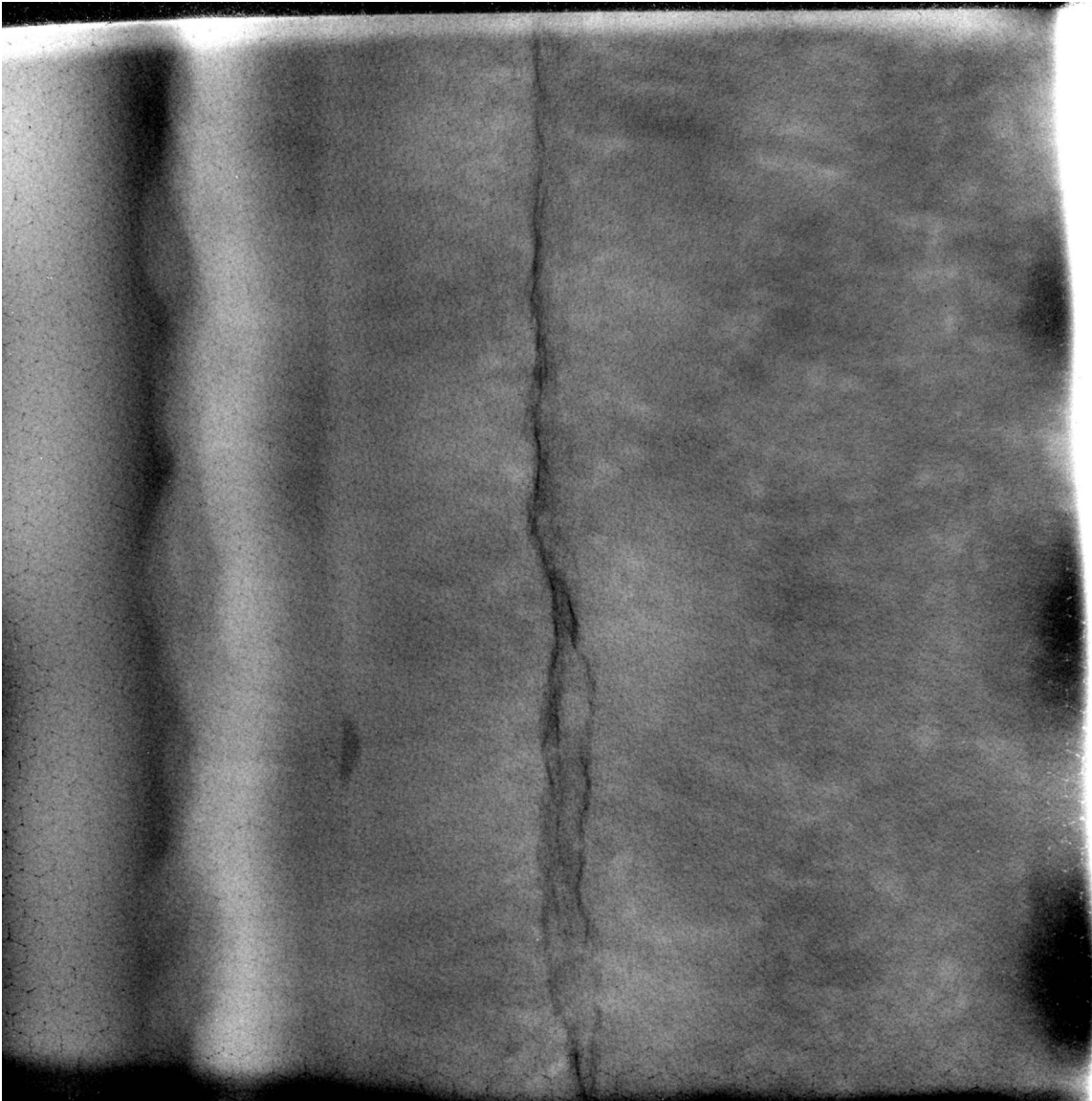


Figure C.157 U7, 7th position (Image size 26,45 x26,45 mm<sup>2</sup>)



P30 MN 220 AD U7 spline 8 bit 512 inv.avi

## U10 (SCC)

$\alpha=10^\circ$  and  $\Theta=6^\circ$ ; From  $-10^\circ$  to  $+10^\circ$ ;  $2^\circ/\text{pos}$ ; 11 positions

X [mm]	X <sub>1</sub>	X <sub>2</sub>	nopx	Z <sub>max</sub> [mm]
27,8	90	260	170	6,2
22,7	81	309	228	8,4
17,5	186	462	276	10,1
12,3	136	386	250	9,2
7,2	149	411	262	9,6

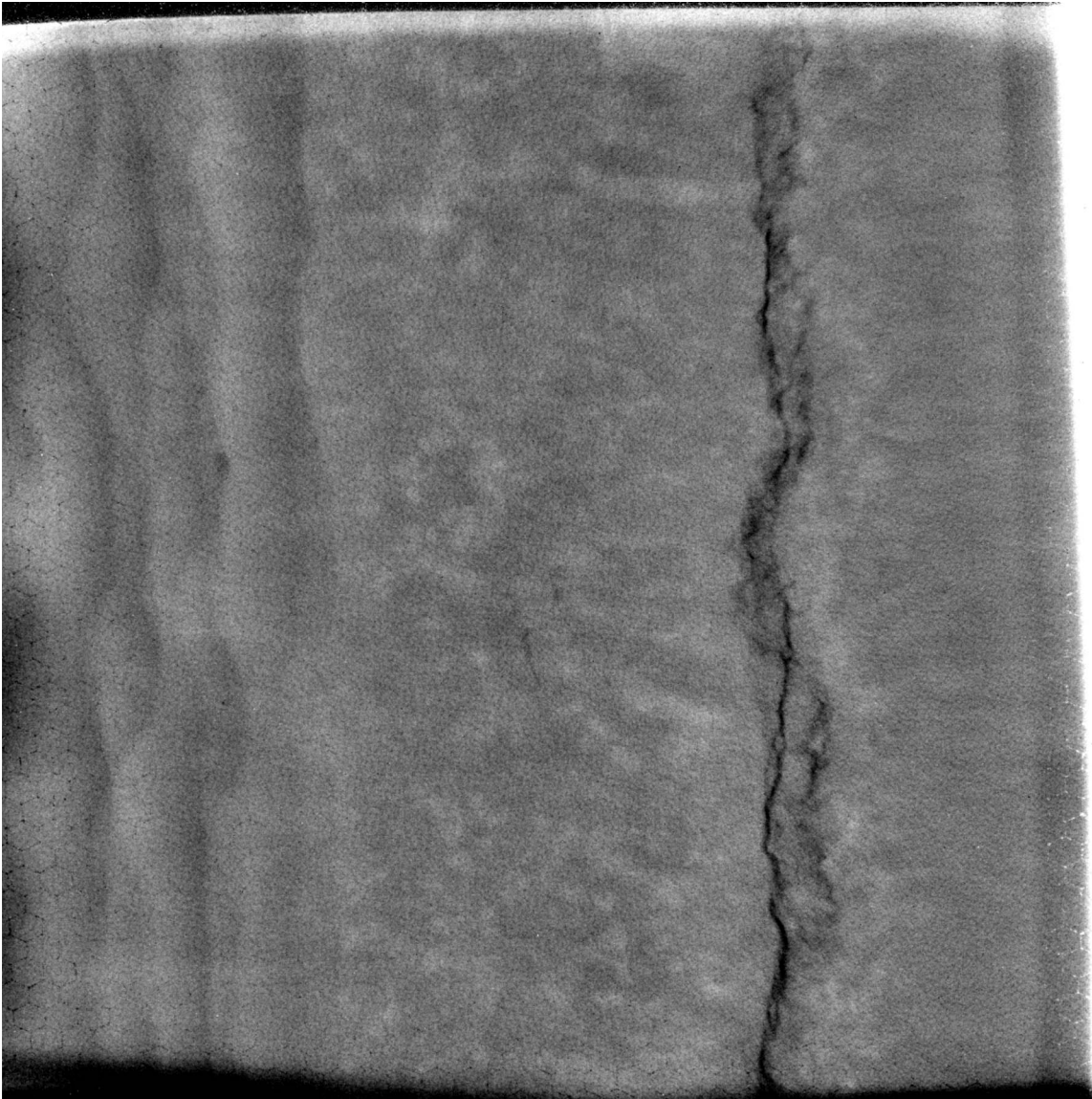


Figure C.158 U10, 6th position (Image size 26,45 x26,45 mm<sup>2</sup>)



P29 MN 220 AD U10 spline 8bit 512 inv.avi

**Defect nr1 (P41)**

$\alpha=8^\circ$  and  $\Theta=8^\circ$ ; From  $-8^\circ$  to  $+8^\circ$ ;  $2^\circ/\text{pos}$ ; 9 positions

X [mm]	X <sub>1</sub>	X <sub>2</sub>	nopx	Z <sub>max</sub> [mm]	Length [mm]
0	86	118	32	1,5	10,7

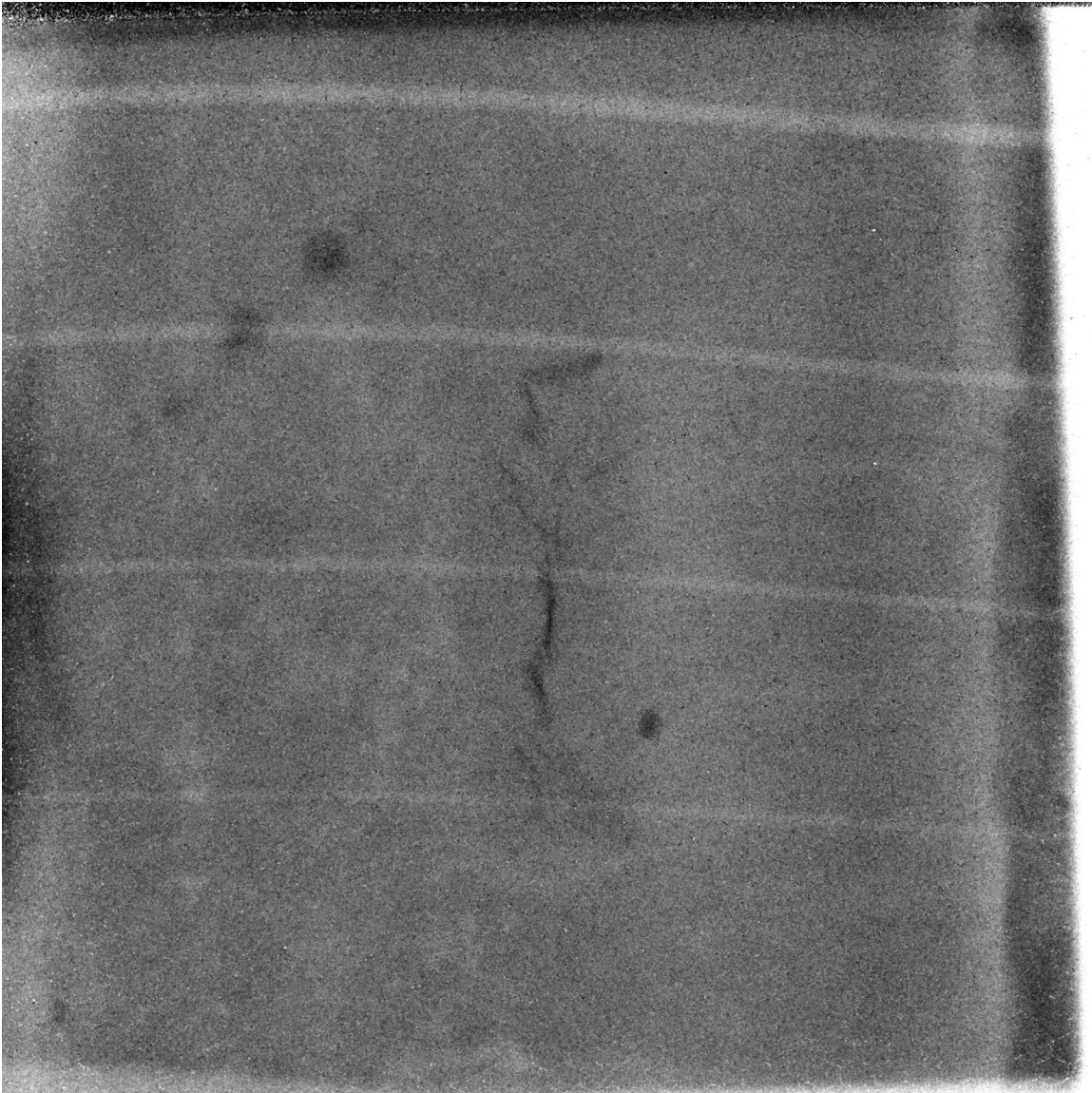


**Figure C.159 Defect nr1, (P41) 3rd position (Image size 26,45 x26,45 mm<sup>2</sup>)**



P41 nr1 0 deg spline 8 bit 512 inv.avi

**Defect nr2 (P41)**

$\alpha=8^\circ$  and  $\Theta=4^\circ$ ; From  $-8^\circ$  to  $+8^\circ$ ;  $2^\circ/\text{pos}$ ; 9 positions

X [mm]	X <sub>1</sub>	X <sub>2</sub>	nopx	Z <sub>max</sub> [mm]	Length [mm]
0	69	112	43	2,0	7,4

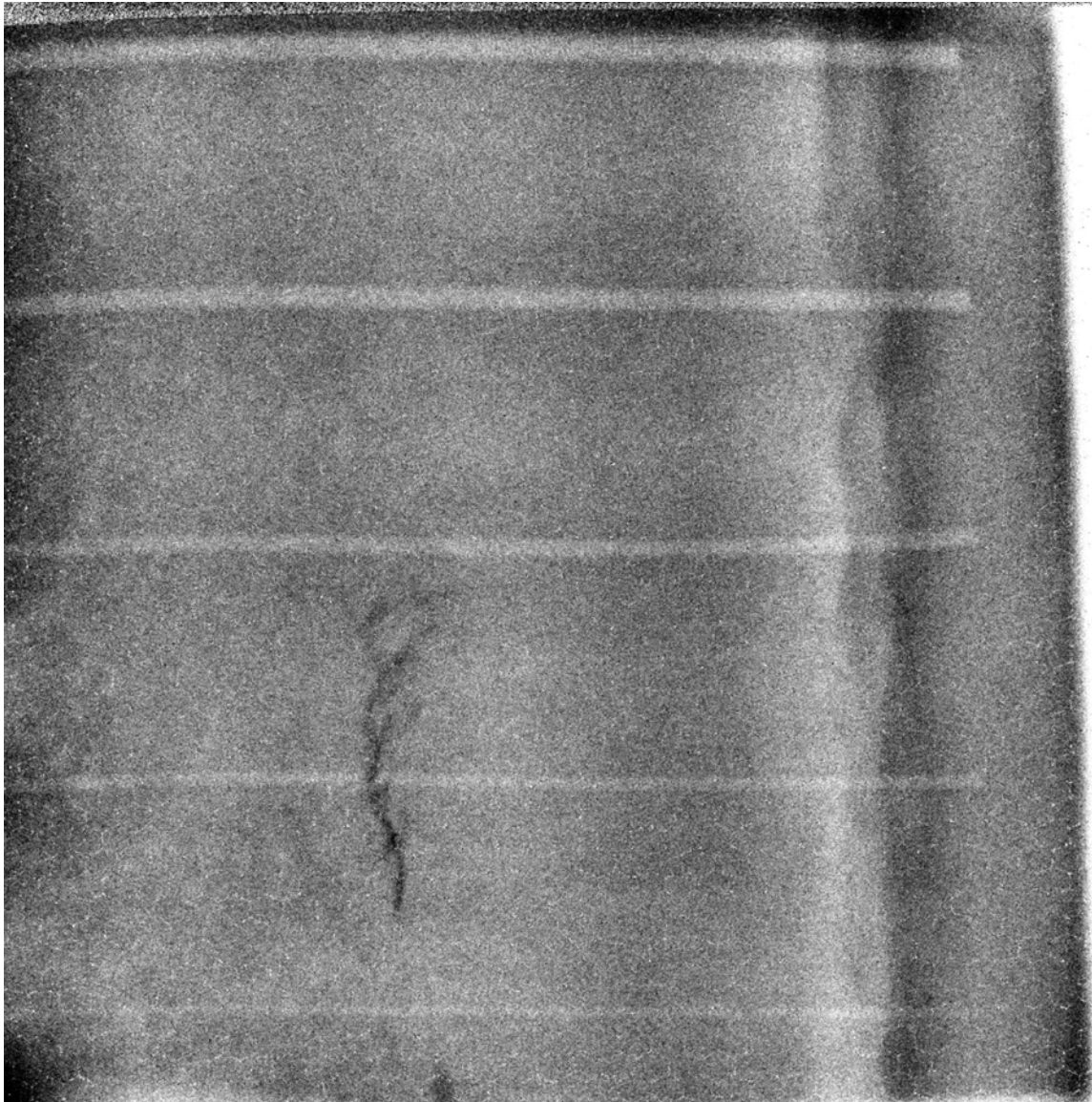


**Figure C.160 Defect nr2, (P41) 2nd position (Image size 26,45 x26,45 mm<sup>2</sup>)**



P41 nr2 28 deg spline 8 bit 512 inv.avi

**Defect nr3 (P41)**

$\alpha=8^\circ$  and  $\Theta=4^\circ$ ; From  $-8^\circ$  to  $+8^\circ$ ;  $2^\circ/\text{pos}$ ; 9 positions

X [mm]	X <sub>1</sub>	X <sub>2</sub>	nopx	Z <sub>max</sub> [mm]	Length [mm]
0	73	116	43	2,0	11,4

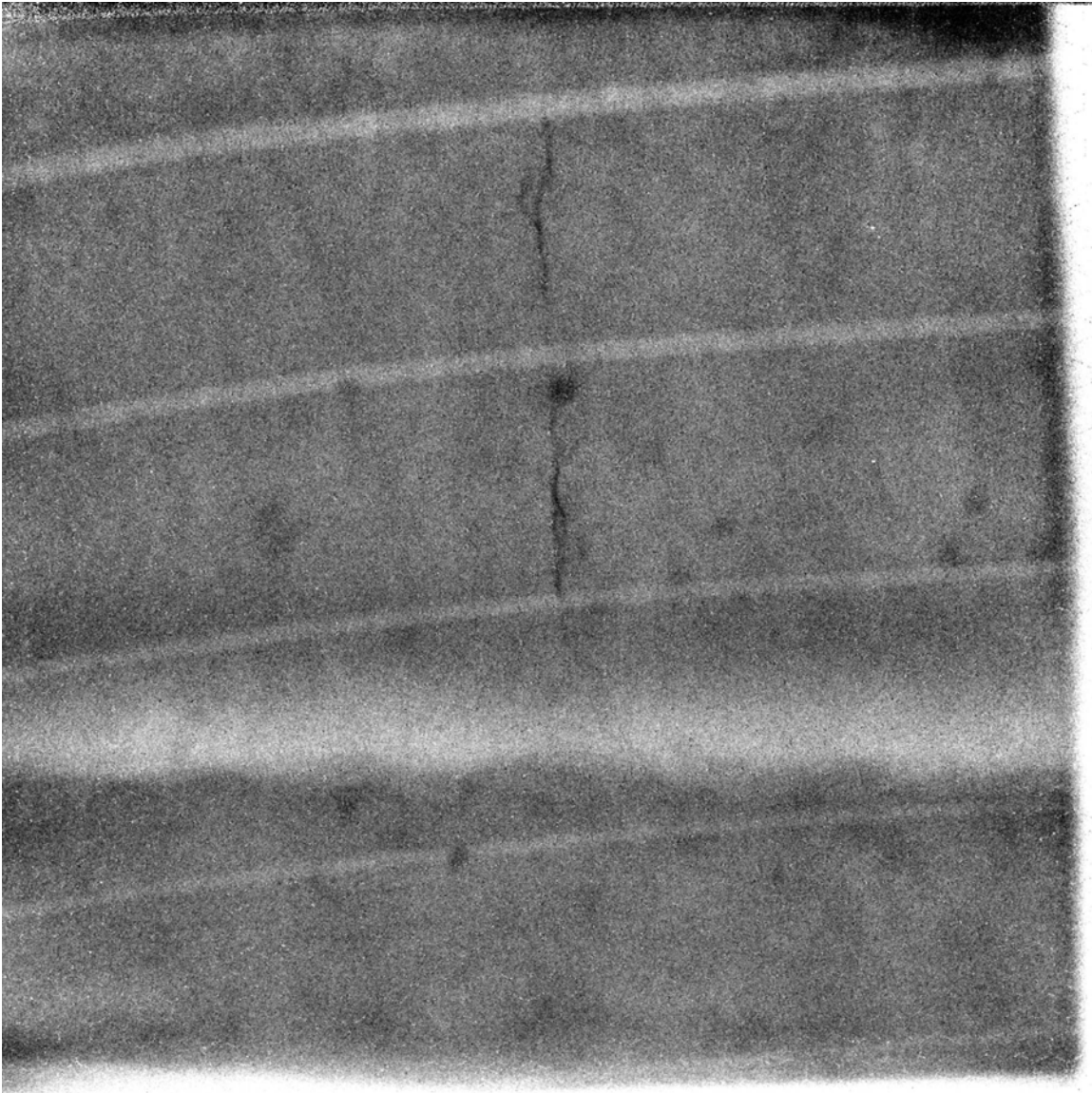


**Figure C.161 Defect nr3, (P41) 6th position (Image size 26,45 x26,45 mm<sup>2</sup>)**



P41 nr3 54 deg spline 8 bit 512 inv.avi

**Defect nr4 (P41)**

$\alpha=8^\circ$  and  $\Theta=4^\circ$ ; From  $-8^\circ$  to  $+8^\circ$ ;  $2^\circ/\text{pos}$ ; 9 positions

X [mm]	X <sub>1</sub>	X <sub>2</sub>	nopx	Z <sub>max</sub> [mm]	Length [mm]
0	97	124	27	1,5*	7,2

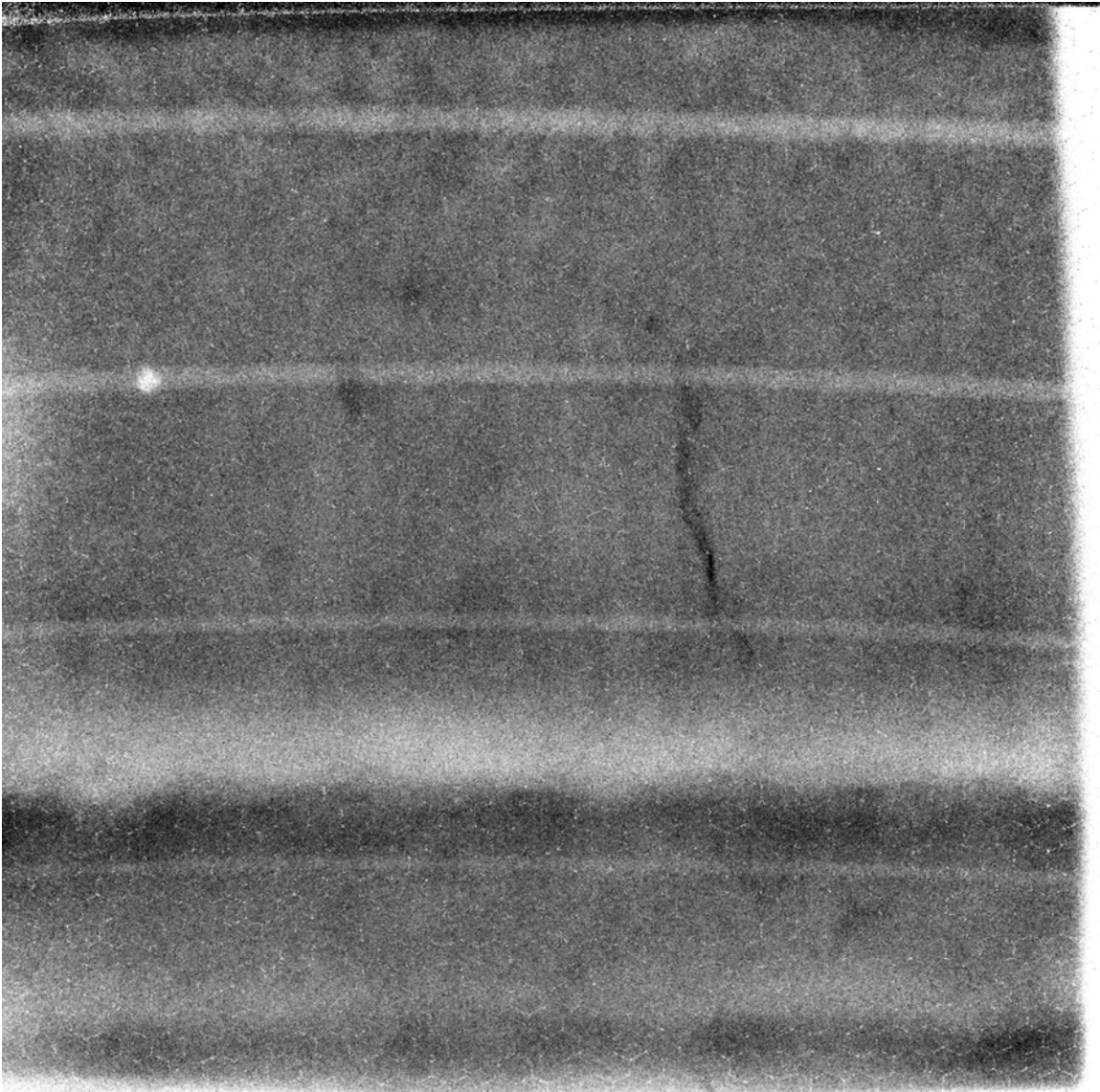


**Figure C.162 Defect nr4, (P41) 2nd position (Image size 26,45 x26,45 mm<sup>2</sup>)**



P41 nr4 77 deg spline 8 bit 512 inv.avi



**Defect nr7 (P41)**

$\alpha=8^\circ$  and  $\Theta=8^\circ$ ; From  $-8^\circ$  to  $+8^\circ$ ;  $2^\circ/\text{pos}$ ; 9 positions

X [mm]	X <sub>1</sub>	X <sub>2</sub>	nopx	Z <sub>max</sub> [mm]	Length [mm]
0	34	237	237	11,0	22,6

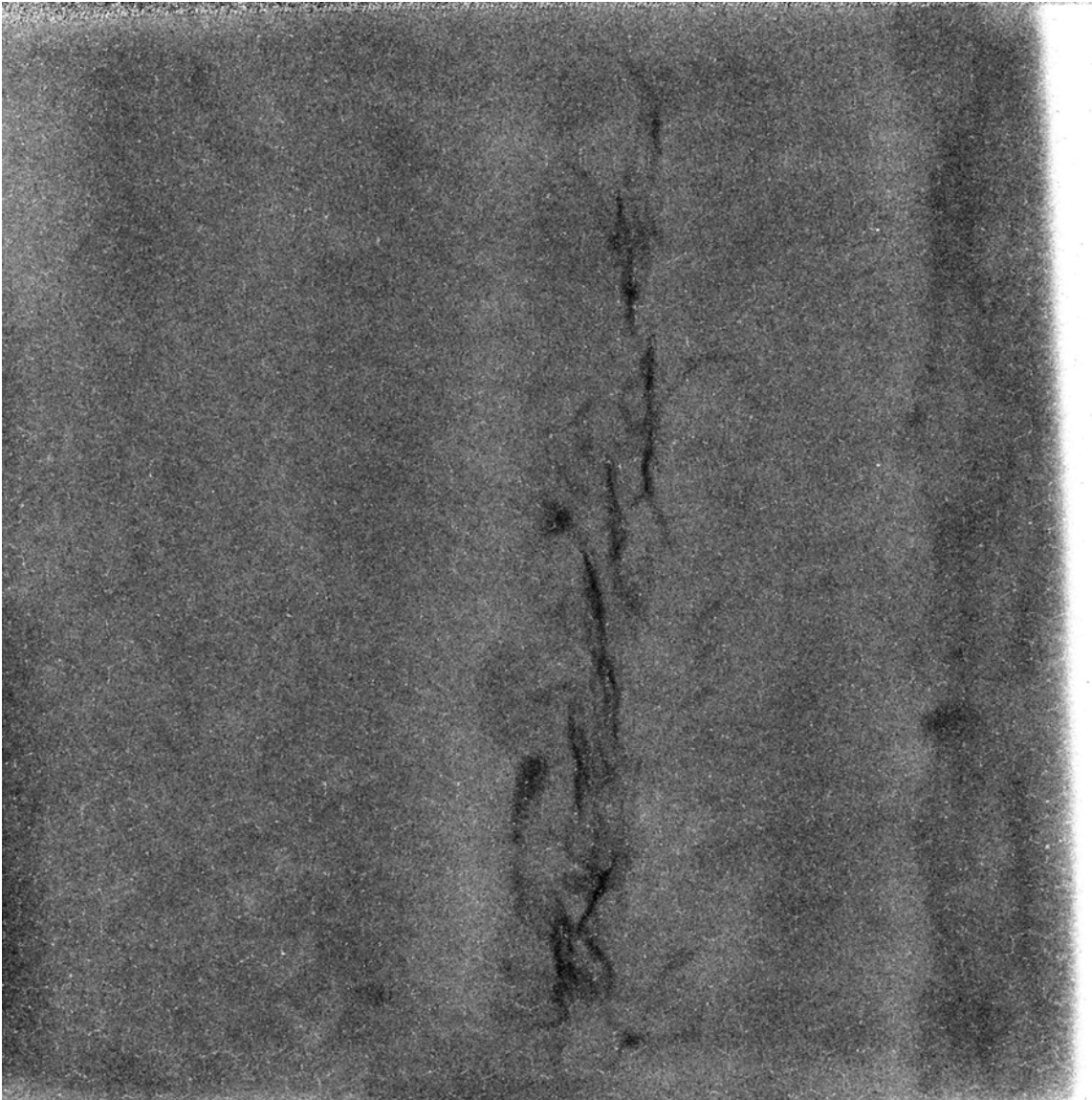


**Figure C.163 Defect nr7, (P41) 8th position (Image size 26,45 x26,45 mm<sup>2</sup>)**



P41 nr7 173 deg spline 8 bit 512 inv.avi

**Defect nr8 (P41)**

$\alpha=8^\circ$  and  $\Theta=2^\circ$ ; From  $-8^\circ$  to  $+8^\circ$ ;  $2^\circ/\text{pos}$ ; 9 positions

X [mm]	X <sub>1</sub>	X <sub>2</sub>	nopx	Z <sub>max</sub> [mm]	Length [mm]
0	116	236	120	5,5	22,7

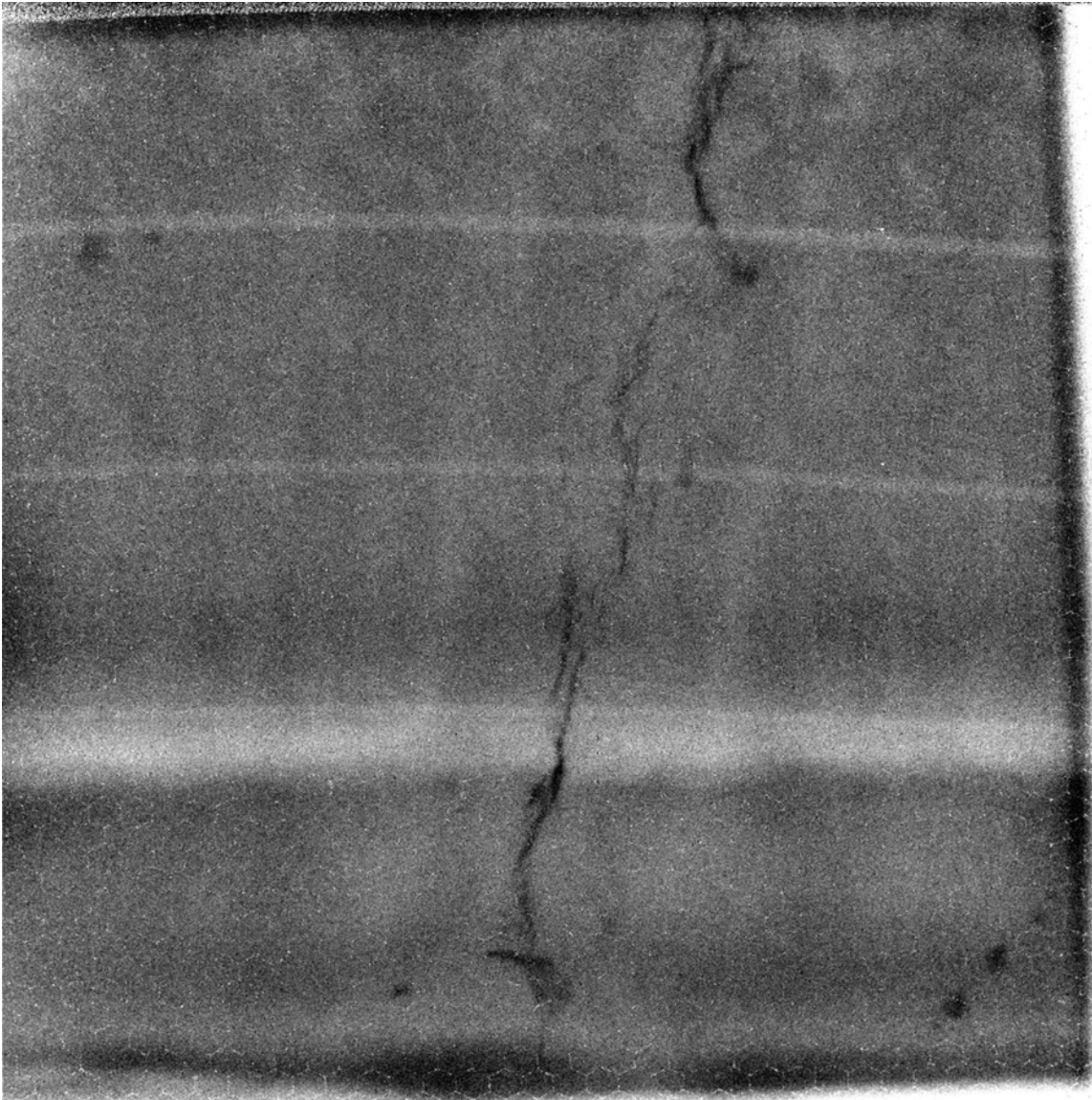


**Figure C.164 Defect nr8, (P41) 6th position (Image size 26,45 x26,45 mm<sup>2</sup>)**



P41 nr8 206 deg spline 8 bit 512 inv.avi

## **C.3 Korea Detailed Technique Descriptions**

### **C.3.1 Nonlinear Resonant Ultrasound Spectroscopy, Technique ID 11-NRUT0**

#### **C.3.1.1 Overview**

##### **Principles of Nonlinear Resonant Ultrasound Spectroscopy**

The studies on nonlinear acoustic effects have focused on identifying structural material characteristics and damage features. Different nonlinear effects include second harmonic generation, modulation of sound by low-frequency vibrations, amplitude-dependent internal friction, and amplitude-dependent resonance frequency shifts. The first applications of the nonlinear acoustic technique for material characterization used measurements of the second harmonic generated by the nonlinear distortion of a primarily sinusoidal acoustic wave propagating in a medium with defects. Later it was realized that harmonic generation analysis is not the only, and not always the best way to implement the effective nonlinear acoustic NDE. Other nonlinear techniques include the cross-modulation (frequency mixing) of low and high-frequency sound and studies of the amplitude dependence of the mode resonance peak in a specimen conducted at Los Alamos National Laboratory. All these techniques are based on nonlinear wave interactions and nonlinear resonances. Due to the use of resonant modes, these methods need much less acoustic power than the travelling-wave methods used before. In particular, acoustic effects due to material hysteresis what is often associated with the crack presence have been observed in these experiments. It was also found that the nonlinear methods turn out to be more sensitive to damage-related structural alterations than any known method based on the measurements of linear parameters such as wave speed and attenuation. It was also confirmed that the macroscopic nonlinear response of a material is largely determined by its microstructure, which is understood as structural inhomogeneities with the scales small as compared to the sample sizes and the acoustic wavelength.

##### **Nonlinear Resonance Frequency Shift**

Resonance frequency shift, together with wave damping in resonance, is analysed as a function of the peak acceleration amplitude. A detailed discussion of the corresponding experimental apparatus can be found in papers published by the Nonlinear Elasticity group of Los Alamos National Laboratory in collaboration with several European laboratories and universities. One example is an experiment with a thin, rectangular beam (400mm × 26mm × 4mm) made of fibre-cemented artificial slate used in roofing constructions. The synthetic fibres (4 mm thick) used in the production process have a principal orientation perpendicular to the length-wise direction of the beam. The beam is excited at its lowest-order flexural (bending) resonance mode by a low-distortion speaker, positioned at 2 cm from the beam middle, parallel to its surface. The sample is suspended with nylon wires at the nodal points of the considered mode. The coupling medium between the specimen and the speaker is air (non-contact excitation). The speaker is driven in discrete frequency steps by a function generator through a high-power amplifier. In order to take the amplitude-frequency response near resonance, 4 to 10 sweeps over the same frequency interval, encompassing the first flexural mode resonance, were made at successively increasing voltages.

##### **Materials Characterization Using Nonlinear Acoustic Parameters**

To characterize the properties of the media, the conventional acoustic NDT technique utilizes linear acoustic parameters, such as sound speed and attenuation coefficient. Similarly, the non-

linear technique employs the non-linear parameter (parameters) for the material characterization. The classical approach to describe the nonlinearity of a homogeneous elastic media is based on Taylor expansion of the dependence between the stress and strain tensors in the material and considers the coefficients of this expansion as the parameters of nonlinearity. In a simple example of one-dimensional longitudinal deformations in an isotropic solid, this expansion can be taken in a scalar form:

$$\sigma = \rho_0 c_1^2 (\varepsilon + \beta \varepsilon^2 + \gamma \varepsilon^3 + \dots), \quad (\text{C.3})$$

where  $\rho_0$  and  $c_1$  are the density and the longitudinal sound speed in the medium, respectively,  $\sigma$  is the stress,  $\varepsilon$  is the strain,  $\beta$ ,  $\gamma$ , ... are the non-linear parameters, which characterize, respectively, the quadratic and cubic non-linearity of the medium.

Typical values of the non-linear parameter  $\beta$  do not exceed 10 for homogeneous media without defects (where nonlinearity is due to the inter-atomic forces acting in the crystal lattice), so that the contribution of the non-linear quadratic term into the relationship (1) is very small for practically all non-destructive strains, and the medium exhibits a linear behavior. The same is even more applicable for the cubic term with the coefficient  $\gamma$ . However, the presence of structural inhomogeneities such as grains, pores, cracks, and other defects is able to increase the nonlinear response of a material by orders of magnitude. This is true for a large variety of natural and constructive material such as rock and many metals.

The practical importance of using the parameters of acoustic nonlinearity as a possible tool for non-destructive testing, including that of the material defects caused by fatigue or external damage has been fully recognized during the last decade. Still, the crucial steps to transition the use of nonlinear acoustic techniques from the laboratory to practical applications is yet to be accomplished. Indeed, the nonlinear properties of many materials are more complicated than described by simple models. An important aspect of "structural nonlinearity" is that stress-strain dependence is hysteretic. In other words, the material behaves differently at the compression and dilatation phases of the loading cycle. This feature, known before in strong static loading, is now known to be present in very low dynamic strains, in the order of  $10^{-7}$ – $10^{-8}$ . The corresponding stress-strain dependence has a singularity and in a simplest case, it reads

$$\sigma = \rho_0 c_1^2 \left[ \varepsilon \pm \eta (\varepsilon^2 - \varepsilon^2_0) \right], \quad (\text{C.4})$$

where  $\eta$  is the coefficient of hysteretic nonlinearity and the "+" and "-" signs are taken for stress increase and decrease phases, respectively. As a result, the observed nonlinear behavior is quite specific; for instance, the resonance frequency shift is proportional to the amplitude of the basic signal rather than to the square of it as could be expected from the "normal" behavior corresponding to the expansion (C.3). To obtain quantitative relationships between the state of the measured characteristics and the state of the material, a reliable theoretical basis must be created.

Recent research has demonstrated that nonlinear acoustic parameters of the material are closely related to the crack size distribution and elastic properties of the defects and, therefore, high acoustical nonlinearity due to cracks can be used for the damage assessment.

In summary;

- As the driving voltage increases, a shifting of resonance frequency is observed.
  - ✓ This resonance peak shifting indicates a nonlinearity of the specimen.
  - ✓ Resonance peak shift and peak width is related to Moduli E and Q-value of the materials.
- Normalized resonance pattern also reflects the nonlinearity.
  - ✓ If the resonance pattern is identical as the driving voltage increases, the specimen shows no nonlinearity (linear elastic response)
  - ✓ Otherwise (if the peak amplitude decreases as the driving voltage increases), the specimen reveals a nonlinear elasticity.

### **C.3.1.2 Equipment Apparatus and Setup the Transducer to the Specimen**

All active acoustic methods of NDE are based on radiation of the required acoustic signals, reception and signal processing. The different regimes of operations require different kinds of radiation signals and different types of processing. The NRUS is a fully digital system that radiates and processes any acoustic signal.

The Nonlinear Resonant Ultrasound Spectroscopy (NRUS) methods are based on excitation of sweep frequency signals in the tested material and measurements of the dependence of the recorded signal amplitude on frequency. In this regime the sweep frequency signal is formed within the PC and is transformed to the transmitter channel of the NRUS system. The developed NRUS software provides radiation of sweep frequency signal in defined frequency band and sweep time. The Amplitude Frequency Responses (AFR) between transmitting and receiving are recorded for various output voltages. The results are presented in the normalized form where the received signal is divided to the system output. In the linear case the measured Normalized Amplitude Frequency Response (NAFR) does not depend on the applied signal amplitude and difference in the Normalized Amplitude Frequency Responses shows the presence of the tested part nonlinearity (Resonance frequency shift and amplitude dependable losses).

Figure C.165 shows a photo for the measurement system of nonlinear resonant ultrasound spectroscopy (NRUS). An arbitrary waveform generator and high power amplifier supply a sinusoidal wave with swept frequency. The piezoelectric elements are bonded on a side of the specimen for generation of the ultrasonic waves and reception of the waves (Figure C.166). In addition, a laser doppler vibrometer (Polytec LDV) was used for an acquisition of the ultrasonic waves (Figure C.167). A PC program controls all the equipment in the system and data acquisition.

In order to get an accurate ultrasonic resonance signals, following equipment are assembled as;

- An arbitrary waveform generator to generate the sinusoidal signals with specific frequency
- An high frequency amplifier to amplify the sinusoidal signal to 1~100 Vpp. The frequency response of the amplifier ranges up to 300 kHz. The output of the amplifier applied to a wide-band piezoelectric transducer to vibrate the specimen with frequency sweep.
- A digital oscilloscope for monitoring the waveform in time domain.

- A PC with software program to sweep the desired frequency range and store and display the spectrum in frequency domain.
- A laser Doppler vibrometer to measure the high frequency vibration or displacement the specimen.

An actual NRUS system is assembled for the Open RRT, shown in Figure C.168.

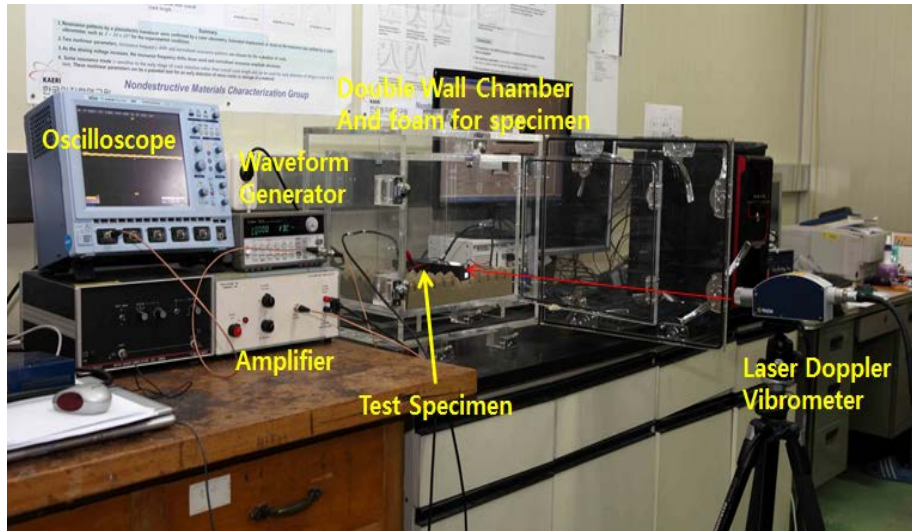


**Figure C.165** Photo of Nonlinear Resonant Ultrasound Spectroscopy (NRUS) with a Laser Doppler Vibrometer

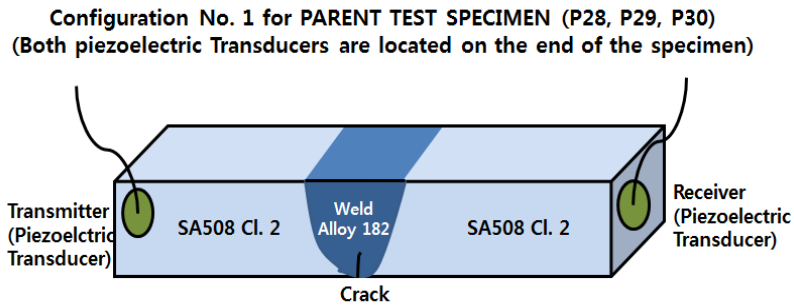


**Figure C.166** Schematic Drawing of the Configuration No. 1 of the Piezoelectric Transducer and the PARENT Specimen for Nonlinear Resonant Ultrasound Spectroscopy

**Configuration No. 2 for PARENT TEST SPECIMEN (P28, P29, P30)**  
 (Both piezoelectric Transducers are located on the top surface of the specimen)

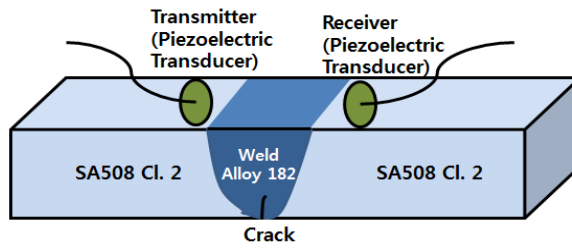


**Figure C.167** Schematic Drawing of the Configuration No. 2 of the Piezoelectric Transducer and the PARENT Specimen for Nonlinear Resonant Ultrasound Spectroscopy

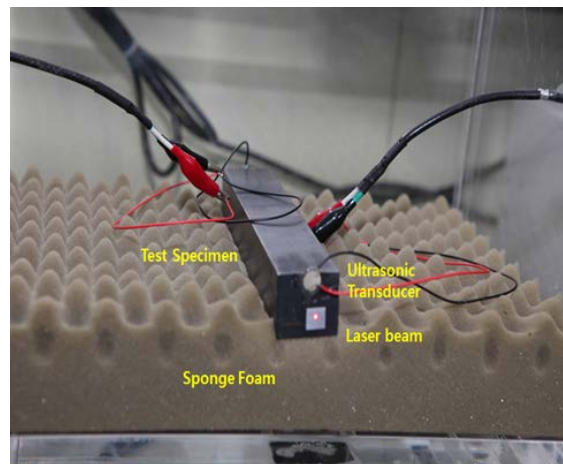


**Figure C.168** Photo Shows a PARENT Specimen (P28) at the NRUS Experiment. The resonance spectrum was acquired by both a piezoelectric transducer and a laser Doppler vibrometer.

### C.3.1.3 Preliminary Estimation of Resonance Frequencies of the Specimens (P28, P29, and P30)

Resonance frequencies and vibration modes are estimated by the LANL RPR code<sup>1</sup> (rectangular parallelepiped model). The specimen (SA 508 cl. 2) was assumed as a low carbon steel with an elastically isotropic material. The input parameters for the estimation are the dimension of the specimen ( $d_1 = 22$  cm,  $d_2 = 3.03$  cm,  $d_3 = 3.5$  cm), density = 7.8 gm/cc and initial guess of  $\epsilon_{11} = 277.0$  GPa,  $\epsilon_{44} = 79.14$  GPa (Cheong et al. 2000).

Table C.1 shows the estimated resonance frequencies and vibration modes for the specimen. Table C.1 lists the first 50 resonance frequencies with the vibration modes and orders. The abbreviations of the vibration modes, "k" are summarized as,

<sup>1</sup> RUSpec software by Magnaflux Quasar Inc.

k=1 uniform translation along x-direction

k=2 rotation about y-axis

k=3 rotation about z-axis

k=4 rotation about x-axis

k=5 volume oscillation

k=6 uniform translation along z-direction

k=7 uniform translation along y-direction

k=8 complex motion.

The number of vibration orders are also listed in the column 'i'.



**Table C.1 Estimated Resonance Frequencies and Vibration Modes for the Specimen P28, P29, and P30**

n	fex	fr	fr [kHz]	%err	wt	k	i
1	0.030078	0.003078	3.08	-89.77	0	7	2
2	0.003489	0.003489	3.49	0.01	0	6	2
3	0.006526	0.006526	6.53	0	0	4	1
4	0.007716	0.007716	7.72	-0.01	0	3	2
5	0.008548	0.008548	8.55	0	0	2	2
6	0.011546	0.011546	11.55	0	0	5	1
7	0.01305	0.01305	13.05	0	0	8	2
8	0.013578	0.013578	13.58	0	0	7	3
9	0.014746	0.014746	14.75	0	0	6	3
10	0.01957	0.01957	19.57	0	0	4	2
11	0.020068	0.020068	20.07	0	0	3	3
12	0.02143	0.02143	21.43	0	0	2	3
13	0.022972	0.022972	22.97	0	0	1	2
14	0.026099	0.026099	26.10	0	0	8	3
15	0.026897	0.026867	26.87	-0.11	0	7	4
16	0.02829	0.02829	28.29	0	0	6	4
17	0.03264	0.03264	32.64	0	0	4	3
18	0.034122	0.034122	34.12	0	0	5	2
19	0.03456	0.03456	34.56	0	0	3	4
20	0.03578	0.03579	35.79	0.03	0	2	4
21	0.04038	0.040384	40.38	0.01	0	8	4
22	0.041924	0.041924	41.92	0	0	7	5
23	0.042493	0.042493	42.49	0	0	6	5
24	0.044754	0.044754	44.75	0	0	1	3
25	0.046332	0.046332	46.33	0	0	2	5
26	0.047535	0.047535	47.54	0	0	4	4
27	0.050986	0.050986	50.99	0	0	6	6
28	0.052126	0.052126	52.13	0	0	3	5
29	0.052191	0.052191	52.19	0	0	2	6
30	0.05225	0.052251	52.25	0	0	8	5
31	0.05272	0.052723	52.72	0.01	0	4	5
32	0.05444	0.054439	54.44	0	0	5	3
33	0.05507	0.055073	55.07	0.01	0	3	6
34	0.05564	0.05564	55.64	0	0	7	6
35	0.05874	0.058742	58.74	0	0	7	7
36	0.05917	0.05917	59.17	0	0	6	7
37	0.05982	0.059824	59.82	0.01	0	8	6
38	0.06006	0.060069	60.07	0.01	0	3	7
39	0.06015	0.060157	60.16	0.01	0	4	6
40	0.06052	0.060518	60.52	0	0	7	8
41	0.06074	0.060745	60.75	0.01	0	4	7
42	0.0609	0.0609	60.90	0	0	8	7
43	0.06132	0.06132	61.32	0	0	1	4
44	0.06134	0.061338	61.34	0	0	5	4
45	0.06137	0.061373	61.37	0	0	3	8
46	0.06187	0.061869	61.87	0	0	2	7
47	0.06228	0.062282	62.28	0	0	1	5
48	0.06266	0.062656	62.66	-0.01	0	8	8
49	0.06282	0.062815	62.82	-0.01	0	7	9
50	0.06492	0.06492	64.92	0	0	8	9

### C.3.1.4 Data Analysis of NRUS Data

#### Examples of NRUS Applications

It is seen that variations of NRUS spectrum for the cracked ring are much higher than for the intact ring. We used steel bearing ring (#1, left specimen of Figure C.169) and two bearing rings made from sintered metal (middle and right specimens of Figure C.169). It was not completely sintered (“green” part) and specimen #2 (middle specimen of Figure C.169) has several cracks that provided high acoustic nonlinearity. Nonlinear amplitude frequency response of intact specimen (#1) is shown Figure C.170 and cracked specimen (#2) shown in Figure C.171.

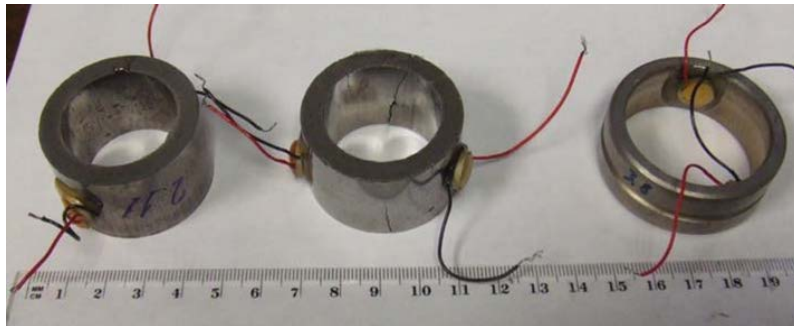


Figure C.169 Reference Tested Specimens

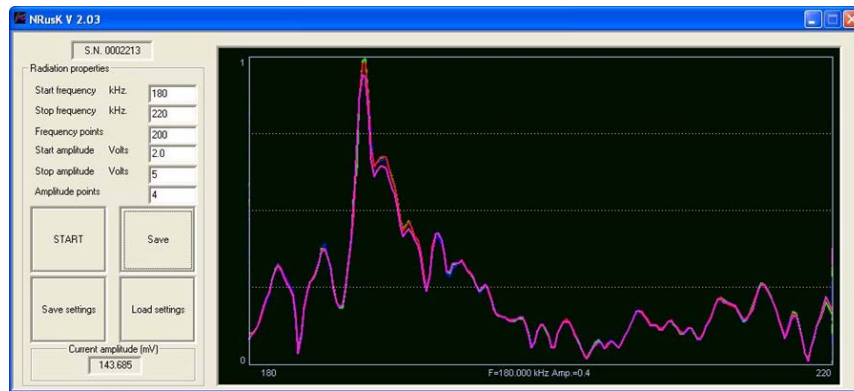
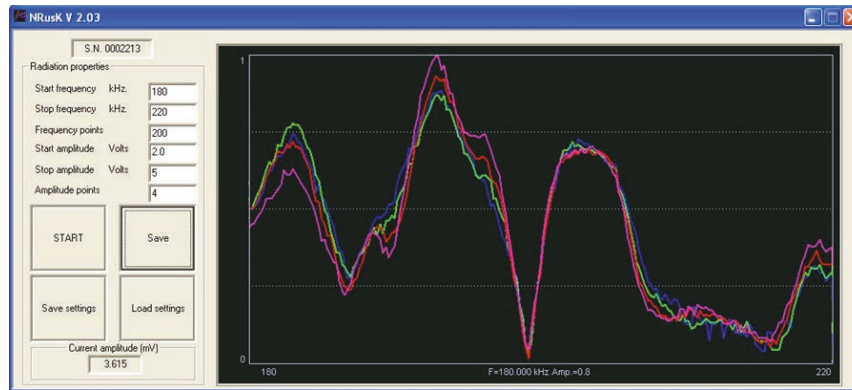
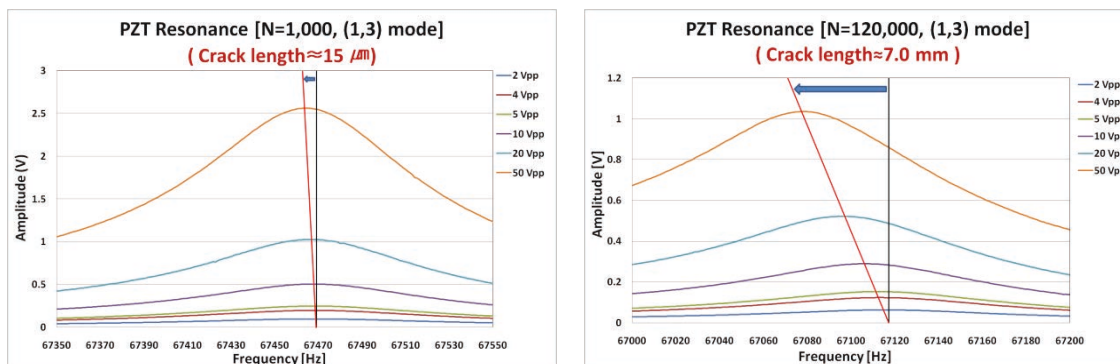


Figure C.170 Measured Nonlinear Amplitude Frequency Response (NAFR) for Intact “Green” Ring (Sample #1) in the Frequency Band 180–220 kHz



**Figure C.171** Measured Nonlinear Amplitude Frequency Response (NAFR) for Cracked “Green” Ring (Sample #2) in the Frequency Band 180–220 kHz

Another example of resonance frequency shift in a CT (Compact Tension) specimen with a stage of crack initiation and a specimen with a long crack, such as crack length of 7 mm are shown in Figure C.172. Resonance pattern from an intact CT specimen shows a little shift of resonance frequency even the driving amplitude varies. It means a little nonlinearity and almost no non-uniformity in the specimen. However, significant amount of the resonance frequency shifts downward is observed in the cracked specimen, as the driving voltage increases. As the crack length is in the range of mm, resonance frequency shifts downward and the normalized amplitude decreases as the driving voltage increases.



**Figure C.172** Resonance Frequency Frequency Shift in (a) CT Specimen in the Early Stage of Crack Initiation (left) and (b) CT Specimen with Crack Length of 7.0 mm (right)

### C.3.2 Pulsed Eddy Current, Technique ID 11-PECT0

PEC testing has been demonstrated to be one of the most effective methods, and is capable of tackling different inspection tasks, such as sub-surface defect detection in complex structures. Among the available conventional NDT methods, eddy current testing (ECT) is the most promising technique to detect flaws in conductive materials. The conventional ECT uses single-frequency sinusoidal excitation for the detection of defects or flaws as a function of changes in voltage, impedance, or phase, because of limited depths of penetration and complexity in a signal analysis ECT was confined to limited applications. Unlike a conventional ECT, PEC uses multiple frequency sinusoidal excitation pulse of the electric current through the excitation coil.

PEC is more economical than other NDT methods. Because of many advantages of PEC over a conventional eddy current method, such as low power consumption owing to a short pulse excitation and the broad band nature of a pulse, PEC has the capability to penetrate different depths in a conductive material and provides the depth information of the defects. Even though the use of PEC has long been considered for the testing of materials, in recent decades, PEC testing has become the subject of wide spread interests in NDT because of its advancement in technologies such as computer data acquisition and digital signal processing. Furthermore, PEC has the capability to measure the thickness, conductivity, and in particular, sub-surface crack measurements, crack reconstruction, and depth estimation.

### **C.3.2.1 Overview**

The PEC testing is the new promising technological approach to NDT, and it has been principally developed for surface, subsurface flaws measurements and corrosion in the multilayered structures. Among the available conventional NDT methods, one of the most used is eddy current testing (ECT) to detect the flaws in conductive materials. Unlike conventional ECT the PEC uses pulse of electric current through the excitation coil. In contrast to the conventional ECT (operates with single sinusoidal frequency), the pulse ECT employ repetitive pulses having short duration in time (having broad band), which yields a signal having frequency contents from DC to several KHz or higher. Skin depth is a function of the resistivity and permeability of the test material, and test frequency. Because the eddy current diffusion depth depends on the excitation frequency the PEC technique has the potential for bringing up deeper information about the tested sample. In order to detect deep crack from the surface, the magnetic field has to penetrate the sample and arrive up to the crack. Therefore, high current and reasonable frequency range are essential for the detection of defects using PEC. In PEC, a response pulse always comes after an excitation pulse is over, so this method is less susceptible to interference, moreover the pulse excitation can minimize the power consumption, which is more capable in the development of portable instruments. Because of the potential advantages of the PEC, prevalent investigations on this technique have been made, such as for detection of subsurface crack and corrosion in aircraft multi-layer structure.

### **C.3.2.2 PEC Equipment**

The block diagram of the PEC system design is shown in Figure C.173. The system consists of a rectangular waveform generator, a probe integrated with an excitation coil and a Hall-sensor, an amplifier to amplify the signal from Hall-sensor, a data acquisition card and a PC with signal processing software. The system works as follows; the waveform generator produces a rectangular waveform with variable frequency and duty cycle. The waveform is fed to a coil driver circuit, which excites the induction coil in the probe with pulsed current. When the probe is mounted on the metal structure, the pick-up sensor will measure the vertical resultant magnetic field, which is the vector sum of the one generated by the excitation coil and the opposing one generated by the induced eddy current in the sample (Primary flux  $\Phi_1$  created by driving coil induces EC in the conducting medium, induced EC produces counter flux  $\Phi_2$ . Now pick-up sensor measures total flux  $\Phi = \Phi_1 + \Phi_2$ .). A voltage amplifier with variable gain amplifies the signal from the pick-up sensor. The A/D card will convert the input signal into digital data ready to be processed by written software in the PC. The software performs communication with the data acquisition card. Signal pre-processing, feature extraction, defect categorization, and the presentation of the results are on the PC monitor.

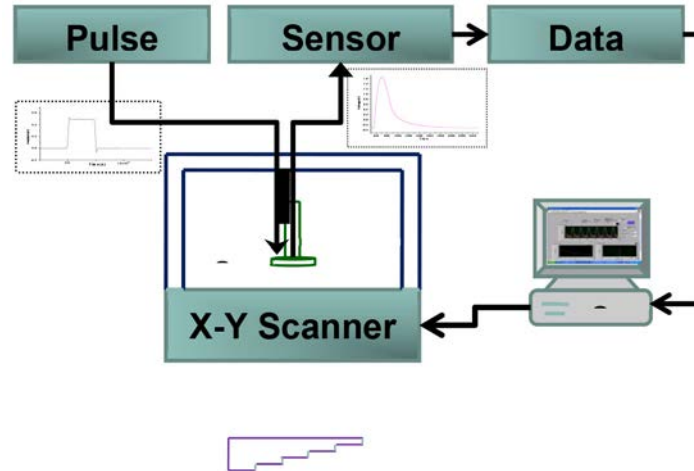


**Figure C.173 Block Diagram of the PEC System**

The amplifier supplies the high current uni-polar (+Ve) pulse to the Driving Coil or exciting coil which is in the PEC probe. With this amplifier we can control the pulse width considering the skin depth of sample (from 1 ms–10 ms) in case of nonmagnetic materials, pulse frequency (500 MHz–50 Hz), and pulse amplitude (max- 100 A). The excitation coil is a copper wire which has square cross section with 1×3 mm having total resistance 0.92 Ω, wound 132 turns on the cylindrical ferrite core. The probe has a 60mm height and 9mm inner diameter, and the Hall-sensor was positioned in the center of probe to detect the induced signal from defects. The cylindrical type ferrite core not only reduces the magnetic leakage but also improves the detection sensitivity by sustaining adequate excitation intensity. The Hall-sensor gives the frequency independent sensitivity from DC to 100 kHz, high spatial resolution having less power consumption with increased sensitivity and simple readout circuitry. When we bring the probe proximity to conducting plate, the steep exciting pulse induces eddy currents and its associated magnetic field dissipates exponentially to approach its steady state. The induced eddy currents flow in the opposite direction to the currents which are flowing in the exciting coil, hence when the probe is placed on the conducting plate, the detected field rises slowly to the maximum peak value.

### **C.3.2.3 Tested Sample and Detection of Crack**

The three kinds of test blocks with ID 28, 29, and 30 provided by ALSTOM, and the flaw types of these test blocks are BWR/NWC SCC Crack, Fatigue Crack, and PWR SCC crack, respectively. The sample was composed by the welding of two base metals, and the composition of base metal is 22NiMoCr37, and the welding metal is alloy 182. A 10 mSec pulse width and 15A excitation current is applied to exciting coil of the probe to test the sample. The PEC probe is fixed to the X-Y scanner to perform the manual scanning on the defect free side of the tested sample. A LabVIEW-based data acquisition program was developed to continuously monitor the variation in the thickness of the sample and is observed on the computer screen. The time domain feature which is the peak value of detected pulse is used for the scanning test to detect the sub-surface cracks in the tested sample.

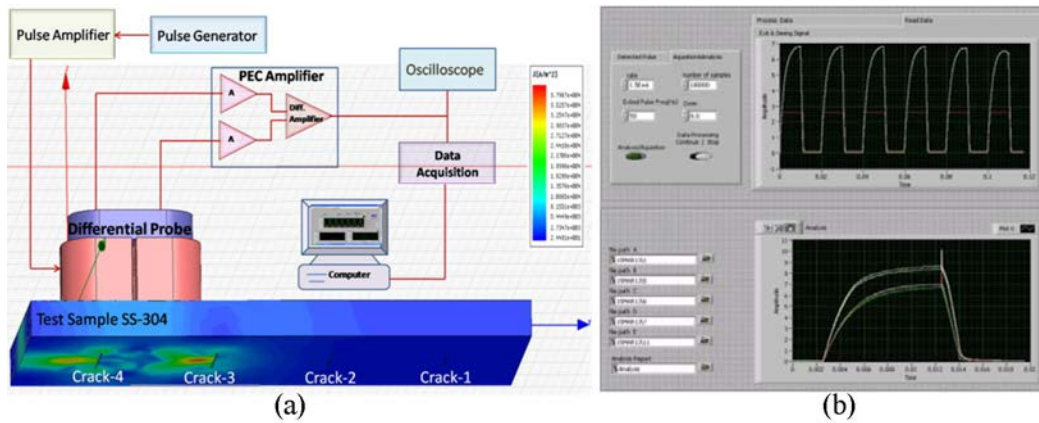


Figure C.174 (a) Configuration of PEC System; (b) LabVIEW Data Acquisition Front Panel



The pulse width (from 1 ms–10 ms)  
 Pulse frequency (500 Hz–50 Hz),  
 Pulse amplitude (max- 100 A).

The excitation coil total resistance 0.92  $\Omega$ ,  
 132 turns on the cylindrical ferrite core.  
 The probe: 60 mm height; 9 mm ID

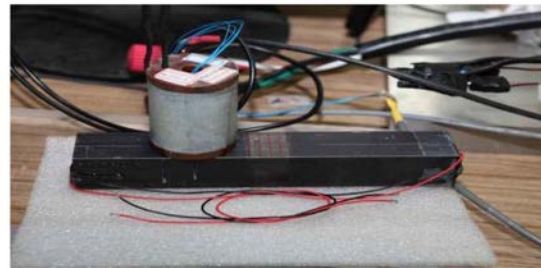


Figure C.175 Pulsed Eddy Current System and Experimental Setup (Probe on Sample)

### C.3.2.4 Configuration of PARENT Test Specimen (P28, P29, P30)

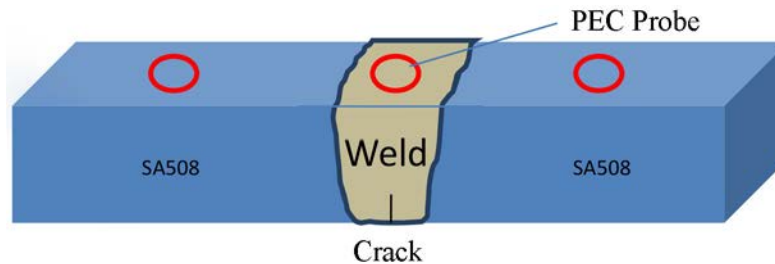
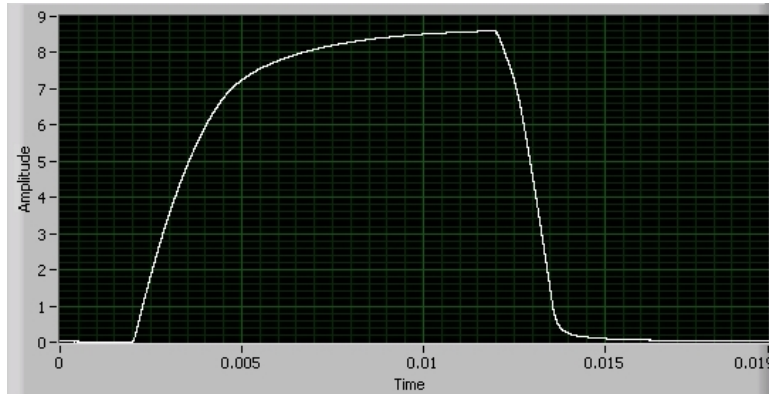


Figure C.176 Schematic of PARENT Test Specimen. PECT probe is located on the opposite side of crack surface.

### C.3.2.5 Experimental Results and Feature Extraction

If the probe placed on the test sample in such a position, then the typical response signal shown in Figure C.177, is the induced signal detected by the Hall-sensor from test block.



**Figure C.177 Typical PEC Signal Induced in the Hall-sensor from the Test Block**

Calibration of PEC signal with standard specimen is essential to obtain a reliable experimental result. Because of no calibration sample is prepared, the validity of experiment was verified using the difference of the PEC peak amplitude obtained in the crack and opposite side (Figure C.178). The base metal of sample block 22NiMoCr37 is ferromagnetic and welding material alloy 182 is nonmagnetic material. Therefore, the PEC amplitude measured in the ferromagnetic part is higher than that of the nonmagnetic part. The y coordinate 10 and 12 cm neighborhood is the interface region between ferromagnetic and nonmagnetic material. The crack is positioned in the neighborhood of y coordinate 11 cm, which shows the minimum PEC signal amplitude.

The important characteristic of detected signal to interpret the results is the peak value of the pulse. The measuring points were selected as a x-y coordinate, the x points were fixed at the center of transverse direction and y points were selected along the longitudinal direction. Figure C.179 show the change of PEC peak amplitude along the coordinate.

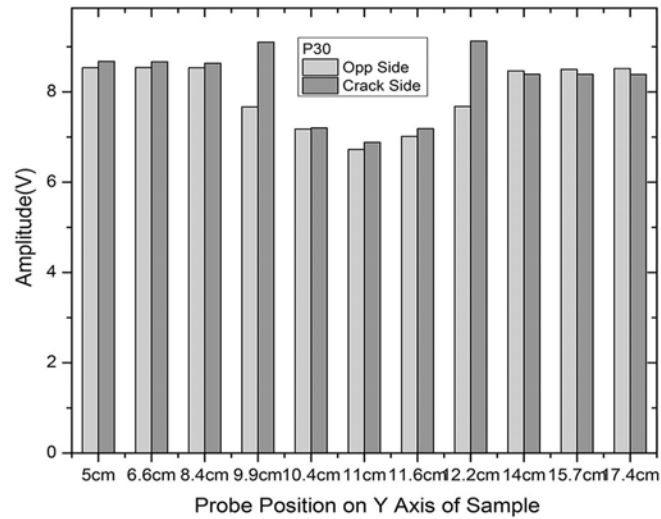
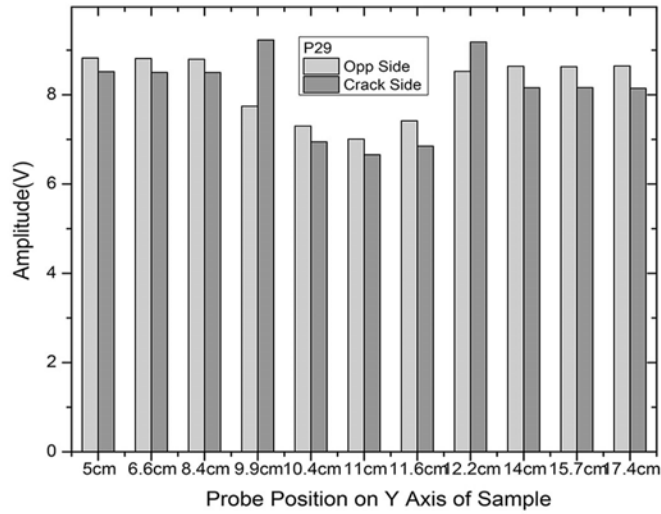
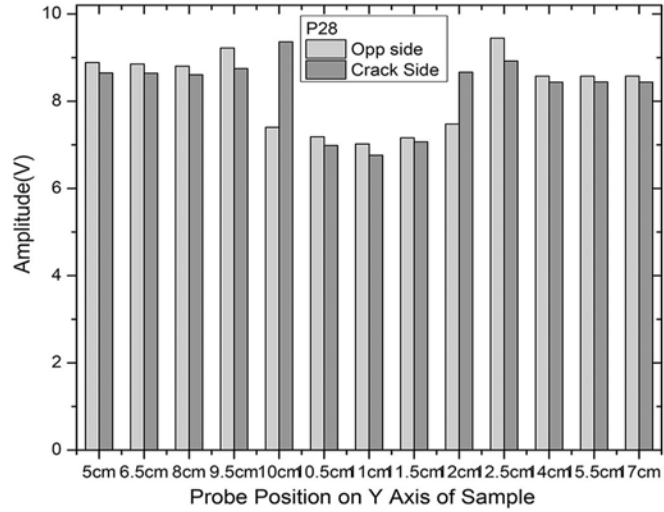


**Figure C.178** The Difference of the PEC Peak Amplitude Obtained in the Crack and Opposite Side for P28, P29 and P30



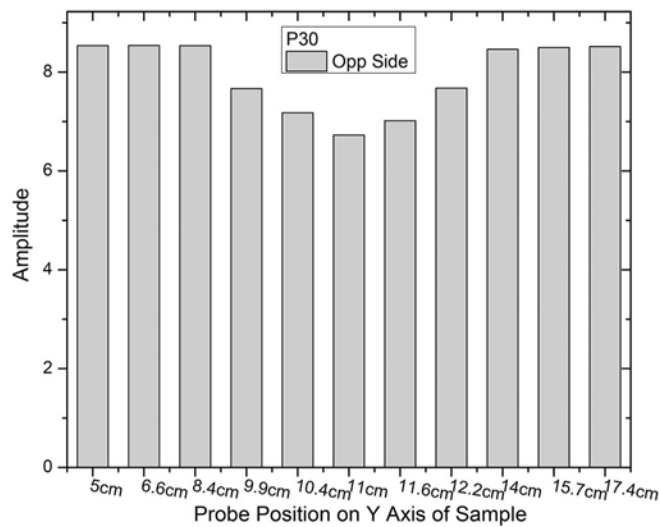
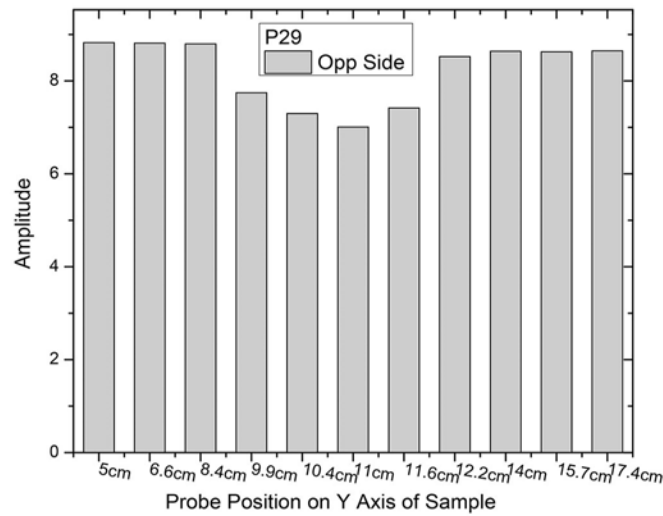
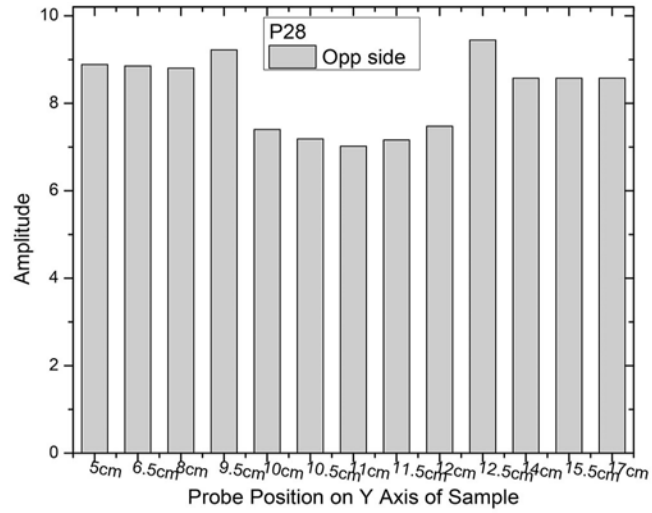


**Figure C.179** The Difference of the PEC Peak Amplitude Obtained in the Crack and Opposite Side for P28, P29 and P30

### **C.3.2.6 Summary**

The nondestructive evaluation (NDE) using PEC to detect the sub surface crack under the thick plate has been performed on the PARENT round robin sample. The PEC amplitude measured in the ferromagnetic part is higher than that of the nonmagnetic part; therefore, it is not certain that the decrements of amplitude are attributed to the defects or nonmagnetic part. The y coordinate 10 and 12 cm neighborhood is the interface region between ferromagnetic and nonmagnetic material. The crack is positioned in the neighborhood of y coordinate 11 cm, which shows the minimum PEC signal amplitude.

## **C.3.3 Phased Ultrasonic Array, Technique ID 20-PA1, 20-PA2**

### **C.3.3.1 Scope**

- This procedure is applicable to ultrasonic examination of dissimilar metal welds and adjacent material utilizing phased array technique (PAUT).
- The objective of examination performed in accordance with this procedure is to accurately detect, length sizing and depth sizing within the specified examination volume.

### **C.3.3.2 Personnel Requirement**

- Personnel performing exams has an experience for equipment setup, calibration, examination and data evaluation.

### **C.3.3.3 Equipment**

- Olympus-Omniscan MXU (16:128) instrument with 8 channels
- Software (TomoView-2.R3) capable of collecting and storing full waveform signals

### **C.3.3.4 Transducer and Wedge**

- Total element: 32 or 64
- Focal range: 40–60 mm
- Frequency: 2.25 or 5 MHz
- Wedge: Angle/Length/Width
- Element size: Length/Width/Pitch

### **C.3.3.5 Calibration**

- Velocity calibration for angle beam probe using IIW radius block
- Instrument linearity check (Screen height/Amplitude control/Transducer values)

- Examination range and signal amplitude calibration
- Sensitivity calibration using calibration block
  - A detailed drawings for calibration block with dimension shall be provided

### C.3.3.6 Inspection Technique

- Examination volume

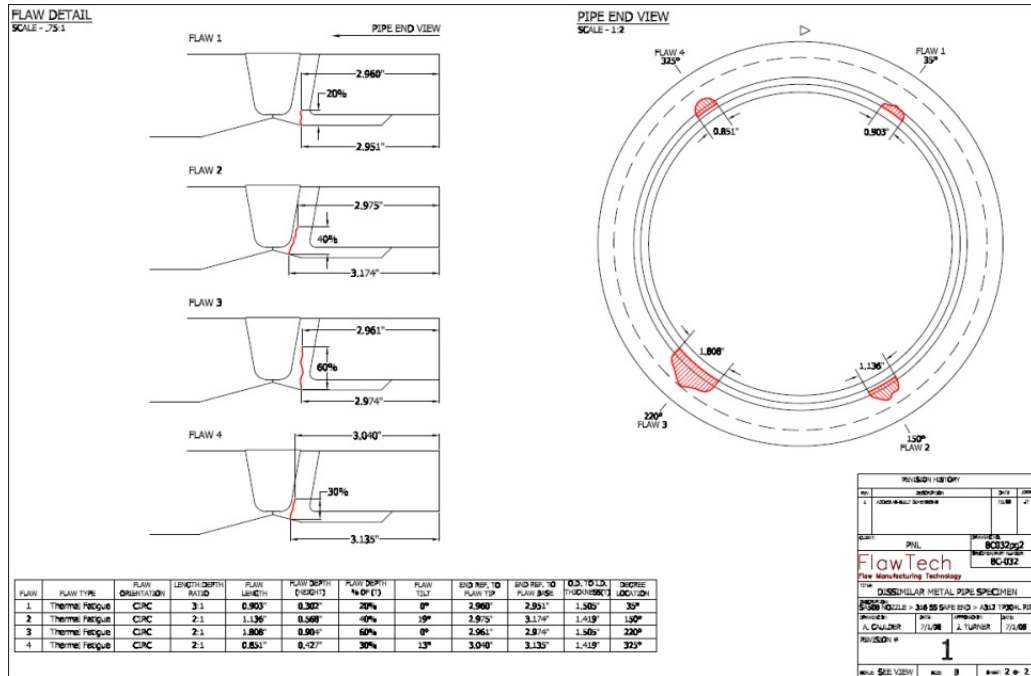


Figure C.180 P1 Specimen

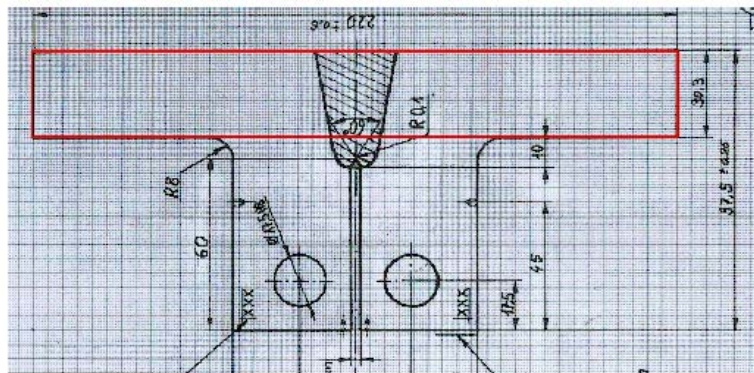


Figure C.181 P28, P29, P30, P31, P32

- Axial examination
  - For examination reflectors oriented parallel with the weld, scanning shall be directed essentially perpendicular to the weld axis from two directions (Up/Down)
- Circumferential examination
  - For examination of reflectors oriented perpendicular with weld, scanning shall be performed along the weld axis in both clockwise and counter-clockwise directions (CW/CCW)
- Scan speed
  - Scan speed shall be not excited 2.0 inches per second for examination
- Overlap
  - Scan pattern shall provide min of 50 % overlap the transmitting element in the indexing direction
- Examination sensitivity
  - Scan image shall be established on the component to be examined and adjust the gain level until the signal response from the inside diameter (ID roll) is between 5 % and 20 % FSH
- All suspected flaw indications, regardless of amplitude, shall be investigated to the extent necessary to provide accurate characterization, identify, and location

#### **C.3.3.7 Inspection Classification**

- Flaw indications
  - All images produced by reflectors within the volume to be examined, regardless of amplitude that cannot be clearly attributed to the geometrical or metallurgical properties of the well configuration shall be considered as flaw indications.
- Non-relevant indication (Geometric/Metallurgical)
  - All image produced by reflectors within the volume to be examined that can be attributed to the geometry of the weld configuration shall be considered as non-relevant indicators.

#### **C.3.3.8 Indication Discrimination**

- Indication has a good image along the length of the component
- Indication provides substantial and unique flaw image

### C.3.3.9 Indication Sizing

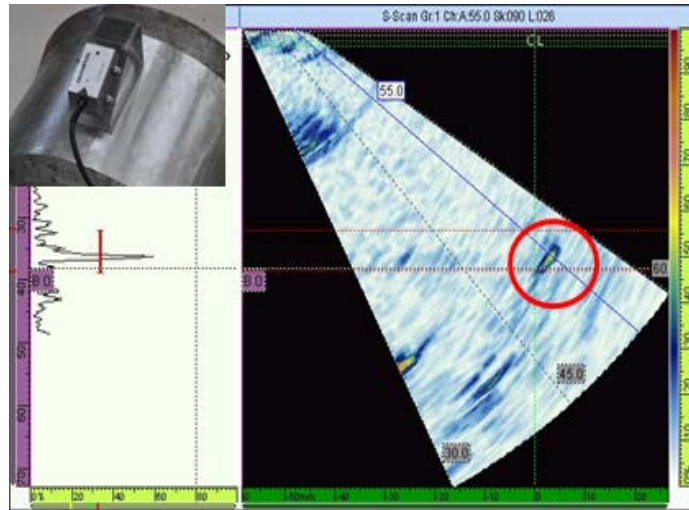
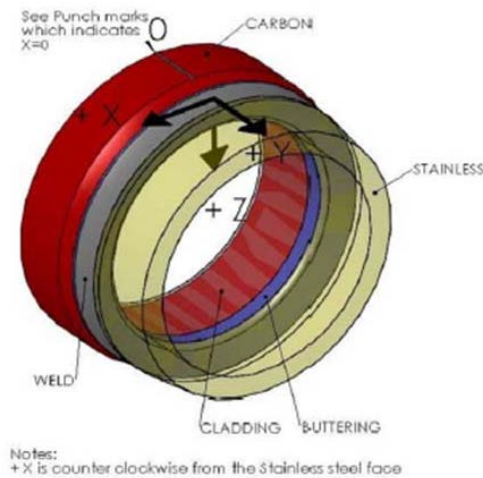


Figure C.182 PAUT Image from Flaw

### C.3.3.10 Recording of Reflectors

- The datum “0” reference points used for recording indications shall be in accordance with the system shown in following figure.



- Flaw indications
  - For flaw indications (images) the following information shall be recorded regardless of amplitude
  - Record the flaw location (Y1 and Y2) from weld center line zone
  - The length dimension (X1 and X2) from “0” reference points
  - The dimension Z1 (upper) and Z2 (lower) through wall

### **C.3.3.11 Examination Reporting**

- Examination data shall be recorded on a data sheet
  - calibration data sheet
  - examination personnel and examination data
  - examination procedure number/revision number
  - equipment serial number, manufacturer, model=
  - search unit angle, manufacturer, serial number, model=
  - search unit frequency, size, mode, shape, beam focus, wedge
  - cable type, length, couplant type
  - signal response amplitude and sweep position obtained from reflectors
  - examination sensitivity and location of reflectors

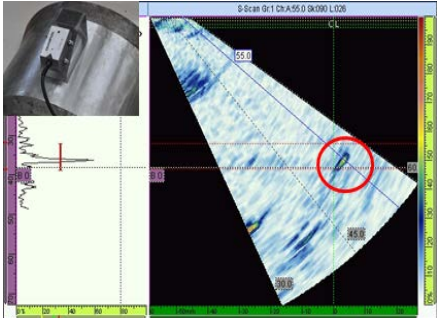


### C.3.3.14 DAG Technique Summary

- Inspection company: KRISS
- Team code : KRISS TEAM 20
- Inspection Procedure: KRISS-PAUT-01
- Specimen: P1, P7, P28, P29, P30, P31, P32
- Inspection type: Manual Phased Array Ultrasonic Examination from OD
- Scan type: Scanning for circumferential flaw (oriented parallel to the weld) and scanning for axial flaw (oriented transverse to the weld)
- Detection

Technique detection	Evaluation methodology detection
PAUT with curved wedge based on reflection from flaw - Pulse echo PAUT probe with 32 elements, 2.25 MHz, reflection (Longitudinal-wave)	Based on PAUT image from echo dynamic pattern and/or signal amplitude - Evaluation of images by PAUT Tx-Rx dynamic focusing algorithm

- Characterization

Technique characterization	Evaluation methodology characterization
PAUT with curved wedge contact technique based on reflection of flaw. - Image by PAUT pulse echo method 	Difference between flaw image and non-relevant indication (geometric/metallurgical) - Whether the images can be clearly attributed to the geometric/metallurgical properties of weld configuration or not - Characterized as embedded flaws if the image doesn't show evidence of flaw from the inside back wall

- Length and width sizing and flaw positioning

Length sizing and positioning	Evaluation methodology sizing and positioning



PAUT with curved wedge contact technique based on reflection of flaw. - Image by PAUT pulse echo method	PAUT equipment provides the size of flaw and position from the sector scan image
--	--

### C.3.4 Ultrasound Infrared Thermography, Technique ID 20-UIR0

#### C.3.4.1 Outline

- Inspection procedures include record of mandatory variable used to determine the defect detection, characterization and defect size
- Procedures written in English (MS Word) (Design/Review/Approved, Procedures/Revision number, Date)
- Before the start of the RRT, documents submit to the supervisor/ supervisor Review
- DAG (Data Analysis Group) Technique Summary writing / submit to the supervisor
  - Brief summary of technique for defect detection, characterization and defect size to ease data evaluation /review

#### C.3.4.2 Mandatory Variable to be Included in Inspection Procedures (IP)

- Weld shape
- Inspection technique
- Used equipment
- Surface emissivity
- Horn type, Frequency, Output
- Thermal imaging equipment calibration
- Defect sizing
- Data acquisition

#### UIR Techniques Essential Variable

- Equipment
- Horn type
- Horn displacement
- Horn contact force

- Ultrasound output
- The contact direction and location of horn
- Defect sizing method
- Lock-in thermography
- Ultrasound duration

### **C.3.4.3 TD Document that must be Included in the Essential Variables**

#### **Scope**

- This procedure is applied to non-destructive examination of dissimilar metal welds and adjacent materials utilizing ultrasound infrared thermography or vibration infrared thermography.
- The objective of examination performed in accordance with this procedure is to accurately detect length sizing and width sizing of defect within the specified examination volume

#### **Personnel Requirement**

- Personnel performing exams has an experience for equipment setup, calibration, examination and data evaluation.

#### **Equipment (ultrasound generator, infrared thermography)**

- Ultrasound generator by UITec–SEE2 Sonic
- Infrared thermography by Flir Cedip siver480

#### **Transducer and Horn**

- Frequency (20 kHz)
- Output (420 W)
- Horn type (Point)
- Contact area (mm<sup>2</sup>)
- Horn material (STS304)

#### **Calibration**

- Frequency and displacement check using ultrasound generator and horn
- Performance test of Infrared thermography camera using blackbody

- Maintenance more than 0.95 of surface emissivity for inspection body using flat black paint

### Inspection Technique

- Examination volume

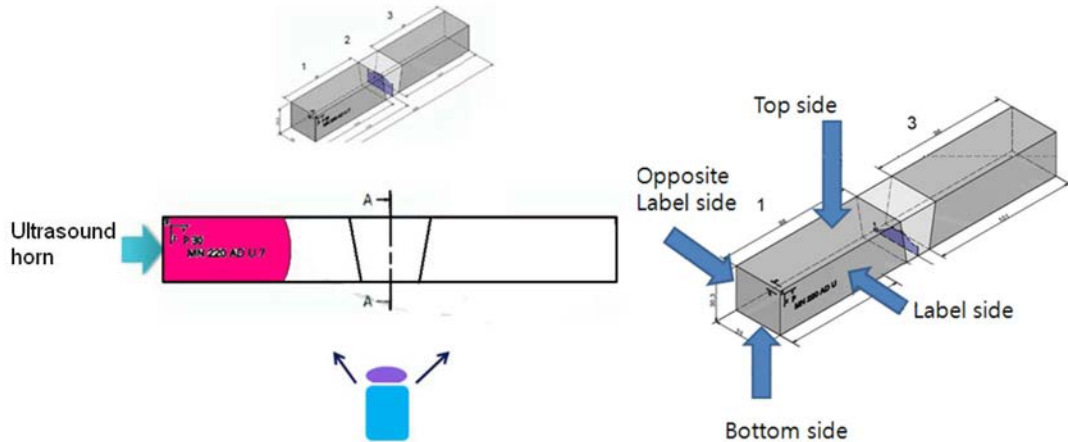


**Figure C.183 P28, P29, P30, P31, P32, P38 Specimen**

- Examination – After occurring ultrasound in a base metal outside of welds and heat-affected zone, examination shall be performed by detecting heat of welds using infrared thermography
- Inspection speed – Inspection speed shall be not exceed 20 minutes after occurring ultrasound
- Examination Sensitivity – After setting the components that can be examined, the contact force shall be adjusted so that displacement containing welds can be in the range of 100  $\mu\text{m}$ .
- All suspected defect indications, shall be investigated to the extent necessary to provide accurate characterization, identify, and location

### Inspection Classification

- Defect indications – All indications produced by infrared thermal image and lock-in phase image with temperature difference within the volume to be examined shall be considered as defect indications, after exciting the basic material near the welds by ultrasonic waves after for a certain amount of time
- Non – relevant indication – All indications produced by infrared thermal image and lock-in phase image without temperature difference within the volume to be examined shall be considered as non-relevant indication, after exciting the basic material near the welds by ultrasonic waves after for a certain amount of time

### Indication Discrimination

- Indication has a healthy image to show temperature difference ( $< 0.15^{\circ}\text{C}$ ) along the position of component
- Indication provides substantial and unique temperature and lock in phase travel

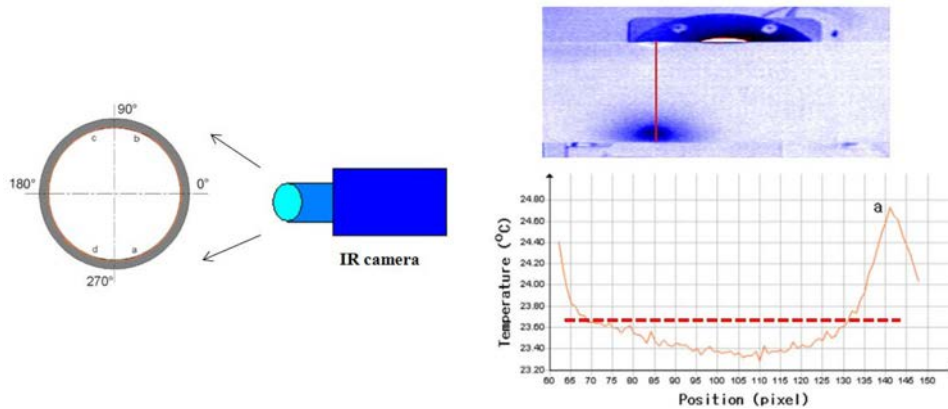


Figure C.184

### Indication Sizing

- Lock-in phase thermography technique
  - Defect size is computed to pixel and measuring image

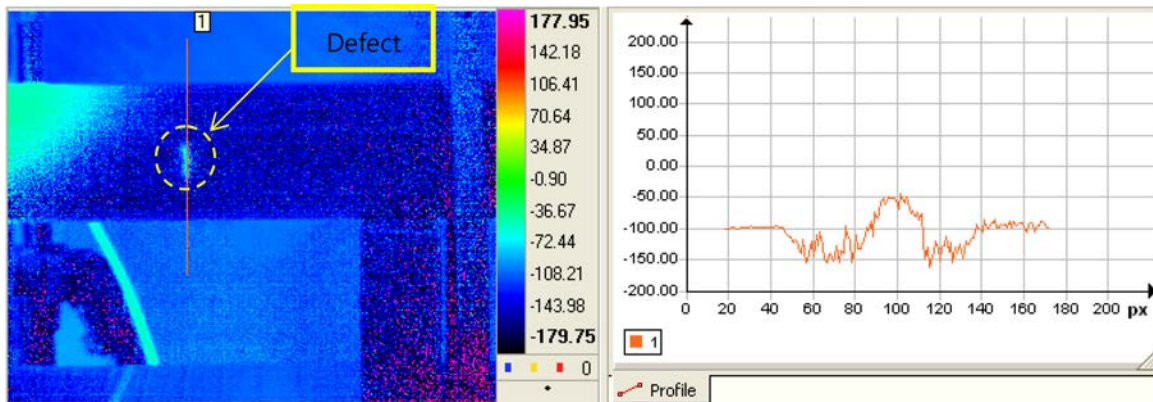
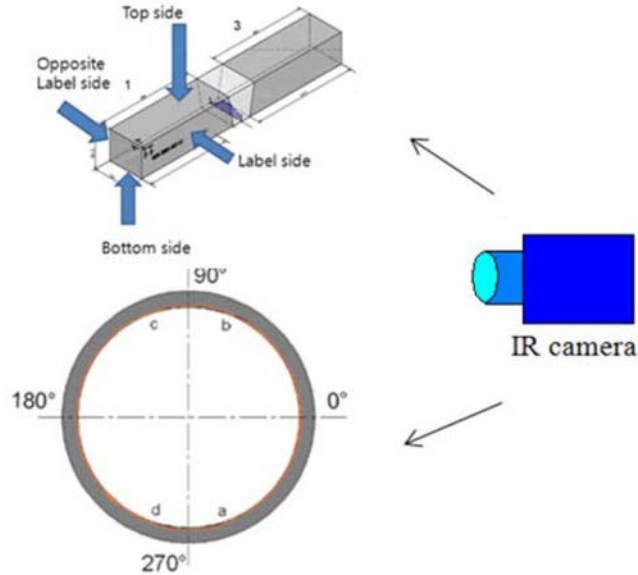


Figure C.185

### Recording of Thermography

- As shown in Figure C.186, the specimen is rotated to 4 directions with  $90^{\circ}$  interval during the test.
- The “0” reference points used for recording indications shall be in accordance with the system shown in Figure C.186



**Figure C.186**

- Defect indications
- For defect indications the following information shall be recorded shown in Figure C.187
  - Record the defect location (Y1 and Y2) from weld center line zone
  - The length dimension (X1 and X2) from “0” reference points
  - The dimension Z1 (Upper) and Z2 (Lower) through wall

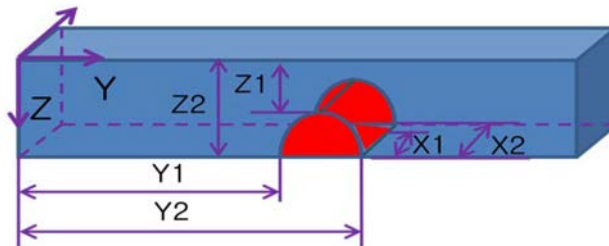


**Figure C.187**

### Examination Reporting

- Examination data shall be recorded on a data sheet
  - Examination personnel and examination data
  - Examination procedure number/revision number
  - Equipment serial number, manufacturer, model

- Search unit angle, manufacturer, serial number, model
- Search unit frequency, size, mode, shape, displacement, horn
- Calibration data sheet

### Calibration Data Sheet for Ultrasound Infrared Thermography

Calibration Data Sheet for Ultrasound Infrared Thermography									
Object of Inspection	Name:Parent RRT	No:P28	Inspection Method:UIR			IR Camera Temperature calibration		Date: 2013. 03. 5	
Inspection Method	Fabricator:Ul-Tech		Model:SEE-SONIC II	Serial No:1372	Black body Tem(°C) : 35.00		Inspected by:	Level:	
Reference Block	No: P28	Nominal Size:		Material: SA508+Alloy18+SA508	Camera Tem(°C) : 35.00		Confirmed by:	Level:	
Transducer Horn	Frequency (kHz)	Fabricator	Model	Serial No	Horn index point (mm²)	Displacement Sensitivity (µm)	distance from horn to welded zone (mm)	Displacement	
1	19.6	Ul-Tech	cone-horn	Cone-1	7 mm²	0.1	110	100 µm	
2									
3									
4									
Remarks:							Signature: _____		

### PARENT RRT Data Sheet

PARENT RRT - DMW TECHNIQUE DATA SHEET											
Procedure ID: 20.2						Tech ID: UIR					
Inspection ID:20,P28.1						Access: OUT					
Test Block ID: P28						Date: 2013/03/05					
Team ID:20											
						Weld Volume Inspected					
Detection: yes						X1: 0.00 mm		X2: 35.00 mm			
Length sizing: yes						Y1: 0.00 mm		Y2: 160.70 mm			
Depth sizing: yes						Z1:0.00 mm		Z2:30.30 mm			
Defect No:	X1 (mm)	X2 (mm)	Y1 (mm)	Y2 (mm)	Z1 (mm)	Z2 (mm)	Defect max Tem(°C)	Defect min Tem(°C)	Surface breaking	Comments	
1			103.84	119.76	18.76	30.30	22.48	21.32	y	Label side view	
-BLANK-											
TEAM SIGN :						INVIIGATOR SIGN:					

### DAG Technique Summary

- Inspection company: KRISS
- Team code: 20.2 ( KRISS TEAM 1)

- Inspection Procedure: 20.2.1 (KRISS-UIR-01)
- Specimen:P28, P29, P30, P31, P32, P38
- Inspection type: Manual Ultrasound Thermography from specimen
- Scan type: The Specimen has been rotated to 4 directions with 90° interval during the test.
- Detection

Technique detection	Evaluation methodology detection
Thermal energy is based on a ultrasound forces <ul style="list-style-type: none"> <li>• Sine wave : 20 kHz</li> <li>• Displacement : 100 μm</li> <li>• Frequency : 30 MHz</li> </ul> UIR technique is based on image of infrared thermography	-Based on temperature, Lock-in phase or amplitude image <ul style="list-style-type: none"> <li>• Evaluation of lock in phase images with temperature distribution through the temperature and position</li> <li>• Temperature difference to evaluate defect is more than 0.15°C</li> </ul> -Hot spot defect images will have measured during the ultrasound excite.

- Characterization

Technique characterization	Evaluation methodology characterization
UIR technique is based on ultrasound forces and infrared thermography <ul style="list-style-type: none"> <li>• Characterization is determination between health area and defect area</li> </ul>	-Temperature difference(T) between defect indication and health indication <ul style="list-style-type: none"> <li>• If <math>T &gt; 0.15^{\circ}\text{C}</math>, the area is classified as a defect, if not the area is classified as a health °C</li> </ul> -All indications produced by infrared thermal image and lock-in phase image with temperature difference within the volume to be examined shall be considered as defect indications

### **DAG Technique Summary**

- Inspection company: KRISS
- Team code: 20.2. (KRISS TEAM 1)
- Inspection Procedure: 20.2.2 (KRISS-UIR-01)
- Specimen: P28 , P29, P30, P31, P32, P38
- Inspection type: Manual Ultrasound Thermography from specimen
- Scan type: The Specimen has been rotated to 4 directions with 90° interval during the test.

- Length & width sizing

Technique length sizing	Evaluation methodology length sizing
UIR technique is based on ultrasound forces and infrared thermography	-If $T > 0.15^{\circ}\text{C}$ , the area is classified as a defect, if not the area is classified as a health $^{\circ}\text{C}$ <ul style="list-style-type: none"> <li>• Evaluation of defect size using spatial resolution of pixel image</li> <li>• Evaluation of lock in phase images with temperature distribution through the temperature difference.</li> </ul> -Hot spot image indications produced by infrared thermal image and lock-in phase image with temperature difference within the volume to be examined shall be measurement as defect size

- Defect positioning

Technique defect Positioning	Evaluation methodology Technique defect positioning
Based on technique for detection, length and width sizing	Based on previous described methodology for detection, length and width sizing <ul style="list-style-type: none"> <li>• X position, along defect, is taken from length sizing</li> <li>• Y position, across defect, is taken from width sizing</li> <li>• Z position, across defect, is taken from width sizing</li> </ul>

### C.3.5 Guided Ultrasonic Wave, Technique ID 21-GW1, 21-GW2

#### C.3.5.1 Overview

##### Introduction of Guided Wave

Guided wave (GW) technique was employed for PARENT Open Test specimen (P4 and P5) to investigate defects size.

Traditional Bulk wave ultrasonic inspection method can do thickness measurements, defect detection and material property characterization in a local area. This technique has disadvantage on large area inspection. Transducer should move point by point to cover a large region to scan whole area. Also, it is difficult to inspect inaccessible structure and area by traditional bulk wave inspection method.



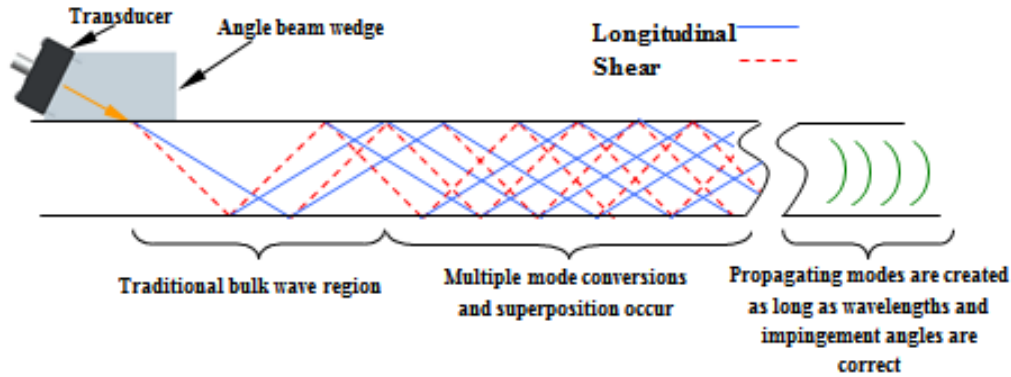


**Figure C.188 Guided Wave Generation and Propagation**

A guided wave inspection technique which is presented on this technical description has different feature compared to conventional bulk wave ultrasonic test. Guided waves are generated with special frequency and excited angle on certain specimen geometry and boundary condition. Once ultrasonic wave is generated as Figure C.188 bulk wave (longitudinal and transverse wave) will propagate on the specimen. Those waves will reflect on the boundary and wave mode conversion will occur to produce guided wave mode with special condition. A guided wave travels along with inspecting material. Guided waves have great advantage on large area inspection due to the propagation on long distance without losing wave energy. However, guided waves include infinite wave mode with different distribution in the structure. This feature makes people hard to analysis and gives more or less sensitivity on different types of defects and loading condition. Guided wave mode and loading condition can be chosen by structure condition and defect size and location, such as on the surface or sub surface.

It is physically and scientifically based approach to generate certain guided wave mode. Guided wave mode is very much dependent on frequency and geometry of specimen. The main characteristic of guided wave is dispersion. Figure C.189 shows guided wave dispersion curve on cylindrical coordinate.

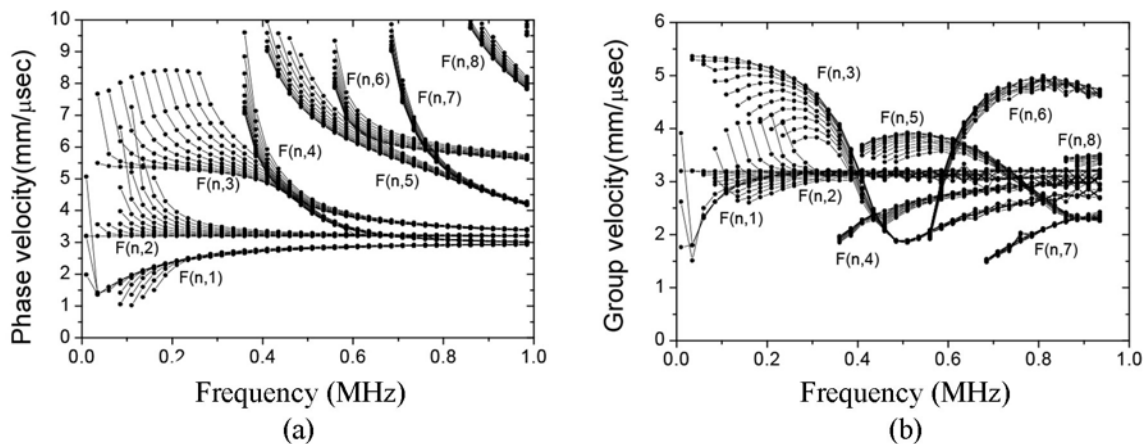


**Figure C.189** Guided Wave Dispersion Curves on Cylindrical Coordinate. (a) Phase velocity dispersion curve, (b) Group velocity dispersion curve

Every possible propagation mode can be shown on a dispersion curve. Through the contribution of advanced computational power and analysis, nowadays, it is possible to deal with advanced understanding and utilization. Wave structure profiles can be obtained for a given structure due to the generation of a dispersion curve. Wave structure profiles can be obtained according to the dispersion curve. How many types of energy are distributed along the thickness of the structure is shown, looking into the profiles of the wave structure. Guided waves ease Structural health monitoring by taking these concepts. Moreover, it is possible to monitor very large areas with great accuracy by using tomographic algorithms with Guided waves. In addition, multiple phased array exciters can be used to focus guided wave energy within structures.

- Pulse echo (PE)

This technique shown as Figure C.190 is the pulse echo method in guided wave inspection technique. Guided waves propagate from the fixed position with a single transducer. The transducer receives the reflected signal from discontinuities. Once we tune the guided wave mode, then the defect distance from the transducer position is based on the wave mode velocity.



**Figure C.190 Pulse Echo Technique**

- Pitch Catch (Pc)

This technique shown as Figure C.191 is the pitch catch method in guided wave inspection technique. Guided waves are generated from one transducer and propagate through the specimen. The other receiving transducer detects the wave signal at the distance from the excitation transducer. If there are any discontinuities on the specimen, the received signal amplitude will be decreased or the wave mode will be changed with respect to specimen thickness.



**Figure C.191 Pitch Catch Technique**

#### **Personnel Requirement for Guided Wave Inspection**

- Personnel performing exams has an experience for equipment setup, calibration, examination and data evaluation.
- Guided wave mode analysis and dispersion curve analysis knowledge.

## Inspection Equipment

- Tone-burst pulser
  - Ritec – Ritec RPR 4000 instrument with high power voltage
- Oscilloscope
  - LeCroy Wave Surfer 42Xs, Sampling rate is 2.5GS/s
- Transducer and Wedge
  - Frequency (500 kHz, 1 MHz, 1.5 MHz, 2.25 MHz)
  - Inspection range (Length with respect to Frequency)
  - Wedge (20° ~ 70°)
- Calibration
  - Wave mode selection
  - Group velocity calibration
  - Measure weld and edge signal

### C.3.5.2 Inspection Technique

#### Examination Volume

- P4 specimen

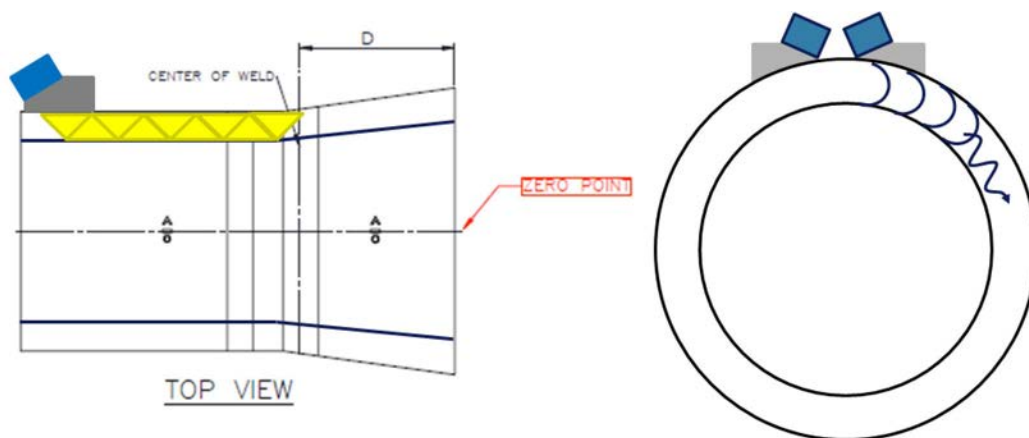
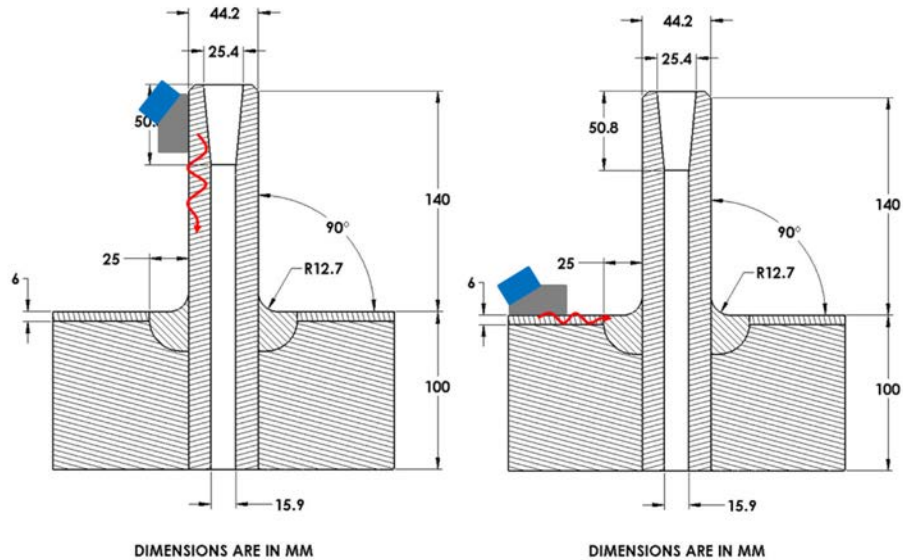


Figure C.192

Guided wave propagates into the specimen. This inspection method can be applied two different ways. First, guided wave is generated from axial direction to the specimen, so reflect signal from defect and weld can be detected by transducer. The other way is generate guided wave along the circumferential direction. Guided wave propagates through the specimen and travel whole specimen volume and receive signal from the other transducer.

- P5 specimen



**Figure C.193**

There are two different way to inspect on P5 specimen. One is generating guided wave on the bottom block. The other way is that generate guided wave from nozzle to weld part. It can detect weld delamination and defect between nozzle and weld.

### **Data Analysis of Guided Wave Signal**

Guided wave can propagate long distance on the inspection specimen. With long propagation distance, there are several features on wave RF signal. Over the distance, it is shown on Figure C.194, over the long distance on the pipe, some key feature information can be found on the signal.

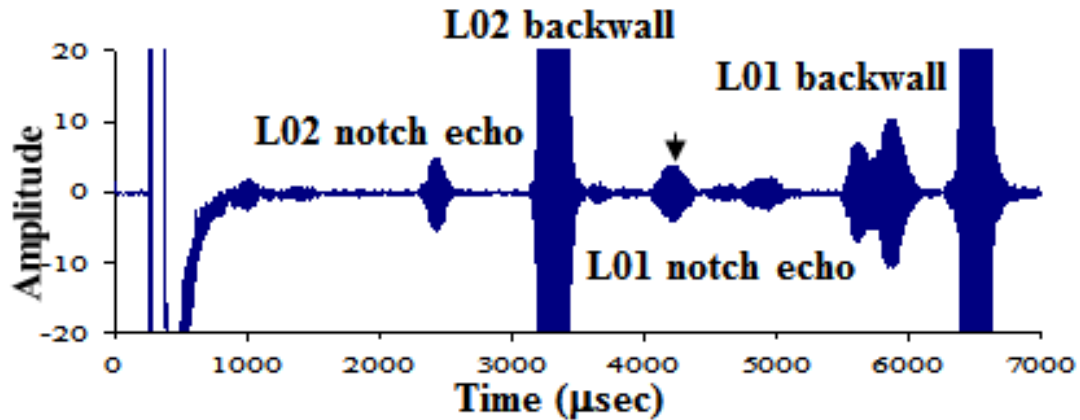


Figure C.194 Guided Wave Inspection Signal on the Long Distance Pipe

### C.3.6 Phased Ultrasonic Array, Technique ID 22-PA-SAFT1, 22-PA-SAFT2, 22-PA-TRT1, 22-PA-TRT2

#### C.3.6.1 Introduction

##### Scope

- This technical description is applicable to ultrasonic examination for dissimilar metal welds and adjacent material utilizing phased array ultrasonic techniques and applicable to the open RRT specimens.
- The objective of examination performed in accordance with this procedure is to accurately detect, length size and depth size for EDM notches, thermal fatigue cracks, fatigue cracks in the specified examination volume.

##### Personnel Requirement

- Personnel performing exams have experience for equipment setup, calibration, examination, time delay setup, signal interpretation, and data evaluation.

##### Specimens

- P29 specimen has one fatigue crack.

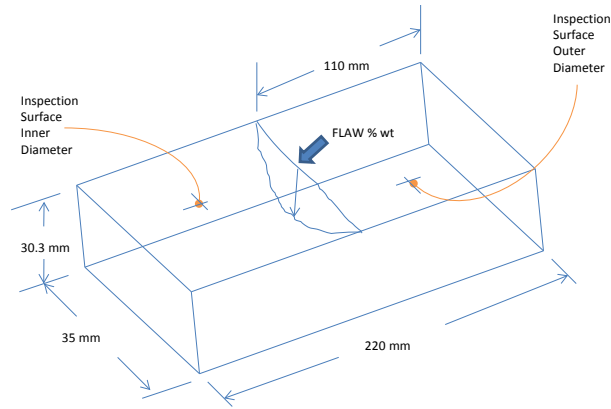


**Figure C.195 Schematic Diagram of P29 Specimen**

### C.3.6.2 Overview of Inspection System

#### System

- Phased Array Ultrasonic Testing System: Olympus Omniscan
- Scanner: Manual Scanner
- Software: Tomoview (collection and storing full waveforms)
  - MATLAB Program is used for determination of time delay using time reversal method.

#### Transducer and Wedge

- Total Number of Element: 16 and 32 Olympus Phased Array Ultrasonic Probes
- Frequency: 2.25 MHz
- Elements Size (Length/Width/Pitch): 44.8 mm/26 mm/2 mm (for 16 elements)  
: 24 mm/24 mm/0.75 mm (for 32 elements)

#### Calibration of System

- Instrument linearity check
- Sensitivity of each element using calibration block:
  - Scanning on the calibration block with scanning phased array ultrasonic probes
  - Checking the received scattering signals from the SDH in the calibration block
  - Adjust amplitude of the received signals to uniform by controlling gain value

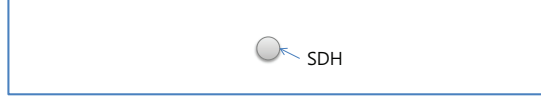


**Figure C.196 Calibration Block**

### C.3.6.3 Inspection Technique

#### Description of Inspection Technique

- To enhance flaw detectability, focusing of ultrasonic waves on a target in an inhomogeneous medium is a key issue.
- Time Reversal Technique provides a very robust technique to focus ultrasonic waves through inhomogeneous media as compared to conventional focusing techniques.

If we consider the wave equation in a lossless fluid medium without body force, we have the wave equation of pressure,  $p(\mathbf{x}, t)$ , as:

$$\nabla^2 p(\mathbf{x}, t) - \frac{1}{c^2} \frac{\partial^2 p(\mathbf{x}, t)}{\partial t^2} = 0 \quad (\text{C.5})$$

In Eq. (C.5), the wave equation contains a second-order time-derivative operator. Thus, if  $p(\mathbf{x}, t)$  is solution of Eq. (C.5), then  $p(\mathbf{x}, -t)$  also is another solution. Time reversal techniques rely on this property. So, if we have a received signal scattered from a flaw located in complex material, we have another wave theoretically that is time reversed one. Thus, using this property, we could precisely focus on a flaw.

The D.O.R.T. method is a detection technique that is derived from the theoretical analysis of TRM. As shown in Figure C.197, the signal received by the  $l^{\text{th}}$  element of the array transducer, which has  $N$  elements, is defined as

$$r_l(t) = \sum_{m=1}^N k_{lm}(t) \otimes e_m(t) \quad (\text{C.6})$$

where  $e_m(t)$  is the input signal applied to the  $m^{\text{th}}$  element,  $k_{lm}(t)$  is the impulse response from the  $l^{\text{th}}$  element to the  $m^{\text{th}}$  element and  $\otimes$  is the convolution in the time domain.

If we take the Fourier transform of Eq. (C.5) and use matrix notation, we have

$$\mathbf{R}(\omega) = \mathbf{K}(\omega) \mathbf{E}(\omega) \quad (\text{C.7})$$

where  $\mathbf{K}(\omega)$ , the transfer matrix, is an  $N \times N$  matrix (Prada et al. 1996). Since we consider the linear-time-invariant system, the new input signal at the  $i^{\text{th}}$  iteration,  $\mathbf{E}^i(\omega)$ , can be defined by

$$\mathbf{E}^i(\omega) = \mathbf{K}^*(\omega) \mathbf{E}^{i-1*}(\omega) \quad (\text{C.8})$$

where \* denotes complex conjugation corresponding to a time reversal. Thus, the received signal at the  $i^{\text{th}}$  iteration,  $\mathbf{R}^i(\omega)$ , can be written as

$$\mathbf{R}^i(\omega) = \left[ \left[ \mathbf{K}(\omega)^* \mathbf{K}(\omega) \right] \mathbf{E}^{i-1}(\omega) \right] \quad (\text{C.9})$$

where  $\mathbf{K}(\omega)^* \mathbf{K}(\omega)$  is called the time reversal operator (Prada et al. 1996).

Based on the assumptions, a linear time-invariant system and lossless medium, the transfer matrix is symmetrical. Thus, the time reversal operator is Hermitian positive. Also, the number of significant eigenvalues of the time reversal operator is equal to the number of well resolved scatterers (Prada et al. 1996). From the eigenvector corresponding to significant eigenvalues, we can obtain the time delays required to focus on the scatterer using Eq. (C.10).

$$\Delta t_i = \frac{\Delta \phi_i}{\omega} \quad (\text{C.10})$$

where  $\phi_i$  is the phase of the eigenvector.

- Procedure of pre-focused time reversal techniques as follow:
  - (1) Exciting ultrasonic waves with pre-calculated time delay using conventional method
  - (2) Received signals are measured by each element of the phased array probe
  - (3) Calculating eigenvalues and eigenvectors using the receive signals
  - (4) Determined number of flaws in the specimen using number of signification eigenvalues
  - (5) Calculating time delay using the eigenvalues for focusing ultrasonic waves on the flaws
  - (6) Re-firing ultrasonic waves using the calculated time delay

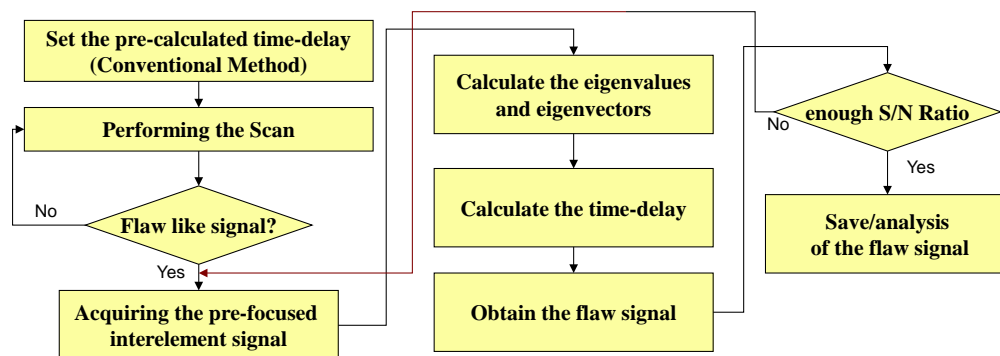


**Figure C.197 Procedure of Pre-focused TR Technique**

### Inspection Classification

- Flaw Indications:



- All indications produced by reflectors, except signals that can be clearly attributed to the geometrical or metallurgical properties of the weld configuration, shall be considered as flaw indication.
- Amplitude of signals and/or image is more than two time bigger than noise could be considered as indications.
- Flaw Location:
  - Location of flaw determines based on time of flight of the flaw indications and sound velocity of the specimen
- Flaw Sizing:
  - Size of the flaw calculate from amplitude of reflected signals from cracks including EDM notches
  - Also, tip echo method (one of Tip Diffraction Methods) will be apply to calculate size of the flaws

### **Examination Reporting**

- Examination reporting is following PARENT RRT guideline:
  - (1) Parent RRT-Procedure Summary Data Sheet
  - (2) Parent RRT-DMW Technique Data Sheet
  - (3) Parent RRT-DMW Inspection Summary Data Sheet
  - (4) Calibration Data Sheet
- Also, provide A-Scan signals and Scan images of detected flaws in the specimens

### C.3.6.4 Appendix

## Calibration Data Sheet

Calibration Data Sheet for Ultrasonic Examination ( Phased Array Examinaion)										Data sheet No.	
Object of Inspection	Name: Parent RRT		No.: P29		Inspection Method: Phased Array UT			Date: 2013.03.05-06			
Inspection Equipment	Fabricator: R/D TECH		Model: TomoScan FOCUS LT		Serial No.: FLJ-1026			Inspected by: Hak-Joon Kim		Level:	
Reference Block	No.: ASTM E164 FTW TYP		Nominal Size:		Material:			Confirmed by:		Level:	
Array Probe	Element Size(mm):	10 x 38.4	Element Pitch(mm):	0.6	Number of Element:	64					
Condition	Evaluation Angle		Freq.	Fabricator	Model	Serial No.	Probe Index Point(mm)	Reference Sensitivity(dB)	EL:Echo Height (CRT%)/ PL: Beam Path Length (mm)		
	Nominal	Measured									
1	45	45	5								
2											
3											
Couplant: Ultra Gel										Cable Length: 2m	
Remarks:										Signature	

PAGE: 12 of 12

## PARENT RRT-Procedure Summary Data Sheet

Round Robin Test Forms for Protocol Revision 17

PNNL

### PARENT RRT – PROCEDURE SUMMARY Data Sheet

Procedure ID: 22.1  
 Procedure Type: PAUT  
 Scan Direction: Axial  
 Length Sizing: yes  
 Scan Type: Man

Team ID: 22  
 Scan Access: OD  
 Detection: yes  
 Depth Sizing: yes

Description for Combining Techniques:

Detection		
Tech-ID	Description	Evaluation Method
1.	PAUT(P-WAVE)	Synthetic Aperture Focusing Technique
2.	PAUT(S-WAVE)	Synthetic Aperture Focusing Technique
3.	PAUT(P-WAVE)	Time Reversal Technique
4.	PAUT(S-WAVE)	Time Reversal Technique

Characterization		
Tech-ID	Description	Evaluation Method
1.	PAUT(P-WAVE)	Echo Dynamic Pattern
2.	PAUT(S-WAVE)	Echo Dynamic Pattern
3.	PAUT(P-WAVE)	Echo Dynamic Pattern
4.	PAUT(S-WAVE)	Echo Dynamic Pattern

Length Sizing		
Tech-ID	Description	Evaluation Method
1.	Amplitude Analysis(P-WAVE)	6DB Method
2.	Amplitude Analysis(S-WAVE)	6DB Method
3.	Amplitude Analysis(P-WAVE)	6DB Method
4.	Amplitude Analysis(S-WAVE)	6DB Method

Depth Sizing		
Tech-ID	Description	Evaluation Method
1.	Amplitude and time Analysis(P-WAVE)	Tip Echo Method
2.	Amplitude and time Analysis(S-WAVE)	Tip Echo Method
3.	Amplitude and time Analysis(P-WAVE)	Tip Echo Method
4.	Amplitude and time Analysis(S-WAVE)	Tip Echo Method

Defect Positioning		
Tech-ID	Description	Evaluation Method
1.	Amplitude and time Analysis(P-WAVE)	Echo Dynamic Pattern, Signal Amplitude, Time Delay
2.	Amplitude and time Analysis(S-WAVE)	Echo Dynamic Pattern, Signal Amplitude, Time Delay
3.	Amplitude and time Analysis(P-WAVE)	Echo Dynamic Pattern, Signal Amplitude, Time Delay
4.	Amplitude and time Analysis(S-WAVE)	Echo Dynamic Pattern, Signal Amplitude, Time Delay

## PARENT RRT-DMW Techniques Data Sheet

**PARENT RRT – DMW TECHNIQUE Data Sheet**

Procedure ID: 22.1  
*team-id seq-no*  
 Inspection ID: 22.P29.1  
*team-id block-id seq-no*  
 Test Block ID: P29  
 Team ID: 22

Tech ID: 1  
 Access: OD  
 Date: 2012/03/05-06

Weld Volume Inspected:

Detection: yes	X1(mm):0	X2(mm):35
Length Sizing: yes	Y1(mm):130	Y2(mm):130
Depth Sizing: no	Z1(mm):0	Z2(mm):0

Defect No	X1 mm	X2 mm	Y1 mm	Y2 mm	Z1 mm	Z2 mm	Y <sub>max</sub> mm	Amp dB	Surface Breaking	Comments
1	0	35	110	110	N/A	N/A	17.5	45	YES	Using Longitudinal Wave, Synthetic Aperture Focusing

**TEAM SIGN:**

**INVIGILATOR SIGN:**

**PARENT RRT – DMW TECHNIQUE Data Sheet**

Procedure ID: 22.1  
*team-id seq-no*  
 Inspection ID: 22.P29.1  
*team-id block-id seq-no*  
 Test Block ID: P29  
 Team ID: 22

Tech ID: 2  
 Access: OD  
 Date: 2012/03/05-06

Weld Volume Inspected:

Detection: yes	X1(mm):0	X2(mm):35
Length Sizing: yes	Y1(mm):130	Y2(mm):130
Depth Sizing: no	Z1(mm):0	Z2(mm):0

Defect No	X1 mm	X2 mm	Y1 mm	Y2 mm	Z1 mm	Z2 mm	Y <sub>max</sub> mm	Amp dB	Surface Breaking	Comments
1	0	35	110	110	N/A	N/A	17.5	45	YES	Using Shear Wave, Synthetic Aperture Focusing

**TEAM SIGN:**

**INVIGILATOR SIGN:**



# PARENT RRT-DMW Inspection Summary Data Sheet

Round Robin Test Forms for Protocol Revision 17

PNNL

## PARENT RRT – DMW INSPECTION SUMMARY Data Sheet

Inspection ID: 22.P29.1  
*team-id block-id seq-no*  
 Test Block ID: P29  
 Team ID: 22

Procedure ID: 22.1  
*team-id seq-no*  
 Date: 2012/03/05-06

Weld Volume Inspected:

X1(mm):0                      X2(mm):35  
 Y1(mm):130                 Y2(mm):150  
 Z1(mm):0                      Z2(mm):0

Defect No	X1 mm	X2 mm	Y1 mm	Y2 mm	Z1 mm	Z2 mm	$V_{max}$ mm	Amp dB	Surface Breaking	Comments
1	0	35	110	110	20.3	30.3	17.5	45	YES	Using Shear Wave(Tech No. 4)

**TEAM SIGN:**

**INVIGILATOR SIGN:**

## C.3.7 Higher Harmonic Ultrasound Technique, Technique ID 30-HHUT0, 30-HHUT1

### C.3.7.1 Overview

#### Introduction of Nonlinear Ultrasonic Technique

We applied the nonlinear ultrasonic technique (NUT), higher harmonic ultrasonic technique (HHUT) for PARENT Open Test specimens (ID 28, 29 and 30) having the crack in DWM to detect the existence of the close crack and measure its depth.

In PARENT Open RRT, we investigated the higher-harmonic generation effect at the crack. Its basic principle is the contact acoustic nonlinearity (CAN) that generates the harmonic frequency components owing to the crack temporarily closed and opened or the nonlinear pressure-displacement relation at the contact interface when ultrasonic waves encounter the imperfect interfaces shown as Figure C.198. As the result, the acoustic wave waveform becomes distorted and the higher harmonic frequency components are generated in the transmitted wave or in the reflected wave from the crack. The magnitude of the harmonic frequency component depends on the crack opening distance (COD) or the contact stiffness of crack interfaces (Abeele and Windels 2006; Biwa et al. 2006; Buck et al. 1978; Jhang 2000; Kim et al. 2006; Solodov et al. 2006; Ulrich et al. 2008).

Thus, it would be possible to detect closed cracks by monitoring the magnitude of the higher harmonic frequency component generated in the transmitted or the reflected wave. Usually, considering up to the second order nonlinearity, the relative nonlinear parameter ( $\beta'$ ) defined by

the ratio of the second order harmonic frequency magnitude to the power of the fundamental frequency magnitude is used as the monitoring parameter, which is convenient for the relative evaluation (Jhang 2000). We were expecting that this parameter would much more sensitive to closed-cracks than the conventional linear characteristics of ultrasonic waves. Many studies have been done for modeling and verifying this phenomenon (Biwa et al. 2006; Buck et al. 1978; Hirsekorn et al. 2006; Kim et al. 2006; Ohara et al. 2003; Solodov 1998).

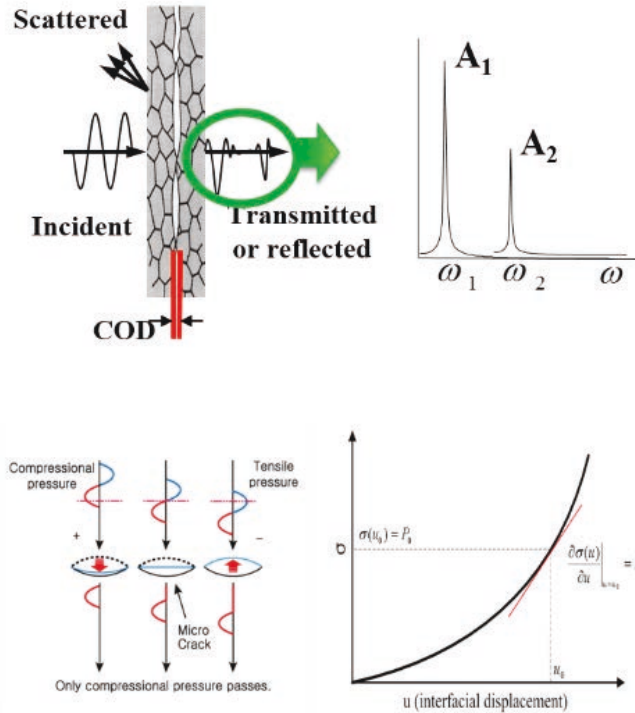


**Figure C.198 The Basic Principle of the Contact Acoustic Nonlinearity**

For the test, we designed the measurement system with PZT transducers and the pneumatic clamping equipment. By doing so, the experimental conditions could be consistent, which assured the reliable measurement of the  $\beta'$ . In our experiments, two kinds of inspection methods were carried out as follows.

- **Pulse echo (PE)**

This technique shown as Figure C.199 is one of common techniques in ultrasonic testing where a pulsed wave is transmitted into the sample and then the reflected signal from discontinuities is received. When we know the wave velocity in the material, we can locate the defect. As the application of this technique for HHUT, we will use the broadband transducer of 5 MHz main-resonance frequency. We generated the longitudinal waves of 3 MHz high power tone burst.

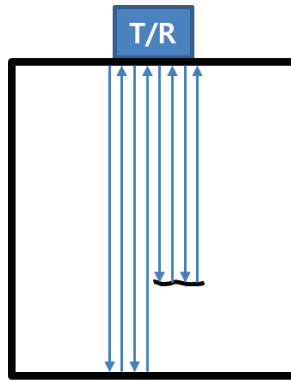


**Figure C.199 Pulse Echo Technique**

- **V-scan (VS)**

In this technique, the ultrasonic beam path follows V-line shown as Figure C.200. The beam path looks V-line when two transducers for transmitting and receiving the ultrasonic are put oppositely within one skip distance space. If a crack exists on the beam path, the amplitude of the received signal will decrease. By doing so, we can identify the existence of a crack. As the application of this technique for HHUT, we used two 45° angle beam transducers. The transducer of 2 MHz main-resonance frequency was used as a transmitter and one of 4 MHz was used as a receiver to measure the harmonic frequency component sensitively.

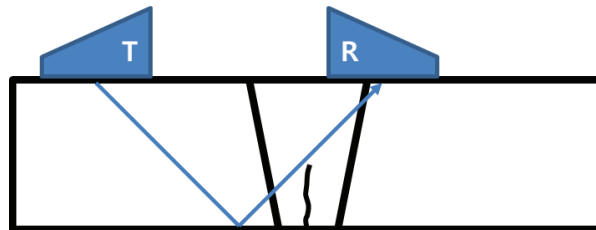


**Figure C.200 V-scan Technique**

### **Sensitivity and Resolution of HHUT**

There is no report on the sensitivity and the resolution of HHUT since it is strongly dependent on the equipment and the measurement skill at the present stage. Instead, we have tried to show the excellence of HHUT in sizing performance by comparing the lengths of defects artificially fabricated in the acrylic and the aluminum specimens by using conventional linear ultrasonic technique (UT) and HHUT. UT measures only the amplitude of the reflection or the transmission signal, whereas HHUT measures nonlinear parameter by measuring the ratio of the fundamental and the second harmonic frequency magnitudes in the transmission or the reflection signal. The measured result showed HHUT was more accurate than UT. Details are shown in below.

- **Acrylic Specimen**

An acrylic specimen was made of two blocks by being contacted together. One of the blocks has flat surface and the other has unevenness on the contacting surfaces. Thus only the outside of uneven area will be contacted. Unevenness was fabricated by polishing with #220 sand

papers. The picture of the specimens is shown as Figure C.201. There are two kinds of specimens with different uneven areas. The change of the contact area according to the contacting pressure is shown as Figure C.202, which was taken by ink print. The initial noncontact area in No. 1 specimen is bigger than that in No. 2 specimen, and the initial axial length of noncontact areas were measured as approximately 40 mm and 30 mm, respectively. According to the increase of pressure, the noncontact area became decreased: The decreasing rate in No. 1 was faster than in No. 2, which means that the unevenness of No. 1 specimen is smaller than No. 2 specimen.

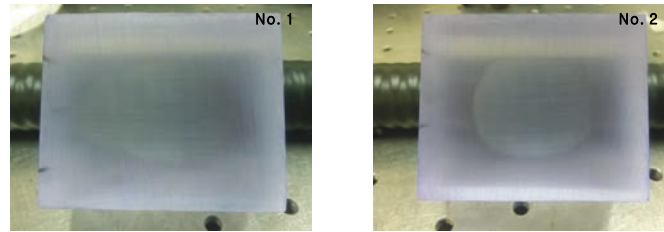


**Figure C.201 Shape of Defects in Acrylic Specimens**

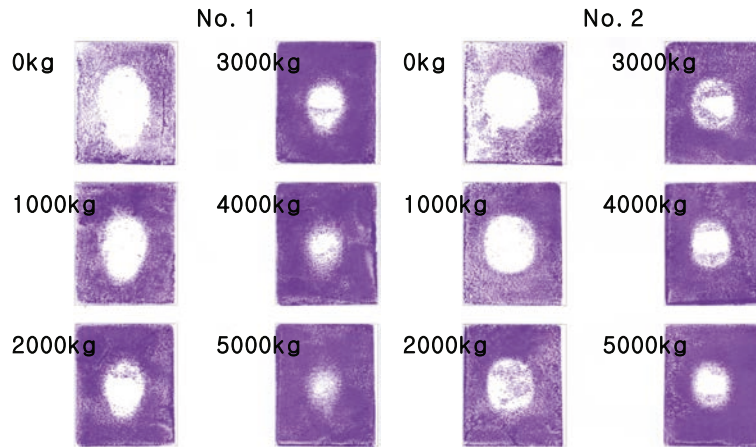


**Figure C.202 The Change of the Contact Area According to the Increase of Contacting Pressure**

When changing the contacting pressure, the result of ultrasonic test is shown as Figure C.203. The left side of the figure shows the result of the linear method, and right side shows the nonlinear parameter using the pulse echo method. The result of the linear method shows the large amplitude at the noncontact area while the nonlinear parameter showed the large amplitude at the boundaries of contact and noncontact interfaces. This means that the boundaries act as partially closed interfaces so that the contact acoustic nonlinearity is activated in maximum there.



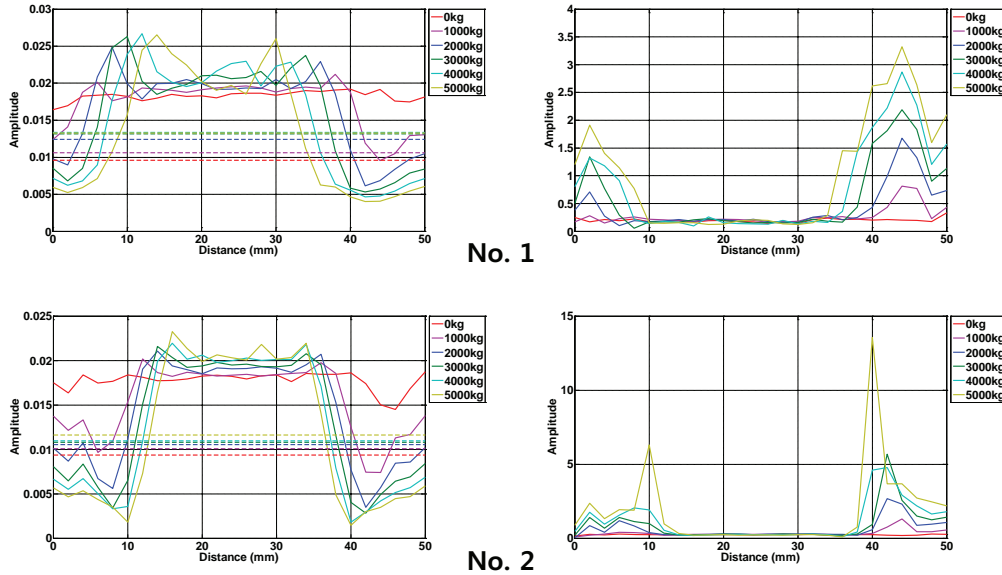


**Figure C.203 Amplitude of (left) –6 dB Method and (right) Relative Nonlinear Parameter**

Table C.2 shows the results of measuring the axial length of the noncontact area by using the 6 dB drop method in UT and by measuring the distance between left and right side peaks of nonlinear parameter in HHUT. UT evaluated the size smaller than the real size. Moreover, the measured size is decreasing by the increase of the contact pressure. On the other hand, HHUT evaluated the size in similar to real size regardless of the contact pressure. These results support the usefulness of HHUT for the detection of closed interfaces and for the improvement of the sizing accuracy.

**Table C.2 Result of Unevenness Size Measurement at Different Loading (dimension in mm)**

Load	No. 1		No. 2	
	6 dB drop method	Consider $\beta'$	6 dB drop method	Consider $\beta'$
0 kg	-	-	-	-
1000 kg	43	43	34.2	38
2000 kg	35	42	29.6	32
3000 kg	30.8	42	27.2	30
4000 kg	28.2	42	25.3	30
5000 kg	24.5	42	23.7	30

- CT Specimen

The dimension of the specimen used in our investigation is shown as Figure C.204, which is a compact tension (CT) specimen of Al6061 material. This specimen was degraded by the fatigue test to initiate a micro-crack from the notch. There are opened cracks around V-notch and closed cracks around crack tip. The measurement size from notch to crack tip is roughly 10 mm.

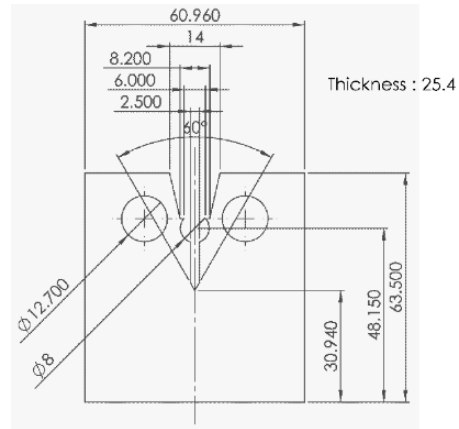


**Figure C.204 Geometry of Specimen (dimension in mm)**

The magnitudes of the fundamental frequency and the second harmonic frequency at different measuring positions along the crack direction from notch are shown as Figure C.205. For this, the pulse echo technique was used. The maximum magnitude of the fundamental frequency appears at 4 mm, and the crack length was measured by 6.5 mm by using 6 dB drop method. On the other hand, the second harmonic magnitude shows the maximum value at 5 mm as well as has large value until 9 mm, which is close to the real size of the crack.

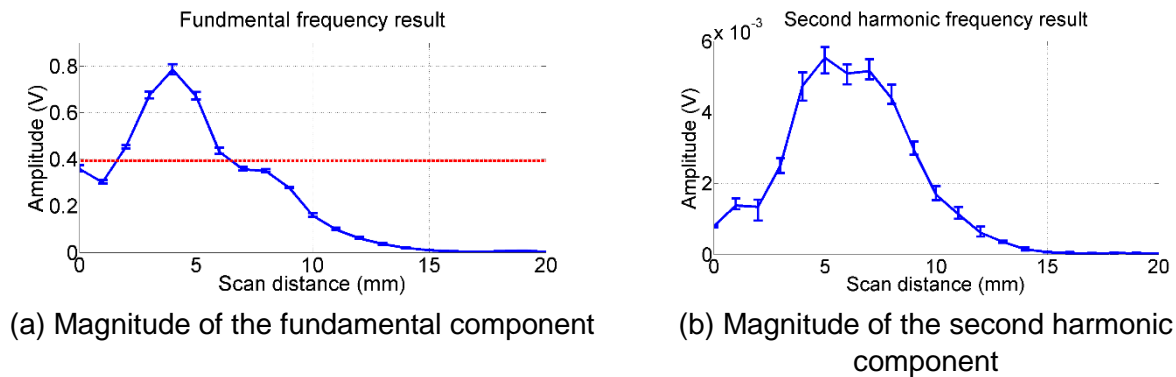


**Figure C.205 Result of Crack Length Using Pulse Reflection Method and Nonlinear Ultrasound**

From this result, we will be able to solve the problem of the conventional ultrasonic technique that is to underestimate the size of the crack. The conventional ultrasonic techniques was sensitive to only the open crack. However, nonlinear ultrasonic technique was sensitive to the

closed crack. Therefore, the evaluation method of the length of the crack using the nonlinear ultrasonic, it may become an important technique to verify the integrity of the structure.

### C.3.7.2 Introduction of the Experimental Equipment and Setup

#### Experimental Equipment

The broadband transducer (Olympus) of 5 MHz main-resonance frequency is shown as Figure C.206(a). The diameter of the transducer is 10 mm. The angle beam transducer (Krautkramer) is shown as Figure C.206(b). The yellow one and the blue one have 2 MHz and 4 MHz main-resonance frequencies, respectively. The size of the transducer is 8 X 9 mm.



(a)



(b)

**Figure C.206 Transducers Used in (a) Pulse Echo Method and (b) V-scan Method**

To generate a high power tone-burst signal, a high-power gated amplifier (RAN-5000 SNAP) was used.



**Figure C.207 High Power Pulser-Receiver (RAM-5000 SNAP)**

In the experiment, the received signal was A/D converted by using NI PCI-5122 board (National Instruments). The board has 100 M/s real time sampling and its resolution is 14 bits.

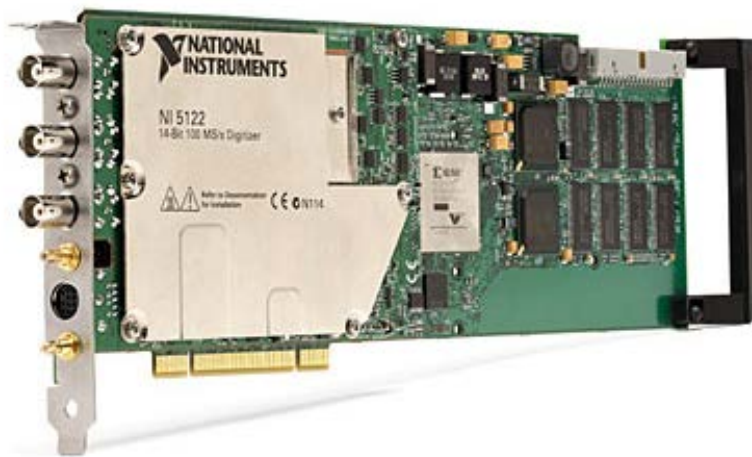


**Figure C.208 A/D Board (NI PCI-5122)**

When the received signal level is too low, it should be amplified. For that, the pulser-receiver 5077PR (Olympus) was used.



**Figure C.209 Pulser-Receiver (5077PR)**

Universal motion controller / driver ESP300 (Newport) was used to move the transducer in the interval of 1 mm. This controller / driver is used with the motorized linear stage M-433 (Newport).



**Figure C.210 Universal Motion Controller / Driver (ESP300)**

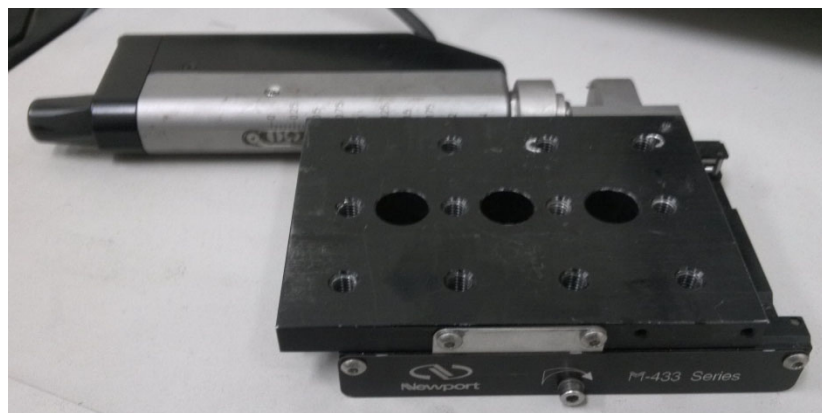


**Figure C.211 The Motorized Linear Stage (M-433)**

And pneumatic system (self-production) was employed to keep constant pressure between transducers and specimens. The loaded pressure was 0.7 MPa.

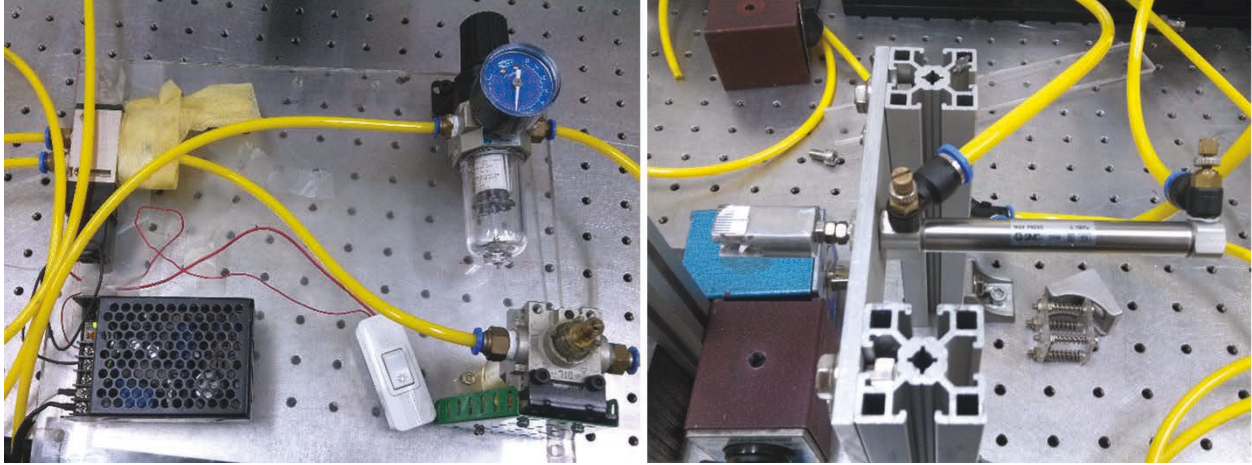


Figure C.212 Pneumatic System

**Experimental Setup (Pulse Echo)**

To apply the pulse-echo method, the experimental system was set shown as Figure C.213. The experimental conditions and parameters were controlled as Table C.3.

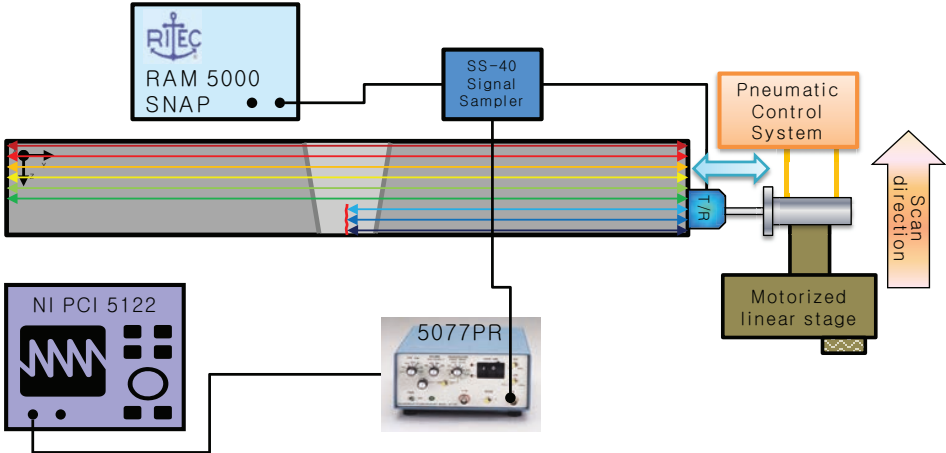


Figure C.213 Experimental Setup

Table C.3 RAM-5000 & 5077PR Setting Condition

RAM-5000 & 5077PR Setting
---------------------------

Frequency	3
No. of Cycle	11
GA Output	50
Gain	+ 30 dB
HPF	1 MHz
LPF	FULL BW

In the pulse-echo method, the specimen was scanned from 23 mm to 7 mm on Z-axis at interval of 1 mm. This Z-axis measurement was conducted repeatedly from 7.5 mm to 22.5 on X-axis at interval of 5 mm.

### C.3.7.3 Experimental Setup (V scan)

To apply the V-scan method, the experimental system was set shown as Figure C.214. The experimental conditions and parameters were controlled as Table C.4.

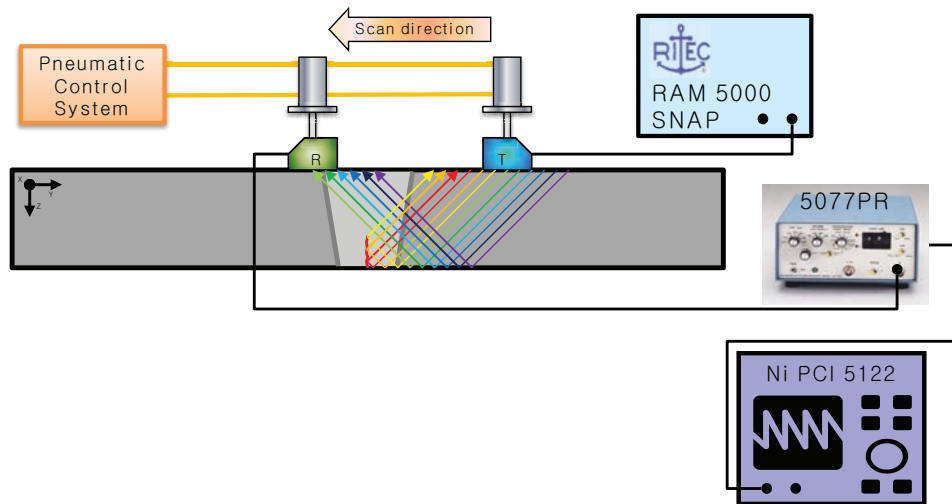


Figure C.214 Experimental Setup

Table C.4 RAM-5000 & 5077PR Setting Condition

RAM-5000 & 5077PR Setting	
Frequency	2
No. of Cycle	11
GA Output	60
Gain	+ 10 dB
HPF	OUT
LPF	FULL BW

In the V-scan technique, the specimen was scanned on Y-axis at interval of 1 mm. Likewise, with the pulse-echo method, the specimen was scanned on X-axis at interval of 5 mm.

#### C.3.7.4 The Data Acquisition Process/Parameters

For acquiring the data by using HHUT method in PARENT specimen, A-scan signal was measured in the way of the pulse-echo method shown as Figure C.215. Select a signal from the full time echo signal by using a fixed time gate, of which time range covers the echo from the welded area only.

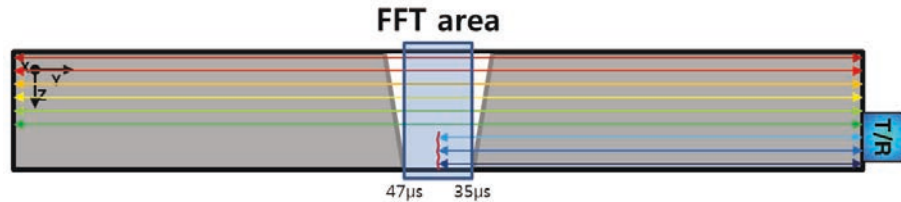


**Figure C.215 The Region of Data Acquire (PE)**

On Z-axis, the scan was carried out from the bottom to the top (23 ~ 7 mm) at interval of 1 mm by using motorized linear stage. On X-axis, the data was manually acquired from 7.5 mm to 22.5 mm at interval of 5 mm. Transducer was placed on the right side of the specimen in order to transmit the ultrasonic wave towards the direction perpendicular to the crack propagation direction. The other information such as the transmit frequency, the number of cycle and the gain of the receiver is tabulated in Table C.3.

In the V-scan method, A-scan signal was acquired shown as in Figure C.216. Select a signal from the full time echo signal by using a fixed time gate, of which time range covers the echo from the welded area only.

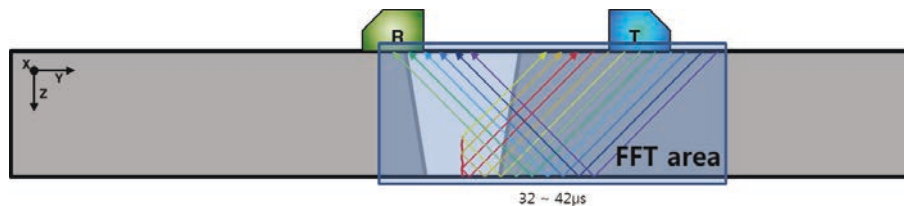


**Figure C.216 The Region of Data Acquire (VS)**

On Z-axis, the receiver was manually moved from 76 mm to 114 mm and the transmitter was manually moved from 136 mm to 174 mm at interval of 1 mm by using motorized linear stage. On X-axis, the data was manually acquired from 7.5 mm to 22.5 mm at interval of 5 mm same as PE. Transducer was placed on the top side of the specimen. The other information such as the transmit frequency, the number of cycle and the gain of the receiver is tabulated in Table C.4.

By converting the scan data from the relevant area same as Figure C.217, the crack size can be measured. Here, Z0 is the first scan point and Z30 is the last scan point.



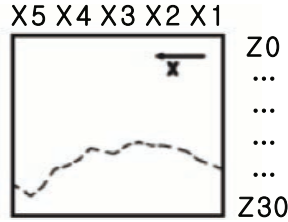


**Figure C.217 The Converted Axis (VS)**

### C.3.7.5 Signal Processing Performed on the Acquired Data

From the acquired data with each method, the magnitudes of the fundamental frequency ( $A_1$ ) and the second harmonic frequency ( $A_2$ ) were obtained by using fast-Fourier transform in the time interval (PE: 35 ~ 47  $\mu$ s, VS: 32 ~ 42  $\mu$ s) presumed to be the crack signal. The relative nonlinear parameter ( $\beta'$ ) was calculated from Eq. (C.11).

$$\beta' = \frac{A_2}{A_1^2} \quad (\text{C.11})$$

Fast-Fourier transform was processed in MATLAB. Here, zero-padding was 200 times to length of the data and any window function was not applied.

### C.3.7.6 Acquired Data Analysis for the Technique

Through the signal processing, the depth of the crack was estimated from the magnitudes of fundamental and the second harmonic frequency components, the relative nonlinear parameter. The estimation algorithm was shown as Figure C.218.

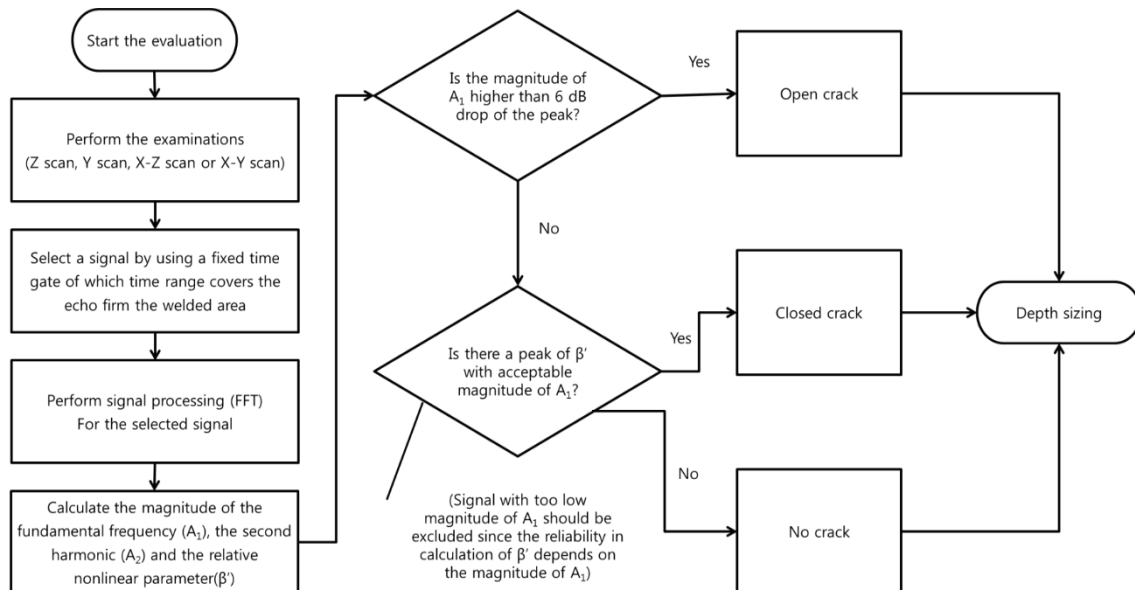


**Figure C.218 Flow Chart for Detection and Depth Sizing of Crack**

### C.3.8 References

- Abeele K and F Windels. 2006. "Characterization and Imaging of Microdamage Using Nonlinear Resonance Ultrasound Spectroscopy (NRUS): An Analytical Model." In *Universality of Nonclassical Nonlinearity*, pp. 369-388, Ch. 23. ed: P Delsanto. Springer, New York.
- Biwa S, S Hiraiwa and E Matsumoto. 2006. "Experimental and Theoretical Study of Harmonic Generation at Contacting Interface." *Ultrasonics* 44, Supplement:e1319-e1322.
- Buck O, WL Morris and JM Richardson. 1978. "Acoustic Harmonic Generation at Unbonded Interfaces and Fatigue Cracks." *Applied Physics Letters* 33(5):371-373.
- Cheong YM, JH Kim, JW Hong and HK Jung. 2000. "Measurement of Dynamic Elastic Constants of RPV Steel Weld due to Localized Microstructural Variation." *Journal of Korean Society of Nondestructive Testing* 20(5):390-396. In Korean.
- Hirse Korn S, M Hirsekorn and PP Delsanto. 2006. "Nonlinear Ultrasonic Transmission Through Thin Bonded Interfaces: Theoretical Background and Numerical Simulations." In *Universality of Nonclassical Nonlinearity*, pp. 231-250, Ch. 15. ed: P Delsanto. Springer, New York.
- Jhang K-Y. 2000. "Applications of Nonlinear Ultrasonics to the NDE of Material Degradation." *IEEE Transactions on Ultrasonics, Ferroelectrics and Frequency Control* 47(3):540-548.
- Kim J-Y, A Baltazar, JW Hu and SI Rokhlin. 2006. "Hysteretic Linear and Nonlinear Acoustic Responses from Pressed Interfaces." *International Journal of Solids and Structures* 43(21):6436-6452.
- Ohara Y, K Kawashima, M Murase and N Hirose. 2003. "Identification of Sintered Irons with Ultrasonic Nonlinearity." In *Review of Progress in Quantitative Nondestructive Evaluation, Vol. 22*, pp. 1257-1264. July 14-19, 2002, Bellingham, Washington. American Institute of Physics, Melville, New York.
- Prada C, S Manneville, D Spoliansky and M Fink. 1996. "Decomposition of the Time Reversal Operator: Detection and Selective Focusing on Two Scatterers." *The Journal of the Acoustical Society of America* 99(4):2067-2076.
- Solodov I, K Pfeleiderer and G Busse. 2006. "Nonlinear Acoustic NDE: Inherent Potential of Complete Nonclassical Spectra." In *Universality of Nonclassical Nonlinearity*, pp. 467-486, Ch. 29. ed: P Delsanto. Springer, New York.
- Solodov IY. 1998. "Ultrasonics of Non-linear Contacts: Propagation, Reflection and NDE-applications." *Ultrasonics* 36(1-5):383-390.
- Ulrich TJ, AM Sutin, RA Guyer and PA Johnson. 2008. "Time Reversal and Non-linear Elastic Wave Spectroscopy (TR NEWS) Techniques." *International Journal of Non-Linear Mechanics* 43(2):209-216.

## C.4 USA Detailed Technique Descriptions

### C.4.1 Eddy Current Technique, Technique ID 7-ECT1

#### C.4.1.1 Overview

The data were taken using an eddy current inspection technique. This is a well-established technique for finding surface defects in conducting materials. In it, a coil is excited with an AC current at one or more frequencies. The magnetic field from the coil induces eddy currents in the test specimen. These eddy currents diffuse through the specimen. Defects in the specimen cause changes in the amplitude and direction of these eddy currents. These changes can be measured as changes in either the impedance of the exciting coil, or as changes in the amplitude and phase of the voltage induced in a second receiving coil. In the technique used here, we employed the receiving coil. This approach is illustrated in the Figure C.219.

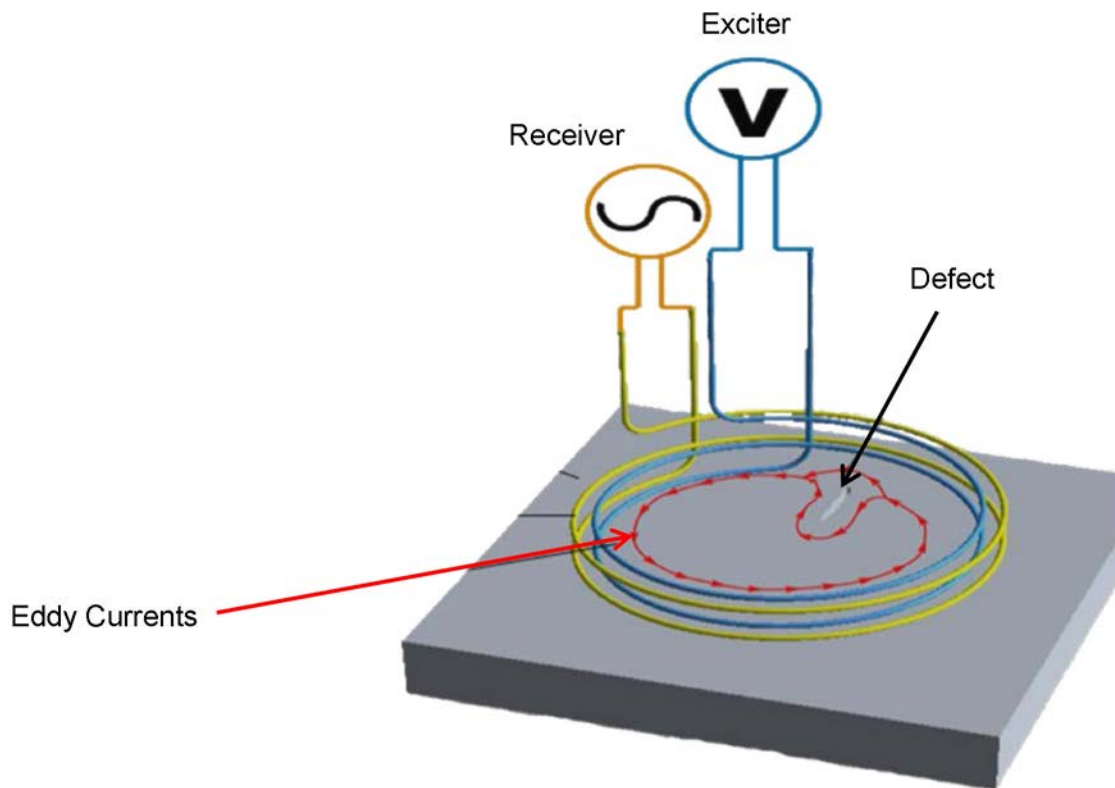


**Figure C.219** Illustration of Eddy Current Testing Flaw Detection Using Separate Exciter and Receiver Coils

In the approach used for these tests, a flexible probe consisting of an array of exciter and receiver coils shown in Figure C.220 was used. The exciter and receiver coils are physically displaced in the test surface plane, as can be seen in the figure; the displacement was chosen to reduce signal variations caused by probe liftoff variations. The largest flaw signal is obtained when the flaw lies along the axis formed by the centers of the two displaced coils. In operation,

the probe is scanned over the surface of the specimen. For these tests, the scanning was performed manually.



**Figure C.220 Flexible Eddy Current Probe and Rigid Adapter Board**

#### **C.4.1.2 NDE Equipment**

A CoreStar Omni 200 ET instrument and a Southwest Research Institute (SwRI) flexible eddy current probe, shown in the Figure C.220, were used. The probe was SwRI Part Number 201115836-003. A rigid adapter board (also shown in Figure C.220), Part Number 201115836-004, was used to connect the flexible array to the eddy current instrument cables. The probe includes 9 coils arranged in 3 rows of 3 coils each. The 3 coils in the center are operated as exciters; each additional row of 3 coils on either side of the exciter row are used as sensors, with the probe operated in driver-pickup mode; that is, one coil is used as an exciter and the other as a receiver, for each channel used. The spacing between the exciters and receivers had been chosen to minimize the effect of liftoff variations based on tests on different (carbon steel) specimens. The probe was operated at a test frequency of 50 kHz. Only a single exciter/receiver coil set on the probe was used for these tests. The probe phase was adjusted so that liftoff variations on the specimens were primarily in the horizontal direction on the instrument. The probe was designed for detection of relatively large flaws on rough welded surfaces, and for operation at frequencies greater than 50 kHz; it was therefore not surprising that there was no significant phase difference information that could be used to estimate flaw depth.

#### **C.4.1.3 Data Acquisition Process**

For the test performed, the instrument was first set up on a calibration plate. The plate is A36 steel; it contains 3 EDM notches. The probe was scanned around the plate; the phase of the display was rotated to make liftoff variations be primarily in the horizontal direction.

For data acquisition, the probe was scanned manually around the penetration, held against the surface by manual pressure. The orientation of the probe was also varied manually; the probe was rotated to maximize the response to any observed defect.

#### **C.4.1.4 Data Analysis**

No additional signal processing was performed on the data. The technique was developed to detect and locate surface-breaking defects. Therefore, analysis consisted primarily of estimating the location of the ends of the flaws.

Flaw position was estimated using a visual technique in order to eliminate the need for a mechanized scanner. Holes were punched in gaps between coils of the probe. Flaw edges were estimated by manually scanning the probe and observing the amplitude of coil pairs that had the largest signal indication. Locations where the amplitude dropped by 6 dB were designated as ends of flaws, and a marker was used to mark the mockup surface through the holes in the probe. Generally, 4 marks were made for each observed flaw. The marks can be seen in the photographs shown with each flaw. The eddy current instrument impedance plane display was recorded at the location of maximum flaw amplitude response.

The position of the marks, and therefore the estimated position of the flaws, was first measured using a coordinate measuring machine (CMM) at SwRI. This machine is maintained in calibration, with an accuracy much better than 0.1 mm. The machine was set up so that it reported X-Y coordinates, with the origin at the plane of the surface of the block and at the center of the penetration. The CMM machine was used to generate position values for the marks that had been placed on the specimens. Flaw ends were estimated by averaging the 2 pairs of locations marked for each flaw. Then the X-Y coordinates were converted into R-theta values for reporting.

After following this procedure, it was noted that the angular positions were generally accurate, but the values of R1 and R2 were too large, especially on blocks P21 and P22. The errors were typically 5 to 9 mm. Visual examination of the photographs showing the flaws and the marks on these blocks clearly showed that the flaw ends were marked much more accurately than reported. Therefore, a different method was used for measuring the locations for blocks P21 and P22. For block P21, which consists of radially oriented EDM notches, the theta values as determined by the CMM were retained. The values of R1 and R2 were determined by measuring the error in pixels in the photographs, and determining a scale factor of pixels per mm using the known flaw length. For block P22, the location of the flaw ends and the marks were measured in pixels. The 2 marks near each flaw end were averaged to provide a position of each flaw end. Then the error in pixels between each actual flaw end and the estimated flaw end was calculated. The error in pixels was converted to mm using the reported flaw length. The same scale factor of pixels to mm was used for both X and Y axes. Then the estimated flaw end locations were converted to mm, and these X-Y coordinates were converted to R-theta coordinates.

#### **C.4.1.5 Self Assessment**

The advantages of this type of ET probe are

- Low cost for the part of the probe that will be subject to wear.
- Possibility of manufacturing with even greater number of coils to ensure 100% coverage with a single scan.
- Fabrication technique ensures accurate manufacturing repeatability.
- Probe flexibility greatly simplifies the motions required of a mechanized scanner, especially in the case of penetrations that are not normal to the vessel surface.

The disadvantage of this approach was

- The use of single layer flexible printed circuit material (used to provide great flexibility) limits the number of turns of the coil; hence, the spatial resolution is limited and the operating frequency had to be kept at 50 kHz or greater.

**PARENT RRT – BMI TECHNIQUE Data Sheet**

Procedure ID: 7.1 Tech ID: 7-ECT1  
 Inspection ID: 7.P21.1 Access: OD  
 Test Block ID: P21 Date: 2012/11/28  
 Team ID: 7

Weld Volume Inspected:

Detection:	Yes	$\theta 1$ :	0	$\theta 2$ :	360
Length Sizing:	Yes	R1:	10	R2:	90
Depth Sizing:	No	Z1:	0	Z2:	0

Defect No	$\theta 1$ Deg.	$\theta 2$ Deg.	R1 mm	R2 mm	Z1 mm	Z2 mm	$R_{max}$ mm	Amp dB	Surface Breaking	Comments
BTE-1	358.5	358.6	27.6	32.1	n/a	n/a	n/a	n/a	yes	See below
BTE-2	269.7	268.8	27.0	33.7	n/a	n/a	n/a	n/a	yes	See below
BTE-3	178.5	177.5	26.3	33.3	n/a	n/a	n/a	n/a	yes	See below
BTE-4	88.9	89.6	22.2	38.2	n/a	n/a	n/a	n/a	yes	See below

Note: Flaw location end points were determined by using an amplitude drop technique and physically marking the probe location at the flaw edges (reference the attached test specimen photos showing the marks made on the block to show flaw location). Each mark was then measured using the BMI coordinate system.

**PARENT RRT – BMI INSPECTION SUMMARY Data Sheet**

Inspection ID: 7.P21.1 Procedure ID: 7.1  
 Test Block ID: P21 Date: 2012/11/28  
 Team ID: 7 Access: OD

Weld Volume Inspected:

Detection:	yes	$\theta 1$ :	0	$\theta 2$ :	360
Length Sizing:	yes	R1:	10	R2:	90
Depth Sizing:	no	Z1:	0	Z2:	0

Defect No	$\theta 1$ Deg.	$\theta 2$ Deg.	R1 mm	R2 mm	Z1 mm	Z2 mm	$R_{max}$ mm	Amp dB	Surface Breaking	Comments
BTE-1	358.5	358.6	27.6	32.1	n/a	n/a	n/a	n/a	yes	
BTE-2	269.7	268.8	27.0	33.7	n/a	n/a	n/a	n/a	yes	
BTE-3	178.5	177.5	26.3	33.3	n/a	n/a	n/a	n/a	yes	
BTE-4	88.9	89.6	22.2	38.2	n/a	n/a	n/a	n/a	yes	

**PARENT RRT – BMI TECHNIQUE Data Sheet**

Procedure ID:	7.1	Tech ID:	7-ECT1
Inspection ID:	7.P22.1	Access:	OD
Test Block ID:	P22	Date:	2012/11/28
Team ID:	7		

		Weld Volume Inspected:			
Detection:	Yes	$\theta 1$ :	0	$\theta 2$ :	360
Length Sizing:	Yes	R1:	20	R2:	90
Depth Sizing:	No	Z1:	0	Z2:	0

Defect No	$\theta 1$ Deg.	$\theta 2$ Deg.	R1 mm	R2 mm	Z1 mm	Z2 mm	$R_{max}$ mm	Amp dB	Surface Breaking	Comments
BHE-1 BHE-2	355.7	4.3	29.6	30.0	n/a	n/a	n/a	n/a	yes	See below
BHE-2	262.0	276.8	27.9	29.5	n/a	n/a	n/a	n/a	yes	See below
BHE-3	166.8	173.0	27.6	32.0	n/a	n/a	n/a	n/a	yes	See below
BHE-4	69.1	110.4	25.0	31.1	n/a	n/a	n/a	n/a	yes	See below

Note: Flaw location end points were determined by using an amplitude drop technique and physically marking the probe location at the flaw edges (reference the attached test specimen photos showing the marks made on the block to show flaw location). Each mark was then measured using the BMI coordinate system.

**PARENT RRT – BMI INSPECTION SUMMARY Data Sheet**

Inspection ID:	7.P22.1	Procedure ID:	7.1
Test Block ID:	P22	Date:	2012/11/28
Team ID:	7	Access:	OD

		Weld Volume Inspected:			
Detection:	yes	$\theta 1$ :	0	$\theta 2$ :	360
Length Sizing:	yes	R1:	20	R2:	90
Depth Sizing:	no	Z1:	0	Z2:	0

Defect No	$\theta 1$ Deg.	$\theta 2$ Deg.	R1 mm	R2 mm	Z1 mm	Z2 mm	$R_{max}$ mm	Amp dB	Surface Breaking	Comments
BHE-	355.7	4.3	29.6	30.0	n/a	n/a	n/a	n/a	yes	
BHE-2	262.0	276.8	27.9	29.5	n/a	n/a	n/a	n/a	yes	
BHE-3	166.8	173.0	27.6	32.0	n/a	n/a	n/a	n/a	yes	
BHE-4	69.1	110.4	25.0	31.1	n/a	n/a	n/a	n/a	yes	

### PARENT RRT – BMI TECHNIQUE Data Sheet

Procedure ID:	7.1	Tech ID:	7-ECT1
Inspection ID:	7.P5.1	Access:	OD
Test Block ID:	P5	Date:	2012/11/28
Team ID:	7		

		Weld Volume Inspected:			
Detection:	Yes	$\theta 1$ :	0	$\theta 2$ :	360
Length Sizing:	Yes	R1:	23	R2:	100
Depth Sizing:	No	Z1:	0	Z2:	0

Defect No	$\theta 1$ Deg.	$\theta 2$ Deg.	R1 mm	R2 mm	Z1 mm	Z2 mm	$R_{max}$ mm	Amp dB	Surface Breaking	Comments
12	11.2	31.5	30.8	31.2	n/a	n/a	n/a	n/a	yes	See below
2	154.0	166.7	42.6	40.6	n/a	n/a	n/a	n/a	yes	See below
3	284.9	286.1	25.7	39.3	n/a	n/a	n/a	n/a	yes	See below

Note: Flaw location end points were determined by using an amplitude drop technique and physically marking the probe location at the flaw edges (reference the attached test specimen photos showing the marks made on the block to show flaw location). Each mark was then measured using the BMI coordinate system.

### PARENT RRT – BMI INSPECTION SUMMARY Data Sheet

Inspection ID:	7.P5.1	Procedure ID:	7.1
Test Block ID:	P5	Date:	2012/11/28
Team ID:	7	Access:	OD

		Weld Volume Inspected:			
Detection:	yes	$\theta 1$ :	0	$\theta 2$ :	360
Length Sizing:	yes	R1:	23	R2:	100
Depth Sizing:	no	Z1:	0	Z2:	0

Defect No	$\theta 1$ Deg.	$\theta 2$ Deg.	R1 mm	R2 mm	Z1 mm	Z2 mm	$R_{max}$ mm	Amp dB	Surface Breaking	Comments
1	11.2	31.5	30.8	31.2	n/a	n/a	n/a	n/a	yes	
2	154.0	166.7	42.6	40.6	n/a	n/a	n/a	n/a	yes	
3	284.9	286.1	25.7	39.3	n/a	n/a	n/a	n/a	yes	



**PARENT RRT – BMI TECHNIQUE Data Sheet**

Procedure ID:	7.1	Tech ID:	7-ECT1
Inspection ID:	7.P7.1	Access:	OD
Test Block ID:	P7	Date:	2012/11/28
Team ID:	7		

Weld Volume Inspected:

Detection:	Yes	$\theta 1$ :	0	$\theta 2$ :	360
Length Sizing:	Yes	R1:	23	R2:	100
Depth Sizing:	No	Z1:	0	Z2:	0

Defect No	$\theta 1$ Deg.	$\theta 2$ Deg.	R1 mm	R2 mm	Z1 mm	Z2 mm	$R_{max}$ mm	Amp dB	Surface Breaking	Comments
1	57.7	57.3	55.3	45.6	n/a	n/a	n/a	n/a	yes	See below
2	109.0	111.5	47.8	55.9	n/a	n/a	n/a	n/a	yes	See below
3	162.5	165.0	27.7	36.4	n/a	n/a	n/a	n/a	yes	See below
4	293.3	298.8	36.7	54.0	n/a	n/a	n/a	n/a	yes	See below

Note: Flaw location end points were determined by using an amplitude drop technique and physically marking the probe location at the flaw edges (reference the attached test specimen photos showing the marks made on the block to show flaw location). Each mark was then measured using the BMI coordinate system.

**PARENT RRT – BMI INSPECTION SUMMARY Data Sheet**

Inspection ID:	7.P7.1	Procedure ID:	7.1
Test Block ID:	P7	Date:	2012/11/28
Team ID:	7	Access:	OD

Weld Volume Inspected:

Detection:	yes	$\theta 1$ :	0	$\theta 2$ :	360
Length Sizing:	yes	R1:	23	R2:	100
Depth Sizing:	no	Z1:	0	Z2:	0

Defect No	$\theta 1$ Deg.	$\theta 2$ Deg.	R1 mm	R2 mm	Z1 mm	Z2 mm	$R_{max}$ mm	Amp dB	Surface Breaking	Comments
1	57.7	57.3	55.3	45.6	n/a	n/a	n/a	n/a	yes	
2	109.0	111.5	47.8	55.9	n/a	n/a	n/a	n/a	yes	
3	162.5	165.0	27.7	36.4	n/a	n/a	n/a	n/a	yes	
4	293.3	298.8	36.7	54.0	n/a	n/a	n/a	n/a	yes	

## C.4.2 Phased Ultrasonic Array, Technique ID 7-PA1, 7-PA2

### C.4.2.1 Overview

The data was taken using an automated ultrasonic phased array contact examination technique that was conducted from the inside surface of each test specimen. The phased array technique allows the use of multiple examination angles generated by a single search unit to improve both detection capability and examination efficiency. The examinations were performed with the UT search unit looking in four directions (toward, away, clockwise, counter clockwise) for detection and sizing of flaws both parallel and transverse to the weld. Flaws are detected and characterized by evaluating fully merged data from all four directions. Detection is based on multi-directional confirmation, signal and spatial characteristics of the flaw. All suspect indications, regardless of amplitude, are investigated to the extent necessary to determine accurate characterization of the nature of the indication. A separate depth sizing examination was conducted after the detection examination to attain the through-wall dimension of each flaw.

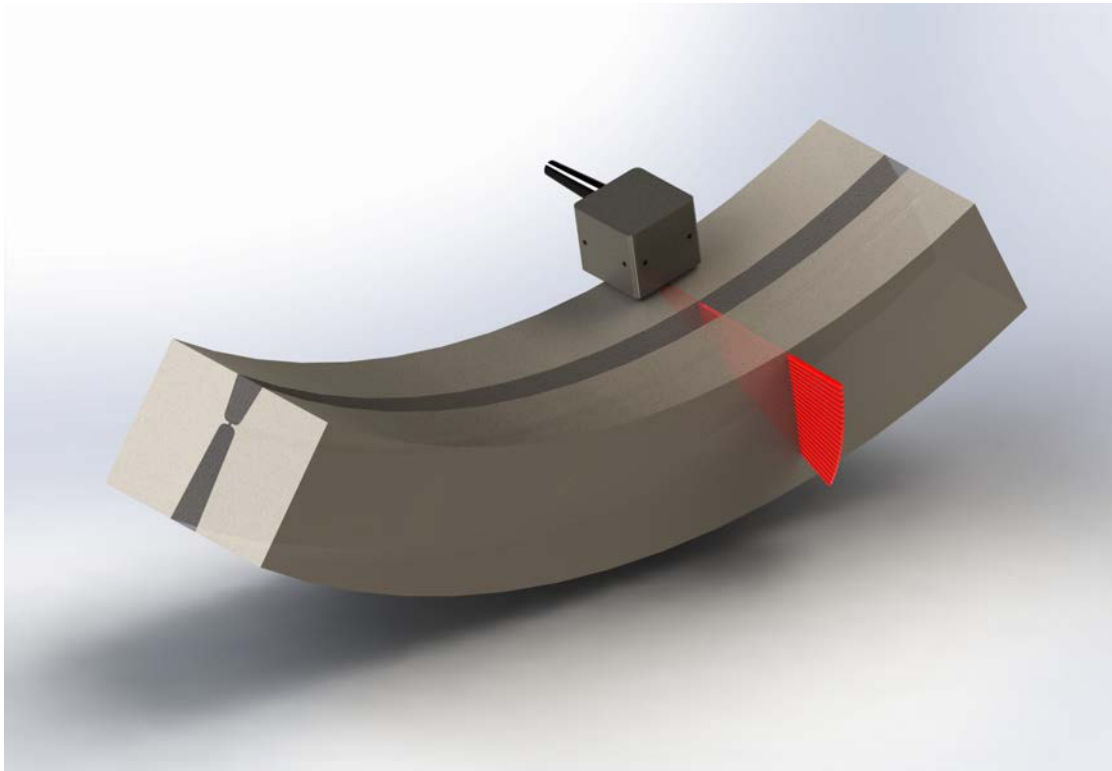


**Figure C.221 Graphical Illustration of Phased Array Examination on Test Block**

### C.4.2.2 NDE Equipment

A Zetec Tomoscan-III PA 32/128 UT instrument was used for data acquisition. This system is capable of handling up to 128 phased array channels. The system utilizes Ultravision acquisition and analysis software, which is Windows-based and uses standard PC hardware for acquisition and analysis. Once the system is set up and calibrated, all of the UT parameter and scan parameter settings can be saved and then recalled for future use. A-scan, B-scan, end-, side-, and C-scan views are available as well as composite views and other options that allow the analyst a broad selection of software analysis tools.

The UT phased array search units for detection and sizing were designed to produce the desired beam angles and waveforms in the DM weld materials, yet be small enough to maintain satisfactory contact when wavy or rough surfaces are encountered on the inside surface of the weld. The 1.5 MHz search unit contains two linear arrays in a pitch-ctach configuration mounted on an integral wedge, which incorporates a roof angle to provide geometric focusing of the two arrays in the near 1/3 of the weld thickness for the examination of the standard ASME Section XI examination volume. The search unit design allows electronic sweeping of the examination angle from 60° to 88° at 2° increments. Calibration of the search units and instrument is attained by using a standard IIW reference block of the same or similar material containing a 1-inch and 4-inch radius that are used for measuring angles, exit points, establishing system delay and reference sensitivity. The 4-inch radius was used to establish system delay and reference sensitivity.

An encoded scanner capable of providing accurate position information was utilized. The scanner was capable of performing scan and indexing movements as required and provided adequate force to keep the search unit coupled to the component surface.

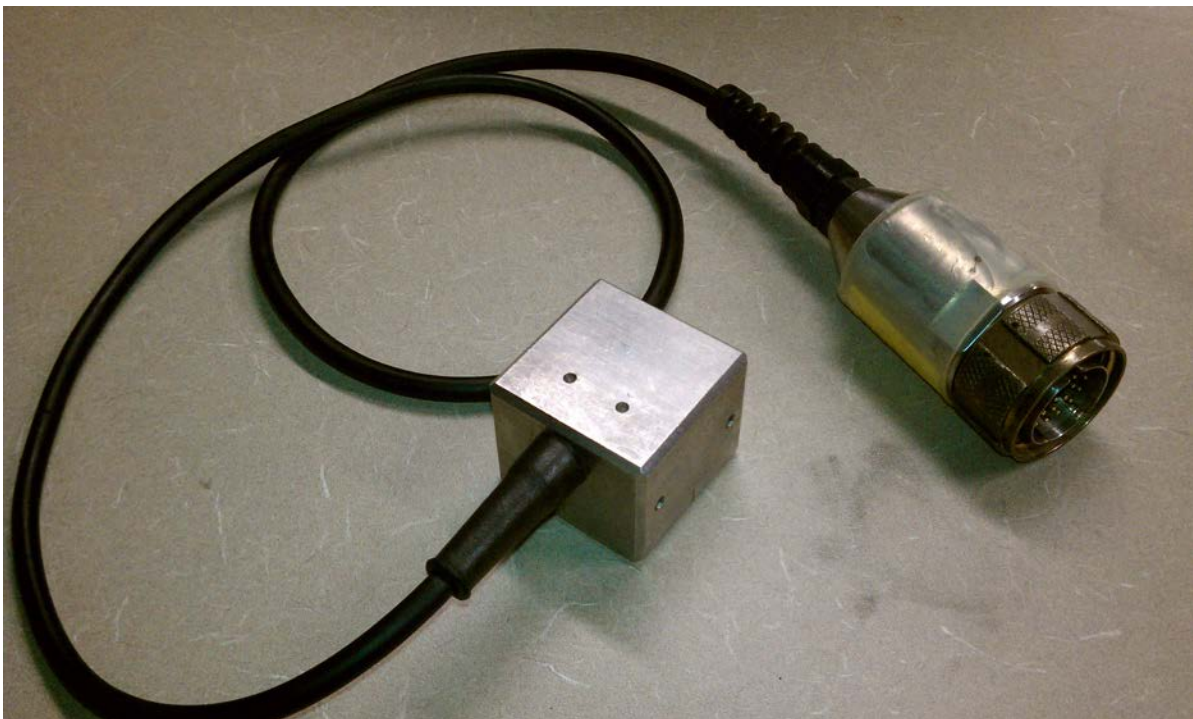


**Figure C.222 22-Element Phased Array Search Unit**

**Data Acquisition Process:** The data acquisition was performed in instrument Log mode with a focal law gain of 14 dB for the detection and length sizing examination and 20 dB for the depth sizing examinations. The Log mode allows the T-III acquisition system to utilize the dynamic gain range of the amplifier. Data acquisition was performed with the scanner moving circumferentially and indexing axially for both axial and circumferential flaws. Beam direction was parallel to the weld for axial flaws and perpendicular to the weld for circumferential flaws. The search unit movement rate did not exceed 2-inches per second for circumferential flaw detection and depth sizing, 1.5-inches per second for transverse flaw detection, and 0.75-inches per second for transverse flaw depth sizing. The maximum increment resolution for detection of

circumferential flaws was 0.15-inches while the maximum increment for detection of axial flaws was 0.05-inches. The maximum increment resolution for depth sizing was 0.10-inches.

### C.4.2.3 Data Analysis

#### Detection

Prior to analyzing data, the Data Analyst ensures the quality of the data by verifying a number of items (20-point checklist is used to verify data quality) and areas not meeting the quality acceptance criteria are re-examined. After the data quality is verified, the appropriate data file is loaded, ensuring that each data file has been fully merged. In all of the volume corrected displays, the cursors are adjusted to envelop the entire scan area. The color palette range is adjusted to provide resolution of the various reflectors throughout the scan and to provide optimum image contrast and to ensure that indications are not masked with the background noise. The volumetric images for each channel are analyzed to identify areas that exhibit deviation from the component geometrical or metallurgical interface responses. Patterns from the VC Top (C) pane that exhibit echo-dynamics in the VC (B) pane are considered flaws. All suspect indications, regardless of amplitude, are investigated to the extent necessary to determine accurate characterization of the nature of the indication. Profilometry data, thickness measurements, contours, and previous data are also utilized in analyzing the detection data. Flaw discrimination is proceduralized and conditions are provided and used by the analyst to determine if a flaw is present and to determine the flaw location including the determination if a flaw is surface breaking. Surface breaking characterization is based on signal and spatial characteristics. The flaw signal will drive to 0 inches on the a-scan when the flaw is surface breaking.

#### Depth Sizing

A data quality assessment is made similar to the detection analysis as previously stated prior to determining the flaw depth. After data quality is determined to be acceptable, the depth sizing evaluation is made as described below for axial and circumferential flaws:

**Circumferential Flaws:** Circumferential depth sizing data is taken using two dual 1.5 MHz 1D linear array probes phasing at a 30°–70° azimuthal scans with 1-degree resolution. Data from two beam directions (Twd & Awy) is considered and an evaluation of the unmerged data is made for several discrete beam angles to establish the flaw depth range and to identify the channel providing the greatest flaw depth. Depth sizing data is then evaluated using full and discrete merges and Z1 and Z2 are identified. Correction values are considered and applied as well as an evaluation of search unit contact that may be affected due to complex inside surface geometry. Search units can tilt when indexing over changing elevations so profilometry data is considered when evaluating sizing data.

**Axial Flaws:** Axial depth sizing data is taken using dual 1.5 MHz 1D linear arrays phasing at a 60°–82° and 40°–46° azimuthal scans with 2-degree resolution. Data from two beam directions (Cw & CCw) is considered. Depth sizing unmerged data from two opposing channels is evaluated to identify Z1 and Z2. Depth measurements are read directly and corrected for cylinder geometry using the software tooling.

#### **C.4.2.5 Self Assessment**

The advantages of this type of technique include:

- Allows the use of multiple elements within a single search unit for multiple inspection angles that can be steered and focused to the examination area of interest.
- The use of multiple inspection angles increases the probability of detection.
- Allows for sectorial scanning and simplification of DMW's with complex geometry.
- A separate detection procedure allows larger indexing for a quicker detection examination.

The disadvantages of this type of technique include:

- A more complex examination technique which requires personnel with proper training and /or experience to implement it.
- A separate depth sizing examination at smaller indexing is required after flaw detection is completed.

#### **C.4.3 Phased Ultrasonic Array, Technique ID 150-PA0**

##### **C.4.3.1 Overview**

The mockup components (P12 & P37) were evaluated using an encoded outside diameter (OD) transmit-receive longitudinal (TRL) ultrasonic phased array technique with continuous flow water coupling. Given that the specimen is composed of carbon and stainless steels (dissimilar metal weld) and is considered large-bore (thickness between 77–79 mm), a phased array probe was chosen with a center frequency of 1.0 MHz for inspection. A frequency of 1.0 MHz will provide excellent penetration into the inner diameter (ID) regions of these components while maintaining good overall flaw characterization resolution as the nominal wavelength in stainless steel is approximately 5 mm. The phased array technique was applied as it is a very versatile and adaptable inspection technique. It can be applied to a multitude of different components due to the ability to apply a variety of focal styles, a range of focal depths and refracted and skewed angles in order to insonify the region or regions of interest with a well-focused beam. This volumetric assessment technique can be used to characterize the length, depth, and location of flaws present in the inspected volume.

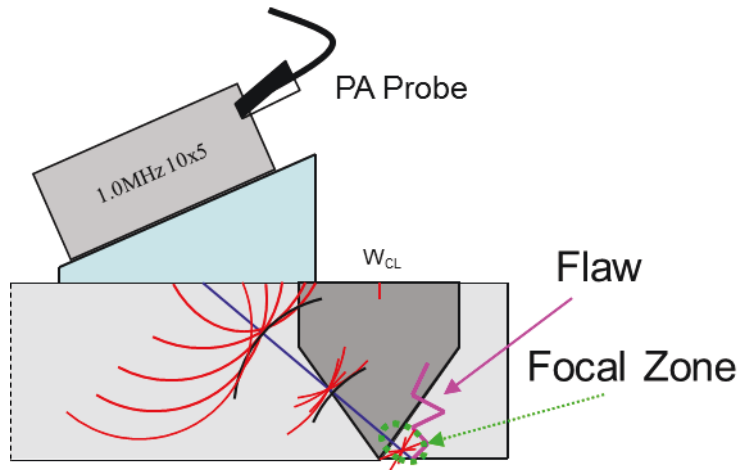


**Figure C.223 Graphic Showing Electronic Focusing Used in Phased Array Technique**

### C.4.3.2 Phased Array Equipment

#### Phased array data acquisition hardware

Data acquisition was accomplished using the DYNARAY<sup>®</sup> system for all PA probes evaluated in this study. This commercially available system is equipped to accommodate a maximum of 256 channels from PA probes and requires the use of Ultravision<sup>®</sup> 3 software. Its frequency pulsing electronics will drive probes in the 0.2–20 MHz range. The laboratory workstation and DYNARAY<sup>®</sup> data acquisition system are shown in Figure C.224.

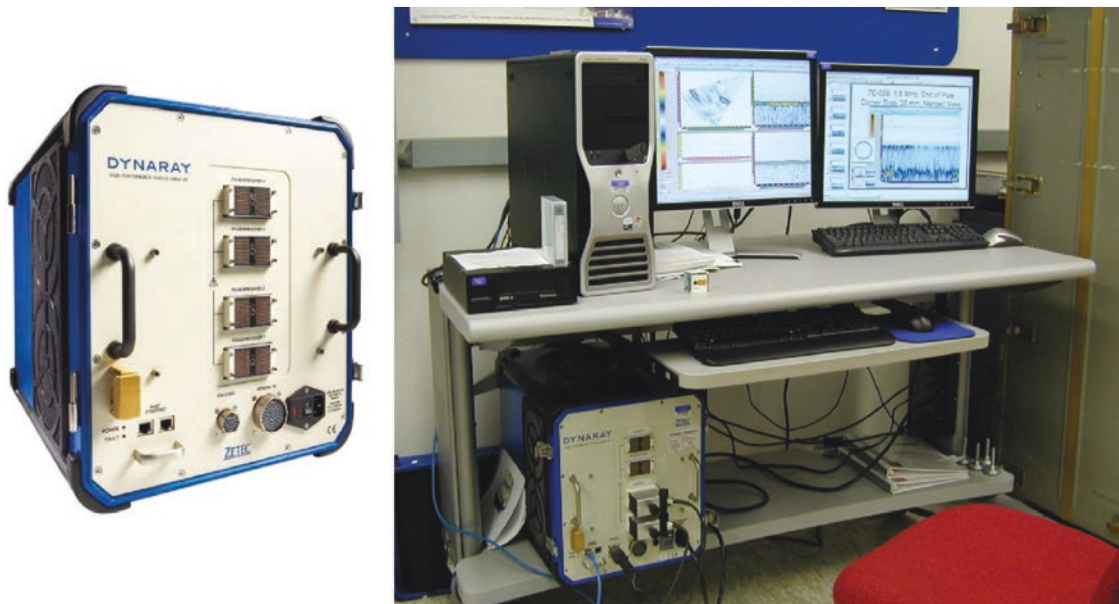


**Figure C.224 Data Acquisition System and Laboratory Workstation. Left: DYNARAY<sup>®</sup> phased array data acquisition system (courtesy of ZETEC<sup>®</sup>). Right: Laboratory workstation for both data acquisition and data analysis, with the DYNARAY<sup>®</sup> system on the lower shelf.**

#### **C.4.3.3 Necessary Equipment and *Function* (Figure C.225)**

- Dynaray Acquisition System (Zetec Inc.)
  - Dynaray Lite will also work – Need minimum of 50 P/R channels
    - *Pulse/Receive phased array probe and collect Phased array data*
- Ultravision 3 software (Zetec Inc.)
  - *Setup focal laws and execute scanning*
- Ultrasonic phased array probe (Imasonic Inc.)
  - *Inspection array*
- Desktop or Laptop computer with Ethernet connection
  - *Run the software for data collection and analysis*
- Motion control drive unit (MCDU) (Zetec Inc.)
  - *Provide power and control for scanner. Relay positional information*
- GPS 1000 Scanner unit (ATCO Inc.)
  - *Provide scan and index motion and special encoding information*

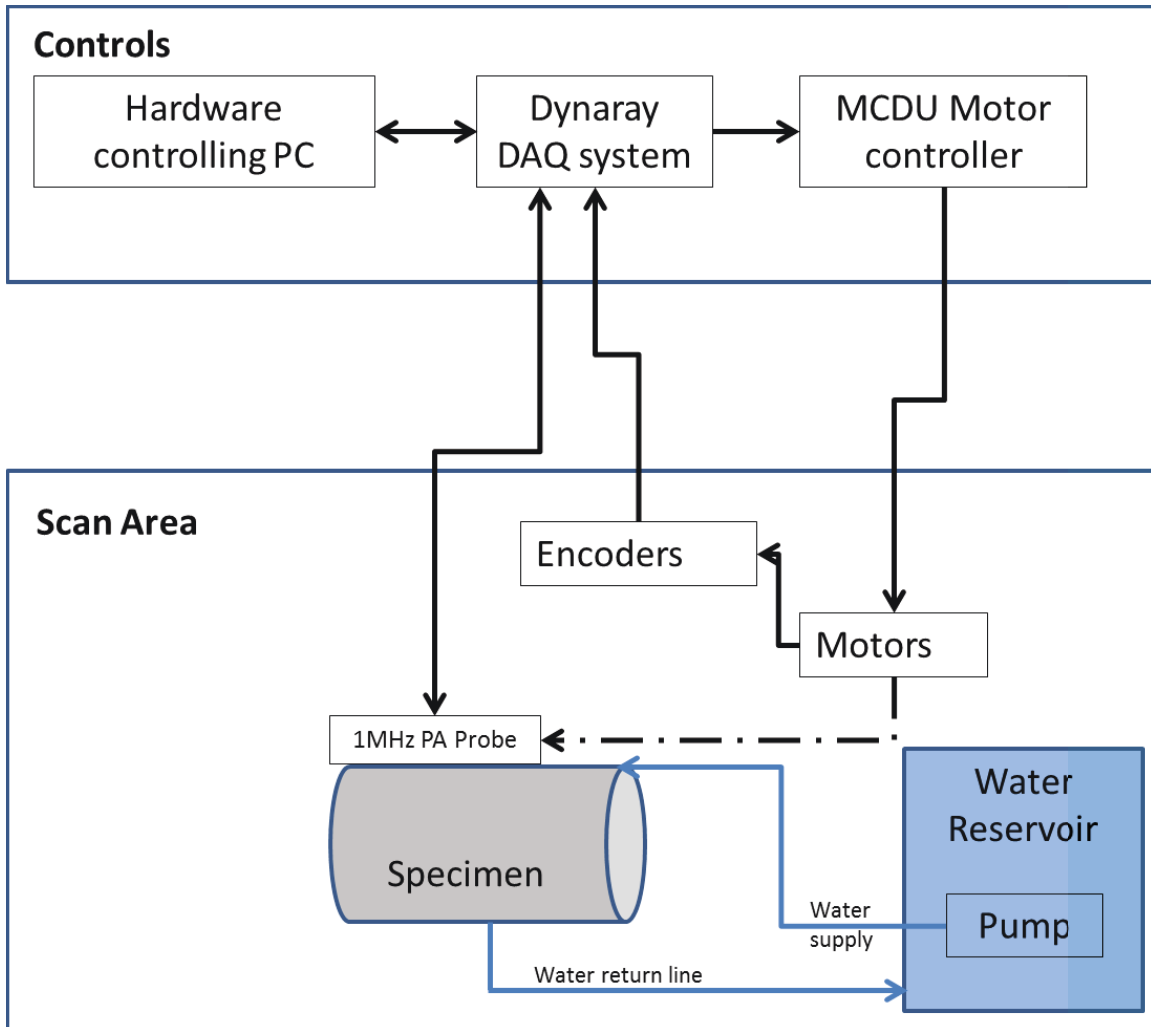


**Figure C.225 Phased Array Data Acquisition Connection Schematic**

### **Phased Array Probe**

The 1.0 MHz Imasonic TRL array (Figure C.226) was originally designed for evaluating inspection effectiveness of PA methods on components with inlays, onlays, and overlays. It consists of two 10-element by 5-element matrix arrays. Each element of the array is 3.5 mm × 3.5 mm with separation of 0.5 mm on each side, thus primary and secondary axis pitch is 4.0 mm. One array is used for transmitting, the other for receiving ultrasonic signals. This probe has a 58% bandwidth (BW) at -6 dB and an approximately 50-mm<sup>2</sup> (1.97-in.<sup>2</sup>) footprint with a customized wedge for data collection in tight geometrical configurations. The 1.0 MHz probe was used with a removable outside diameter (OD) contoured Rexolite wedge assembly with a wedge angle of 15 degrees. The probe's nominal wavelength in stainless steel is 5.31 mm (0.21 in.) at its average center frequency of 1.1 MHz. Skew angles of ±20 degrees were possible with this array.



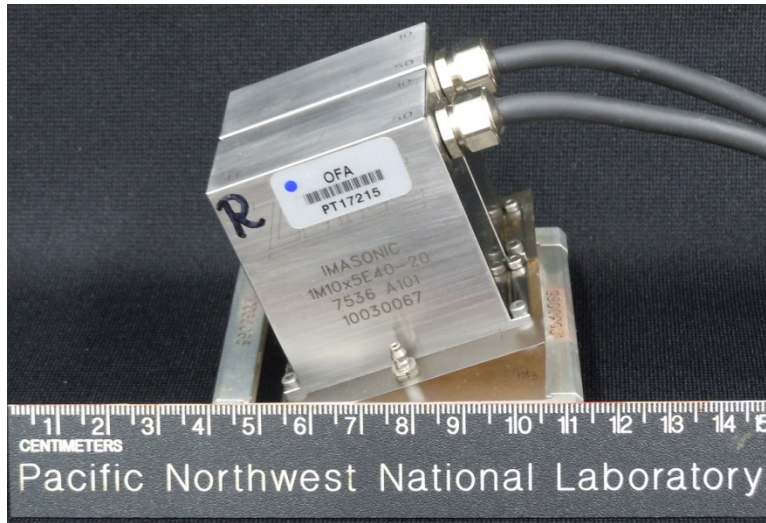


**Figure C.226 1.0 MHz Transmit-Receive Phased Array Probe**

#### **C.4.3.4 Data Acquisition Process and Parameters**

##### **Focal Law Development**

Before a phased-array probe can be used to perform an examination, a set of focal laws must be produced to control the firing of individual elements. The focal laws are inputs to the Ultravision<sup>®</sup> control software, which determines specific elements to excite at specific times to allow for proper beam-forming in the material to be examined. The focal laws also contain details about the angles being generated, the focal point of the sound field, the delays associated with the wedge and electronics, and the orientation of the probe. The inspection team uses a software package contained in the Ultravision<sup>®</sup> 3 software program for producing focal laws known as the “ZETEC<sup>®</sup> Advanced Focal Law Calculator.” The software package performs two functions: 1) focal law generation and 2) simulation of the ultrasonic field produced by the probe when using the generated laws. The user enters the physical information about the PA probe, such as the number of elements and the sizes of the elements, and the wedge information, such as the wedge angle and the wedge size, into the program. The desired angles and focal distances are then entered, and the software generates the needed delays for each element to produce the desired beam steering and focusing in the material. The software beam simulation produces a simple image of the probe on the wedge, ray-tracing to show the focal depth and steering desired, and density mapping to enable the viewer to see how well the sound field responds for a particular angle and whether grating lobes exist that may be detrimental to the examination. Figure C.227 shows an example of the ray tracing for a probe on the left with the sound field density mapping on the right. It should be noted that this simulation is performed in isotropic material; that is, the velocity of sound is maintained throughout any angle for a particular wave mode, which is not really the true state for CASS, but enables the user to estimate sound field parameters and transducer performance for optimal array design and focal law development.

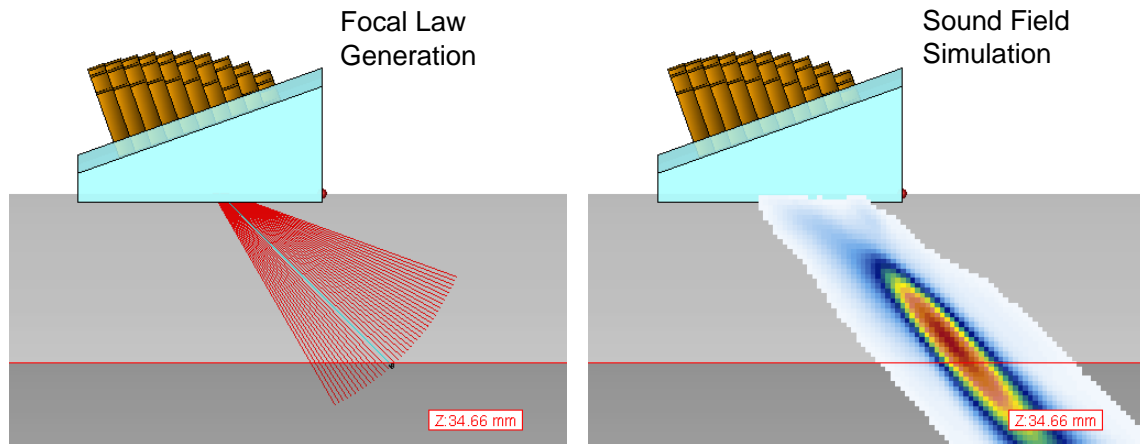
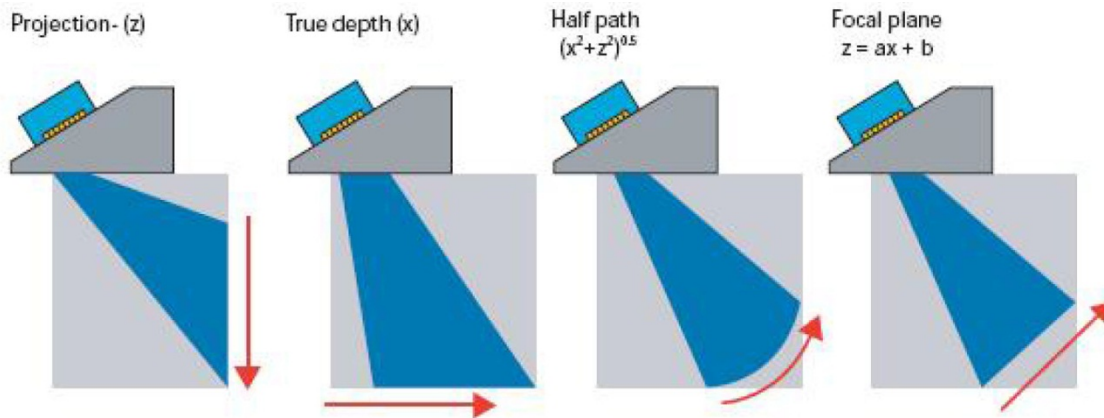


**Figure C.227 The ZETEC® Advanced Phased Array Calculator is Useful for Generating Focal Laws (left) and Simulating the Sound Field for the Focal Law (right) to Determine Beam Characteristics**

#### **Data Acquisition Parameters**

- 1.0 MHz 2×(10×5) element matrix array
  - Transmit-Receive Longitudinal
  - Each element pulsed with 500 ns negative 200V square wave excitation (Dynaray)
  - True Depth and Half Path focusing techniques (Figure C.228)
  - 20–60 degree azimuthal angle sweep, 3 degree increment
  - 0,±10 degree skew angles
- Outside Diameter (OD) inspection
  - Raster scan resolution: 1.0 mm scan, 1.0 mm index
  - Automated and encoded
- OD contoured Rexolite wedge
  - 15 degree wedge angle
- 0 pt., coordinates and scan conventions followed from test block information sheet
- Continuous water loop used for ultrasonic coupling between the wedge and the component
- Circumferential scans (looking for axially oriented flaws)
  - Collect data in clockwise and counter clockwise directions

- Axial scans (looking for circumferentially oriented flaws)
  - Collect data from up-stream and down-stream locations
- Target Focus: Inner Diameter Regions
  - ID connected flaws (cracks)



1. Projection – focusing in a specific vertical plane. Parameters: distance from probe reference point, sweep angles (start, stop, interval), skew angle(s).
2. True depth – focusing at specific constant depth with all angles focused at this depth. Parameters: focusing depth, sweep angles (start, stop, interval), skew angle(s).
3. Half-path – sound path held constant as beam is swept. Parameters: sound path length, sweep angles (start, stop, interval), skew angle(s).
4. Focal plane – arbitrary user-defined plane of focus. Low angle path length, high angle path length, sweep angles (start, stop, interval), skew angle(s).

**Figure C.228 Beam Focusing Options for Phased Array Probes**

#### C.4.3.5 Signal Processing of the Phased Array Data

- Ultravision 3 software was used to reconstruct the phased array data into images. No additional filtering or manipulations of the data were conducted.

#### C.4.3.6 Analysis of the Phased Array Data

- Phased array image analysis was conducted using Ultravision 3 software to display a variety of images including: (Figure C.229)
  - A-Scan (time-amplitude) along selected angles
  - C-Scan (Top View) scan vs. index axes – location and length of flaw
  - B-Scan (Side View) scan vs. ultrasound axes – depth of flaw

- D-Scan (End View) index vs. ultrasound axes – length and depth of flaw
- Detection
  - Strong response signal(s) present in the ID region of component
    - o Signal strength above background noise levels to be considered (greater than 6 dB above background)
- Characterization
  - Detected signals will be length sized using a -6 dB and loss of signal (LOS) method in the D-Scan view
  - Depth sizing will be assessed by measuring maximum flaw extent in the B- and/or D-Scan view(s)
  - Overall flaw circumferential and axial location assessed with C-Scan view

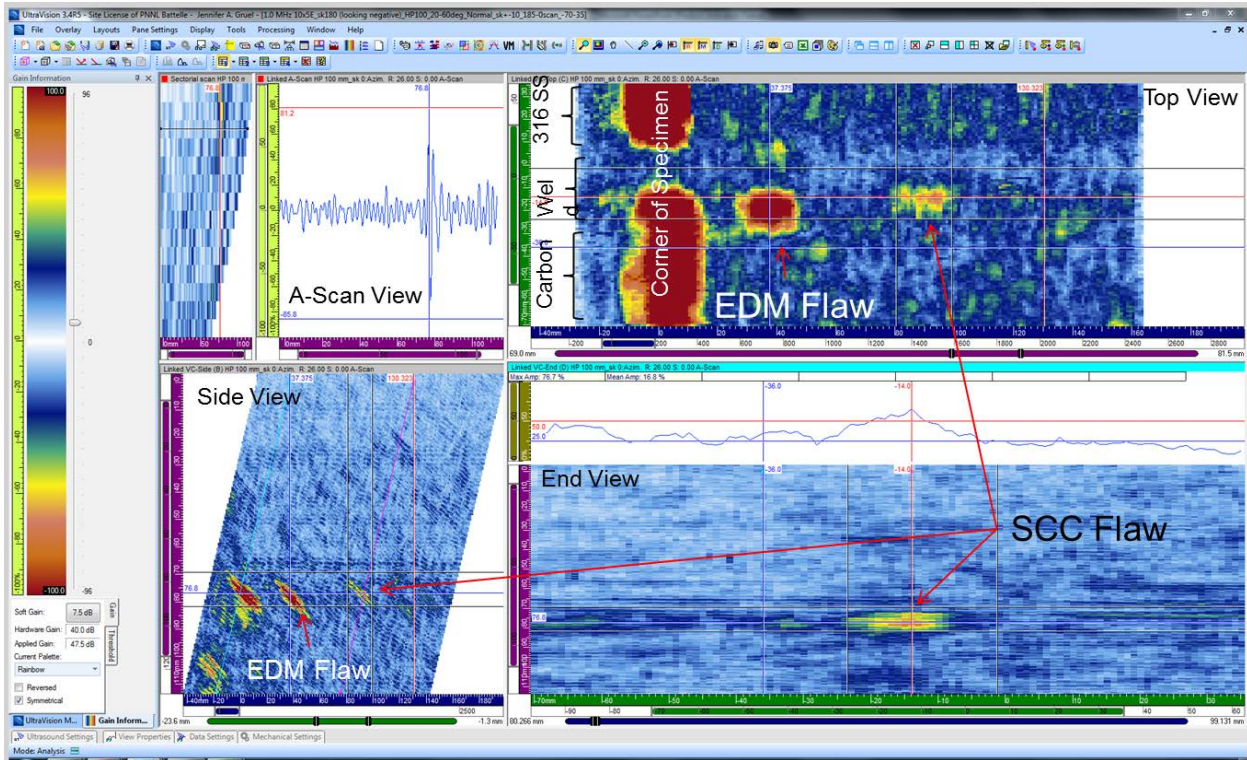
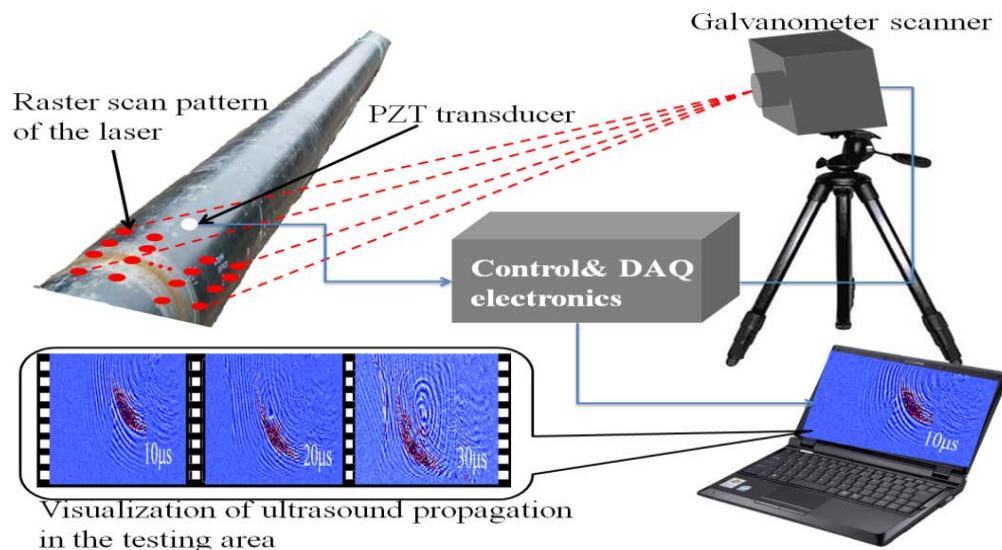


Figure C.229 Example of Phased Array Image Data

#### C.4.4 Laser Ultrasound Visualization Method, Technique ID LUV0, LUV-ASW0, LUV-BSW0

Figure C.230 illustrates the laser ultrasound visualization system for material nondestructive evaluation/testing. The proposed laser ultrasound visualization system is a fully standalone,

self-contained and battery-powered sensor unit. It consists of four major components: laser pulse energy delivery system, a miniature piezoelectric transducer (PZT), control and data acquisition electronics, and a laptop computer for signal processing and visualization. The processes for defect/ flaw inspections are as follows: The sensor unit will be placed at a standoff distance from the object under testing with the galvanometer scanner facing the surface of the testing areas. The end user will push a button, which will generate a trigger signal to start the inspection process. Control signals will be generated by the sensor electronics and sent to the pulsed laser and the galvanometer scanner. Consequently, the laser pulses are precisely delivered onto different locations of the testing object, and swept in a raster scan pattern. As the laser pulses are delivered onto each spot, they generate local heating, which induces minute surface motions. Such a surface motion propagates through other area of the object, thus leading to the generation of ultrasound pulses. It should be emphasized that the laser pulse energy used for the ultrasound generation is several orders of magnitude lower than the laser material damage threshold, thus causing no damages to testing object. A PZT transducer will be placed at a convenient location by the end user on the outer surface of the testing object to detect the ultrasound pulses. The PZT sensor signals will be recorded and stored in a laptop computer. After a complete scan in the testing area, the stored ultrasound propagation data will be processed and displayed. The ultrasound signal propagation characteristics in the testing area can be mapped with laser ultrasound generations at different spots. Those signals will be in the form of a movie clip for the end users to visualize the ultrasound signal propagation characteristics. Consequently, defects including mechanical cracks, stress corrosion cracks, voids, welding flaws etc., can all be easily visualized without any complicated pattern recognition algorithm, ultrasound modeling tools or a well-trained technician. Any maintenance personnel should be able to operate the proposed sensor without any difficulty because the detections of those defects are straightforward. For example, small mechanical cracks inside the testing structure will act as ultrasound wave scatterers, which lead to the formation of ring patterns around those cracks in the ultrasound propagation images.



**Figure C.230 A Schematic of the Envisioned Laser Ultrasound Visualization System Used for Inline Pipeline Integrity Assessment**

It should be noted that the underlying principle of proposed laser ultrasound visualization technique is similar to the traditional ultrasound testing in that the ultrasound propagation

characteristics in the specimens are monitored, based on which various defects and the state of the specimen can be detected and identified. One distinct difference between the proposed laser ultrasound and the traditional ultrasound testing is that the proposed method allows the defect detection and identification based on two dimensional images instead of only an one-dimensional waveform. This is because the ultrasound wave propagations in real-world structures are very complicated, as a lot of propagation modes and features could arise due to multiple wave bouncing from various boundaries, weld seams, walls and interfaces. Consequently, those one-dimensional waveforms are heavily convoluted, and the detections of specific features are very challenging. Often, very complicated modeling works are required, making it difficult to interpret the ultrasound data. The proposed laser ultrasound technique, however, can form the two dimensional images to reveal the ultrasound wave propagations in structures. The defects present in structures with complicated shapes and configurations can be directly visualized.

The merits of the proposed laser ultrasound visualization sensor system and its advantages over other techniques are listed below:

1. **Compact, lightweight, and portable:** Using a compact, lightweight and low power consumption fiber laser, the whole laser ultrasound sensor system will have a size ~12"×12"×8", weigh around 20 lbs, and can be powered by a 24V battery. The compactness, lightweight and portability of the proposed laser ultrasound visualization system makes it practical to be used in the field.
2. **Capable of detecting a wide variety of defects:** Defects including cracks (partial or full cracks), delamination/debonding, voids, porosity, foreign particle inclusions, moisture ingress, and material fatigue and work hardening can all be detected using the proposed sensor.
3. **Compatible with complex shapes and configurations:** With the proposed laser ultrasound system, there is no need to control the laser incidence angle and laser focus, thus making it possible to inspect objects with any arbitrary shapes and configurations.
4. **High sensitivity and good spatial resolution:** The combination of using short ns- laser pulse for ultrasound generation and miniature PZT transducers for ultrasound detection enables very high signal to noise ratio, thus leading to very high sensitivity in defect detection. Additionally, the laser ultrasound system should allow very good spatial resolution (i.e., hundreds of micrometer to ~1 mm) in detecting defected area.
5. **High measurement throughput:** The high measurement throughput is a direct result of the high speed enabled by the laser galvanometer scanner, which can scan in both x and y direction with a maximum speed of 2 m/s.
6. **Easy and safe to the operators:** In the traditional ultrasound technique, the defect detection is based on one-dimensional waveforms. The data interpretations are not straightforward and typically involve complicated modeling. The proposed laser ultrasound system, however, allows defect detection and identification based on visual images of the ultrasound propagation characteristics in the testing object. Additionally, compared to the X-ray tomography technique, the laser ultrasound visualization system is much safer to the operators, as it does not involve any harmful radiations.

## **C.5 Japanese Detailed Technique Descriptions**

### **C.5.1 Phased Array Asymmetrical Beam TOFD and Phased Array Twin Probe, Technique ID 29-PA-ATOFD0, 29-PA-ATOFD1, 29-PA-ATOFD2, 29-PA-TP0**

The TOFD method can precisely measure crack depth, but is not suitable for materials with high ultrasonic attenuation, such as stainless steel cast piping, austenitic stainless steel piping welds and dissimilar welds in vessel nozzles in nuclear power plant equipment.

Two kinds of scanning methods have been developed with a phased array system along with a method for analysis of the data (Ishida and Kitasaka 2013).

One of these scanning methods is a TOFD method with asymmetrical ultrasonic beams of a transmitter and a receiver (hereafter PA-ATOFD method; phased array asymmetrical beam TOFD method”).

The other is a phased array twin probe method with a transmitter and a receiver (hereafter PA-TP method).

An analysis method synthesizes plural scanning data with different refraction angles and path lengths (hereafter “MA method; multi-angle synthesis method”) acquired by the PA-ATOFD or the PA-TP method.

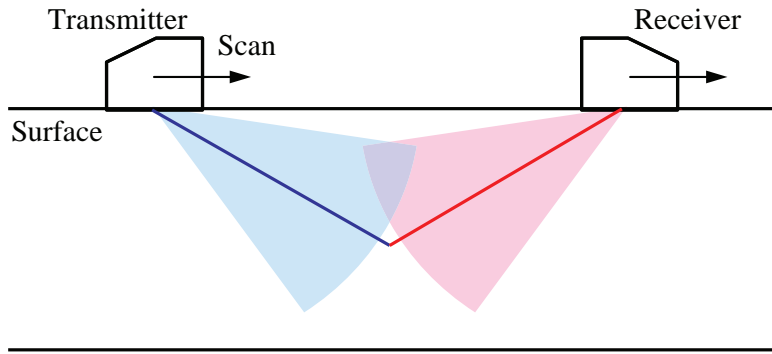
#### **C.5.1.1 Principle of Scanning and Synthesis Methods**

##### **Phased Array Asymmetrical Beam TOFD Method (PA-ATOFD Method)**

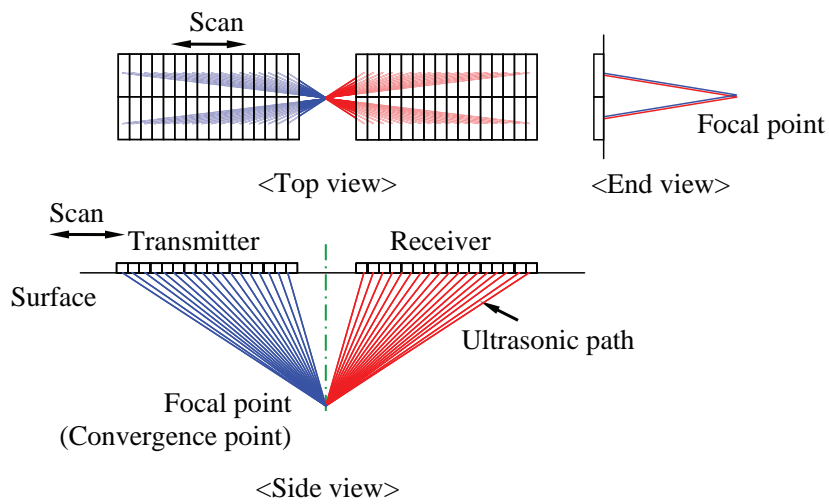
Figure C.231 illustrates a schematic diagram of the conventional TOFD method. Two probes with a single element are used for the transmitter and receiver. To change the refraction angle with a reflection source it is necessary to change the probes with another incident angle or the distance between the transmitter and receiver.

Figure C.232 illustrates a schematic diagram of the phased array TOFD method. We can set the focus and convergence point of the ultrasonic beams of the transmitter and receiver at arbitrary different positions in a material. However, to change the refraction angle with a reflection source it is necessary to change the distance between the transmitter and receiver.

Figure C.233 illustrates a schematic diagram of the phased array asymmetrical beam TOFD method. Ultrasonic beams with different refraction angles and path lengths of the transmitter and receiver are set at an arbitrary focal and convergence point in the material in order to acquire the tip echo of the SCC with different refraction angles. Furthermore, the scanning data are synthesized with different refraction angles and different depths of focus point. This synthesis is expected to enable us to distinguish easily the echo from reflected sources and noise.



**Figure C.231 Conventional TOFD Method**



**Figure C.232 Phased Array TOFD Method**

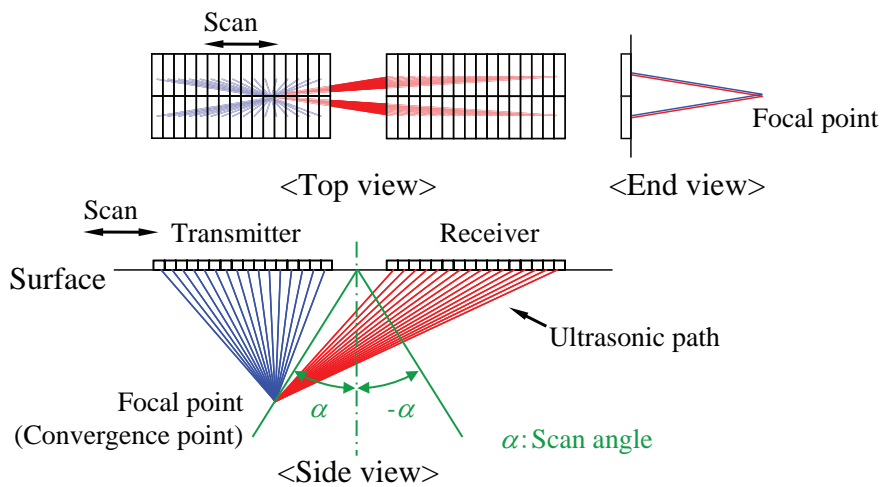


**Figure C.233 Phased Array Asymmetrical Beam TOFD Method (PA-ATOFD Method)**



## Phased Array Twin Probe Method (PA-TP Method)

Figure C.234 shows a schematic drawing of a phased array twin probe method. In the longitudinal (back/forth) direction to the incidence of ultrasound waves, the element arrangement in this direction can focus the ultrasonic beam on different refracting angles and different focus point depths. The elements were arranged in right/left directions to focus the ultrasonic beam at different depths in this direction as well.

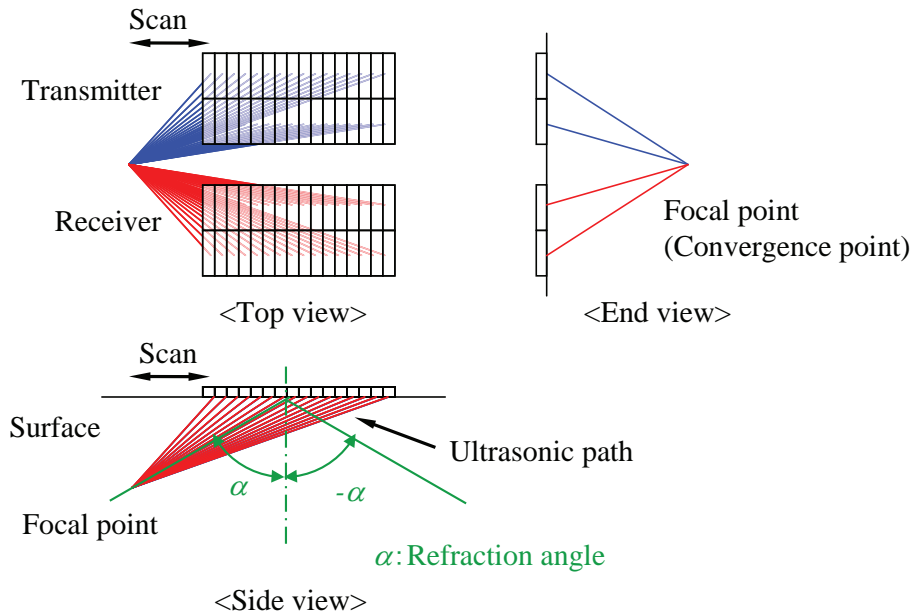
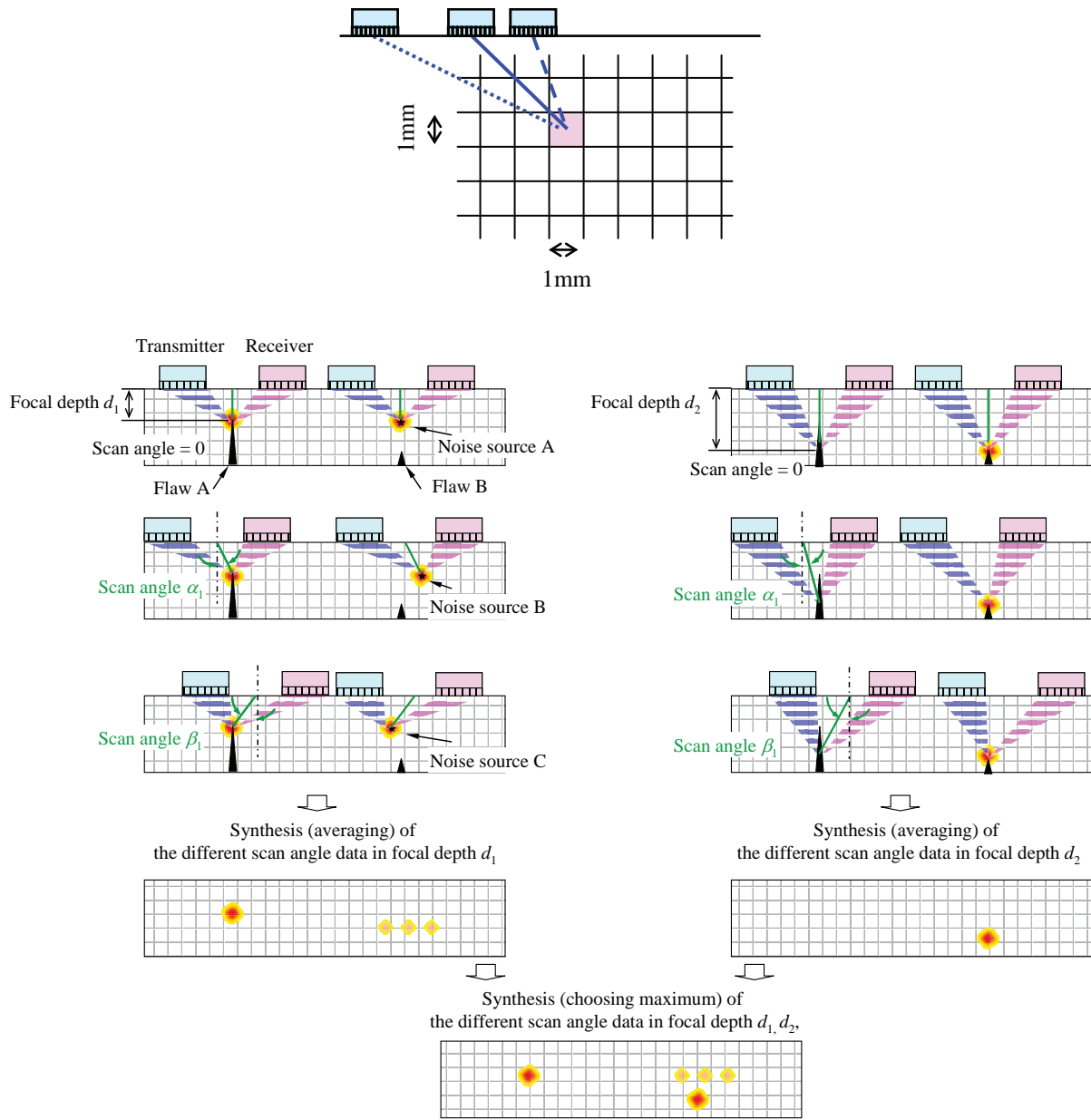


Figure C.234 Phased Array Twin Probe Method

## Multi-angle Synthesis Method (MA Method)

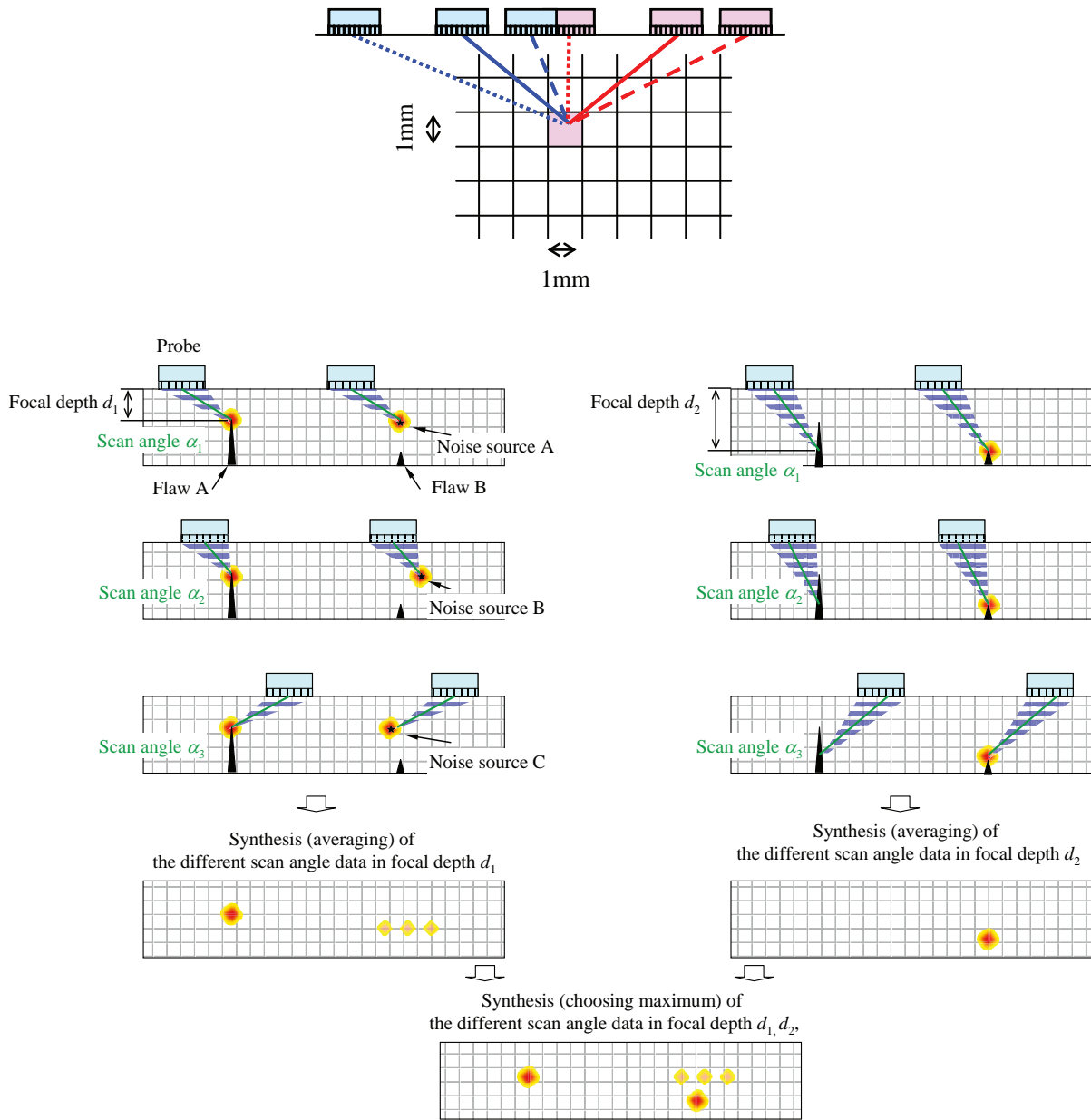
Figure C.235 illustrates the multi-angle synthesis method. The scanning data are synthesized with different scan or refraction angles and different depths of focal point. This synthesis is expected to enable us to distinguish easily the echo from reflected sources and noise.

The scanning data are synthesized by an original calculation program on a PC.



(1) Synthesis of PA-ATOFD method data

Figure C.235 Multi-angle Synthesis Method (MA Method) (1/2)



(2) Synthesis of PA-TP method data

Figure C.235 Multi-angle Synthesis Method (MA Method) (2/2)

### C.5.1.2 Inspection Procedure

#### PA-ATOFD Method

##### (A) Procedure

1. Scan and acquire data by PA-ATOFD method
2. Determine an analysis section for B-scan analysis by MA method analysis
3. Analyze and draw a B-scope image by MA method analysis

### (B) Equipment

- Transducer (Figure C.236, Table C.5)
  - 2×16 matrix array (Inner surface (near crack side))
  - 4×8 matrix array (Inner surface (near crack side))
  - 10×25 matrix array (Outer surface (far crack side))
  - Transducers are fit with a wedge on the surface of the specimen.
- Pulser/Receiver (Figure C.237)
  - Zetec Dynaray (256ch P/R)
- Delay setting / Imaging software (Figure C.237)
  - Zetec Ultravision<sup>(1)</sup>
- Scanner (Figure C.237)
  - X-Y

### (C) Calibration

- Use reference block with side drilled hole to calibrate echo height and path length
  - ( $\phi$ 3mm, 4, 8, 12 ~ 36, 40 mm depth)

### (D) Scan

- Scan direction            Perpendicular to the crack surface
- Scan pitch                1 mm
- Index pitch               2 mm
- Scan angle                +40 ~ -40 deg. (maximum)
- Images                    B, C, D-scope (Ultravision)  
                                  B-scope (MA method)

### (E) MA Method Analysis

- PC

---

(1) The delay time of the array probe was originally set by the inspection team..

- Synthesis calculation program on the MATLAB
- Imaging                      B-scope
- Synthesis pitch            1 mm

**PA-TP Method**

(A) Procedure

1. Scan and acquire data by PA-TP method
2. Determine an analysis section for B-scan analysis by MA method analysis
3. Analyze and draw a B-scan image by MA method analysis

(B) Equipment

- Transducer (Figure C.236, Table C.5)
  - 10×25 matrix array (Outer surface (far crack side))
  - Transducers are fit with a wedge on the surface of the specimen.
- Pulser/Receiver (Figure C.237)
  - Zetec Dynaray (256ch P/R)
- Delay setting / Imaging software (Figure C.237)
  - Zetec Ultravision
- Scanner (Figure C.237)
  - X-Y

(C) Scan

- Scan direction              Perpendicular to the crack surface
- Scan pitch                    1 mm
- Index pitch                   2 mm
- Scan angle                    +45 ~ -45 deg. (maximum)
- Images                        B, C, D-scope (Ultravision)  
                                       B-scope (MA method)

(D) MA Method Analysis

- PC
- Synthesis calculation program on the MATLAB
- Imaging                      B-scope
- Synthesis pitch            1 mm

**Table C.5 Array Transducers**

Type	2×16 Matrix Array	4×8 Matrix Array	10×25 Matrix Array
Frequency (MHz)	2.25	2.25	2
Elements	32	32	250
Array of elements (width × length)	2×16	4×8	10×25
Size (mm) (width × length)			
Element	7.4×1.8	3.8×1.8	3.8×3.0
Aperture	14.9× 31.8	15.8×15.8	39.8×79.8



(1) 2×16 matrix array



(2) 4×8 matrix array



(3) 10×25 matrix array



(4) Example of probe with the wedge

**Figure C.236 Transducer**



**Figure C.237 Measurement Set-up (Example for the Specimen P37)**

### **C.5.1.3 Team's Assessment of the Technique Based on the Round-Robin Test Results**

#### **Met Our Expectation**

- Better result by PA-TP method with MA method for the outer surface scan.
  - PA-TP method gives us a defect position by the corner echo. But PA-ATOFD method gives us a tip echo only. It is difficult to discriminate a tip echo directly by PA-ATOFD.
  - But for the inner surface scan, PA-ATOFD method gives us a defect position by lack of the signal.

#### **To be Improved**

- Develop a coupling supply system for the large aperture transducer.
  - We frequently met lack of coupling (glycerin paste) on the scanning surface.
- Determine the best transducer specification of the PA-ATOFD method for the inner surface.
  - We could not detect the tip echo of the deep defect (20mm~) on the inner surface by our PA-ATOFD probe. This result tells us necessity of the larger aperture probe.

Further detailed assessment should be evaluated with defect destructive information.

## C.5.2 Three-Dimensional Synthetic Aperture Focusing, Technique ID 17-SAFT1

### C.5.2.1 Principle

Synthetic Aperture Focusing Technique (SAFT) is used to construct an ultrasonic image from ultrasonic signals obtained with several transmitter-receiver combinations. When an array transducer is used for the acquisition of these ultrasonic signals, ultrasonic waves transmitted by one selected transducer element are received by all the transducer elements. By shifting the element used for the transmitter, the ultrasonic signals for every transmitter-receiver combination are collected.

Let  $\mathbf{x}_i$  be the position of the transmitter,  $\mathbf{x}_j$  be the position of the receiver and  $\mathbf{x}$  be the position of a defect. Here we suppose that an ultrasonic wave transmitted from  $\mathbf{x}_i$  is reflected at  $\mathbf{x}$  and received at  $\mathbf{x}_j$  (Figure C.238). The distance between  $\mathbf{x}_i$  and  $\mathbf{x}$  is denoted by  $r_i = |\mathbf{x}_i - \mathbf{x}|$ , and the distance between  $\mathbf{x}_j$  and  $\mathbf{x}$  is denoted by  $r_j = |\mathbf{x}_j - \mathbf{x}|$ . If the wave velocity is given by  $v$ , the propagation time from  $\mathbf{x}_i$  to  $\mathbf{x}_j$  via  $\mathbf{x}$  is calculated by  $t_{ij} = (r_i + r_j) / v$ .

Conversely, the sum of the distances  $r_i + r_j$  can be calculated with the wave velocity  $v$  and the propagation time  $t_{ij}$ , which can be derived from the ultrasonic signals obtained with the receiver. If the total travel distance  $r_i + r_j$  is known, the defect position  $\mathbf{x}$  can be narrowed down. The defect position  $\mathbf{x}$  should be on the circumference of the ellipse determined by the conditions that its focal points are  $\mathbf{x}_i$  and  $\mathbf{x}_j$  and the sum of the distances from any point on this ellipse to these focal points is  $r_i + r_j$ . A different transmitter-receiver combination provides a different ellipse on the circumference of which the defect position  $\mathbf{x}$  is located. Then, multiple transmitter-receiver combinations specify the defect position  $\mathbf{x}$ .

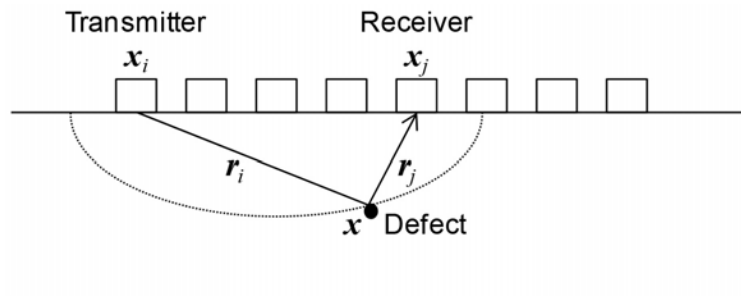


**Figure C.238 One Combination of Transmitter and Receiver**

Let us denote the ultrasonic signals obtained with the combination of the transmitter at  $\mathbf{x}_i$  and the receiver at  $\mathbf{x}_j$  by  $u_{ij}(t)$ , which is a function of time. Because the signal amplitude becomes large at the time when the ultrasonic wave reflected by the defect arrives at the receiver,  $u_{ij}(t_{ij})$  is expected to have a large amplitude. By using the definitions shown above,  $u_{ij}(t_{ij})$  can be expressed as



$$u_{ij}(t_{ij}) = u_{ij} \left( \frac{r_i + r_j}{v} \right) = u_{ij} \left( \frac{|\mathbf{x}_i - \mathbf{x}| + |\mathbf{x}_j - \mathbf{x}|}{v} \right).$$

This expression implies that, for an arbitrary position  $\mathbf{x}$ ,  $u_{ij}(t_{ij})$  has a large amplitude when a defect exists at  $\mathbf{x}$ . To construct an ultrasonic image by SAFT, a data array is prepared to store the accumulation of  $u_{ij}(t_{ij})$  for each discrete point  $\mathbf{x}$  in the target area of a test object. After the ultrasonic signals  $u_{ij}(t)$  are acquired by measurement for each  $i$  and  $j$ , the accumulation  $S(\mathbf{x})$  is calculated by

$$S(\mathbf{x}) = \sum_{i=1}^N \sum_{j=1}^N \left| u_{ij} \left( \frac{|\mathbf{x}_i - \mathbf{x}| + |\mathbf{x}_j - \mathbf{x}|}{v} \right) \right| \quad \text{for each } \mathbf{x},$$

where  $N$  is the number of the elements of the array transducer. Then,  $S(\mathbf{x})$  itself provides an ultrasonic image that shows high intensity at the place where a defect may exist.

In the above example, the transducer elements are linearly aligned, but the idea of SAFT can be expanded for an array transducer that has a two-dimensional array of transducer elements to deal with three-dimensional ultrasonic images. That is called three-dimensional SAFT (3D SAFT).

The feature and advantages of 3D SAFT UT technique is shown in Figure C.239 as compared with the principle of usually used UT technique such as conventional angle beam technique and phased array technique (Komura and Furukawa 2010).

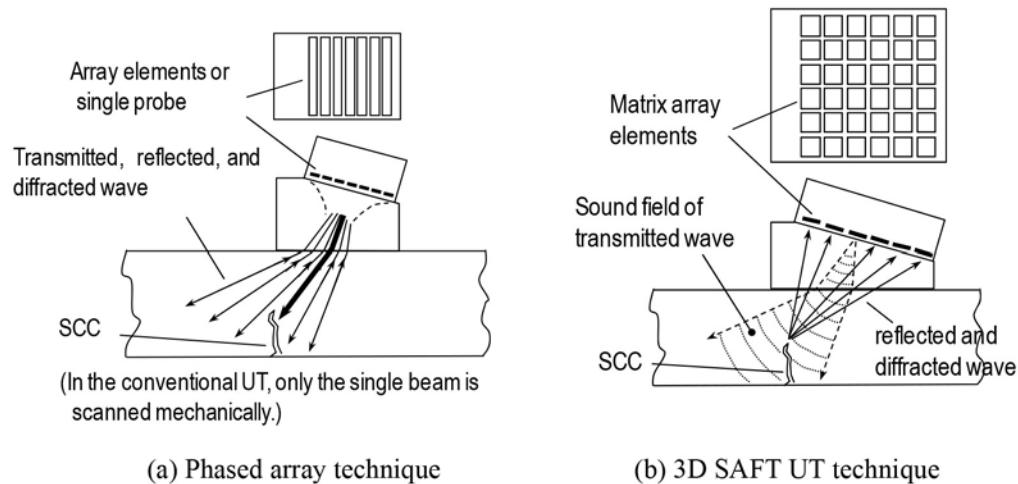


**Figure C.239** The Difference of Principle between Phased Array Technique and 3D SAFT UT Technique

In the case of conventional angle beam technique and phased array technique shown in Figure C.239(a), the ultrasonic beam is transmitted to the particular direction, and returned beam from the same direction as to the transmitted direction caused by the reflection and/or diffraction of defects, geometrical and metallurgical discontinuities. The imaging results of inspection show the image which is observed from particular direction of beam transmitted. Then the noise echoes, such as geometrical and metallurgical echo, are displayed in the same

way as the defect indication. Therefore it is difficult to discriminate the defect indications from noise echoes. Furthermore it required the probe scanning in order to transmit the UT beam to the exact position of SCC opening and SCC tip, and to acquire the inspection data under the suitable conditions.

In the case of 3D-SAFT UT, on the other hand, UT beam is transmitted by one element of matrix array probe, and reflected or diffracted UT wave from the opening of SCC, face of SCC, and tip of SCC is detected by transmitted element and other all elements of matrix array probe. This action is repeated for transmitting by all matrix array elements. Then the data of (the number of line elements  $\times$  the number of column elements) are stored in the memory of equipment. These all data are used to the calculation of SAFT processing as shown in Figure C.238, and 3D image within the inspected volume are displayed. By this 3D image data, three 2D images, C-scan/B-scan/D-scan image, are drawn.

In this 3D-SAFT technique, the waveform data which have different beam path by the combination of transmitted element and received element are used for the image calculation. Therefore obtained defect image is the image which is constructed by the data of different view directions. Then, random signals such as metallurgical noises are eliminated each other and SN ratio of true defect is increased. Furthermore this performance of 3D-SAFT is achieved by the inspection without probe scanning. It means the possibility of monitoring the SCC growth at the fixed position.

### C.5.2.2 Equipment

Figure C.240 shows the inspection system used for this measurement. The inspection instrument is Matrixeye™ 256ch manufactured by Toshiba corporation (Karasawa et al. 2009). The ultrasonic transducer consists of 16 $\times$ 16 transducer elements and its nominal frequency is 2 MHz. The wedge combined with the transducer is an angle beam wedge made of polystyrene, and its nominal refraction angle is 45° for longitudinal waves in stainless steel. Table C.6 provides more detailed information.

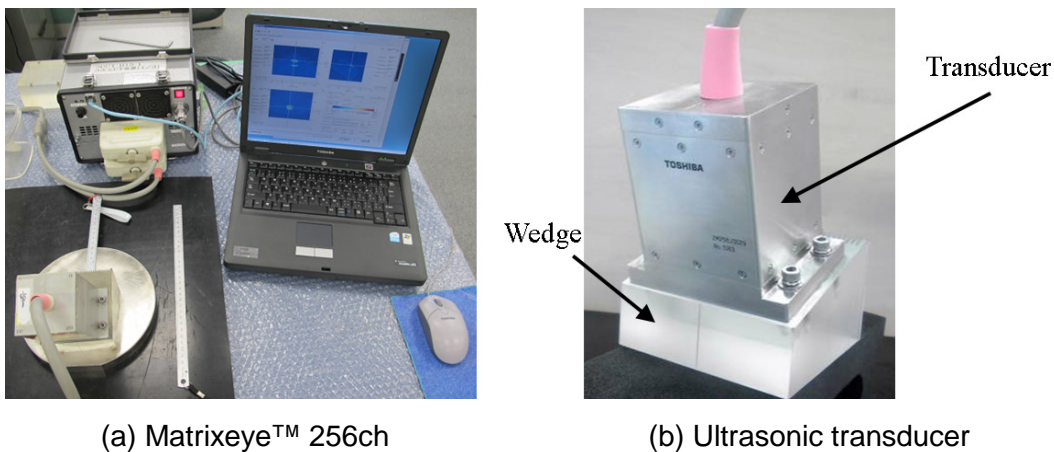


**Figure C.240 Inspection System**

**Table C.6 Detailed Information about Inspection System**

Item	Description
Testing method	Direct coupling

Couplant	Sonicoat
Frequency	2 MHz
Transducer elements	16x16 (3 mm-pitch)
A/D sampling	30 MHz
Wedge	Polystyrene (2,360 m/s)
Sound velocity of test object	5,750 m/s
Refraction angle (calculated)	45.1°
Gain	30 dB
Averaging	8
T/R pattern	Ttidori-Rall

### C.5.2.3 Data Acquisition

Defects are open on the inner surface of the pipe specimens. The inspections are carried out from the outer surface of the specimens. The transducer is placed in such a way that the incident direction is perpendicular to the longer direction of the defect. The inspection is performed toward both sides of the defect (Figure C.241). Figure C.242 shows how the transducer is actually placed. The contact surface of the wedge is flat for the ENSI blocks, and it is respectively contoured for the pipe specimens to be matched to the specimen surface where the transducer is placed for each case that the incident direction is the axial or circumferential direction.

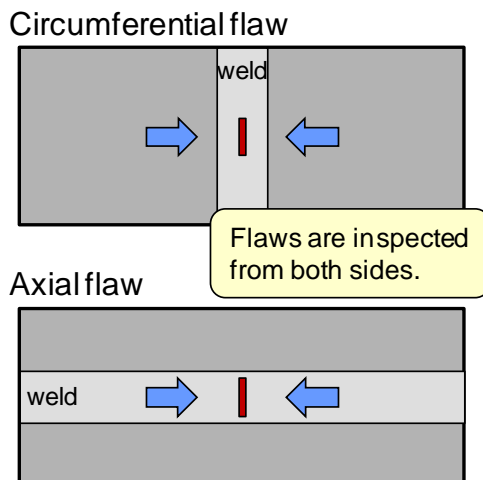
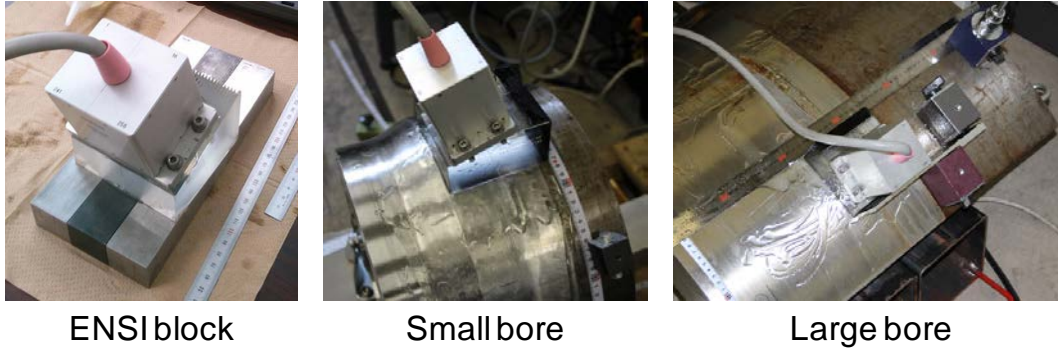
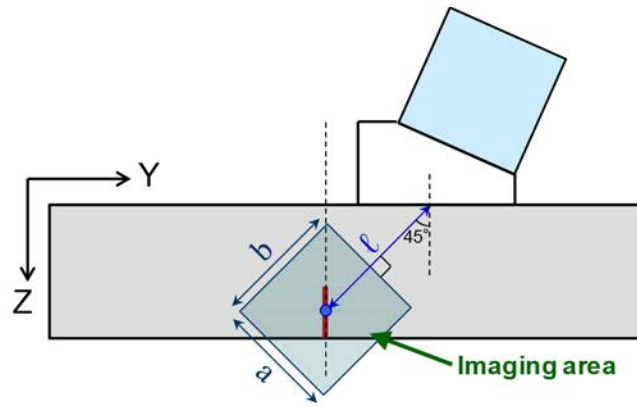


Figure C.241 Inspection Direction

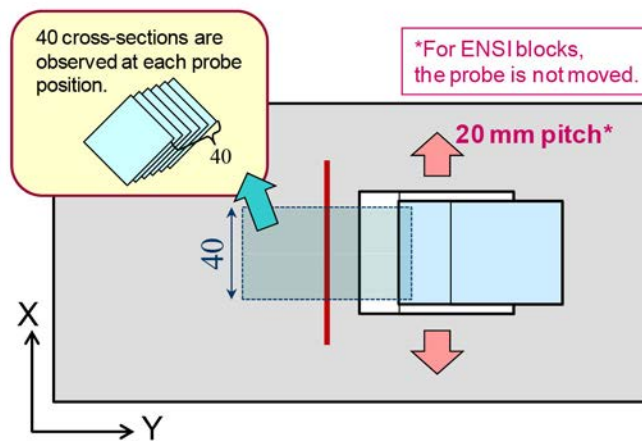


**Figure C.242 Probe Placement**

Figure C.243 shows the inspection conditions. The  $x$ ,  $y$  and  $z$  coordinates are defined as shown in Figure C.243 (this definition does not always correspond with the coordinates of a specimen). Because the locations and sizes of the defects are disclosed, the transducer is placed as the “central beam axis” bumps on the defect plane (the plane that includes a defect surface such as a crack face) at the distance  $\ell$  from the incident point. Here the “central beam axis” means the central beam axis when all the transducer elements are regarded as one transducer element. After the ultrasonic signals for every transmitter-receiver combination are recorded, three-dimensional SAFT data is generated based on the principle explained in Section C.5.2.1. The center point of the area where the data is generated is the point at the distance  $\ell$  from the incident point along the center beam axis. The size of the  $y$ - $z$  cross-section of the area is determined by the length  $a$  in the direction parallel to the central beam axis and the length  $b$  in the direction perpendicular to the central beam axis. Table C.7 shows the values  $\ell$ ,  $a$  and  $b$  determined for each specimen. The length of the area in the  $x$  direction is fixed to 40 mm.



(a) Cross-sectional view



(b) Top view

**Figure C.243 Inspection Conditions**

**Table C.7 Parameters for Imaging Range**

	$l$ (mm)	$a$ (mm)	$b$ (mm)
ENSI Block	42.5	45	50
Large bore pipe specimen	80	100	120
Small bore pipe specimen	43	80	70

From the three-dimensional SAFT data, two-dimensional SAFT images are constructed on several cross-sections to examine the inside of the specimen. At one position of the transducer, SAFT images are constructed on 40  $y$ - $z$  cross-sections (20 cross-sections on either side of the center section) at 1-mm pitch in the  $x$  direction. If the SAFT images obtained at one transducer position are insufficient for evaluating a whole defect, the transducer is moved along the longer direction of the defect with a 20-mm pitch, and the SAFT images are obtained at each position. Also, when the images are not clear enough to evaluate a defect, the transducer is moved forward toward the defect to obtain better images.

When an axial defect on a pipe specimen is evaluated, a specimen surface has a curvature in the incident direction as shown in Figure C.244. The transducer is placed with this curvature taken into consideration. However, the  $x$ ,  $y$  and  $z$  coordinates of the data acquisition software for

this measurement are the same relative to the transducer as the transducer is placed on a flat plate. Because the PARENT protocol prescribes, for the pipe specimens, the  $x$  and  $y$  coordinates go along the outer surface of the specimen and the  $z$  coordinate is perpendicular to the outer surface of the specimen, the prescribed coordinates become inclined with increasing distance from the transducer in the circumferential direction, which causes an error between these two coordinate systems. As a result, although the true  $z$  direction is perpendicular to the outer surface of a pipe specimen, a defect perpendicular to the outer surface of the pipe specimen is considered to be inclined with respect to the  $z$  direction of the coordinate system of the data acquisition software when the specimen surface has a curvature in the incident direction. In this case, the  $z$  component of the defect size is shortened.

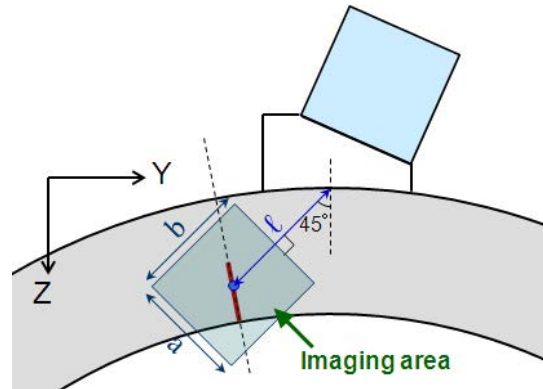


**Figure C.244 Inspection Conditions for Axial Defect of Pipe Specimens**

Let us consider the error due to the above-mentioned problem. The central angle of the arc between the incident point and the defect plane is given by

$$\theta = \arctan\left(\frac{\ell}{\sqrt{2r_{OD} - \ell}}\right),$$

where  $\ell$  is the distance between the incident point and the defect plane along the center beam axis, and  $r_{OD}$  is the outer radius of the pipe specimen. If the true  $z$  component of the defect size is  $d$ , the  $z$  component shown by the data acquisition software is  $d \cos\theta$ , and then the difference between them is  $d(1 - \cos\theta)$ , which is the percentage of the true  $z$  component. This percentage is 1% for the large bore pipe specimens and 3.5% for the small bore pipe specimens. In this inspection, this error is less than 1 mm. Therefore, any correction is not made for this error in this inspection.

If bottom echoes are not obtained in the measurement, the bottom surface is assumed to be the level at the depth equal to the pipe wall thickness below the incident point. However, when the inner surface of the specimen has a curvature in the incident direction, the  $z$  coordinate of the inner surface is not constant along the incident direction in the coordinate system of the data acquisition software. Then, this causes an error if bottom echoes are not obtained in the measurement because the  $z$  component of the defect size is obtained by the difference of the  $z$  coordinates between the tip of the defect and the assumed bottom surface. Let  $r_{ID}$  be the inner radius of the pipe specimen. The  $z$  coordinate of the inner surface where the defect is located is lower than that of the assumed bottom surface by the distance  $r_{ID}(1 - \cos\theta)$ . Therefore, the  $z$

component of the defect size is shortened due to this gap. In this inspection, any correction is not made for this gap either.

#### C.5.2.4 Data Analysis

After the acquisition of the three-dimensional SAFT data, the defect profile is derived from SAFT images. Figure C.245 shows the accumulated images on  $x$ - $y$  (C-scan),  $y$ - $z$  (B-scan) and  $z$ - $x$  (D-scan) planes that are obtained by adding up values of the SAFT data along the direction perpendicular to each plane. In these images, the  $z$ - $x$  plane corresponds to the defect plane (this coordinate system corresponds to that of a specimen only when the defect extends in the circumferential direction). In the image on the  $z$ - $x$  plane, the strong indications a little below the center are induced by the corner echoes, and the weak indications that shape the elliptical outline above the center are formed by the defect tip echoes.

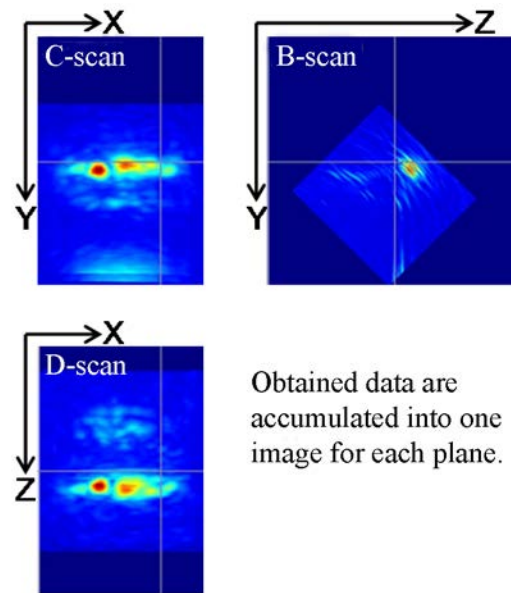


**Figure C.245** Accumulated Images Obtained by Merging SAFT Images (when the defect extends in the circumferential direction)

Figure C.246 shows the derivation of defect profile. The left image of Figure C.246 is obtained by binarizing the accumulated image on the  $z$ - $x$  plane with the noise level used as the threshold. The noise level is determined from a set of the SAFT images. This binarized image represents the defect shape. The SAFT images on the  $y$ - $z$  plane are closely examined one by one to locate the tip and corner echo positions as coordinate values, which results in the right graph in Figure C.246. In this process, a significant indication is distinguished from a strong noise by considering the positional relation between the corner indications and the tip indications, the continuity of indications, and the tendency for indications to follow the movement of the transducer. The defect depth and length are determined from these results. In this data analysis, an indication that cannot be characterized as a noise on systematic criteria is evaluated as a significant indication even if that indication obviously seems to be a noise because its positional relation is unlikely for a defect.

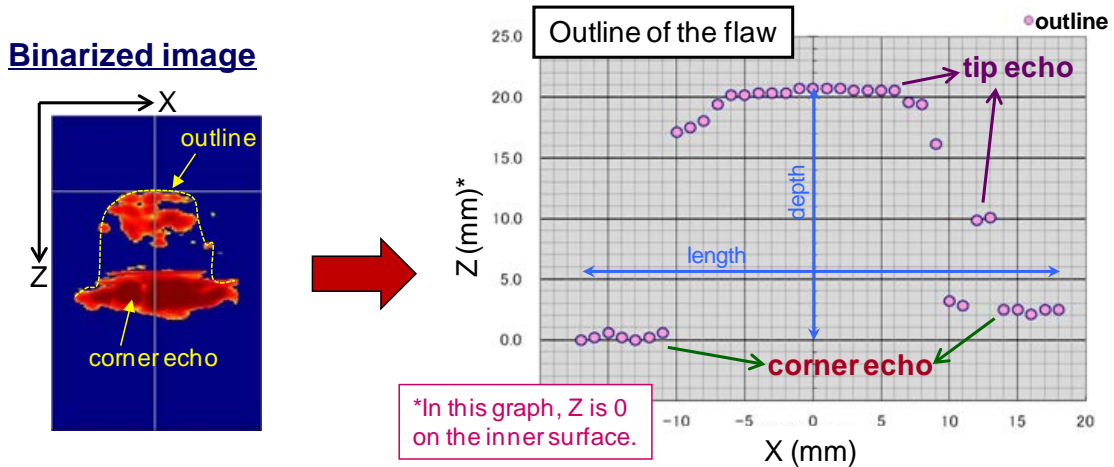


**Figure C.246 Derivation of Defect Profile**

If strong indications are found around the bottom surface just below defect tip indications, that defect is considered as a surface-breaking defect. The point of the peak value in the indications around the bottom surface is taken as the representative point of the bottom surface. A point in the tip indications is selected as the defect apex in such a way that the distance in the z direction between this point and the representative point of the bottom surface is maximized. The depth of a defect is defined by this distance in the z direction. When indications are not obtained around the bottom surface and only tip indications are obtained, the bottom surface is determined as the level at the depth equal to the pipe wall thickness below the incident point.

To obtain the defect length, each end of a defect is determined as the point where the amplitude of an indication around the bottom surface becomes less than the noise level. When indications spread over a wide range around the bottom surface and it is difficult to determine the ends of the indications, the point where the distance from the bottom surface first becomes less than 1 mm is taken as an end of the defect. When no indication is found around the bottom surface, it is decided that the defect length cannot be obtained.

On a data sheet of the round robin test, the position and the dimensions of a defect is reported as the x, y and z coordinates that describe a defect area, which is the smallest cuboid that can contain the defect. When a defect area is set up from a measurement result, a defect area is considered as a two-dimensional rectangular area perpendicular to the x-y plane, parallel to the longer direction of the defect and including the defect apex. The edges of the defect area are determined by the defect apex and both ends of the defect.

As mentioned in Section C.5.2.3, a defect is inspected from both sides of the defect. To report the x, y and z coordinates of a defect area, the measurement results for both sides of the defect should be combined. From the two measurement results, two defect areas are obtained for each defect. If the perpendicular distance between the two defect areas is less than or equal to 10 mm, the conclusive defect area is reported as the smallest cuboid that contains the two defect areas. If the perpendicular distance is greater than 10 mm but the tip indications of these measurement results intersect with each other, the two defect areas are treated as one conclusive defect area and its range in the direction perpendicular to the two defect areas is made  $\pm 5$  mm from the middle point of the two defect areas. Besides, if the above-mentioned conditions are not satisfied but any special reason is found such as profile symmetry of both sides and correlation of the distributions of indications, the conclusive defect area is reported in



the same manner as the above second case. In the other cases, the two defect areas are considered to be caused by independent defects and each area is individually reported as a conclusive defect area.

### **C.5.2.5 Team's Assessment of the Technique Based on the Round Robin Test Results**

Whereas phased array ultrasonic testing has a low accuracy for crack depth sizing at a steep slope of the crack profile, 3D SAFT can obtain the overall profile of the crack and an accurate depth estimate even at such a steep part.

Although the specimens P1 and P37 include internal cracks, it is difficult to catch an indication of the lower end of an internal crack because strong indications around the bottom surface obscure weak indications due to the lower end of an internal crack. Therefore, it had to be considered that the lower end of an internal crack reaches the bottom surface.

In this round robin test, since the defects exist in the nickel-based alloy welds and several specimens have about 80 mm-thick walls, ultrasonic testing results are subject to strong attenuation. 3D SAFT has difficulty generating high-amplitude ultrasonic waves and sometimes cannot even detect a defect because 3D SAFT uses a transducer that consists of many small transducer elements. Therefore, the results show low detectability of the defects especially for measuring the axial defects, which require ultrasonic waves to travel a long distance inside weld metal. Meanwhile, 3D SAFT obtained the approximate profiles of the detected defects and can be expected to estimate the profile of a defect in a nickel-based alloy weld unless ultrasonic attenuation causes a significant problem. Although the results of the defect profile estimation cannot be evaluated for lack of the information of the true profiles, most of the sizing errors are acceptable and it is considered that 3D SAFT provided reliable defect profile estimation.

### **C.5.3 Subharmonic Phased Array for Crack Evaluation, Technique ID 6-SHPA1, 6-SHPA2, 6-SHPA3, 6-SHPA4**

#### **C.5.3.1 Overview**

Crack can be detected by ultrasound if cracks are open, since ultrasound is strongly scattered by the crack. However, if cracks are closed because of compressive residual stress and/or the oxide films generated between crack faces, ultrasonic inspection can cause the underestimation or nondetection of cracks since ultrasound penetrates through the closed crack. To detect and measure defects, a crack imaging method, subharmonic phased array for crack evaluation (SPACE) was used. SPACE is on the basis of the subharmonic generation by short-burst waves and the phased array algorithm with frequency filtering. There are two types of SPACE. One is SAW SPACE which uses surface acoustic wave (SAW), where the array transducer is positioned on the crack opening side through a wedge designed to generate SAW. SAW SPACE is used to detect defects and measure their lengths. The other one is Bulk SPACE which uses bulk longitudinal wave, where the array transducer is positioned on the opposite of crack opening side. Bulk SPACE is used to measure the depths of defects.

#### **C.5.3.2 Principle**

The schematic of SAW SPACE is shown in Figure C.247. SAW SPACE uses a surface acoustic wave (SAW). A PZT array transducer with a wedge was used to generate intense ultrasound by focusing. The phased array equipment is MultiX LF (produced by M2M). Each element of the PZT array transducer was excited by a three-cycle burst of a frequency of 3.5 MHz with 150 V

following a delay law for transmission focusing. The scatterings of fundamental and subharmonic waves occur at the open and closed parts of defects, respectively. The scattered waves received by the PZT array transducer are analog-to-digital converted. Subsequently, they are digitally filtered at fundamental and subharmonic frequencies, where the sampling frequency was 50 MS/s. After their phased shift following the delay law for reception focusing, they are summed. Finally, the root-mean-square (RMS) value is calculated as the intensity at a focal point. This process is repeated over a scan area with a step to create images. The image is created in sequence for each transmission focal point. The images for all transmission focal points can be merged. The fundamental array (FA) and subharmonic array (SA) images obtained can indicate the open and closed parts of cracks, respectively.

The schematic of Bulk SPACE is shown in Figure C.248. A PZT array transducer was used to generate and receive ultrasound by focusing. The phased array equipment are MultiX LF (produced by M2M) and PAL (produced by KrautKramer). Each element of the PZT array transducer was excited by a three-cycle burst with 150 V following a delay law for transmission focusing. We selected the input frequency of 2 MHz, 5 MHz, and 7 MHz, depending on specimens. The scattering of fundamental and subharmonic waves occur at the open and closed parts of defects, respectively. The scattered waves received by the PZT array transducer are analog-to-digital converted. Subsequently, they are digitally filtered at fundamental and subharmonic frequencies. After their phased shift following the delay law for reception focusing, they are summed. Finally, the root-mean-square (RMS) value is calculated as the intensity at a focal point. This process is repeated over a scan area with a step to create images. The image is created in sequence for each transmission focal point. The images for all transmission focal points can be merged. The FA and SA images obtained can indicate the open and closed parts of cracks, respectively.

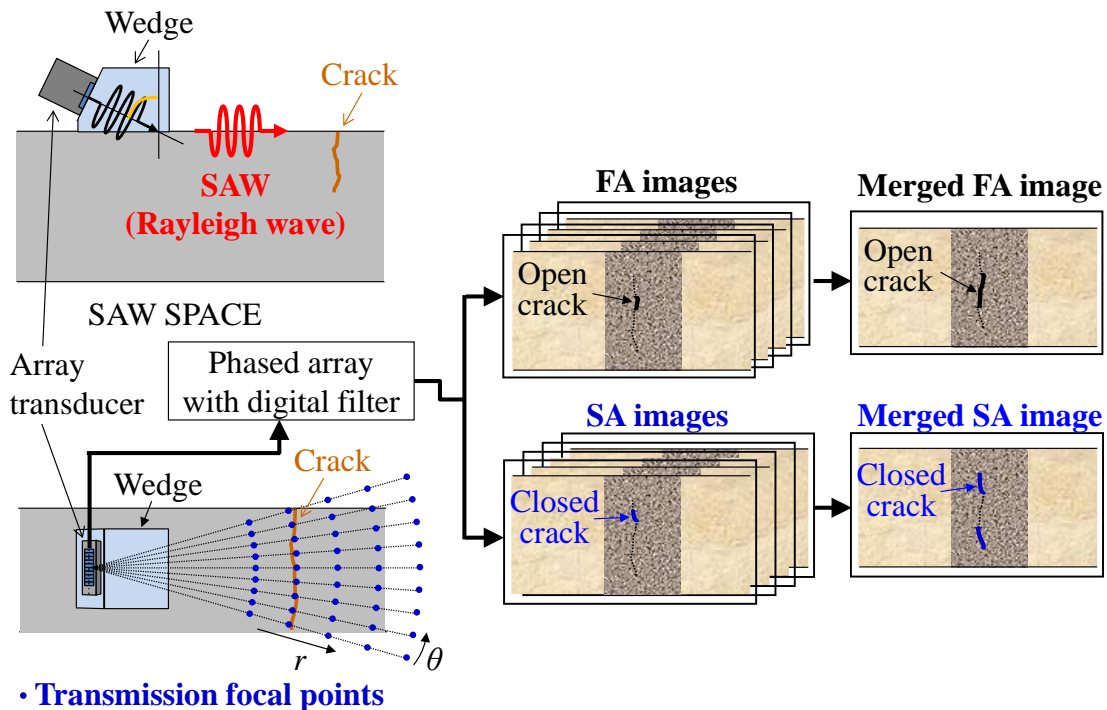


Figure C.247 Schematic of SAW SPACE

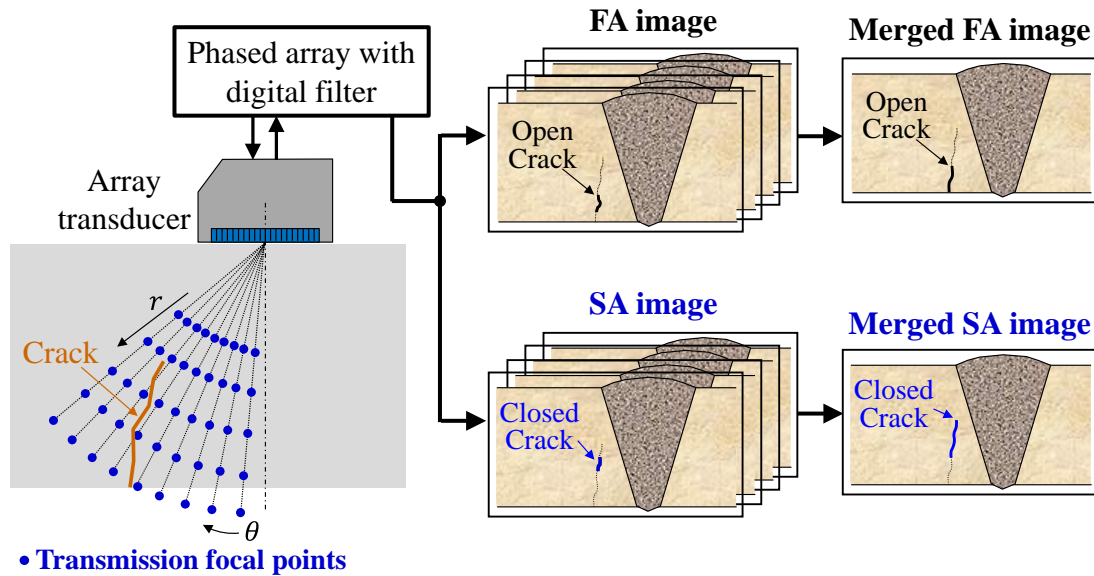


Figure C.248 Schematic of Bulk SPACE

### C.5.3.3 Procedure and Technique

We selected four techniques, which are SHPA01, SHPA02, SHPA03, and SHPA04 as follows:

- [SHPA0]
  - FA image (5 MHz) of Bulk SPACE
  - Phased array apparatus: PAL produced by KrautKramer
  - Probe: PZT array transducer (5 MHz, 32 el, 0.5 mm pitch, 10 mm width) produced by Imasonic
  - Input frequency: 5 MHz
  - Input voltage: 100 V
  - Scanning condition:
    - Focus on transmission: depth=15 mm–45 mm (3.5-mm step),  $\theta=10^\circ \sim 60^\circ$  ( $1^\circ$  step)
    - Focus on reception: depth=15 mm–45 mm (3.5-mm step),  $\theta=10^\circ \sim 60^\circ$  ( $1^\circ$  step)
- [SHPA1]
  - FA image (2 MHz) of Bulk SPACE
  - Phased array hardware: PAL (produced by KrautKramer)

- Probe: PZT array transducer (2 MHz, 32 el, 0.5 mm pitch, 10 mm width) produced by JapanProbe
- Input frequency: 2 MHz
- Input voltage: 100 V
- Scanning condition:
  - Focus on transmission: depth=15 mm–45 mm (3.5-mm step),  $\theta=10^\circ \sim 60^\circ$  (1° step)
  - Focus on reception: depth=15 mm–45 mm (3.5-mm step),  $\theta=10^\circ \sim 60^\circ$  (1° step)
- [SHPA2]
  - SA image (3.5 MHz) of Bulk SPACE (f/2)
  - Phased Array Hardware: MultiX-LF produced by M2M
  - Probe: PZT array transducer (5 MHz, 32 el, 0.5 mm pitch, 10 mm width) produced by Imasonic
  - Input frequency: 7 MHz
  - Input voltage: 150 V
  - Scanning condition:
    - Focus on transmission:  $r=14 \text{ mm}–42 \text{ mm}$  (7-mm step),  $\theta=6^\circ–65^\circ$  (1° step)
    - Focus on reception: 0.5-mm step
- [SHPA3]
  - FA image (3.5 MHz) of SAW SPACE
  - Phased array hardware: MultiX-LF produced by M2M
  - Probe: PZT Array transducer (5 MHz, 32 el, 0.5 mm pitch, 10 mm width) produced by Imasonic
  - Input frequency: 3.5 MHz
  - Input voltage: 100 V
  - Scanning condition:
    - Focus on transmission:  $r=39.5 \text{ mm}$ ,  $\theta=-14^\circ \sim 15^\circ$  (1° step)

- Focus on reception:  $r=39.5$  mm,  $\theta=-14^{\circ}\sim 15^{\circ}$  ( $1^{\circ}$  step)

#### C.5.3.4 Self Assessment of the Technique Based on the Round Robin Test Results

In this measurement, we used flat PZT array transducer because the curvature of the specimen is not so large. On the other hand, our techniques can be applied to specimens with a large curvature by using flexible array transducer or a shoe conformable to the curvature with a delay law under the consideration of curvature.

Specimens P1, P4, P28-P32 were measured by subharmonic phased array for crack evaluation (SPACE). As a result, most cracks were visualized in FA images, suggesting that they were open. On the other hand, hiped EDM (P4, Nos. 1 and 2) were visualized in SA images, suggesting that they were closed. Thus, it was proved that SPACE was capable to detect all the cracks of each specimen, and to measure their lengths and depths. In addition, the importance of the subharmonic waves with lower frequency than the incident wave was verified to detect and measure closed defects in highly attenuating objects with coarse grains or textures.

#### C.5.4 Large Amplitude Excitation Subharmonic UT, Technique ID 18-LASH1, 18-LASH2

##### C.5.4.1 Overview of LASH Technique

LASH (Large Amplitude Subharmonic) technique develops to combine with a SPACE measurement system as shown in Figure C.249. When larger amplitude ultrasound is incident to the crack subharmonic wave sometime generate at the crack. For the imaging of these subharmonic images, commercial phased array system is applied using aperture synthesis processing and additional digital filter. However amplitude of transmitted ultrasound is limited because larger voltage burst wave of SPACE will be damage to the usual transducers. Thus, LASH technique is expected to break this limitation of SPACE in industrial inspection.

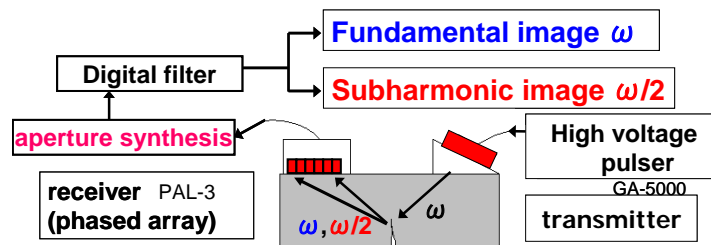
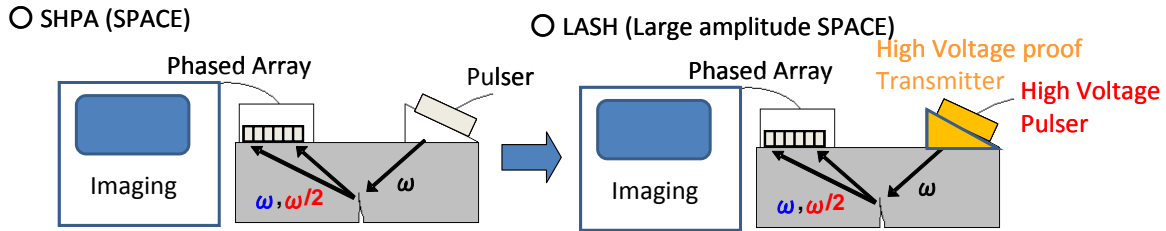


Figure C.249 Schematic Diagram of Basic SPACE System

The schematic diagram of LASH (Lager amplitude SPACE) system is shown in Figure C.250. Only the ultrasonic transmission components were improved from usual SPACE. We must be focus whether the LASH system has an advantage in crack tip echo identification of low S/N ratio for conventional SPACE system or not.



**Figure C.250 Schematic Diagram of Improved LASH System**

For the high voltage excitation of SPACE without any damage in transducer, the structure of transducer must improve to proof up to 2000 V excitation as shown in Figure C.251. Since the fabricated temperature of process is 600 °C which is higher than the Curie point of the PZT, repolarization process with the DC voltage of 1000 V/mm during 30 minutes at 200 °C in silicon oil bath is applied after the fabrication of the transducer. We have developed two techniques of high voltage pulser (include the transformer coil system) and laminated transducer system as the LASH techniques. In this study high voltage pulser up to 1000V excitation was used for the large amplitude ultrasound transmission. We call tech ID 18-0 for 400 V excitation LASH measurement system which is as same excitation voltage as conventional SPACE measurement, and tech ID 18-1 for high voltage excitation LASH measurement system.

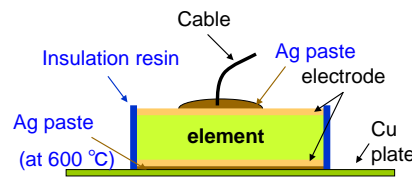


**Figure C.251 Improvement for High Voltage Transducer**

In comparison of the spatial resolution with conventional inspection imaging and the SPACE, our SPACE system applied here is a laboratory system which used 32 element phased array and 8 bit RF signals for subharmonic imaging by aperture synthesis improving the old commercial phased array system. Therefore, obtained images may be inferior to the one by modern phased array systems (e.g., 128 element and 10 bit) in measurement sensitivity or in spatial resolution. However the most important point here is whether the SPACE technique has an advantage in crack tip echo identification or not in case that the estimated crack tip show lower S/N ratio in conventional inspections. If the advantage of SPACE can be found for even some of the cracks, higher resolution and sensitivity can be improved by replacing the old phased array system of present SPACE to the modern commercial phased array system in future.

#### **C.5.4.2 Inspection Procedures for Open Specimens**

Since all the positions of cracks in each our measurement specimens were open, we positioned the transducers to given crack positions and only the detectability of crack tips were investigated using LASH. In these measurements, single B-scope was measured by aperture synthesis procedures with LASH system.

Furthermore only for the cracks in which crack tips can be clearly observed in subharmonic B-scope images, three dimensional B-scope images were measured using the encoder system with 1.3 mm pitch as shown in Figure C.252 to estimate of the three dimensional crack shape. Reconstruction of the three dimensional B-Scope images was made at the parallel positions along the weld line. Since this scanning equipment with encoder also fabricated for laboratory use, fairly good image can be obtained for flat surface specimen of P-28 ~ P-32, however significant measurement can't be made for large curved surface specimens of P-1 and P-12. Thus, B-scan image at the center position of each given crack position was measured as a standard inspection data and a three dimension image with encoder system obtained as an optional one in this report.

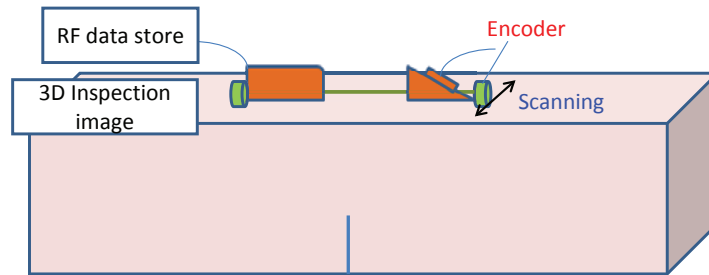


**Figure C.252 Three Dimensional Inspection with Encoder**

### C.5.4.3 Experimental Results

#### Small Flat Specimen

Representative B-scan images at the center of given crack position of P28 specimen were shown in Figure C.253. Left image was a fundamental 5 MHz image (correspond to conventional inspection of linear ultrasound) and right one was a subharmonic 2.5MHz image. Red line shows a position of a back surface and black dot line shows a crack tip from the given crack position.

B-scan images for specimen P30, P31 and P32 were shown in Figures C.254–C.256. All the images were obtained by 1000 V excitation which expected to obtained the highest S/N ratio of crack tip echo comparing to the one by standard 400 V excitation of conventional SPACE.

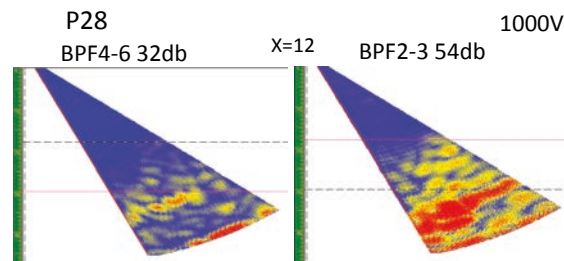


**Figure C.253 B-Scope Image of P28 Specimen**

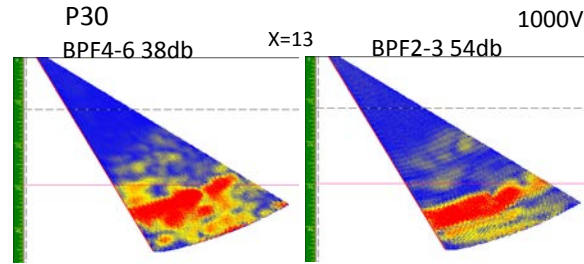


**Figure C.254 B-Scope Image of P30 Specimen**

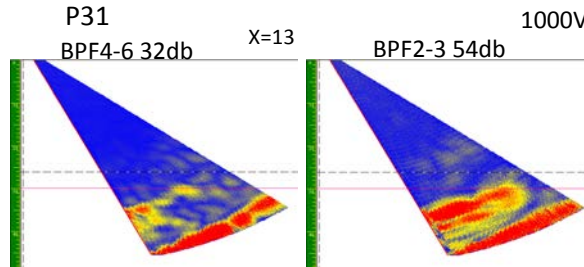


**Figure C.255 B-Scope Image of P31 Specimen**

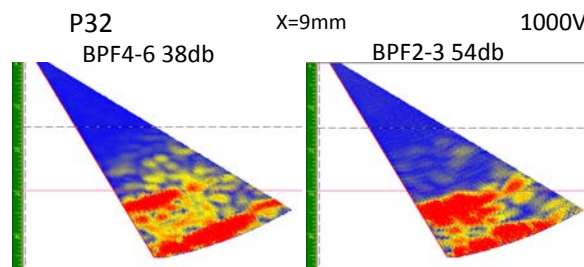
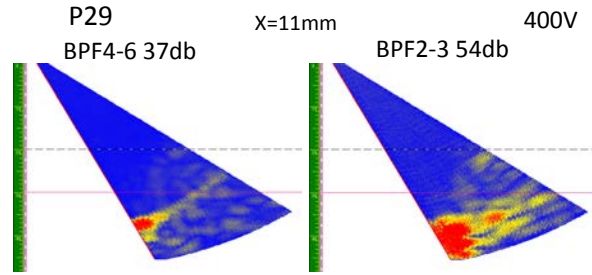


**Figure C.256 B-Scope Image of P32 Specimen**

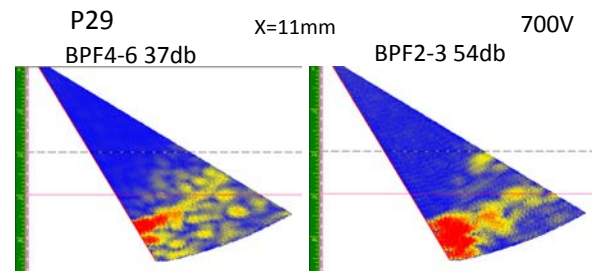
Measurement condition of amplitude and applied band path filter for each imaging were described in top of each figure. All the obtained images of specimen P28, P30, P31 and P32 show low S/N ratio in crack tip echo detection due to the large backscattering from microstructure around the welding area. Only in P28 image in Figure C.253, crack tip could be detected especially in right subharmonic image. However in all the specimens crack tip cannot be clearly detected both by linear and nonlinear ultrasound measurement.

B-scan images for specimen of P29 for the excited voltage of 400V, 700V and 1000V were shown in Figure C.257(a), (b), (c).

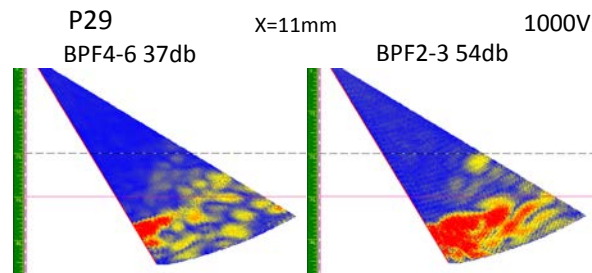




(a) 400V Excitation



(b) 700V Excitation



(c) 1000V Excitation

### Figure C.257 B-Scope Image of P29 Specimen

Comparing with the fundamental left images, crack tip echo could be obtained clearly in subharmonic right images for all excitation voltage and S/N ratio and the detectability of crack tip echo were increasing according to the excitation voltage. In fundamental linear images of left one, any crack tip echoes could not be detected due to large backscattering noise. For the detection of the crack tip in P29 specimen, thus, especially LASH technique was extremely effective. Since we can clearly detect the crack tip echo for P28 and P29 specimens, three dimensional imaging procedures using encoder were applied. Sample of the results were shown in Figure C.258. Upper one was 3D view and lower one was cross-section view. Left one was fundamental images and right one was subharmonic images.

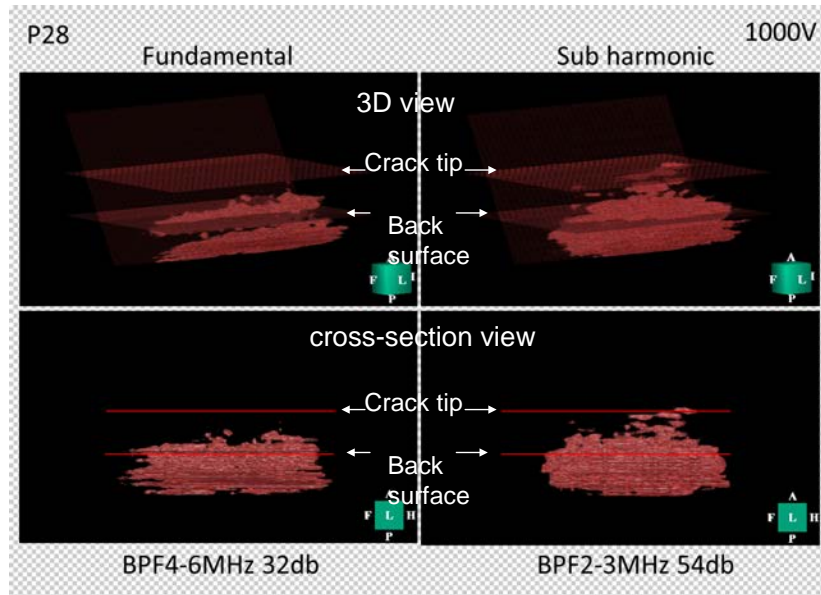


**Figure C.258 Three-D View and Cross-section View of P29 Specimen with 1000V Excitation**

Hatchings in 3D images were the given positions of crack tip and back surface. Though we show the 3D images only for the specimens P28 and P-29 in this report, significant crack tip could not be obtained because of large scattering noise in other 3D images for other specimens.

### Large Specimens

Though we tried to detect the cracks of BMI specimens, the curved specimen surface and large thickness of the specimen did not match our measurement setup because our system had been developed in laboratory use for a flat and small specimen.

Representative B-scan images at the center of the given position of SCC in P12 specimen with 1000V excitation were shown in Figure C.259.

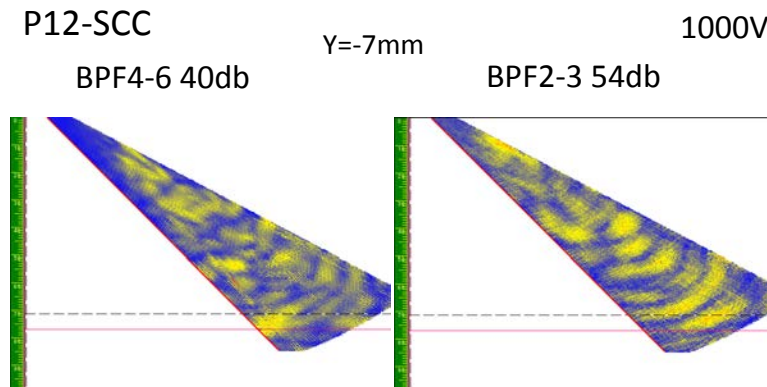


**Figure C.259 B-Scope Image of SCC in P12 Specimen**

Both in left fundamental image and right subharmonic image, crack tip cannot be detected due to the extremely large scattering noise. This might be caused by the bad couplant condition due

to the curved surface and to the large thickness of the specimen P12. For the comparison, B-scan images of EDM notch in specimen P12 with 1000V excitation with no filter were shown in Figure C.260.

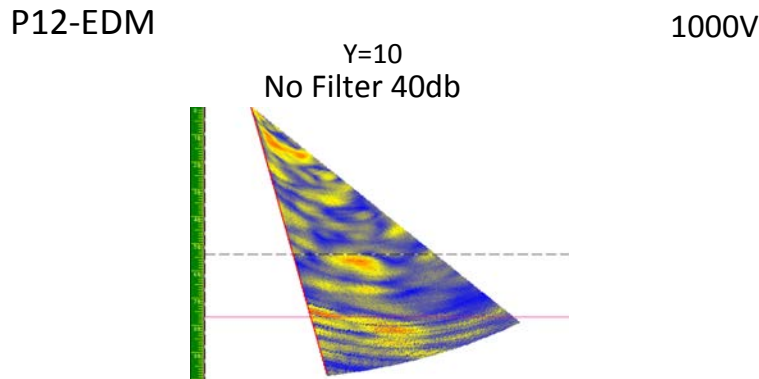
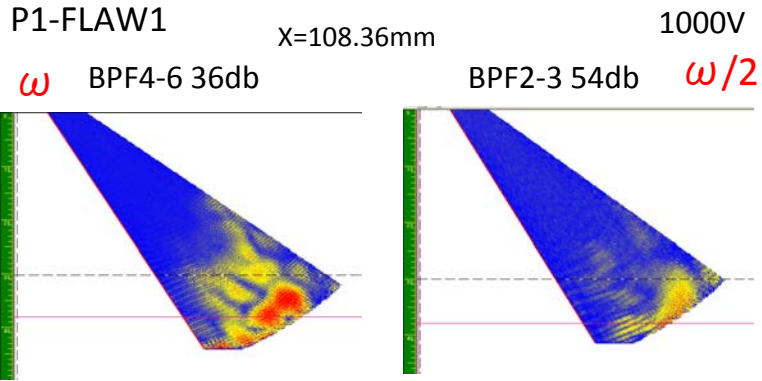


**Figure C.260 B-Scope Image of EDM Notch in P12 Specimen**

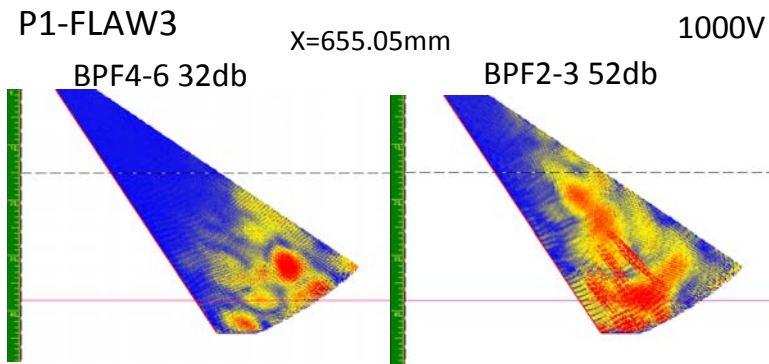
Though EDM notch tip could be recognized at the given position of dotted line due to the large amplitude of tip echo, extremely large scattering echoes were also observed. B-scan images of flaws 1, 3, 4 in specimen P1 are shown in Figure C.261(a), (b), (c). All the images were obtained by 1000 V excitation which expected as higher S/N ratio of flaw tip echo.

Since the thickness of the specimen P1 was thinner than specimen P12, scattering noises from microstructures were lower than one of P12 specimen. However, both in left fundamental image and right subharmonic image, crack tip echo cannot be detected for the flaw-1, 3, 4. B-scan images of flaw 2 in specimen P1 with the excited voltage of 400V, 700V and 1000V are shown in Figure C.262(a), (b), (c).

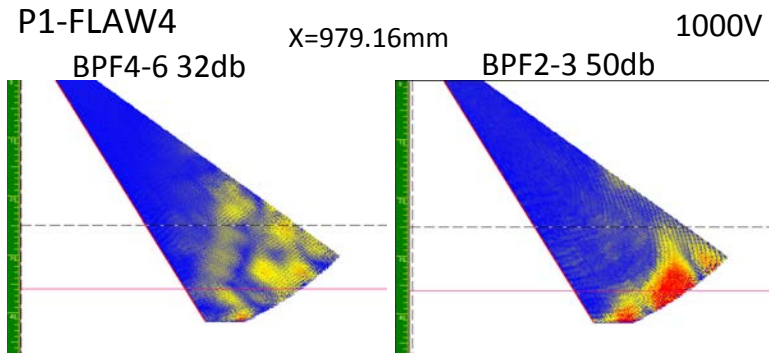
Since Flaw-2 show lower scattering noise than one of other flaws, crack tip echo might be detected extremely in higher voltage subharmonic images using LASH technique. However S/N ratio of flaw tip echo was not enough and further improvement of the measurement setup especially for curved surface specimen will be expected.



(a) Flaw 1

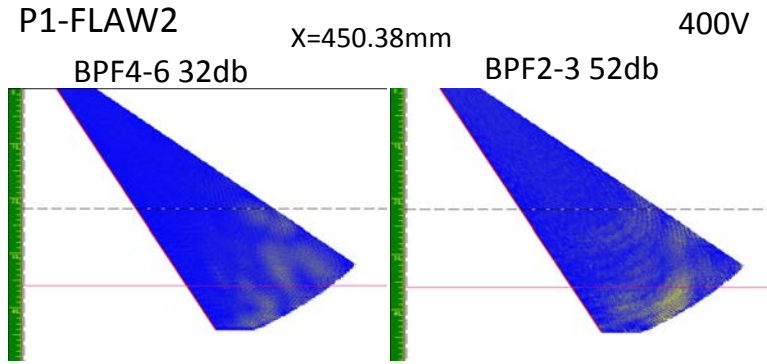


(b) Flaw 3

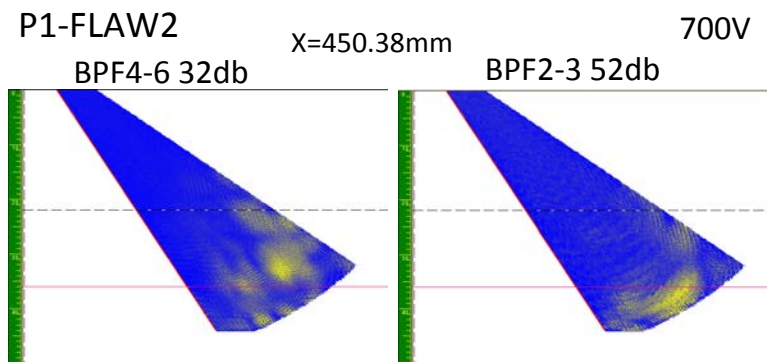


(c) Flaw 4

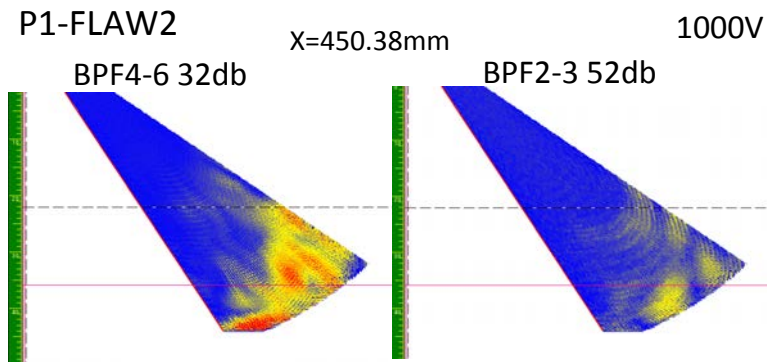
Figure C.261 B-Scope Images of Flaws in P1 Specimen



(a) 400V Excitation



(b) 700V Excitation



(c) 1000V Excitation

**Figure C.262 B-Scope Images of Flaw 2 in P1 Specimen**

**C.5.4.4 Assessment of LASH Technique for the Round Robin Test**

We applied LASH techniques with high voltage SPACE of nonlinear imaging inspection system up to 1000 V excitation to the five small and two large DMW specimens and obtained following conclusions.

1. About the crack in small specimen P-28, 29 and the Flaw-2 in large specimen, LASH technique up to 1000V was effective for the detection of the flaw tip echo comparing with the conventional linear ultrasound technique and conventional SPACE technique.
2. However an improvement of the measurement setup especially for couplant to curved surface specimen will be required. Larger amplitude ultrasonic incident and the improvement of the S/N ratio in subharmonic inspection image will also be required.

## **C.5.5 Higher Harmonic UT, Technique ID 27-HHUT1, 27-HHUT2, 27-HHUT3**

### **C.5.5.1 Overview**

Higher harmonic ultrasonic testing (HHUT) detects waveform distortion of the ultrasonic waves scattered at cracks or SCC in comparison with the incident sinusoidal tone-burst wave as higher harmonic amplitudes. Different from the conventional UT based on the acoustic impedance difference, HHUT is free from the grain boundary scattering noise, therefore it can detect closed cracks and SCC with high S/N ratio.

We apply an immersion higher harmonic imaging technique (HHIT) for detecting cracks and SCC.

### **C.5.5.2 Principle of Higher Harmonic UT and Higher Harmonic Imaging**

#### **Waveform Distortion and Harmonic Generation**

Ultrasonic propagation across cracks and SCC in metals could be modeled as shown in Figure C.263. The cracked face has high stiffness for compressive stress, however, it has far lower stiffness in tensile stress. When a sine burst wave is sent for a cracked face, the transmitted wave across the face is severely deformed. The fast Fourier transformation (FFT) of the transmitted wave has many higher harmonics in frequency domain as shown in Figure C.264. By using an analog high pass filter with appropriate cut-off frequency, we could extract desired higher harmonics.

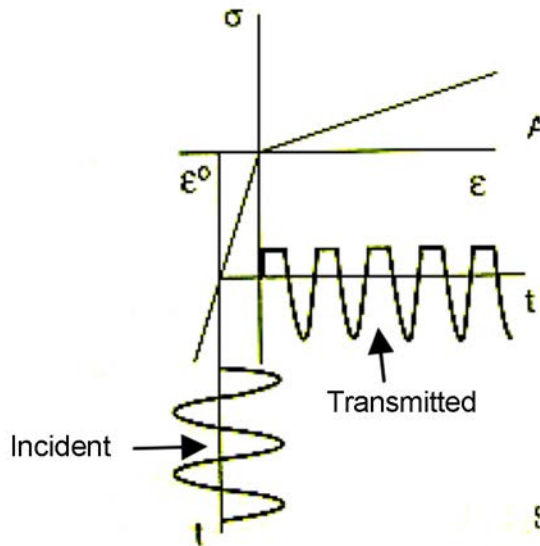


**Figure C.263 Waveform Distortion of the Incident Sine Wave at Crack Face**

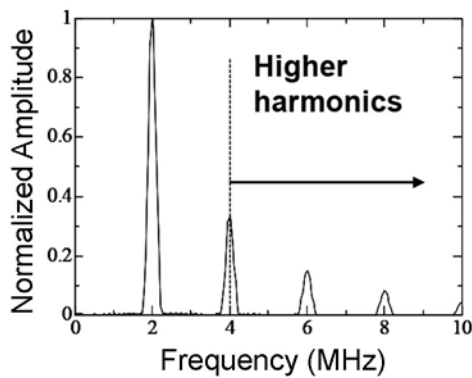


**Figure C.264 Extraction of Higher Harmonics Using Analog High Pass Filter**

### **Immersion Higher Harmonic Imaging of Cracks and SCCs**

The higher harmonic imaging system is composed of a sine burst wave pulser, a focused transducer, an in-plane scanning unit, analog high pass filters, an A/D wave memory and imaging software. The burst wave pulser, RITEC RPR-4000, transmits high power sinusoidal wave with low noise of harmonics. The higher harmonic waveforms scattered at cracks or SCC are extracted by using the analog high pass filter and stored in the wave memory and the harmonic amplitude is mapped on X-Y plane.

The main units of the imaging system are shown in Figures C.265–C.267. For angular incidence, the transducer is mounted on the attachment shown in C.267.

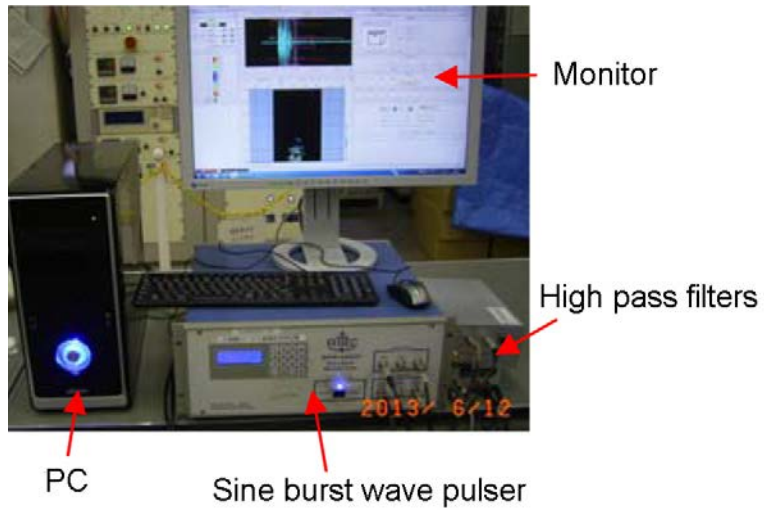


**Figure C.265 Higher Harmonic Imaging System**

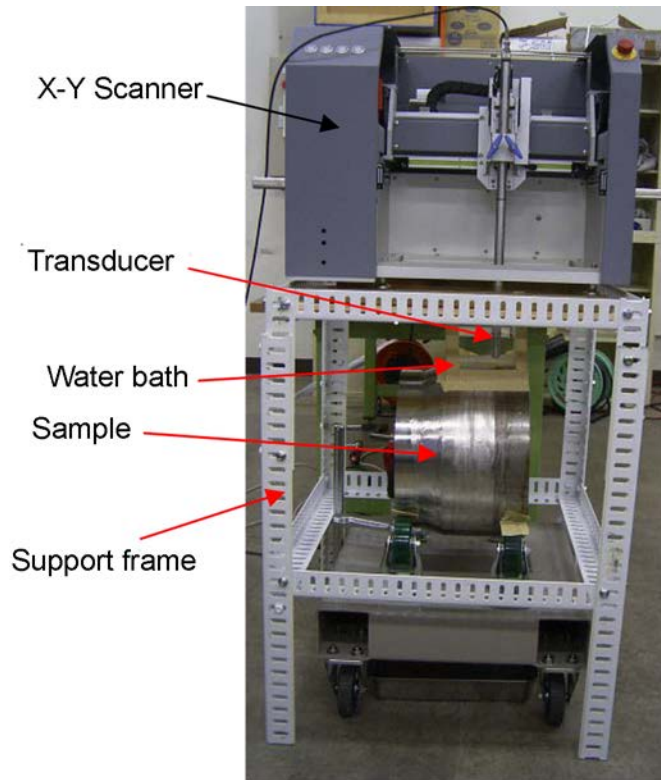


**Figure C.266 Measurement Setup for Normal Incidence**



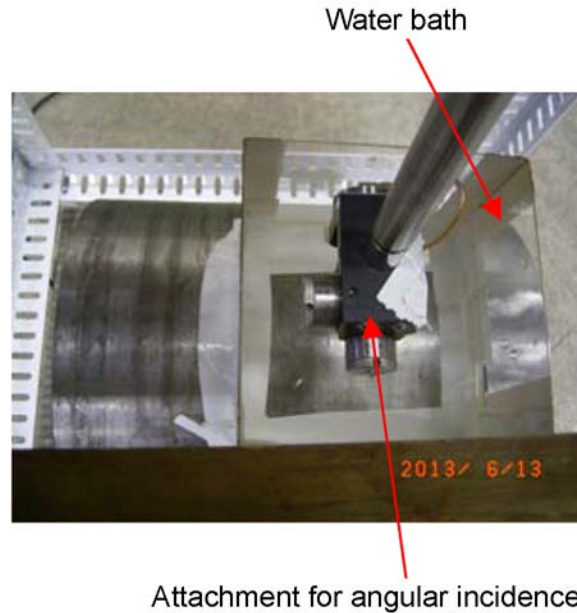


**Figure C.267 Measurement Setup for Angular Incidence**

Examples images of crack or SCC are shown in Figures C.268 and C.269. These images are constructed by using imaging software of InsightScan and InsightAnalysis. The C-scan images in Figures C.268 and C.269 are the best images of crack or SCC corresponding to the slice gates shown in Figure C.270.

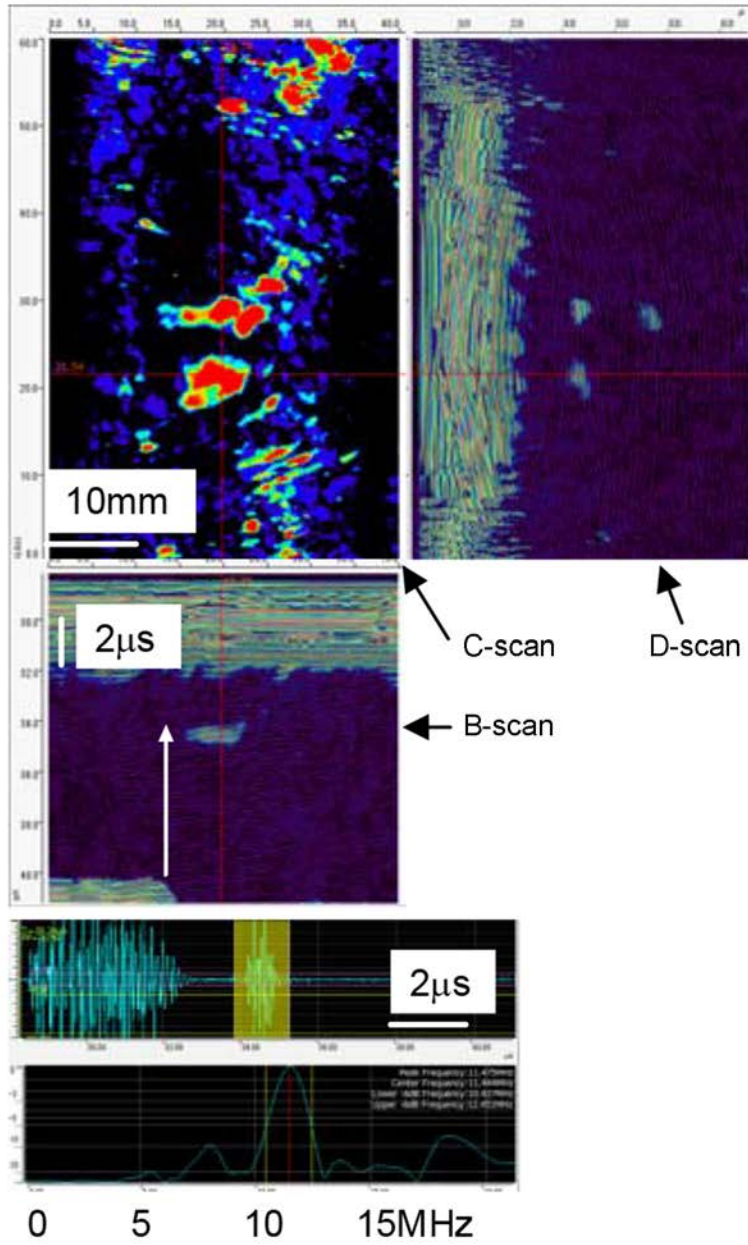


Figure C.268 Example of C-, B-, and D-scan Images, Waveforms and FFT of Normal Incidence

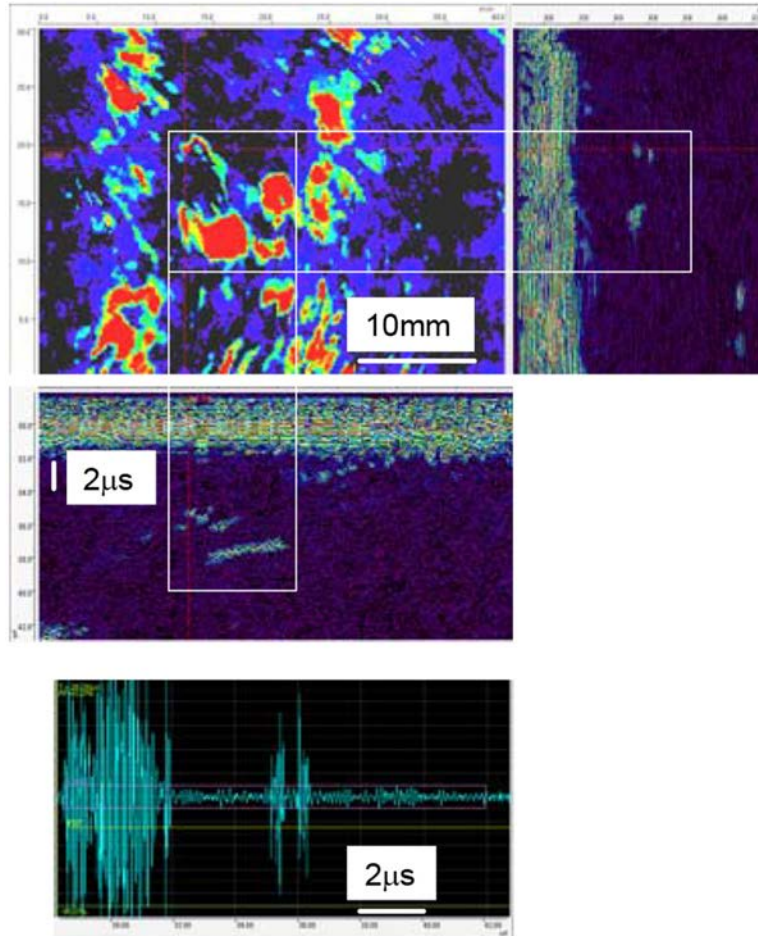
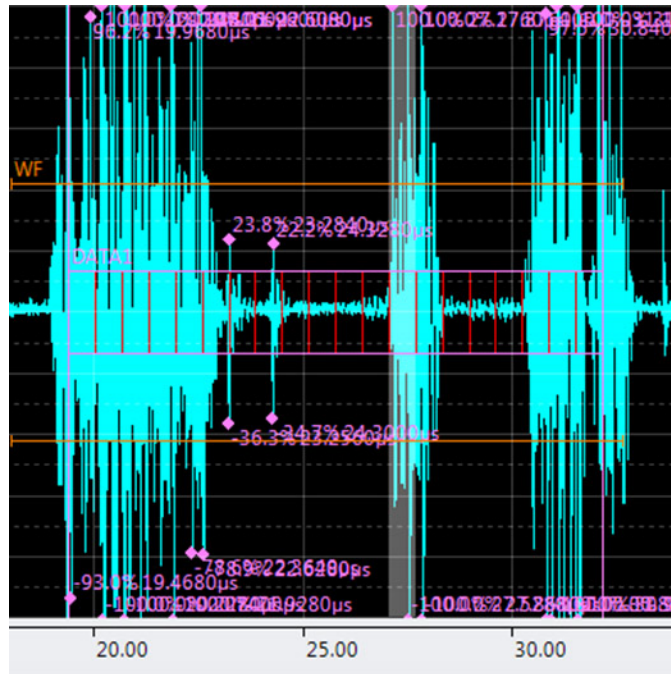


Figure C.269 Example of C-, B-, and D-scan Images and Waveforms of Angular Incidence



**Figure C.270 Slice of Gates for C-scan**

The B- and D-scan images show the horizontal and vertical cross-section along the horizontal and vertical red line in the C-scan image. The waveform at the cross point of the horizontal and vertical red lines is shown.

In this in-plane X-Y scanning, as shown in Figure C.271, the ultrasonic beam is deflected away from the focus depending on the incident point. Thus the length of circumferential crack or SCC is underestimated.

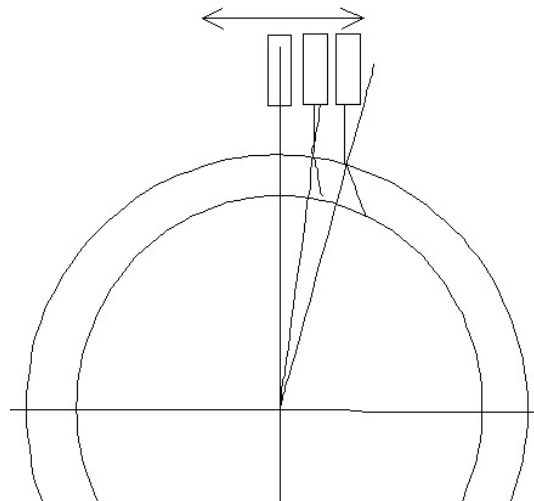


**Figure C.271 Beam Deflection by In-plane Scanning**

### **C.5.5.3 Inspection Technique by Normal Incidence**

#### **Setting**

- Transducer: Frequency 5 MHz, Focal length 76 mm, element diameter 9.6 mm
- Transmission: 4 MHz, 3 cycle, 240V
- High-pass filter: 8 MHz
- Receiver gain: around 54 dB with 8 MHz high-pass filter
- Angle of incidence: 0 (normal)

#### **Imaging**

- Scan pitch 0.25 mm (X, Y)
- Slice gate for C-scan (20 division)
- Scanning velocity : 20-30 mm/s
- Display: C, B & D
- Imaging higher harmonic: 3<sup>rd</sup> harmonic (12 MHz)

#### **Calibration**

- No calibration because of no suitable calibration blocks for HHUT.

### **C.5.5.4 Inspection Technique by 5-degree Angular Incidence**

#### **Setting**

- Transducer: Frequency 5 MHz, Focal length 76 mm, element diameter 9.6 mm
- Transmission: 4 MHz, 3 cycle, 240V
- High-pass filter: 8 MHz
- Receiver gain: around 54 dB with 8 MHz high-pass filter
- Angle of incidence: 5 degree for cylinders.

#### **Imaging**

- Scan pitch 0.25 mm (X, Y)
- Slice gate for C-scan (20 division)

- Scanning velocity : 20-30 mm/s
- Display: C, B & D
- Imaging higher harmonic: 3<sup>rd</sup> harmonic (12 MHz)

**Calibration**

- No calibration because of no suitable calibration blocks for HHUT.

**C.5.5.5 Inspection Technique by 2-degree Angular Incidence for Rectangular Blocks**

**Setting**

- Transducer: Frequency 5 MHz, Focal length 76 mm, element diameter 9.6 mm
- Transmission: 3.5 MHz, 2 cycle, 240V
- High-pass filter: 10 MHz
- Receiver gain: around 58 dB with 10 MHz high-pass filter
- Angle of incidence: 2 degree

**Imaging**

- Scan pitch 0.25 mm (X, Y)
- Slice gate for C-scan (20 division)
- Scanning velocity: 20-30 mm/s
- Display: C, B & D
- Imaging higher harmonic: 3<sup>rd</sup> harmonic (10.5 MHz)

**Calibration**

- No calibration because of no suitable calibration blocks for HHUT.

	<b>Pipe</b>	<b>Square Block</b>
Frequency of burst waves	4	3.5
Cycles of burst waves	3	2
Frequency of high-pass filter	8 MHz	10 MHz
Angle of incidence	0 or 5 degree	2 degree

## C.5.6 Orthogonal Coil Array Eddy Current, Technique 16-ECT1

### C.5.6.1 Overview

*Eddy Current Testing* (ECT) is one of nondestructive testing methods using electromagnetic interaction and has high detectability for surface breaking cracks. A test object should be made of a conductive material. ECT is performed with a probe that consists of a single or multiple coils. When a probe is placed on the surface of a test object and an alternating current is applied to a coil of the probe, a magnetic field is induced around the coil (this process is called *excitation*). This magnetic field penetrates into the surface of the test object and generates a circulating current, which is called eddy current, in the test object. If a defect exists in the test object, the defect interferes with this current flow. Then, a coil of the probe can detect a change of the magnetic field caused by this current flow and show where the defect exists (this process is called *detection*).

An ECT array probe has several coils so as to inspect a wider area at once.

### C.5.6.2 Equipment

The equipment used in this inspection is a commercial ECT system that consists of an inspection instrument R/D Tech MS5800 and a ZETEC ECT array probe (E342024D). Figure C.272 shows the appearance of this ECT array probe. This ECT array probe has 24 coil elements aligned in two rows. Each of 24 output channels of the system outputs ECT signals obtained with the corresponding coil element. Figure C.273 shows the coil layout of this ECT array probe. Each coil element is 3 mm-wide orthogonal coils that are formed by two coils vertically standing on the contact surface and orthogonal to each other. According to the specification, the center-to-center distance of the two coil rows is 6.65 mm, and the intervals of coils in a row are 4.89 mm. The system employs the impedance (IMP) mode in which both coils of a coil element are used for both excitation and detection, and the transmit-receive (TR) mode in which one coil is used for excitation and the other is used for detection. Because preliminary experiments showed the IMP mode provided better results than the TR mode, only the IMP mode is used in this inspection. The excitation frequency is set to 200 kHz.



Figure C.272 ECT Array Probe

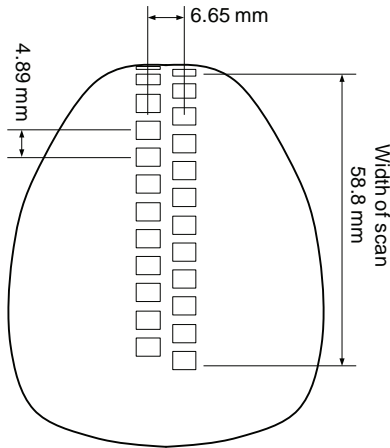


**Figure C.273 Coil Layout of ECT Array Probe**

### C.5.6.3 Data Acquisition

The ECT array probe is placed on the inner surface of a test block in such a way that the coil rows are perpendicular to the weld line of the test block. The probe is moved along the weld line to inspect the surface of an area around the weld line (Figure C.274). In this round-robin test, the length of the coil rows can cover the whole areas where the defects exist with one line or one circle of movement.

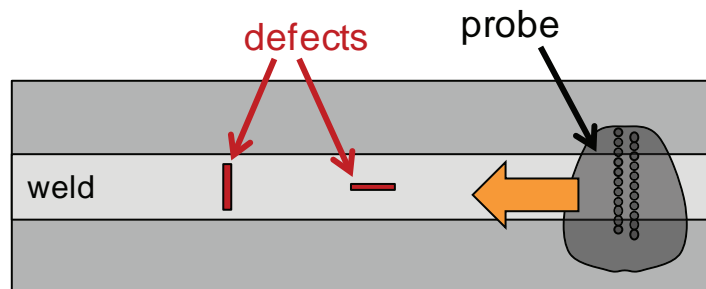


**Figure C.274 Scanning Procedure**

For the pipe test blocks, while the probe is fixed to have contact with the inner surface of a test block, the test block is rotated on a rotating rack to make the probe scan an area around the weld line (Figure C.275). The wire end of a wire encoder is attached to the outer surface of a pipe test block so as to acquire the probe position (Figure C.276).



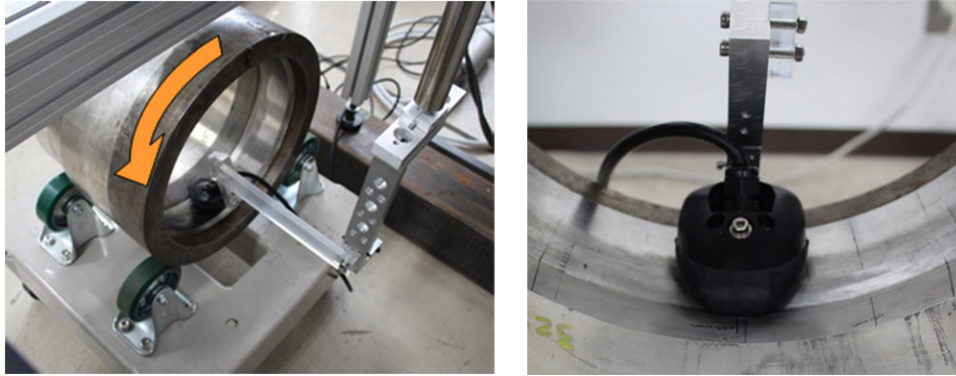


**Figure C.275 Probe Placement on Pipe Test Blocks**

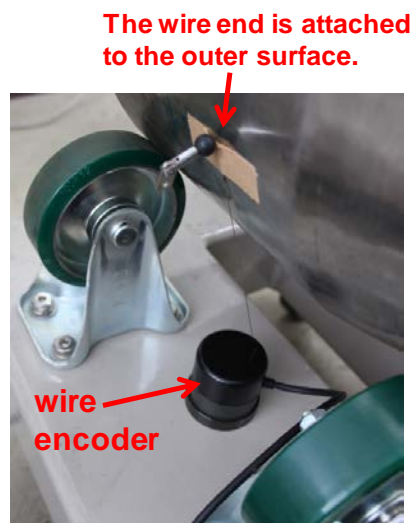


**Figure C.276 Wire Encoder Attached to Pipe Test Blocks**

For the BMI test blocks, a test block is placed on a turntable, and the probe is fixed on an inspected surface of a test block in such a way that the front edge of the probe touches the tube in the center of the test block. Then, the test block is rotated on the turntable to make the probe scan an area around the weld line (Figure C.277). The wire end of a wire encoder is attached to the outer edge of the turntable to acquire the moving distance of the outer edge of the turntable. Since the diameter of the turntable is 400 mm, the rotation angle is obtained by dividing this moving distance by 200 mm.

For the rectangular test blocks, since the inspected surface is flat, an electric scanner is used to make the probe scan the inspected surface (Figure C.278). Only for these test blocks, the probe is placed on a test block in such a way that the coil rows are parallel to the weld line and moved across the weld line because the rectangular test blocks are elongated in the direction perpendicular to the weld line. Figure C.278 shows two blocks are placed together. The right block is placed for positioning the probe.



**Figure C.277 Probe Placement on BMI Test Block**

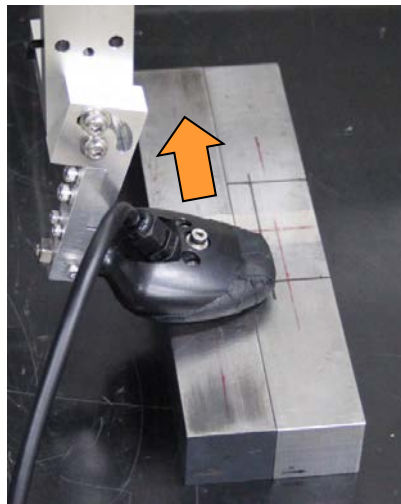


**Figure C.278 Probe Placement on Rectangular Test Blocks**

#### **C.5.6.4 Signal Processing**

Since the pipe and BMI test blocks are rotated manually, the intervals of the points to sample ECT signals are not constant. To analyze ECT signals smoothly, ECT signals at regular intervals are calculated from the measured ECT signals by using linear interpolation. In this inspection, these intervals are set to 0.1 mm.

Figure C.279 shows distributions of signal amplitude obtained by inspecting a reference block with the equipment explained above. The reference block has four narrow slits that are made by wire electrical discharge machining (EDM) across the full width of the block. The depths of these EDM slits are 1 mm, 2 mm, 3 mm and 4 mm from the left. As shown in Figure C.279(a), raw signals often include noises mainly due to the contact condition between the probe and the inspected surface. The differences in the contact conditions among the coil elements give rise to

noises that make stripes in a signal distribution. To reduce noises, the following noise reduction methods are applied. Note that ECT signals are alternating current (AC) signals and have two components ( $V_x$ ,  $V_y$ ) that can provide signal amplitudes and signal phases.

### **Average Noise Reduction**

A signal is regarded as a noise according to the following criteria.

1. The beginning of a signal sequence

The signals at  $N_{av}$  points from the beginning of a signal sequence of each channel are always regarded as noises.

2. Small signals

A signal the amplitude of which is less than  $V_{th}$  is regarded as a noise.

3. Signals similar to the average of recent noises

A signal is regarded as a noise when the magnitude of the difference between this signal and the average of the noises at the previous  $N_{av}$  points is less than  $V_{th}$ .

When this average of the noises is calculated, the noise at a point where the signal is not regarded as a noise is defined as the average of the noises at the previous  $N_{av}$  points at that point.

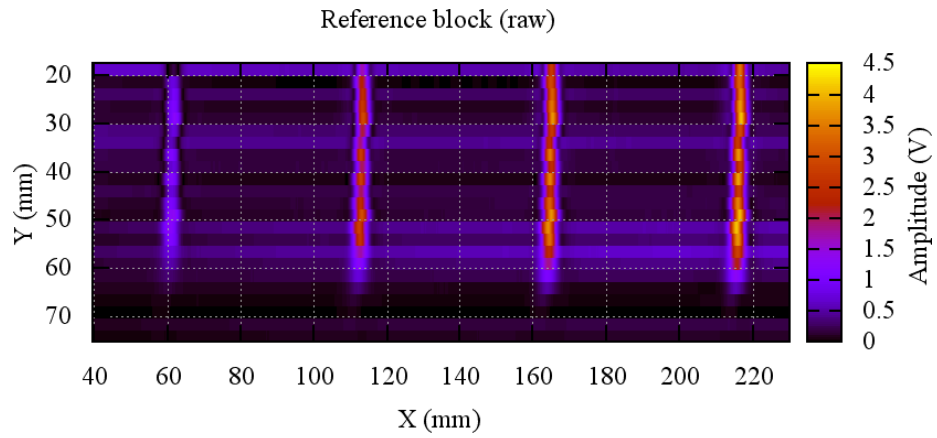
4. Signals similar to the interim average of noises

A signal is regarded as a noise when the magnitude of the difference between this signal and the interim average of the noises at the points preceding that point is less than  $V_{th}$ .

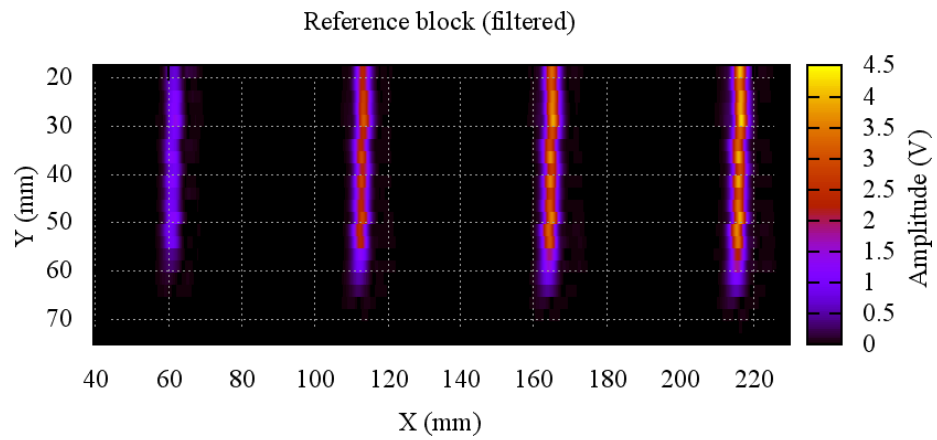
When this average of the noises is calculated, the noise at a point where the signal is not regarded as a noise is defined as the average of the noises at the previous  $N_{av}$  points at that point.

Then, the average of the noises at the previous  $N_{av}$  points is subtracted from an ECT signal at each point. At the  $N_{av}$  points from the beginning of a signal sequence, the interim average of the noises at the preceding points is subtracted from an ECT signal at each point.

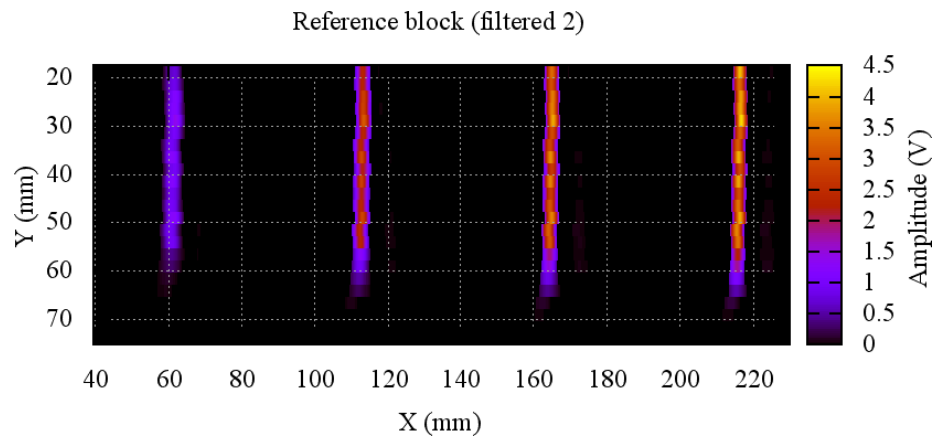
The difference of the material properties between base metal and weld metal causes a significant change of an ECT signal when the probe is moved across the border between them. Because the rectangular test blocks P28, P29, P30, P31, P32, P38 and P42 have a defect in the welded part, only a small part around the defect is analyzed for these test blocks to focus on the welded part and avoid picking up indications due to a material difference. However, in the case of P38, the defect exists on the border of base metal and weld metal, and the area preceding the defect is base metal. Therefore, the average noise reduction is applied backward to a sequence of ECT signals for P38.



(a) Raw signals.



(b) Signals after average noise reduction is applied.



(c) Signals after phase filter is applied.

**Figure C.279 Distributions of Signal Amplitude**

## Phase Filter

If noises cannot be eliminated enough by the average noise reduction, a phase filter is applied.

When the excitation frequency is 200 kHz, the signal phase of an indication of a crack parallel to the coil rows tends to have a value around  $130^\circ$ , and the signal phase of an indication of a crack perpendicular to the coil rows tends to have a value around  $-50^\circ$ . Then, to detect a crack parallel to the coil rows, the ECT signals are removed at the points where the signal phases are out of the range  $[100^\circ, 160^\circ]$ . Also, to detect a crack perpendicular to the coil rows, the ECT signals are removed at the points where the signal phases are out of the range  $[-80^\circ, -20^\circ]$ .

The above-mentioned noise reduction methods are applied and the parameters are set as follows.

Test Block	Average Noise Reduction	Phase Filter
P1	$N_{av}=50, V_{th}=0.2 \text{ V}$	Not applied
P4	$N_{av}=50, V_{th}=0.1 \text{ V}$	Not applied
P5, P7, P41	$N_{av}=25, V_{th}=0.3 \text{ V}$	Not applied
P12	$N_{av}=25, V_{th}=0.3 \text{ V}$	Applied
P28, P29, P30, P31, P32, P38, P42	$N_{av}=25, V_{th}=0.3 \text{ V}$	Applied

### C.5.6.5 Data Analysis

A defect indication is defined as a continuous region where the signal amplitude is more than or equal to 0.1 V and the maximum signal amplitude of the region is more than or equal to 0.5 V. If the minimum gap of two defect indications is less than or equal to 5 mm, these two defect indications are treated as one defect indication.

If the aspect ratio of a defect indication is more than or equal to 1.5, the defect is considered as an axial or circumferential defect. An axial or circumferential defect is defined as a defect that goes through the point of the maximum amplitude of the indication, has a length in the axial or circumferential direction and does not have a width. The length of an axial or circumferential defect is set to the length of the defect indication in the axial or circumferential direction, respectively. If the aspect ratio is less than 1.5, the size of a defect is answered as the minimum rectangle that can include the defect indication. In any case, the defect depth is not evaluated.

Furthermore, the length of two adjacent axial or circumferential defects is determined according to ASME Boiler & Pressure Vessel Code Section XI IWA-3400.

A preliminary experiment shows the maximum signal amplitude of an indication of a subsurface EDM slit is about 0.2 V although the distance between the inspected surface and the top of the

slit is less than 0.5 mm. Then, all detected indications are considered as surface-breaking defects.

### **C.5.6.6 Team's Assessment of the Technique Based on the Round Robin Test Results**

Except the defects of the BMI test block P7, all the defects of the inspected test blocks were detected. From this result, it can be said that these defects can be sufficiently detected with a commercial ECT system. For the defect of P7, more detailed analysis is required to clarify the exact cause of the detection failure and verify whether these weld solidification cracks are appropriate to simulate PWSCC.

Although most of the defect indications are sufficiently clear, reducing more noises in the signals provides more accurate information to discriminate and evaluate defects. More study is expected to find a more appropriate way to place the probe and an effective signal processing method.

### **C.5.7 Advanced Eddy Current, Technique ID 33-AECT1**

#### **C.5.7.1 Overview**

Eddy current testing (ECT) is an analysis using electromagnetic induction whereby flaws in conductive materials can be detected. A pancake coil carrying current is placed near the test specimen. When an alternating current is supplied to the coil, the magnetic field is changed through interaction between the specimen and the eddy current generated near the surface of the specimen. Variations in the phase and amplitude of the eddy current can be detected using a receiver coil.

A differential probe is used that easily distinguishes signals from a flaw and background noise, because the flaw detection signal features a characteristic loop. However, the drawback is that this signal is hard to detect by simple scanning and placement of the detection coils. The signal is only significant when the pair of coils scans in a direction perpendicular to the longitudinal direction of the flaw. In contrast, if the scan is parallel, the flaw signal is weaker.

The probe used in the present method has four detection coils which are arranged inside one exciting coil. Hence, both perpendicular and parallel defect signals can be obtained irrespective of scanning direction of the probe over the flaw. Moreover, the technique is robust against lift-off noise.

In this study, the detection performance and sizing performance of the length are evaluated using the multi-probe.

#### **C.5.7.2 Principle of Advanced ECT Method (Multi-probe)**

##### **Overview and Operating Principle of the Multi-probe for ECT**

Figure C.280 shows a schematic of the coil arrangement of the multi-probe. The multi-probe has four detection coils which are arranged inside a circular exciting coil. The detection coils are labeled 1–4 in a clockwise sense; coils 1 and 3 are aligned perpendicular to the scanning direction, whereas coils 2 and 4 are aligned parallel. Irrespective of scan direction, it is possible to obtain flaw signals parallel, perpendicular, and at 45° to the scanning direction by taking differences in the detection signals of pairs of coils.

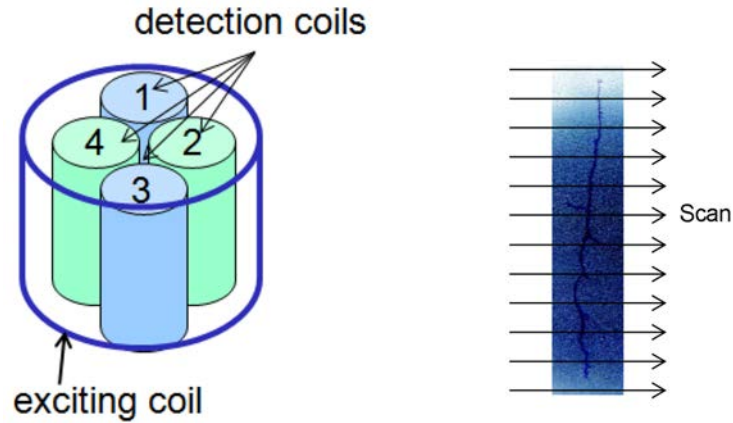


**Figure C.280 Overview of the Coil Arrangement and Scanning Procedure of the Multi-probe**

An example of a measurement of thermal fatigue specimen is presented. Figure C.281 shows the dye-test results of a crack resulting from thermal fatigue. Figure C.282 shows the detection signal obtained from each of the detection coils. Additionally, Figure C.283 shows the amplitude of the differential signal of coil pairings 1-2, 1-3, 1-4, and 2-4. The flaw can be evaluated in detail based on these defect signals. Branching cracks are seen in Figure C.281 and can also be inspected.



**Figure C.281 Results of a Dye Test of a Crack Produced by Thermal Fatigue**

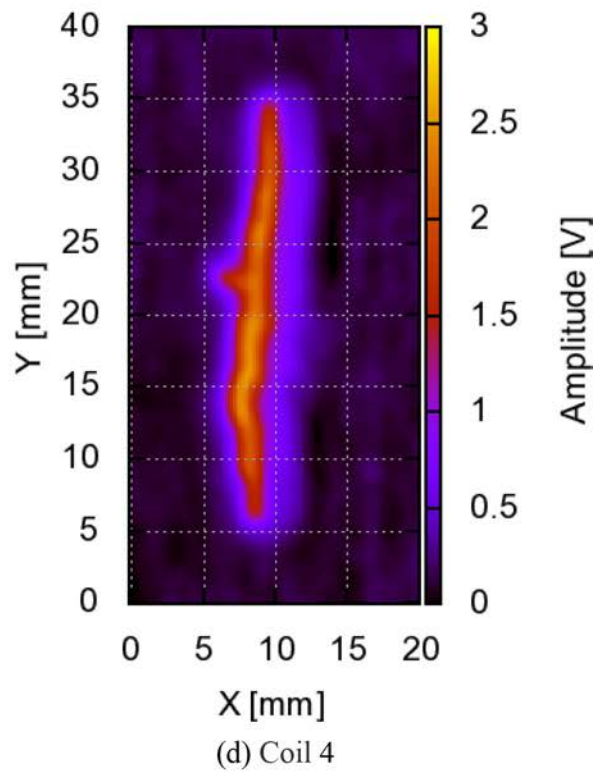
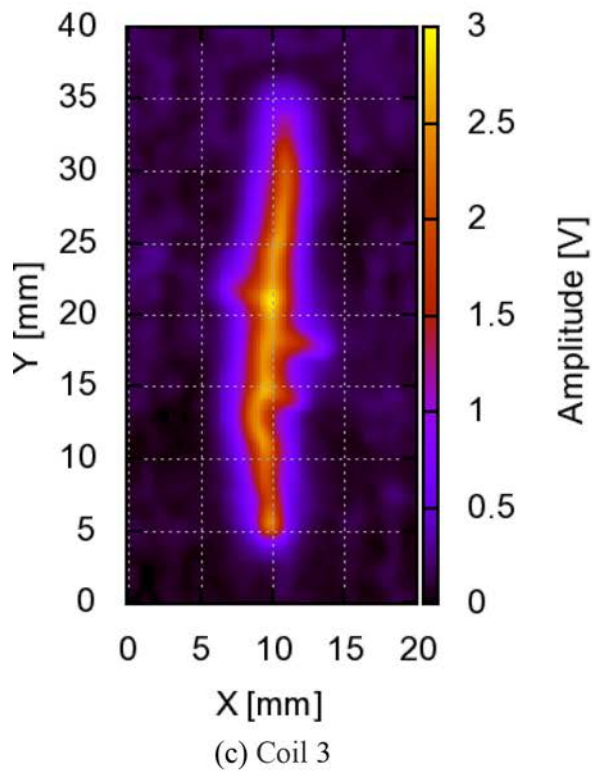
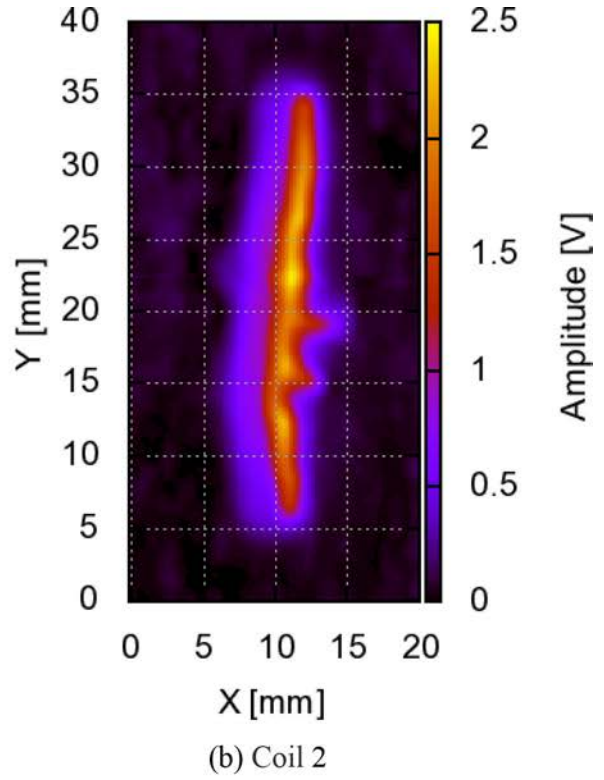
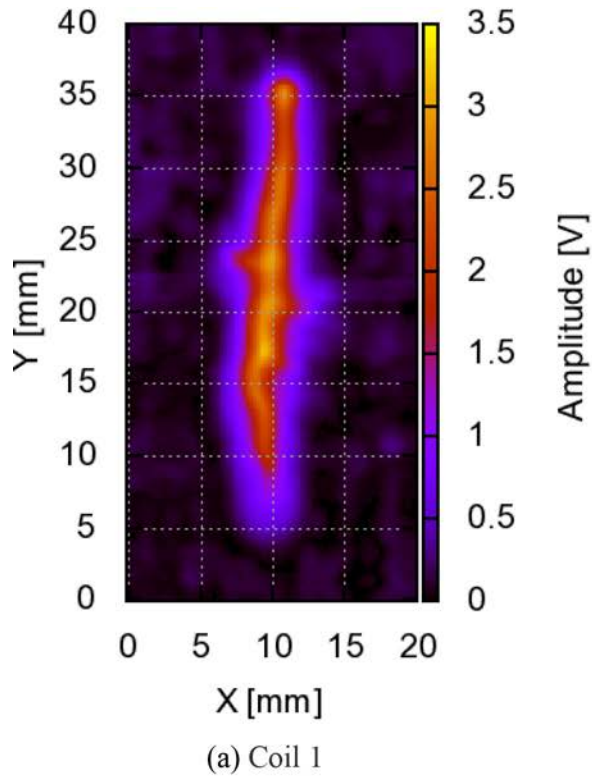
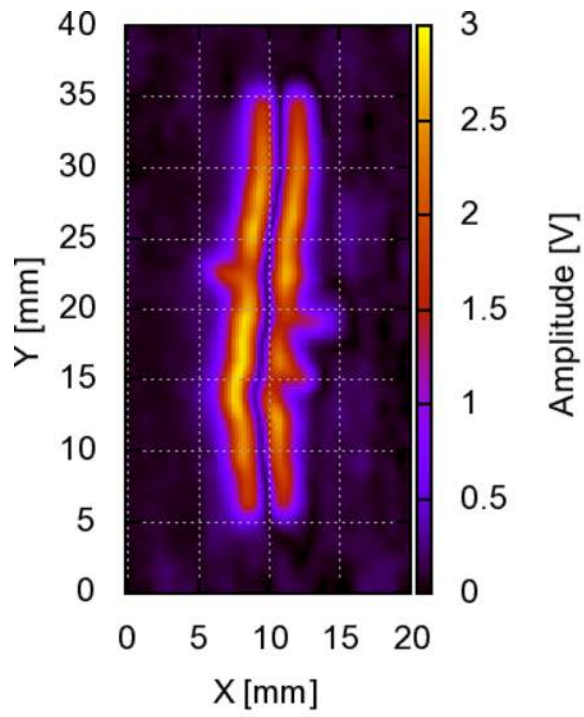
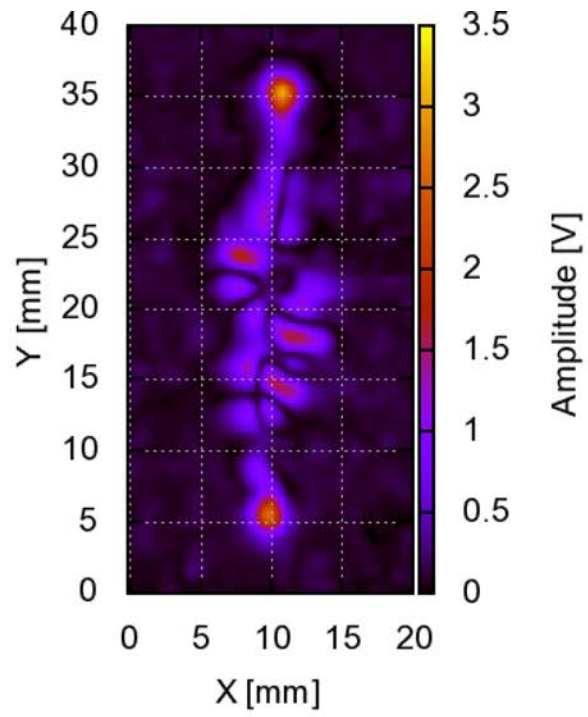


Figure C.282 ECT Signals from Detection Coils 1–4

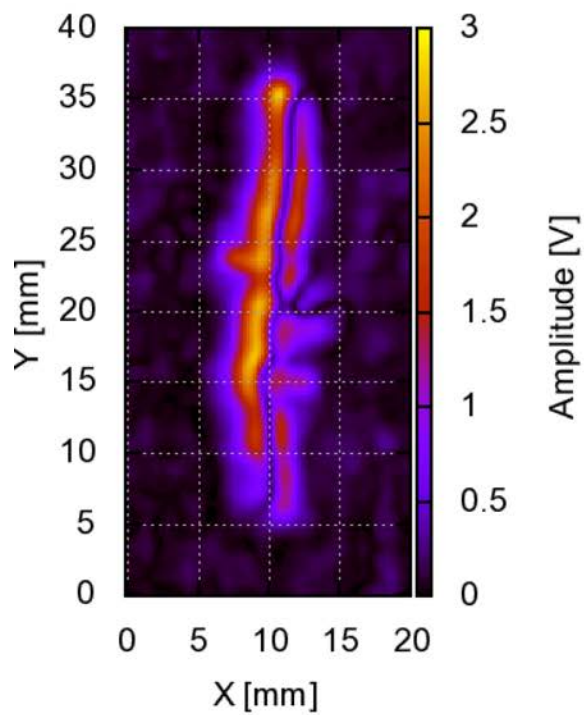




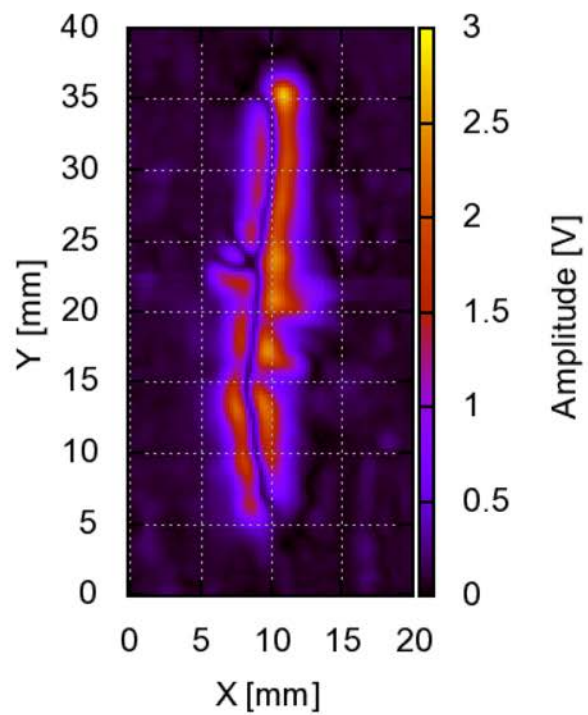
(a) Coils 2 and 4



(b) Coils 1 and 3



(c) Coils 1 and 2



(d) Coils 1 and 4

**Figure C.283 Differential Signals from the Various Coil Pairings**

## ECT System with the Multi-probe

Figure C.284 shows a schematic diagram of the ECT system. The ECT was conducted with an ECT multi-channel flow detector (48CH flow detector, Aswan Electronics Co., Ltd., Osaka, Japan), multi probe, motorized XY stage or rotation stage, stage controller, and a DAQ pad or data logger. The multi-probe is of differential-type consisting of five pancake coils, one excitation coil and four detection coils. The excitation coil with 100 turns has an outer diameter of 5 mm, an inner diameter of 4.2 mm, and a height of 5 mm. The detection coils, each with 300 turns, have an outer diameter of 1.5 mm, an inner diameter of 0.7 mm, and a height of 1.3 mm. The test frequency in this study is 100 kHz.

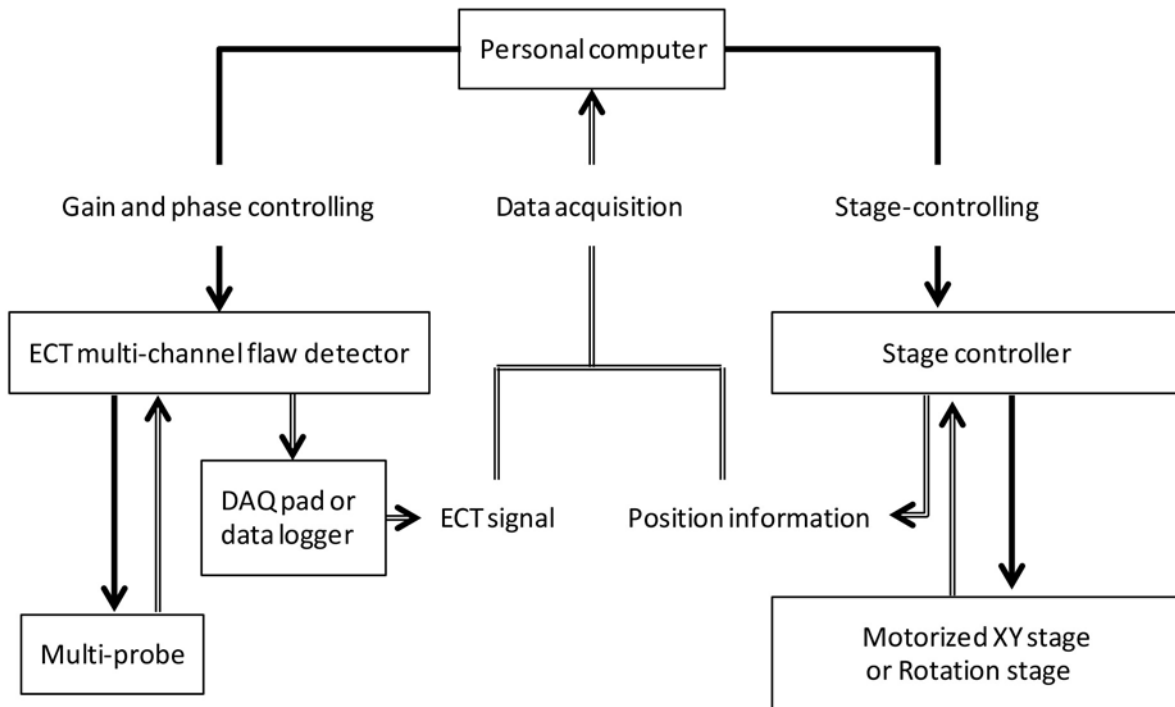


**Figure C.284 Results of a Dye Test of a Crack Produced by Thermal Fatigue**

### Scanning Method and Data Collection Method

The motorized XY stage or the rotation stage is used in conducting probe scans. The motorized XY stage is used in taking measurements of various specimens labeled Test Blocks P28, P29, P30, P31, P32, P38, P42, P46, and P12. The rotation stage is used in taking measurements of Test Blocks P37, P41, P5, and P7. When using the motorized XY stage, analog signals from the flow detector are converted into digital signals by the DAQ pad to be stored as data on the PC. When using the rotation stage, the detection signals are recorded on the PC using a data logger.

## Calibration of ECT Signal

Calibrations were conducted so that the EC signals from a 2-dimensional slit with depth of 1 mm and width of 0.33 mm have an amplitude of 1 V and a phase of  $90^\circ$ . The four detector coils are calibrated in the same way. The specimen material is Inconel 600; its dimensions are 20 mm in thickness, 200 mm in length, and 75 mm in width.

Figure C.285 shows the calibrated signal of the four detection coils. Figure C.286 shows the differential signal of coil pairs 1-3 and 2-4. These differential signals feature a characteristic figure-of-eight shape with an angle of inclination of nearly  $90^\circ$ .

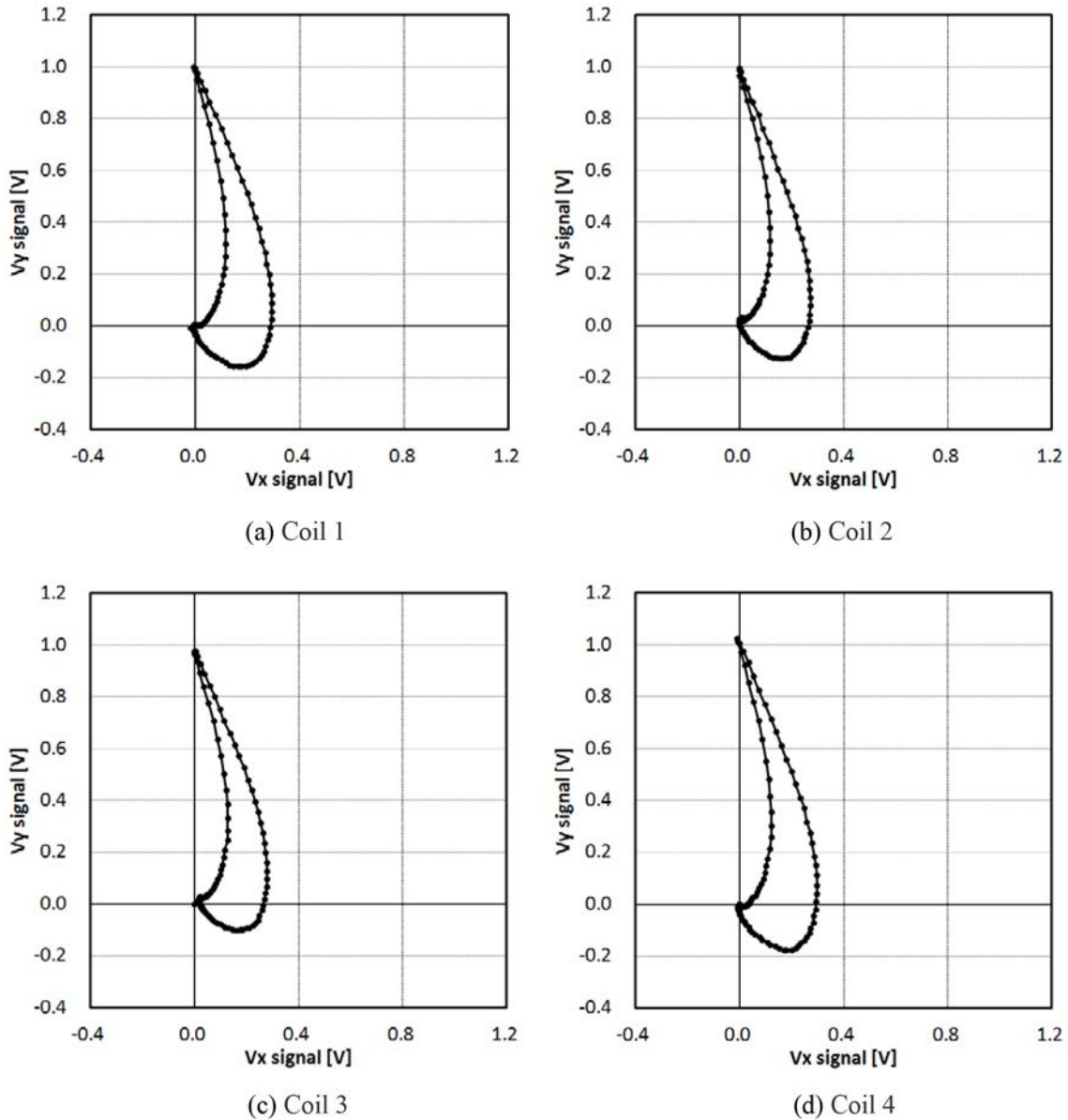
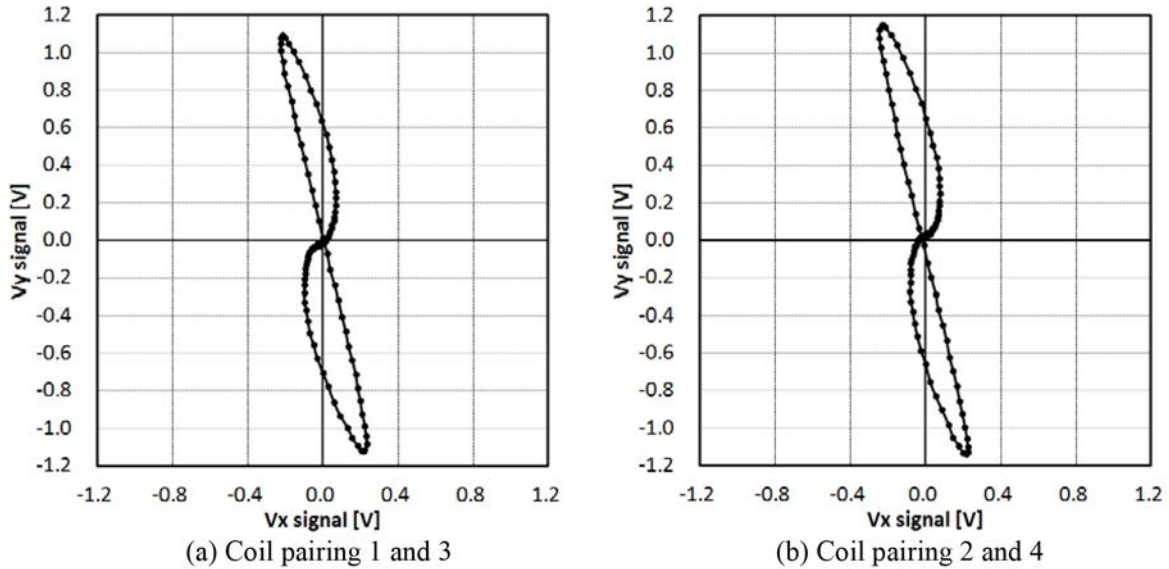
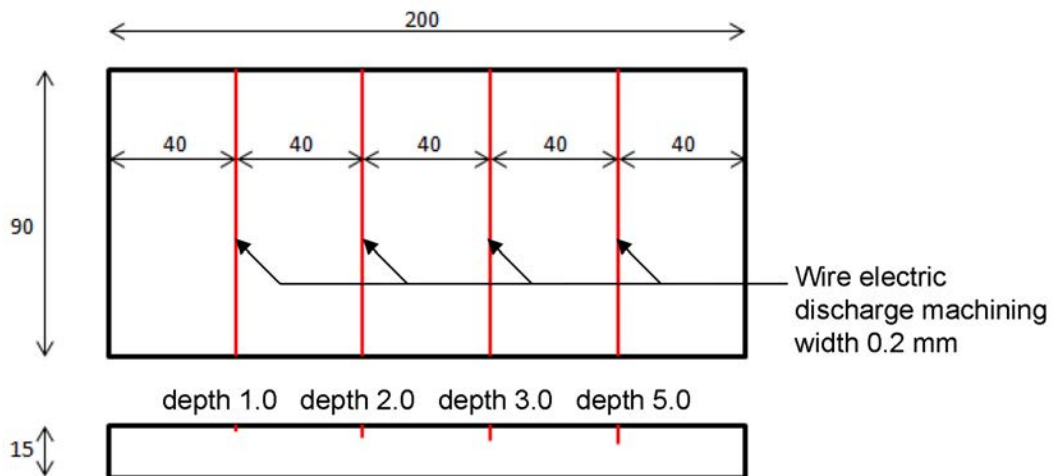


Figure C.285 Calibrated Signals from the Four Detection Coils



**Figure C.286 Differential Signals from the Multi-coil**

For this study we prepared type-316 stainless-steel plate specimens each etched with a 2-dimensional slit of width 0.2 mm but various depths of 1.0, 2.0, 3.0 or 5.0 mm, as illustrated in Figure C.287. Figure C.288 shows the results of measurements of these slits using the multi-probe. These results show that the amplitude varies with slit depth, but the phase does not change significantly.



**Figure C.287 Dimensions of the Type-316 Stainless Steel Plate Specimen**

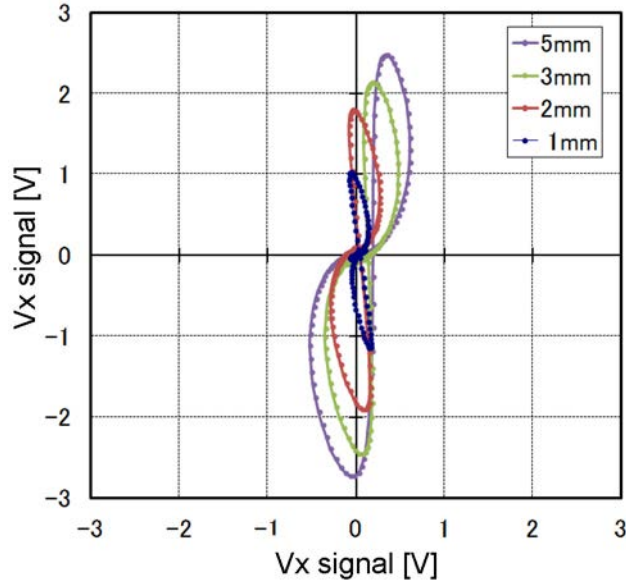


**Figure C.288 ECT Signals from Slits of Various Depths**

**Signal Processing Method**

Figure C.290 shows the  $V_y$  and  $V_x$  signals of Test Block P28 obtained by scanning from +22.5 to -22.5 mm along the X-axis direction about the center ( $Y=0$ ). The signal change in position at 10 mm and -10mm on the the X-axis are influences from the boundary of the weld and the base metal. The defect signal is the signal change about  $X=0$  mm. Figure C.291 shows a typical Lissajous waveform. In particular, Figure C.291(a) is a Lissajous waveform of the detection signal along the X-axis from -22.5 mm to 25 mm. The large amplitude signal that is inclined at  $30^\circ$  is a signal change resulting from influences from the weld. Figure C.291(b) shows an enlargement of the Lissajous waveform corresponding to the flaw. This signal is characteristic of a flaw signal with its angle of inclination at nearly  $90^\circ$ . The amplitude at the center of the Lissajous waveform will not necessarily be 0 V because of influences of lift-off and the weld. Hence, the phase is calculated as the inclination of the changing signal between steps of the scan. The phase  $\theta$  is calculated from the inclination between the  $(V_x, V_y)$  signal of the  $n^{\text{th}}$  and  $(n+1)^{\text{th}}$  turning points,

$$\theta = ATAN \left[ \frac{(V_{y(n+1)} - V_{y(n)})}{(V_{x(n+1)} - V_{x(n)})} \right],$$

where  $V_{x(n)}$  and  $V_{y(n)}$  are the values of  $(V_x, V_y)$  of the  $n^{\text{th}}$  turning point. Figure C.292 shows the phase results calculated using the amplitude and a threshold of  $80\text{--}110^\circ$ . The phase of  $80\text{--}110^\circ$  near  $X=1$  mm confirms the presence of a flaw at this position.

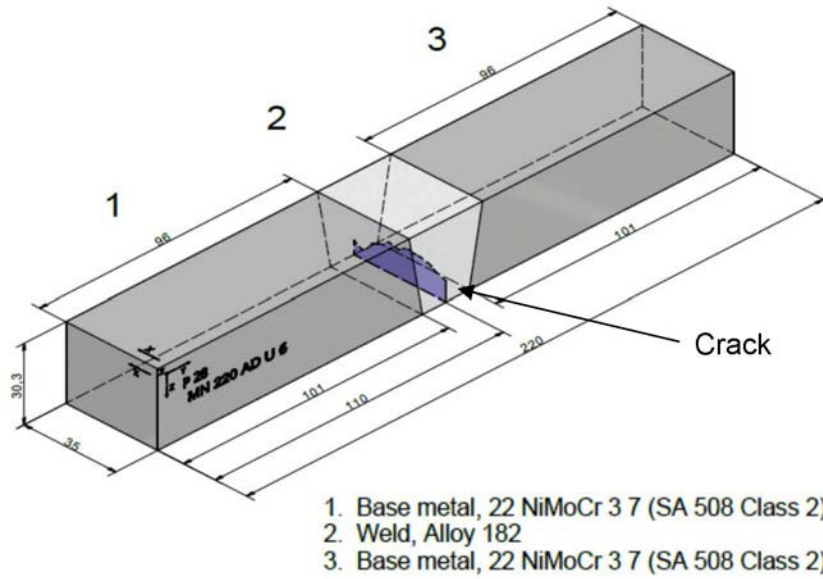


Figure C.289 Composition and Dimensions of Test Block P28

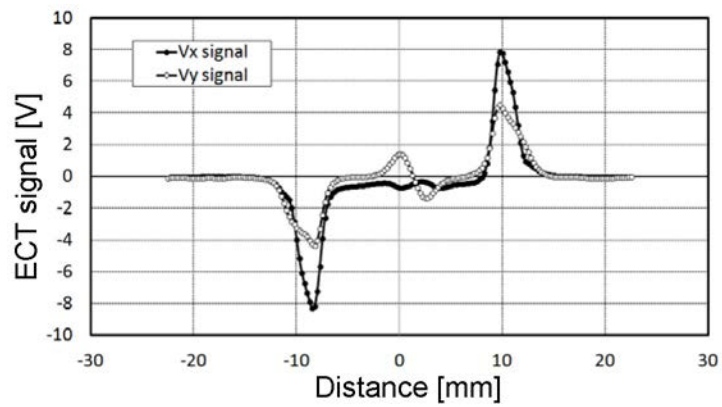
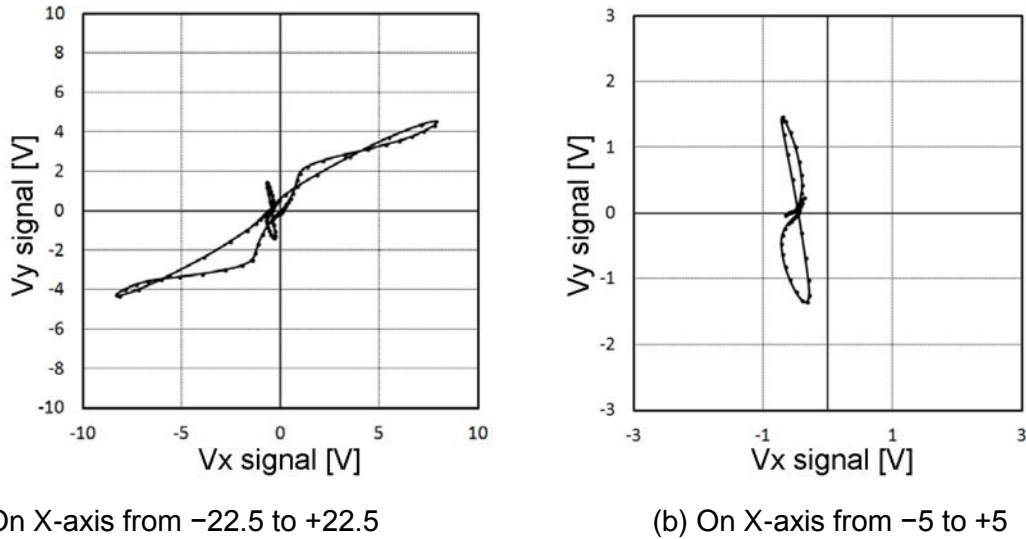
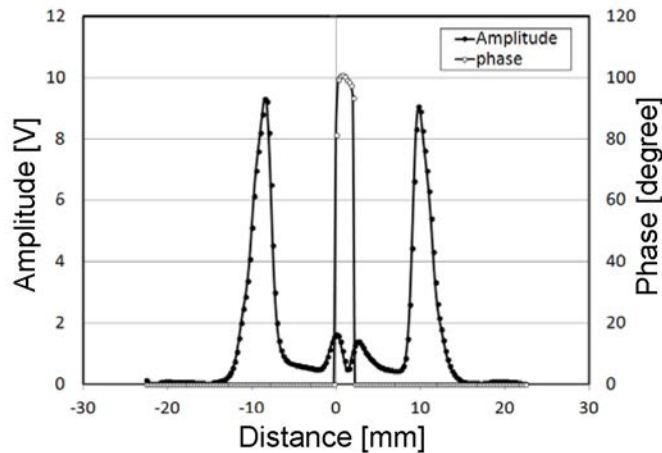


Figure C.290 ECT Signals Vx, Vy of Test Block P28 on Y=0



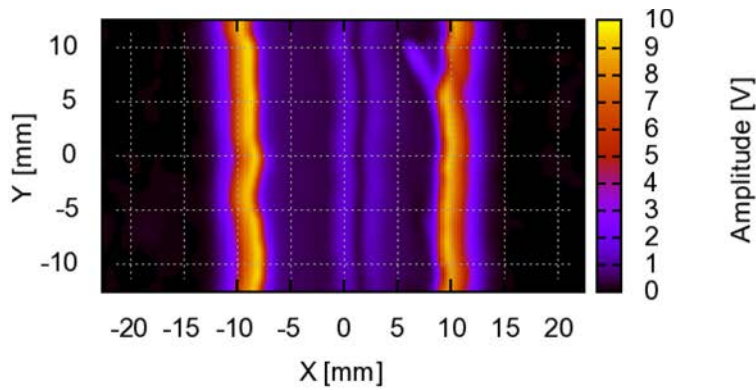
**Figure C.291 Lissajous Waveform of Test Block P28 on Y=0**



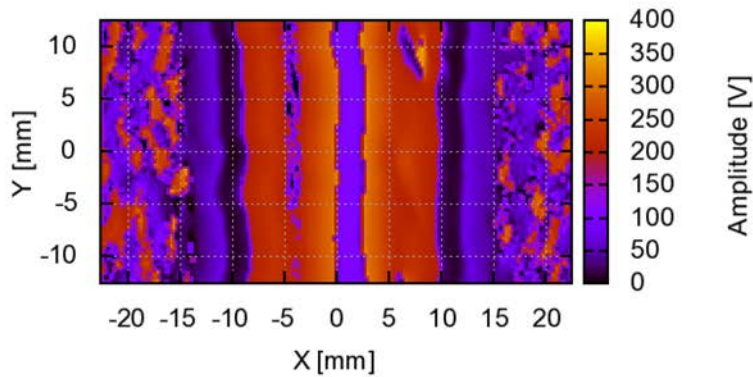
**Figure C.292 Amplitude and Phase of Test Block P28 on Y=0**

Figure C.293 shows a C-scan display of Test Block P28. Specifically, Figure C.293(a) gives the amplitude of the flaw signal which is smaller than the noise signal from the boundary of the base material and welds, Figure C.293(b) gives the phase of the signal, and Figure C.293(c) displays the results from the analysis. The threshold for the amplitude is set so that the absolute value of the difference between  $V_y(n+1)$  and  $V_y(n)$  is more than 0.1V, whereas that of the phase is set at 80–110°. The threshold of amplitude is 25% or more of amplitude which is determined from the calibration signal and the scan pitch. Additionally, if the significant value does not appear continuously three times or more, the phase is 0°. The flaw, colored orange in Figure C.293(c), has a length determined from the result of the analysis.

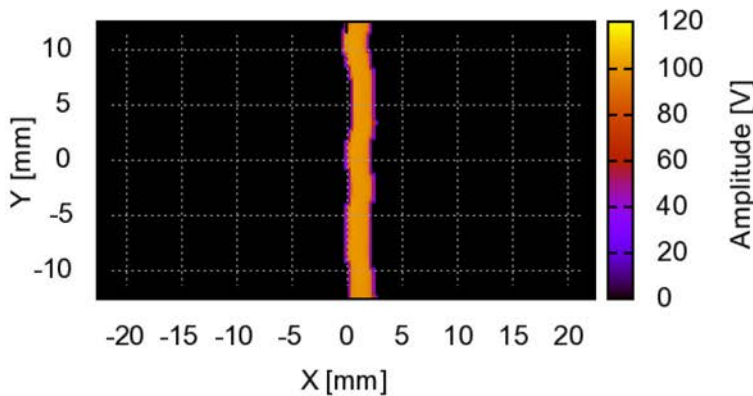
The length of the flaw is evaluated based on the signal disappearance instructions length from the analysis result. If the plural defects are adjacent and intermittent, the length is determined by ASME XI IWA-3400 “Linear flaws detected by surface or volumetric examinations.”



(a) Amplitude of ECT signal of Test Block P28



(b) Phase of ECT signal of Test Block P28



(c) Phase of the flaw

**Figure C.293 C-scan Display of Test Block P28**

**C.5.7.3 Inspection Method for the Test Blocks of P28, P29, P30, P31, P32, P38, P42, P46, and P12**

Figure C.294 shows experimental setup for ENSI-Blocks. The motorized XY stage is used in scanning the probe over Test Blocks P28–P32, P38, P42, P46, and P12. At each measurement point, the probe measures the ECT signal recorded along with the scanning position information and stored on the PC. The scan is taken at intervals of 0.25 mm in both X and Y directions.



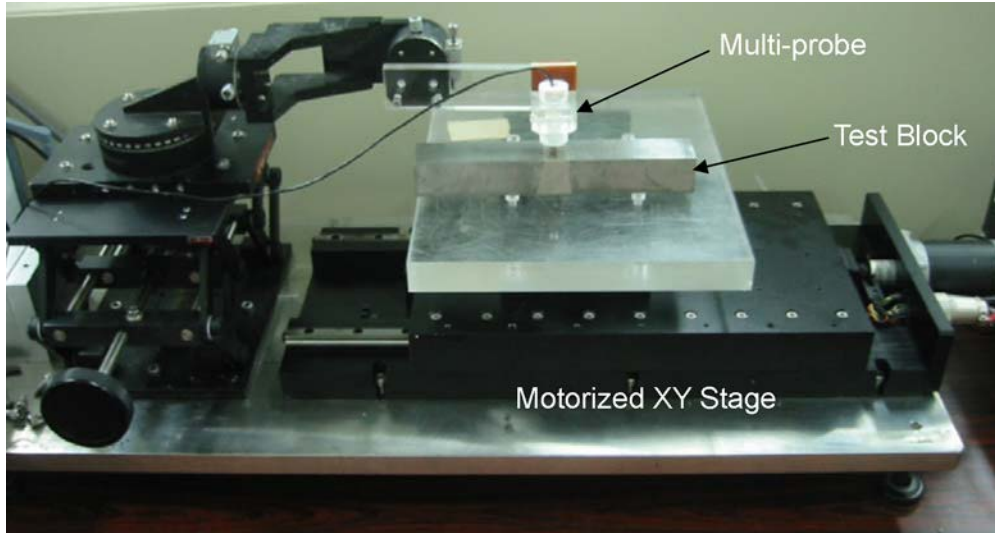


**Figure C.294 Experimental Setup for ENSI-Blocks**

**C.5.7.4 Inspection Method for the Test Blocks of P37, and P41**

Figure C.295 shows experimental setup for Small DMW P41 using rotation stage. The rotation stage is used to scan the probe for Test Blocks P37 and P41. The probe is scanned over the inner surface of the pipe in conducting the flaw detection test, as shown in Figure C.296. The measuring angle and rotational speed of the rotation stage are controlled by the stage controller. The Y-axis positioning of the probe is performed manually using a feed screw. The ECT signal and time measurements are collected using the data logger. The measurement position (measurement angle) is calculated from the angular speed of the rotation stage and the elapsed time. Finally, the angular measurement is converted to a distance from an origin 0 on the outer peripheral.

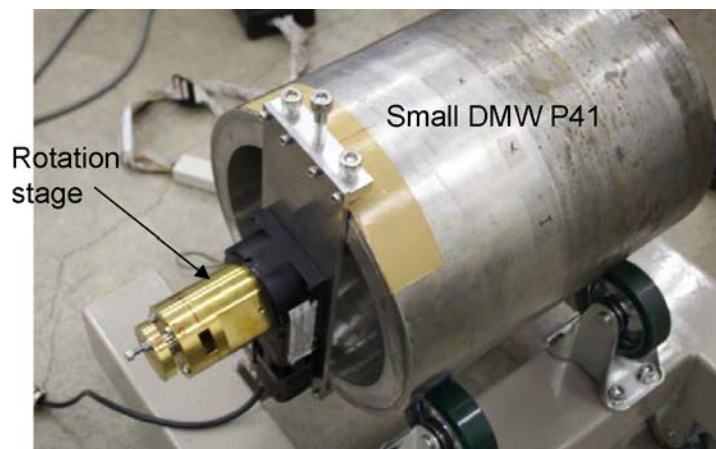


**Figure C.295 Experimental Setup for Small DMW P41 Using Rotation Stage**

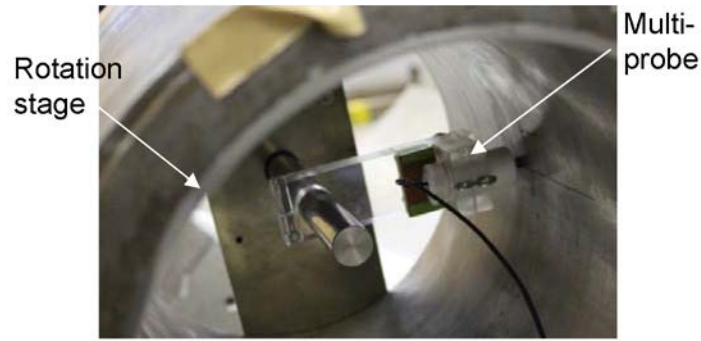


**Figure C.296 Photo of Multi-probe Inside the Pipe**

### **C.5.7.5 Inspection Method for the Test Blocks of P5, and P7**

Figure C.297 shows experimental setup for Small DMW P41 using rotation stage. The rotation stage is used to scan the probe over Test Blocks P5 and P7 (BMI; Bottom Mounted Instrumentation) to perform flaw detection around the pipe, as shown in Figure C.298. The measuring procedure is the same as in Procedure-2. The ECT signal and elapsed time measurements are recorded using the data logger. The measurement position (measurement angle) is calculated from the angular speed of the rotation stage and elapsed time measurements.

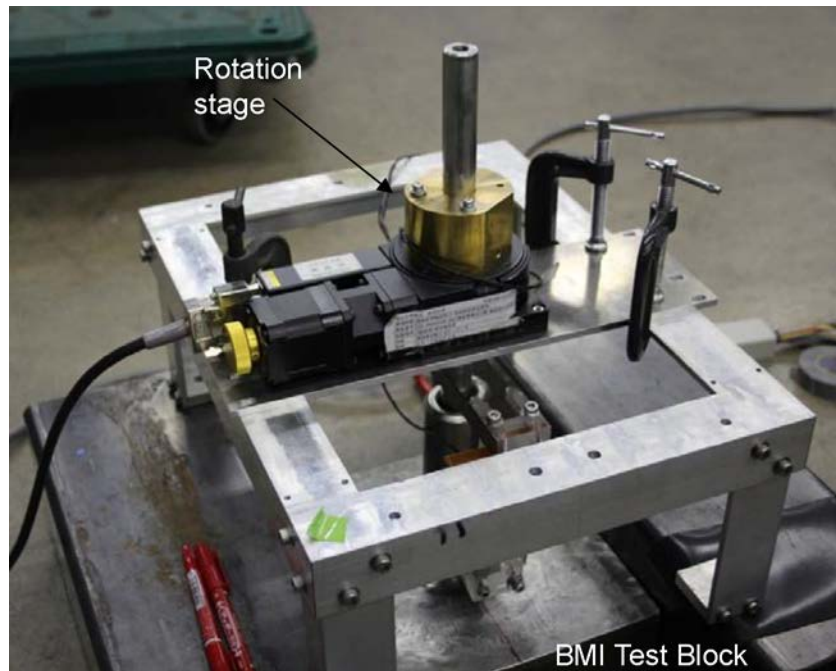


**Figure C.297 Experimental Setup for BMI Using Rotation Stage**

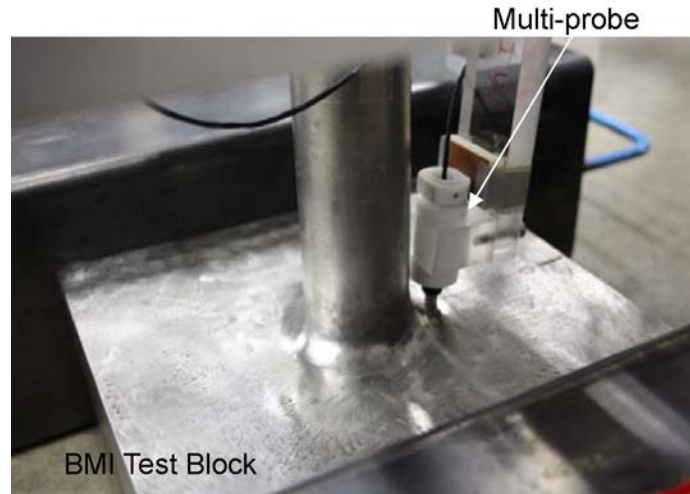


**Figure C.298 Status of Multi-probe**

### **C.5.7.6 Team's Assessment of the Technique, Based on the Round Robin Test Results**

1. What is the purpose and advantage of the emerging technique (what problem was it developed to solve)?
  - The present probe consists of differential receivers and an exciter surrounding receivers, and this configuration allows high detectability to small cracks according to the experience obtained by the team. In addition, the receiving unit of the probe has two pairs of differential coils which are aligned perpendicular to each other. Using two sets of differential signals, the probe can detect and evaluate flaws having various directions without rotating the probe. Moreover, the technique is robust against lift-off noise.
2. Provide a brief assessment of the results of your testing, specifically regarding the ability of the technique to detect and size (length/depth) flaws?
  - Small Test Blocks (P28, P29, P30, P31, P32, P38, P42, P46), DMW Test Blocks (P12, P37, P41) and BMI Test Blocks (P5, P7) were evaluated using the multi-probe for eddy current testing.
  - The flaws located in the weld could be detected, and the length values were evaluated with relatively good accuracy.
  - However, the signals of flaws lying on the bond of welds include the large amount of noise and length sizing for these flaws did not work well. In the case of closed flaws, the detectability is low.
3. Were there any problems/issues that limited application of the technique to the test blocks?
  - How often was the technique usable to its full extent (for example, could the technique only be applied to the flat ENSI test blocks, but not to curved surfaces)?

- In the case of manual inspection of BMI, due to the curvature of welds of penetrating pipes, it is difficult to keep constant inclinations, which lead large noises of measurements.
- If there were limitations of the technique, please provide your ideas about how these limitations may be overcome in the future.
  - It is necessary to apply a scanner which automatically positions the probe keeping the inclination with respect to the weld lines.

## C.5.8 Controlled Excitation Eddy Current, Technique ID 5-CEECT1

### C.5.8.1 Overview

The technique applied is based on eddy current inspection. The uniqueness of the technique is that it would enable to evaluate the depth of deep flaws more quantitatively than conventional eddy current testing.

The physics in action of the technique, which is illustrated in Figure C.299, is basically identical that of conventional eddy current testing. That is, the technique emits an alternating magnetic field to conductive media to induce eddy currents, and senses the magnetic fields that the induced eddy currents generate in order to detect and evaluate a flaw. Measurements are carried out on the surface where a flaw opens, and signals are obtained as a function of the position of a probe. The amplitude and the phase of the signals are used to estimate the position, surface length, and the depth of a flaw. The uniqueness stems from the use of a probe consisting of vertical exciters and a horizontal detector situated away from the exciters. The physical background of the technique is explained in Yusa et al. (2011) together with several experimental validations.

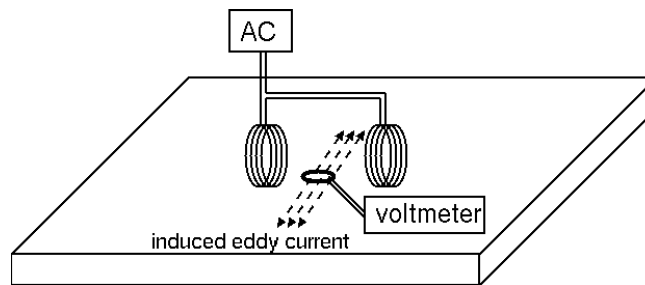


**Figure C.299 Physics in Action**

Signals obtained through the technique are maximized above the edges of a flaw, which can be used to estimate the position and the surface length of the flaw. The depth of a flaw is evaluated on the basis of the relation between the phase of a signal and the depth of a flaw obtained through experiments or numerical simulations conducted to gather signals due to artificial slits with known depths. Whereas these approaches are basically same with those used in conventional eddy current testing, the technique has such advantage that the phase of signals changes clearly with the depth of a flaw even though the flaw is several times deeper than the depth of penetration as depicted in Figure C.300.

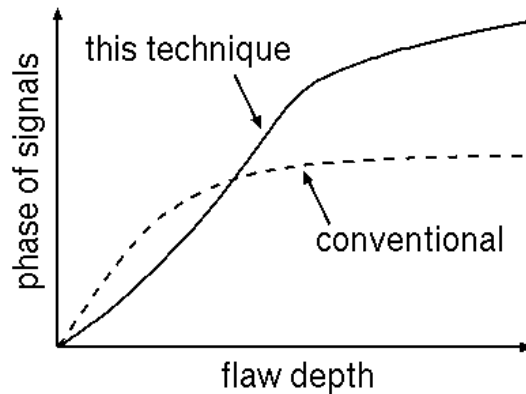


**Figure C.300 The Advantage of the Technique**

One of the largest problems about the technique is that the effect of flaw parameters on measured signals is not fully revealed. Whereas earlier studies have confirmed the depth of a flaw affects signals significantly, they have also revealed that the length of a flaw has a large effect on signals. This implies that the technique is sensitive to the cross-sectional profile of a flaw much more than conventional eddy current testing, and it is likely that sophisticated inversion is needed to quantitatively evaluate the depth of a flaw. The studies revealed that the technique cannot show advantage over conventional eddy current testing if the surface length of a flaw is shorter than approximately 20 mm, whose physical background has not been fully revealed yet. An exciting frequency of 50 kHz has been used in earlier studies; no quantitative evaluation on the effect of frequency has been conducted so far. Consequently, the limitation of the technique in flaw evaluation has not been clarified. Another practical drawback is that the probe used for the technique is much larger than those used for the conventional eddy current testing. This makes it difficult to scan non-flat surfaces.

### **C.5.8.2 NDE Equipment Used to Implement the Technique**

The schematic diagram of the equipment is illustrated in Figure C.301. An AC current is supplied to the exciter to induce eddy currents inside the target, and signals are measured by a lock-in amplifier. The signals are gathered by a PC through an A/D converter. Important pieces of equipment are listed below.

- Function synthesizer (WF1974, NF Corporation)
  - The function synthesizer generates sinusoidal voltage to excite the exciter. The frequency and the amplitude of the voltage in this experiment were 50 kHz and 15Vpp, respectively.
- Bipolar amplifier (HSA4051, NF Corporation)
  - The bipolar amplifier was used to amplify the voltage generated by the function synthesizer and to feed sufficiently large exciting current to the exciters. The amplification in this experiment was set to 40 times.

- Oscilloscope (1001B, Tektronix, Inc.)
  - The oscilloscope monitored the exciting current by measuring the voltage of the shunt resistance to measure the amplitude of exciting current and to confirm that the current exhibits no obvious distortion.
- Lock-in amplifier (LI5640, NF Corporation)
  - The lock-in amplifier was used to measure detector signals. The voltage of the shunt resistance, which was measured by the oscilloscope, was used as reference signals. The lock-in amplifier displayed both in-phase and quadrature components of the signals, and output them as DC signals ranging  $\pm 10V$ .
- A/D converter (NR-500, Keyence Japan)
  - The A/D converter was used to convert the output of the lock-in amplifier, which is in analog, into digital signals that can be recorded by the PC connected with the A/D converter with USB.
- PC
  - The PC, which is an ordinary PC with Windows 7, recorded the data using dedicated data logger software, Wave Logger (Keyence Japan).

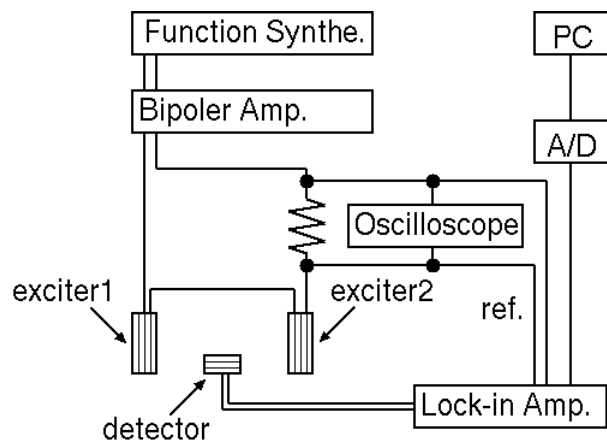


**Figure C.301 Connection Diagram**

Probe utilized is shown in Figure C.302. The probe had two vertical exciters and one horizontal detector. The two vertical exciters generate magnetic fields with the same polarity, which induces a directional eddy current directly below the detector. The distance between the exciters was set to either 54 or 12 mm. Note that the technique requires situating the detector away from the exciters in order that measured signals changes clearly with the depth of a flaw. Therefore, when the distance is 12 mm, the measurements become basically same with conventional eddy current testing, and signals measured are used only to detect flaws.

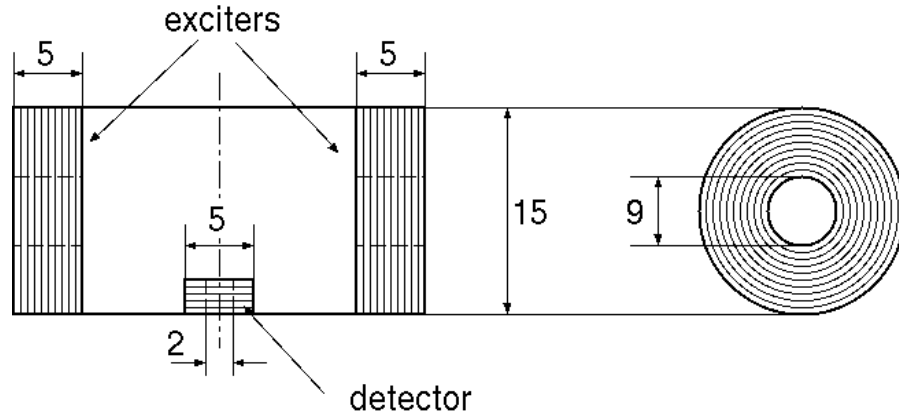


**Figure C.302 Probe**

### **C.5.8.3 Data Acquisition Process/Parameters**

- Automated or manual: manual
- Encoded or not: no
- Access surface on test blocks: surfaces where the flaw opens
- Data acquisition speed: 10 kHz

Details are given in the reports.

### **C.5.8.4 Signal Processing Performed on the Acquired Data**

There is no signal processing performed on the data.

### **C.5.8.5 Acquired Data Analysis Process for the Technique**

Signals due to a flaw are distinguished from noise on the basis of the fact that a flaw should provide two signal maximums whose phases are opposite to each other as illustrated in Figure C.303. It should be noted however, this assumes that a flaw has a symmetric boundary profile. It is likely that this approach does not work well if a flaw has an extremely complicated boundary profile.

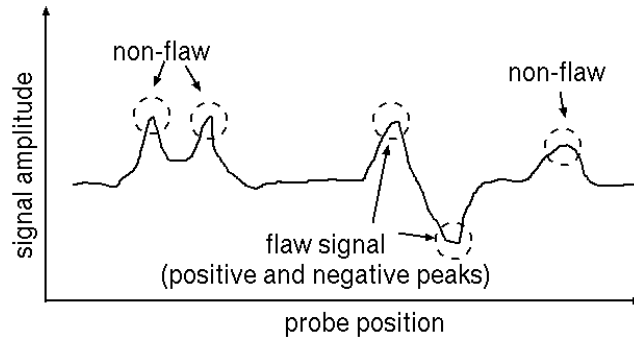


**Figure C.303 Distinguishing Flaw/Non-flaw Signals**

The depth of a flaw is evaluated on the basis of the phase of measured signals, as mentioned above. More specifically, the trajectory of the measured signals is displayed on two-dimensional plane to evaluate the phase of the signals,  $\theta$ , as shown in Figure C.304. Then, the depth of a flaw is estimated using a calibration curve obtained through experiments or numerical simulations conducted to gather signals due to artificial slits with known depths.

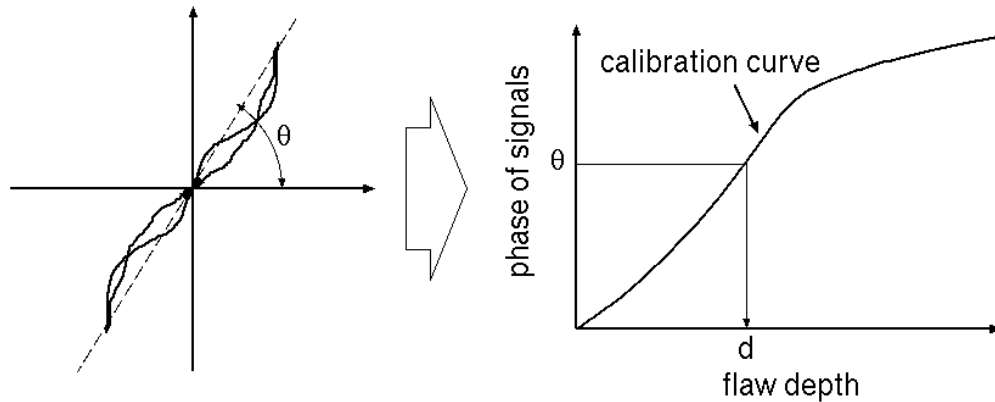


**Figure C.304 Evaluating the Depth of a Flaw**

#### **C.5.8.6 Team's Assessment of the Technique, based on the Round Robin Test Results**

The technique was developed to overcome that conventional eddy current does not provide clear information about the depth of flaws due to the skin effect. Whereas studies conducted so far in laboratories using flat plate specimens have demonstrated the effectiveness of the technique, it was not possible to size the flaws used in the round robin test. Furthermore, not all the flaws were clearly detected using the technique. Problems that limited the application of the technique to the test blocks are as follows.

1. Low signal-to-noise ratio due to the welds
  - The welds caused relatively large noise, which made it difficult to evaluate signals to size the flaws. More quantitative information about the position of probe, which would be obtained using stages, would enable signal processing to enhance signal-to-noise ratio by taking consideration of the spatial distribution of measured signals.
2. Difficulty in inspecting curved surfaces



- Since the probe needs to be large, inspecting surface with a curvature led to a large lift-off and small signal amplitude.

## C.5.9 Microwave Near-field Microscope, Technique ID 28-MM1, 28-MM2

### C.5.9.1 Overview

Microwave is an electromagnetic wave having a frequency from 300 MHz to 300 GHz. It has an advantage of propagating well in air. Therefore, a coupling medium is not necessary when nondestructive inspection is carried out. Microwave induces a current on the crack surface, when microwave irradiates a metal surface where a crack is present. Therefore, a conductor loss is created due to the current flowing on the crack surface. This feature enables us to detect cracks on the metal surface.

An open-ended coaxial line sensor which supports transverse electromagnetic (TEM) waves without cutoff frequency for the fundamental TEM mode was used because the operating frequency band can be broad, and it is possible to decrease the size of aperture for increasing the spatial resolution. A network analyzer was used to generate a continuous wave signal which was fed to the open-ended coaxial line sensor and to measure the amplitude of the reflection coefficient. The amplitude of the reflection coefficient was used to evaluate the depth of a crack.

### C.5.9.2 Principle of Microwave Near-field Microscope Technique

#### Open-ended Coaxial Line Sensor

Figure C.305 shows the distribution of the electric field at the sensor aperture. For the fundamental TEM mode, the electric field is only in the radial direction between inner and outer conductors.

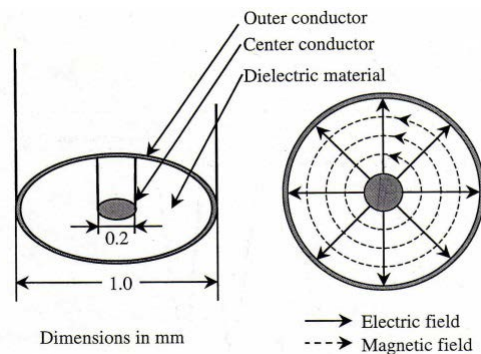


**Figure C.305 Distribution of the Electric Field at the Sensor Aperture**

The microwave is irradiated from sensor to sample. We detect the crack from the reflection of wave. Figure C.306 shows the amplitude of the reflected wave measured by scanning a crack in a sample at the frequency of 110 GHz. The shape of graph indicates the result of the interaction of the microwave with the crack. When the crack is located between the inner and outer conductors under the sensor, the sum of the components of the electric field that is perpendicular to the crack takes its maximum value, thereby the conductor loss reaches the maximum value. Therefore, the value of amplitude shows the largest decrease. However, when the crack is located under the center of the sensor, no conductor loss will be generated, since

the elected field is parallel to the crack. Moreover, two decreased peaks of the value of amplitude can be obtained as shown in Figure C.306, since the crack passes twice between the inner and outer conductors under the sensor. Consequently, a W-shaped characteristic signal was obtained.

Hence, the average of the two peaks,  $P_1$  and  $P_2$  shown in Figure C.306, was used to calculate the amplitude difference  $\Delta A$ .

$$\Delta A = \frac{P_1 + P_2}{2} \quad (C.12)$$

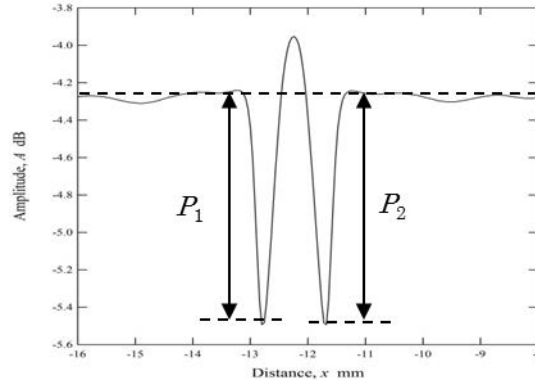


**Figure C.306 Amplitude of Reflected Wave Measured by Scanning a Crack**

### Evaluation of Crack Depth

The depth of a crack is evaluated based on microwave propagation theory. Crack is modeled as a parallel plate waveguide. Equation for evaluating the depth of the crack is obtained by considering the relationship between the crack depth and reflection coefficient as

$$d = \frac{\Delta A}{40(\log_{10} e)\alpha_M} \quad (C.13)$$

where,  $\alpha_M$  is a constant depending on the crack shape and sensor dimension.

### C.5.9.3 Experimental Procedure for P1, P4, P12, P21, P23, P24, and P41

#### Data Acquisition

The photograph of a vector network analyzer is shown in Figure C.307. The frequency band of the vector network analyzer used for manual measurement is possible to propagate microwave from 10 MHz to 67 GHz. In this experiment, the test was performed with the frequency of 67 GHz. The sensor used for manual measurement in which an open-ended coaxial line was fixed by encasing in epoxy resin was shown in Figure C.308. The amplitude difference was obtained by scanning a crack perpendicular to the crack length direction. The measurement was carried out in manual raster scanning. Direction of scanning was perpendicular to the crack direction. A crack was measured with the scan pitch of 33 points/sec.

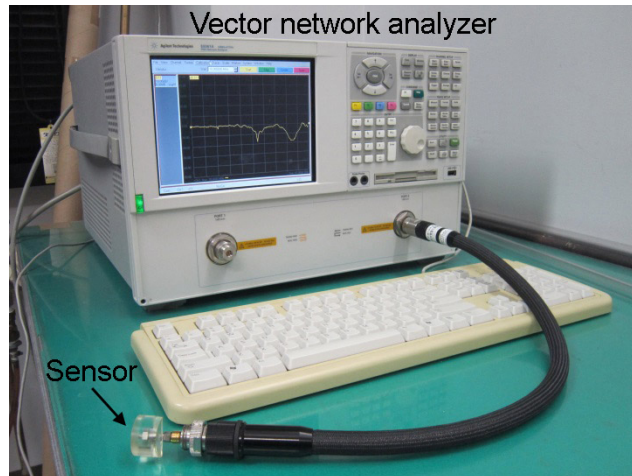


**Figure C.307 Photograph of Vector Network Analyzer and Sensor**



**Figure C.308 Photograph of Open-ended Coaxial Line Sensor**

### **Signal Processing and Evaluation**

The graph like Figure C.306 can be drawn from the data obtained by scanning the crack. Based on the graph, the average value of the two peaks was determined and the crack depth was evaluated by substituting the value in Equation (C.13).

### **C.5.9.4 Experimental Procedure for P28, P29, P30, P31 and P32**

#### **Data Acquisition**

Experimental method and principle are based on the above measurement. The photograph of the microwave microscope is shown in Figure C.309. A network analyzer, which is designed to process the amplitude and phase of the transmitted and reflected waves from the network, was used to generate a continuous wave signal which is fed to an open-ended coaxial line sensor. The photograph of open-ended coaxial line sensor is shown in Figure C.310. The operating frequency was 110 GHz, the standoff distance between the sensor and the sample was 60  $\mu\text{m}$ . The measurements were carried out in automated raster scanning and scan direction pitch is 0.04 mm and step direction pitch is 1 mm.

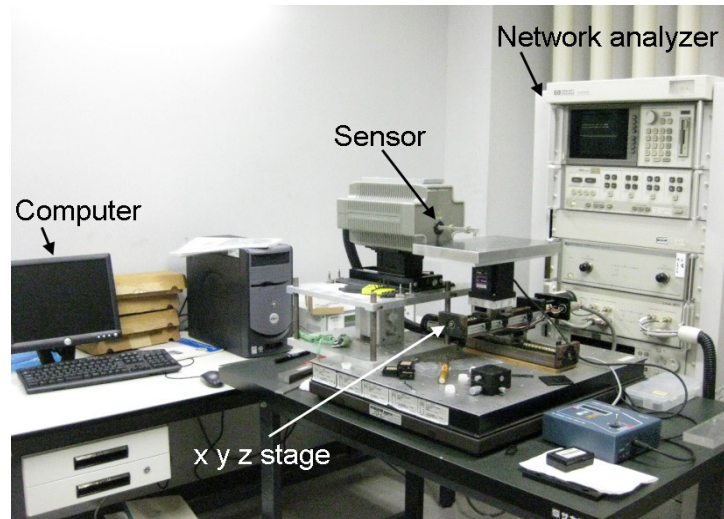


**Figure C.309 Photograph of Microwave Microscope**

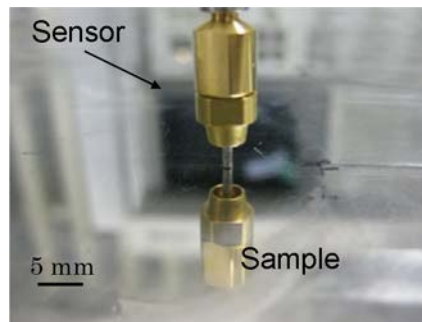


**Figure C.310 Photograph of Open-ended Coaxial Line Sensor**

### **Signal Processing and Evaluation**

The measured amplitude of reflected wave was imaged as C-scan, and the crack length on the sample surface was measured. In addition, at the position of maximum amplitude difference, the crack depth was evaluated by substituting it in Equation (C.13).

### **C.5.9.5 Team's Assessment of the Technique, Based on the Round Robin Test Results**

#### **The Purpose and Advantage of the Emerging Technique**

Microwave has an advantage of propagating well in air. Therefore, a coupling medium is not necessary when nondestructive inspection is carried out. In addition, open-ended coaxial line sensor supports transverse electromagnetic (TEM) waves without cutoff frequency for the fundamental TEM mode. Therefore, the operating frequency band can be broad, and it is possible to decrease the size of aperture for increasing the spatial resolution.

#### **A Brief Assessment of the Results of the Testing**

EDM slits on the curved surface can be detected, and the cracks length can be evaluated correctly. However, fatigue cracks could not be detected. The evaluation of the depth is

impossible in both. Some cracks in flat ENSI test blocks can be detected, and the cracks length can be evaluated, but the others could not be detected.

### **Limitation of the Technique to the Test Block**

On the curved surface, the technique only could be applied to EDM slits. And, it is difficult to scan rough surface. So, it cannot be applied to cracks on welding part. Since microwave has high sensitivity, it is susceptible to surface roughness, i.e., standoff distance between a sensor and a sample surface. Therefore, in advance, it should be considered to remove the noise by measuring the surface shape with a laser displacement meter.

### **C.5.10 References**

Ishida H and J Kitasaka. 2013. "Development of a Phased Array TOFD UT Method to Measure the Depth of SCCs in Dissimilar Metal Weld." In *9th International Conference on NDE in Relation to Structural Integrity for Nuclear and Pressurized Components*, pp. 754-762. May 22-24, 2012, Seattle, Washington. NDT.net, Rheintalstr, Germany. <http://www.ndt.net/article/jrc-nde2012/papers/120.pdf>.

Karasawa H, T Ikeda, S Matsumoto, T Hamajima and H Isobe. 2009. "3D-SAFT Ultrasonic Inspection Equipment "Matrixeye™". In *Proceedings of the Seventh International Conference on NDE in Relation to Structural Integrity for Nuclear and Pressurised Components*, pp. 669-683. May 12-14, 2009, Yokohama, Japan. European Commission Joint Research Centre, Luxembourg. <http://www.ndt.net/article/jrc-nde2009/papers/97.pdf>.

Komura I and T Furukawa. 2010. "Improvement of SCC Depth Sizing Capability by 3D-SAFT UT Method in Ni Alloy Weld." In *Proceedings of the Eighth International Conference on NDE in Relation to Structural Integrity for Nuclear and Pressurised Components*, pp. 831-837. September 29-October 1, 2010, Berlin, Germany. European Commission Joint Research Centre, Luxembourg.

Yusa N, Y Sakai and H Hashizume. 2011. "An Eddy Current Probe Suitable to Gain Information about the Depth of Near-side Flaws Much Deeper than the Depth of Penetration." *NDT & E International* 44:121-130.









**BIBLIOGRAPHIC DATA SHEET**

(See instructions on the reverse)

**NUREG/CR-7236, Vol. 1**

2. TITLE AND SUBTITLE

**Results of Open Testing for the Program to Assess the Reliability of  
Emerging Nondestructive Techniques**

3. DATE REPORT PUBLISHED

MONTH

**August**

YEAR

**2017**

4. FIN OR GRANT NUMBER

V6286

5. AUTHOR(S)

R. M. Meyer, A. E. Holmes, and P. G. Heasler

6. TYPE OF REPORT

Technical

7. PERIOD COVERED (Inclusive Dates)

8. PERFORMING ORGANIZATION - NAME AND ADDRESS (If NRC, provide Division, Office or Region, U. S. Nuclear Regulatory Commission, and mailing address; if contractor, provide name and mailing address.)

Pacific Northwest National Laboratory  
P.O. Box 999  
Richland, WA 99352

9. SPONSORING ORGANIZATION - NAME AND ADDRESS (If NRC, type "Same as above", if contractor, provide NRC Division, Office or Region, U. S. Nuclear Regulatory Commission, and mailing address.)

Division of Engineering  
Office of Nuclear Regulatory Research  
U.S. Nuclear Regulatory Commission  
Washington, DC 20555-0001

10. SUPPLEMENTARY NOTES

11. ABSTRACT (200 words or less)

The U.S. Nuclear Regulatory Commission (NRC) conducted agreements with organizations in Finland, Japan, South Korea, Sweden and Switzerland to establish the Program to Assess the Reliability of Emerging Nondestructive Techniques (PARENT) whose goal was to investigate the performance of current and emerging nondestructive examination (NDE) procedures and techniques to find flaws in nickel-alloy welds and base materials. This was performed by conducting a series of open and blind international round-robin tests on a set of nickel alloy piping components that included large-bore dissimilar metal welds (LBDMW), small-bore dissimilar metal welds (SBDMW), and bottom-mounted instrumentation (BMI) penetration welds. The project was divided into open and blind testing to separate the evaluation of novel techniques implemented by nonqualified teams (open testing) from the evaluation of more established techniques implemented by commercial inspection service providers (blind testing). This report is focused on documenting the open testing activity and results. The open testing portion of PARENT was performed with knowledge of true-state information in the open test blocks provided to teams conducting tests. As a result, no detection performance analyses were performed on open test data. Thus, the evaluation of open test data is based on statistical analyses of sizing data and qualitative review of data response images.

12. KEY WORDS/DESCRIPTORS (List words or phrases that will assist researchers in locating the report.)

Nondestructive Examination, Stress Corrosion Cracking, Dissimilar Metal Welds,  
Ultrasonic Testing, Probability of Detection

13. AVAILABILITY STATEMENT

unlimited

14. SECURITY CLASSIFICATION

(This Page)

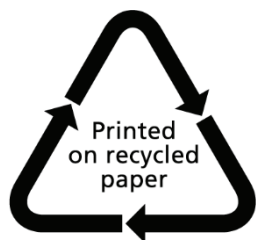
unclassified

(This Report)

unclassified

15. NUMBER OF PAGES

16. PRICE



Federal Recycling Program





UNITED STATES  
NUCLEAR REGULATORY COMMISSION  
WASHINGTON, DC 20555-0001

OFFICIAL BUSINESS



@NRCgov



**NUREG/CR-7236, Vol. 1**

**Results of Open Testing for the Program to Assess the Reliability of Emerging  
Nondestructive Techniques**

**August 2017**